DIRECT CONVERSION OF NUCLEAR RADIATION ENERGY

George H. Miley

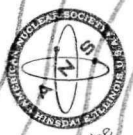

Prepared under the direction of the American Nuclear Society for the United States Atomic Energy Commission

DISCLAIMER

Direct Conversion of Nuclear Radiation Energy

American Nuclear Society
and
U. S. Atomic Energy Commission

MONOGRAPH SERIES ON
NUCLEAR SCIENCE AND TECHNOLOGY

JOHN GRAHAM, Series Editor
American Nuclear Society

ADVISORY COMMITTEE

ROBERT W. DICKINSON, Liquid Metals Engineering Center
GORDON E. HANSEN, Los Alamos Scientific Laboratory
JOHN INGLIMA, Consolidated Edison
NORMAN H. JACOBSON, American Nuclear Society
FRANK E. JAMERSON, General Motors Research Laboratory
LESTER L. KINTNER, U. S. Atomic Energy Commission
JOHN R. LAMARSH, New York University
WILLIAM E. LOEWE, Lawrence Radiation Laboratory
DAVID A. McCUTCHAN, Westinghouse Astronuclear Laboratory
JACK M. RAVETS, Westinghouse Electric Corporation
CLIFFORD E. WEBER, U. S. Atomic Energy Commission

MONOGRAPH TITLES AND AUTHORS

Reactor Noise, Joseph A. Thie
System Analysis of Nuclear Reactor Dynamics, Lynn E. Weaver
The Foundations of Nuclear Transport Theory, S. G. Yip and R. K. Osborn
Alkali Metal Handling and Systems Operating Techniques, J. W. Mausteller, F. Tepper, and S. J. Rodgers
Irradiation Effects in Nuclear Fuels, J. A. L. Robertson
Water Coolant Technology of Power Reactors, Paul Cohen
Nuclear Reactor Instrumentation (In-Core), James F. Boland
Reactivity Coefficients in Large Fast Power Reactors, Harry H. Hummel and David Okrent
Techniques in Fast Reactor Critical Experiments, W. G. Davey and W. C. Redman

TID-25612

Direct Conversion of Nuclear Radiation Energy

GEORGE H. MILEY

Nuclear Engineering Program
University of Illinois
Urbana–Champaign Campus

Prepared under the direction of the
American Nuclear Society
for the
Division of Technical Information
United States Atomic Energy Commission

Published by

AMERICAN NUCLEAR SOCIETY

Library of Congress Catalog Card Number: 70 – 155742
Printed in the United States of America

Foreword

This monograph is one of a series developed through the joint efforts of the American Nuclear Society and the Division of Technical Information of the U. S. Atomic Energy Commission. The purpose of the undertaking is to cover very specific areas of nuclear science and technology and thus help to advance the peaceful applications of nuclear energy.

While the monographs are primarily directed toward the operational scientist or engineer concerned with the applications of nuclear energy, they should also be helpful to students of science and engineering who otherwise might have little opportunity to study information within the special area of each monograph.

In looking forward to many dramatic accomplishments in peaceful uses of nuclear energy, the American Nuclear Society is pleased to cooperate with the U. S. Atomic Energy Commission in developing this series of monographs to help reach these achievements.

John Graham
Monograph Editor
American Nuclear Society

Blank Page

Preface

Interest in direct conversion of nuclear energy into other useful forms dates back almost to the discovery of radioactivity itself. In fact, in 1900, Madame and Pierre Curie reported the detection of a voltage associated with radium decay, and, in 1913, H. G. J. Moseley reported the operation of a high-voltage nuclear battery using radium.

The advent of the nuclear reactor and the "atomic age" brought an increased interest in the development of simpler, more esthetically pleasing, and more reliable conversion processes than represented by conventional turbo-machinery.

The possibility of an improved conversion efficiency also offered attractive rewards such as the extension of fuel reserves, the reduction of costs, and the reduction of thermal pollution. Simultaneously, the growth of new and varied power requirements due to our expanding "energy based" society and space exploration created a demand for new approaches to energy conversion.

However, a bulk of the research and development effort in direct energy conversion in the past decade has been concerned with approaches such as thermoelectricity, thermionics, and magnetohydrodynamics, all of which involve heat cycles. This monograph, on the other hand, is devoted to methods for converting nuclear radiation directly *without resorting to a heat cycle.* These concepts follow from the early discoveries by the Curies and by Moseley and generally involve the direct collection of the primary charged particles released in a nuclear reaction or by decay, or, alternately, they involve the separation and collection of ion pairs produced as the primary radiation interacts with surrounding matter. The utilization of such methods is in its infancy. Unfortunately, they have been relegated to a position of curiosity and are generally given only passing thought for instrumentation or low-power "batteries." I contend, however, that they offer some truly unique characteristics that should be exploited. Hopefully, this monograph will make some contribution in this direction since it represents a first attempt to bring a number of such concepts together in a unified treatment.

Several points about the presentation should be noted:

1. Concepts are discussed without stressing the distinction between devices for instrumentation and power sources with the hope that a cross fertilization of ideas may serve to strengthen both areas. It is not uncommon for useful high-power conversion devices to grow out of a beginning in instrumentation. The evolution of high-powered thermionic diodes from electron tube concepts is a well-known example.

2. Although the input energy is restricted to nuclear radiations, the form of the output energy is not restricted. By default, this monograph includes only the concepts that lead to electrical output. However, I contemplate a second book in which the conversion process is generalized to include other final energy forms, e.g., coherent laser radiation, chemicals, etc.

3. No specific attempt is made to "sell" the concepts on the basis of efficiency, power-to-weight ratio, etc. Where information of this type is presented, it is done with the realization that more studies, particularly experimental tests, are required before the situation can be evaluated.

The first six chapters stress fundamentals rather than detailed designs or applications, which are left for Chap. 7. Advances in the state of the art are most likely to come through an expanded understanding of fundamentals, and they should be of a more lasting value. In fact, it is my fond hope that the applied information presented in Chap. 7 will be quickly outmoded.

Another motivation is that these fundamentals generally have wider application than in cell design alone, and this may provide an important link with other technical areas; e.g., charged-particle transport such as treated here may be of interest to workers in space shielding, chemonuclear processing, microdosimetry, etc.

Chapter 2 treats the basic energy conversion, i.e., the conversion of particle kinetic energy to potential energy. This may appear almost elementary since it is governed by simple conservation laws. Still it often holds surprises for persons who have not received a prior introduction to the balances involved. Chapter 2 also introduces the concept of an "ideal cell," which neglects energy losses in the fuel layer, secondary electrons, leakage currents, etc. Since a heat cycle is not involved, the ideal cell, rather than the Carnot cycle, defines the maximum obtainable efficiency. This is most significant. One always wants to know if the ultimate efficiency is worth the effort — if not, there is no reason to continue the study or, in the present case, the monograph! Furthermore, the ideal cell provides a "yardstick" for evaluation of actual cell performance.

The following chapters successively attack the phenomena that cause deviations from ideal performance.

Chapters 3 and 4 treat charged-particle transport theory. The numerous charged particles involved, ranging from electrons to fission fragments, present a real problem. Their passage through matter differs considerably in detail; consequently it might appear that each should be treated separately, thus preventing a generalized cell analysis. This dilemma is circumvented by developing a simplified energy–charge loss model in Chap. 3 that can be adapted with reasonable accuracy to any one of the particles through two adjustable parameters. This model is then used in Chap. 4 to incorporate transport effects in cell analysis.

Chapter 5 presents a fundamental description of secondary electron production. A special treatment based on parts of the transport theory of Chaps. 3 and 4 is developed. The emphasis placed on this problem stems from the fact that secondaries play a unique dual role. In many cells, they are a leakage current, which must be stopped; on the other hand, cells can be designed to collect secondary electrons, and, in this case, they serve as the primary charge carrier.

Chapter 6 discusses leakage currents and associated problems ranging up to and including voltage breakdown. From a design point of view, this material may be of the most immediate importance. Most practical cells are leakage-current limited, and their success relies on appropriate design measures to combat leakages. Unfortunately these areas are poorly understood. For example, a comprehensive theory of voltage breakdown in vacuum has only recently been developed, which, in itself, still leaves some unanswered questions; however, in the present case, yet another question arises: "Does the intense radiation field encountered in cell operation affect breakdown?" The other phenomena discussed—radiation-induced conductivity, space-charge storage, and sputtering—involve equally sticky questions.

Chapter 7 discusses designs and applications to date. Ideally, the theory developed in the earlier chapters would be compared with experimental data, but, unfortunately, few clean, well-controlled experiments that could be used to test theoretical models have been carried out.

Finally, a short listing of questions is included in Appendix G. Although this monograph is not primarily intended as a text, the inclusion of questions may prove useful if parts of the book are used in class situations. Also, since answers are given to some questions, this appendix may be used by persons attempting intensive self study.

An extensive, although not exhaustive, listing of references is included. An attempt has been made to make key developments reason-

ably self-sufficient. However, if appropriate review articles are available, the reader is referred to them. Unfortunately some important works appear solely in limited-distribution laboratory reports. An arbitrary choice was made to include such references since this may facilitate direct communication with the workers or organizations involved if the need arises, but a reasonably detailed presentation of pertinent material is generally included in these cases.

Finally, a warning should be voiced. At this early stage of development, it is difficult to present the precise, elegant derivations that would be possible in dealing with a subject having a long history of intensive research. Thus, simplified theories designed to stress concepts and interrelations are used extensively. This is not bad as such; however, there is always the danger of a limited range of validity, which is no doubt true in some of the present treatment, especially where experimental data are scarce. Consequently the reader is cautioned to keep an open and inquiring mind.

Acknowledgments

Many people have contributed to this monograph in various ways. Frank Jamerson of the General Motors Research Laboratories read an early draft. Jim Anno of the Battelle Memorial Institute and Cliff Heindl of the Jet Propulsion Laboratory performed a critical review of the first draft. Their many suggestions and continued encouragement were an invaluable aid.

Various people read and commented on specific sections, including Neil Schilmoeller, University of Illinois, Chap. 1; Ernest Lyman, University of Illinois, sections on vacuum breakdown; and Elmer Lewis, Northwestern University, sections on the Dirac chord method.

Much of the writing and work made use of the facilities of the Nuclear Engineering Program at the University of Illinois, and, in this respect, the help and encouragement offered by Marvin Wyman is gratefully acknowledged.

Selected portions of the text and problems were used by students during a course on Direct Energy Conversion at the University of Illinois in the summer of 1968 and at Cornell University in the fall of 1969. Their many questions and suggestions and their enthusiasm made the effort seem worthwhile, even during darker moments.

Many of the original calculations contained herein were carried out by Paul Thiess, a doctoral candidate in Nuclear Engineering at the University of Illinois, with the assistance of Patricia Squires. In the

process Mr. Thiess made a number of vital comments and suggestions and played a major role in the formulation of several sections, including those on topping cycles, two-region calculations, energy–range relations, and sputtering. He also aided in proofreading, and his active interest was a continuing source of help and encouragement.

The section on the Gamma Electric Cell was largely shaped by discussions with Henry T. Sampson, whose Ph. D. thesis involved an experimental study of such a cell. A visit with Bernard Gross also produced many ideas in this regard.

A number of others provided hard-to-obtain reports, sent prepublication papers, figures, etc., and, although such instances are too numerous to list here, each effort was appreciated.

The perseverance, good humor, and hard work of the ANS Monograph Series Editor, John Graham, were essential to the successful completion of the task. Without his help in keeping things moving, there can be no doubt but that the whole project would have come to a grinding halt long before even Chap. 2 was finished. The careful work of the Editorial Branch, AEC Division of Technical Information Extension, Oak Ridge, is also gratefully acknowledged.

Last but not least, the members of the author's family, who endured the ordeal in good spirits, deserve a vote of thanks.

George H. Miley
University of Illinois

February 1970

Blank Page

Contents

1

Introduction

1-1 BACKGROUND

The growing number of nuclear reactors and the resulting increase in availability of radioisotopes have stimulated interest in methods of extracting energy from these sources and converting it to the form required in a particular application. For many purposes electricity is the most convenient form for energy transmission so the problem of converting nuclear energy to electricity is fundamental.

Ironically, the primary particles released in nuclear fission (fission fragments) are charged, and so are such common radioisotopic decay products as alpha and beta particles. As a result, one must begin in all these cases with moving charged particles—i.e., an electric current. Gamma photons are a major exception to this argument; however, they primarily interact with matter by energy transfer to electrons, so once again an electric current is produced.

This argument may sound good at first, but it is open to several questions: "Will the direction of motion of the charged particles be such that a *net* migration of charge will occur?" (Otherwise this cannot really be called an electrical current.) And, "If there is a net migration, is there some way to collect the charge?" The answer is yes to both of these questions, and this monograph is, in fact, directed at expanding on this point. (The author plans to publish a second book that will discuss what can be done if one decides not to collect the primary charged particles directly but wants instead to make use of the ionization and excitation created by them. However, to provide further perspective, a brief discussion of this approach is included in the present chapter.)

These concepts can perhaps be best understood by considering some possible energy conversion cycles that start with fission or radioisotope sources. The possible application to a controlled thermonuclear reactor is also discussed in later sections.

1-2 NUCLEAR RADIATION ENERGY CONVERSION CYCLES

The general problem is demonstrated by Fig. 1.1. The initial energy released in fission or radioisotope decay resides largely in

the kinetic energy of a charged particle (Stage 1). Energy conversion cycles based on the principle of collecting these particles and hence converting their kinetic energy to potential energy are called "Direct-Collection Cycles."

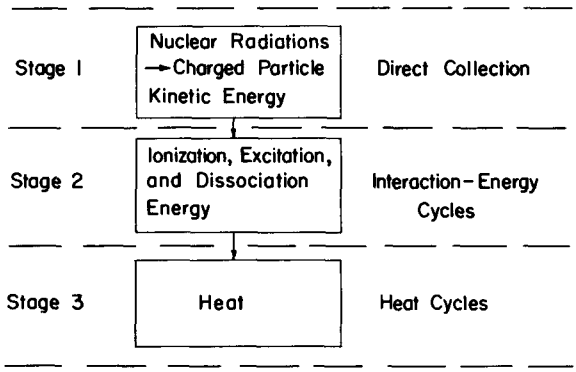

Fig. 1.1—Various stages of nuclear radiation energy conversion.

If direct collection is not used, the charged particle will interact with matter such that its kinetic energy is converted to ionization, excitation, and dissociation (Stage 2). Cycles designed to operate on one or more of these energy forms are termed "Interaction-Energy Cycles."

Unless one of these cycles is used to interrupt the energy flow, the natural final form is heat (Stage 3). Most of the better known conversion cycles start at this point and involve heat cycles.

It is evident that direct collection represents the most direct cycle in the sense of involving the fewest steps. Interaction-Energy Cycles are intermediate in directness, while heat cycles are least direct. (The reader should be cautioned not to confuse directness with efficiency. As is shown later, the most direct cycle may not necessarily be the most efficient.)

The heat cycle is also distinguished from the other two cycles from a thermodynamic point of view. The second law restricts the maximum conversion efficiency of a heat cycle operating between temperatures T_H and T_C (absolute temperatures) to the Carnot efficiency η_C given as

$$\eta_C = \frac{T_H - T_C}{T_H} = 1 - \frac{T_C}{T_H}. \tag{1.1}$$

Since cycles based on direct collection or interaction energy do not involve the conversion of heat energy, they are not restricted by this law. This does not imply, however, that their efficiencies will automa-

tically be larger than the Carnot efficiency since there are other limiting factors One objective of this monograph is to point out and study these factors.

1-3 DIRECT-COLLECTION AND INTERACTION-ENERGY CONCEPTS

Direct-Collection and Interaction-Energy Cycles have received little attention to date, so it is important at this point to introduce some of the underlying concepts

1-3.1 Direct Collection

An example of one type of direct-collection device is shown in Fig. 1.2, and it will serve to illustrate the concept.

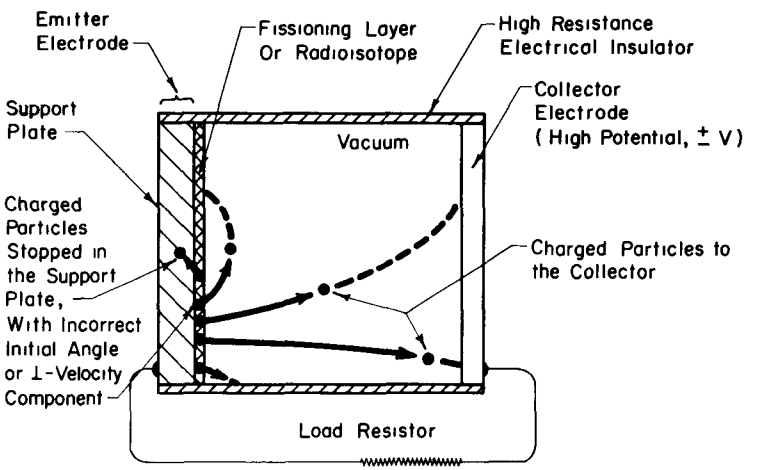

Fig. 1 2 — An example of one type of Direct-Collection Cell.

This device, which we will term a "cell," can be visualized simply as a self-charging capacitor. The two electrodes are electrically insulated, and a vacuum is used between them to allow the flow of the high-energy charged particles from the fuel layer to the collector. The fuel layer must be quite thin so that particles born in it have a chance to escape; thus the support plate is required for mechanical strength. Unfortunately, those particles emitted in the direction of the support plate are stopped in it due to their short range.

A load resistor is inserted between the two electrodes so that as charged particles reach the collector a potential builds up on it. When

this happens subsequent particles leaving the emitter must overcome this potential barrier in order to reach the collector. The basic energy conversion step in the cell occurs when the kinetic energy of the particle is converted to potential energy via the potential barrier. A current is thus forced through the load resistor.

(a) *Voltage and Efficiency Considerations*

Direct-Collection Cells are typically high-voltage, low-current devices. This is a direct consequence of the nature of the charged particles involved: fission fragments have energies of the order of 80 MeV and carry a charge of +20e. Thus, if all their kinetic energy were converted to potential energy, roughly $(80 \times 10^6)/20$ or 4×10^6 V would be obtained. Equivalent voltages and other data are summarized in Table 1.1 for typical charged particle sources of interest here. Except for some beta emitters and ions from a fusion reactor, the voltages are of the order 10^6 V; thus, if a significant portion of the kinetic energy is to be converted, a potential barrier of this order of magnitude is required.

In fact, if the particles all had the same initial energy *and* possessed a direction of motion perpendicular to the collector, the optimum barrier potential would be exactly equal to the voltage equivalent of the kinetic energy. Then, if possible radiation losses during deceleration are neglected, every particle would have just sufficient kinetic energy to overcome the barrier and would give complete conversion; i.e., 100% conversion of kinetic energy to potential energy would be achieved.

Unfortunately, most charged particle sources of interest involve distributions in both energy and angle of emission. If a simple collector is used, the optimum barrier potential inevitably involves a compromise. If the potential is too low, the conversion from kinetic to potential energy is inefficient. Yet higher potentials automatically prevent a fraction of the particles from reaching the collector, because they either originate with a low energy or their initial direction is "wrong," causing too small a velocity component perpendicular to the barrier. While a barrier height can be selected to optimize the conversion efficiency, this involves a compromise between these factors so that the efficiency must fall below 100%.

The optimum potential is roughly equal to the voltage equivalent of the average particle energy for distributed energies, or, in the important case of a monoenergetic source with an isotropic angular distribution, the optimum is approximately equal to half the voltage equivalent to the particle's initial energy. While the precise value depends on a number of factors including the type of source, the fuel

Table 1.1—TYPICAL CHARGED PARTICLES

Particle	Source	Avg. Energy, $\langle T_0 \rangle$ (MeV)	Half-life	Avg. Charge, q (Units of Electron Charge e)	Approximate $V_{max} = T_{max}/q$ (MV)
Fission fragment	n (^{235}U) f.f.*	≈80		+20	+4
Lithium-7	n (^{10}B) Li†	0.84		+3	+0.3
Alpha	^{210}Po	5.3‡	138 days	+2	+2 to +3
	n (^{10}B)α†	1.5			+0.75
Beta or electron	^{3}H	0.006‡	12 years	−1	−0.02
	^{144}Ce	0.06	285 days		−0.2
	^{85}Kr	0.5	10 years		−1.3
	^{90}Sr/^{90}Y	0.22 (0.90)§	28 years (64 hr)		−2.2
	γ (Compton interaction)	Order of 1			Order of −1
Deuterium, tritium, helium-3	Working ions, fusion reactor	0.01 to 0.15		+1 to +3	+0.003 to 0.5

*Two fragments having a distribution of energies around 97 MeV and 65 MeV are emitted.

†This reaction yields both ^{7}Li and an alpha particle.

‡Alpha emission is approximately monoenergetic, whereas β emission involves a continuous spectrum. In the latter case V_{max} is based on the maximum value of T_0 assuming that $\langle T \rangle \approx 0.4 T_{max}$.

§Values in parentheses are for ^{90}Y.

layer thickness, and the cell geometry, clearly cells designed for optimum energy conversion efficiency must operate in the kilovolt to megavolt range.

The conversion efficiency, kinetic to potential energy, depends strongly on cell geometry, charged particle energy-charge losses during transport, and leakage currents, and these factors are discussed in detail in later chapters. It should suffice here to note that efficiencies for ideal cells (neglecting all transport and leakage current losses) range from about 7% for isotropic emitter parallel plate cells to 100% for a point-emitter spherical-collector cell. Actual devices will no doubt fall somewhere in between these extremes. However, at the present stage of development, it is difficult to assess accurately the importance of losses, so the efficiency range achievable in practice remains uncertain.

Finally, it should be stressed that efficient power production is not always the major objective. Some applications (e.g., in instrumentation) require only a current source. In such cases, high voltages are not necessary or even desirable, and the cell is essentially operated in a shorted condition.

(b) *Current and Power Density Estimates*

Currents obtainable from Direct-Collection Cells vary considerably depending on the cell design and also on the amount and type of radiation source (fuel) used. To illustrate some typical values and to pinpoint some of the key design parameters involved, simplified calculations of currents and power densities are carried out in Appendix A for three different cases: a fission or nuclear reactor source; a beta emitter (^{90}Sr); and an alpha emitter (^{210}Po). The results are summarized in Table 1.2; however, it should be stressed that they are quite approximate and only intended to indicate the orders of magnitude involved.

Table 1.2—SUMMARY OF ESTIMATED CURRENT AND POWER DENSITIES

Source	Voltage (V)	μA/cm^2	We/cm^3
Fission	2×10^6	0.8	0.5
^{90}Sr/^{90}Y	1.1×10^6	0.06	2.3×10^{-2}
^{210}Po	2.5×10^6	0.03	2.5×10^{-2}

As expected, the current densities are quite low, falling in the range of microamperes per square centimeter. However, because of the high voltages involved, the power densities turn out to be quite respectable, demonstrating that a high-powered cell is practical from the point of view of size (weight, cost, and other factors must also be con-

sidered, but as shown in Chap. 7, these too may be favorable for certain applications).

The fact that such high voltages are necessary for high power densities represents a serious complication. As will be shown repeatedly in these discussions, the development of the technology necessary to maintain the required voltages is a key problem. Many of the cells built to date, particularly the so-called "nuclear batteries," have, for one reason or another, operated at a voltage too low to offer good efficiencies or power densities. This has helped propagate the misconception that Direct-Collection Cells are *necessarily* low power devices.

1-3.2 Interaction-Energy Cells

Interaction-Energy Cells (I-E Cells) are defined here as any device that directly converts the ionization and/or excitation produced by the interaction of nuclear radiation(s) with matter into a new energy form. In sharp contrast to Direct-Collection Cells which are limited in output to electrical energy, I-E Cells are capable of producing a variety of output energy forms. The main possibilities are illustrated in Fig. 1.3.

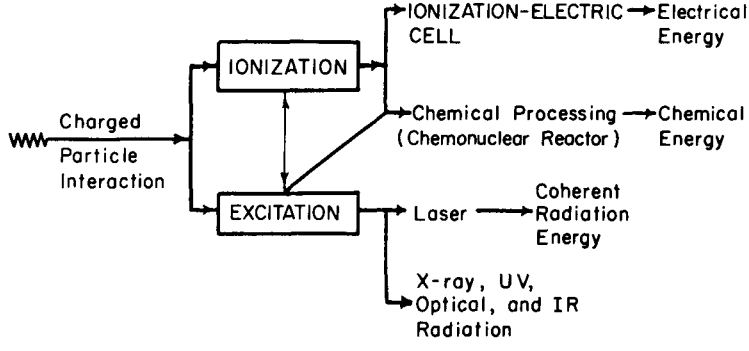

Fig. 1.3 — Relation of Interaction-Energy Cells.

If the ion-electron pair created in the process of ionization can be separated, an electrical output is possible, and such devices are termed Ionization-Electric Cells.

The ionization and excitation energy can also be utilized in other ways. Since various chemical reactions proceed via either ionized or free radicals, chemical processing is another important possibility. If the radiation source is a nuclear reactor, the "cell" is commonly termed a "chemonuclear unit". Although this represents an exceedingly important area, it is not included in this monograph since adequate coverage has been provided in other books and review articles (e.g., see Refs. 1-6).

Finally, radiation of a wavelength different from the input can be obtained. The decay of excited states and recombination of ionized species may lead to the emission of radiation ranging from x-ray to infrared wavelengths, and these radiations represent a potentially useful energy form. The nuclear radiation pumped laser (to be discussed in some detail in the author's second book) is a specific example of a device designed to capitalize on this route. Conventional laser systems use flash lamps, high voltage supplies, or radio-frequency oscillators to supply or pump energy into the system. The use of nuclear radiation pumping appears feasible, but this approach is still in an early research stage.

At this point, we select the Ionization-Electric Cell from these various possibilities for a more detailed study. As pointed out earlier, from a mechanistic point of view, it is the next logical step for electrical output after Direct-Collection Cells. Thus, an understanding of it may provide more perspective relative to direct collection, which is of principle concern in this monograph.

(a) *The Ionization-Electric Cell Concept*

As illustrated in Fig. 1.4(a), the cell consists simply of two electrodes separated by a gas, solid, or liquid. Ion pairs, created in the inter-electrode region by radiation, are separated by a potential difference ΔV illustrated in Fig. 1.4(b). (The shape of the potential curve will depend upon the cell design and operating conditions; the curve shown is only for illustrative purposes.) The separated charges result in a net current flow in the external circuit and the load resistor.

The description up to this point may sound much like a conventional ionization chamber used for radiation detection. The distinction, however, comes from the way in which ΔV is created. The ionization chamber uses a battery for a bias voltage. The chamber then acts as a radiation dependent impedance in the circuit so that the battery supplies a net energy input. On the other hand, if ΔV is created by some "inherent" or internal mechanism, it is possible to obtain a net energy output, and this is the key to the Ionization-Electric Cell.

One way of accomplishing this is to construct the electrodes from materials having different work functions, in which case $\Delta\phi$ of Fig. 1.4(b) represents the work function difference. An electron reaching the electrode at "d" falls through a potential corresponding to that electrode's work function. Then, in passing through the external circuit, it may suffer a voltage drop across the load and still enter the other electrode at a potential equal to its Fermi level (hatched levels in the figure). Provided

$$I > \phi \tag{1.2}$$

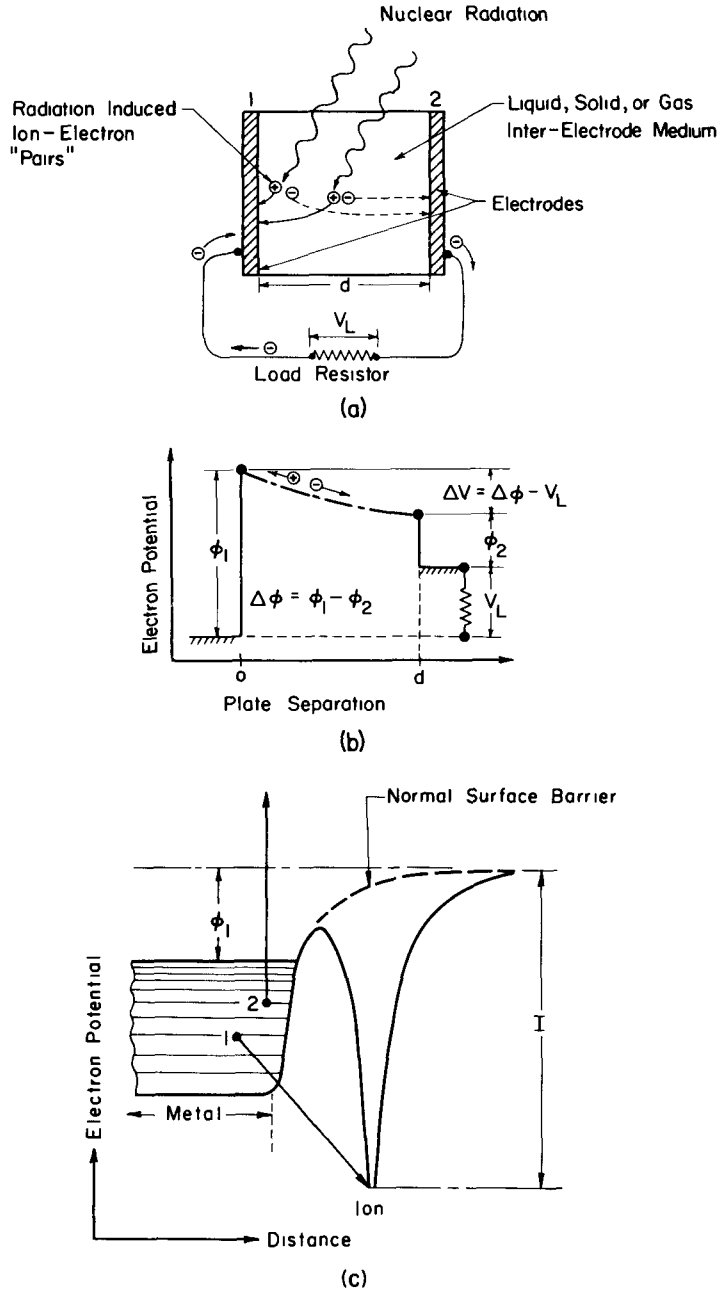

Fig. 1.4 — Schematic illustration of the Ionization-Electric Cell. (a) The Ionization-Electric Cell concept. (b) An illustrative potential diagram. (c) Electron-ion recombination at the electrode surface. The normal surface barrier is modified by the approach of the ion, and electron (1) tunnels directly to the ground state of the ion. Excess energy is given to electron (2), which, depending on the energy, may escape the surface. This is called direct Auger neutralization.[7]

the electron can then recombine with an ion with ionization potential I that has been forced to the electrode by the internal potential difference. This requirement arises because the ion must "draw" the electron across the work function barrier as illustrated schematically in Fig. 1.4(c).

The internal potential difference as shown in Fig. 1.4(b) is given by

$$\Delta V = \Delta\phi - V_L. \tag{1.3}$$

This relation is consistent with one's intuition, e.g., the maximum current should occur when ΔV is maximum. This corresponds to a short circuit ($V_L = 0$), in which case ΔV goes to $\Delta\phi$. On the other hand, the current for an open circuit is zero. This indicates a null driving force ($\Delta V = 0$), in which case the open circuit voltage is simply $\Delta\phi$.

The work function difference technique has been used with gaseous interelectrode material. Another method, which is restricted to solid state devices, is to use a p-n semiconductor junction to create a voltage gradient. Finally, in gaseous devices a temperature difference between the electrodes has been found to create a voltage difference.

(b) *Ionization-Electric Cell Efficiency Considerations*

As stressed earlier, neither Direct-Collection nor Ionization-Electric Cells involve a heat cycle, and hence, neither is limited to Carnot efficiencies. However, there is a fundamental difference between the two cells.

It is shown in Chap. 2 that it may be possible to minimize losses in Direct-Collection Cells and approach 100% efficiency simply by judicious selection of cell geometry and construction. In contrast, the Ionization-Electric Cell faces a fundamental obstacle to approaching this goal. Since it operates by separation of ion pairs, the energy associated with excitation is lost. Thus its efficiency is limited by the condition

$$\eta \leq \frac{I}{I + I^*} = \frac{I}{W} \tag{1.4}$$

where I is the first ionization potential for gases or the valence to conduction band energy gap for solids, and I* represents the energy going into excitation in the general sense, i.e., including excess kinetic energy given to the ion and electron and energies larger than I associated with ionization via ejection of inner shell electrons. (In cases where ionization is produced via excitation as an intermediate step, e.g., Penning mixtures[7], I* is to be interpreted as the part of the excitation energy not passed on to ionization. Hence, (I + I*) represents the total energy lost per ion pair created, denoted by W.)

This limitation reflects the proliferation of energy forms with passage through the various stages illustrated in Fig. 1.1. It is, in fact, this randomization of energy forms that, from a mechanistic point of view, leads to the Carnot efficiency limitation in the third or heat cycle stage.

The limitation imposed by Eq. (1.4) depends strongly on the material involved. For example, W ≈ 20 to 40 eV/ion pair for gases for a remarkable range of energies and types of radiation[8]. Thus, for helium (I ≈ 24.6 eV), the limiting efficiency is roughly 85%; for cesium vapor (I ≈ 3.9 eV), it is roughly 13%; etc. On the other hand, W values for solids are generally an order of magnitude lower than for gases, but the energy gap is correspondingly lower so the division of energy is not necessarily improved. For example, silicon with a gap of ≈1.1 eV has W ≈ 3.5 eV/pair, which gives a maximum efficiency of ≈ 31%.

While the limiting efficiency only depends on I and W, many additional parameters determine the actual efficiency of a specific design. These include the fraction of the incoming radiation absorbed in the inter-electrode medium, possible recombination and other losses of the ion pairs prior to collection, and the magnitude of $\Delta\phi$ and its effectiveness for charge separation.

(c) *Current and Power Densities*

The cell design, particularly the selection of the inter-electrode medium and the radiation source, can lead to wide variations in output currents and power densities. For comparison purposes, we will again consider the reactor fission-fragment source used in the earlier Fission-Electric Cell example. However, we will now assume that the ionization-electric concept is used to obtain electrical output.

First, we must decide whether to use a solid, liquid, or gaseous device. The solid, because of its density, has the advantage of strongly absorbing radiation, leading to compact, high-power density devices. However, radiation damage may be limiting. Liquids and gases may, with proper selection, be used to avoid this problem. Little is known about liquid-state cells, so quite arbitrarily helium at 1 atm pressure is used in the following example.

A cross section of a typical cell array in the reactor is shown in Fig. 1.5. The design is similar to the Fission-Electric Cell (Fig. 1.2), but the space between electrodes is now filled with helium.

As before a thickness roughly equal to the fragment range in uranium (10 μ) is used in order to maximize the emergent fragment current. However, the plate spacing d should be selected so that the fragments lose most or all of their energy via ionization and excitation of helium. Thus, a spacing equal to the fragment range in the gas is selected—roughly 11 cm for helium at 1 atm.

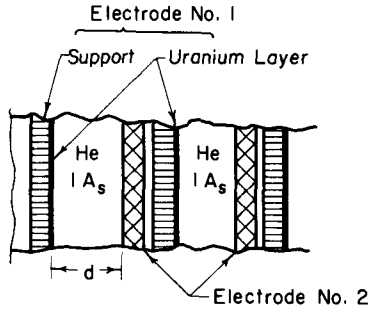

Fig. 1.5 — Cross section of several cells in the reactor Ionization-Electric Cell example.

Table 1.3 — SUMMARY OF ESTIMATED CHARACTERISTICS FOR THE IONIZATION-ELECTRIC CELL OF FIG. 1.5*

Neutron Flux [n/(cm^2 sec)]	Recombination Included	Fraction of Ion Pairs Collected	Current Density† (A/cm^2)	Power Density (We/cm^3)
10^{14}	No	1.0	0.35	2.7×10^{-2}
10^{14}	Yes	1.4×10^{-5}	5.0×10^{-6}	3.9×10^{-7}
10^{5}	Yes	0.4	1.4×10^{-10}	1.1×10^{-11}

*For a 11-cm spacing with helium at 1 atm.

†A 1-V work function difference was assumed in all calculations. Ohmart has built a cell with a work function difference of ≈0.9 V, while the design by Thomas assumed 1.67 V but used stacked cells to obtain 73.5-V output (p. 250, Ref. 24).

The cell currents and power densities are estimated in Appendix A-2, and the results are summarized in Table 1.3.

If no recombination of the ion pairs were to occur, it is seen that quite reasonable current and power densities would be obtained; however, recombination cannot be ignored, and this causes a serious reduction in the output densities. Larger work function differences or the use of a filling gas with a lower recombination coefficient would help, but large gains in these directions do not seem feasible with present technology. As indicated by the calculation for a neutron flux of 10^5, a reduction in the ion pair production source (hence the ion and electron densities) will reduce the losses due to recombination. While this leads to an improved efficiency, it results in even lower current and power densities. Unless future developments get around this problem, this would seem to restrict the Ionization-Electric Cell to low power applications, e.g., instrumentation, battery supplies, etc. In fact, because of their simplicity, reliability, and low cost, such cells are already marketed commercially as detectors in radiation level and thickness gauges[9].

1-3.3 Barrier Analogies

An analogy may give some further perspective to the concepts discussed thus far, which have stressed that direct radiation energy conversion basically involves the conversion of charged particle kinetic energy into potential energy. Intuitively, this is done by erecting a potential barrier in the path of the particle. Ironically, the problem is complicated in the case of nuclear radiations because the kinetic energy per particle is characteristically so large. A single barrier must then, by definition, be large, leading to the high voltages required in Direct-Collection Cycles. As illustrated by the dam analogy in Fig. 1.6, an alternate approach is a series of smaller barriers, but this also presents problems.

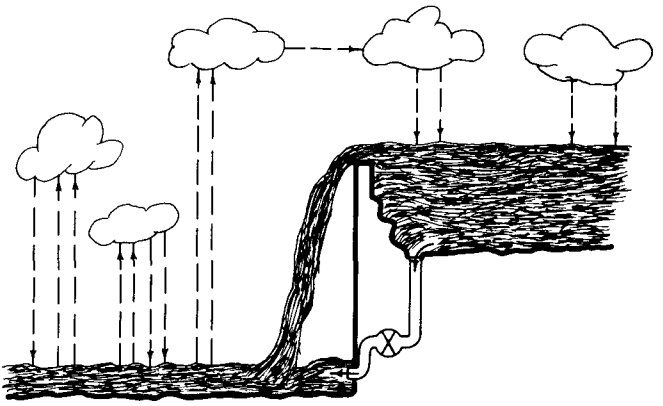

Fig. 1.6(a) — A single-stage hydroelectric dam. (Analogous to single-collector Direct-Collection Cells. As illustrated, unless all clouds have sufficient height — particles have sufficient energy — they will not be able to overcome the barrier.)

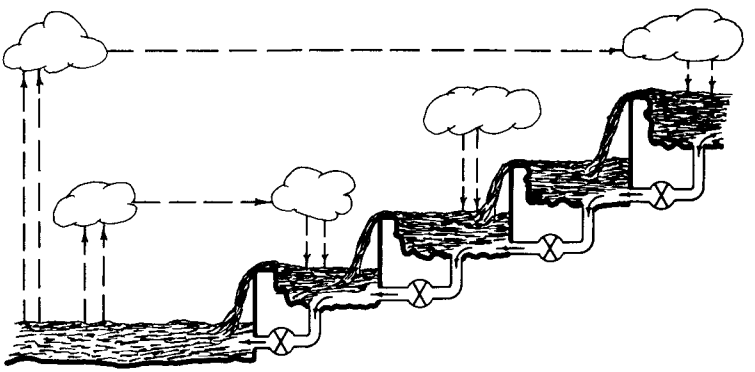

Fig. 1.6(b) — A multistage unit. (Analogous to Multiple-Collector Cells or Ionization-Excitation Cycles. Here the variable barrier height compensates for variations in cloud altitude — particle energy.)

At the risk of carrying the analogy too far, this can be used to illustrate some of the points made in the preceding analyses. Certainly the single stage approach is the most direct, and it is the simplest to optimize. One simply selects the dam height to maximize the potential head, to minimize overflow losses, and to offer minimum interference for the return of water to the reservoir via the clouds. However, two key questions must be raised: Can such a high dam be built without danger of collapse (voltage breakdown)? Will the clouds be distributed in elevation such that the dam prevents passage of the lower ones (corresponding to variations in particle energies and angles)? If either is a problem, it may be necessary to resort to a series of barriers or a multistage approach.

The use of multiplate collectors with varying potentials, discussed in Sec. 1-3.4(b), represents such an alternative for Direct-Collection Cells, but unfortunately such arrangements have received little attention to date. (The DVE Cell, discussed later in Chap. 2, represents another somewhat more subtle variation that, in effect, has an infinite number of stages!)

Interaction-Energy Cells also represent a multistage approach where the ionization and/or excitation potentials provide the individual stages. The difficulty with this approach is that the cells conceived to date have involved outer-shell electrons so the potential barriers are inherently small (relative to nuclear radiation energies) and there is little freedom to select optimum sizes and combinations of heights. Thus, to obtain a reasonable choice of barriers, there is a strong motivation to develop a cycle based on ionization-excitation of inner-shell electron levels or possibly nuclear levels, but methods to do this have not been devised.

In theory a multistage unit might be as efficient as one with a single stage; however, this is not easy because of the many practical problems involved. In the dam analogy, one must worry about where the clouds release their rain, the individual efficiences of each turbo-generator, etc. There are simply more ways that losses can enter, and in practice, they probably would. In addition, Fig. 1.6(b) probably should include a side-stream to permit water from upper stages to bypass the lower ones completely. This would be analogous to the inability of the Ionization-Electric Cell to utilize excitation energies.

1-3.4 Relation to Other Conversion Methods

Having gained some understanding of Direct-Collection and Interaction-Energy Cycles, we are in a position to question how they relate to other conversion methods, and this is illustrated schematically in Fig. 1.7, which is an expansion of the earlier stage diagram (Fig. 1.1). As shown, the path involving heat production can be split into two main

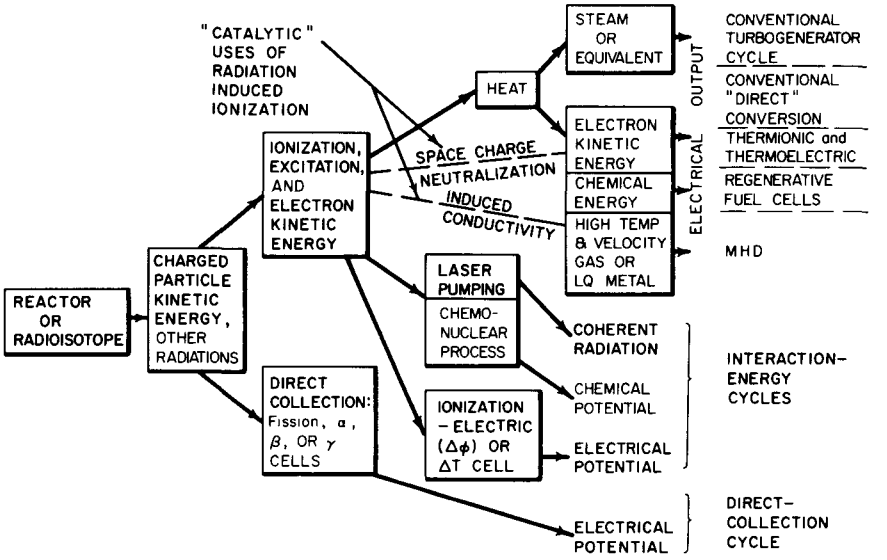

Fig. 1.7 — Relation of various Energy-Conversion Cycles.

routes: One goes through a conventional turbogenerator cycle such as has been used on all existing central nuclear-electric power stations to date. The second route, involving thermionic, thermoelectric, MHD, or fuel cell units, is of particular interest because these four, plus photovoltaic methods, are the major concepts commonly included in "Direct Energy Conversion" (e.g., Refs. 10 and 11). Since the same term has been applied to the subject matter discussed here, some confusion is likely. Strictly speaking, Fig. 1.7 illustrates that thermionics, etc., when used with a nuclear source, are not "direct" in terms of the number of conversion steps involved. However, the term "Direct Energy Conversion" has come to mean, by virtue of common usage, methods that "... convert energy to electricity using *fewer* intermediate steps" than the turbogenerator system (Ref. 10, p. 1).

While the present comments may be critical of the nomenclature or jargon, they are not meant to infer that direct collection, because it is single step and hence "direct," is the "best" method for nuclear energy conversion. The question of "best" is much more complex. In fact, there is not even a unique answer since "best" can only be interpreted in terms of a specific application.

(a) *Combination Cycles*

It should be feasible to combine either a Direct-Collection or an Interaction-Energy Cell with a heat cycle. In fact, as illustrated in Fig. 1.8, there are several possible ways of coupling the two through the "waste heat" from the radiation cells. The concept of combining

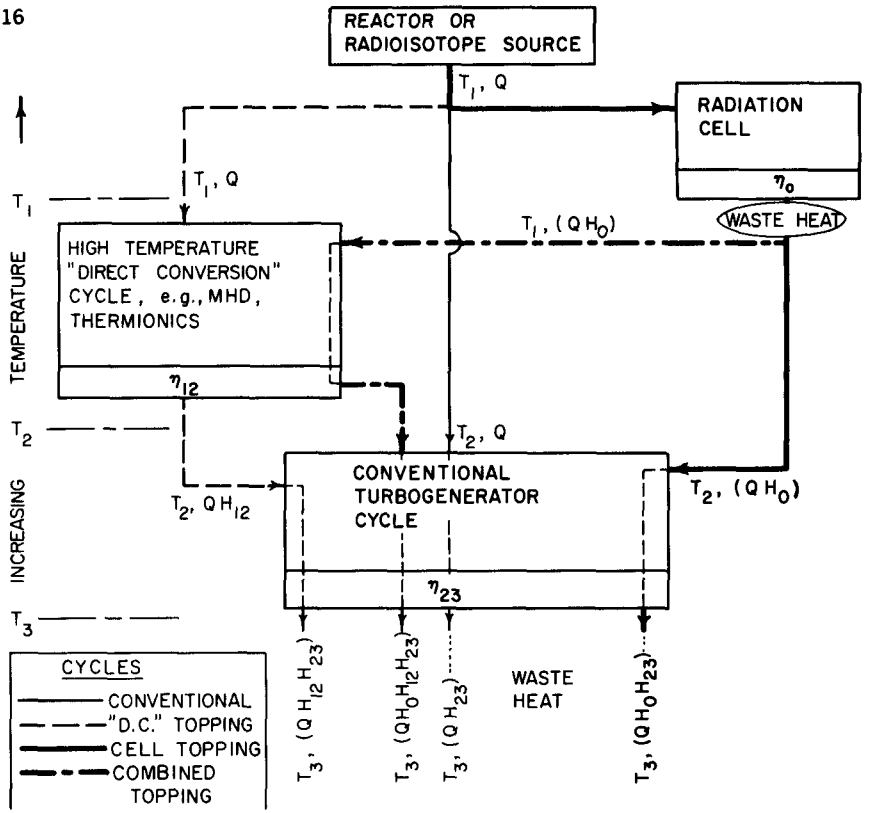

Fig. 1.8 — Possible topping cycles involving Radiation Cells. Cycle efficiencies are indicated as η_{ij}, where the subscripts refer to the temperature difference involved, i.e., $(T_i - T_j)$. (η_0 is independent of temperature.) The temperature and waste heat energy values, $QH_{ij} \equiv Q(1-\eta_{ij})$, are indicated at various points. The electrical output for a given cycle will be the difference between the entering and exit energy values, e.g., for the radiation cell, this is: $[Q-(QH_0)] = \eta_0 Q$.

various cycles is not new, but it has received renewed interest in recent years with the advent of high temperature concepts such as MHD and thermionics. They make it possible to consider using higher temperatures which, depending on the source, may be available but are not utilized in conventional steam or gas turbines because of metallurgical considerations. For example, steam turbines are generally limited to temperatures less than $\approx 600°C$, while gas turbines are restricted[12] to $700-900°C$.

A unit making use of the upper or "top" temperature range is commonly called a "topper," and the process is called "topping"[12]. This is illustrated in Fig. 1.8 by the path leading directly from the source to the high temperature–direct conversion cycle on the left, thence to the turbogenerator. The temperature leaving the topper (T_2 in Fig. 1.8) is generally taken to be the same as the inlet temperature to the turbogenerator if it were used separately (note the direct

path in Fig. 1.8 from the source to the turbogenerator). Since the temperature range employed by the turbogenerator is unaffected, its efficiency is unchanged.

Since, as shown in Fig. 1.8, combined cycles involving radiation pass energy from the source through the cells first,* they too can be viewed as "toppers." However, there is one important difference· Because these cells do not involve a thermodynamic cycle, they can essentially reject heat at the highest temperature permitted by the source itself (labeled T_1). As a consequence, they could even serve as a topper for a high temperature thermionic or MHD cycle (see the dashed line in Fig. 1.8). Further, it would be possible to combine all three cycles if the thermionic or MHD unit in turn served as a topper for the turbogenerator.

Some numerical examples of the effect of topping are worked out in Appendix A-3, where it is shown that even a low efficiency topper may be attractive; e.g., use of a nuclear cell with 10% efficiency with a 35% efficient turbogenerator results in a fractional increase in the overall efficiency of 19% (giving an overall efficiency of 42%). For a fixed output power, this corresponds to a reduction in the energy input requirement of ≈16% and a decrease in the waste heat rejected of ≈24%. This has direct meaning in terms of reduced fuel costs, heat dump requirements, and thermal pollution. (Thermal pollution, concerned with possible damage that thermal discharge from power plants may inflict on the natural environment, has received considerable attention recently, e.g , see Ref. 13.)

While these results are impressive, consideration must be given to the added cost and complexity associated with adding the topper. However, it should be stressed that cost is not always the most significant basis for a decision for or against topping. Like it or not, society may be forced to pay more to reduce thermal pollution. In space applications the entire system, including the added topping unit, must often compete with alternatives on the basis of power to weight ratio criteria. Other special requirements may favor one approach over another, and the radiation cell topping concept would be ideal where simultaneous requirements for both high- and low-voltage currents exist. Likewise, ionization–excitation cells producing chemicals or coherent radiation might have unique advantages in situations requiring these outputs along with electrical energy. A dual chemical-processing, steam unit is another combination that has received some consideration[14,15]

*This is valid for situations like the Fission-Electric Reactor where the source energy initially resides in the kinetic energy of the charged particles used in the Direct-Collection Cell. However, in some instances (e.g., conversion of gamma radiation energy entering a reactor shield via a Gamma-Electric Cell as discussed later in Chap. 7), the cell operates on energy that has *by-passed* the heat cycle. It then acts as an auxiliary converter rather than a topper, and the analysis must be modified accordingly.

(b) *Combination and Multiplate Cells*

Aside from integrating nuclear cells with heat cycles, a variety of ways of combining various cells themselves can be envisioned. Coupled cells using different sources, or Direct-Collection and Interaction-Energy combinations, are termed *combination* cells.

Multiplate (emitter and/or collector) arrangements are often involved in combination cells, although they may just as frequently be used in single cell construction. It is impossible to consider all of the possibilities here, but a few examples are illustrated in Fig. 1.9. They should be considered in view of four key reasons for designing in this direction, namely to:

- permit operation on two or more different types of radiation emitted from a given source.
- obtain a maximum emitter–collector surface area in the minimum volume.
- achieve lower potential differences between successive plates.
- compensate for differences in particle ranges and energies.

The design illustrated in Fig. 1.9(a) uses alternate alpha and beta emitters so that each plate serves a dual role as both emitter and collector. This might also be possible in a cell using only one type of emitter. However, different load resistors or fuel layer thicknesses would be required from plate to plate. Otherwise the particle emission and arrival rates would just balance for any given plate, making it impossible to build up a net charge or potential.

In the cell of Fig. 1.9(b), a collimated gamma radiation beam interacts with the electrodes to produce high energy Compton electrons. (Electrode materials are typically selected with low atomic number so that, with gammas in the low MeV range, Compton production is favored; however, the photoelectric effect and pair-production can give a significant contribution in some cases.) The preferential forward direction of motion of these electrons gives rise to an electrical current, and this is an example of a multiplate, vacuum type Gamma-Electric Cell (solid dielectric insulators can also be used as described in Chaps. 2 and 7).

Gamma radiation, being more penetrating than Compton electrons, is partially transmitted through the emitter–collector plates while the electrons are stopped. Since the gamma intensity is attenuated somewhat by each plate, the number of electrons emitted also progressively decreases. As a result more electrons arrive at a given plate than leave, so provided correct load resistors are selected, a potential will build up.

Also note that each electron "sees" only the potential barrier represented by the voltage difference between two plates. Thus, by this cascade effect, barring voltage breakdown, the total voltage dif-

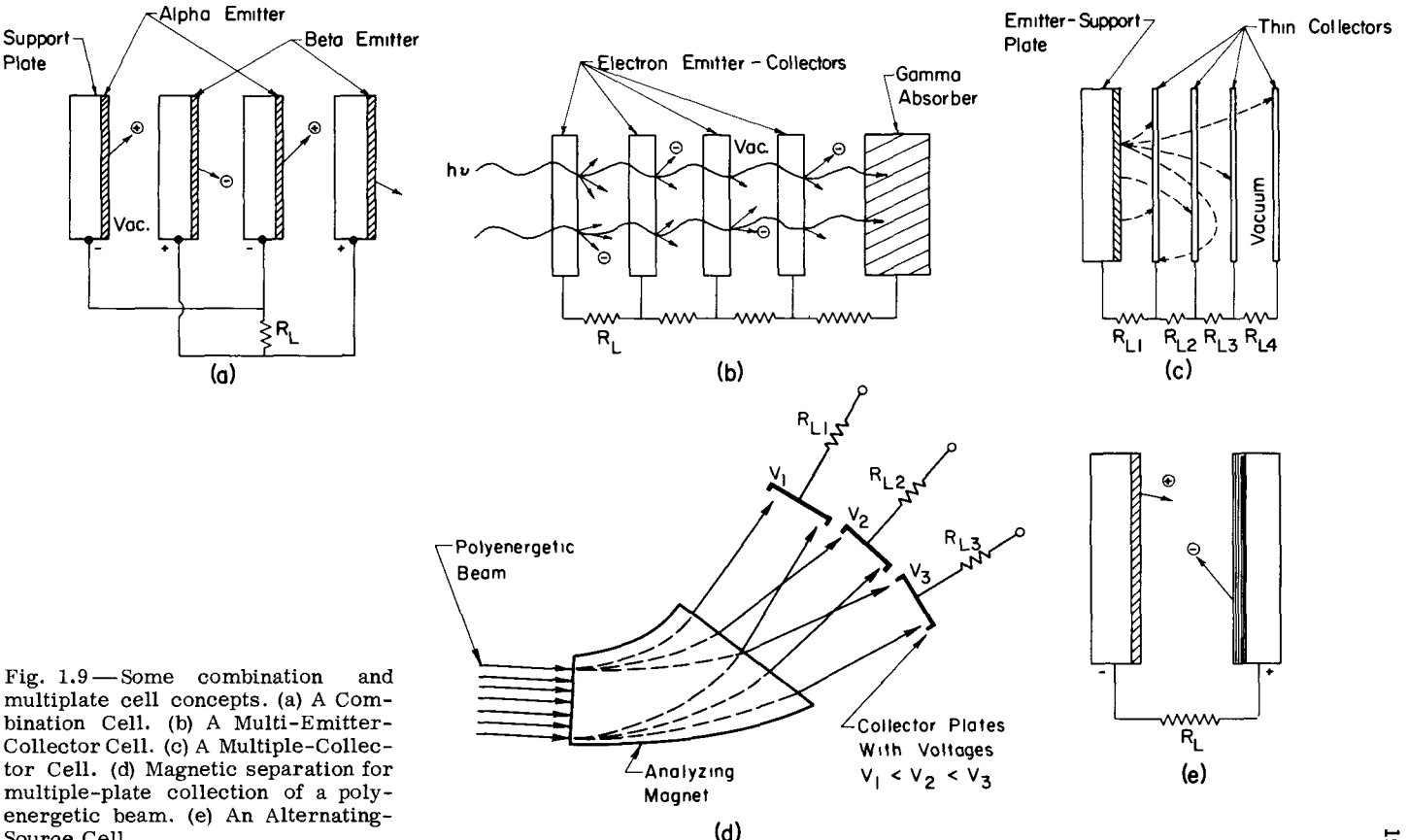

Fig. 1.9 — Some combination and multiplate cell concepts. (a) A Combination Cell. (b) A Multi-Emitter-Collector Cell. (c) A Multiple-Collector Cell. (d) Magnetic separation for multiple-plate collection of a polyenergetic beam. (e) An Alternating-Source Cell.

ference (first emitter to gamma absorber) could greatly exceed the voltage equivalent of the gamma photons or the Compton electrons. (As will be seen later, the same effect is an inherent characteristic of even a 2-electrode solid dielectric Gamma-Electric Cell.)

The next illustration, Fig. 1.9(c), uses a number of thin collectors. Depending on their energy and direction, the charged particles may pass through several collectors before stopping. In fact, some of those unable to overcome the potential and reach a given collector, say the third one, may be stopped in one of the intervening collectors, e.g., the second one, instead of returning to the emitter. While such a design would offer a choice of voltages, represented by R_{L1}, R_{L2}, etc., in the figure, it has some disadvantages. The emitter area is preserved; hence, the currents are of the same magnitude as for the equivalent 2-plate design. Also, its efficiency would no doubt be impaired because a fraction of the particles pass through one or more plates and suffer energy losses in doing so.

An interesting variation has been considered to collect charged particles emerging from a mirror-type thermonuclear fusion device[16]. The collector plates are replaced by a series of vapor filled cells. High-energy particles escaping from the fusion device undergo charge exchange collisions in the vapor, and the resulting low-energy charged particles are swept out of the vapor by transverse fields created by appropriate electrodes. This approach avoids some of the problems inherent in the use of a solid collector plate, but detailed studies of efficiencies, other leakage effects, etc., have not been published to date. The use of a series of collectors, progressively increasing in potential, is particularly important in connection with a device such as a thermonuclear reactor where the charged particles have a wide spread of energies. Lower-energy particles are collected by the first collectors whereas higher-energy particles pass through to the high potential collectors. This offers the possibility of quite high conversion efficiencies in comparison to a single collector cell operating at a unique potential which is "off-optimum" for lower- or higher-energy particles.

The basic principle of this approach is illustrated in Fig. 1.9(d) where a magnetic field is used to energy-analyze a multienergy beam. The resulting beams are collected by plates having voltages, i.e., load resistances, "mated" to the various beam energies. This is equivalent, in concept, to the cell of Fig. 1.9(c), but the losses inherent in the transmission of particles through collection plates are now avoided. Neglecting leakage currents and resistive losses in the magnet (these are truly extraneous losses since, by definition, no work is expended in the defection of the particles by the magnetic field) a 100% efficiency can be approached in the limit of many plates.

The final example, Fig. 1.9(e), a slight modification of Fig. 1.9(a), uses two plates alternately coated with positive and negative particle

emitters. Such an arrangement would potentially give larger currents without increasing the plate area; however, the use of two or more sources introduces an added complexity from a practical point of view.

Other aspects, e.g., the effect of secondary electron emission, should be considered in evaluating any of these designs. These problems, as well as a consideration of other possible designs, will be deferred until later.

Ultimately the choice between simple cells versus combination and/or multiplate cells is reduced to weighing the benefits of the latter against the increased complexity and cost of construction.

1-4 NUCLEAR RADIATION INDUCED IONIZATION AS A "CATALYST" IN OTHER CONVERSION DEVICES

The basic objective of the Ionization-Electric Cell is the conversion of nuclear radiation energy via a cycle involving induced ionization. However, another important way that radiation induced ionization might be used is to "aid" or increase the efficiency of the heat conversion process in thermal cycles. In this role it acts as a "catalyst." Its presence improves the process, but the conversion of the heat energy, not radiation energy, is the basic objective. Two important examples, space charge neutralization in thermionics and induced conductivity in MHD, are illustrated by the dotted lines in Fig. 1.7. Both will be discussed in more detail in the author's second book, but a brief description is instructive here.

Space charge neutralization is a key problem in successful operation of thermionic diodes. (For a general description of thermionic diode theory and operation, see Refs. 10 and 11). As the current is increased, electrons leaving the emitter "see" a dense cloud of electrons ahead in the gap. Unless corrective measures are taken, this "space charge" barrier seriously reduces the current and hence the efficiency of the diode.

Early designs used a close spacing which reduced space charge by simply limiting the gap volume available to electrons, but the spacings required (of the order of 0.001 cm) caused extreme mechanical problems. Another early approach used crossed electric-magnetic field techniques. Unfortunately, electron leakage currents are serious, and the device is considerably more complicated than the simple diode.

Introduction of ions into the inter-electrode gap represents the most common current approach. Two basic considerations are involved: first, sufficient ions must be produced; and second, the energy required for ion production should be minimized since it is not recovered.

Cesium has been used extensively as a fill gas because of its low ionization potential. However, ionization by contacting it with the hot

emitter surface has encountered difficulties because of the high temperatures required, and the alternate approach of using higher cesium pressures to achieve volume ionization through electron collisions also has some disadvantages. The increased resistance to electron flow across the gap and the associated energy losses and decrease in current reduce the operating efficiency, but this approach is presently accepted as the "standard" method.

Auxiliary electrode methods, photoionization, and nuclear radiation induced ionization have been considered, but they have not yet received sufficient study to permit a final evaluation.

In theory at least, the nuclear radiation route is ideally suited to a converter employing a reactor or radioisotope power source. First, a nuclear power source has associated with it "excess" nuclear radiations that, having failed to produce heat in the diode emitter, are lost from the thermionic cycle. If these radiations could be used to produce the required ions, the energy going into the ion production would in a sense be "free." Second, the high energy of the nuclear radiation makes it feasible to exploit fill gases other than cesium since the ionization potential is no longer a critical parameter. For example, Jablonski et al.[17] have considered the use of various noble gases, and they point out that these gases: are less corrosive than cesium; have electron–neutral atom cross sections 100 to 10^3 times smaller than for cesium, thus reducing the plasma resistance and associated losses; and permit lower operating temperatures compared to devices using surface ionization.

However, these gains are not obtained without some penalties, and it is still not clear that sufficient ionization can be obtained. This appears to be virtually impossible using gamma radiation; hence, for a reactor source, the obvious route is via fission fragments. This brings us back to the problem of getting fragments out of the fuel layer, and it brings in additional questions, too; e.g., will the diode performance be harmed as the plasma is slowly contaminated by fission products (fragments)?

The use of nuclear radiation to enhance electrical conductivity in MHD presents a similar situation. (References such as 10–12 review the basic concepts of MHD.) The power produced by a gas cycle MHD unit is proportional to the electrical conductivity of the gas, which is in turn a function of the ionization density. The normal method for obtaining the required ionization is by using high temperatures and by simultaneously seeding the gas, i.e., by adding small quantities of an alkali metal with a low ionization potential. However, the temperatures required are generally quite high, and one must contend with the corrosive seed material. Thus, alternate non-thermal ionization techniques have received some attention, and this is of particular importance if an MHD unit is to be used with a nuclear reactor source. The reactor,

in comparison with a flame source, presents a major difficulty because heat must be generated in solid fuel elements and transferred to the gas. This seriously limits temperatures and makes thermal ionization marginal even with seeding.

In fact, a recent study at Los Alamos Scientific Laboratory[18] concluded that the "extensive (developmental) programs required do not appear justified since ... no significant gains in power economy can be predicted that will allow the nuclear-MHD plant to compete with conventional nuclear power plants." It should be stressed that these remarks refer strictly to *thermal* ionization techniques. The authors gave only a "cursory" consideration to non-thermal processes because the methods have not yet been demonstrated experimentally, and the temperature range expected (<3400°R) is within the obtainable range of gas turbine development, which would be a formidable competitor.

Despite these problems, the bleak outlook for thermal ionization would seem to force attention to turn eventually to non-thermal methods. Of the various possibilities, the arguments for considering nuclear radiation ionization closely parallel those used in the case of thermionics. The radiation energy is "free," and the working gas can be selected without regard to ionization potential. However, there is an important additional consideration in MHD. The MHD channel itself probably cannot be placed in the reactor core because of the resulting complications for both the core and magnet design. One solution is to irradiate the entrance nozzle, and the problem then boils down to obtaining sufficient ionization density as the gas flows into and down the channel. Some preliminary studies indicate that a high speed helium-3 gas flow might work (e.g., Ref. 19). An alternate approach that has some merit is to select a gas, such as nitrogen, having a long lifetime (metastable) excited state which, upon excitation in the entrance, can then decay and produce ionization in the channel itself[20].

No doubt there are other concepts where the "catalytic" effect of radiation induced ionization might be advantageous; for example, electrogasdynamics[21]. A source of ions alone is needed, but a sweeping field technique to remove electrons preferentially from the radiation region might be one possible attack.

1-5 STATUS OF CELL DEVELOPMENT

A detailed discussion of Direct-Collection Cell development is presented in Chap. 7. At this point, we would simply like to gain a general "feeling" for the state of the art. This discussion is best divided into three parts following the three main areas of cell applications: instrumentation; low output power supplies; and high output power supplies.

Table 1.4—CELLS AVAILABLE COMMERCIALLY

Common or Trade Name of Cell	Type of Cell (Insulator)	Typical Radiation Involved	Output Power	Uses	Unique Characteristics	Monograph Section or References
I. Instrumentation						
a. Semirad detector (Secondary Electron Mixed Radiation Dosimeter)	D–C* (vacuum)	Secondary electrons (recoil protons) produced by external gamma radiation (fast neutrons)	†	Radiation monitors, particularly for in-core measurements, pulsed reactors, and nuclear explosions	Small, rugged; linear in very high intensity fields, fast time response; fairly insensitive to temperatures, etc., gamma compensation possible	Sec. 7–6
b. Compton diode	D–C (vacuum or dielectric)	Compton electrons produced by external gamma radiation	†	Same as for Semirad	Same as for Semirad	Sec. 7–5
c. "Self-powered" neutron detectors	D–C (dielectric)	Beta particles produced by external neutron flux	†	Same as for Semirad	Same as for Semirad	Sec. 7–4.2
d. Semiconductor neutron detectors	I-E‡ (semiconductor)	All types of external radiation	†	Radiation detection, spectroscopy	Small size, high energy resolution	Ref. 22
e. Ohmart measuring cell	I-E (dielectric spacer, gas filled)	External gamma or beta radiation	†	Detector element in density, and liquid-level gauges	Simple, rugged, dependable	Ref. 9
f. Alphatron	I-E	Internal alpha source	†	Vacuum pressure gauge ($\geq 10^{-4}$ Torr)	No filament to burn out or sag, can be exposed to atmosphere, linear response; long life	Ref. 23
II. Low-Output Power Source						
a. Nuclear batteries	D–C (vacuum or dielectric)	Internal radioisotope source, mainly β emitters	<1-mW	Timing circuit; instrumentation, electric detonator, or watch and clock power	Simple, rugged, long life, insensitive to temperature, pressure, gravity, constant current up to relatively high voltages	Sec. 7–4.2

*D–C = Direct-Collection.
†Essentially a short circuit, also may be biased with an external power supply or battery.
‡I-E = Ionization-Electric.

As indicated in Table 1.4, most of the cells commercially available fall under the heading of nuclear radiation detection instrumentation. The Semirad detector, Compton diode, and "self-powered" neutron detector have gained a unique place for measurements involving high radiation intensities, e.g., in pulsed reactors, nuclear explosions, etc. As a result, considerable research has been devoted to their development, and they show considerable sophistication in such matters of importance to detection as linearity, insensitivity to the radiation energy spectrum, and time response. These cells are based on direct collection, but the Ionization-Electric Cell concept has also been used as illustrated by the semiconductor detector and Ohmart Cell. Because of their high-energy resolution, semiconductor detectors have assumed a prime role in nuclear radiation spectroscopy, and they have perhaps received more research and development effort than any other detector listed here[22].

The traditional ionization chamber might be included as an example of the Ionization-Electric Cell, but in a strict sense, this is not correct since an external bias supplies the *sole* driving force for collection. (An external bias may be used in the other cells to enhance collection, but other "driving forces" are also present—i.e., the particle kinetic energy in direct-collection concepts and an internal electric field in the semiconductor junction. In brief, the key question is: will the cell operate at all without a bias? The latter examples would; the ionization chamber will not.) The Ohmart Cell is a "cousin" of the ionization chamber, but it uses a work function difference concept as described earlier. In contrast to the other detectors, relatively little research outside of the effort by the Ohmart Corporation[9] has been devoted to this cell.

The alphatron, a vacuum pressure gauge, demonstrates another instrumentation application. However, its cost is relatively high and care is required for the safe use of the radioisotope, and these items have prevented a wide usage of this gauge[23]. Like the ion chamber, it generally uses an external bias; however, because of its unique built-in source, it has been included in Table 1.4.

While the basic concepts may be similar, the transition from instrumentation to a power source is not an easy one. For example, consider the time period involved during which thermoelectric generators evolved from thermocouple concepts, or thermionic generators evolved from electron tube concepts. It is also interesting that two ingredients were required for the transition: the development of new materials and a new mental attitude by the designer.

In the case of nuclear cells, it would appear that this transition has slowly but surely begun. In the low power range (<1 mW) the so-called "nuclear battery" has an established place for special purpose requirements. In fact, the number of nuclear batteries in operation greatly

exceeds the number of well publicized SNAP generators[24]. This has been attributed to the low unit cost of the batteries, and it is certainly not surprising when one reflects on the number of ordinary chemical batteries that have been built relative to, say, coal fired electric generating stations. However, the low unit cost combined with fairly loose efficiency and power density requirements for nuclear batteries have had one serious consequence: Relatively little effort has been put into basic research. It is easy enough to build a device that meets these requirements, and as a result, the design techniques have remained more as an art than a science.

This brings us to high output power sources. As indicated in the preceding sections, there is no fundamental reason to restrict nuclear cells, particularly of the Direct-Collection type, to low power levels. This point has also been noted by Corliss and Harvey[24], and their explanation throws considerable light on the situation. They observe:

> The most compelling reason for the very unequal division of development effort (between nuclear cells and heat cycles) seems to be in the powerful momentum built up by the heat engines during the Project Feedback studies, the prototype Mound Laboratory experiments, and the early SNAP work. If the first definitive requirement for radioisotopic power had been in the 1-watt range rather than at the 500-watt level, it is quite possible that nuclear batteries might have been developed with the same urgency and intensity that was lavished on heat engines. In the early 1950's, it was very difficult to see how nuclear batteries, then mainly laboratory curiosities producing microwatts or less, could be magnified to 500 watts, a power multiplication of 10^9. It was far easier to conceive of scaling highly developed turbomachinery downwards in power. In this way, but perhaps not with the logic stated so explicitly, the main radioisotopic power efforts were committed to the heat-engine approach.

Some results from efforts to develop high-power cells are listed in Table 1.5 (pp. 28-29).

Most experiment studies have concentrated on open circuit voltage build-up tests. The one exception, Linder and Christian's Beta Cell, was operated with a load at 365 kV. Its efficiency of 20% is the highest *measured* efficiency reported to date. However, the output power was only about 30 mW, and at the time of their study there was no motivation to go to higher powers.

Recent experiments involving Fission, Alpha, and Gamma Cells have all demonstrated voltages in the 20- to 50-kV range, but this is still an order of magnitude lower than that assumed in most design studies. Various leakage currents prevented larger voltages in the Alpha and Gamma Cells, whereas equipment limitations stopped the tests of the Fission-Electric Cell. In each of these cases, it appears feasible to obtain higher voltages, but some design modifications and improved techniques are undoubtedly necessary to achieve the design values.

Several design studies for space propulsion applications are noted in Table 1.5. The high voltages delivered by Direct-Collection Cells are ideally suited for the accelerating potential in an electric-ion propulsion system. The nuclear cell approach should be favorable, provided the operating conditions assumed (i.e., voltages and currents) can be achieved in practice, and numerous other applications will no doubt develop once cell performance is proved.

The design proposed for coupling to a mirror-type thermonuclear reactor stands out as involving a high-power output while offering an extremely high efficiency. The latter is possible because the cell can be located external to the reactor, yet it appears to be possible to obtain a well-collimated incident beam of charged particles. In contrast, the other cells in Table 1.5 involve a fairly wide distribution of particle directions.

In conclusion, it would appear that studies of high-power cells are in their infancy, and it is simply too early to evaluate their ultimate potential or feasibility. While the attainment of high voltages is certainly a key problem involved in the development of high-power cells, there are numerous others, some of which are indicated in Table 1.6.

When heavy charged particles break through or enter the surface of a solid, many secondary electrons are emitted. The total charge associated with them may, in fact, be larger than that of the primary particle, and, if the latter is a positive particle, the secondary electrons may introduce an unwanted leakage current. Attempts to suppress or control secondaries using grids and magnetic means have met with only partial success to date.

The fuel layer itself is often so thin that its manufacture requires special techniques. Durability is, of course, important, and in addition, it would be desirable to be able to refuel without disassembling the cell. Electroplating techniques may be a possible solution in some cases.

Even if the cell operates, it may not be desirable to use the high-voltage dc output directly. Suitable step-down or dc to ac transformers which mate with the typically high impedance characteristic of the cells require special techniques. It might be noted, however, that a high-voltage dc output may be more convenient than initially expected. There has, in fact, been a trend in this direction in the electrical power field, e.g., L. Lessing in "DC Power's Big Comeback"[25] describes the development of high-voltage ($\approx$750 kV) dc transmission lines for the low-cost bulk movement of power. He goes on to point out that "the rediscovery of dc in high-voltage power transmission raises several arresting possibilities" such as economic transmission from remote sites by underground or underwater transmission.

Little actual experience has been obtained with high-power cells, and perhaps because of this many of the design studies reported to date have suffered from obviously minimal engineering design. For

Table 1.5—SOME HIGHLIGHTS OF RECENT CELL STUDIES

Type Cell	Source	Maximum Voltage (Cause of Limit)	Comments About			Investigator(s) and Year	Monograph Section
			Current	Power	Efficiency		
Fission-Electric							
Experimental	^{235}U layer in core	20 kV (maximum magnetic field current)	——— Open circuit ———			Krieve, 1966	7-2
Conceptual design	Gas cooled reactor for space propulsion	1 MV with 1-cm gaps	25 A	25 MWe, 3–6 kg/kWe less shields; or 0.2 W/cm^3	5–10%	Mokski, 1967	7-2
Thermonuclear-Electric							
Conceptual design	Mirror-type controlled thermonuclear reactor	100 to 500 kV (corresponds to maximum ion energy)	≈2 kA	≈500 MWe	90–95%	Post, 1969	7-7
Alpha-Electric							
Experimental	5 Ci ^{210}Po	≈50 kV (microdischarging)	——— Open circuit ———			Plummer et al., 1967	7-3

Beta-Electric							
Experimental	250 mCi ^{90}Sr	365 kV (internal breakdown)	$\approx 10^{-9}$ A short circuit	3×10^{-4} We	20%	Linder and Christian, 1952	7-4.2
Conceptual design	$^{144}Ce/^{144}Pr$ for electrostatic propulsion	700 kV	0.14 A	100 kW , 0.35 kg/kWe with 5 mg/cm^2 collector, or 6×10^{-5} W/cm^3	27%	Mickelsen and Low, 1963	7-4.1
Gamma-Electric							
Experimental	Reactor radiation	$\approx$20 kV open circuit (leakage currents)	10^{-6} A per (cm^2 R)/h short circuit			Sampson, 1967	7-5
Ionization-Electric							
Experimental	Gamma radiation, from 11 μCi ^{110}Ag with 4.8 atm argon	0.86 V (work function difference)	0.9×10^{-11} with $R_L = 10^{11}$ Ω	7.3×10^{-12} W $\approx 6 \times 10^{-15}$ W/cm^3	0.02%	Ohmart, 1951	
Conceptual design	44 mCi tritium with 2 atm argon	1.67 V/cell, 44 cells in series giving 73.5 V open circuit	0.8×10^{-9} A (short circuit)	10^{-8} We, $\approx 10^{-10}$ W/cm^3	0.6%	Thomas, 1953	

Table 1.6—SOME PROBLEMS ASSOCIATED WITH THE DEVELOPMENT OF HIGH-POWERED CELLS

1. *Voltage build-up,* including the elimination or minimization of
   (a) vacuum voltage-breakdown and/or micro-discharging
   (b) radiation induced conductivity in insulators
   (c) radiation damage to insulators
   (d) surface and other leakage currents
   (e) sputtering at either or both electrodes
2. *Secondary electron control,* requiring
   (a) improved grid and/or magnetic suppression techniques
   (b) minimization of electron reflection
   (c) reduction of secondary electron leakage currents from outer surfaces
3. *Source preparation* such as the
   (a) preparation of durable thin fuel layers
   (b) development of refueling methods
   (c) minimization of sputtering of fuel onto other surfaces
4. *Utilization of the characteristic high-voltage, low-current, dc output,* involving the development of efficient
   (a) step-down transformers
   (b) dc to ac conversion techniques
5. *Improved designs* to provide
   (a) adequate heat removal
   (b) lightweight shielding for special applications
   (c) rugged mechanical design in a geometry offering high conversion efficiency

example, several studies have simply ignored the need to remove waste heat or to provide radiation shielding despite the fact that these features would require drastic design changes.

These and associated problems are discussed further in later chapters. It is clear, however, that an intensive effort will be required before reasonably suitable solutions are found, and in the process, new problems may develop. Still, it should be stressed that there is every reason to believe solutions can be found. There are really only two questions: "How soon?" And, "What will the limiting problem(s) be?"

REFERENCES

1 M. Burton and J L. Magee (Eds.), *Advances in Radiation Chemistry,* Vol. 1, Wiley-Interscience, New York, 1969.

2. G. H. Miley and J J. Martin, The High Temperature Irradiation of the N-Heptane-Hydrogen System, *A I Ch E Journal, 7* 593 (1961).

3. M. Steinberg, Chemonuclear Reactors and Chemical Processing, in *Advances in Nucl. Sci. and Tech.,* E. J. Henley and H. Kouts (Eds.), Vol. 1, pp. 247-333, Academic Press Inc., New York, 1962.

4. B. Manowitz, M. Steinberg, J. W. Sutherland, P. Harteck, S. Dondes, and J. H. Cusack, The Development of Chemonuclear Processes, in *Proc. of the Third Int. Conf. on the Peaceful Uses of Atomic Energy, Geneva, 1964* Vol. 15, pp. 322-331, United Nations, New York, 1965

5. M. Steinberg, Chemonuclear and Radiation Chemical Process Research and Development, *Isotopes and Rad. Tech., 4,* 2: 142-155 (Winter 1966–67).
6. M. Steinberg, Status Report of Chemonuclear Reactor and Radiation Chemical Processing, BNL-11262, Brookhaven National Laboratory, April 1967.
7. E. W. McDaniel, *Collision Phenomena in Ionized Gases,* p. 260, John Wiley and Sons, New York, 1964.
8. R. D. Evans, *The Atomic Nucleus,* McGraw-Hill, New York, 1955.
9 Bulletin No. G C-2, The Ohmart Corporation, Allendorf Drive, Cincinnati, Ohio (1967).
10. S. W. Angrist, *Direct Energy Conversion,* Allyn and Bacon, Inc., Boston, Mass., 1965.
11. G. W. Sutton, *Direct Energy Conversion,* McGraw-Hill, New York, 1966.
12. K. H. Spring, *Direct Generation of Electricity,* pp. 12-18, Academic Press, New York, 1965.
13. J. R. Clark, Thermal Pollution and Aquatic Life, *Scientific American, 220,* 3 18 (1969).
14 Bernard Manowitz, The Industrial Future of Radiation Chemistry, *Nucleonics, 11,* 10 18-20 (1953).
15. P. Harteck and S. Dondes, Producing Chemicals with Reactor Radiation, *Nucleonics, 14,* 7 22 (1956).
16. R. F. Post, Mirror Systems Fuel Cycles, Loss Reduction and Energy Recovery, UCRL-71753, Lawrence Radiation Laboratory, Livermore, Calif., Sept. 8, 1969.
17. F. E. Jablonski, C. B. Leffert, R. Silver, R. F. Hill, and D. H. Loughridge, Space Charge Neutralization by Fission Fragments in the Direct Conversion Plasma Diode, *J. Appl. Phys., 30,* 12 2017 (1959).
18. L. A. Booth, The Prospects for Nuclear Reactor–MHD Commercial Power Production, *J. of Engineering for Power,* 345 (October 1966).
19. J. Braun, On Helium Plasma Through Neutron Irradiation, *Plasma Physics (J. of Nucl. Energy Part C), 6,* 407 (1964).
20. B. Manowitz, J. Powell, and M. Zucker, Non-Equilibrium Ionization by Metastable Excited Species in Nuclear MHD Cycles, *Proceedings, MHD–EHD Conference,* Brookhaven National Laboratory, March 1967.
21. M. C. Gourdine and D. H. Malcolm, Feasibility of an EGD High Voltage Power Source, *Proc., 19th Annual Power Sources Conference,* pp. 163-165, PCS Publications Committee, Red Bank, N. J., May 1965.
22. J. M. Taylor, *Semiconductor Particle Detectors,* Butterworths, Inc., Washington, D. C., 1963.
23. A. Guthrie, *Vacuum Technology,* pp. 181-184, John Wiley and Sons, New York, 1963.
24. W. R. Corliss and D. G. Harvey, *Radioisotopic Power Generation,* Prentice-Hall, Inc., Englewood Cliffs, N. J., 1964.
25. L. Lessing, DC Power's Big Comback. *Fortune, 174* (September 1965).

2

Basic Concepts in Direct Collection

We have seen that all direct-collection concepts convert kinetic energy into potential energy using the motion of a charged particle in an electric field. The charged particle may originate from fission, fusion, radioactive decay, or the interaction of nuclear radiation with matter. A complete analysis of a given concept includes charged particle transport effects and leakage currents, which will be discussed in later chapters. At present, however, we will study an *idealized* cell where such effects are neglected. This provides a simple introduction to the basic concept and also establishes the maximum obtainable output current and efficiency for a given geometry. As such, it presents a convenient "yardstick" or reference for evaluating the performance of actual cells.

2-1 CHARGED PARTICLE MOTION IN ELECTRIC FIELDS

The theory of charged particle motion in electric fields has been extensively developed in connection with electron tubes, accelerators, etc[1–4]. These applications often require a precise knowledge of the electron trajectory in three dimensional space, and the details of the calculation can be quite complex. Fortunately, the present applications are not so much concerned with a precise calculation of the trajectory as with the question: "Does the particle reach the collector?" Thus, we require only a few select calculational techniques. For convenience, these relations are derived in Appendix B. Since high-velocity electrons may be encountered in the important case of Beta Cells, relativistic corrections are retained.

2-2 ANALYSIS OF IDEALIZED CELLS

Direct-Collection Cells fall into two broad categories: plate and volume emitters. There are two basic types of Plate-Emitter Cells. One uses a coating of radioactive or fissioning material deposited on a support plate. In the other, charged particles (e.g., Compton electrons) are emitted due to the interaction of radiation in the plate, possibly due to an external radiation source. Typically a vacuum is maintained between

the emitter and collector plates so that electrical insulation is provided with a minimum of interference with passage of the charged particles. A solid or liquid dielectric may be used in some instances where transport losses are not important and it is desirable to reduce costs and provide a more rugged construction

There are also two basic types of Volume-Emitter Cells. In one, the emitting material is in a gaseous form or it is dispersed throughout a solid or fluid. This medium is then surrounded by a thin solid electrical insulator (e.g., a glass container) with an external collector electrode. Another type of volume emitter is simply composed of a solid dielectric material placed between two conducting plates. Collimated radiation impingent upon this cell drives electrons out of the dielectric and into one of the conducting plates.

In the present chapter "ideal-cell" versions of both types of cells are considered with the ideal cell defined by the following assumptions

(1) *Energy-charge losses during transport of the charged particles are neglected* Such losses will occur as the particles emerge from the fuel layer in the Plate-Emitter Cell or when they pass through the emitter medium and solid dielectric in the Volume-Emitter Cell.

(2) *All leakage currents are neglected* Leakage currents will occur in high-voltage devices such as these cells due to a variety of mechanisms. In addition to normal ohmic and surface leakage currents, radiation induced conductivity in the electrical insulators, secondary electron emission, and sputtering of surfaces may be important. Also, the maximum voltage in a practical device is often limited by voltage breakdown which may be viewed as a catastrophic leakage current! Possible backscattering and transmission of the charged particles through the collector plate are also viewed as leakage currents and they, along with the aforementioned currents, will be neglected.

(3) *Space charge effects are neglected* The current densities involved are typically small enough that particle trajectories can be calculated to good accuracy without including forces due to space charge build-up between the electrodes or self-magnetic fields caused by the beam This approximation will also be carried over to more detailed calculations in Chap. 4. (The Thermonuclear-Electric Cell, described later in Sec 7-7, represents an important case where space charge effects must be considered.)

(4) *Radiation losses are neglected* Possible radiation emissions due to deceleration or other interactions of the charged particles may be important in some special cells, but may be neglected in most cases.

(5) *A unique charged carrier is assumed* Cells using fission or beta sources will involve a distribution of particle energies, etc. However, in the ideal cell all particles are assigned a single kinetic energy T_0, a mass m_0, and a unique charge $+q_0$ (or $-q_0$). This assignment basi-

cally permits the selection of a unique operating voltage such that the efficiency and currents calculated are maximum values.

(6) *Isotopic and fission sources are assigned an isotropic angular distribution (lab system) for particle emission. Recoil sources, such as electrons from Compton scattering, are assigned an approximate average forward emission distribution.* An accurate angular distribution for emission must be used to represent the source, even in the ideal cell. The reason is simple. If all particles were emitted straight forward in the direction of the collector, the calculation would be trival under assumptions 1 to 5. For non-relativistic particles, the maximum conversion efficiency (kinetic to potential energy) would simply be 100%! Other distributions will give lower efficiencies, so the ideal-cell calculation in effect gives the reduction in efficiency due to the detailed angular distribution and geometry of the source.

The ideal-cell analysis presented here has been strongly influenced by the early studies of the Fission-Electric Cell by Safonov[5], Schock[6], Heindl[7], and Miley[8]; the Beta Cell study by Cohen[9]; the Alpha Cell studies by Plummer et al.[10]; and the Gamma-Electric Cell studies by Gross and Murphy[11,12] and Sampson and Miley[13,14]. However, in contrast to these studies which focused on specific devices, the present discussion is an attempt to achieve a more general point of view.

In the following sections we first consider the three classical configurations—plane, cylindrical, and spherical geometries—for "plate" cells. Following this, the volume emitter is discussed.

2-3 IDEALIZED PARALLEL-PLATE CELLS

The two basic types of parallel-plate cells are illustrated in Figs. 2.1(a) and (b). Both are reduced to the idealized geometry of Fig. 2.1(c) by assuming that all particles originate on the surface of the emitter plate. This is equivalent to neglecting energy losses during escape of the particles from the emitter. It also implies that the emitter is thin relative to the electrode spacing or that it is a sufficiently good electrical conductor so that particles do not experience a significant change in potential until they leave the emitter surface.

The plates are taken to be essentially infinite in length and width so the complication of end effects can be ignored. We begin by analyzing steady state operation with the collector at a potential V^+ relative to the emitter. This suggests positively charged particles, but application of the equations to negative particles only involves a sign change. The actual value of V^+ will depend on the load resistance used in the electrical circuit connecting the electrodes.

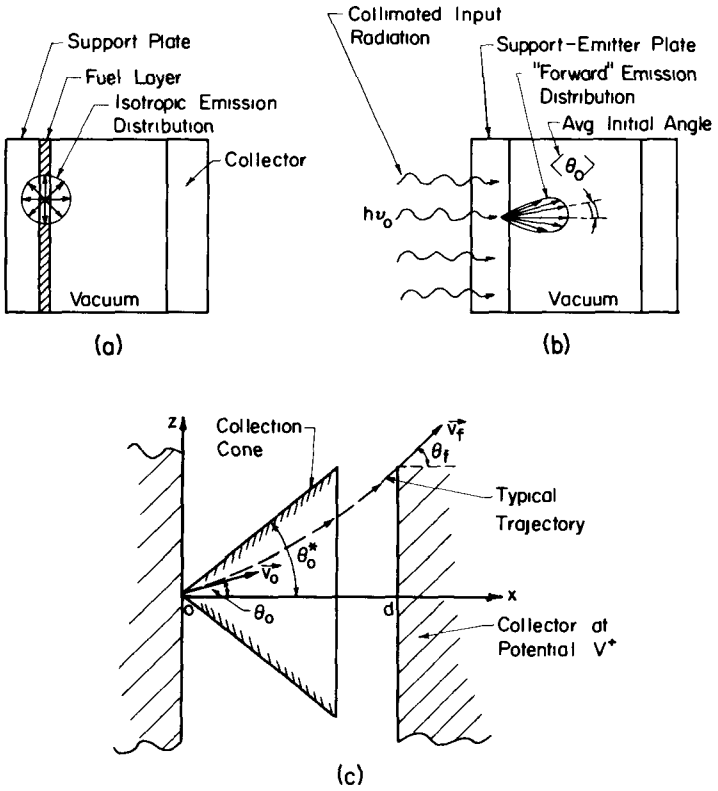

Fig. 2.1 — The parallel-plate cell. (a) Isotropic emission due to a fission or radioisotope fuel layer (b) Forward emission of particles ejected by the interaction of a collimated radiation beam in the emitter plate. (c) Geometry for the idealized cell. Here, S_0 particles/(cm^2 sec) are emitted from the surface with charge q, mass m, and kinetic energy T_0.

Consider a particle originating at the emitter surface with velocity $\vec{v}_0$ which reaches the collector with a residual velocity $\vec{v}_f$. Conservation of energy, Eq. (B.10),* requires that

$$qV^+ = [m(v_0) - m(v_f)]c^2 \tag{2.1}$$

where $m(v_j)$ is the relativistic mass corresponding to speed v_j and c is the speed of light (j = 0 or f)

*Equation numbers that include alphabetic characters refer to the appropriate appendix, in this case Eq. (B.10) of Appendix B.

Since there is no force in the z direction, this component of linear momentum is conserved, and from Eq. (B.14):

$$v_0\, m(v_0) \sin\theta_0 = v_f\, m(v_f) \sin\theta_f \tag{2.2}$$

where, as shown in Fig. 2.1(c), θ_f is the angle with the x-axis upon collection.

2-3.1 The Collection Cone

The particle will be collected if

$$0 \leq \theta_f \leq \frac{\pi}{2}\,. \tag{2.3}$$

The limit of $\theta_f = \pi/2$ corresponds to the case where the particle approaches the collector tangentially, and we will define the corresponding *initial* angle as θ_0^*. If the initial angle exceeds θ_0^*, the particle will not have a large enough initial x-component of velocity to reach the collector, and it will "fall back" to the emitter. Thus particles with initial angles in the range

$$0 \leq \theta_0 \leq \theta_0^* \tag{2.4}$$

are collected, and this defines the "collection cone" of Fig. 2.1(c).

Since θ_0^* corresponds to a θ_f of $\pi/2$, we use this in Eq. (2.2) and solve for the speed at that angle

$$v_f^* = \left[\frac{v_0^2 \sin^2\theta_0^*}{1 - (v_0/c)^2 \cos^2\theta_0^*}\right]^{1/2} \tag{2.5}$$

where we have used Eq. (B.7) for m(v).

Substitution of v_f^* into Eq. (2.1) gives

$$qV^+ = m(v_0)\, c^2\left[1 - \sqrt{1 - \left(\frac{v_0}{c}\right)^2 \cos^2\theta_0^*}\right] \tag{2.6}$$

which, upon solving for $\cos\theta_0^*$, yields

$$\theta_0^* = \cos^{-1}\sqrt{\Delta} \tag{2.7}$$

where

$$\Delta \equiv \frac{\beta}{\chi(R,\beta)} \tag{2.8a}$$

with

$$\beta = \frac{qV^+}{T_0} \tag{2.8b}$$

and

$$\chi(R,\beta) = \frac{R-1}{R-\beta} \tag{2.8c}$$

where

$$R = 2\left(1 + \frac{m_0c^2}{T_0}\right). \tag{2.8d}$$

As discussed in Appendix B-1.2, T_0 is the particle's *initial* kinetic energy, defined as

$$T_0 = [m(v_0)\ c^2 - m_0c^2] \tag{2.8e}$$

where the other symbols have been defined previously.

2-3.2 Relativistic Corrections

With Eq. (2.7), the collection zone is completely defined, and we are in a position to evaluate the number of particles reaching the collector for a particular voltage and angular distribution of emission. However, before doing this, we will digress for a moment to consider the physical significance of Δ and the associated parameters defined in Eq. (2.8).

This is perhaps best done indirectly by noting that in the nonrelativistic limit ($v_0/c \ll 1$) the quantity R approaches infinity so that, by Eq. (2.8c), $\chi \rightarrow 1.0$. Then according to Eq. (2.8a), Δ and β are identical. Now, the meaning of β is more obvious. It is a "reduced voltage" defined as the ratio of the operating voltage V^+ to T_0/q, the latter representing the voltage equivalent to complete conversion of the kinetic energy T_0 into potential. Thus T_0/q is the maximum obtainable voltage, so β gives the ratio of the operating to the maximum voltage. By analogy then, we see that Δ must represent a generalized reduced voltage including relativistic effects. The factor χ in Eq. (2.8a) corrects for energy associated with the relativistic mass increase that is lost, i.e., unconverted to potential, if the particle reaches the collector with a significant velocity. Since the remaining velocity depends on the collector voltage β, χ turns out to be a function of β.

It is interesting to note that, if $\beta = 1$, $\chi \rightarrow 1$ regardless of R. This is explained by noting that $\beta = 1$ represents a maximum or open cir-

cuit voltage; in which case, $\theta_0^* = 0$, and the only particles collected are those which are emitted normal to the surface having kinetic energy exactly equal to zero at the collector surface. Thus, any energy initially tied up in an increased mass has been fully converted to translational energy and thence to potential energy. At any other voltage some of the particles corresponding to $\theta_0 < \theta_0^*$ will be left with a finite velocity at the collector and hence will carry some unavailable energy.

Some feeling for the importance of the relativistic correction can be gained from Fig. 2.2, where χ is plotted as a function of the reduced

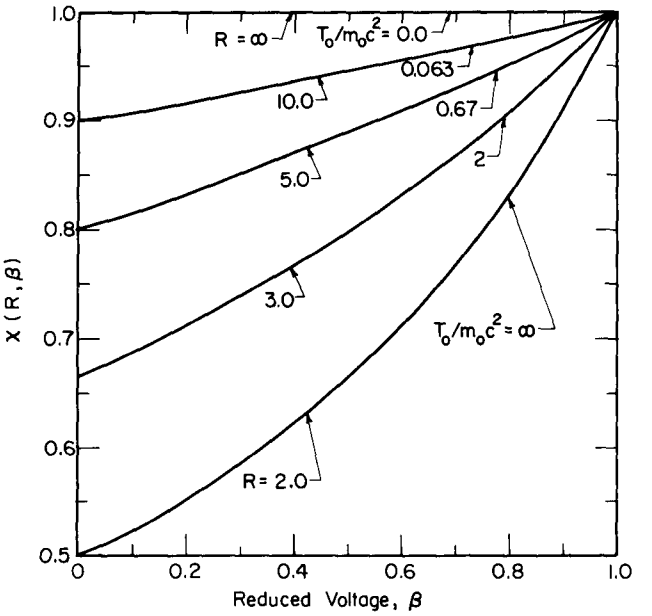

Fig. 2.2 — The relativistic correction factor.

voltage β for various values of R. Values of R are given in Table 2.1 for typical sources of interest here. Note that R is bounded such that

$$2 \leq R \leq \frac{4c^2}{v_0^2} (\approx \infty) \tag{2.9}$$

where the lower limit is the extreme relativistic case while ∞ corresponds to non-relativistic particles. It is seen from Table 2.1 and Fig. 2.2 that for all practical purposes $\chi \approx 1$ for the various sources except for certain beta emitters like ^{85}Kr and ^{90}Sr and gamma induced Compton currents. Since Beta and Gamma Cells are quite common and important, we will retain the relativistic correction in the remaining

Table 2.1—TYPICAL VALUES OF R

Particle	Mass (amu)	Source	Average Energy (MeV)	R
Betas	0.55×10^{-3}	^{3}H	0.006	1.7×10^{2}
		^{144}Ce	0.06	19
		^{85}Kr	0.5	4
		$^{90}Sr/^{90}Y$	1.1	2.9
		Compton	Order of 1	3
Alpha	4.003	^{210}Po	5.3	1.4×10^{3}
		Fusion (D-T)	3.5	2.2×10^{3}
		$n(^{10}B)\alpha$	1.5	5.0×10^{3}
^{7}Li	7.018	$n(^{10}B)Li$	0.84	1.8×10^{4}
Proton	1.007	≈1 MeV neutron recoil	Order of 1	1.9×10^{3}
		Fusion (D-^{3}He)	14.7	1.4×10^{2}
Fission fragment	≈96 (light) ≈140 (heavy)	$n(^{235}U)ff$	98 67	1.8×10^{3} 3.9×10^{3}

sections of this chapter and results will be presented with R as a parameter.

2-3.3 Current—Voltage Characteristics

The current density J (A/cm^2) of the collector is found by integration over the solid angle subtended by the collection cone, i.e.,

$$J(\Delta) = S_0 q \int_0^{\theta_0^*} P(\theta_0) \sin \theta_0 \, d\theta_0 = S_0 q \int_{\mu_0^*}^{1} P(\mu_0) \, d\mu_0 \tag{2.10}$$

where S_0 is the particle emission rate per square centimeter of emitter surface, q is their charge in coulombs, $P(\theta_0)$ is the angular distribution of emission, and μ_0 is defined as cosine θ_0. We have required that $P(\mu_0)$ be normalized such that

$$\int_{-1}^{+1} P(\mu_0) \, d\mu_0 = 1.0. \tag{2.11}$$

As discussed earlier, fission and isotopic sources can be assigned an isotropic angular distribution so that

$$P(\mu_0) = \tfrac{1}{2} \qquad \text{(isotropic)}. \tag{2.12a}$$

In addition, to illustrate the case where a recoil source (e.g., Compton scattering) is used, we will also consider

$$P(\mu_0) = \delta(\mu_0 - \bar{\mu}) \qquad (\bar{\mu} > 0) \qquad \text{(forward)} \tag{2.12b}$$

where $\bar{\mu}$ is defined as the cosine of the average scattering angle, $\langle\theta_0\rangle$, illustrated in Fig. 2.1(b).* While somewhat crude, the use of an average angle will give some feeling for the forward emission case without the lengthy algebra required for more exact distribution. This model may also be used to represent the important case of a Thermonuclear-Electric Cell (Sec. 7.7). Magnetic fields are employed in this cell to obtain a well-collimated ion beam that approaches the ideal of $\bar{\mu} = 1.0$.

Some typical values of $\bar{\mu}$ are given in Table 2.2 for the important case of Compton scattering, and as expected, the distribution is

Table 2.2— AVERAGE ANGLE AND ENERGIES FOR COMPTON ELECTRONS

Gamma Energy (MeV)	Average Compton Electron Properties	
	MeV	$\bar{\mu}$
1.25	0.59	0.85
6.13	3.92	0.96
10.0	6.80	0.98

strongly peaked forward. The same concept can be applied to proton scattering by fast neutrons, high-energy electrons (δ-rays) ejected by fast ions, etc. Returning to Eq. (2.10), we can now carry out the integration

$$\frac{J(\Delta)}{S_0 q} = \begin{cases} \frac{1}{2}(1 - \sqrt{\Delta}) & \text{(isotropic)} \quad (2.13a) \\ 1 - h(\sqrt{\Delta} - \bar{\mu}) & \text{(forward)} \quad (2.13b) \end{cases}$$

*The symbol $\delta(x)$ will be used throughout the text to represent the *Dirac Delta function*. It is defined to have the properties

$$\delta(x) = \lim_{\epsilon \to 0} \begin{cases} 0 & [x < -(\epsilon/2)] \\ 1/\epsilon & [-(\epsilon/2) < x < (\epsilon/2)] \\ 0 & [x < (\epsilon/2)]. \end{cases}$$

It is normalized such that

$$\int_{-\infty}^{\infty} \delta(x)\, dx = 1.0.$$

An immediate consequence of these properties is that

$$\int_{-\infty}^{\infty} f(\xi)\, \delta(\xi - y)\, d\xi = f(y).$$

where h(x) is a step function such that

$$h(x) = \begin{cases} 1 & (x > 0) \\ 0 & (x \leq 0) \end{cases} \tag{2.14}$$

and Δ was defined earlier in Eqs. (2.7) and (2.8). As expected, J is a maximum when $\Delta = 0$, corresponding to a short circuit.

In the case of isotropic emission, the short-circuit value is half of the total current from the source ($S_0 q$) because half of the particles are directed into the emitter support and lost. With forward emission, this does not happen, so all particles are collected under no load conditions.

For voltage calculations, it is convenient to use the short-circuit current to define a fractional current $J_F(\Delta)$ given by

$$J_F(\Delta) = \frac{J(\Delta)}{J(0)} . \tag{2.15}$$

A plot of the fractional current is shown in Fig. 2.3 as a function of the reduced voltage β for various values of the relativistic parameter R. [Equation (2.8) was used to write Δ as a function of β and R for this

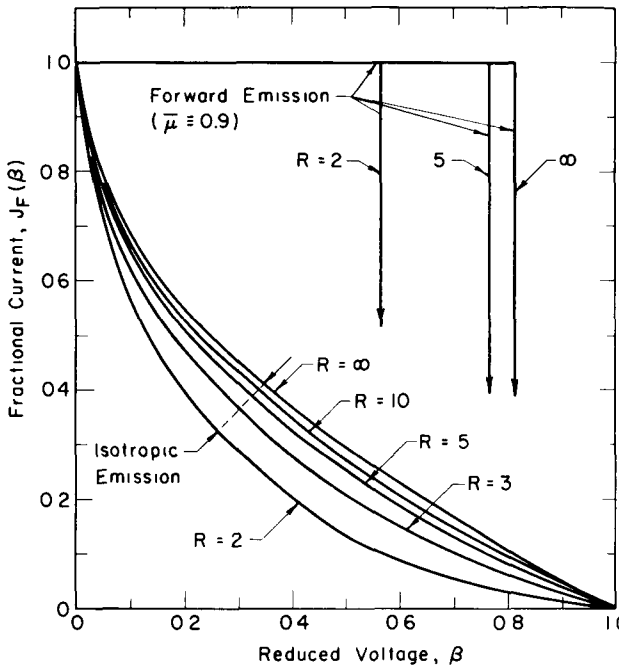

Fig. 2.3 — Fractional current vs the reduced voltage for an ideal planar cell.

plot.] Forward emission is illustrated using $\bar{\mu} = 0.9$, which, as seen in Table 2.2, is typical of Compton scattering.

With a voltage present, some of the particles are unable to overcome the potential barrier so J_F is reduced—gradually in the isotropic case and in a step-like fashion in the idealized forward emission case.

According to Eq. (2.13b), the fractional voltage β_m corresponding to this step or maximum voltage for forward scattering occurs when $\sqrt{\Delta} = \bar{\mu}$. Use of Eq. (2.8) then gives

$$\beta_m = \frac{R}{2}\left[1 - \sqrt{1 - \frac{4(R-1)\bar{\mu}^2}{R^2}}\right]. \tag{2.16}$$

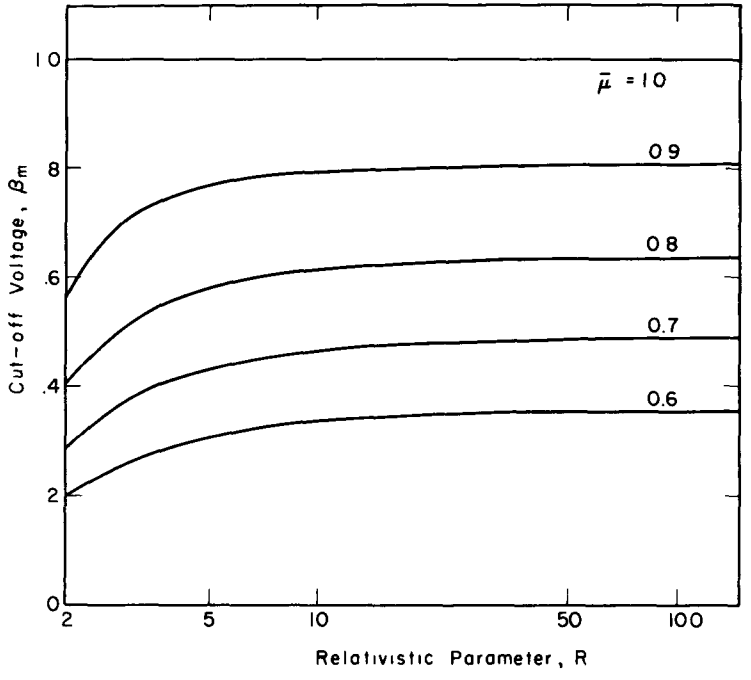

Fig. 2.4—Maximum or cut-off voltage vs R for forward emission.

For convenience this is plotted in Fig. 2.4 for select values of $\bar{\mu}$. Note the limiting values are:

$$\beta_m = \begin{cases} \bar{\mu}^2 & (R = \infty, \text{ non-relativistic}) \quad (2.16a) \\ 1 - \sqrt{1 - \bar{\mu}^2} & (R = 2, \text{ relativistic limit}). \quad (2.16b) \end{cases}$$

The physical interpretation of this result is quite simple. As β increases, the collection cone, according to Eq. (2.7), continually decreases until it is smaller than the cone defined by $\bar{\mu}$, after which nothing more can be collected. The intersection of the two cones defines β_m.

The discontinuity obviously occurs because we have assumed an idealized delta function angular distribution. While this will not occur in practice, it is not a bad approximation for strongly peaked distributions such as Compton scattering. The actual distribution will simply cause a "rounding" of the step function.

As in Fig. 2.3, we will continue in future plots to illustrate forward emission for the arbitrary values of $\bar{\mu} = 0.9$ and R = 2, 5, and ∞. The results can, however, be easily adjusted for other parameters using Fig. 2.4.

Another feature of the current–voltage curves of Fig. 2.3 deserving comment is that, for a fixed value of β, larger currents occur as R increases toward infinity—the non-relativistic case. Care must be exercised in the interpretation of this observation since, for a given type of particle, T_0 decreases as R increases. Then, since the reduced voltage β is normalized to (T_0/q), the requirement that it remain constant implies that the operating voltage V^+ must increase with decreasing R. This in effect forces the more relativistic particles to face a larger barrier and reduces the current below the R = ∞ line.

This point is vividly illustrated by the alternate presentation of the isotropic emission case shown in Fig. 2.5. Here J_F is plotted

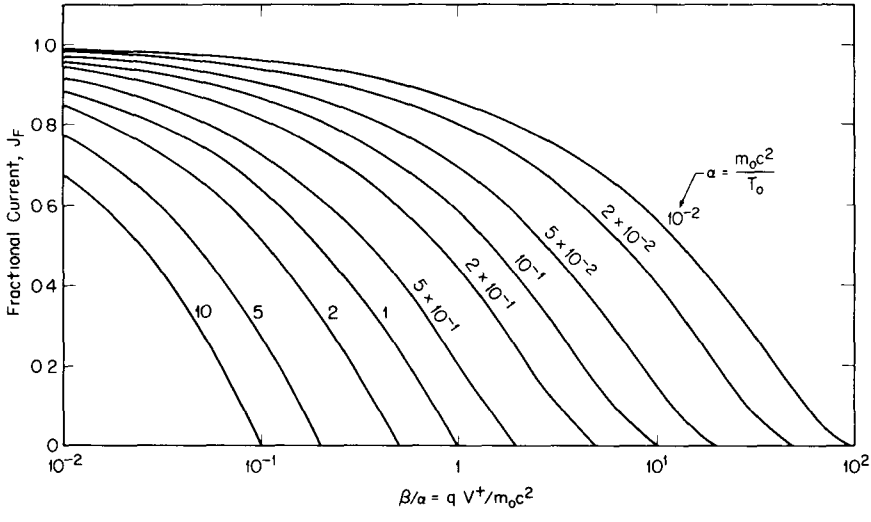

Fig. 2.5—Alternate plot of the current–voltage characteristic.

against qV^+/m_0c^2 instead of β. This represents a simple transformation since

$$\frac{qV^+}{m_0c^2} = \frac{\beta}{\alpha} \tag{2.17}$$

where

$$\alpha \equiv \frac{m_0c^2}{T_0} \rightarrow \begin{cases} \infty & \text{(non-relativistic case)} \\ 0 & \text{(relativistic limit).} \end{cases} \tag{2.17a}$$

The relativistic correction factor of Eq. (2.8c) may now be written in terms of β/α and $1/\alpha$:

$$\chi = \left[\frac{2 + 1/\alpha}{2(1 + 1/\alpha) - \beta/\alpha}\right]. \tag{2.18}$$

As one would expect, this figure shows for a given voltage V^+ that the current increases with decreasing α, i.e., with increasing initial particle energy.

Note that here, due to the different initial energies, the various curves end at different maximum voltages, whereas the previous "β-plot" normalized all the curves to the same end point. This affords a convenience in presentation so β-plots are generally preferred. However, they can be misleading unless the preceding point of interpretation is kept in mind.

2-3.4 Cell Efficiency

The idealized cell efficiency η_c^* is defined as

$$\eta_c^* = \frac{\text{(power output)}}{\text{(power input associated with charged particles)}}$$

$$= \frac{J(V^+)\ V^+A_c}{S_0T_0A_E} = \frac{J(\beta)\ \beta\ A_c}{S_0q\ A_E} \equiv \frac{I(\beta)\ \beta}{S_Tq}. \tag{2.19}$$

The collector and emitter areas, A_c and A_E, respectively, are included because of the normalization of J and S_0 to a unit area. Of course, in the parallel-plate case the area ratio is unity. Otherwise, it is convenient to introduce the *total* current I and the *total* source-emission rate S_T.

Note that the power input is defined as that associated with the initial energy of the charged particles and not the total energy input to the cell. The difference is most easily illustrated in the case of a cell

operating on Compton electrons. Only a fraction of the total energy input represented by the energy carried by the gamma beam will be transferred to Compton electrons. Many gammas may pass through the emitter plate without scattering, and others may undergo unwanted reactions such as pair production and photoelectric emission. Thus, the overall efficiency η_T^* is related to the cell efficiency by the relation

$$\eta_T^* = \eta_{cr} \cdot \eta_c^* \tag{2.20}$$

where η_{cr} represents the fraction of the total input energy that is transferred to the current carrying charged particles. While η_{cr} is typically small for a gamma source, it may approach unity for isotope and fission sources.

Although the overall efficiency is of ultimate importance, at this point we are mainly interested in the cell efficiency since it is a direct measure of the conversion of kinetic to potential energy. In fact, note that for a plate-type cell (as opposed to the DVE cell discussed later) an alternate definition of η_c^* is

$$\eta_c^* = \frac{\begin{matrix}\text{(particles per sec} \\ \text{reaching the collector)}\end{matrix} \times \begin{matrix}\text{(change in potential} \\ \text{energy per particle)}\end{matrix}}{\begin{matrix}\text{(particles per sec} \\ \text{emitted by the source)}\end{matrix} \times \begin{matrix}\text{(initial kinetic} \\ \text{energy per particle)}\end{matrix}}. \tag{2.21}$$

If we use the current relations given in Eqs. (2.13a and b), Eq. (2.19) or (2.21) becomes

$$\eta_c^* = \begin{cases} \dfrac{\beta}{2}(1 - \sqrt{\Delta}) & \text{(isotropic)} \quad (2.22a) \\ \beta\,[1 - h(\sqrt{\Delta} - \bar{\mu}) & \text{(forward).} \quad (2.22b) \end{cases}$$

These results are plotted in Fig. 2.6. In either case, it is seen that the maximum obtainable efficiency decreases with decreasing R, i.e., more relativistic particles. This is because some of the energy associated with the relativistic-mass increase is always unavailable for conversion.

An equation for the point of maximum efficiency for isotropic emission can be found by setting $d\eta_c^*/d\beta = 0$. This gives

$$\beta_P^3 - \frac{3R\beta_P^2}{2} + \frac{1}{4}(R + \frac{9}{4}R^2 - 1)\beta_P + \frac{R(1-R)}{4} = 0 \qquad \text{(isotropic)} \tag{2.23a}$$

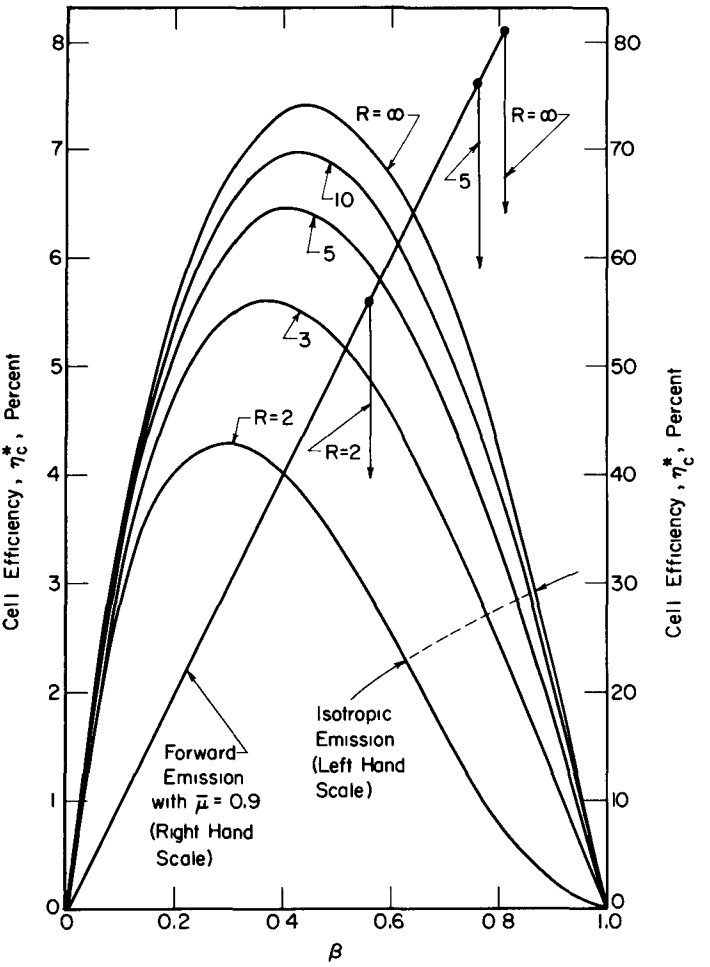

Fig. 2.6 — Efficiency vs reduced voltage for an ideal planar cell.

where β_P is the fractional voltage corresponding to the maximum efficiency for a given value of R.

In forward emission, the maximum efficiency occurs at the cut-off voltage, so the corresponding equation is

$$\beta_P^2 - R\beta_P + (R-1)\bar{\mu}^2 = 0 \qquad \text{(forward)}. \tag{2.23b}$$

In the non-relativistic limit ($R \to \infty$), the solution is found to be

$$\beta_P = \begin{cases} 4/9 & \text{(isotropic)} \quad (2.24a) \\ \bar{\mu}^2 & \text{(forward)} \quad (2.24b) \end{cases}$$

corresponding to maximum efficiencies of 7.42% and $\bar{\mu}^2$, respectively, in agreement with Fig. 2.6.

2-3.5 Electrode Heating

Any kinetic energy that is not converted to potential energy will ultimately be converted to heat. As discussed in Chap. 1, this heat may be of value in topping cycles. If not, it simply represents an energy loss, but in any case, provisions may be needed to insure proper heat removal so that the electrode structure is not harmed.

The division of the heat energy deposition rate between the emitter and collector will vary, depending upon the operating voltage. The energy deposited in the emitter per square centimeter per second, labeled E_E, is given by the rate of energy released by the source less that carried away to the collector; i.e.,

$$E_E(\Delta) = S_0T_0 - J(\Delta)\frac{T_0}{q}. \tag{2.25}$$

Use of the earlier current relations gives

$$\frac{E_E(\Delta)}{S_0T_0} = \begin{cases} \frac{1}{2}(1+\sqrt{\Delta}) & \text{(isotopic)} \quad (2.26a) \\ h(\sqrt{\Delta}-\bar{\mu}) & \text{(forward).} \quad (2.26b) \end{cases}$$

This result is shown in Fig. 2.7(a). Naturally as the voltage increases more particles "fall back" to the emitter causing increased heating in it. Note that even in the short-circuited condition ($\Delta = 0$), half of the particles in the isotropic case end up in the emitter; hence this scale begins at 0.5. For the simplified forward distribution, all particles escape from the emitter until a critical voltage is reached, which forces them all to fall back to the emitter.

The energy deposition rate per square centimeter in the collector is simply the excess kinetic energy carried by the particles reaching the collector; consequently,

$$E_c(\Delta) = \frac{J(\Delta)}{q}[T_0 - qV^+] \tag{2.27}$$

and substitution for $J(\Delta)$ gives

$$\frac{E_c(\Delta)}{S_0T_0} = \begin{cases} \frac{1}{2}(1-\beta)(1-\sqrt{\Delta}) & \text{(isotropic)} \quad (2.28a) \\ (1-\beta)[1-h(\sqrt{\Delta}-\bar{\mu})] & \text{(forward).} \quad (2.28b) \end{cases}$$

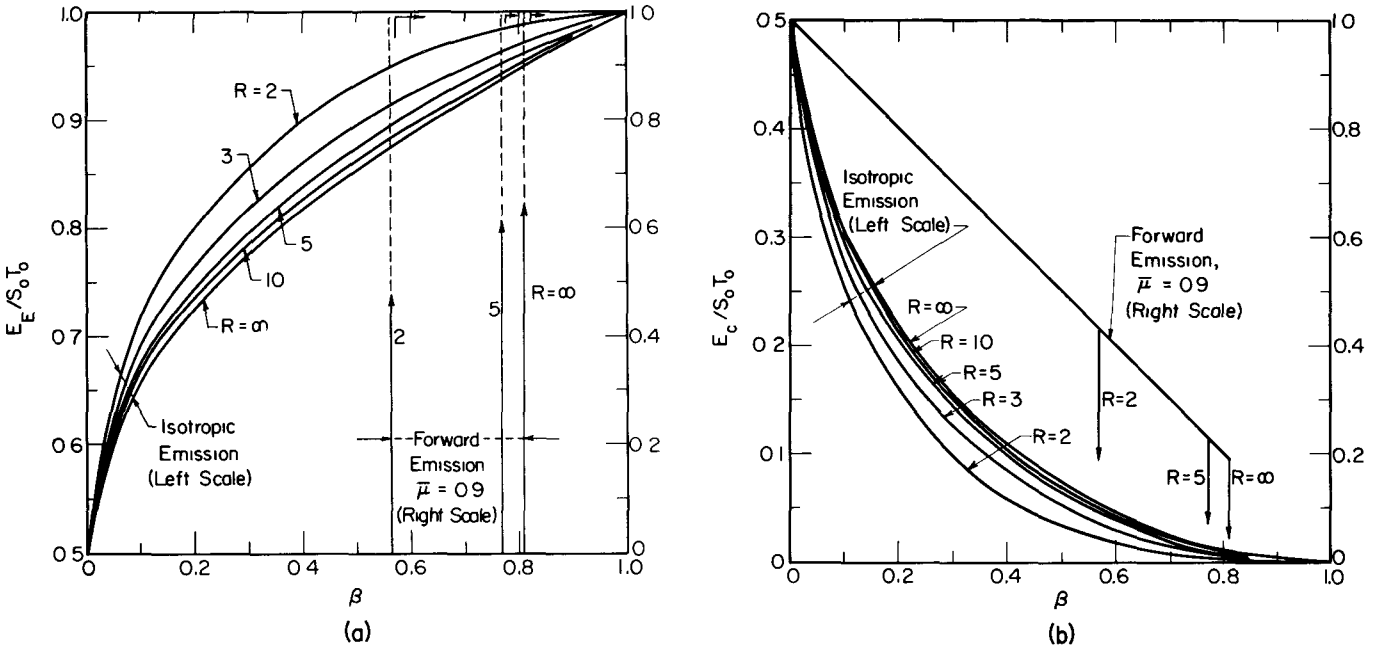

Fig. 2.7 — Electrode heating curves for an ideal planar cell. (a) Emitter heating. (b) Collector heating.

As shown in Fig. 2.7(b), collector heating decreases with increasing voltage. At higher voltages fewer particles reach the collector, and those that do have less excess energy (the latter point explains the linear decrease in the heating curve for forward emission although the current remains constant below the maximum or "cut-off" voltage).

It will be noted that in the range of operation of $\beta \approx 0.4$ to 1.0, corresponding to the maximum efficiency, the heating of the emitter dominates. As a result, the ability to cool this electrode may be a critical factor in cells designed for high power.

2-3.6 Energy-Angle Distribution at the Collector

The detailed energy-angle distribution of particles striking the collector may be important in some designs. For example, in space applications it may be important to minimize the weight of the collector. A particle striking the surface at an oblique angle will not require as thick a collector as one entering perpendicularly. If weight is critical, it may be desirable to select a thickness that will stop only those particles entering at angles larger than some select value, say 30° from the perpendicular. (A detailed design for an electrostatic propulsion unit that permitted some transmission is discussed in Sec. 7-4.1. This involved a spherical design in which the collector represented a significant portion of the cell weight.)

Another reason for interest in the energy-angle distribution is that, as shown later in Chap. 5, this is an important factor in the determination of the secondary electron yield at the collector.

In the present case, the energy of a particle reaching the collector is easily found from conservation of energy as given in Eq. (2.1). The angular distribution, however, requires more algebra.

First, Eqs. (2.1) and (2.2) are combined to give a relation between the initial and final direction cosines μ_0 and μ_f, respectively, with Δ, defined in Eq. (2.8), as a parameter. The result is

$$\mu_f^2 = 1 - \left(\frac{1 - \mu_0^2}{1 - \Delta}\right). \tag{2.29}$$

The final and initial angle distributions are related by the normal method of change of variable in density functions, i.e.,

$$P(\mu_f) = P(\mu_0)\left|\frac{d\mu_0}{d\mu_f}\right| \tag{2.30}$$

where $P(\mu_j)\, d\mu_j$ is the probability that a particle will have a direction cosine lying in $d\mu_j$ at μ_j. Evaluation of the derivative using Eq. (2.29) gives:

$$P(\mu_f) = \frac{(1 - \Delta)\mu_f \, P(\mu_0)}{\sqrt{\mu_f^2 + \Delta \, (1 - \mu_f^2)}}. \tag{2.31}$$

After renormalization such that the integral of $P(\mu_f)$ over the collection cone ($\mu_f > 0$) is unity for any voltage Δ, the two cases of interest here result in distributions of the form:

$$P(\mu_f) = \begin{cases} \dfrac{(1 + \sqrt{\Delta})\mu_f}{\mu_f^2 + \Delta(1 - \mu_f^2)} & \text{(isotropic)} \quad (2.32a) \\ \delta\left(\mu_f - \sqrt{\dfrac{\bar{\mu}^2 - \Delta}{1 - \Delta}}\right) & \text{(forward).} \quad (2.32b) \end{cases}$$

The isotropic case is shown in Fig. 2.8, where $P(\mu_f)$ is plotted as a function of μ_f for select Δ.

For a short circuit ($\Delta = 0$), there is no potential present to distort the initial distribution so $P(\mu_f)$ also turns out to be isotropic, i.e., $P(\mu_f) = 1/2$. However, as Δ increases (increasing voltage), the distribution becomes more and more peaked in the forward direction.

In the simple forward emission model there is a one-to-one relation between μ_f and $\bar{\mu}$, and this is shown graphically in Fig. 2.9. Note that $\mu_f = \bar{\mu}$ for a short circuit ($\Delta = 0$) while the intercept for $\mu_f = 0$ corresponds to the maximum voltage point observed in earlier plots.

2-3.7 Voltage Build-up Times and Periodic Discharge Operation

The calculations thus far have assumed steady state operation. Voltage build-up characteristics are of interest in connection with start-up and also for special applications like timing circuits.

The cell may be viewed as a parallel plate capacitor with capacitance C defined as

$$C = \epsilon_0 \frac{A_c}{d} = \frac{Q^+}{V^+} \tag{2.33}$$

where Q^+ is the total charge on the collector plate, A_c is its area, d is the plate spacing, and ϵ_0 is the dielectric constant for vacuum.

We visualize that an open circuit condition is used during the voltage build-up. At some point, the cell is discharged by suddenly switching the load into the circuit. Since leakage currents are neglected in the ideal cell, the entire cell current contributes to the voltage build-up, i.e.,

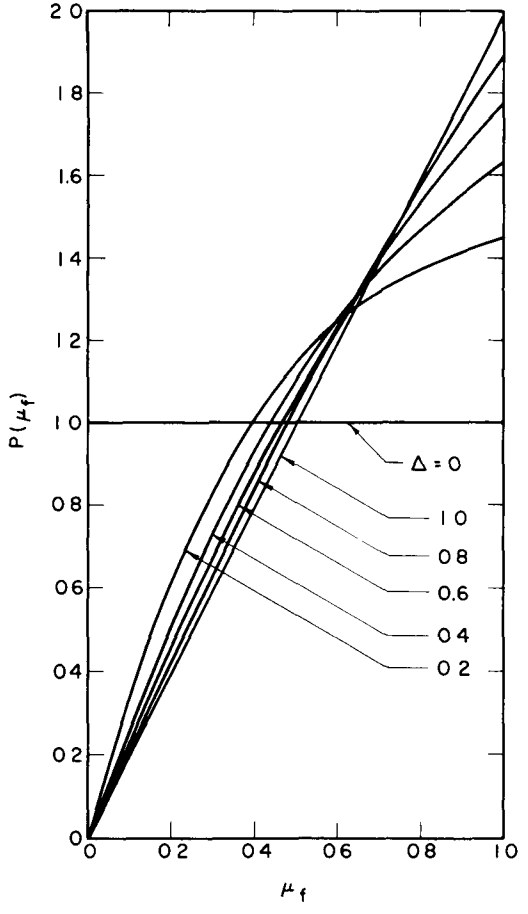

Fig. 2.8—Angular distribution of particles reaching the collector. (For isotropic emission.)

$$\frac{dQ^+}{dt} = A_c\, J(\beta). \tag{2.34}$$

Combining Eqs. (2.33) and (2.34) and integrating from time t = 0 to t_β corresponding to a reduced voltage β gives

$$\frac{t_\beta}{t_0} = \int_0^\beta \frac{d\beta'}{J_F(\beta')} \tag{2.35}$$

where t_0 is a characteristic time constant defined as

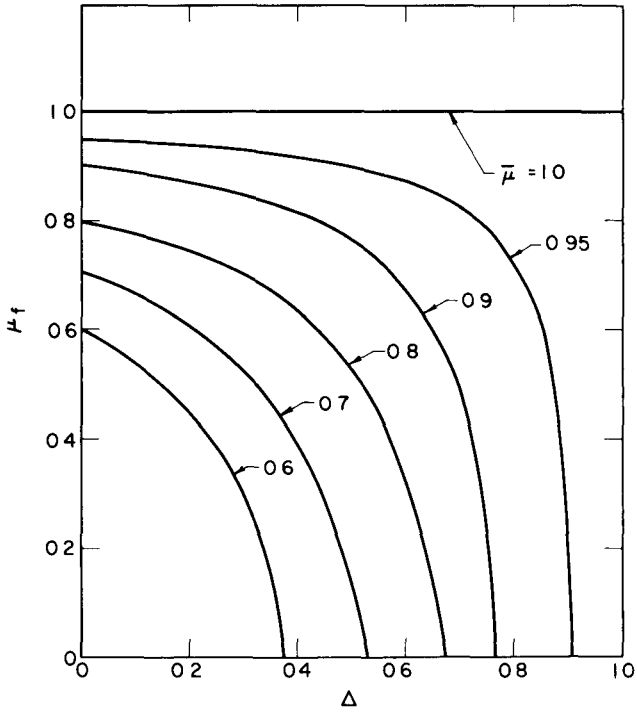

Fig 2.9 — Direction cosine at the collector vs reduced voltage. (For forward emission.)

$$t_0 = C\left[\frac{T_0/q}{I(0)}\right] \equiv CR_c \tag{2.36}$$

and I(0) is the short-circuit current or A_c J(0). Here the quantity $(T_0/q)/I(0)$, the maximum voltage divided by the short circuit current, represents a resistance which we define as the "cell impedance" R_c, so t_0 can be identified as a conventional RC time constant. (The significance of the cell impedance is discussed further in Chap. 6.)

The integration indicated in Eq. (2.35) may now be carried out with the earlier results for the fractional current $J_F(\beta)$. The result for the *isotropic emission* case is found to be

$$\frac{t_\beta}{t_0} = \frac{R-1}{R-2}\ln\Omega - \sqrt{R-1}\,\arcsin\gamma \tag{2.37}$$

where

$$\Omega \equiv \frac{\left(1-\frac{\beta}{R-1}\right)\left(R-2\beta+(R-2)\sqrt{\frac{\beta(R-\beta)}{R-1}}\right)}{\left(1-\beta\right)\left(R-2\beta-(R-2)\sqrt{\frac{\beta(R-\beta)}{R-1}}\right)} \tag{2.38a}$$

$$\gamma \equiv \frac{2}{R}\sqrt{\beta(R-\beta)}. \tag{2.38b}$$

Considerable simplification occurs for the limiting values of R; namely,

$$\frac{t_\beta}{t_0} = \begin{cases} 2\ln\left[(1-\sqrt{\beta})^{-1} - \sqrt{\beta}\right] & (R=\infty) \quad (2.39a) \\ \left[\frac{\beta+\sqrt{\beta(2-\beta)}}{1-\beta}\right] - \arcsin\sqrt{\beta(2-\beta)} & (R=2) \quad (2.39b) \end{cases}$$

A plot of t_β/t_0 is shown in Fig. 2.10. The forward emission case is also shown, and being somewhat simpler it perhaps provides added insight. In this case, integration of Eq. (2.35) gives

$$\frac{t_\beta}{t_0} = \begin{cases} \beta & (\beta < \beta_m) \quad (2.40a) \\ \infty & (\beta > \beta_m) \quad (2.40b) \end{cases}$$

where β_m, defined in Eq. (2.16), is the maximum voltage achievable in steady state operation. The linear dependence of t_β on β occurs for $\beta < \beta_m$ because the charging current is independent of β. However, there is a discontinuity at the maximum voltage where t_β approaches ∞.

The curves for isotropic emission are also nearly linear at very low voltages ($\beta < 0.2$), but since the charging current is reduced as β increases, t_β increases dramatically at higher β. An infinite time is required to reach $\beta = 1.0$ since the current goes to zero at this limit.

These results can also be used to calculate the cell efficiency, ϵ_c^*, for periodic discharge operation. Since cell currents are typically small, we will assume that the discharge time can be neglected relative to the charging time. Then ϵ_c^* is defined in a manner similar to the steady state efficiency (Sec. 2-3.4), namely:

$$\epsilon_c^* = \frac{(\text{energy stored in time } t_\beta)}{\begin{array}{c}(\text{particle kinetic energy} \\ \text{released in time } t_\beta)\end{array}} = \frac{E_s(\beta)}{S_0 T_0 t_\beta A_E} \tag{2.41}$$

where, by analogy with a capacitor, the stored energy is given as

$$E_s(\beta) = \frac{1}{2} C(V^+)^2 = \frac{CT_0^2}{2q^2} \beta^2. \tag{2.42}$$

Combining these equations, we find

$$\epsilon_c^* = \frac{J(0)\beta^2/2qS_0}{t_\beta/t_0} \tag{2.43}$$

which is plotted in Fig. 2.11 using t_β/t_0 from the previous results.

It is seen that the efficiency for periodic operation is always less than that for steady state operation shown in Fig. 2.6. Since the voltage

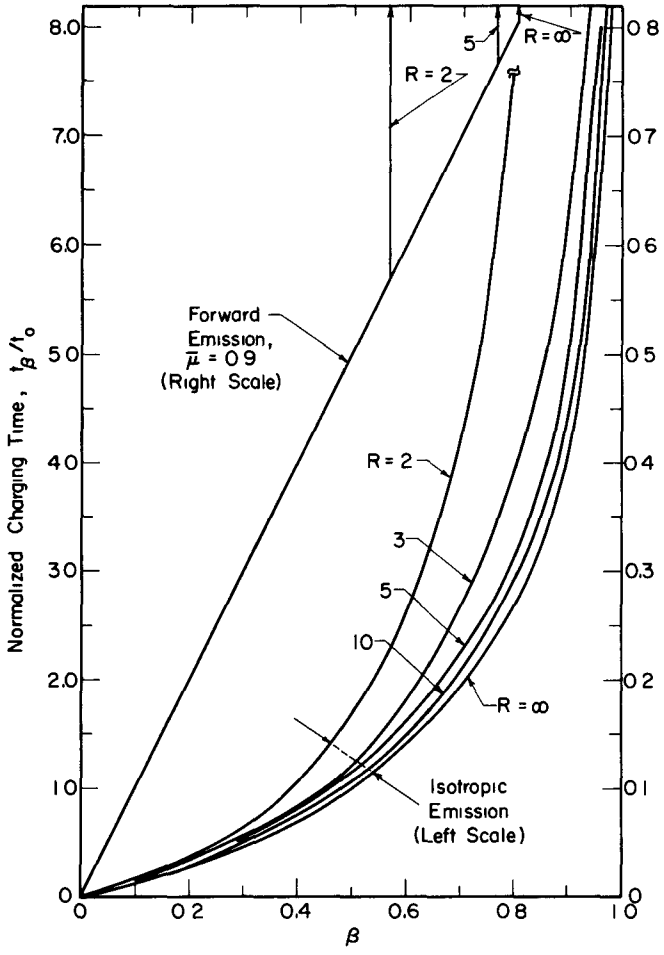

Fig. 2.10 — Open-circuit charging time for an ideal planar cell.

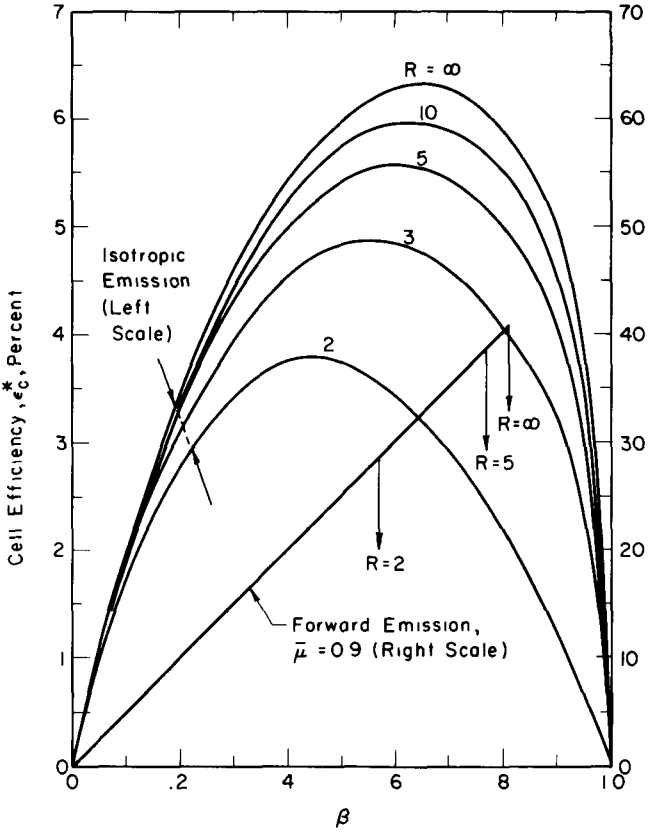

Fig. 2.11—Cell efficiency for an ideal planar cell charged periodically to the reduced voltage β.

varies from zero to its value β at discharge, much of the time it is "off-optimum." For example, we saw earlier that the voltage build-up is linear with time in the forward emission case. Thus the average voltage for charging from 0 to β is simply $\beta/2$. Since the current is constant, the efficiency will be just half of that corresponding to steady state operation at β and indeed this is seen to be the case. For isotropic emission the time spent at higher voltages dominates so that the difference between steady state and periodic operation is much less; e.g., $[\epsilon_c^*]_{max} \approx 6.3\%$ vs $[\eta_c^*]_{max} \approx 7.4\%$ for $R = \infty$.

2-4 IDEALIZED SPHERICAL ELECTRODE CELLS

The geometry described here consists of concentric emitter and collector electrodes as shown in Fig. 2.12. The analysis is somewhat

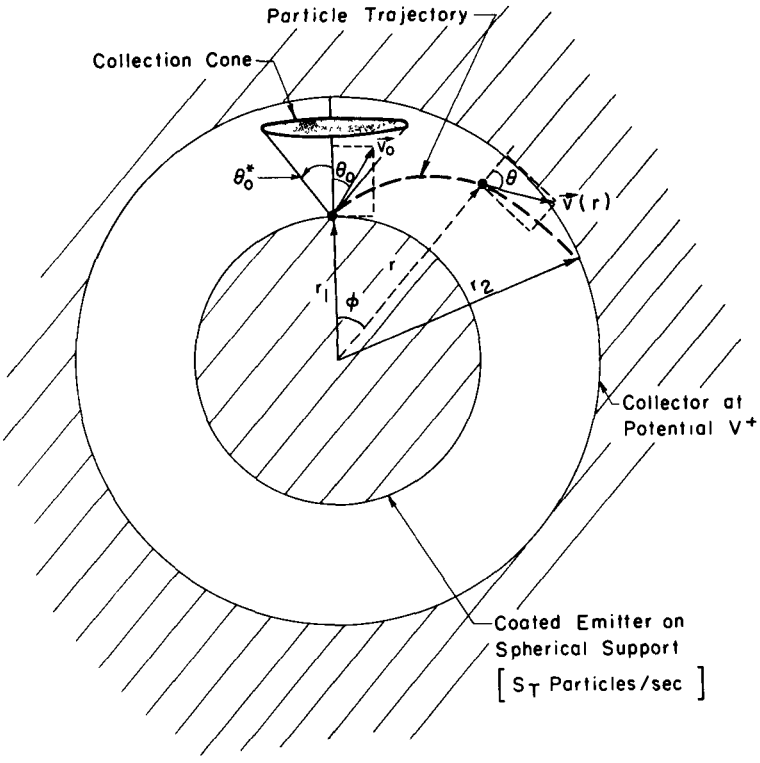

Fig. 2.12—Geometry of the idealized spherical cell.

more complicated than for parallel plate, so we shall consider current-voltage and efficiency calculations in some detail.

Again we will restrict our attention to isotropic emission, i.e., we will assume that the emitter has a thin coating of radioactive or fissioning material. Once the isotropic case is solved, the extension to forward emission is quite straightforward; however, this is left to the reader. For one reason, the spherical geometry does not readily lend itself to forward scattering. An internal source-scatterer might approach forward emission; however, the important case of an external source illustrated earlier in Fig. 2.1 will, in general, not work because the beam will always hit some parts of the electrode "off-normal."

As before, we assume that any particle hitting the support plate–emitter is absorbed. This ignores the possibility of reflection or transmission of particles entering almost tangentially to the emitter surface. However, such events should not be frequent enough to cause a serious error. We must remember though that the assumption of

complete absorption fails for small inner radii, i.e., as $r_1 \to 0$. (In practice, this may not be a problem since structure requirements will generally require larger values of this radius.)

2-4.1 Current–Voltage Characteristics

Consider a particle born with velocity $\vec{v}_0$ as shown in Fig. 2.12. The electric field created in the cell represents a central force, so that, as discussed in Appendix B-1.2, the particle trajectory will be in a single plane.

Conversion of energy again requires that

$$qV^+ = [m(v_0) - m(v_f)]c^2 \tag{2.44}$$

where v_f is the final velocity at the collector, i.e., at $r = r_2$.

For spherical geometry, conservation of angular momentum is used in place of linear momentum. Using Eq. (B.20), we can write

$$r_1 v_0\, m(v_0) \sin \theta_0 = r_2 v_f\, m(v_f) \sin \theta_f. \tag{2.45}$$

Following the procedure used for the parallel plate case, we search for the maximum initial angle θ_0^* that the particle can have and still be collected. This occurs when the angle at the collector θ_f is just equal to $\pi/2$ or, alternately, when θ_0 itself reaches $\pi/2$. (This limit, which we will designate as a "surface limit," comes from our assumption that all particles striking the emitter are absorbed.) If θ_f is set equal to $\pi/2$, Eq. (2.45) gives

$$\theta_0^* = \sin^{-1}\left[\frac{r_2}{r_1}\frac{v_f\, m(v_f)}{v_0\, m(v_0)}\right] \tag{2.46}$$

which must be solved simultaneously with Eq. (2.44). The result is

$$\theta_0^* = \max.\begin{cases} \sin^{-1} 1 & \text{(surface limit)} \qquad (2.47a) \\ \sin^{-1}\left(\dfrac{r_2}{r_1}\sqrt{1-\Delta}\right) & \text{(potential limit).} \qquad (2.47b) \end{cases}$$

The characteristic parameter Δ which originally occurred in the parallel plate analysis [Eq. (2.8)] again appears here.

In this case it is convenient to deal with the total current rather than the current density. If S_T is the total emission rate (particles per second) from the source, integration over the collection cone shown in Fig. 2.12 gives the total current $I(\Delta)$ in amperes as

$$\frac{I(\Delta)}{(S_T q/2)} = \begin{cases} 1 & (\Delta < \Delta_M) \qquad (2.48a) \\ 1 - \sqrt{1 - \left(\frac{r_2}{r_1}\right)^2 (1 - \Delta)} & (\Delta > \Delta_M) \qquad (2.48b) \end{cases}$$

where

$$\Delta_M = \left[1 - \left(\frac{r_1}{r_2}\right)^2\right]. \qquad (2.49)$$

The dividing value of Δ, labeled Δ_M, corresponds to the point where the two limits on θ_0^* given in Eqs. (2.47a and b) are equal.

A plot of this voltage–current characteristic is shown in Fig. 2.13 for selected values of the radius ratio r_1/r_2, and the two extreme

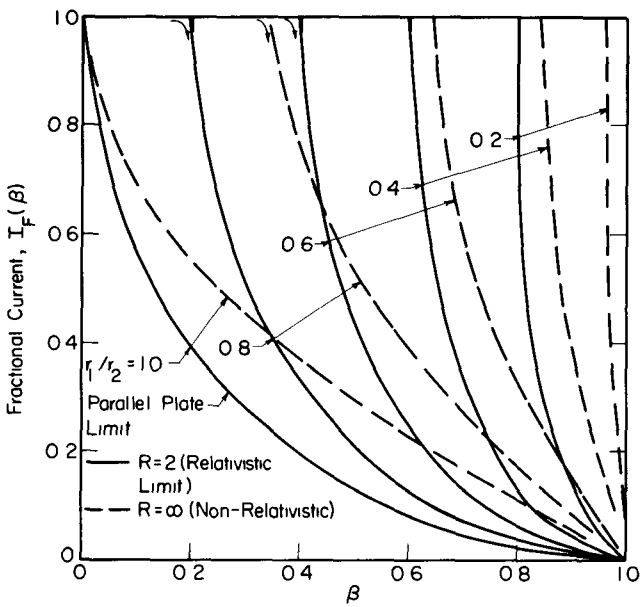

Fig. 2.13—Current–voltage characteristics for an ideal spherical cell. (Isotropic emission, r_1 = inner and r_2 = outer radius.)

values of R—namely, R = ∞ (non-relativistic) and R = 2 (relativistic limit). As before, Eqs. (2.8a to d) have been used to convert from Δ to a β-plot.

The fractional current is defined as before, i.e.,

$$I_F(\beta) \equiv \frac{I(\beta)}{I(0)}. \qquad (2.50)$$

Note that the short-circuit value in the present case is $S_T q/2$, which is exactly half of the source emission current. As stressed earlier, the reason is that a perfectly absorbing source sphere is assumed so half of the particles are lost to it upon birth.

The curves in Fig. 2.13 generally display a region of constant current followed by a rapid decrease above some critical voltage. The constant region can be explained by noting that even if a particle leaves the source at $\theta_0 = \pi/2$, it will, unlike the parallel plate case, have a non-zero component of momentum directed toward the collector. This is illustrated schematically in Fig. 2.14, where the initial

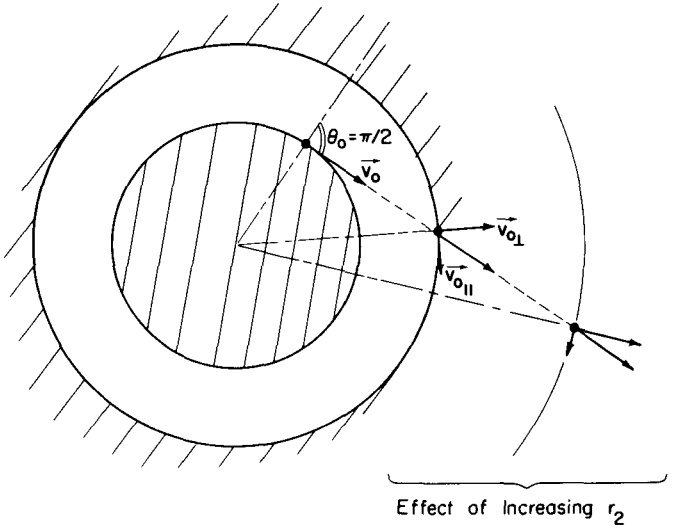

Fig. 2.14 — Momentum components in spherical cells.

velocity vector is extended and divided into parallel and perpendicular components. As a result, the voltage must build up to a finite value before it can nullify the perpendicular momentum component. It is also seen that as r_2 increases, the perpendicular component is increased at the expense of the parallel component. Then a larger voltage is required before the current begins to decrease.

In the limit as $r_2 \to \infty$, all particles will be collected up to the limiting voltage, $\beta = 1.0$. As would be expected, this characteristic of spherical geometry is shown in the next section to lead to a corresponding gain in efficiency as compared to the parallel plate case.

It will be noted that the spherical results fall between two extremes. If absorption in the source sphere is ignored, in the limit as $r_1/r_2 \to 0$, the results are identical to the parallel plate forward emission case where $\overline{\mu} = 1.0$. At the other extreme, as $r_1/r_2 \to 1.0$, the re-

sults reduce to the parallel plate calculations for isotropic emission. Thus in a sense, spherical geometry can be viewed as partly compensating for isotropic emission so that even using radioisotopic fuel, etc., one can begin to approach the ideal of forward emission.

2-4.2 Efficiency

The current from the previous section can be used to calculate the cell efficiency, η_c^*, following the definition given in Eq. (2.19). The result is shown in Fig. 2.15.

The linear increase in efficiency which occurs at lower voltages corresponds to the constant current region. Thus the maximum efficiency occurs for the limiting case of $r_2 \to \infty$, i.e., $r_1/r_2 = 0$. Again, because half of the particles are absorbed in the source sphere, the maximum is 50%. However, it is obvious that, if the source is transparent (perhaps due to a small r_1 relative to the particle range), the efficiency can approach 100%! This is, in effect, equivalent to the case of forward emission with $\overline{\mu} = 1.0$ discussed earlier.

This result is most encouraging since it seems to point the way to a practical method of obtaining high efficiencies with isotropic emission. However, a number of problems are inherent. First, there are mechanical problems associated with supporting the source sphere. (They are not insurmountable, however, and such designs are discussed in Chap. 7.) Second, the requirement of small r_1/r_2 leads to either a low power output or alternately a low power density. The power restriction occurs if small r_1/r_2 is obtained by making $r_1 \to 0$ since the source volume is then reduced. If the alternate route of making r_2 large is adopted, the total volume will be large, forcing small power densities. Also, as r_2 is increased, the weight associated with the collector increases as $(r_2)^2$ if its thickness is held constant. This may be a serious problem if the unit weight is critical as is commonly true in space applications. Thus, some engineering compromise must be made between efficiency, weight, and power requirements.

2-4.3 Other Characteristics

Because the spherical cell is an important, highly efficient geometry, the following additional characteristics are included as Figs. 2.16 to 2.18:

(1) collector and emitter heating curves.
(2) charging time curves.
(3) cell efficiency plots for periodic operation.

Again, results are shown for the two limiting cases of R = 2 and ∞ for various radii ratio.

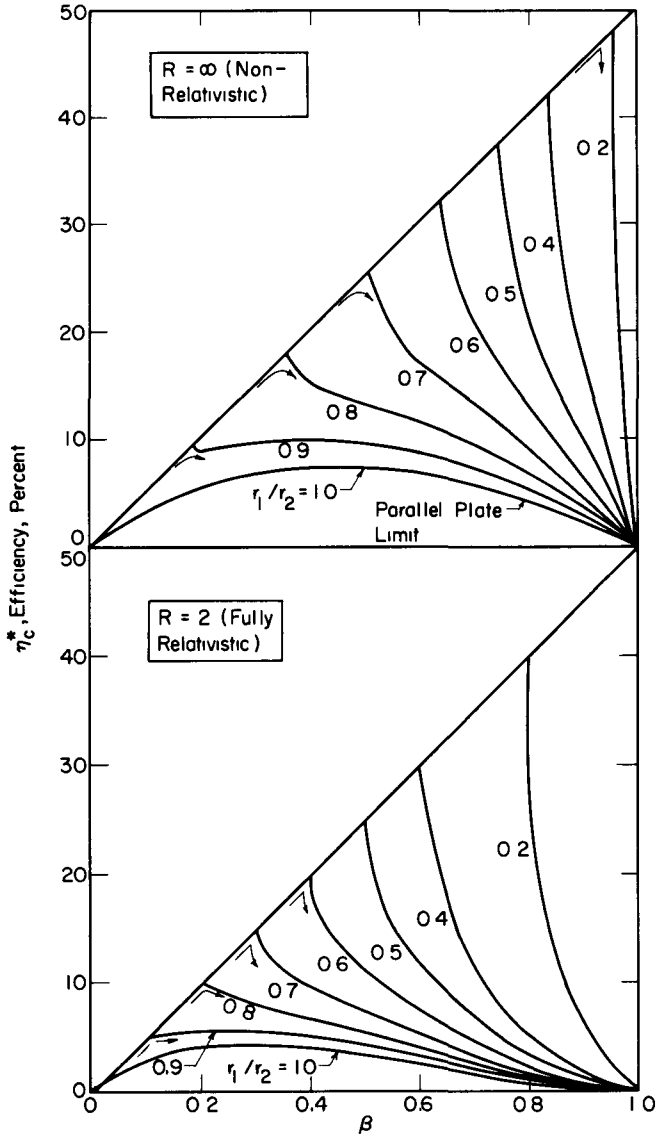

Fig. 2.15 — Cell efficiency vs reduced voltage for an ideal spherical cell. (Assumes isotropic emission and an absorbing source sphere.)

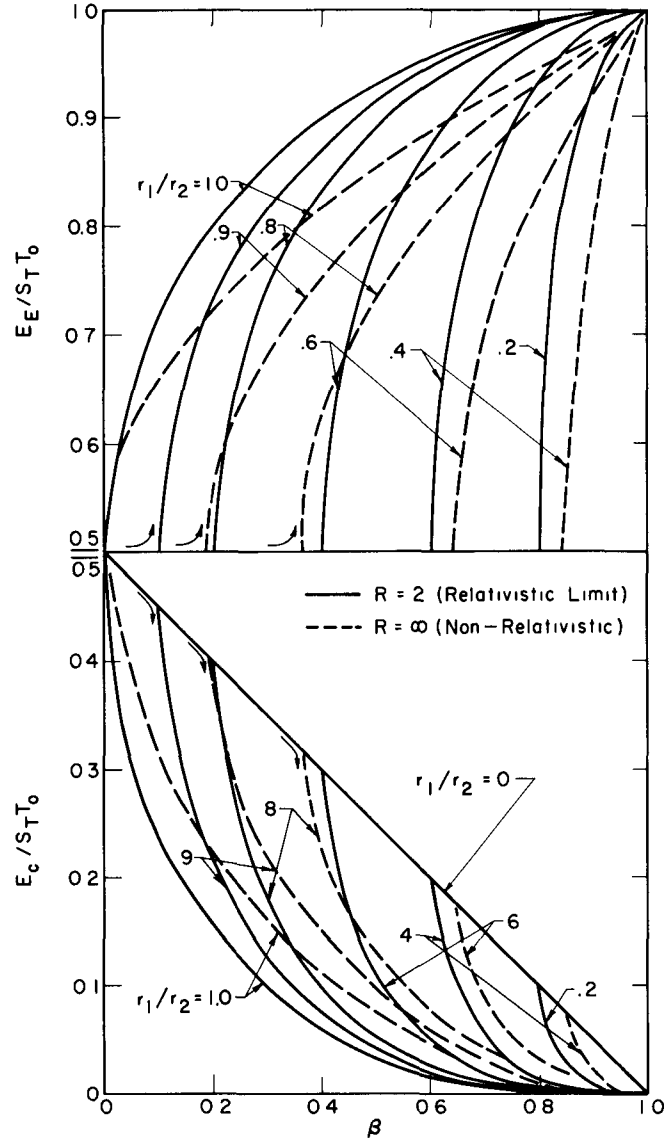

Fig. 2.16 — Electrode heating curves, ideal spherical cells. (For isotropic emission; absorbing source sphere.)

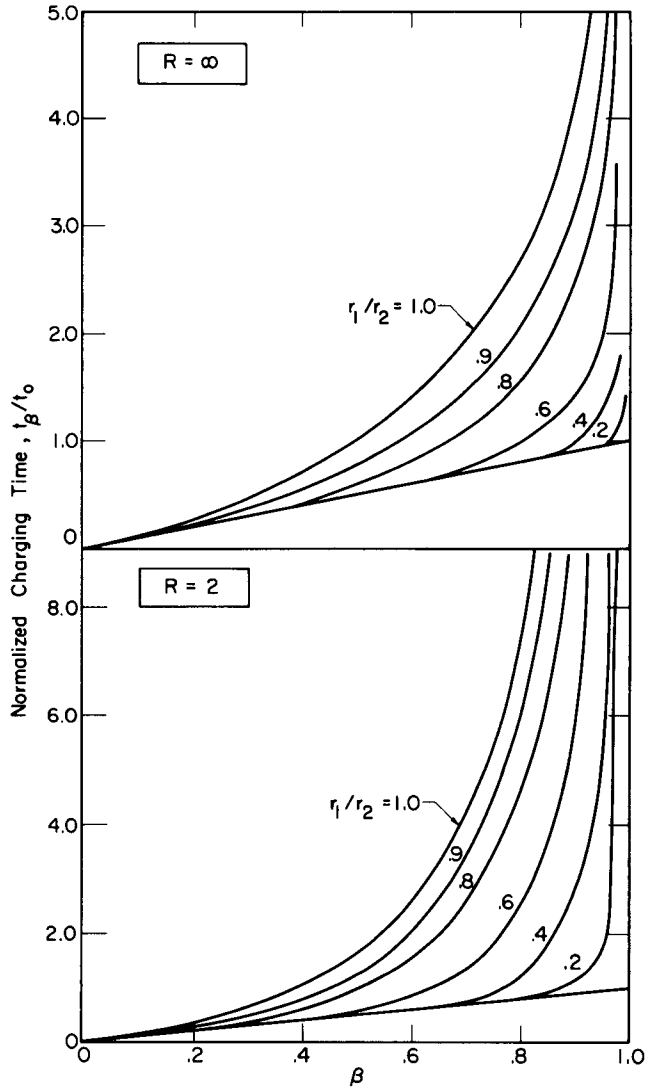

Fig. 2.17 — Open-circuit voltage build-up curves, ideal spherical cells.

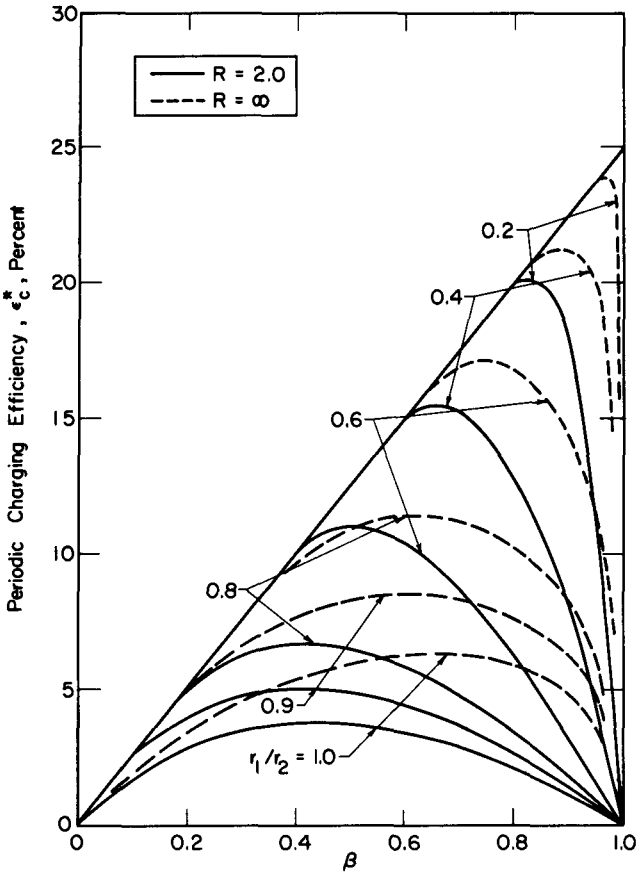

Fig. 2.18 — Periodic charging efficiency for an ideal spherical cell.

The figures are reasonably self-explanatory. As expected, the limiting envelopes for $r_1/r_2 = 0$ are consistent with the results for a parallel plate cell with forward scattering with $\bar{\mu} = 1.0$. Thus the charging time is a linear function of voltage, and the periodic charging efficiency is also linear and reaches a maximum value of 25%, which, for reasons noted earlier, is half of the steady state value. The limiting curves for $r_1/r_2 = 1.0$ again agree with the parallel plate isotropic-emission case.

2-5 IDEALIZED CYLINDRICAL CELLS

A concentric cylindrical geometry such as illustrated in Fig. 2.19 is considered next. Infinite length cylinders are assumed so that end

effects can be neglected. This should be a good approximation for the typical case of a large length to diameter ratio.

As with spherical cells, only isotropic emission is considered here, and it is envisioned that the outer surface of the inner cylinder is coated with a radioisotope or fissioning material while the outer cylinder serves as the collector. Again, the source cylinder is assumed to be a perfect absorber of the charged particles.

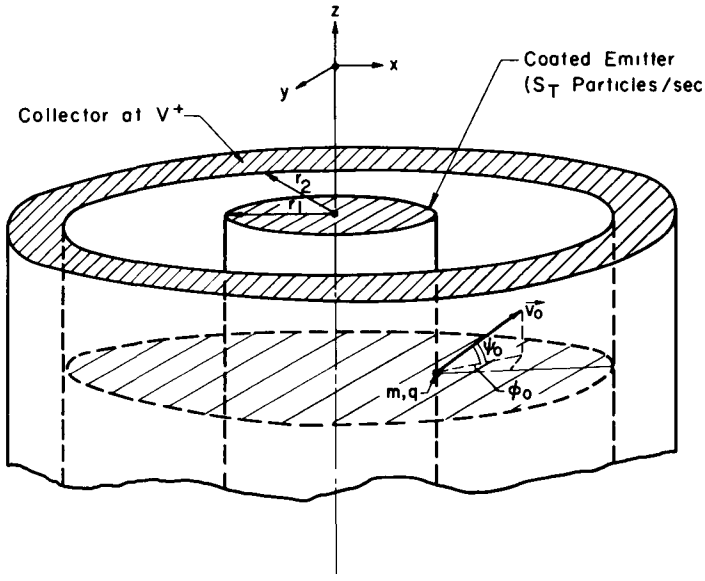

Fig. 2.19 — Concentric cylinder geometry.

The analysis is quite similar to that for the parallel plate and spherical cases; however, there are several important differences. For this reason the current–voltage characteristic is derived in some detail, but other calculations are not included.

2-5.1 Current–Voltage Characteristics

Again, we consider the conservation equations for a charged particle leaving the emitter with an initial velocity $\vec{v}_0$ and arriving at the collector with a velocity of $\vec{v}_f$ (Fig. 2.19). Corresponding subscripts are applied to the angles involved. The angle ψ is measured relative to a plane perpendicular to the z-axis, and ϕ is measured in this plane as shown. Then the conservation laws, as derived in Appendix B-1.2, are:

•*Energy*

$$qV^+ = [m(v_0) - m(v_f)]c^2 \tag{2.51}$$

•*Linear momentum* in the z direction

$$v_0\, m(v_0) \sin \psi_0 = v_f\, m(v_f) \sin \psi_f \tag{2.52}$$

•*Angular momentum*

$$r_1 v_0\, m(v_0) \cos \psi_0 \sin \phi_0 = r_2 v_f\, m(v_f) \cos \psi_f \sin \phi_f. \tag{2.53}$$

Recall that the earlier analysis required only two equations whereas three are now necessary. This adds some complexity.

To find the condition where the particle just reaches the collector, we again set ϕ_f equal to $\pi/2$ and solve these equations for the maximum value of ψ_0 in terms of the initial conditions and the radius ratio r_1/r_2. This gives

$$\psi_0^* = \cos^{-1}\left[\frac{\Delta}{1 - \left(\frac{r_1}{r_2}\right)^2 \sin^2 \phi_0}\right]^{1/2} \tag{2.54}$$

where Δ, defined in Eq. (2.8), again enters this limit.

Since, in this case there is no longer rotational symmetry about $\vec{r}$, the collection volume is distorted from the conical shape visualized in the parallel plate and spherical cases. Still, we can visualize placing a sphere of unit radius around the particle q in Fig. 2.19, and we calculate the collection current by finding the fraction of the sphere's surface which falls within allowed values of ψ_0 and ϕ_0. The current per unit length $I_l(\Delta)$ due to a source strength of S_l particles/(sec cm-length) is then

$$I_l(\Delta) = \frac{S_l q}{\pi} \int_0^{\phi_0^*} d\phi_0 \int_0^{\psi_0^*} \cos \psi_0\, d\psi_0 \tag{2.55}$$

where isotropic emission is explicitly assumed. As before, the asterisk denotes maximum values of the angles, and the fact has been used that the total collection area is four times that contained in a quadrant cut out by planes perpendicular and parallel to $\vec{z}$, which contain $\vec{r}_1$ (Fig. 2.19).

The angle ψ_0 is similar to that of the plane electrode case in that it will always be limited by the operating voltage rather than by a requirement that the emitted particles have directions which allow escape from

the fuel layer. (We again refer to these two possibilities as "potential limited" and "surface limited," respectively.) This is because the velocity component in the direction of the force vanishes when $\psi_0 = \pi/2$, so the value predicted by Eq. (2.54) will automatically be less than $\pi/2$.

In contrast, the angle ϕ_0 is similar to the angle in spherical geometry in that it may be either potential or surface limited. The former limit is found from Eq. (2.54) by setting $\cos \psi_0 = 1$, while the surface limit is again $\pi/2$.

These limits are more conveniently expressed in terms of a dividing voltage, in which case

$$\phi_0^* = \begin{cases} \pi/2 & (\Delta \leq \Delta_M) \quad (2.56a) \\ \sin^{-1}\left(\frac{r_2}{r_1}\sqrt{1-\Delta}\right) & (\Delta > \Delta_M) \quad (2.56b) \end{cases}$$

where

$$\Delta_M = \left[1 - \left(\frac{r_1}{r_2}\right)^2\right]. \quad (2.57)$$

Current–voltage curves based on Eq. (2.55) and these limits are presented in Fig. 2.20. The first integration over ψ_0 was carried out analytically, but the remaining integration was done numerically. The fractional current shown is again normalized by the short-circuit value, and for convenience Δ has been converted to a β-plot.

As might have been anticipated, these curves in general fall between the parallel plate and spherical cases for an isotropic source. The limit $r_1/r_2 = 1.0$ corresponds to the parallel plate case. Then, as r_1/r_2 is decreased, the current always falls off more rapidly than the corresponding spherical curves with the same r_1/r_2. Further, in the limit where $r_1/r_2 = 0$, the current is no longer a constant as it was in the spherical case. This is because the initial energy of the particles associated with the axial or z-component of momentum is not useful in overcoming the potential barrier.

Analytic expressions may be obtained for three limiting cases. First, under short-circuit conditions, i.e., as $\Delta \to 0$, both ψ_0^* and ϕ_0^* are $\pi/2$. Then integration of Eq. (2.55) gives

$$I_l(0) = \frac{1}{2} S_l q \qquad (\Delta = 0). \quad (2.58)$$

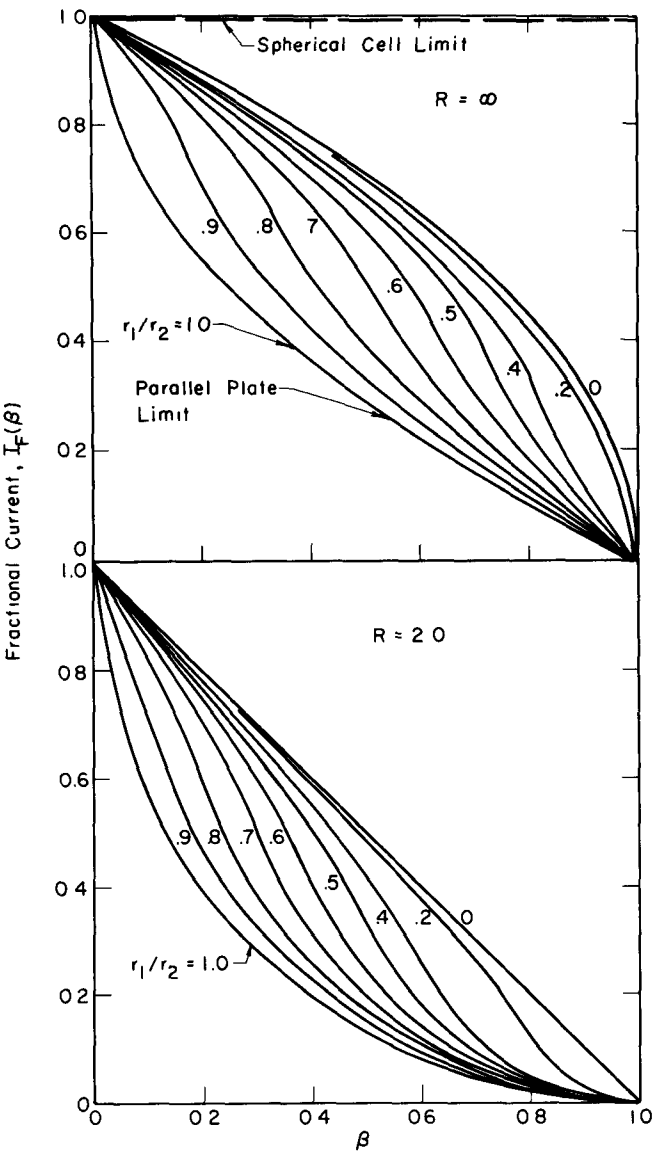

Fig. 2.20 — Current–voltage characteristics for an ideal cylindrical cell.

The factor of 1/2 is due to the perfectly absorbing source rod assumed here. As with the sphere, a thin rod might permit partial transmission, in which case the current could be potentially doubled.

In the limit as $r_1/r_2 \to 0$, $\phi_0^* = \pi/2$ [Eq. (2.56a)] is valid over the entire range of Δ from 0 to 1.0. Using this limit and the appropriate form of ψ_0^* from Eq. (2.54) gives

$$\frac{I_l(\Delta)}{S_l q/2} = \sqrt{1-\Delta} \qquad \left(\frac{r_1}{r_2} = 0\right). \tag{2.59}$$

In the opposite extreme where $r_1/r_2 \to 1$, Eq. (2.56b) is valid for all Δ, and direct integration leads to the parallel plate result, Eq. (2.13a).

2-5.2 Efficiency

Cell efficiencies, based on the definition of Eq. (2.19) and using the current from Eq. (2.55), are shown in Fig. 2.21. As anticipated, these results are again intermediate between those for the plane and sphere. The maximum efficiency of 19.2% occurs at $\beta = 0.67$ for $r_1/r_2 = 0$ in the non-relativistic limit. A convenient analytic expression for this result follows directly from Eq. (2.59), in which case

$$\eta_c^* = \frac{\beta}{2}\sqrt{1-\beta}\,. \tag{2.60}$$

The voltage corresponding to the maximum point is then easily found by equating the derivative $d\eta_c^*/d\beta$ to zero and solving for β.

As before, the efficiency can potentially be doubled if absorption in the source rod is eliminated. However, as in the spherical case, attempts to increase the efficiency through this approach or through the use of a small r_1/r_2 ratio must result in a compromise between the efficiency and the power level–power density.

While the ultimate efficiency of the cylindrical cell is generally less than that for a spherical cell, it occurs at a somewhat lower voltage. Since voltage breakdown places a serious limitation on the maximum practical voltage, this combined with its convenient geometry (from a mechanical point of view) may make the cylindrical cell quite attractive. In fact, the two limiting curves in Fig. 2.21 show that in the range of β from 0 to about 0.3 the cylindrical and spherical efficiencies are comparable while a significant gain is achieved relative to the parallel plate case.

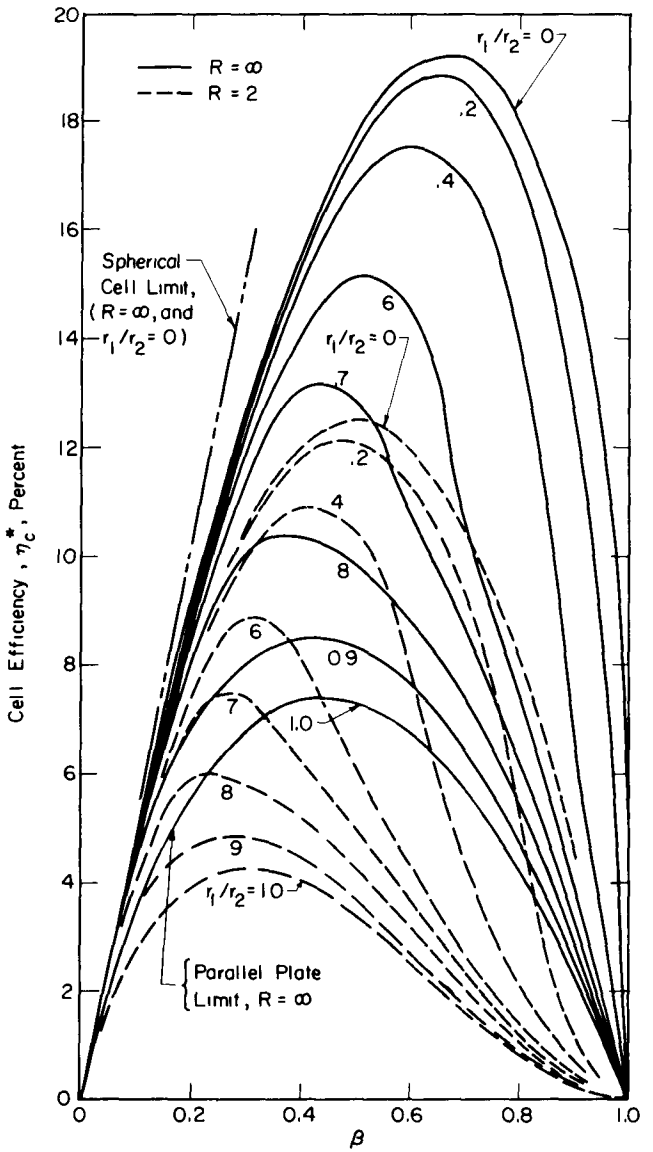

Fig. 2.21 — Cell efficiency for an ideal cylindrical cell. (For isotropic emission and an absorbing source cylinder.)

2-6 IDEAL VOLUME-EMITTER CELLS

Two basic types of Volume-Emitter Cells are illustrated in Fig. 2.22a and b. Figure 2.22a shows a spherical collector lined with a dielectric and filled with a conducting medium that serves as the emitter (Conducting-Volume-Emitter or CVE Cell). An example of this type of cell is one that uses ^{85}Kr gas as the emitter. The gas would be a fairly good conductor since it would be partially ionized by the beta radiation. Such cells typically use a glass dielectric coated on the outer surface with a layer of copper or aluminum and have a sealed

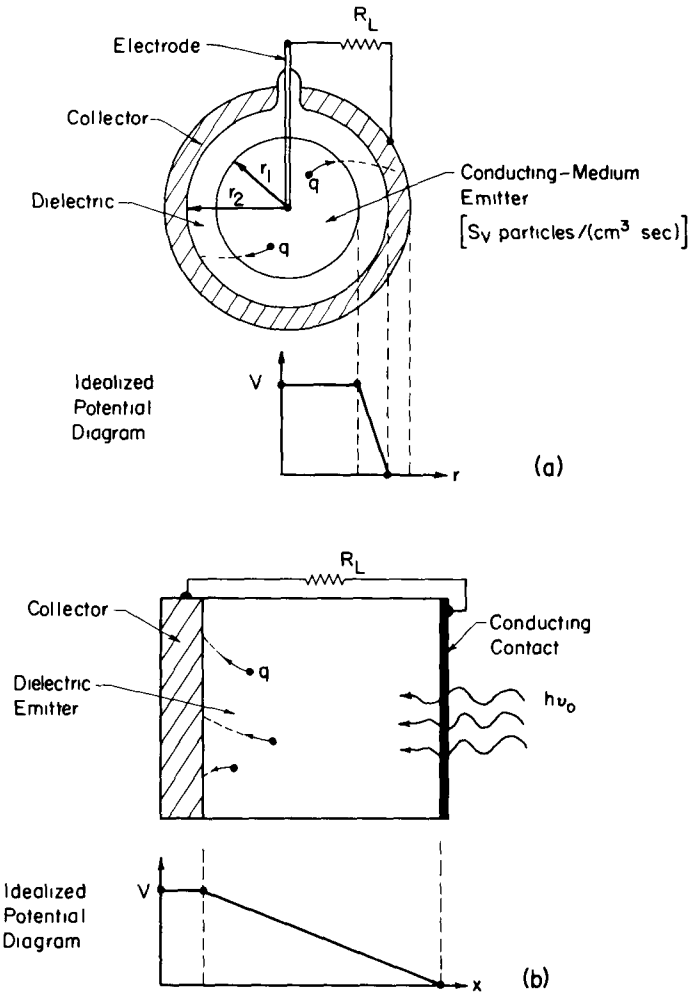

Fig. 2.22 — Volume-emitter designs. (a) A Conducting-Volume-Emitter (CVE) Cell. (b) A Dielectric-Volume-Emitter (DVE) Cell.

lead-through wire to provide electrical contact with the gas. The gas itself in effect serves as the emitter electrode.

Although this concept is easily extended to other geometries, only the spherical case is treated here. As shown in the earlier sections, there is a strong motivation to use spherical geometry because of its high efficiency. Further, in contrast to plate cells, such a geometry is simpler in this case since mechanical problems associated with support of the source are avoided.

The second type of Volume-Emitter Cell, shown in Fig. 2.22(b), collects particles originating in the dielectric itself (Dielectric-Volume-Emitter or DVE Cell). While this might be envisioned as a radioactive source distributed throughout the dielectric, the most important situation is where particles are scattered out of the dielectric due to collimated radiation from an external source. An example is the Gamma-Electric Cell in which impinging gamma radiation generates a Compton electron current in a dielectric such as polyethylene. Because collimated radiation is used, parallel plate geometry is most convenient and is considered here.

The most important difference between these two types of Volume-Emitter Cells arises from their potential diagrams. As illustrated by the idealized potential diagrams (neglecting possible space charge effects) in Fig. 2.22, the dominant potential gradient occurs across the dielectric in both cells. Thus, in the CVE cell, all of the particles must overcome the same barrier in order to reach the collector. In contrast in the DVE cell, the barrier that is "seen" by a particle depends on where the particle is born. We will find this results in marked differences in the operating characteristics of these cells.

2-6.1 Analysis of an Ideal CVE Cell

On the basis of the assumption that the volume emitter is a good conductor, the voltage drop across the interior of the CVE cell is essentially negligible (Fig. 2.22). Then, since ideal-cell theory neglects transport energy losses, a particle born in the interior of the emitter volume can reach the inner surface of the dielectric (radius r_1) without a change in kinetic energy. Thus, for the purpose of analysis, the volume source can essentially be replaced by an equivalent thin spherical shell source at r_1 with strength

$$S_T = S_V \frac{4}{3} \pi r_1^3 \qquad \text{(particles/sec)} \tag{2.61}$$

where S_V[particles/(cm^3 sec)] are emitted in the volume. These approximations should in fact be fairly accurate for such cells. The conductivity need not be very high before the potential drop across the emitter is small relative to the cell output voltage. In addition, the

diameter and the fill pressure of the emitter gas will generally be selected to maximize particle escape, automatically insuring low transport energy losses in the emitter.

Isotropic emission should be a good approximation for a radioactive gas emitter such as envisioned here. Thus, using the equivalent spherical source, we can reduce this idealized analysis to that developed earlier for the spherical plate cells because, if we neglect transport energy losses through the dielectric, there is no difference (from a mathematical point of view) between it and a vacuum.

Intuitively, however, this does not seem quite fair! For one thing, the thicker the dielectric, the better, relative to voltage breakdown. Thus, the thickness of the dielectric will generally represent a compromise between this and the desire for a thin region required to maximize particle transmission.

Recognizing that particle transmission may then be considerably less than 100%, we will attempt to incorporate a correction for this into the analysis. We do this by assigning a range (maximum distance of travel) for the particles in the dielectric. Although the use of a range implies particle slowing, in the spirit of the ideal cell, we will continue to ignore transport energy losses as such. Thus, our results will certainly overestimate currents, efficiencies, etc., but this is expected for the ideal cell. Still, by including absorption (i.e., the range), we prevent the results from being completely unrealistic.

The range λ is incorporated into the analysis as illustrated in Fig. 2.23. Once the trajectory (marked by arrows) in the dielectric exceeds the range, the particle is stopped or absorbed. To keep the analysis as simple as possible, we will adopt the "straight-line" approximation, i.e., the range limited trajectory is approximated by a straight line defined by the direction cosine at r_1.* Also, since in general the dielectric thickness $d \ll r_1$, we will neglect the curvature in evaluating θ_0^* (Fig. 2.23) so that

$$\theta_0^* \approx \cos^{-1}(d/\lambda) \tag{2.62}$$

where, in order that the transmission be non-zero,

$$d/\lambda < 1.0. \tag{2.63}$$

Equation (2.62) represents the maximum allowed angle θ_0^*, and in effect

*Note that this approximation applies only to the *limiting* trajectory. The trajectories for particles starting at smaller initial angles are still determined by conservation of energy and momentum and hence will be curved except for the zero voltage case. Thus the straight-line approximation is not as serious a limitation as might be thought at first.

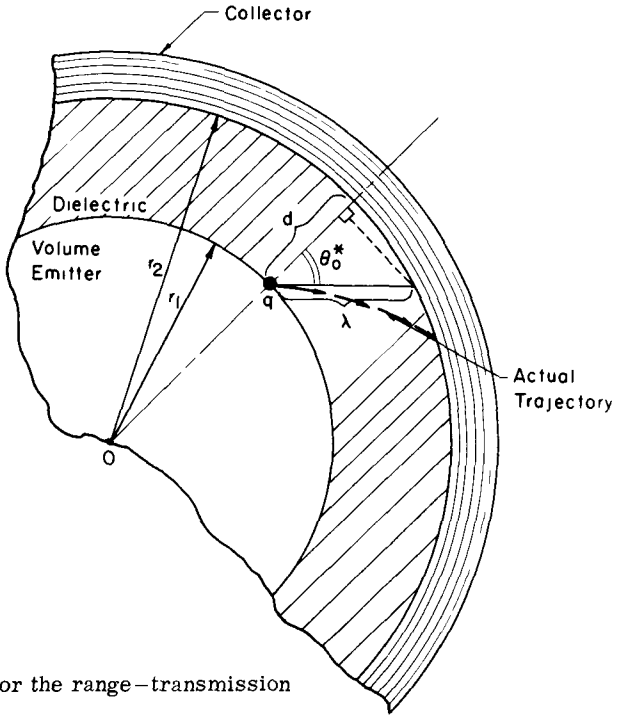

Fig. 2.23 — Geometry for the range–transmission approximation.

replaces the "surface limit" [Eq. (2.47a)] in the spherical plate cell analysis.

With this modification, the current of Eq. (2.48) becomes

$$\frac{I(\Delta)}{S_T q} = \begin{cases} 1 - \dfrac{d}{\lambda} & (\Delta < \Delta_d) \quad \text{(straight-line limit)} \qquad (2.64a) \\ 1 - \sqrt{1 - \left(\dfrac{r_2}{r_1}\right)^2 (1 - \Delta)} & (\Delta > \Delta_d) \quad \text{(potential limit)} \qquad (2.64b) \end{cases}$$

where the dividing voltage is

$$\Delta_d = 1 - \left(\frac{r_1}{r_2}\right)^2 \left[1 - \left(\frac{d}{\lambda}\right)^2\right]. \qquad (2.65)$$

The factor 1/2 does not appear in the source normalization because we have, in effect, assumed a "non-absorbing source support" by neglecting absorption in the emitter medium.

This result is illustrated in Fig. 2.24 for a cell with $r_1/r_2 = 0.5$ in the non-relativistic limit. The cell efficiency shown was calculated

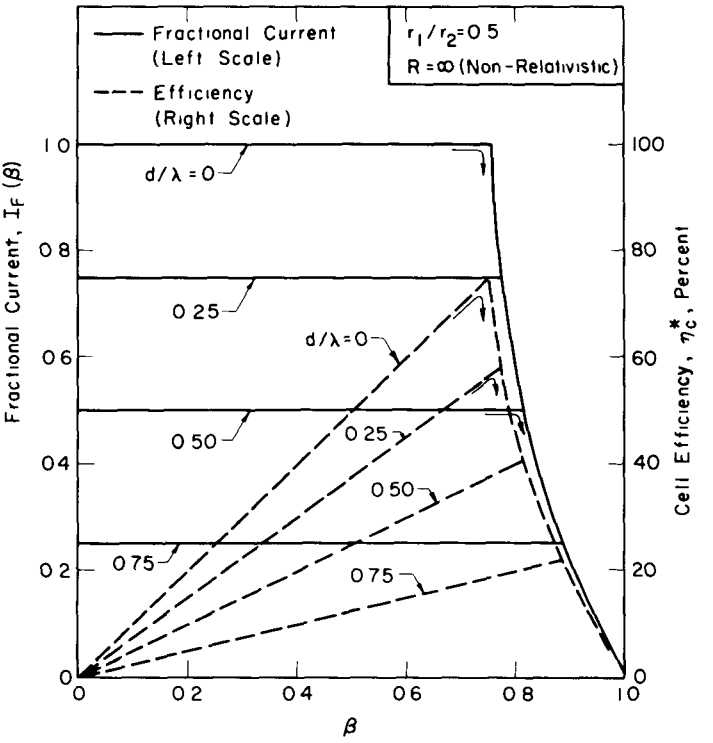

Fig. 2.24 — Effect of dielectric thickness in the ideal CVE cell.

in the conventional fashion using Eq. (2.19) and the current from Eq. (2.64). The current is reduced linearly as d/λ is increased. However, the dividing voltage always lies along the $d/\lambda = 0$ curve, and hence, it increases with d/λ. Physically, this is because as d/λ increases, the maximum angle defined by $\cos^{-1}(d/\lambda)$ decreases. Hence, absorption represents a more severe restriction and dominates until larger voltages are attained.

Since the maximum cell efficiency occurs at the dividing voltage, it too occurs at higher voltages as d/λ is increased. For this reason the maximum efficiency is not quite decreased in proportion to d/λ; e.g., in this case ($r_1/r_2 = 0.5$), the maximum efficiency for $d/\lambda = 0$ is about 75% whereas for $d/\lambda = 0.5$ it falls to 40% — a reduction by a factor of 0.53. This effect will become more pronounced as the slope of the dividing voltage line is reduced, i.e., for increasing r_1/r_2 ratio [see Eq. (2.65)].

Because absorption in the emitter has been neglected, the efficiencies, like the current, are increased by a factor of two over the ideal spherical cell with an absorbing support. This makes them quite

attractive despite the reduction due to d/λ. However, in order for this to be achieved in practice, the source density ρ_s and radius must be restricted such that $(\rho_s r_1) \ll \lambda_s$, where λ_s is the particle range (g/cm^2) in the source material. This amounts to restricting the total source strength, so once again one is faced with a compromise between efficiency and power level–power density.

There is also a serious question as to whether or not the voltages required for optimum efficiency can be contained with reasonable values of d/λ. Hence, although the CVE cell appears to be very attractive in idealized calculations, it may well face more serious practical limitations than its counterpart, the plate type cell.

2-6.2 Analysis of an Ideal DVE Cell

In sharp contrast to any of the cells studied to this point, particles emitted in the DVE cells are born in a region containing a potential gradient. Thus the potential barrier presented to a particle depends on *where it is born* As a result, the derivation of the potential diagram for the dielectric region is a key step in the analysis. The idealized diagram in Fig. 2.25 neglects space charge effects, however, with charged particles being scattered in and out of various regions of the dielectric, it is not at all obvious that this is reasonable. The question seems even more urgent since, as discussed in Chap. 6, electrons are effectively trapped at the end of their track due to the low conductivity of the dielectric. The resulting space charge build-up has actually caused a breakdown or fracture during irradiation of certain dielectrics. (This is discussed further in Chap. 6.) However, in the present analysis we will continue to neglect space charge effects. This is rationalized as follows

Entering radiation can be pictured as driving charged particles through the dielectric as illustrated in Fig. 2.25. The particles may be visualized as moving in short hops either if the dielectric thickness exceeds their range or if the potential gradient is so steep that it seriously retards particle progress.

At this point, it is helpful to consider the Gamma-Electric Cell as a specific example; then the particles are Compton electrons due to gamma irradiation.* The range of 1-MeV electrons in a typical dielectric, such as polyethylene, is only a few millimeters. Since, in contrast to the CVE cell, the dielectric now can be larger than the range without

*Electrons will also be produced by the photoelectric effect and pair production. However, because low-Z dielectrics are of interest here and because of their markedly forward scattering, Compton electrons will dominate during bombardment by gamma radiation in the low MeV range.

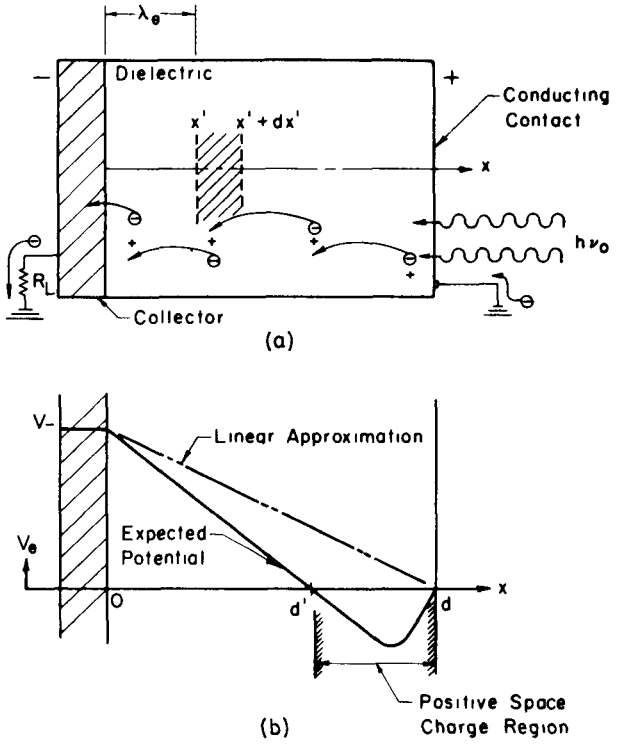

Fig. 2.25 — Operation of the ideal DVE cell. (a) Transport of electrons through the dielectric. (Note that the charge balance is maintained except for a region near the conducting contact.) (b) The resulting potential diagram.

preventing operation, a thick dielectric will probably be selected to minimize ohmic leakage currents and the danger of breakdown.

As we will see shortly, cell performance depends on the gamma intensity near the collector; therefore, the dielectric cannot be made so thick that gamma attenuation becomes serious. Fortunately, this restriction is not too severe since the mean free path for 1-MeV gamma rays in these dielectrics is of the order of 20 cm.

In summary, as a typical case we will consider a dielectric that is thick relative to the Compton electron range but thin relative to the gamma mean free path. The immediate consequence of the latter is that the Compton source rate throughout the volume is essentially uniform. Further, as illustrated in Fig. 2.25, in the interior of the dielectric (between $x = 0$ and d'), as many electrons are driven into a differential volume such as dx' on the average as are driven out of it. Space charge build-up is thus prevented in this region. However, near the face of the cell where the radiation enters, more electrons are

driven out of a unit volume than enter it, and this will create a local positive space charge region.

This charge will build up either until breakdown occurs or alternately until local ohmic leakage currents due to the electric fields involved become large enough to balance the excess Compton current. In the present analysis we will assume that the latter occurs. Further, we assume that the magnitude of the space charge and the relative dimensions d′ and d are such that the linear approximation of Fig. 2.25 is not totally unrealistic.

An additional point should be noted here: If the gamma radiation passes through the collector, it will "drive" electrons out of the back face of the cell, and this loss could be comparable with the current collected! To prevent this, a fairly thick, dense material such as lead will be used for the collector to attenuate or stop the gamma radiation.

Having decided on the potential diagram, we are in a position to calculate the current–voltage characteristic. We will again consider the average angle forward scattering model introduced earlier. Also, to gain further insight into the problem without the lengthy algebra required by using the full Klein–Nishina differential cross section, we will simultaneously consider a simple cosine distribution to represent scattering. In summary these two distributions are

$$P(\mu_0) = \begin{cases} \delta(\mu_0 - \bar{\mu}) & \text{[average angle, forward emission (avg. angle, f.e.)]} \quad (2.66a) \\ \left.\begin{array}{ll} 2\mu_0 & (\mu_0 > 0) \\ 0 & (\mu_0 < 0) \end{array}\right\} & \text{[cosine distribution, forward emission (cosine, f.e.)]} \quad (2.66b) \end{cases}$$

where $P(\mu_0)$ is normalized as indicated in Eq. (2.11).

The cosine distribution was not considered earlier. However, it is easily shown that, if it is used in the parallel plate analysis of Sec. 2-3.3, the resulting form of $J(\Delta)$ is

$$J(\Delta) = S_0 q(1 - \Delta) \qquad \text{(cosine, f.e.)}. \tag{2.67}$$

The analysis can proceed from here in either of two equivalent ways. In one, the charge induced in the collector due to the individual "hops" of the electrons is calculated and summed over all the electrons. This is the most general approach and *must* be used in the analysis of fast transients. However, for *steady state* operation, the current crossing any plane perpendicular to the x-axis must be a constant. Thus an alternate approach is to calculate the current crossing the dielectric–collector interface. For voltage calculations, this is the

easiest approach, and we shall use it here. (Restrictions inherent in this approach and the significance of ohmic-leakage currents, displacement currents, and space-charge effects are discussed further in Sec. 6-4.2.)

First, note that all electrons crossing the collector–dielectric interface must originate within a distance equal to one range from the interface. Hence, the calculation is reduced to finding the current driven out of this volume—i.e., the volume defined by λ_e in Fig. 2.25 where λ_e is the maximum range for Compton electrons. (The range is used here in much the same spirit as in the CVE cell analysis—transport energy losses will still be neglected.) An expanded view of this region is shown in Fig. 2.26.

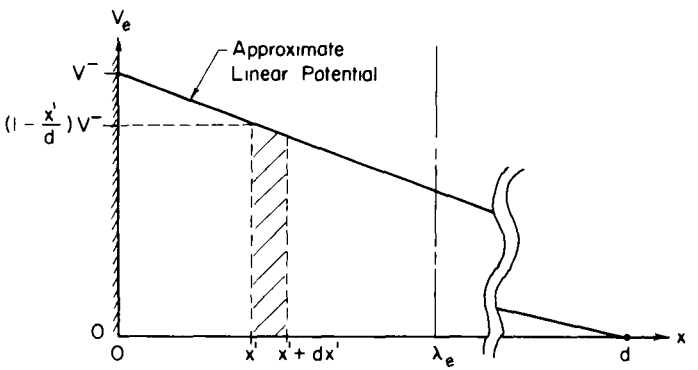

Fig. 2.26—Collection volume near the collector.

The current is found by considering a volume element dx′ at x′. This element can be visualized as a plane source of strength S_V dx [particles/(cm^2 sec)], where S_V is the volume emission rate [particles/(cm^3 sec)]. A particle emitted in dx′ starts at a potential $(1 - x'/d)V^-$, and thus it must overcome a potential difference of $(x'/d)V^-$ in order to reach the collector. This plane will contribute a differential current density, dJ_V, and the total current can be found by integrating over all allowed dx′.

Since we are neglecting transport energy losses, the problem presented by the plane source in dx′ is essentially equivalent to a parallel plate cell operating at voltage $(x'/d)V^-$. Thus, the results obtained earlier for these cells can be used with V^+ replaced by $(x'/d)V^-$. However, there is one difference: the particle trajectory cannot exceed the range λ_e. Again, in the determination of this limit we will use a straight-line approximation for the range limited trajectory (but not the voltage limited trajectory). Then, the equivalent of Eq. (2.7) for the limiting angle is

$$\theta_0^* = \min. \begin{cases} \cos^{-1} y & \text{(range limited)} \quad (2.68a) \\ \cos^{-1} \sqrt{\Delta(y)} & \text{(potential limited)} \quad (2.68b) \end{cases}$$

where y is a nondimensional distance defined as x'/λ_e and $\Delta(y)$ represents a modified form of Eq. (2.8a)

$$\Delta(y) = \frac{U\lambda_e y(R - U\lambda_e y)}{R - 1} \tag{2.69}$$

with U defined as the gradient of the reduced voltage across the cell; i.e.,

$$U \equiv \frac{\beta}{d} . \tag{2.70}$$

The gradient U for this type of cell is a more significant quantity than β alone, since the ability of a particle to reach the collector now depends on its location (x') and the voltage gradient *rather* than the absolute voltage.

With these results, we can immediately write the differential current for the two cases of interest by analogy with Eq. (2.13). Then, for the average angle forward emission model, we obtain

$$\frac{dJ_y}{Svq\lambda_e} = \begin{cases} [1 - h(y - \bar{\mu})]\, dy & (U/U_M < 1) \quad (2.71a) \\ [1 - h(\sqrt{\Delta(y)} - \bar{\mu})]\, dy & (U/U_M > 1) \quad (2.71b) \end{cases}$$

with

$$U_M \equiv \frac{\beta_m}{\bar{\mu}\lambda_e} \tag{2.72}$$

where β_m is the reduced voltage cut-off defined earlier in Eq. (2.16) and Fig. 2.4.

Equation (2.71a) corresponds to lower values of the gradient U, where θ_0^* is range limited [cf., Eq. (2.68a)], whereas Eq. (2.71b) corresponds to the potential limited case. The dividing gradient U_M is found by equating the value of y, where the arguments of the step functions in Eqs. (2.71a and b) vanish.

The physical basis for this is as follows: We see from Eq. (2.72) that U_M is the maximum gradient that a particle traveling a distance $\bar{\mu}\lambda_e$ can overcome. But as illustrated in Fig. 2.27, $\bar{\mu}\lambda_e$ corresponds to the maximum distance measured along the x'-axis that a particle can

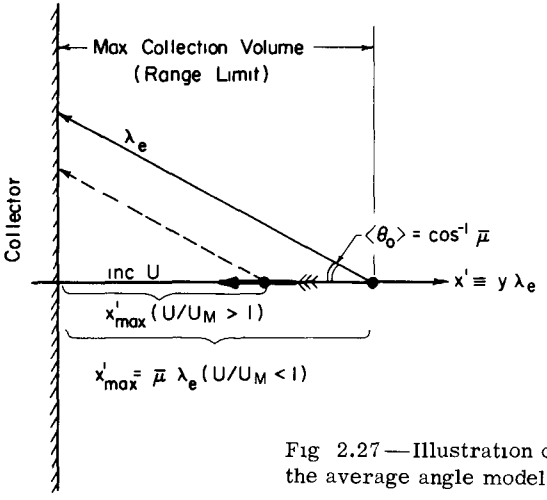

Fig 2.27—Illustration of range and potential limits for the average angle model.

travel under any conditions due to the range limitation. Once U exceeds U_M, the maximum distance becomes potential limited and will always be less than $\bar{\mu}\lambda_e$. Note that there is no *"cut-off" gradient*! Since particles are emitted throughout the dielectric, some will always be close enough to reach the collector until U = ∞.

The corresponding result for the cosine emission distribution is found in a similar fashion, and the differential current for this case is

$$\frac{dJ_V}{S_V q\lambda_e} = \begin{cases} [1 - \Delta(y)]\,dy & (0 < y < y_d) \\ (1 - y^2)\,dy & (y_d < y < 1) \end{cases} \quad (U\lambda_e < 1) \qquad (2.73a,\ 2.73b)$$

$$[1 - \Delta(y)]\,dy \quad \left(0 < y < \frac{1}{\lambda_e U}\right) \quad (U\lambda_e > 1). \qquad (2.74)$$

The various limits are somewhat more complicated and require explanation. For lower gradients $U\lambda_e < 1$, the two limits for θ_0^* result in a dividing value of y found by equating the arguments in Eqs. (2.68a and b). thus,

$$y_d = \frac{U\lambda_e R}{(R-1) + (U\lambda_e)^2}. \qquad (2.75)$$

This situation is illustrated in Fig. 2.28 A particle starting at y_1, which is less than y_d, is so close to the collector that its maximum initial angle is limited to the collection zone defined by the potential

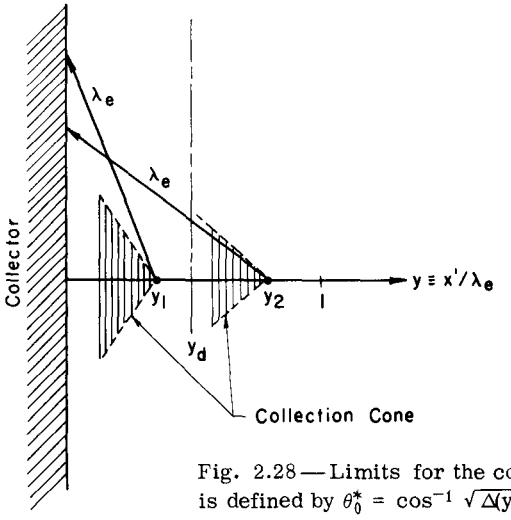

Fig. 2.28 — Limits for the cosine model. (The collection zone is defined by $\theta_0^* = \cos^{-1}\sqrt{\Delta(y)}$.)

barrier. The collection zone is somewhat smaller for a particle starting at y_2, but as indicated, the maximum angle is now limited by the range λ_e.

Now, once the gradient exceeds a value such that $U\lambda_e > 1$, the particle is always potential limited. [Note that the smallest value of $U\lambda_e$ in Eq. (2.75) satisfying $y_d = 1$ is 1.0. This is also consistent with the earlier average angle condition $U/U_M = 1$ since, for $\bar{\mu} = 1$, $U_M \to 1/\lambda_e$]. In this case, the maximum value of y, designated y_{max}, where a particle can originate and still reach the collector, is found from a simple energy balance. This corresponds to a particle with $\mu_0 = 1$, so the required balance is

$$\frac{x'_{max}}{d} \quad V^- = \frac{T_0}{q} . \tag{2.76}$$

Rearrangement and use of earlier definitions gives

$$y_{max} = \frac{1}{\lambda_e U} \tag{2.77}$$

which agrees with the limit used in Eq. (2.74). (Note: Since the particle is traveling straight forward, all the kinetic energy can be converted so the balance is independent of relativistic corrections involving R.)

The differential currents are now integrated over y to find the total current. The results are

Average angle, f.e.

$$\frac{J_V}{S_V q \lambda_e} = \begin{cases} \bar{\mu} & (U/U_M < 1) \quad (2.78a) \\ \dfrac{\bar{\mu} U_M}{U} & (U/U_M > 1) \quad (2.78b) \end{cases}$$

Cosine, f.e.

$$\frac{J_V}{S_V q \lambda_e} = \begin{cases} \dfrac{2}{3} - \theta(U\lambda_e) & (U\lambda_e < 1) \quad (2.79a) \\ \dfrac{1/\lambda_e}{U}\left[1 - \dfrac{1}{R-1}\left(\dfrac{R}{2} - \dfrac{1}{3}\right)\right] & (U\lambda_e > 1) \quad (2.79b) \end{cases}$$

where

$$\theta(U\lambda_e) = \left\{\frac{y_d^3}{3}\left[\frac{(U\lambda_e)^2 + 1}{R-1}\right] - \frac{U\lambda_e R}{2(R-1)} y_d^2\right\} \quad (2.80)$$

with y_d as defined in Eq. (2.75).

The main features of these results, along with efficiencies, are illustrated in Fig. 2.29 for the non-relativistic case ($R = \infty$). In this limit several simplifications occur. First, in the average angle model, since $\beta_M \to \bar{\mu}$, the dividing gradient U_M becomes $\bar{\mu}/\lambda_e$. Also in the cosine model $\theta(U, \lambda_e)$ reduces to $\frac{1}{6}(U\lambda_e)^3$. For convenience in the plot, we identify U_M for the cosine model with $1/\lambda_e$.

For the average angle model, for U less than U_M, the current is seen to be constant since all particles born in the volume $\bar{\mu}\lambda_e$ are collected. Above $U = U_M$, the collection volume decreases inversely with U, going to zero asymptotically as $U \to \infty$. The cosine distribution leads to the same general shape, but the current decreases somewhat before U reaches U_M. This is expected because particles born near the plate with large initial angles θ_0 will be potential limited (Fig. 2.28). Thus, the number of these particles collected will decrease as U increases. Then, once U exceeds U_M, the whole collection volume begins to decrease in the same fashion as for the average angle model, and the current decreases rapidly.

It is interesting that the short-circuit current for the cosine model is $(\frac{2}{3})\, S_V q \lambda_e$. This result is consistent with the average angle model since, as shown by comparison with Eq. (2.78a), it implies that $\bar{\mu} = \frac{2}{3}$, which corresponds to averaging μ_0 over $P(\mu_0)$ given in Eq. (2.66b).

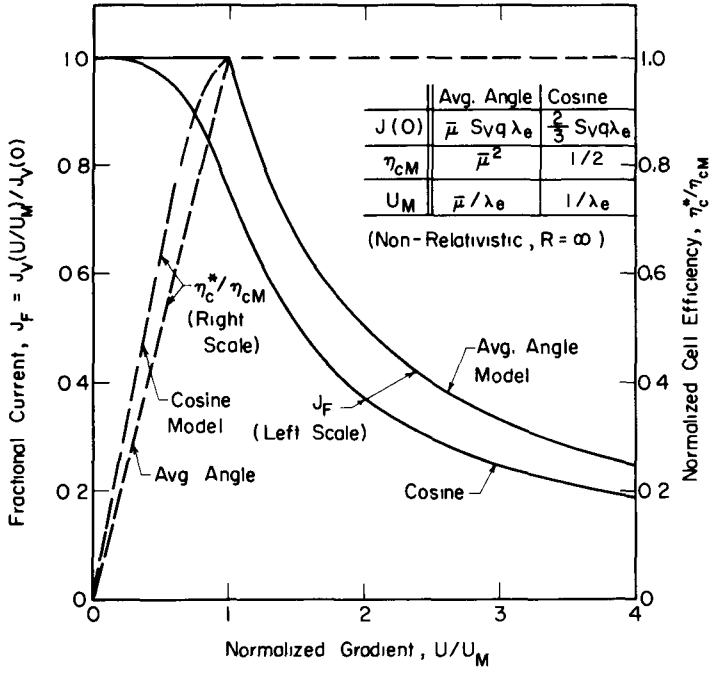

Fig. 2.29 — Current and efficiency plots for the average angle and cosine model representations of a DVE cell.

The efficiencies shown in Fig. 2.29 again follow from the definition given in Eq. (2.19), and, for the average angle model,

$$\eta_c^* \equiv \frac{JV^-}{S_V T_0 d} = \eta_{cM} \begin{cases} U/U_M & (U/U_M < 1) \\ 1 & (U/U_M > 1) \end{cases} \tag{2.81a, 2.81b}$$

where the maximum efficiency η_{cM} is given by

$$\eta_{cM} = \bar{\mu}\lambda_e U_M \xrightarrow{R=\infty} \bar{\mu}^2. \tag{2.82}$$

[Due to electron "hopping," discussed later, Eq. (2.21) *cannot* be used for η_c^*.] Likewise, for the cosine model we obtain

$$\eta_c^* = \eta'_{cM} \begin{cases} \dfrac{\lambda_e U\ \theta(U\lambda_e)}{\left[1 - \dfrac{1}{R-1}\left(\dfrac{R}{2} - \dfrac{1}{3}\right)\right]} & (U\lambda_e < 1) \\ 1 & (U\lambda_e > 1) \end{cases} \tag{2.83a, 2.83b}$$

where

$$\eta'_{cM} = \left[1 - \frac{1}{R-1}\left(\frac{R}{2} - \frac{1}{3}\right)\right] \xrightarrow{R=\infty} \frac{1}{2}. \tag{2.84}$$

The shape of the efficiency plot for the DVE cell is different from that for any of the previous cells studied. A constant region is reached for U above U_M, and this corresponds to the region where the current decreases inversely with voltage so that the voltage–current product is constant.

The maximum efficiency for the average angle model reduces to $\bar{\mu}^2$ in the non-relativistic limit. This is because both the collection volume and the dividing gradient U_M are proportional to $\bar{\mu}$.

There is an interesting aspect of the efficiency results that deserves comment. Note that, if $\bar{\mu} = 1$ (i.e., if all particles are scattered straight forward), the average angle model predicts a maximum efficiency of 100%. Since a similar result was obtained for the plate cells, this may not seem to surprising. Yet, it must be remembered that, in this case, the electrons reaching the collector originate from different points in the dielectric. Thus, each "sees" a different barrier so that it is difficult to understand how 100% of the particle kinetic energy is converted to potential. However, the point is this: The efficiency in Eq. (2.81) involves the current times the *total* cell voltage V^-. In essence this means that each electron collected is given credit for overcoming the entire voltage barrier regardless of its point of origin. This is not unreasonable. As illustrated earlier in Fig. 2.25, the electrons move in short "hops"; thus the motion of all four electrons in this figure might be replaced by a single electron moving across the entire cell.

In this sense, the DVE cell is a type of multistage barrier such as discussed in the dam analogy of Chap. 1, Sec. 1-3.3. This results in some unique features. The most obvious has already been alluded to — namely, the results in Fig. 2.29 are independent of the actual cell thickness but only depend on the voltage gradient. It is tempting then to consider quite thick cells as a possible means of building up very high voltages. While it is possible to go in this direction, a limit is soon reached because gamma-ray attenuation, assumed negligible here, will become important. On the basis of this logic, it is clear that an optimum cell thickness exists. However, we are not in a position to evaluate this problem now because, once gamma-ray attenuation enters, space charge effects must also be considered.

One important practical problem with the DVE cell should be noted. It is difficult to maintain a high resistivity due to radiation induced conductivity and damage to the dielectric. Thus leakage cur-

rents due to such effects will probably be quite important relative to plate-vacuum type cells. The DVE cell does, however, have some advantage over the CVE-type cell in this respect, since thicker dielectrics can be used.

In conclusion, we see that the cell efficiencies for the ideal DVE cell appear to be quite attractive. However, it is apparent that, if gamma radiation is the input, the overall efficiency may still be quite low because only a fraction of the gammas can be absorbed in a cell of reasonable length. This represents a real problem since the key to the high cell efficiency is the forward scattering of Compton electrons. While a different source might be considered, if its angular distribution of emission is less favorable, there may be a marked decrease in cell efficiency. In fact, a similar analysis shows the maximum ideal-cell efficiency to be reduced to about 16% for isotropic emission. Further, isotropic emission produces an obvious space charge problem near the collector–dielectric interface so it is not even clear that such a source would work. (Other than this, the generation of a net current might be achieved by use of a thick collector and a very thin electrode on the opposite end of the cell. A potential difference would be developed by stopping particles in the collector while allowing a loss of particles at the thin electrode via transmission.)

2-7 SUMMARY

The ideal-cell results define the maximum or limiting performance that can be expected from a specific geometry and type of cell. Results found for the maximum cell efficiency and the reduced voltage and fractional current at the point of maximum efficiency are summarized in Table 2.3. The use of normalized parameters eliminates the dependence on the specific type of charged particle involved. The results shown here do, however, assume non-relativistic particles. Some cases, particularly cells involving betas or Compton electrons, may require a relativistic correction such as developed in the preceding sections.

The limiting efficiencies in Table 2.3 range from about 6 to 7% for a plane plate cell with isotropic emission to values over 50% for spherical geometry or plane cells with forward emission. There is obviously a strong motivation to use cylindrical or spherical geometry and/or forward emission. There are, of course, pros and cons relative to either approach, and in a specific application, there may not even be a choice. Forward emission is not possible except where special sources, such as gamma induced Compton electrons, are available and can be used. Unfortunately in such cases, the transfer of energy from the entering radiation to the charged particle (not included in

Table 2.3—SUMMARY OF TYPICAL IDEAL-CELL RESULTS

Geometry and Angular Distribution	β (or U) at η_c^*(max.)	η_c^*(max.) %	J_F at η_c^*(max.)
I. Plate Cells			
Plane*			
Isotropic	0.445	7.42	0.33
Forward ($\bar{\mu} = 0.9$)	0.81	81.0	1.0
($\bar{\mu} = 1.0$)	1.0	100.0	1.0
Plane, periodic discharge*†			
Isotropic	0.65	6.3	
Forward ($\bar{\mu} = 0.9$)	0.81	40.5	
Cylindrical*‡§	0.667	19.2	0.058
Spherical*‡§	1.0	50.0	0
II. Volume-Emitter Cells			
Conducting-Volume Cells (CVE)*			
Spherical; $d/\lambda = 0.5$‡§	0.81	41.0	0.5
Dielectric-Volume Cells (DVE)			
Plane Geometry:			
Forward ($\bar{\mu} = 0.9$)	$0.9/\lambda_e$	81.0	1.0
Forward, cosine	$1/\lambda_e$	50.0	0.75

*Assumes any particle hitting the source support is absorbed.
†All other cases are for steady state operation.
‡Isotropic emission.
§For the limit where the radius ratio $(r_1/r_2) \rightarrow 0$.

evaluating *cell* efficiencies) may be inefficient. An important exception is the use of a Direct-Collection Cell with a controlled thermonuclear reactor. As discussed in Chap. 7, a collimated ion beam, equivalent to forward emission, is obtained with magnetic fields, and efficiencies exceeding 95% have been predicted for *this part* of the cycle. (Depending on the fusion reaction employed, not all of the energy is released as charged-particle kinetic energy.)

The alternate approach of going to cylindrical or spherical geometry also has some restrictions. First, the efficiency is best for low inner to outer radii ratios, and this in turn implies a compromise with the power level or power density may be necessary. For the spherical cell in particular, the voltage is high and the fractional current is low in the range of maximum efficiencies.

The spherical CVE cell gets around the awkward problem of supporting the source, but leakage currents, breakdown, and radiation damage to the dielectric insulator seriously limit it as well as the DVE cell.

When considering geometries, we should remember that, as Plummer et al.[10] point out, there are a number of hybrid or compromise geometries lying somewhere between the sphere and cylinder. Thus, the choice is not just between these extremes.

As stressed earlier, the quantities in Table 2.3 are independent of the type of charged particle involved. Still *absolute* currents and voltages will be determined by the particle and the characteristics of the source. These and many other factors, such as its specific activity, cost, half-life, shielding requirements, etc., enter into the selection of a source. Such considerations, as related to radioisotopes, have been discussed elsewhere (e.g., see Refs. 15 and 16). However, the use of a nuclear reaction, such as $n(^{235}U)ff$ or $n(^{10}B)\alpha$, would probably involve a nuclear reactor. This represents a more complex system, and the only detailed consideration of such units is for the Fission-Electric Cell as described in Chap. 7.

However, some specific points of importance to cell operation should be noted:

(1) Because of the voltage breakdown problem, there is a strong motivation to consider particles with a lower kinetic energy voltage equivalent, i.e., lower T_0/q. As seen from Table 1.1, this tends to favor certain beta emitters.

(2) The ideal-cell analysis assumes a monoenergetic energy spectrum. In general, a spectrum will exist, and if it is wide, the operating voltage will of necessity represent a compromise, which lies above the optimum for lower-energy particles but below the optimum for high-energy particles. Alpha emitters approach the ideal of monoenergetic spectrum and hence have some advantage in this respect. Otherwise, as discussed in Chap. 1, a multiplate collector may be required to compensate for the spread in source energies.

(3) Many of the losses neglected in the ideal-cell analysis are strongly influenced by the type of particle involved, and this may be an important factor in the final selection of a source. Examples are energy losses during particle transport and leakage currents due to secondary electron emission, sputtering, and backscattering, which are considered in the following chapters.

It is obvious, then, that the source selection involves a number of factors that must be weighed against each other relative to a specific application.

In conclusion, limiting efficiencies from the ideal-cell analysis indicate some attractive possibilities for nuclear cells. The key question remaining is "How serious are the losses and voltage limitations?" The remainder of this monograph is devoted to answers and/or to developing techniques to answer this question.

Cells built thus far have generally been limited to only a fraction of the ideal-cell efficiency. Since there is no law of nature to prevent us from approaching the ideal, the limiting factor is ultimately the ingenuity of the designer! This presents a real challenge and demands that we continue to study and widen our understanding of the fundamental

processes associated with the parasitic losses. The following chapters are presented in this spirit. Thus, rather than provide a "design manual" or solutions to the problems, the presentation is intended to provide some insight and background in the problem areas.

REFERENCES

1. J. Millman and S. Seely, *Electronics*, 2nd ed., Chap. 2, McGraw-Hill Book Company, Inc., New York, 1951.
2. R. L. Ramey, *Physical Electronics*, Chap. 11, Wadsworth Publishing Company, Belmont, Calif., 1961.
3. W. W. Harman, *Fundamentals of Electronic Motion*, McGraw-Hill Book Company, Inc., New York, 1953.
4. J. R. Pierce, *Theory and Design of Electron Beams*, D. Van Nostrand Company, Princeton, N. J., 1954.
5. G. Safonov, *Direct Conversion of Fission to Electric Energy in Low Temperature Reactors*, Rand Report RM-1870, Rand Research Corp., Santa Monica, Calif., January 1957.
6. A. Schock, *A Direct Nuclear Electrogenerator—Analysis of Cylindrical Electrode Configuration*, Fairchild Aircraft Corp., Deer Park, N. Y., AFOSR-TN-59 590 (1959).
7. C. J. Heindl, *Efficiency of Fission Electric Cells*, Tech. Report No. 32-105, Jet Propulsion Laboratory, Pasadena, Calif., May 1961.
8. G. H. Miley, "Fission Fragment Transport Effects as Related to Fission-Electric-Cell Efficiencies," *Nucl. Sci. Eng., 24* 322 (1966).
9. A. J. Cohen, *A Numerical Analysis of Direct Nuclear Electrogenerator Cells That Use Cerium-144 Beta-Emitting Radioisotope Sources*, Report NASA-TN D-2070, NASA Lewis Research Center, Cleveland, Ohio, November 1963.
10. A. M. Plummer, W. J. Gallagher, R. G. Mathews, and J. N. Anno, *The Alpha-Cell Direct-Conversion Generator*, NASA Report CR-54256, Battelle Memorial Institute, Columbus, Ohio, Nov. 30, 1964.
11. B. Gross, "The Compton Current," *Zeitschrift fur Physik, 155:* 479 (1959).
12. B. Gross and P. Murphy, "Currents from Gammas Make Detectors and Batteries," *Nucleonics, 19,* 3: 86 (1961).
13. G. H. Miley and H. T. Sampson, "Gamma-Electric Cell Theory and Experiment," *Proc. Inter. Conf. on Energetics*, pp. 238-251, Univ. of Rochester, August 1965, Am. Soc. Mech. Eng., New York, 1965.
14. H. T. Sampson and G. H. Miley, "High Voltage Gamma-Electric Cell Operation," *Nucl. Appl., 5:* 145 (1968).
15. H. L. Davis, "Isotope Costs and Availability; Radionuclide Power for Space—Part I." *Nucleonics, 21,* 3: 61 (1963).
16. W. R. Corliss and D. G. Harvey, *Radioisotopic Power Generation*, Prentice-Hall, Englewood Cliffs, N. J., 1964.

3

Charged Particle Transport

3-1 INTRODUCTION

The energy loss that is incurred by a charged particle as it passes through the source layer itself and through other parts of the cell such as the solid insulator in volume emitter designs is one of the important parasitic losses in an actual cell. This energy appears initially as ionization and excitation of the atoms in the material, and eventually it disappears as heat. Since the charged-particle ranges involved are often only a fraction of a centimeter or so in solids, the losses may be quite significant.

As charged ions slow down, they tend to pick up electrons and are eventually neutralized. This is an associated effect, which is especially pronounced for fission fragments but of lesser importance for other ions of interest such as alpha particles.

Before discussing how these effects influence cell performance, we must gain some background in the fundamentals of charged particle transport theory. This background is provided in the present chapter while applications to cell calculations are given in Chap. 4.

It is only possible to "scratch the surface" of this theory here. The interested reader is referred to any one of a number of detailed treatments, e.g., Refs. 1 to 7. The present development uses Ref. 1 to a large extent as a starting point, but, to facilitate the cell analysis, we soon "strike out on our own" to construct simple range–energy–charge relations.

3-2 ION SLOWING THEORY

The average energy loss per centimeter of travel $-dE/dr$ is the fundamental quantity of interest to us. Since most cells will utilize ions in the 1- to 10-MeV range, we will restrict the discussion to non-relativistic cases, i.e., $-dE/dr \rightarrow -dT/dr$ (Appendix B-1).

A quantum mechanical calculation based on the Born approximation is commonly used to evaluate $-dT/dr$. In this derivation, there is a fundamental assumption that the amplitude of the scattered wave

function is much smaller than that for the incident wave. This, it turns out, implies that[1]

$$\frac{qe}{\hbar v} \ll 1 \tag{3.1}$$

where v is the ion's speed, e is the unit of electronic charge, $\hbar$ is Planck's constant divided by 2π, and q is the net electronic charge of the ion. The charge q is defined here in units of e; therefore, if z is the charge number or the number of missing electrons,

$$q \equiv ze. \tag{3.2}$$

If the converse is true, i.e., if

$$\frac{qe}{\hbar v} \gg 1 \tag{3.3}$$

then Block[8] and Williams[9] have shown that the quantum mechanical derivation should be replaced by one based on classical mechanics. Block has derived an expression for the energy loss that combines both extremes. His result is

$$-\frac{dE}{dr} = -\frac{dT}{dr} = \frac{4\pi e^2 q^2}{m_e v^2} NB \tag{3.4}$$

$$B \equiv Z \left\{ \ln \frac{2m_e v^2}{I} + \psi(1) - \operatorname{Re} \psi \left(1 + i \frac{qe}{\hbar v}\right) \right\} \tag{3.5}$$

where

$$\psi(x) \equiv \frac{1}{\Gamma(x)} \frac{d}{dx} \Gamma(x) \tag{3.6}$$

and

$$I \approx (11 \pm 3)Z \qquad \text{(in eV)}. \tag{3.7}$$

The term B is called the "stopping number," whereas $-dE/dr$ is the "stopping power"; N and Z refer to the atoms per cubic centimeter and nuclear charge number for the stopping material; m_e is the mass of an electron; $\Gamma(x)$ is the gamma function of x; and I, the geometric mean excitation and ionization potential, is approximately related to Z as indicated by Eq. (3.7) (see p. 645, Ref. 2, for a detailed plot of I vs Z).

The real part of ψ is denoted by Re ψ. Properties of the gamma function and the related Psi function $\psi(x)$ are discussed on pages 258-259 of Ref. 10, and a plot of $\psi(x)$ is shown in Fig. 3.1. In the limit

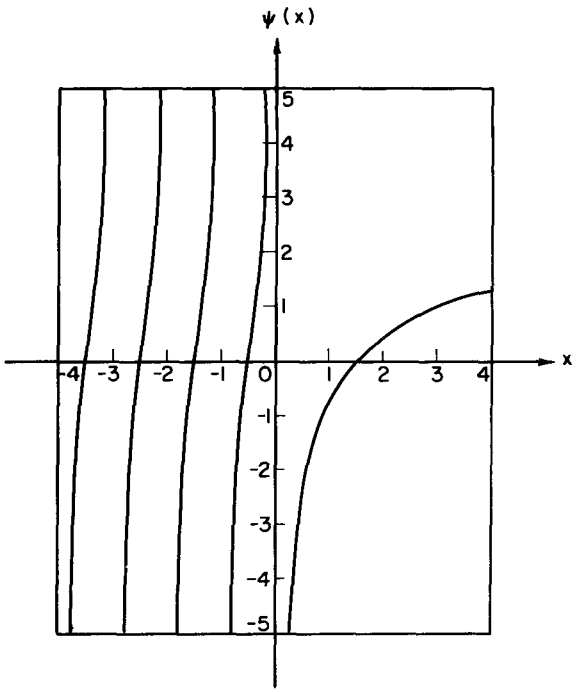

Fig. 3.1 — The Psi function. (From Abramowitz and Stegun, Ref. 10.)

where $qe/\hbar v \to 0$, the Psi functions cancel in Eq. (3.5), and we get the quantum mechanical limit of the stopping number

$$B \approx Z \ln \frac{2m_e v^2}{I} \qquad \left(\frac{qe}{\hbar v} \ll 1\right). \tag{3.8}$$

Conversely, if $qe/\hbar v$ is large, we find from Fig. 3.1 that

$$\psi(1) = -0.577 \tag{3.9}$$

and, using Eq. (6.3.19) of Ref. 10 for $y \to \infty$,

$$\text{Re}\,\psi(1 + iy) \approx \ln y + \frac{1}{12\,y^2} + \frac{1}{120\,y^4} + \ldots \tag{3.10}$$

so that retaining the leading term

$$\mathrm{Re}\,\psi\left(1+i\frac{qe}{\hbar v}\right)\approx \ln\frac{qe}{\hbar v}\qquad\left(\frac{qe}{\hbar v}\gg 1\right) \tag{3.11}$$

Upon substitution of Eqs. (3.9) and (3.11) into (3.5), the stopping number reduces to the classical limit

$$B\approx Z\ln\frac{1.123\,m_e v^3}{\omega qe}\qquad\left(\frac{qe}{\hbar v}\gg 1\right). \tag{3.12}$$

Here

$$\omega\equiv I/\hbar \tag{3.13}$$

is identified with an average oscillation frequency of the electrons in the stopping material atoms.

One serious problem still remains: These derivations treat the charge q as a unique number, independent of the charged particle's speed. However, as the particle slows down, electrons will gradually be attached to it until, at the end of its track, it is neutralized. This variation in charge is quite complex, but we can crudely visualize the situation as follows: As long as the particle's speed is considerably larger than the orbital speed of electrons in the stopping material atoms, electron capture will not occur. However, once these speeds are comparable, neutralization will begin. This argument implies that the particle will remain fully ionized so long as its kinetic energy T is

$$T\gg\frac{M}{m_e}E_I \tag{3.14}$$

where M/m_e is the ion-electron mass ratio and E_I is the energy associated with the ionization potential for electrons in the stopping material. This restriction applies to both results for B obtained above, i.e., both Eqs. (3.8) and (3.12). However, it does allow us to classify these results further, since

$$\frac{qe}{\hbar v}=\frac{Ze^2}{\hbar v}\left(\frac{q/e}{Z}\right)=\frac{Ze^2}{\hbar v}\left(\frac{z}{Z}\right). \tag{3.15}$$

But, the speed of K shell electrons is of the order of $Ze^2/\hbar$ so that, if $z/Z\ll 1$, the parameter $qe/\hbar v$ will remain small over a reasonable range of v, and Eq. (3.8) will be valid over much of the track. This is true for alpha particles ($z=2$), lithium ($z=3$), etc., in heavy stopping materials. Fission fragments are the major exception since, at the start of their track, $z\approx 20$. Then, not only must we apply Eq. (3.12),

but the charge q will vary over the entire track. Because of these complications, we will treat fission fragments separately and first turn our attention to ions with low charge.

3-3 LOW-q ION SLOWING

3-3.1 Energy Regions

Because of electron capture, it is necessary to divide the ion's track into three energy regions.

(1) *Region I* (High Speed):

$$\frac{Mc^2}{2} \gg T \gg \frac{M}{m_e} E_I .$$

In this case the particle is fully ionized, i.e., q is constant and Eq. (3.8) applies. Fortunately, the logarithmic term will only vary slowly with energy, so we can obtain a working form by using an average value of B. Thus, using Eq. (3.4), we find

$$-\frac{dT}{dr} \approx \frac{C_I}{T} \tag{3.16}$$

with

$$C_I \equiv \frac{2\pi Me^2q^2}{m_e} N\bar{B} \tag{3.17}$$

$$\bar{B} \equiv Z \ln\left(\frac{4m_e T}{MI}\right) \tag{3.18}$$

where $\bar{B}$ represents an average over energy or, more crudely, B evaluated at some average energy.

(2) *Region II* (Intermediate Speeds):

$$\frac{M}{m_e} E_I \geq T \geq \frac{M}{2} v_m^2 .$$

The quantity v_m represents the maximum speed of an electron in the stopping material if it is visualized as a Fermi electron gas. Bohr[11] has derived an approximate theory for this energy region assuming that several inner electrons are ineffective (also see Ref. 1). Bohr's result is

$$-\frac{dT}{dr} \approx \frac{C_{II}}{\sqrt{T}} \tag{3.19}$$

$$C_{II} = \frac{16\pi q^2 Z^{1/3}\hbar N}{m_e \sqrt{2/M}} \cdot \tag{3.20}$$

(3) *Region III* (Low Speeds):

$$T \lesssim \frac{M}{2} v_m^2 \ .$$

Fermi and Teller[12] have analyzed this problem (reviewed in Ref. 1) in an approximate fashion by representing the stopping material as a Fermi gas; then

$$-\frac{dT}{dr} = C_{III} \sqrt{T} \tag{3.21}$$

with

$$C_{III} = \frac{4}{3\pi} Ry \frac{m_e}{\hbar} \sqrt{\frac{2}{M}} \ln\left(\frac{\hbar v_m}{e^2}\right) \tag{3.22}$$

where Ry is the Rydberg Energy, $m_e e^4/2\hbar^2$.

3-3.2 A Simplified Model

In summary, we see that all three energy regions lead to an approximate expression of the form

$$-\frac{dT}{dr} \approx \frac{C}{T^n} \tag{3.23}$$

where

Energy Region	C	n
I	Eq. (3.17)	1
II	Eq. (3.20)	1/2
III	Eq. (3.22)	−1/2 .

(3.24)

We are generally most concerned with Regions I and II since the largest part of the particle's energy loss occurs in this portion of the track. Region II may in fact extend to fairly high energies. For example, consider alpha particles slowing in oxygen, where E_I for the K shell is about 540 V, so these electrons begin to participate when the alpha-particle energy is about 4 MeV. Fortunately, these inner elec-

trons are not completely effective due to screening (pp. 170-176, Ref. 1). However, by the time the alpha-particle energy drops to 1 MeV, the L shell or valence electrons become involved and the electron capture is quite significant.

This behavior is illustrated in Fig. 3.2 for alpha-particle slowing in air. As shown in Fig. 3.2(a), the alpha remains almost fully ionized

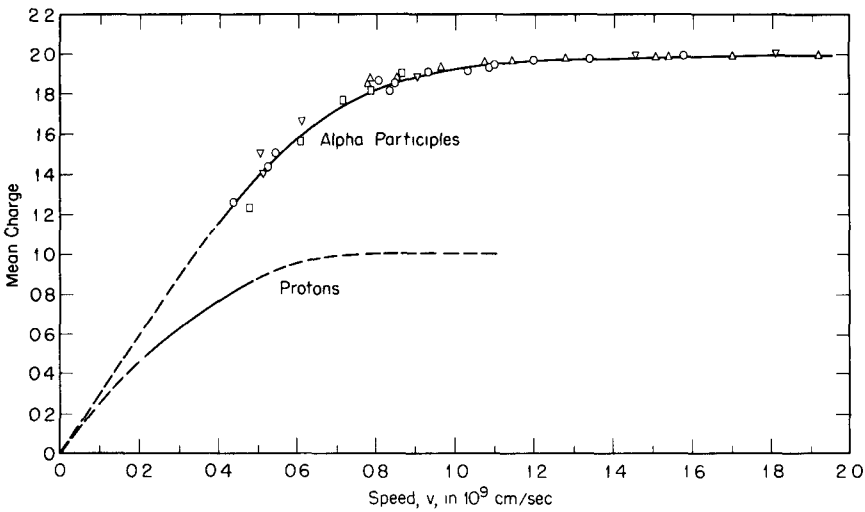

Fig. 3.2(a) — Charge variation for alpha particles and protons slowing in air. Mean charge. (From Evans, Ref. 2. Includes data collected from several investigators.)

until about 2 MeV where the mean charge begins to decrease rapidly such that, near the end of the track, it is proportional to the speed. In this case, Fig. 3.2(b) stresses the point that the mean charge is in reality an average over many particles in the beam. An individual particle will carry a charge of 0, +1e, or +2e as shown.

As we might have anticipated, Eqs. (3.23) and (3.24) show a marked difference between the energy loss in going from Regions I and II to Region III, where the particle is essentially neutralized. In fact, n changes sign. There is a lesser difference between I and II.

We might expect the values given in Eq. (3.24) to be somewhat inaccurate due to the approximations inherent in their derivation. Thus we will assume that Eq. (3.23) is a reasonable form for the slowing law, but we will search for appropriate values of C and n to force a fit to experimental data. In doing this, in the spirit of earlier comments, we will concentrate on Regions I and II and ignore Region III.

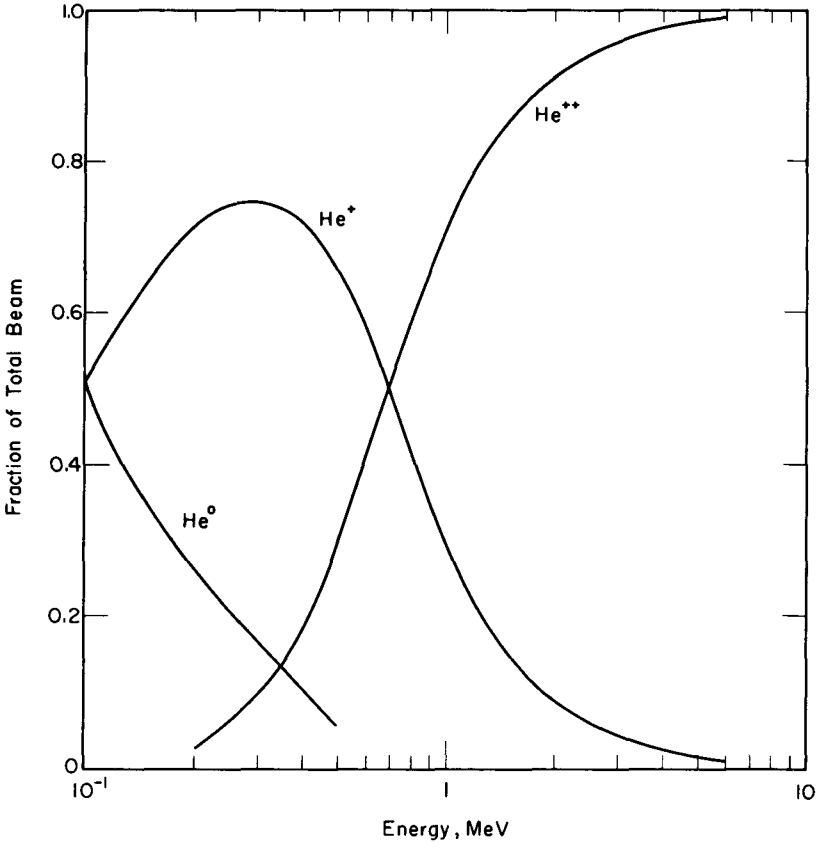

Fig. 3.2(b) — Charge variation for alpha particles and protons slowing in air. Charge equilibrium for alpha particles. (From Berthelot, Ref. 7.)

Equation (3.23) is most conveniently fit to experimental data by introducing the concept of $\lambda(T_0)$, the mean range of an ion born with kinetic energy T_0.

This concept rests on the assumption that the ion track can be approximated by a straight line as illustrated in Fig. 3.3(a). Since the ion–electron mass ratio M/m_e is large, the ion's energy loss per interaction will be small and the straight-line assumption should be reasonably accurate. Some deviations will still occur, and as illustrated in Fig. 3.3(b) we might expect some distribution of path lengths around the mean value $\lambda(T_0)$. This effect is termed "straggling."

Fortunately, straggling is not too important for ions such as alphas and protons, i.e., the distribution of ranges illustrated in Fig. 3.3(b) is quite narrow for these particles. While it might be pos-

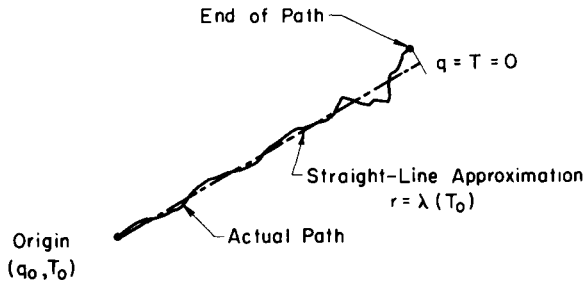

(a)

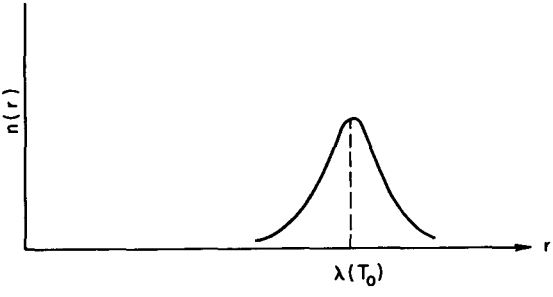

(b)

Fig. 3.3 — Charged particle transport concepts. (a) The straight-line approximation. (Larger deflections occur near the end of the track where "hard" collisions are more likely.) (b) Schematic straggling curve. Here, $n(r)$ represents the number of particles traveling a distance r per unit distance.

sible to improve our straight-line theory by the introduction of straggling parameters, in the interest of simplicity we will not do this here. Straggling is much more important for electron transport, and it will be discussed in more detail in Sec. 3-5.3. If it is desired, the method of analysis developed there can be used for ions with only minor changes.

The straight-line assumption allows direct integration of Eq. (3.23)

$$\int_0^{\lambda(T_0)} dr = -\int_{T_0}^{0} \frac{T^n}{C}\, dT \tag{3.25}$$

or

$$C = \frac{T_0^{n+1}}{(n+1)\,\lambda(T_0)}\,. \tag{3.26}$$

Substitution of C back into Eq. (3.23) gives $-dT/dr$ in terms of the range and the fitting parameter n; therefore,

$$-\frac{dT}{dr} = \frac{T_0}{(n+1)\,\lambda(T_0)} \left(\frac{T_0}{T}\right)^n . \tag{3.27}$$

We can now derive an energy–distance or "slowing-down" law by integrating Eq. (3.27) from 0 to r and T_0 to T. This gives

$$\frac{T}{T_0} = \left(1 - \frac{r}{\lambda(T_0)}\right)^{1/(n+1)} . \tag{3.28}$$

Note that the average range $\lambda(T_0)$ depends on the initial energy T_0, and in fact from Eq. (3.26)

$$\lambda(T_0) \propto T_0^{n+1}. \tag{3.29}$$

Finally, combining Eqs. (3.27) and (3.28), we can write $-dT/dr$ in terms of r

$$-\frac{dT}{dr} = \frac{T_0}{(n+1)\,\lambda(T_0)} \left[1 - \frac{r}{\lambda(T_0)}\right]^{-n/(n+1)} . \tag{3.30}$$

3-3.3 Application to Alphas and Protons

We will use Eqs. (3.26) through (3.30) as the working set for low-q ions. They contain two parameters: the slowing-down parameter n, and the range $\lambda(T_0)$. Both depend on the type of particle involved. The range also depends on the stopping material and hence must be re-evaluated for each problem; however, n turns out to be amazingly constant, independent of the stopping material. This is extremely important, and, in fact, it is this property of n that makes the model so convenient.

We will first illustrate the evaluation of n for alpha particles, again using data for slowing in air (Fig. 3.4). Experimental data for ThC′ alpha rays is shown in Fig. 3.4(a) along with curves for values of n ranging from 0.1 to 0.5. Clearly there are two regions involved—above a MeV or so, $n \approx 0.5$ is the best fit; however, at lower energies the slope shifts closer to $n \approx 0.1$. The change in slope is not surprising. It is probably associated with charge neutralization, which as seen from Fig. 3.2(a), also starts at approximately 1 MeV.

According to Eq. (3.29) the value of $n = 0.5$ predicts that the alpha range will vary as $T_0^{1.5}$. This corresponds to the classic "Geiger Rule" for alpha ranges, which has been used extensively for initial energies between 4 and 10 MeV (p. 652, Ref. 2). For high energies (10 to

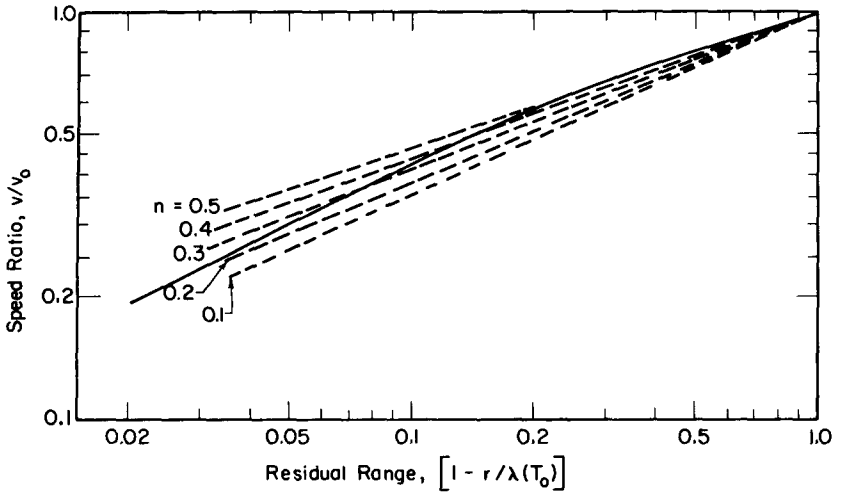

(a)

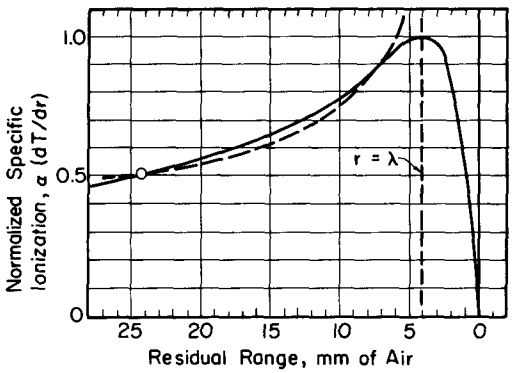

(b)

Fig. 3.4—Comparison of the simplified slowing model with alpha-particle data. (a) Energy–range correlation for alpha particles. [The solid line is a replot of data from p. 649 of Evans, Ref. 2, for ThC′ alpha particles in air. (T_0 = 8.78 MeV; $\lambda(T_0)$ = 8.57 cm).] (b) Bragg curve for an alpha particle in air. [The solid line is from p. 69 of Berthelot, Ref. 7; the dashed line is based on Eq. (3.30) normalized at 24 mm with $(1 - r/\lambda) \rightarrow 0$ at 4 mm.]

200 MeV), Evans[2] has reported that Wilson and Brobeck derived a range relation in which n is about 0.8. It is interesting that he shows that composite range data by Briggs for natural α-rays is well fit by $n \approx 0.63$.

One might question the use of a single value of n in these range correlations. Although a particle may start at 4 MeV, during slowing it clearly must also pass through the lower energy range where n changes! However, for alpha particles and high-energy protons, since $(n + 1)$ is positive, the value of n corresponding to the initial energy tends to dominate. This can be illustrated by dividing the range into two energy regions corresponding to $0 < T < T_1$ and $T_1 < T < T_0$, where T_0 is the initial energy. Then, if Eq. (3.25) is revised to reflect this, we find

$$\lambda(T_0) = \int_0^{T_1} \frac{dT}{(-dT/dr)} + \int_{T_1}^{T_0} \frac{dT}{(-dT/dr)}$$

$$= \frac{T_0^{n+1}}{(n+1)C}\left[1 + \frac{(n+1)C}{(n'+1)C'}\,\frac{T_1^{n'+1}}{T_0^{n+1}} - \left(\frac{T_1}{T_0}\right)^{n+1}\right] \tag{3.31}$$

where the prime indicates parameters for the lower energy region. Since $C' \approx C$ and $n' < n$, the bracketed quantity approaches unity for $T_1/T_0 \ll 1$.

Another aspect of the simplified model is illustrated in Fig. 3.4(b), where it is compared with the well-known Bragg Curve for alpha particles in air. As the particle slows, it interacts more effectively to produce a larger ionization density per unit track despite its partial neutralization. Thus, a peak occurs near the end of the track.

As seen from the figure, the simplified model reproduces the general shape of the curve quite well except near the peak. As seen from Eq. (3.30), for cases like this where $n > 0$, $(dT/dr) \to \infty$ as the residual range goes to zero. This introduces an error. Further, unless care is taken to adjust the range λ so that $(1 - r/\lambda)$ goes to zero at the peak of the curve, the calculated curve will be even more in error. Fortunately however, as long as the main portion of the curve is fit well, transport problems of interest here can still be evaluated fairly accurately.

A somewhat different presentation of slowing-down data is shown for protons in Fig. 3.5. Here the "atomic stopping cross section" ϵ defined as

$$\epsilon = -\frac{1}{N}\frac{dT}{dr} \qquad (\text{eV cm}^2) \tag{3.32}$$

is plotted as a function of energy for slowing in six different materials.

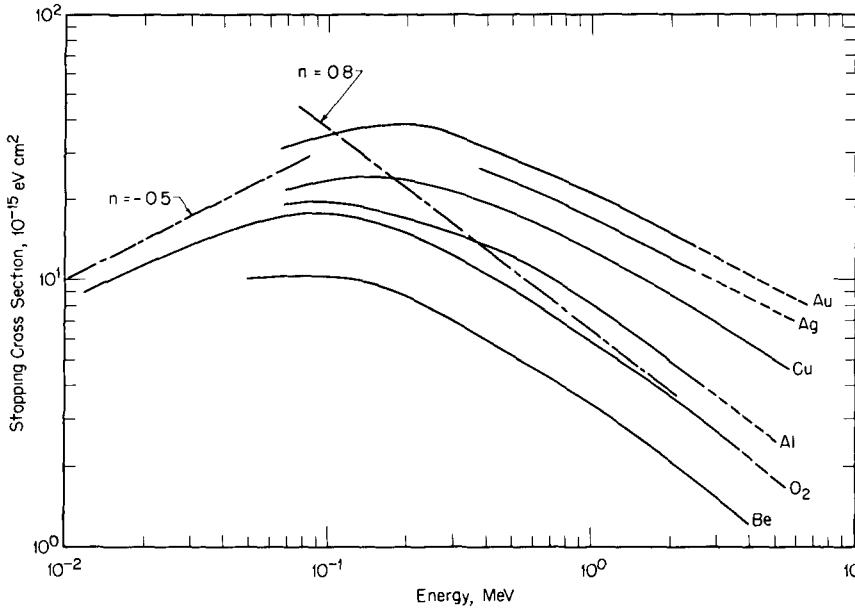

Fig. 3.5 — The slowing correlation for protons. (The solid curves are plots of atomic stopping cross sections based on data from Whaling, Ref. 6.)

Here N (atoms/cm^3) applies to the stopping material. By comparison with Eq. (3.23), we see that

$$\ln \epsilon = -n \ln T + \ln \frac{C}{N} \tag{3.33}$$

where C is given by Eq. (3.26). Thus, the slope of the curves in Fig. 3.5 gives $-n$. As illustrated, for energies above ≈ 1 MeV, $n = 0.8$ gives a good fit. (In an earlier study, Evans[13] also recommended this value for use in space shielding calculations.) However, for protons there is a drastic change in slope at lower energies and in fact n changes sign. Below ≈ 0.1 MeV, $n \approx -0.5$ fits the data in Fig. 3.5. On the other hand, Wahling[6] suggests -0.25 based on other range–energy data.

It should be noted that Fig. 3.5 is a good illustration of the near constancy of n for such widely different substances as O_2 and Au. Curves for 16 additional materials including both gases and metals are presented in Ref. 6, and all show similar trends.

In contrast to n, the range $\lambda(T_0)$ depends strongly on the stopping material and must be re-evaluated for each problem. A number of

correlations are available,[1–7] but for convenience a particularly simple range–energy nomograph devised by R. Wilson (pp 222-227, Ref. 1) is reproduced in Fig. 3 6. This nomograph is probably accurate to within several percent over the ranges included. To use it, connect the energy and Z by a straight line and extend the line to the range

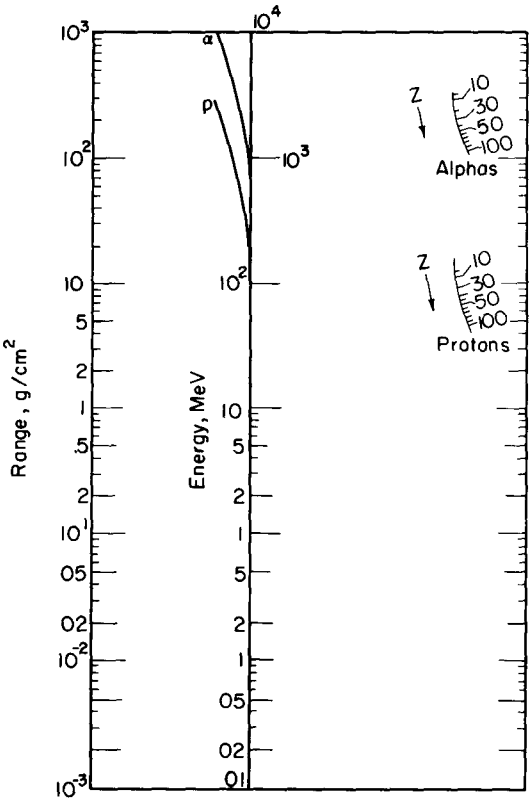

Fig 3.6 — Range–energy nomograph for low-q particles (From Bethe and Ashkin, Ref. 1, due to unpublished work by R. R. Wilson. Left scale range in grams per square centimeter Middle scales kinetic energy in MeV. Upper-right scales atomic number Z of stopping material To use, connect range, energy, and Z by a straight line) For convenience the range scale has been extended to smaller values here.

scale. At non-relativistic energies use the straight middle energy scale.

For example, to find the range of a 10-MeV alpha particle in aluminum, connect Z = 13 on the upper right scale and $T_0 = 10$ on the middle scale. Extrapolation gives a range of 1.5×10^{-2} g/cm^2, or,

since aluminum has a density of 2.7 g/cm^3,

$$\lambda_{Al}(10 \text{ MeV}) = \frac{1.5 \times 10^{-2}}{2.7} = 5.6 \times 10^{-3} \text{ cm}. \tag{3.34}$$

One final problem should be noted in connection with evaluation of $\lambda(T_0)$. As discussed earlier, there is some difficulty in fitting a Bragg curve unless an adjusted or "extrapolated range" is used. This is a direct result of neglecting energy Region III in the development of the slowing law. Thus, it may be desirable to use an "extrapolated range" based on an extrapolation of the experimental data for energies in Region II rather than the actual measured range. This is illustrated schematically in Fig. 3.7. Fortunately the difference between these ranges is normally quite small so values taken from the nomograph of Fig. 3.6 can be used directly as a first approximation.

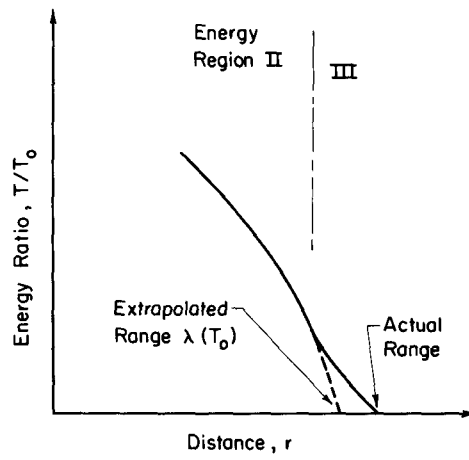

Fig. 3.7—Schematic illustration of the extrapolated range. (The difference between ranges is exaggerated for clarity.)

3-4 FISSION FRAGMENT SLOWING

Fission fragments differ from alpha particles, protons, etc., in two important respects. Both their mass and initial charge are significantly larger. Also, a distribution of masses and charges results from the fission process. Because these factors strongly influence slowing down, we will first briefly review fragment properties. (A complete discussion is presented by Hyde in Ref. 14.)

3-4.1 Fission Fragment Properties

Cells might utilize either spontaneous or neutron induced fission, and we will consider ^{235}U as a representative example. The well-known mass yield or mass distribution curve[15] for thermal neutron fission of ^{235}U is reproduced in Fig. 3.8. In addition to the mass curve, the initial energy distribution for the fragments is required. This may be calculated from the mass distribution as indicated in Appendix C, or alternately an experimental curve[16] such as shown in Fig. 3.9 may be used. A useful, approximate analytic representation for the energy distribution suggested by Redmond et al.[17] is

$$S_j(T_0) = \begin{cases} 0.685 \exp\left[-\alpha (T_0 - 67)^2\right] & (j = 1) \\ \exp\left[-\gamma (T_0 - 98)^2\right] & (j = 2) \end{cases} \tag{3.35}$$

where $S_j(T_0)$ represents the number of fragments born in the j*th* group (1 = heavy, 2 = light) at energy T_0 per unit energy. The constants are $\alpha = 0.00693$ and $\gamma = 0.0177$, and this correlation is valid for $0 \leq T_0 \leq 115$ MeV.

Since both the energy and mass distribution curves are quite narrow, it is often sufficiently accurate to define heavy and light fragment groups having average parameters as indicated in Table 3.1. Note that the initial electronic charge q_0 has a very narrow distribution and can essentially be thought of as unique rather than an average value.[14]

3-4.2 Fragment Slowing

Typical energy–range[18] and Bragg[19] curves for fission fragments are shown in Fig. 3.9. The striking contrast between these curves and the earlier alpha-particle curves of Fig. 3.4 can be explained as follows. Unlike low-q ions, the fission fragments undergo electron capture over their entire track; hence, $-dT/dr$ is a maximum at the beginning of the track where q is a maximum. Due to their mass, fission fragments suffer significant nuclear collisions, particularly as they approach neutrality, and this accounts for the peaks at the end of the tracks. These collisions are quite effective. Discounting grazing incidents, less than 10 collisions are required to stop the fragment (p. 670, Ref. 2).

Using the data of Table 3.1, we can easily show that $qe/\hbar v$ is of the order of 2 to 3 over most of the range of a fission fragment; consequently, the electronic interaction can be represented by Eq. (3.12)—the classical case. Nuclear collisions introduce an additional term,[1] so that $-dT/dr$ becomes

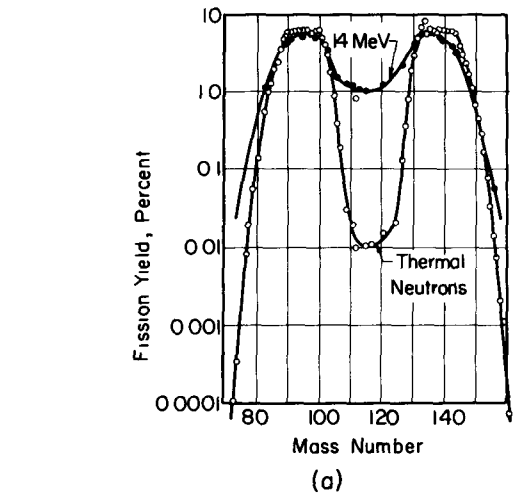

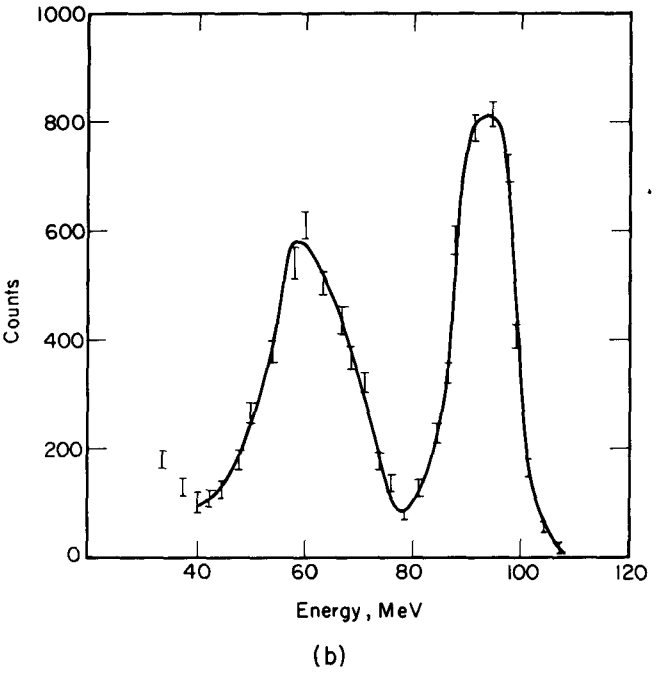

Fig. 3 8 — Fission fragment energy and mass-distribution curves for ^{235}U. (a) Mass distribution for fission of ^{235}U. (From Katcoff, Ref. 15.) (b) Energy distribution for thermal neutron fission of ^{235}U. (From Brunton and Thompson, Ref. 16. The data shown have not been corrected for an ionization loss of about 7 MeV per fragment.)

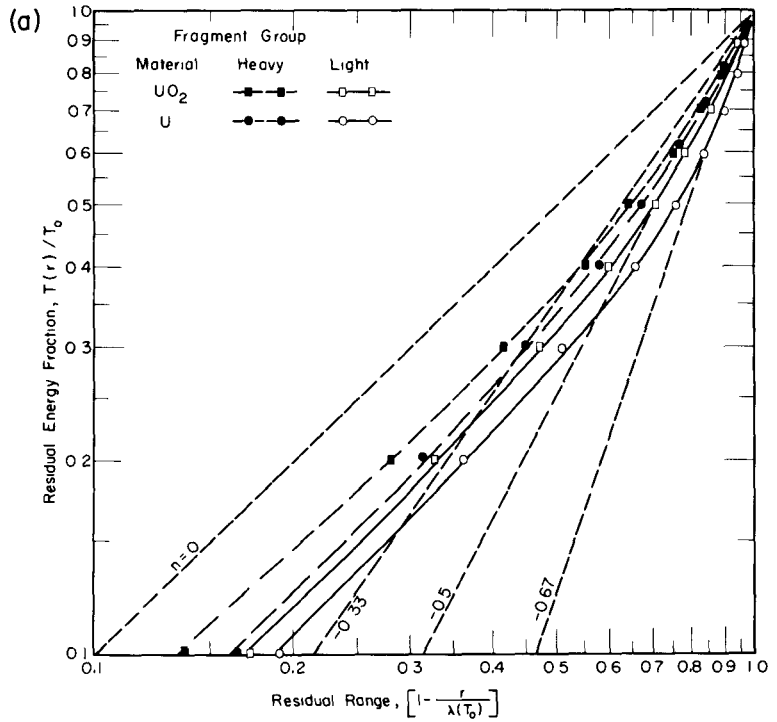

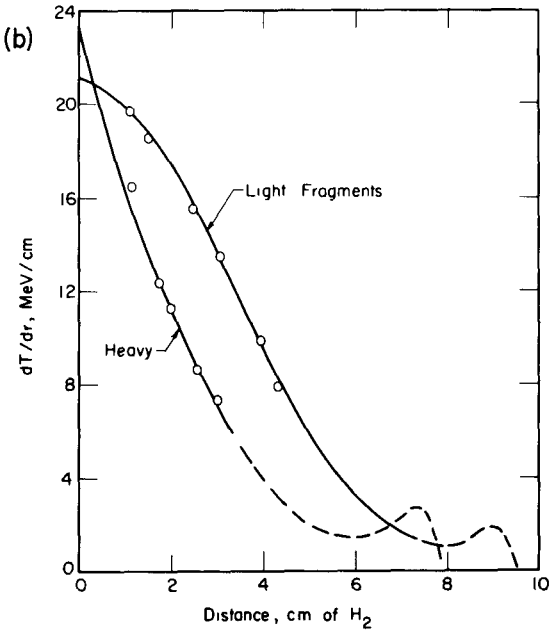

Fig. 3.9 — Slowing curves for fission fragments. (a) Energy–range curves for U and UO_2. (From Miley, Ref. 18. Points shown were estimated using experimental data for other materials as described in Ref. 18.) (b) Bragg curve for slowing in H_2. (From Evans, Ref. 2.)

$$-\frac{dT}{dr} = \frac{4\pi e^2 q^2(v)}{m_e v^2} N \left(B_e + \frac{e^2 Z_f^2 Z m_e}{M_f q^2(v)} B_n \right) \tag{3.36}$$

where

$$B_e = Z \ln \left(\frac{1.123 m_e v^3}{\omega q(v) e} \right) \tag{3.37}$$

$$B_n = Z \ln \left[\frac{M_f M v^2 a_{12}^{sc}}{(M_f + M) Z_f Z e^2} \right]. \tag{3.38}$$

The term B_e is the electronic stopping number; B_n is the corresponding quantity for nuclear collisions; subscript f indicates fragment proper-

Table 3.1 — AVERAGE FISSION FRAGMENT PARAMETERS FOR SLOW NEUTRON INDUCED FISSION*

	^{233}U	^{235}U	^{239}Pu
T_0 (total), MeV	163 ± 2	165 ± 2	172 ± 2
T_{01}, MeV†	66	67	72
T_{02}, MeV	97	98	100
v_{01}, cm/nsec	0.96	0.97	1.00
v_{02}, cm/nsec	1.42	1.41	1.39
M_{f1}, amu	139	140	140
M_{f2}, amu	95	96	100
q_{01}		+22e (+15e)‡	
q_{02}		+20e (+16e)	

*From Hyde, Ref. 14.

†In this notation a subscript zero indicates the initial condition, 1 indicates the heavy group and 2 the light group.

‡As discussed in the text, values in the parentheses should be used as the initial equilibrium values in Eq. (3.39).

ties; a_{12}^{sc} is the impact parameter beyond which energy losses go to zero due to screening; and the charge q has been written as q(v) since it depends on the fragment's speed. Other quantities have been defined previously.

The charge–speed relation was first investigated by Bohr[11,20,21] using the Fermi–Thomas statistical model. He found

$$q(v) \approx Z_f^{1/3} \frac{\hbar v^m}{e^2} \equiv q_0 \left(\frac{v}{v_0} \right)^m \tag{3.39}$$

with m assigned a value of 1.0. Early experiments by Lassen[22] indicated that this was reasonably accurate for heavy particles but that $m \approx 1/2$ should be used for the light fragments. However, more recent data by Fulmer and Cohen[23] indicate that, to the contrary, m is about

1.1 for heavy fragments and about 1 for light fragments. A plot of their data is reproduced in Fig. 3.10. Their results also indicate that the fragment charge almost instantaneously drops from an initial value of ≈ 20 e to ≈ 16 e. Once it reaches the latter "equilibrium value," further reduction follows Eq. (3.39).* Thus the equilibrium values of Table 3.1 should be used for q_0 in applying Eq. (3.39).

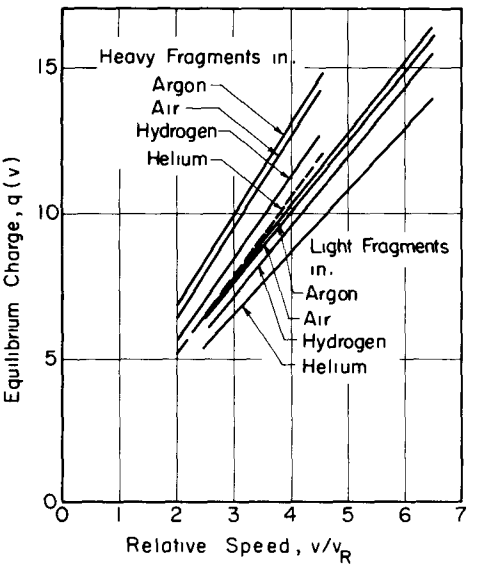

Fig. 3.10—The charge q(v) for fission fragments. (From Fulmer and Cohen, Ref. 23. The speed v is normalized by $v_R = \hbar/e^2$.)

In the spirit of the previous analysis of low-q ions, we begin by neglecting B_n in Eq. (3.36) on the basis that nuclear collisions are only important over a relatively small distance at the end of the track [see Fig. 3.9(b)]. Substitution of q(v) from Eq. (3.39) into (3.36) gives

$$-\frac{dT}{dr} = \frac{4\pi e^2 q_0^2}{m_e v^{2(1-m)} v_0^{2m}} NB_e \tag{3.40}$$

*Actually, as shown by recent experiments, q_0 depends on the density of the target material [see H. D. Betz et al., *Phys. Lett., 22,* 643 (1966)]. Differences may be large; e.g., the average charge on heavy ions may be almost twice as large in a solid as in a gas. It has, in fact, been suggested that this effect might be utilized as the basis for a uranium-ion accelerator [see G. Hortig, *IEEE (Inst. Elec. Electron. Eng.), Trans. Nucl. Sci., NS-16,* No. 3, Pt. I, 75 (1969)].

$$B_e = Z \ln \frac{1.123\, m_e v^{3-m} v_0^m}{\omega q_0 e} \tag{3.41}$$

Since m is of the order of 1, B_e has roughly the same dependence on v as in the quantum mechanical limit given in Eq. (3.8). Again, arguing that the logarithmic term is slowly varying, we can use an average value $\bar{B}_e$, so Eq. (3.40) becomes

$$-\frac{dT}{dr} = \frac{C_f'}{T^{(1-m)}} \tag{3.42}$$

$$C_f' \equiv \left[\frac{4\pi e^2 q_0^2}{m_e (2/M_f)^{(1-m)} v_0^{2m}}\right] N\bar{B}_e. \tag{3.43}$$

Alternately, more flexibility is afforded if, by analogy with the low-q ion results, we write B_e as

$$B_e = [B_e]_{v=v_0} \left(\frac{T}{T_0}\right)^K. \tag{3.44}$$

For example, $K = \frac{1}{2}$ gives $B_e \propto v$. In this formalism, we get

$$-\frac{dT}{dr} = \frac{C_f}{T^S} \tag{3.45a}$$

$$S \equiv 1 - (m + K) \tag{3.45b}$$

where

$$C_f = \frac{C_f' [B_e]_{v=v_0}}{\bar{B}_e \cdot T_0^K}. \tag{3.46}$$

We adopt Eq. (3.45a) as our working equation. It is of the same form as Eq. (3.23) for low-q ions; hence, Eqs. (3.27) through (3.31) are valid if n is replaced by S and C is replaced by C_f.

It is understood that, if the light and heavy group formalism is to be adopted, S and C_f may be different for the two groups, and in later sections, we use the subscript j to indicate this. As before, j = 1 indicates the heavy group; j = 2, the light group.

Miley[18] has reviewed the correlation of this result with experimental data available up to January 1965. On the basis of transmission measurements such as shown in Fig. 3.9, he found the values for S_j given in Table 3.2, but pointed out that $S_1 = -0.5$ and $S_2 = -0.67$ give better agreement with integral data — that is, fragment energy spectra

Table 3.2—VALUES OF S_j BASED ON TRANSMISSION DATA*

	S_j	
j	$0.4 < T/T_0 < 1.0$	$0 < T/T_0 < 0.4$
1	−0.48	0
2	−0.6	0

*From Miley, Ref 18; based on data in Fig 3 9 Note that n = S_j in the figure

measurements for various fuel-layer thicknesses. More recent integral data by Kahn et al.[24] indicate that $S_1 = S_2 = -0.5$ is to be preferred. Thus, there remains some discrepancy between the transmission measurements and integral spectra studies.

If we select $S_1 = S_2 = -0.5$ and assume $m_1 = m_2 = 1.0$, then from Eq. (3.45b) K (the exponent on B_e) is 0.5, which implies that $B_e \propto v$. This corresponds to the result for low-q ions in Energy Region II, and it is in agreement with independent arguments advanced by Walton (p. 208, Ref. 5).

We still need to evaluate the mean range $\lambda(T_0)$ for fission fragments, and several correlations have been presented. One of the earliest was due to Bohr,[11] who derived the ratio of the range of a fission fragment to that of an alpha particle of the same initial speed v_0

$$\frac{\lambda(T_0)}{\lambda_\alpha(M_\alpha T_0/M_f)} \approx \frac{7}{2}\left(\frac{A_f M_f}{Z_f^{2/3}}\right)\frac{e^4}{\hbar^2 T_0} \tag{3.47}$$

where A_f, M_f, and Z_f are the mass number, mass, and nuclear charge number of the fragment, respectively, and M_α is the alpha-particle mass. This can be used in connection with the earlier nomograph (Fig. 3.6) for λ_α.

However, better accuracy can be obtained by using an empirical correlation such as presented by P. W. Frank[25]

$$\lambda(T_0) = \left(0.03910 + 0.02020\,\frac{M}{Z^{1/2}}\right)\frac{T_0^{2/3}}{\rho} \tag{3.48}$$

where the quantities without subscripts refer to the stopping material. (With ρ in mg/cm^3 and T_0 in MeV, λ is in cm.) This correlation, based on a least squares fit to data from eleven different materials, originated from the suggestion by Alexander and Gazdik[26] that

$$\lambda(T_0) \propto T_0^{2/3}. \tag{3.49}$$

Referring back to Eq. (3.29), we see that this implies $S = -1/3$. This choice is at variance with the S values suggested by both Miley[18] and Kahn et al.[24] The latter recognized this discrepancy and used the same data as Frank[25] to obtain a correlation consistent with $S = -1/2$

$$\lambda(T_0) = \left(0.0968 + 0.0497 \frac{M}{Z^{1/2}}\right) \frac{M_f^{1/2} T_0^{1/2}}{Z_f^{2/3} \rho}. \tag{3.50}$$

Figure 3.11 compares these correlations with Niday's data[27] for slowing in uranium metal. Because fission leads to a spread in nuclear

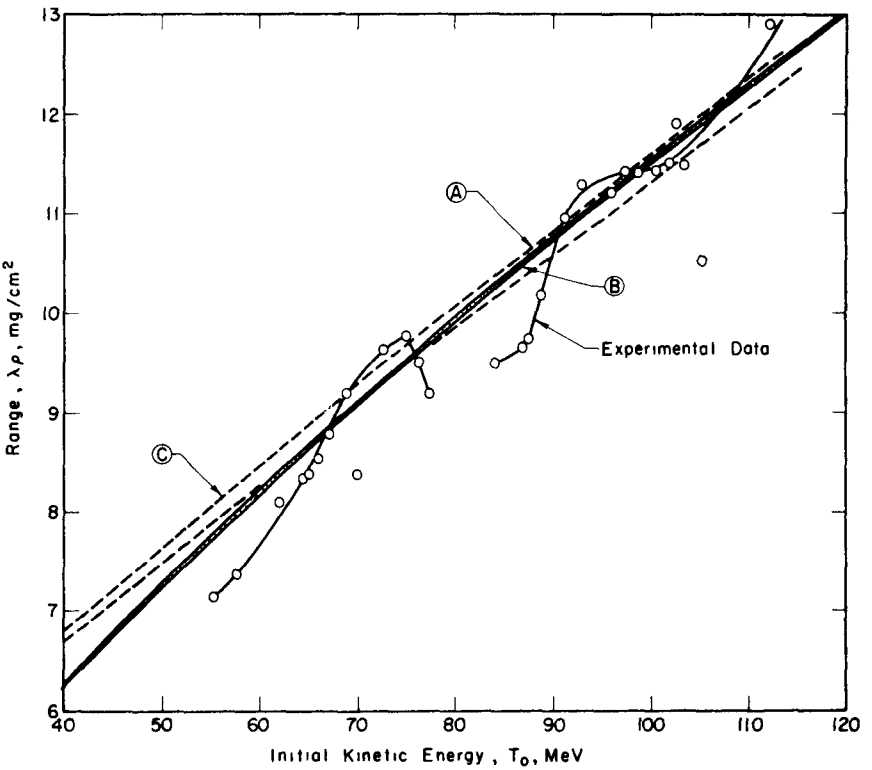

Fig. 3.11 — Fission fragment range correlations. (The data points were calculated from Niday's original range–mass data (Ref. 27) using Eq. (C.8), Appendix C. Curve A is based on Eq. (3.49), normalized to 8.95 mg/cm^2 at 67 MeV. Curve B, which is quite similar to A, represents Frank's correlation [Eq. (3.48)] with M = 235 and Z = 92. Curve C is based on the correlation by Kahn et al. [Eq. (3.50)]; Z_f is from Hyde, Ref. 14. The region between the dashed lines represents the spread due to the normal distribution of Z_f.)

charge Z_f for a fixed initial energy T_0, Kahn's correlation is represented as a band of finite width. Actually, for the range of energies involved, there is not too much difference between the various correlations. They give the average slope of the experimental data fairly well, but do not include the fine structure.

3-5 ELECTRON SLOWING

The relatively small mass of the electron leads to additional complexities in electron slowing theory:

(1) Relativistic corrections are more likely to be important.

(2) In addition to collisional processes, bremsstrahlung represents a significant energy loss mechanism for higher-energy electrons.

(3) Large angle scattering is more likely than for heavy ions, in which case an electron can lose a significant fraction of its energy in a collision. Thus, straggling is much more pronounced than for ions, and the concepts of straight-line motion and average range have meaning only in terms of the average behavior of a large population.

(4) Secondary electrons produced during the slowing process can be important—e.g., delta-ray electrons from hard collisions can result in significant side branching outside the path of the primary beam. And, near the end of the electron track a significant portion of the secondary electrons may be almost as energetic as the primary particle so the distinction between them becomes somewhat nebulous.

3-5.1 Energy–Range Relations

Using Moller's formula[28] for electron–electron scattering, Bethe[1] developed the following expression for ionization energy losses during electron slowing

$$\left[-\frac{dT}{dr}\right]_{\text{ionization}} = \frac{4\pi e^4}{m_0 v^2} NB_e \tag{3.51}$$

$$B_e = \frac{Z}{2}\left\{\ln\frac{m_0 v^2 T}{2I^2(1-\gamma^2)} - (2\sqrt{1-\gamma^2} - 1 + \gamma^2)\ln 2 + 1 - \gamma^2 + \frac{1}{8}(1-\sqrt{1-\gamma^2})^2\right\} \tag{3.52}$$

where m_0 is the rest of the electron, γ is the speed ratio v/c, and the other symbols are as defined earlier. For $\gamma \ll 1$, the stopping power reduces to

$$B_e = Z \ln \frac{m_0 v^2}{2I} \sqrt{\frac{e_b}{2}} \tag{3.53}$$

where e_b is the base of the natural logarithm. For very high speeds where $T \gg m_0c^2$, the stopping power becomes

$$B_e = \frac{Z}{2}\left(\ln \frac{T^3}{2m_0c^2I^2} + \frac{1}{8}\right). \tag{3.54}$$

The total energy loss per unit path length can be thought of as the sum of the losses considered above for ionization processes and that due to bremsstrahlung or radiative processes. Thus,

$$\frac{dT}{dr} = \left[\frac{dT}{dr}\right]_{\text{ionization}} + \left[\frac{dT}{dr}\right]_{\text{radiation}}. \tag{3.55}$$

The calculation of radiation losses is rather involved, but for non-relativistic electrons, it is given approximately as (p. 614, Ref. 2)

$$\left[\frac{dT}{dr}\right]_{\text{radiation}} \approx \frac{16}{411} \frac{e^4 N Z^2}{m_0 c^2} \qquad (T \ll m_0c^2). \tag{3.56}$$

For expressions valid at higher energies, the reader is referred to the review by Koch and Motz[29] and also the calculations by Berger and Seltzer (pp. 209-212, Ref. 4).

Radiation losses tend to dominate at higher energies, whereas ionization losses are most important at low energies. The energy at which the two losses are equal is defined as the critical energy T_c, and it may be found from the empirical expression (p. 215, Ref. 4)

$$T_c \approx \frac{800}{Z + 1.2} \qquad \text{(in MeV)}. \tag{3.57}$$

In most cases of interest for Direct-Collection Cells, the electron energies involved will be less than the critical value; consequently, we will neglect radiation losses in the following discussion.

A comparison of Eqs. (3.51) and (3.52) with the earlier relations for ions [Eqs. (3.4) and (3.5)] shows that they differ only in the form of the stopping number (in fact, since the electron charge is fixed, $q(v) = e$, the complexity of charge variation is removed). For example, the non-relativistic stopping number for electrons, Eq. (3.53), differs from the

corresponding expression for ions [Eq. (3.8)] simply by the additional numerical factor $1/4\sqrt{e_b/2}$ in the argument of the logarithm.*

We might argue again that, since the stopping number will not vary rapidly with energy, electron slowing should be reasonably well represented by Eqs. (3.27) through (3.30) developed earlier for low-q ions and fission fragments. This is not without precedence. The so-called "Thomson–Whiddington Law" (p. 623, Ref. 2; Refs. 30 to 32), long used in the x-ray literature, represents the range of soft electrons as

$$\lambda(T_0) \propto T_0^2. \tag{3.58}$$

Recalling that the energy loss model of Eq. (3.23) gives a range proportional to T_0^{n+1} [see Eq. (3.29)], we see that this is consistent with n = 1. Workers interested in secondary electron emission have also commonly used n = 1 (p. 264, Ref. 33). Recent studies of cathode- and radio-luminescence[34] have used similar correlations, and in this connection, Everhart[35] found n = 1.22 gives a good fit to experimental data for aluminum oxide films.

Further insight into the selection of n can be gained by reviewing the widely used range–energy correlation for electron slowing in aluminum devised by Katz and Penfold.[36] Using a collection of experimental data available up to 1951, they found the correlations

$$\lambda_{Al}(T_0) \approx \frac{412}{\rho} T_0^{(1.26-0.0954 \ln T_0)} \qquad (0.1 < T_0 < 2.5 \text{ MeV}) \tag{3.59a}$$

$$\lambda_{Al}(T_0) \approx \frac{530}{\rho} T_0 - 0.039 \qquad (2.5 < T_0 < 20 \text{ MeV}) \tag{3.59b}$$

where ρ is the density (mg/cm^3) of aluminum. A plot of this correlation along with some experimental data is shown in Fig. 3.12. The Katz–Penfold correlation gives an excellent fit; however, if one selects 1/2 MeV as a dividing energy, a reasonable approximation suggested by Evans[2] is

$$\lambda_{Al}(T_0) \propto T_0^2 \qquad (0.1 < T_0 < 0.5 \text{ MeV}) \tag{3.60a}$$

$$\lambda_{Al}(T_0) \propto T_0 \qquad (0.5 < T_0 < 20 \text{ MeV}). \tag{3.60b}$$

*This factor is due to two considerations: (1) In electron scattering the electron emerging with the higher energy is defined as the primary one so the maximum energy loss is $\frac{1}{4}$ mv^2 rather than $\frac{1}{2}$ mv^2. (2) A correction has been included to account for scattering of identical particles both having spin $\frac{1}{2}$.

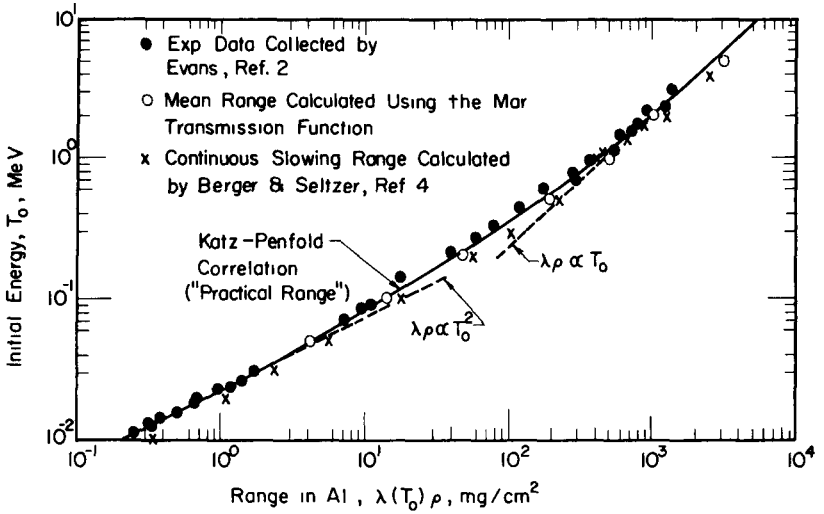

Fig. 3.12 — Electron range–energy relations for aluminum.

Thus, $n \approx 1$ is indicated for energies below $\frac{1}{2}$ MeV and $n \approx 0$ for higher energies.

3-5.2 Ranges

Again, absolute values of the range are needed for a given material. Comprehensive listings of calculated ranges have been prepared by Nelms[37] and more recently by Berger and Seltzer (see pp. 228-268 of Ref. 4). For convenience, some representative values from the latter are given in Table 3.3.

Table 3.3 — REPRESENTATIVE ELECTRON RANGES*

Medium†	T_0 (MeV)	$\lambda(T_0)$ (cm)					
		0.5	1.0	1.5	2.0	3.0	5.0
H_2	(8.375×10^{-5})	1.0×10^3	2.5×10^3	4.1×10^3	5.6×10^3	8.7×10^3	1.5×10^4
C	(2.22)	0.089	0.22	0.37	0.50	0.77	1.29
Al	(2.69)	0.083	0.20	0.33	0.45	0.69	1.13
Fe	(7.87)	0.031	0.076	0.12	0.17	0.25	0.41
Pb	(11.34)	0.029	0.067	0.10	0.14	0.20	0.31
U	(19.0)	0.018	0.041	0.064	0.085	0.12	0.19

*Calculated values from Ref. 4.
†Densities (g/cm³) are given in parentheses under each material.

A convenient analytic correlation is not readily available. Several authors[38,39] suggest generalizing the Katz–Penfold correlation for aluminum by multiplying $\lambda(mg/cm^2)$ of Eq. (3.59) by the factor (A/Z)(13/27) where A and Z are for the material of interest. To test this, a plot of $\lambda\rho/(\lambda\rho)_{Al}$ vs Z was developed in Fig. 3.13 using ranges for various materials from Ref. 4. The points in this graph represent a plot of (A/Z)(13/27).

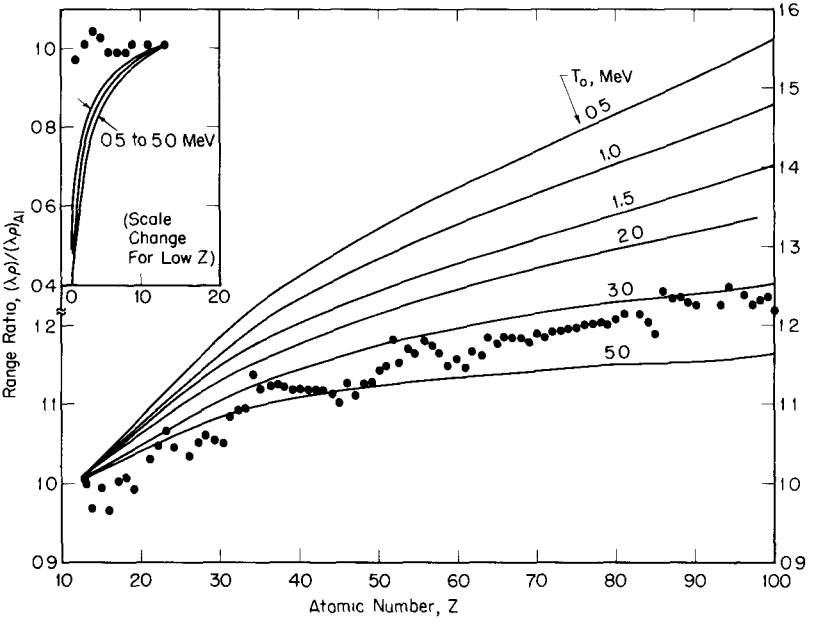

Fig. 3.13 — Electron range variation with atomic number. (The data points represent $(^{13}/_{17})(A/Z)$. The solid lines are based on values from Table 3.3 and similar calculations by Berger and Seltzer, Ref. 4.)

As can be seen, the points coincide fairly well with the curve for an initial energy of 3 MeV, but curves for other energies deviate considerably. A rough correlation including this energy dependency is found to be $(13A/27Z)(3/T_0)^{0.12}$ where T_0 (MeV) is the initial energy. However, this result cannot be used for $Z < 13$.

The range relations presented up to this point are for a discrete initial energy T_0. However, electrons from beta decay and Compton interactions that have a broad initial energy distribution are often of interest in nuclear cells. This is not a problem in cell calculations since, as is shown in later chapters, the range is ultimately integrated over the actual source energy distribution. However, for rough cal-

culations, it may be of interest to have an average or "effective" range for the electrons from these sources. Two such correlations should be noted. An effective Compton electron range correlation for aluminum developed by Curran et al.[40] is shown as a function of the incident gamma-ray energy in Fig. 3.14. Also, it has been shown (p. 627, Ref. 2) that an effective range for electrons from beta decay is found if the maximum or end-point energy of the beta spectrum is used for the energy in the Katz–Penfold relation.

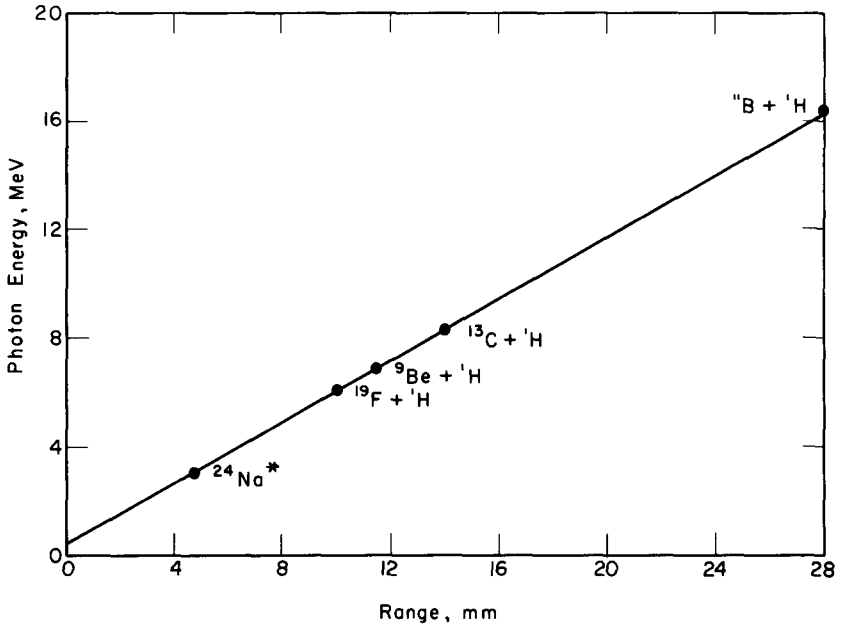

Fig. 3.14—Effective range in aluminum of electrons produced by gamma rays, as a function of the gamma-ray energy. (From Bethe and Ashkin, Ref. 1, based on data by Curran, Dee, and Petrzilka, Ref. 40.)

3-5.3 Straggling

Straggling is especially important for electrons, which, due to their low mass, may suffer large angle scattering during slowing [Fig. 3.15(a)]. This introduces two effects: (1) The *actual path length traveled* by the electron will differ considerably from the *range or crow-flight distance.* (2) If a number of particles are involved, there will be a distribution of both path lengths and ranges around their mean values. These concepts are illustrated in Fig. 3.15(b), which is based on data by Williams,[32] who recorded 145 individual electron histories for 19.6-MeV electrons slowing in oxygen at 1-atm pressure.

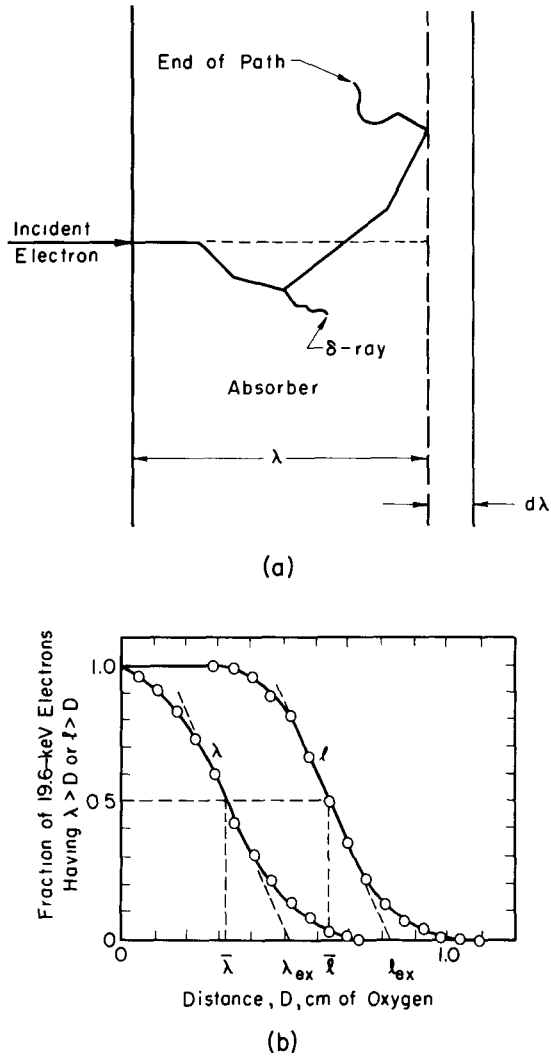

Fig. 3.15—The difference between the mean range and the mean path length. (Adapted from Evans, Ref. 2.) (a) Schematic diagram of an electron path. Because it is multiply scattered while traversing the absorber of thickness $\lambda + d\lambda$, the electron does not emerge. If the absorber had been of thickness λ, the electron would have just penetrated it and be said to have a range λ. The total path length l is measured along the actual path of the electron and is always considerably greater than λ. (b) The distribution of path lengths l and of range λ for 19.6-keV electrons in oxygen at 0° C and 1-atm pressure: $\bar{\lambda} = 0.32$ cm = mean range, $\lambda_{ex} = 0.52$ cm = extrapolated range, $\bar{l} = 0.64$ cm = mean path length, $l_{ex} = 0.82$ cm = extrapolated path length, and $\sqrt{2/\pi}\,(l_{ex} - \bar{l}) = 0.14$ cm $= 0.22\,\bar{l}$ = standard deviation of l about $\bar{l}$. The mean path length is 1.24 times the extrapolated range, under these conditions. (Based on data by Williams, Ref. 32.)

The distributions show considerable spread, and in this case the mean path length was about twice the mean range.

The difference between the path length and range introduces a serious problem from a theoretical point of view. Energy loss calculations generally yield the average loss per unit path traveled, whereas the simplified energy loss model of the previous section involves an average loss per unit range. However, this difficulty can be partially circumvented if experimental energy–range data are used to determine n and $\lambda(T_0)$ in the simplified model so that it is automatically normalized to the average energy loss per unit range. While expedient, this approach fails to provide information about the energy spread involved. In other words, while Eq. (3.28) defines a mean energy, the inherent differences in path length will lead to a distribution of energies around this mean, and this is sometimes termed "energy straggling."

Some further insight can be gained through the experimental results of Fig. 3.16. This shows the energy distribution for electrons transmitted through various thicknesses of mica due to an impingent beam at 0.21 MeV—the energy spread clearly increases with thickness. Also, note that the various spectra are asymmetric. This is a general characteristic of electron straggling, which we will recall later.

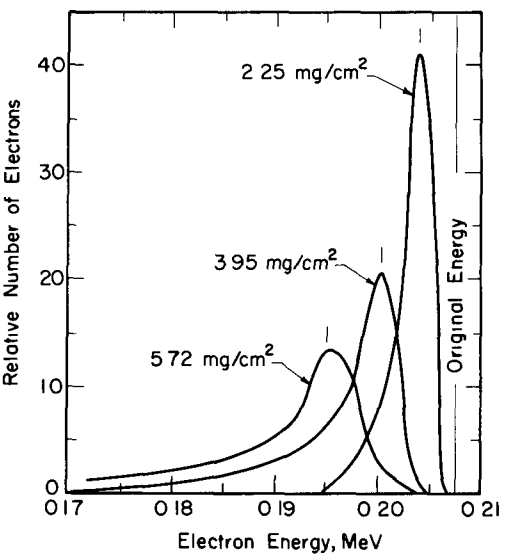

Fig. 3.16—Electron transmission through mica (From Evans, Ref. 2. Transmission through mica of monoenergetic electrons from the 0.2065-MeV conversion line of RaB. The position of the shifted peaks gives the most probable energy loss. Note that it is obviously different from the average energy loss, because the peaks are asymmetric The data for this figure are based on results by White and Millington as reported by Evans.)

To study this effect quantitatively, it would be desirable to find a mathematical expression for the distribution of energies for a fixed range. In the present treatment, however, it is more convenient to calculate the range distribution, and this, in effect, gives the same information. We begin by defining $P(\lambda,T_0)\,d\lambda$ as the probability that a particle of initial energy T_0 will have a range lying between λ and $\lambda + d\lambda$. Thus, the probability that a particle will travel a crow-flight distance greater than r, defined as the *transmission probability* $T(r,T_0)$, may be found by the integration

$$T(r,T_0) = \int_r^\infty P(\lambda,T_0)\,d\lambda. \tag{3.61}$$

Also, an average range can be defined as

$$\langle\lambda(T_0)\rangle = \int_0^\infty r\,P(r,T_0)\,dr. \tag{3.62}$$

A common assumption for *ion transport* is that $P(\lambda,T_0)$ is Gaussian, i.e.,

$$P(\lambda,T_0) = \frac{1}{2S}\exp\left[-\left(\frac{\pi}{4S^2}\right)(\lambda-\bar{\lambda})^2\right] \tag{3.63}$$

where $\bar{\lambda}$, the mean range, is approximately* equal to $\langle\lambda\rangle$, and S, defined as the straggling parameter, is related to the standard deviation

$$S^2 = \frac{\pi}{2}\langle(\lambda-\bar{\lambda})^2\rangle \tag{3.64}$$

In general, S must be determined from experimental data, and this is discussed in Refs. 1 and 2.

A corresponding treatment for electrons is not readily available. In light of Fig. 3 16, a non-symmetrical distribution might be expected rather than a Gaussian; indeed, studies of energy loss distribution for electrons passing through thin plates have resulted in variants of the Vavilov distribution. This is perhaps the most fundamental approach to the problem to date, and it is briefly discussed in Appendix C. However, the Vavilov distribution is cumbersome to use in cell calculations and is limited to thin plates. An alternate approach that avoids some of these problems is the use of an empirical correlation such as obtained

*The Gaussian distribution is normalized on the interval $-\infty \leq \lambda \leq \infty$, thus $\bar{\lambda}$ corresponds to use of Eq. (3 62) with the lower limit extended to $-\infty$. However, for a sharply peaked distribution the difference can be ignored

by Mar[41] based on Monte Carlo calculations. His results are given as a transmission probability expressed as a modified exponential

$$T(r, T_0) = \exp\left[-\frac{Dr^b}{T_0^c}\right] \tag{3.65a}$$

where

$$D \equiv \left(\frac{0.585\ Z^{-0.271}}{\rho}\right)^{-b} \tag{3.65b}$$

$$b \equiv 0.484c \tag{3.65c}$$

$$c = 14.5Z^{-0.48} \approx \frac{14.5}{\sqrt{Z}} \tag{3.65d}$$

where Z is the atomic number and ρ is the density (g/cm^3) of the stopping material.

A plot of this function is shown in Fig. 3.17 for various energy electrons in aluminum. [Note the similarity to Fig. 3.15(b).]

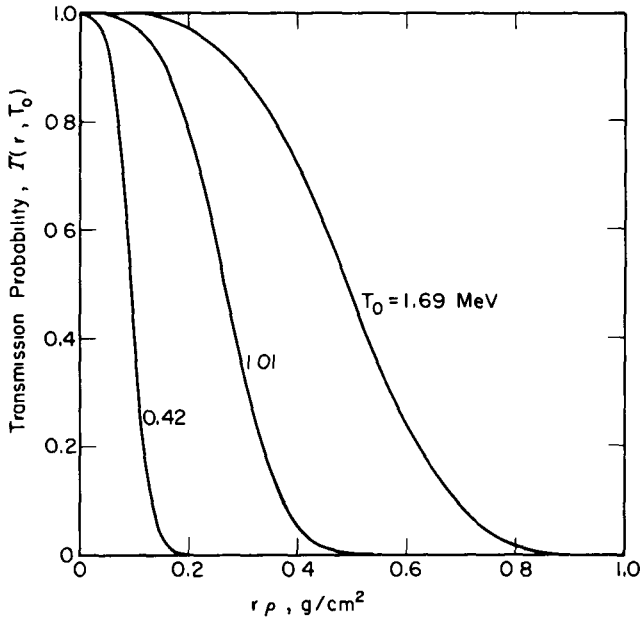

Fig. 3.17 — The Mar transmission probability for electrons impinging on aluminum.

As a partial check on its accuracy, we can use Mar's transmission function to calculate the mean range. This is possible, since from Eq. (3.61),

$$P(\lambda, T_0) = -\left[\frac{d\,T(r, T_0)}{dr}\right]_{r=\lambda}. \tag{3.66}$$

Ranges based on this relation and Eq. (3.62) are compared with the Katz–Penfold correlation in Fig. 3.12 presented earlier, and excellent agreement is indicated. (Actually this is surprising; since the Katz–Penfold correlation is for "practical ranges", only the shapes of the curves are expected to be similar.) However, there does appear to be one difficulty with this correlation: Other calculations indicate that the variation of range with Z does not agree with the results of Fig. 3.13. The cause for this discrepancy is not clear and requires further study. Still, Eq. (3.65) should provide an approximate correction for straggling, and because of its utility, it will be used in later calculations.

One immediate consequence of straggling is that it is possible to define a number of different types of ranges. The experimentalist typically reports an extrapolated range (Fig. 3.7) called the "practical range." The Katz–Penfold correlation is such a range based on the extrapolation of measurements of the ionizing power of electrons passing through aluminum plates of various thicknesses.[2] A slightly different result is obtained if the number of transmitted electrons is measured instead of ionizing power.

Another range used by experimentalists is the "maximum" range λ_m, which corresponds to a thickness that will essentially stop all electrons. (A rule of thumb[42] is that extrapolated range corresponds to about 2% transmission in contrast to less than 0.1% for λ_m.)

Theoretical studies, however, often deal with average values, and Eq. (3.62) is one possible definition of an average range. Several others frequently used should also be noted.

The ranges in Table 3.3 were calculated using a continuous slowing representation of electron transport. This gives an average energy loss per unit path (dT/dS), where the path length S is essentially a range rather than the actual trajectory. The corresponding range is then given as

$$\lambda(T_0)_{c.s.d.a.} \equiv \int_0^{T_0} \frac{dT}{(-dT/dS)} \tag{3.67}$$

and the National Academy Subcommittee on Penetration of Charged Particles recommends that this be termed the "c.s.d.a." (continuous

slowing-down approximation) range.[4] While it is an average value, it should not be expected to agree precisely with Eq. (3.62).

Others have based an "average" range on the most probable energy T_P of the transmitted electrons (Fig. 3.16). If the change in T_P per unit thickness is $(dT_P/d\tau)$, then

$$\lambda_P(T_0) \equiv \int_0^{T_0} \frac{dT}{(-dT_P/d\tau)} \tag{3.68}$$

which is called the "probable" range. Since, as stressed earlier, transmitted electron energy distributions are asymmetric, λ_P will generally be different from $\lambda_{c.s.d.a.}$ and $\langle\lambda\rangle$.

Cosslett and Thomas[42] have reviewed the relation between these and some other possible definitions in some detail. One of their conclusions is that, "broadly speaking," the extrapolated range varies in a manner similar to the mean energy range. However, they note that the maximum range varies more nearly like the most probable range.

This proliferation of definitions is admittedly confusing unless considerable care is exercised in the use of ranges. Depending on the accuracy desired in a given calculation, the differences may or may not be significant. Some feeling for this can be obtained by returning to Fig. 3.12. It is now recognized that the two calculations included are based on different definitions, neither of which is expected to give a "practical range" like the Katz–Penfold correlation. The spread between the various values is of the order of 10 to 30%. (Note that, as predicted by Cosslett and Thomas, all three curves have the same shape.) If an uncertainty of this order of magnitude is not acceptable, the only solution is to do away with the range concept and instead use a full transmission function such as Eq. (3.65) in calculations. Unfortunately, this adds considerable complexity to the calculations.

3-6 SUMMARY OF CHARGED PARTICLE SLOWING

It has been shown that, to a first approximation, charged particle slowing can be represented by the simplified energy loss and range–energy laws of Eqs. (3.27) and (3.28)

$$-\frac{dT}{dr} = \frac{T_0}{(n+1)\,\lambda(T_0)} \left(\frac{T_0}{T}\right)^n \tag{3.69}$$

$$\frac{T}{T_0} = \left(1 - \frac{r}{\lambda(T_0)}\right)^{1/(n+1)}. \tag{3.70}$$

The slowing parameter n is primarily a function of the type of charged particle involved. Typical values of n are summarized in Table 3.4 along with the charge-fitting parameter m discussed below. While n may depend weakly upon the properties of the stopping material, it remains surprisingly constant over a wide range of materials of varying atomic number and density.

Charge neutralization may also occur during slowing, in which case Eq. (3.39) offers a first approximation for the variation of the charge with the particle's speed or energy:

$$\frac{q(T)}{q_0} = \left(\frac{T}{T_0}\right)^{m/2}. \tag{3.71}$$

Some typical values of m are also included in Table 3.4. Alpha particles, protons, and other low-q ions undergo neutralization only at low speeds (order of 1 MeV or less), but fission fragment neutralization sets in almost immediately upon birth.

Table 3.4—SUMMARY OF TYPICAL VALUES* OF n AND m

Particle	n	m	Energy Range (MeV)
Alpha	0.5	0	>1
	0.1	1	<1
Proton	0.8	0	>½
	−0.25 to −0.5	1	<0.1
Fission fragment	−0 5	1	
Electron	1	0	<½
	0	0	>½

*Note The values shown are only approximate. As discussed in the text, more accurate values may be found for a given situation by restricting the correlation to the specific range of energies and materials of interest

The range $\lambda(T_0)$ depends strongly on both the nature of the stopping material and the charged particle. To be consistent with Eqs. (3.27) and (3.28), the energy dependence of the range should follow the form of Eq. (3.26)

$$\lambda(T_0) = \frac{T_0^{n+1}}{(n+1)C} \tag{3.72}$$

where C involves various properties of the particle and stopping material such as illustrated by Eqs. (3.17), (3.20), and (3.22) for low-q ions or Eqs. (3.43) and (3.46) for fission fragments. In practice, how-

ever, $\lambda(T_0)$ is typically obtained from experimental data such as Wilson's nomograph (Fig. 3.6) for low-q ions, Kahn's correlation [Eq. (3.50)] for fission fragments, and the Katz–Penfold correlation [Eq. (3.59)] for electrons.

The energy and range involved in Eqs. (3.27) and (3.28) are mean values based on electronic interactions. In practice, a distribution about the mean exists due to straggling, which results from large angle scattering and possibly nuclear collisions. This is most severe for electrons, but an approximate straggling correction is possible using the Mar transmission function of Eq. (3.65) or the Vavilov distribution of Appendix C-2.

REFERENCES

1. H. A. Bethe and J. Ashkin, "Passage of Radiations Through Matter," in *Experimental Nuclear Physics,* Vol. 1, pp. 166-358, E. Segre (Ed.), John Wiley and Sons, New York, 1953.
2. R. D. Evans, *The Atomic Nucleus,* Chaps. 18 and 22, McGraw-Hill Book Company, Inc., New York, 1955.
3. S. V. Starodubtsev and A. M. Romanov, *The Passage of Charged Particles Through Matter,* Translated from Russian, Israel Program for Scientific Translations, Jerusalem, 1965.
4. *Studies in Penetration of Charged Particles in Matter,* Nuclear Science Series Report No. 39, Committee on Nuclear Science, National Academy of Sciences–National Research Council, Washington, D. C., 1964.
5. G. N. Walton, "Fission Recoil and Its Effect," in *Progress in Nuclear Physics,* Vol. 6, pp. 193-229, O. R. Frisch (Ed.), Pergamon Press, New York, 1957.
6. W. Whaling, "The Energy Loss of Charged Particles in Matter," in *Handbuch der Physik,* Vol. 34, pp. 193-217, Julius Springer, Berlin, 1958.
7. Andre Berthelot, *Radiations and Matter,* Leonard Hill Books, Limited, London, 1958.
8. F. Block, "Zur Bremsung Rasch Bewegter Teilchen Beim Durchgang Durch Materie," *Ann. Physik, 16:* 285 (1933).
9. E. J. Williams, "Application of Ordinary Space–Time Concepts in Collision Problems and Relation of Classical Theory to Born's Approximation," *Rev. Mod. Phys., 17:* 217 (1945).
10. M. Abramowitz and I. A. Stegun (Eds.), "Handbook of Mathematical Functions," *Nat. Bureau of Standards, Appl. Math Ser., 55:* (1964).
11. N. Bohr, "The Penetration of Atomic Particles Through Matter," *Kgl. Danske Videnskab. Selskab. Mat.-Fys Medd., 18:* 8 (1948).
12. E. Fermi and E. Teller, "The Capture of Negative Mesotrons in Matter," *Phys. Rev., 72:* 399 (1947).
13. R. D. Evans, "Principles for the Calculation of Radiation Dose Rates in Space Vehicles," NASA Report No. 63270-05-01, Arthur D. Little, Inc., Boston, Mass., July 1961.
14. E. K. Hyde, *The Nuclear Properties of the Heavy Elements*-III; *Fission Phenomena,* Prentice-Hall, Englewood Cliffs, N. J., 1964.
15. S. Katcoff, "Fission-Product Yields from Neutron-Induced Fission," *Nucleonics, 18,* 11: 203 (1960).
16. D. C. Brunton and W. B. Thompson, "Energy Distribution of Fission Fragments from ^{239}Pu," *Can. J. Res., 28A:* 498 (1950).

17 R. F Redmond, R. W Klingensmith, and J. N. Anno, "Energy Spectrum of Fission Fragments Emitted from Thin Layers of Uranium Dioxide," *J Appl Phys., 33* 3383 (1962).
18 G. H Miley, "Fission Fragment Transport Effects as Related to Fission-Electric-Cell Efficiencies," *Nucl Sci. Eng., 24* 322 (1966).
19 N. O Lassen, "On Energy Loss by Fission Fragments Along Their Path," *Phys Rev , 75* 1762L (1949).
20. N. Bohr, "Scattering and Stopping of Fission Fragments," *Phys Rev , 58* 654 (1940).
21 N. Bohr, "Velocity–Range Relation for Fission Fragments," *Phys Rev , 59* 270 (1941)
22 N. O. Lassen, "On the Variation Along the Range of the $H\rho$-Distribution and the Charge of the Fission Fragments of the Light Group," *Phys Rev , 69* 137 (1946).
23. C. B Fulmer and B L. Cohen, "Equilibrium Charges of Fission Fragments in Gases," *Phys Rev , 109* 94 (1958).
24. S Kahn, R. Harman, and V Forgue, "Energy Distribution of Fission Fragments from Uranium Dioxide Films," *Nucl Sci Eng , 23* 9 (1965).
25. P W Frank, "Recoil Range of Fission Fragments," WAPD-BT-30, pp. 47-51, Bettis Atomic Laboratory, Pittsburgh, Pa., 1964.
26 J. M Alexander and M. F. Gazdik, "Recoil Properties of Fission Products," *Phys Rev , 120* 874 (1960).
27 J. B Niday, "Radiochemical Study of the Ranges in Metallic Uranium of the Fragments from Thermal Neutron Fission," *Phys Rev , 121* 1471 (1961).
28. Chr. Moller, "Zur Theorie des Durchgangs Schneller Elektronen Durch Materie," *Ann Physik, 14* 531 (1932)
29. H W. Koch and J W. Motz, "Bremsstrahlung Cross-Section Formulas and Related Data," *Rev Mod Phys , 31* 920 (1959)
30. R Whiddington, "The Transmission of Cathode Rays Through Matter," *Proc Roy. Soc. (London), A86* 360-370, 1911.
31 R. Whiddington, "The Transmission of Cathode Rays Through Matter," *Proc Roy Soc (London), A89* 554-560, 1913
32. E. J. Williams, "The Rate of Loss of Energy by β-Particles in Passing Through Matter," and "The Loss of Energy by β-Particles and Its Distribution Between Different Kinds of Collisions," *Proc Roy Soc (London), A130* 310-327 and 328-346, 1931.
33. A. J. Dekker, "Secondary Electron Emission," in *Solid State Physics, Advances in Research and Applications,* F. Seitz and D. Turnbull (Eds.), Vol. 6, pp 251-311, Academic Press, New York, 1958.
34. G. F J. Garlick, "Cathode and Radioluminescence," in *Luminescence of Inorganic Solids,* P. Goldberg (Ed.), pp. 685-727, Academic Press, New York 1966.
35. T. E Everhart, "Simple Theory Concerning the Reflection of Electrons from Solids," *J Appl Phys , 31* 1483 (1960).
36. L. Katz and A S. Penfold, "Range–Energy Relations for Electrons and the Determination of Beta-Ray End-Point Energies by Absorption," *Rev Mod Phys , 24* 28 (1952).
37. A. Nelms, "Energy Loss and Range of Electrons and Positrons," *NBS Circular 577* (1956), and *Supplement to NBS Circular 577* (1958), National Bureau of Standards, Washington, D. C.
38. L. E. Glendenin, "Determination of the Energy of Beta Particles and Photons by Absorption," *Nucleonics, 2,* 1 12 (1948)
39. A J. Cohen, "A Numerical Analysis of Direct Nuclear Electrogenerator Cells That Use Cerium 144 Beta-Emitting Radioisotope Sources," NASA TN D-2070, NASA Lewis Research Center, November 1963.

40. S. C. Curran, P. I. Dee, and V. Petrzilka, "The Excitation of γ-Radiation in Processes of Proton Capture by Light Elements," *Proc. Roy. Soc. Series A, 169,* 269-289, 1938.
41. B. W. Mar, "Electron Shielding Codes for Evaluation of Space Radiation Hazards," Document No. D2-90414, Boeing Aircraft Corp., Seattle, Washington, June 1963.
42. V. E. Cosslett and A. N. Thomas, "Penetration and Energy Loss of Electrons in Solid Targets," in *The Electron Microprobe,* pp. 262-268, T. D. McKinley, K. F. J. Heinrick, and D. B. Wittry (Eds.), John Wiley and Sons, Inc., New York, 1966.

4

Application of Charged Particle Transport Theory to Cell Calculations

The charged particle transport theory developed in Chap. 3 is now applied to some typical cell calculations. The slowing model of Eqs. (3.27) and (3.28) is used to represent particle energy losses during transit through the fuel and/or insulator layers, and the possibility of charge neutralization is included via Eq. (3.39). As stressed in Chap. 3, these equations are quite general, so it is not necessary to identify the specific type of charged particle under consideration.

The objectives of this chapter are to develop methods of analysis and to provide an insight into the magnitude and importance of the losses. To accomplish this with a minimum of complexity, we will assume the following:

• The fuel and/or insulators are represented as *flat plates.* As discussed in Chap. 2, there is a strong incentive to consider other geometries; however, if the curvature is not too great, the flat plate analysis may carry over directly. Otherwise, the analysis must be redone for the actual geometry involved. Unfortunately, although the method of attack is similar, such calculations are frequently tedious and best done numerically.

• Except for Sec. 4-5, which deals primarily with gamma interactions, an *isotropic source* angular distribution is used. As pointed out in Chap. 2, this is realistic for radioisotope and fission sources.

• *Relativistic effects are neglected* Where required, a correction for these effects can be made following the methods developed in Chap. 2. However, this would generally necessitate numerical solutions, and, since the corrections involved are frequently small, such calculations are not included here.

• A single value of the energy-loss parameter n of Eqs. (3.27) and (3.28) is used, although, as discussed in Chap. 3, it may depend on the energy range involved. On the basis of the argument used earlier in connection with range-energy correlations, the high-energy region often dominates, so it is reasonably accurate to evaluate n at the particle's initial energy. If desired, it is fairly straightforward but tedious to divide the calculations into different energy regions with different n's.

4-1 CURRENT CALCULATIONS

Before applying the theory developed in Chap. 3 to cell calculations, it is necessary to develop a familiarity with current calculations. The treatment of currents presented here has been greatly influenced by studies described in Refs. 1–6 and, likewise, the applications to cell analysis by Refs. 7–13. However, in both cases, a number of original features and results are included in the present development.

Several different currents—the particle current, energy current, and charge current—are of interest, and they will be considered in order in the following sections.

4-1.1 Angular and Total Particle Currents Using a Point-Kernel Method

Consider the plane fuel layer shown in Fig. 4.1, which is infinite in the x and y directions and has a thickness τ. Charged particles are

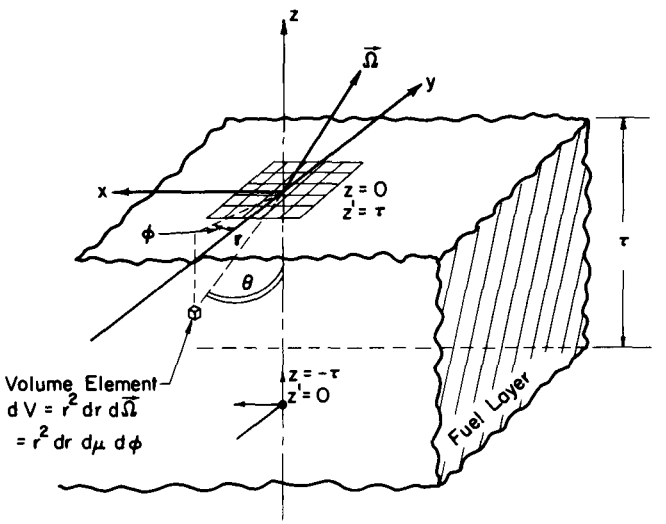

Fig. 4.1 — Plane emitter, spherical coordinate system.

assumed to be born in the layer according to a time independent source distribution $S(\vec{r},T_0,\vec{\Omega})$, which represents the number of particles born per second at $\vec{r}$ per unit volume having a kinetic energy T_0 per unit energy and direction $\vec{\Omega}$ per unit steradian. This source might be due to radioisotope decay, fissioning, Compton scattering, etc.

The mean range in the layer for a particle with initial energy T_0 is designated as $\lambda(T_0)$, or in cases where the meaning is clear, simply as λ.

We begin by calculating the particle current, $J(\tau,\vec{\Omega};\, r,\vec{\Omega}',T_0)\, d\vec{\Omega}\, dr\, d\vec{\Omega}'$, which is defined as the number of particles per second per unit area with directions lying between $\vec{\Omega}$ and $\vec{\Omega}+d\vec{\Omega}$, crossing a surface perpendicular to the z-axis at $z' = \tau$ (or $z = 0$), having been *born* with an energy T_0 with an initial direction between $\vec{\Omega}'$ and $\vec{\Omega}' + d\vec{\Omega}'$ and having traveled a distance lying between r and r + dr before reaching the surface. In this notation, properties associated with the source and the particle trajectory prior to reaching the surface of interest follow the semicolon. After some experience, this may not be necessary, but we will retain the full notation here since it is of considerable aid in understanding the logic behind many of the calculations. (The only danger is that one may forget and associate one of these variables with the current rather than the source. The energy T_0 is an excellent illustration. While the source energy is T_0, particles comprising the current at τ will have some other energy T, where $T < T_0$ due to the energy loss they suffer in traveling a distance r.)

The source associated with the volume element dV can be visualized as a point source of strength $S(\vec{r},T_0,\vec{\Omega}')\, dV$, in which case

$$\begin{aligned} &J(\tau,\vec{\Omega};r,\vec{\Omega}',T_0)\, d\vec{\Omega}\, dr\, d\vec{\Omega}' \\ &\quad = (\hat{z}\cdot\vec{\Omega})[K(r,\vec{\Omega}'\rightarrow\vec{\Omega},T_0)\, d\vec{\Omega}\,][S(\vec{r},T_0,\vec{\Omega}')\, dV\,] \\ &\quad = (\hat{z}\cdot\vec{\Omega})\,\frac{T(r,T_0)}{r^2}\cdot\delta(\vec{\Omega}'-\vec{\Omega})\, S(\vec{r},T_0,\vec{\Omega}')\, r^2\, dr\, d\vec{\Omega}\, d\vec{\Omega}' \qquad (4.1) \end{aligned}$$

where $K(r,\vec{\Omega}'\rightarrow\vec{\Omega},T_0)$, the solution or Green's function for a point emitter, has been written as a product of the two factors $T(r,T_0)/r^2$ and $\delta(\vec{\Omega}'-\vec{\Omega})$. The first factor is the product of a $1/r^2$ geometric attenuation times the transmission function $T(r,T_0)$, which represents the probability that a particle of initial energy T_0 will travel a distance r without being stopped or absorbed. The second factor $\delta(\vec{\Omega}'-\vec{\Omega})$ is simply a statement that the particle travels in a straight-line path. Canceling the factors of r^2 and integrating over all possible source angles, we obtain

$$\begin{aligned} J(\tau,\vec{\Omega};r,T_0)\, dr\, d\vec{\Omega} &= \int_{\Omega'} d\vec{\Omega}'\, [J(\tau,\vec{\Omega};r,\vec{\Omega}',T_0)\, dr\, d\vec{\Omega}] \\ &= S(\vec{r},T_0,\vec{\Omega})\; T(r,T_0)\; \mu\, d\mu\, d\phi\, dr \qquad (4.2) \end{aligned}$$

where μ is the direction cosine, i.e., $\cos\theta$. If the transmission probability $T(r,T_0)$ is evaluated using the mean range concept, it is by definition

$$T(r,T_0) = 1 - \int_0^r dr'\ \delta[r' - \lambda(T_0)] \equiv h[\lambda(T_0) - r]$$

$$= \begin{cases} 1 & [r < \lambda(T_0)] \quad (4.3a) \\ 0 & [r \geq \lambda(T_0)]. \quad (4.3b) \end{cases}$$

Note that, as indicated, $T(r,T_0)$ can be conveniently written in terms of the step function $h(x)$ introduced earlier in Eq. (2.14). This function will be used as a compact form in later equations.

This should be quite accurate for ions, but, due to straggling, it will be less accurate for electrons. For the latter, we will consider the possibility of using the Mar transmission function in Sec. 4-1.8.

For the remainder of the development, we will assume that the source is independent of r and ϕ, then

$$S(\vec{r},T_0,\vec{\Omega}) \rightarrow \frac{S(T_0,\mu)}{2\pi} \quad (4.4)$$

and integration over ϕ gives

$$J(\tau,\mu;r,T_0)\ d\mu\ dr = S(\mu,T_0)\ T(r,T_0)\ \mu\ d\mu\ dr. \quad (4.5)$$

The total angular current $J(\tau,\mu;T_0)$ is now found by integration over r, which gives

$$J(\tau,\mu;T_0) = S(\mu,T_0)\ \mu \int_0^{\tau/\mu} h[\lambda(T_0) - r]\, dr$$

$$= S(\mu,T_0)\ \mu \cdot \begin{cases} \lambda(T_0) & [0 \leq \mu \leq \tau/\lambda(T_0)] \quad (4.6a) \\ \tau/\mu & [\tau/\lambda(T_0) \leq \mu \leq 1]. \quad (4.6b) \end{cases}$$

If the plate is thick, i.e., if $\tau > \lambda(T_0)$, Eq. (4.6a) is to be applied for all μ between 0 and 1. Otherwise for a thin plate, both Eqs. (4.6a and b) must be retained.

The total current, independent of angle, is found by integration over μ, but first the angular dependence of the source must be specified. We elect to assume an isotropic source such that

$$S(\mu,T_0) \rightarrow \frac{1}{2} S(T_0). \quad (4.7)$$

This is a good assumption for sources due to fission and radioactive decay, but the Compton process, discussed in later sections, illustrates an important case where a non-isotropic angular representation must be used. Using the isotropic source and Eqs. (4.6a and b), we find that

$$J(\tau;T_0) = \int_0^1 J(\tau,\mu;T_0)\, d\mu = \frac{\tau\, S(T_0)}{2}\left[1 - \frac{\tau}{2\lambda(T_0)}\right] \qquad [\tau \leq \lambda(T_0)]. \tag{4.8}$$

This result is valid for a thin plate; otherwise, only Eq. (4.6a) contributes to the integral so that

$$J(\tau;T_0) = \frac{S(T_0)}{4}\,\lambda(T_0) \qquad [\tau \geq \lambda(T_0)]. \tag{4.9}$$

This expression is quite general and gives the current for any type of particle leaving a thick plate provided the source is uniform and isotropic. (It has also been used in reverse to determine the mean range $\lambda(T_0)$; e.g., Faraggi and Garin-Bonnet[14] measured the particle current leaving the surface of a uranium foil undergoing a known fission rate and then solved Eq. (4.9) for the fragment range.)

4-1.2 The Energy Spectrum of the Particle Current

In addition to the total particle current, we are often interested in the energy spectrum of the particles crossing the surface. This can be found immediately from the basic equation for $J(\tau,\vec{\Omega};r,T_0)$ given in Eq. (4.2) since, if a particle of original energy T_0 travels a distance r, it will have a unique energy given by the energy–range law. Then, since $J(\tau,\vec{\Omega};r,T_0)$ is a density function in r, it may be transformed according to

$$|J(\tau,\vec{\Omega},T;T_0)\, dT| = |J(\tau,\vec{\Omega};r,T_0)\, dr| \tag{4.10}$$

$$J(\tau,\vec{\Omega},T;T_0) = \frac{S(\vec{r},\vec{\Omega},T_0)\; T(r,T_0)\; (\vec{z}\cdot\vec{\Omega})}{|dT/dr|}. \tag{4.11}$$

Again assuming a uniform isotropic source and evaluating $|dT/dr|$ by Eq. (3.27), we find that

$$J(\tau,\mu,T;T_0) = \frac{(n+1)\,\lambda(T_0)\,S(T_0)}{2T_0}\left(\frac{T}{T_0}\right)^n \mu \qquad (0 \leq T \leq T_0). \tag{4.12}$$

The probability $T(r,T_0)$ has been dropped since the requirement that the kinetic energy T be positive is entirely equivalent. Care must be taken in integrating over μ to find $J(\tau,T)$. If the plate is thin so that $\tau \leq \lambda(T_0)$, a critical energy $T_{\tau n}$ occurs when $r = \tau$ in the energy–range law (Eq. 3.28); thus, it is defined as

$$\frac{T_{\tau n}}{T_0} = \left[1 - \frac{\tau}{\lambda(T_0)}\right]^{1/(n+1)} \qquad [\tau \leq \lambda(T_0)]. \tag{4.13}$$

The subscript n is included as a reminder that $T_{\tau n}$ depends on the choice of n. Then, for $T_{\tau n} \leq T \leq T_0$, integration over all μ is allowed and

$$J(\tau,T;T_0) = \int_0^1 J(\tau,\mu,T)\, d\mu$$

$$= \frac{(n+1)\,\lambda(T_0)\,S(T_0)}{4T_0}\left(\frac{T}{T_0}\right)^n \qquad (T_{\tau n} \leq T \leq T_0). \tag{4.14}$$

Note, for thick plates, $T_{\tau n} \to 0$ and Eq. (4.14) is applicable over the entire range of energies involved. However, for a thin plate it is also necessary to consider the energy interval $0 \leq T \leq T_{\tau n}$, in which case the integration must be cut off at $\mu = \tau/r$ and

$$J(\tau,T;T_0) = \int_0^{\tau/r} J(\tau,\mu,T)\, d\mu$$

$$= \frac{(n+1)\,\lambda(T_0)\,S(T_0)}{4T_0}\left(\frac{T}{T_0}\right)^n \left(\frac{\tau}{r}\right)^2 \qquad (0 \leq T \leq T_{\tau n}). \tag{4.15}$$

The distance r in this result is related to energy by the energy–range law [Eq. (3.28)]; then

$$r^2 = \lambda^2(T_0)\left[1 - \left(\frac{T}{T_0}\right)^{n+1}\right]^2 \tag{4.16}$$

and Eq. (4.15) becomes

$$J(\tau,T;T_0) = \frac{(n+1)\,S(T_0)\,\tau}{4T_0[\lambda(T_0)/\tau]\left[1-(T/T_0)^{n+1}\right]^2}\left(\frac{T}{T_0}\right)^n \qquad (0 \leq T \leq T_{\tau n}). \tag{4.17}$$

Equations (4.14) and (4.17) define the complete spectrum for a thin fuel layer.

The physical explanation for the energy intervals associated with these equations can be best understood by referring to Fig. 4.2. Particles traveling a distance $r \leq \tau$ can come from anywhere within the hemisphere defined by $r = \tau$, and their energy must lie in the interval $T_{\tau n} \leq T \leq T_0$ since one coming from the plate surface would have energy T_0, whereas one coming from the surface of the hemisphere would have energy $T_{\tau n}$. In this region, all angles are allowed (i.e., $0 \leq \mu \leq 1$). For a thin plate where $\tau < \lambda(T_0)$, the distance r can exceed τ for some directions, and if r is fixed, the range of μ must be terminated where r intersects the back plate surface. This limits μ to the interval $0 \leq \mu \leq \tau/r$, and, since a particle coming from this region

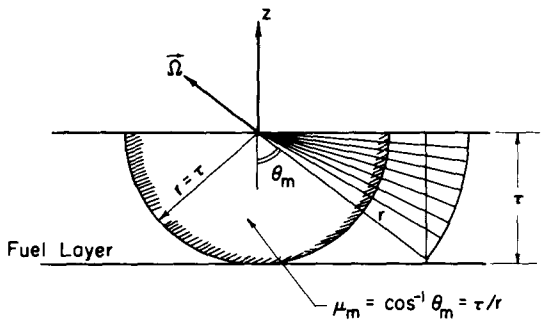

Fig. 4.2—A cross section of the fuel layer showing integration limits.

originates outside of the hemisphere, it must have an energy lying within the interval $0 \leq T \leq T_{\tau n}$.

Energy spectra calculations based on these results are shown in Fig. 4.3 for a fairly thin fuel layer ($\tau/\lambda = 0.25$) and a thick layer ($\tau/\lambda = 1.0$), respectively. Note, particularly in the case of a thick plate, that the low-energy region of the spectra tends to dominate for fission fragments or low-energy protons ($n < 0$) whereas the high-energy region dominates for others such as alpha particles. This is consistent with the observation of Chap. 3 that the Bragg curve decreases with distance of travel faster for fission fragments than for alpha particles. In other words, high-energy fission fragments slow most rapidly, and this causes the low-energy region of the escaping fragment current to be favored.

These results are, of course, all for a monoenergetic source energy. If a continuous source spectrum is involved, (cf. beta decay or ^{235}U fission) a final integration over initial energies is required. For example, for fission fragment calculations, $S_j(T_0)$ from Eq. (3.35) can be used, and the current becomes

$$J(\tau, T) = \sum_{j=1}^{2} \int_{T}^{\infty} \left[\frac{J(\tau, T; T_0)}{S(T_0)}\right] S_j(T_0)\, dT_0. \tag{4.18}$$

Special care must be taken for intermediate plate thickness where $\lambda(T_0) < \tau$ for low initial energies but $\lambda(T_0) > \tau$, i.e., the plate is thin, for higher energies in the source spectrum. The basic problem involved then is to decide when to use Eq. (4.17), as opposed to Eq. (4.14), for $J(\tau, T; T_0)$ required in the integration.

This is done as follows: A critical value of the initial energy, labeled T_{0c} and given by

$$T_{0c} = \frac{T}{[1 - \tau/\lambda(T_{0c})]^{1/(n+1)}} \tag{4.19}$$

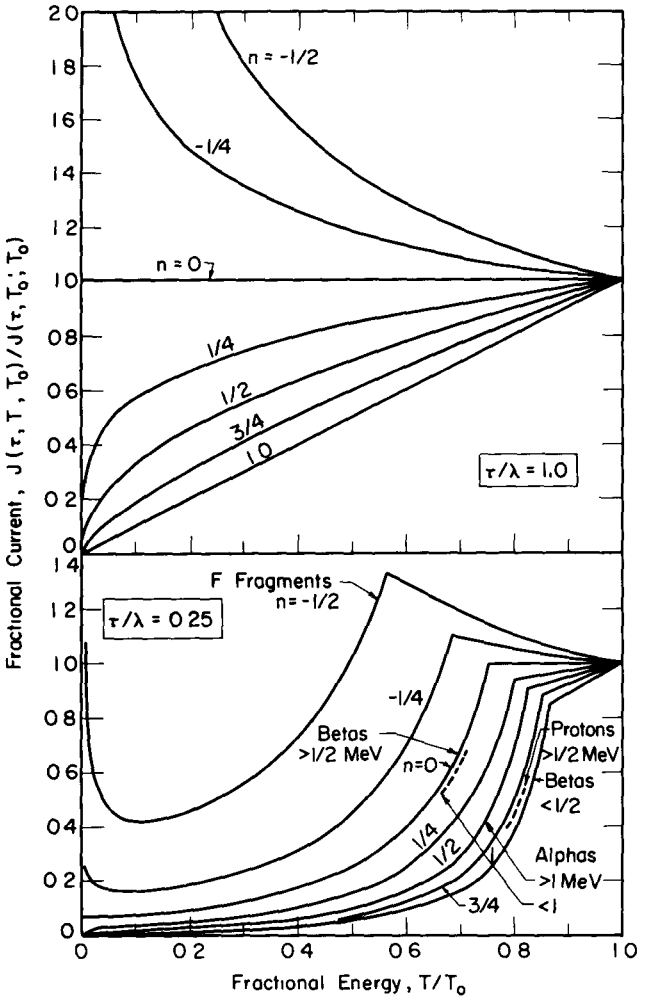

Fig 4.3 — Current spectra for a monoenergetic source for two fuel-layer thicknesses

is defined such that a particle starting with this energy can pass through the fuel thickness τ and just reach the surface with energy T. Then, any particle that originates within the hemisphere defined by $r = \tau$ in Fig. 4.2 must have started with an energy $T_0 < T_{0c}$ in order to reach the surface with energy T, and this corresponds to the zone of integration leading to Eq. (4.14). Conversely, particles from outside the hemisphere must have $T_0 > T_{0c}$; thus, the integration over initial energies can be divided into two regions, giving

$$J(\tau,T) = \sum_{j=1}^{2}\left\{\int_{T}^{T_{0c}}\left[\frac{J_A(\tau,T;T_0)}{S(T_0)}\right]S_j(T_0)\,dT_0 + \int_{T_{0c}}^{\infty}\left[\frac{J_B(\tau,T;T_0)}{S(T_0)}\right]S_j(T_0)\,dT_0\right\} \tag{4.20}$$

where the subscripts "A" and "B" refer to Eqs. (4.14) and (4.17), respectively.

Figure 4.4 shows $J(\tau,T)$ calculated from Eq. (4.20) for several values of τ for fission fragments passing through UO_2 ($\lambda \approx 11\ \mu$). Results for the two sets of values of n_1 and n_2 suggested in Sec. 3-4.2 are compared with experimental data reported by Redmond et al.[6] The $n_1 = n_2 = -\frac{1}{2}$ curve provides the closest representation at 2.94 μ, but it introduces an exaggerated light fragment peak (80-MeV) for the 0.84-μ case. Still, the agreement must be considered adequate, and this lends confidence to the present calculational technique. (Similar calculations and additional experimental data of this type are presented in Appendix D in connection with Dirac chord calculations.)

4-1.3 The Energy Current

The *energy current* J_E defined as

$$J_E(\tau,\mu,T;T_0) \equiv J(\tau,\mu,T;T_0)\,T \tag{4.21}$$

represents the kinetic energy carried by the particle current. It may be evaluated by using Eq. (4.12) for the particle current, in which case

$$J_E(\tau,\mu,T;T_0) = \frac{(n+1)\,\lambda(T_0)\,S(T_0)}{2}\left(\frac{T}{T_0}\right)^{n+1}\mu. \tag{4.22}$$

The angular dependence may be removed by integrating between the limits for μ used in Eqs. (4.14) and (4.15). Integration over T then yields the total energy current

$$J_E(\tau;T_0) = \int\!\!\int J_E(\tau,\mu,T;T_0)\,d\mu\,dT = \frac{(n+1)\,\lambda(T_0)\,S(T_0)\,T_0}{4}\,Y_{n+1}^{n+1}[T_{\tau n}/T_0,\ \tau/\lambda(T_0)] \tag{4.23}$$

where the function Y is defined as

$$Y_K^{\nu}(\alpha,\beta) = \int_{\alpha}^{1} y^k\,dy + \beta^2\int_{0}^{\alpha}\frac{y^k}{[1-y^{\nu}]^2}\,dy. \tag{4.24}$$

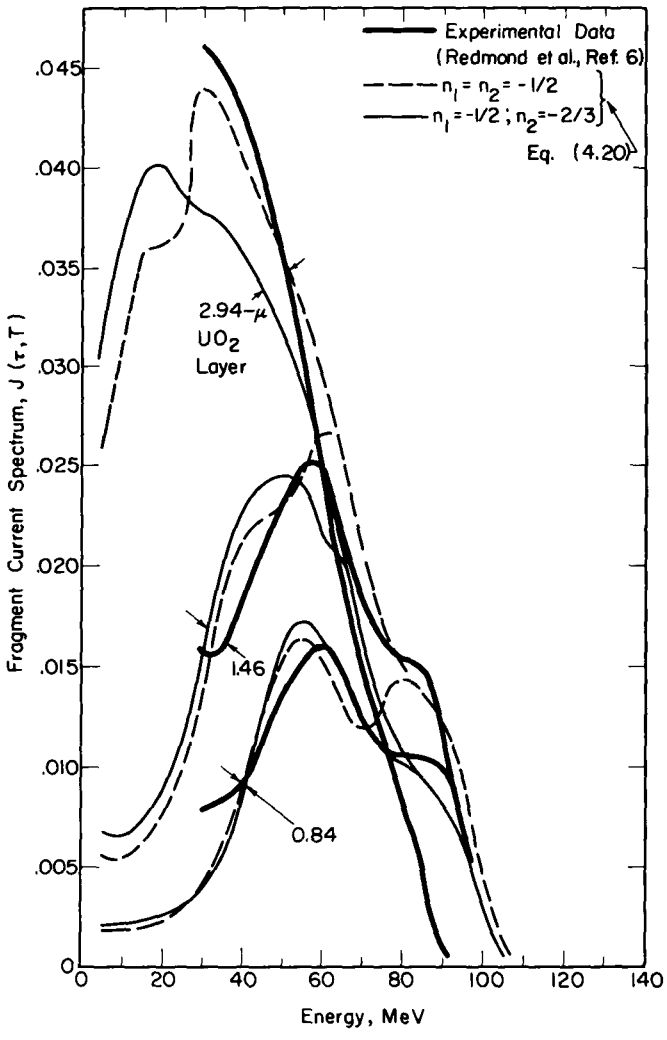

Fig. 4.4—Calculated and measured current spectra for fission fragments from UO_2 plates. (After Miley, Ref. 4.)

The energy current is particularly important for the determination of ionization–excitation rates. This can be shown by considering the continuity equation for energy flow

$$\nabla \cdot \vec{J}_E(z) = S_E(z) - L_E(z) \tag{4.25}$$

where $S_E(z)$ represents an energy production rate (source) while $L_E(z)$ is the energy loss rate—both being per unit volume at z. Thus, if the

region under consideration is free of sources, then $L_E(z)$ (which ultimately determines ionization and excitation rates) is simply equal to $\nabla \cdot \vec{J}_E(z)$. This concept is applied later in the two-region calculations of Sec. 4-4.

The energy current at τ can also be used to evaluate the average energy $\langle T \rangle_\tau$ associated with the particle current emerging from the plate, which, by definition, is given as

$$\langle T \rangle_\tau = \frac{\int T\, J(\tau, T; T_0)\, dT}{\int J(\tau, T; T_0)\, dT}$$

$$= \frac{J_E(\tau; T_0)}{J(\tau; T_0)}$$

$$= \frac{Y_{n+1}^{n+1}[T_{\tau n}/T_0,\ \tau/\lambda(T_0)]}{[2\tau/(n+1)\lambda](1 - \tau/2\lambda)} T_0. \tag{4.26}$$

The function Y was defined in Eq. (4.24). This is most easily evaluated for a thick plate $[\tau > \lambda(T_0)]$, in which case $T_{\tau n} \to 0$, and

$$Y_K^V(0,\beta) \to \frac{1}{K+1} \tag{4.27}$$

so that

$$\langle T \rangle_\tau \to \frac{n+1}{n+2} T_0 \qquad [\tau \gtrsim \lambda(T_0)]. \tag{4.28}$$

Thus, for a *thick plate,* the average energy for fission fragments ($n = -\frac{1}{2}$) is approximately $\frac{1}{3}\, T_0$; for alphas >1 MeV ($n = \frac{1}{2}$) it is about $\frac{3}{5} T_0$; etc. For *thin plates* $\langle T \rangle_\tau$ depends on both $\tau/\lambda(T_0)$ and n, and a plot based on Eq. (4.26) is shown in Fig. 4.5.

4-1.4 The Charge Current Density

The charge current density J_q is defined as

$$J_q(\tau, \mu, q; T_0, q_0) \equiv J(\tau, \mu, q; T_0, q_0)\, q \tag{4.29}$$

where $J(\tau, \mu, q; T_0, q_0)$ is the particle current written as a function of q instead of energy T. Multiplication of J by q gives the charge associated with this particle current. (We call this a charge current *density* to avoid confusion with the electrical current which is not normalized to a unit area. The term density was not used previously since particle currents are generally normalized in this manner by convention.) If

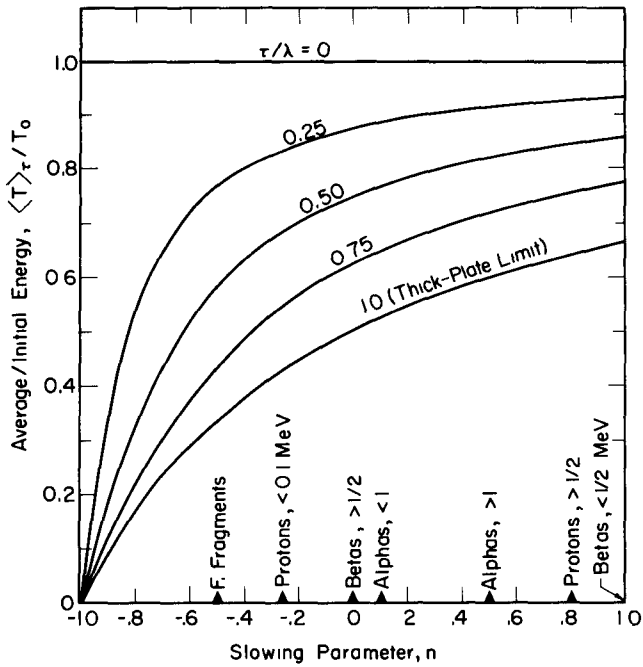

Fig. 4.5 — Average energy of the particle current as a function of plate thickness and the slowing parameter n.

charge neutralization does not occur, q equals q_0 independent of the particle's speed, and

$$J_q(\tau,\mu,q;T_0,q_0) = J(\tau,\mu;T_0)\ \delta(q_0 - q)\ q_0$$

$$= \frac{S(T_0)}{2}\ \mu\ \delta(q_0 - q)\ q_0 \begin{cases} \lambda(T_0) & [\tau/\lambda(T_0) \geq \mu \geq 0] \quad (4.30a) \\ \tau/\mu & [1 \geq \mu \geq \tau/\lambda(T_0)] \quad (4.30b) \end{cases}$$

where we have used Eq. (4.6) for the particle current. The total charge current density is found by integrating over all μ and q.

$$J_q(\tau;T_0,q) = \int\int J_q(\tau,\mu,q;T_0,q_0)\ d\mu\ dq$$

$$= \begin{cases} [S(T_0)/2]\ \tau[1 - \tau/2\lambda(T_0)]\ q_0 & (\tau < \lambda) \quad (4.31a) \\ [S(T_0)/4]\ \lambda(T_0)\ q_0 & (\tau > \lambda). \quad (4.31b) \end{cases}$$

If charge neutralization does occur, we must use Eq. (3.39), which, when combined with the slowing law, gives

$$\frac{q(r)}{q_0} = \left[1 - \frac{r}{\lambda(T_0)}\right]^{1/l} \tag{4.32a}$$

where

$$l \equiv \frac{2(n+1)}{m}. \tag{4.32b}$$

In addition to the initial energy, the initial charge of the source must be specified, and this is done by assuming a uniform isotropic source

$$S(T_0, q_0, \mu) = \frac{S(T_0, q_0)}{2}. \tag{4.33}$$

The current $J(\tau, \mu, q; T_0, q_0)$ is found from the particle current involving r using the transformation method of Sec. 4-1.2, which gives

$$J(\tau, \mu, q; T_0, q_0) = \frac{J(\tau, \mu; r, T_0, q_0)}{|dq/dr|}. \tag{4.34}$$

Combining Eqs. (4.5), (4.29), (4.32), and (4.34), we find

$$J_q(\tau, \mu, q; T_0, q_0) = \frac{l\,\lambda(T_0)\,S(T_0, q_0)}{2}\left(\frac{q}{q_0}\right)^l \mu. \tag{4.35}$$

Integration over μ to eliminate the angular dependence follows the same procedure as used for Eqs. (4.14) and (4.15), and this yields

$$J_q(\tau, q; T_0, q_0) = \frac{l\,\lambda(T_0)\,S(T_0, q_0)}{4}\left(\frac{q}{q_0}\right)^l \times \begin{cases} 1 & (q_0 \geq q \geq q_c) \quad (4.36a) \\ [(\tau/\lambda(T_0))]^2\,[1 - (q/q_0)^l]^{-2} & (q_c \geq q \geq 0) \quad (4.36b) \end{cases}$$

where the dividing charge q_c is given by

$$\frac{q_c}{q_0} = \left[1 - \frac{\tau}{\lambda(T_0)}\right]^{1/l}. \tag{4.37}$$

The total charge current density is found by integration over q, i.e.,

$$J_q(\tau;T_0,q_0) = \int J_q(\tau,q;T_0,q_0)\,dq$$

$$= \frac{l\,\lambda(T_0)\,S(T_0,q_0)}{4}\,q_0\,Y_l^l[q_c/q_0,\ \tau/\lambda(T_0)] \tag{4.38}$$

where Y was defined earlier in Eq. (4.24).

This may be used to find the average charge $\langle q\rangle_\tau$ associated with the particle current emerging from a plate of thickness τ, in which case we find

$$\langle q\rangle_\tau = \frac{J_q(\tau;T_0,q_0)}{J(\tau;T_0,q_0)}$$

$$= \frac{Y_l^l[q_c/q_0,\ \tau/\lambda(T_0)]}{Y_{l-1}^l[q_c/q_0,\ \tau/\lambda(T_0)]}q_0. \tag{4.39}$$

Curves for the average charge $\langle q\rangle_\tau$ as a function of l for various plate thicknesses τ/λ are presented in Fig. 4.6. It is clear that $\langle q\rangle$ is strongly dependent on l (i.e., the energy and charge loss parameters

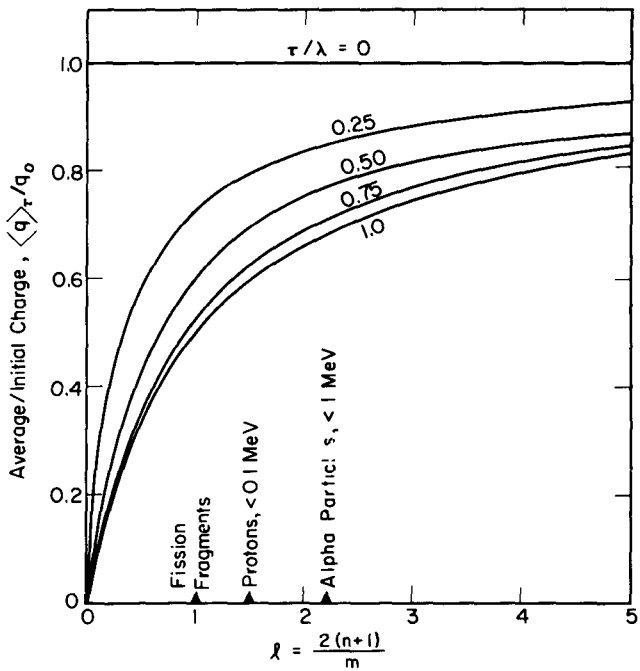

Fig. 4.6 — Average charge for particles leaving fuel layers of various thicknesses.

n and m), but the plate thickness is not overly important once τ/λ exceeds ≈ 0.5.

In general, numerical calculations were required to obtain these results; however, an analytic solution can easily be obtained for the limiting case of a thick plate where $q_c = 0$. Then, using Eq. (4.27), we obtain

$$\langle q \rangle_\tau = \frac{l}{l+1}\, q_0. \tag{4.40}$$

For example, using $n = -\frac{1}{2}$ and $m = 1$ (i.e., $l = 1$) as representative for a fission fragment, we find that $\langle q \rangle_\tau \rightarrow \frac{1}{2}\, q_0$ or + 10e.

4-1.5 Relation to Flux

The angular flux $\phi(\tau, \mu, T; T_0)$ is defined as the number of particles per second having a direction μ per unit μ and an energy T per unit T passing through a square centimeter of a plane at τ oriented such that it is perpendicular to the direction defined by μ. The angular current $J(\tau, \mu, T; T_0)$ was normalized to a plane at $z' = \tau$ perpendicular to the z-axis; hence, as seen from Fig. 4.7, the flux is

$$\phi(\tau, \mu, T; T_0) \equiv \frac{J(\tau, \mu, T; T_0)}{(A_\phi / A_J)} = \frac{J(\tau, \mu, T; T_0)}{\mu}. \tag{4.41}$$

Using Eq. (4.12) for J, we find

$$\phi(\tau, \mu, T; T_0) = \frac{(n+1)\, \lambda(T_0)\, S(T_0)}{2T_0} \left(\frac{T}{T_0}\right)^n \tag{4.42}$$

and the "scalar flux" is found by integration over μ, which gives

$$\phi(\tau, T; T_0) = \frac{(n+1)\, \lambda(T_0)\, S(T_0)}{2T_0} \left(\frac{T}{T_0}\right)^n \times \begin{cases} 1 & (T_{\tau n} \leq T \leq T_0) \qquad (4.43a) \\ [\tau/\lambda(T_0)]\, [1 - (T/T_0)^{m+1}]^{-1} & (T_{\tau n} \geq T \geq 0). \qquad (4.43b) \end{cases}$$

The scalar flux should no longer be thought of in terms of particles crossing an area at τ; rather, it represents the total track length per second of particles having kinetic energy T per unit energy per unit volume at τ. This is consistent with the conventional definition used in reactor analysis (pp. 63-68, Ref. 15).

The flux and not the current should be used with a cross section to define a reaction rate (e.g., ionization or excitation rates). Thus, the

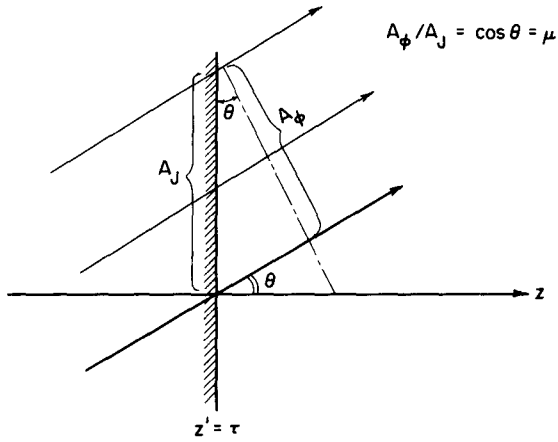

Fig. 4.7 — Relation between the angular current and flux.

reaction rate (for a given process "y") per unit volume is

$$[\text{R.R.}(\tau,\text{T})]_y = \Sigma_y(\tau,\text{T})\ \phi(\tau,\text{T}) \tag{4.44}$$

where $\Sigma_y(\tau,\text{T})$ is the macroscopic reaction cross section or the probability per unit track length of interaction y taking place with particles of energy T.

There are some situations where it is possible to bypass the calculation of the flux. For example, as discussed in connection with the continuity equation for energy [Eq. (4.25)], the energy loss rate in a source-free medium can be found directly from the current since it is equal to $\nabla\cdot\vec{J}_E$. Then, if the process "y" depends on the energy deposited (ionization is an example), the reaction rate can be evaluated directly. This technique is exploited later in Sec. 4-4.

4-1.6 Plane Kernels

The preceding current derivations were based on the integration of the solution for an elemental volume source over the entire volume of the fuel or source plate. More precisely, a point kernel or point Green's function was integrated over the actual source distribution. An alternate, but entirely equivalent, approach would be to start with a plane kernel and integrate over the plate volume. This in effect envisions the fuel plate as being composed of many plane sources sandwiched together to form the plate source.

Since plane kernels are especially useful in some calculations (e.g., multiregion slab problems), their derivation is illustrated in Appendix D-1 and a table of common kernels is included.

4-1.7 The Escape Probability

The escape probability E is defined as the fraction of the particles born in a fuel layer that escape. This can be calculated directly from the current; e.g., for the slab case with Eqs. (4.8) and (4.9) it is

$$E_{\tau,\frac{1}{2}}(T_0) = \frac{J(\tau;T_0)}{S(T_0)\,\tau} = \begin{cases} \frac{1}{2}\left[1 - \frac{\tau}{2\lambda(T_0)}\right] & [\tau \le \lambda(T_0)] \qquad (4.45a) \\ \frac{1}{4}\frac{\lambda(T_0)}{\tau} & [\tau \ge \lambda(T_0)] \cdot \qquad (4.45b) \end{cases}$$

The subscript $\frac{1}{2}$ is a reminder that this is based on "one-sided emission;" consequently, if a support or obstacle to emission on the back side of the plate is not present, Eq. (4.45) should be multiplied by a factor of two.

If the source has a distributed energy spectrum $S(T_0)$, the total escape probability is found by integration over the source spectrum

$$E_\tau = \frac{\int_0^\infty E_\tau(T_0)\, S(T_0)\, dT_0}{\int_0^\infty S(T_0)\, dT_0} \cdot \qquad (4.46)$$

It is often convenient in the application of this concept to other geometries to present the results in terms of the dimensionless quantity

$$\xi(T_0) \equiv \lambda(T_0)\frac{A}{V_s} \qquad (4.47)$$

where A/V_s is the surface to volume ratio of the solid[2]. In effect, this gives the ratio of the volume that particles escape from $(A\lambda)$ to the total volume. The utility of ξ is discussed further in Appendix D-2.2. For the slab case above, it is seen that

$$E_{\xi,\frac{1}{2}}(T_0) = \begin{cases} \frac{1}{2}\left[1 - \frac{1}{2\xi_{\frac{1}{2}}(T_0)}\right] & \left[\frac{1}{\xi_{\frac{1}{2}}(T_0)} \le 1\right] \qquad (4.48a) \\ \frac{1}{4}\,\xi_{\frac{1}{2}}(T_0) & \left[\frac{1}{\xi_{\frac{1}{2}}(T_0)} \ge 1\right] \qquad (4.48b) \end{cases}$$

where, due to our assumption of one-sided emission, $\xi_{\frac{1}{2}}(T_0)$ is based on the surface area of one side of the plate only; i.e., $\xi_{\frac{1}{2}} = \lambda(T_0)/\tau$. The full surface area is normally used for other geometries.

4-1.8 Straggling Effects

A correction for straggling can be included by using the approximate expressions for the transmission functions discussed earlier in

Sec. 3-5.2, namely,

$$T(r,T_0) = \begin{cases} \frac{1}{2}\,\mathrm{erfc}[y(r)] & (r > \bar{\lambda}) \\ \frac{1}{2}\,\{1 + \mathrm{erf}[y(r)]\} & (r < \bar{\lambda}) \end{cases} \quad [\text{Gaussian (ions)}] \tag{4.49a, 4.49b}$$

$$T(r,T_0) = \exp\left(-\frac{Dr^b}{T_0^c}\right) \quad [\text{Mar (electrons)}] \tag{4.49c}$$

where

$$D \equiv \left(\frac{0.585Z^{-0.271}}{\rho}\right)^{-b} \tag{4.50a}$$

$$b = 0.484\ c \tag{4.50b}$$

$$c = 14.5Z^{-0.48} \approx \frac{14.5}{\sqrt{Z}} \tag{4.50c}$$

$$y(r) \equiv \frac{\sqrt{\pi}}{2S}\left|(r - \bar{\lambda})\right|. \tag{4.50d}$$

Equations (4.49a and b) come from the integration of the Gaussian probability given in Eq. (3.63), where S and λ were also defined.

These functions can now be substituted into Eq. (4.5), and the integration over r can be carried out. The distinction between a "thick" and a "thin" plate discussed relative to Eqs. (4.6a and b) is no longer applicable since the transmission functions only vanish as $r \to \infty$. Thus, the limits are always from 0 to τ/μ and the integral involved becomes

$$\int_0^{\tau/\mu} T(r,T_0)\,dr = \begin{cases} \bar{\lambda} + i\,\mathrm{erfc}[y(0)] - i\,\mathrm{erfc}\left[y\left(\frac{\tau}{\mu}\right)\right] & \text{(Gaussian)} \quad (4.51a) \\ \frac{T_0^{c/b}}{bD^{1/b}}\,\gamma\left[\frac{1}{b};\left(\frac{\tau}{\mu}\right)^b\frac{D}{T_0^c}\right] & \text{(Mar)} \quad (4.51b) \end{cases}$$

where $\gamma(a;x)$ is the incomplete gamma function defined as (p. 260, Ref. 16)

$$\gamma(a;x) = \int_0^x \exp(-t)\,t^{a-1}\,dt \tag{4.52}$$

and $i\,\mathrm{erfc}(x)$, one of the repeated integrals of the error function, is given as (p. 299, Ref. 16)

$$i\,\mathrm{erfc}(x) = \frac{1}{\sqrt{\pi}} \exp(-x^2) - x\,\mathrm{erfc}(x). \tag{4.53}$$

These results may now be integrated over μ, as was done in Eq. (4.8), to find the current $J(\tau;T_0)$. Numerical evaluation of the integrals is required for an arbitrary thickness. Results of such calculations are not available; however, we can make some general observations.

For a thick plate, it is easy to show that these results are consistent with the average range model provided the average range $\langle\lambda(T_0)\rangle$ is defined according to Eq. (3.62). In this case, τ and hence the upper limit of Eq. (4.51) goes to ∞, and the following identity is obtained from the integration by parts and the use of Eqs. (3.62) and (3.66)

$$\begin{aligned}\langle\lambda(T_0)\rangle &= \int_0^\infty r\,P(r,T_0)\,dr = -\int_0^\infty r\left(\frac{dT}{dr}\right)\,dr \\ &= \int_0^\infty T(r,T_0)\,dr\,.\end{aligned} \tag{4.54}$$

Here $[r\,T]_0^\infty$ has been set equal to zero since T vanishes exponentially at ∞.

Reading Eq. (4.54) backwards, we see for a very thick plate that $\int_0^\infty T\,dr$ reduces to $\langle\lambda\rangle$, which is precisely the result obtained for the average range model, Eq. (4.6a). (To simplify the notation, brackets were not used earlier to indicate the average range.) This result may also be verified by direct integration of the transmission functions, although a slight discrepancy will be carried through the Gaussian distribution because, as noted in Chap. 3, it is normalized between $-\infty$ and $+\infty$ rather than 0 and ∞.

At the other extreme (thin plates), it may be argued intuitively that straggling tends to reduce the current below the average range model result which predicts that all particles born within a distance equal to the average range away from the surface will escape. However, the straggling distribution indicates that even some of these particles will be stopped. Physically, this is because some are scattered into a direction almost parallel to the surface before they reach it, and these dominate over those scattered into a direction that enhances escape. As the plate gets thicker and thicker, the current approaches the average range model. More and more particles are born beyond one average range length from the surface, but, due to the transmission distribution, they still have a finite probability of escaping. This tends to compensate for those born near the surface that fail to escape, and, in the limit of an infinite plate, the average range model current is recovered.

4-2 THE DIRAC CHORD METHOD—SHORT-CIRCUIT-CURRENT CALCULATIONS FOR OTHER GEOMETRIES

E. E. Lewis[2] has shown that the Dirac chord method, originally developed by Dirac[17] (see also Ref. 18 and pp. 373-377 of Ref. 15) to calculate neutron escape probabilities for purely absorbing media, can be quite useful in short-circuit calculations. A major advantage is that the extension to other geometries is greatly simplified if the chord distribution is available—this includes the sphere, infinite cylinder, hemisphere, oblate spheroid, and oblate hemispheroid (pp. 21-42, Ref. 18). However, it should be noted that, if the distribution is not available, the method may involve as much labor as, if not more than, the direct approach developed in the preceding sections.

Unfortunately, it does not appear possible to use the Dirac chord method in two important situations; namely, cell analysis for voltage conditions or the multiregion problem. Still, because of its utility in short-circuit and escape-probability calculations, the Dirac chord method is covered in some detail in Appendix D-2, where calculations of escape probabilities, particle current energy spectra, and average particle energy losses in the solid for cylinders and spheres are discussed.

4-3 CELL VOLTAGE—CURRENT CALCULATIONS

Several techniques can be used to calculate cell voltage–current characteristics including energy losses in the emitter layer. Two will be illustrated by the coated parallel-plate cell of Fig. 4.8.

The analysis is restricted to steady state operation with the collector maintained at a potential V^+ by a load resistance placed between it and the emitter. The emitter "fuel"-layer thickness is designated as τ, and the plate separation as d. The fuel layer might be a radioisotope, uranium, or any other source of charged particles.

To concentrate on the effect of a finite fuel-layer thickness, we continue to ignore other possible loss mechanisms, namely: any particles hitting either the support or collector plate are assumed to be absorbed; the space between plates is taken to be a perfect vacuum so no energy nor charge losses occur in this region; and secondary-electron emission, sputtering, etc., are ignored.

The charged particle source is assumed to be uniformly distributed throughout the emitter layer, and an *isotropic angular distribution* is used.

Particles are assigned a unique initial charge and energy q_0 and T_0, but this is not a restrictive assumption because it is always possible

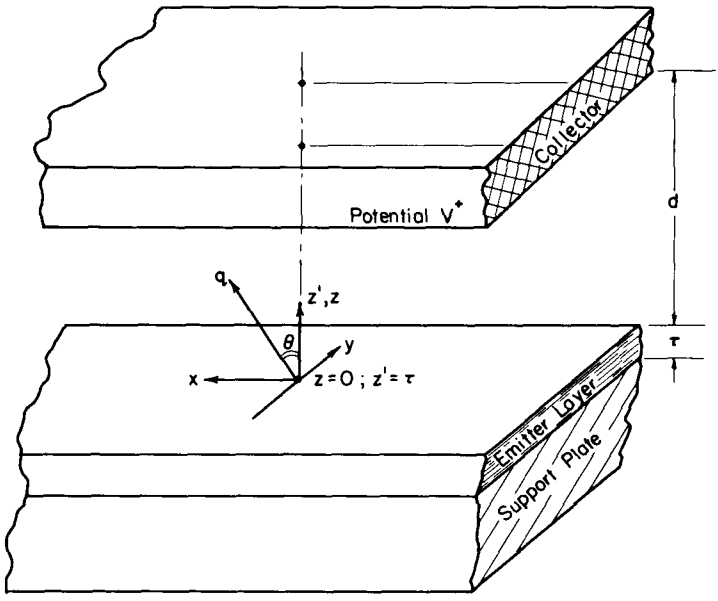

Fig. 4.8 — Coated parallel-plate geometry.

to integrate over the actual energy and charge spectra. For simplicity, we ignore relativistic effects, but if necessary, corrections can be made in much the same fashion as in Chap. 2.

4-3.1 Short-Circuit Current ($V^+=0$)

Under short-circuit conditions, all particles escaping the emitter layer will be collected. Thus, the cell short-circuit-current density $J_q(0)$ is simply equal to the charge current density (Sec. 4-1.4) evaluated at τ, or

$$J_q(0) = \langle q \rangle_\tau \, J(\tau; T_0, q_0) \equiv J_q(\tau; T_0, q_0) \tag{4.55}$$

where $J_q(\tau; T_0, q_0)$ can be evaluated using Eqs. (4.31) or (4.38) depending on whether or not q varies with energy. If q is in coulombs, J_q will be in amperes per square centimeter of plate surface. Equation (4.55) can also be written in terms of the escape probability, in which case by definition

$$J_q(0) = \langle q \rangle_\tau \, S(T_0, q_0) \, \tau \, E_{\tau,\frac{1}{2}}(T_0) \tag{4.56}$$

The escape probability $E_{\tau,\frac{1}{2}}$ can be taken from Eq. (4.45) for slabs, or, if other geometries are involved, the values summarized in Table D.2

of Appendix D can be used. In the latter case, if the charge varies, its average value may be found from Eq. (4.39).

4-3.2 Voltage—Current Analysis (Method A)

The analysis required here is identical to that used earlier for the idealized cell except that now the source can be visualized as the current emerging at the layer surface. This current has an energy, charge, and angle distribution that is different from the one encountered in the idealized cell so it is necessary to start with the complete current distribution function given in Eq. (4.12) as*

$$J(\tau,\mu,T;T_0) = \frac{(n+1)\,\lambda(T_0)\,S(T_0)}{2T_0}\left(\frac{T}{T_0}\right)^n \mu. \tag{4.57}$$

Now, consider the non-relativistic formulation of Eqs. (2.1) and (2.2) for conservation of energy and linear momentum

$$q_\tau V^+ = \frac{1}{2}\,m\,(v_\tau^2 - v_d^2) \tag{4.58}$$

$$mv_\tau \sin\theta_\tau = mv_d \sin\theta_d \tag{4.59}$$

where the subscripts τ and d indicate the fuel plate and collector surfaces, respectively. As before, the particle having the minimum energy required for collection will approach the collector tangentially so $\sin\theta_d \to 1$. In this limit, the conservation equations become

$$q_\tau V^+ = \frac{1}{2}\,mv_\tau^2(1-\sin^2\theta_\tau) = \frac{1}{2}\,mv_\tau^2\cos^2\theta_\tau \equiv T_{\tau z}^-. \tag{4.60}$$

The energy $T_{\tau z}^-$ is identified as the energy *associated* with the z-component of the velocity v_τ^-. (Energy is of course not a vector so this should not be thought of as the z-component of the energy). The superscript $(-)$ is used to indicate a minimum value. Equation (4.60) defines the minimum z-component of velocity $(v_\tau^-)_z$, i.e., the minimum value of $T_{\tau z}^-$ that a particle can have upon leaving the fuel layer and still be collected. It is important to note that this minimum can occur in *two* ways: For a fixed speed v_τ at the surface, the direction cosine μ_τ could assume a minimum value. Alternately, for a fixed direction cosine, the

*It should be stressed that the current energy spectrum is not of itself sufficient except for short-circuit calculations. The angular distribution must also be known for voltage analysis. This implies that techniques like the Dirac chord method are limited to short-circuit analysis.

speed v_τ could be a minimum. We will use both conditions later. [Another point to note in using Eq. (4.60) is that if charge neutralization occurs, q_τ will be a function of the energy of the particle at the surface, hence $T_{\tau z}$, as shown later in Eq. (4.67).] But first it is desirable to find out how to use the energy $T_{\tau z}$ in current calculations. To do this, we transform the particle current energy spectrum from T to T_τ. (Where the intention is clear, the subscript τ will be omitted for brevity.)

$$J(\tau,\mu,T_z;T_0) = J(\tau,\mu,T;T_0)\left|\frac{dT}{dT_z}\right|$$

$$= \frac{(n+1)\,\lambda(T_0)\,S(T_0)}{2T_0}\left(\frac{T_z}{T_0}\right)^n \mu^{-2n-1} \tag{4.61}$$

where we have used the relation

$$T_z = \mu^2 T. \tag{4.62}$$

The charge current density collected is then found by integration such that

$$J_q(V^+;T_0) = \int_{\mu^-}^{\mu^+} d\mu \int_{T_z^-}^{T_z^+} dT_z\; J(\tau,\mu,T_z;T_0)\; q(T_z). \tag{4.63}$$

The order of integration used here is a deliberate selection which has been found most convenient. The superscripts + and − indicate maximum and minimum values, respectively. These limits are a function of the emitter-layer thickness for a "thin" layer ($\tau < \lambda$), and their determination is a key point in the analysis. We will analyze the thin plate case first since it represents the most general situation, and results for a thick layer can easily be obtained as a limiting case.

[We could have derived Eq. (4.63) equally well by starting with the charge current density given in Eq. (4.35) and using the relation

$$J(\tau,\mu,T_z;T_0)\; q(T_z) = J_q(\tau,\mu,q;T_0,q_0)\left|\frac{dq}{dT_z}\right|. \tag{4.64}$$

This follows directly from the definition of the charge current density, and the fact that, if μ is fixed, q and T_z are uniquely related so $|dq/dT_z|$ can be evaluated as shown later.]

A cross section of the emitter or fuel layer and the support plate structure is shown in Fig. 4.9. This is similar to the geometry used earlier in Chap. 2 for the plane electrode cell, but now a finite emitter layer is included.

The angle θ_τ^+ is defined as the maximum possible emission angle, i.e., the maximum value of θ_τ in Eq. (4.60). This implies a maximum energy at the surface, which in turn requires that the particle is born at the emitter surface so that its energy is not degraded in traversing

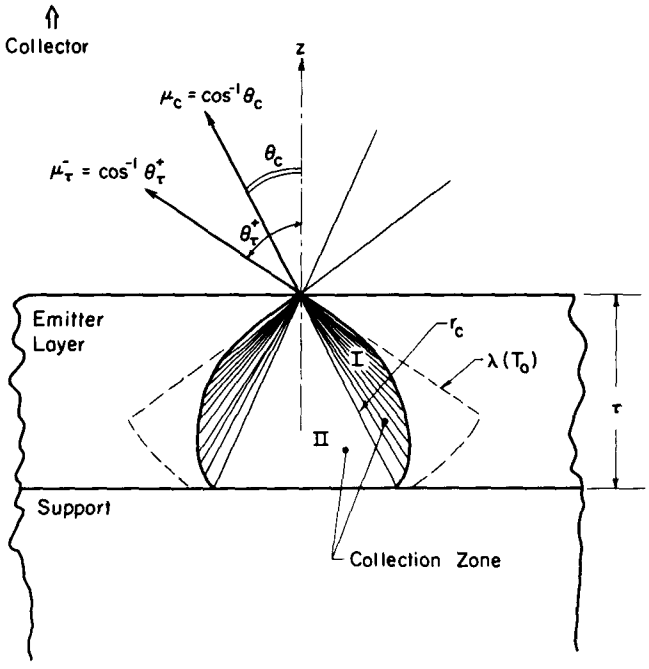

Fig. 4.9 — Cross section of a thin emitter layer showing the maximum and critical emission angles.

the fuel layer. Such a particle would have an energy T_0 and a charge q_0 at the surface, and application of Eq. (4.60) gives

$$\mu^- = \cos^{-1}\theta_\tau^+ = \sqrt{\frac{q_0 V^+}{T_0}} \equiv \sqrt{\beta_0}. \tag{4.65}$$

Note that β_0 represents the fractional voltage based on the *initial* energy and charge T_0 and q_0, respectively, and that θ_τ^+ is identical to the limiting angle obtained for the ideal cell [Eq. (2.7)]. The thickness of the emitter layer has no bearing on the properties of a particle born on the surface, so in this limit the distinction between the present case and the ideal cell vanishes.

The maximum value of T_z also occurs when the particle is born on the surface, and, for a fixed value of μ, T_z^+ is found from Eq. (4.62) to be

$$T_z^+ = \mu^2 T_0. \tag{4.66}$$

At this point, it is necessary to introduce the concept of a critical angle θ_c, illustrated in Fig. 4.9. Consider the envelope representing

the maximum distance a particle can travel in the layer and still have sufficient energy left to reach the collector. The critical angle corresponds to the condition where this envelope intersects the bottom surface of the emitter layer. Its value can be determined from conservation requirements described by Eq. (4.60). The left hand side of this equation is first expanded by use of the charge–energy relation of Eq. (3.39)

$$q_\tau V^+ = q_0 \left(\frac{T_\tau^-}{T_0}\right)^{m/2} V^+ = T_0\beta_0 \left(\frac{T_{\tau z}^-}{T_0}\right)^{m/2} \mu_\tau^{-m} . \tag{4.67}$$

When this expression is substituted back into Eq. (4.60), it is found that

$$T_{\tau z}^- = T_0 \beta_0^{2/(2-m)} \mu_\tau^{2m/(m-2)} \tag{4.68}$$

which defines the minimum energy associated with the z-component of velocity that a particle of direction cosine μ_τ can have and still be collected. Returning to Fig. 4.9, we see that the critical angle θ_c is defined such that such a particle will have traveled a distance r_c. Geometry gives

$$r_c = \frac{\tau}{\mu_c} \qquad [r_c \leq \lambda(T_0)] \tag{4.69}$$

and substitution of this relation into Eq. (3.28) yields

$$\left[T_{\tau z}^-\right]_{\mu_\tau = \mu_c} = \mu_c^2 T_{\tau c} = \mu_c^2 T_0 \left[1 - \frac{\tau}{\mu_c \lambda(T_0)}\right]^{1/(n+1)} . \tag{4.70}$$

This expression is now set equal to Eq. (4.68) with the latter evaluated at $\mu_\tau = \mu_c$, giving

$$\mu_c^2 T_0 \left[1 - \frac{\tau}{\mu_c \lambda(T_0)}\right]^{1/(n+1)} = T_0 \beta_0^{2/(2-m)} \mu_c^{2m/(m-2)} . \tag{4.71}$$

After rearrangement, we obtain

$$\beta_0^{2[(n+1)/(2-m)]} \mu_c^{2[(n+\epsilon)/(m-2)]} - \mu_c + \frac{\tau}{\lambda(T_0)} = 0 \tag{4.72}$$

where

$$\epsilon = n + \frac{m}{2} + 1. \tag{4.73}$$

This is the defining relation for μ_c, which is seen to be a function of the reduced voltage β_0 and the fractional layer thickness τ/λ. A plot of μ_c vs β_0 for selected values of τ/λ, n, and m is shown in Fig. 4.10. It turns out that the solutions for n = m = 0 and n = $-\frac{1}{2}$, m = 1 are identical. They require the solution of a quadratic equation from which it is found that

$$\mu_c = \frac{\tau}{2\lambda(T_0)}\left[1 + \sqrt{1 + 4\left(\frac{\lambda}{\tau}\right)^2 \beta_0}\right] \qquad \begin{matrix}(m = n = 0)\\ \text{or}\\ (n = -\frac{1}{2},\ m = 1)\ .\end{matrix} \tag{4.74}$$

Other values of n and m involve cubic and higher-order equations and are best solved numerically. It can be seen from either Eq. (4.72) or (4.74) that, when $\beta_0 = 0$, $\mu_c \to \tau/\lambda(T_0)$. This is consistent with our earlier calculations; e.g., note the angular limits on the charge current density in Eq. (4.30). Another limitation is that μ_c cannot be smaller than μ^-, defined by Eq. (4.65), so that while a formal solution of Eq. (4.72) may exist, nothing can be collected beyond this limit.

This can be summarized by the requirement

$$\mu_c \geq \text{max. } [\sqrt{\beta_0},\ \tau/\lambda(T_0)] \tag{4.75}$$

and these limits are apparent in Fig. 4.10.

Again, referring to Fig. 4.9, we see that the critical angle divides the allowed collection angles into two regions:

$$\text{Region I} \qquad \sqrt{\beta_0} \leq \mu \leq \mu_c \tag{4.76a}$$

$$\text{Region II} \qquad \mu_c \leq \mu \leq 1\ . \tag{4.76b}$$

The allowed range for T_{rz} must then be found within each region. The maximum value T_z^+ will always occur for a particle originating at the surface; hence, it is the same for both regions and is given by Eq. (4.66) discussed earlier.

However, the minimum values are region dependent, and a particle originating from Region I can come from anywhere within the fuel layer so long as it reaches the surface with sufficient energy to be collected. This requirement has already been considered and corresponds exactly to Eq. (4.68). In contrast, the minimum energy T_z^- for Region II occurs when the particle originates at the lower surface of the emitter layer. Such a particle will travel a distance τ/μ, so that T_z^- can be found directly from the energy–range relation

$$T_z^- = \mu^2 T_0\left[1 - \frac{\tau}{\mu\,\lambda(T_0)}\right]^{1/(n+1)} \qquad \text{(Region II)}. \tag{4.77}$$

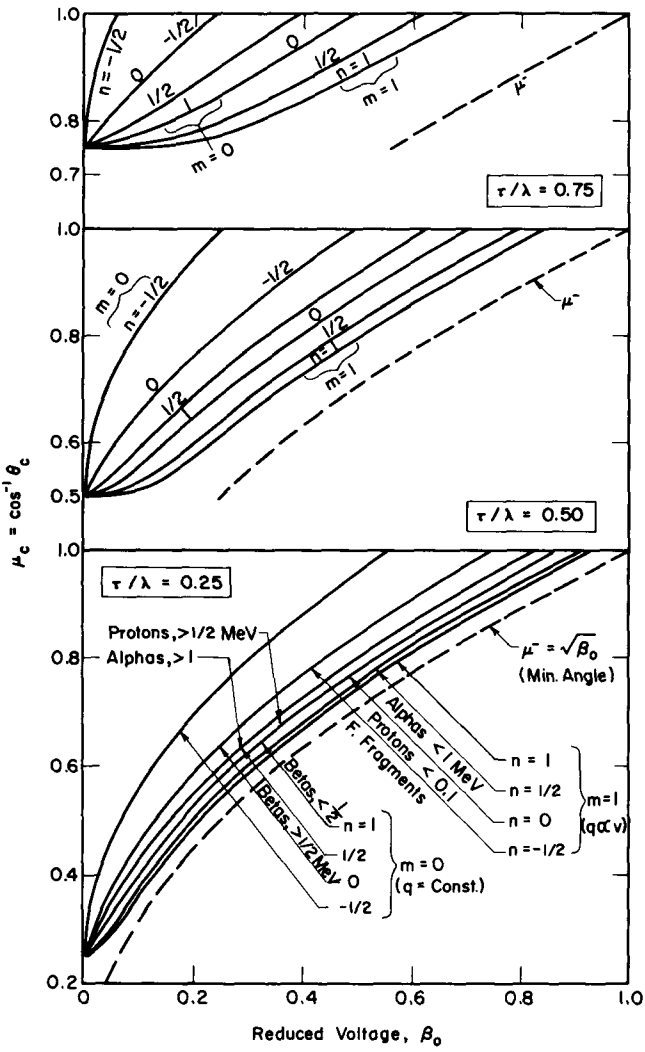

Fig. 4.10 — The critical angle θ_c as a function of reduced voltage. (For several plate thicknesses.)

These limits are summarized in Table 4.1. The charge current density may now be found by carrying out the integrations indicated in Eq. (4.63), which gives

$$J_q(\beta_0, \tau/\lambda) = J_q^{I} + J_q^{II} \tag{4.78}$$

where I and II refer to the two regions of Table 4.1 and the corresponding currents are given by

TABLE 4.1—INTEGRATION LIMITS

	Region I	Region II
μ^+	μ_c	1
μ^-	$\sqrt{\beta_0}$	μ_c
T_z^+	$\mu^2 T_0$	$\mu^2 T_0$
T_z^-	$T_0 \beta_0^{2/(2-m)} \mu^{2m/(m-2)}$	$\mu^2 T_0 \left[1 - \frac{\tau}{\mu\, \lambda(T_0)}\right]^{1/(n+1)}$

$$J_q^I = J_{qt}(0) \begin{cases} \mu_c^2 - \beta_0 + \beta_0^{2\epsilon/(2-m)} \ln \dfrac{\beta_0}{\mu_c^2} & (n = -m) \quad (4.79a) \\ \mu_c^2 - \beta_0 + \dfrac{(2-m)\beta_0}{2(n+m)} \left[(\mu_c^{4(n+m)/m-2} \beta_0^{2(n+m)/2-m} - 1)\right] & (n \neq -m) \quad (4.79b) \end{cases}$$

$$J_q^{II} = J_{qt}(0) \left[1 - \mu_c^2 - 2\left(\frac{\tau}{\lambda}\right)^2 \int_{1-\tau/\mu_c\lambda}^{1-\tau/\lambda} dV\, \frac{V^{\epsilon/(n+1)}}{(1-V)^3}\right]. \quad (4.80)$$

The quantity $J_{qt}(0)$ represents the short-circuit current for a thick plate, which is given by

$$J_{qt}(0) = \frac{(n+1)\, \lambda(T_0)\, S(T_0, q_0)\, q_0}{4\epsilon} \quad (4.81)$$

where ϵ was defined in Eq. (4.73).

These results are considerably simplified in the limit of a thick plate where by definition, $\mu_c = 1$, $\tau/\lambda(T_0) \geq 1$, and $J_q^{II} \to 0$ so that

$$J_q(\beta_0) = J_q^I = J_{qt}(0) \begin{cases} 1 - \beta_0 + \beta_0 \ln \beta_0 & (n = -m) \quad (4.82a) \\ 1 - \beta_0 + \dfrac{(2-m)\beta_0\, (\beta_0^{2(n+m)/2-m} - 1)}{2(n+m)} & (n \neq -m). \quad (4.82b) \end{cases}$$

The charge current is shown in Figs. 4.11(a), (b), and (c) for selected values of τ/λ, m, and n. These curves were calculated using a combination of analytic and numerical methods since analytic forms for μ_c and also the integral in Eq. (4.80) can only be obtained for certain values of m and n. As expected, the currents shown decrease with increasing voltage. The effect of charge loss (i.e., of m) can be most easily seen in Fig. 4.11(c) for a thick plate. For a fixed value of n

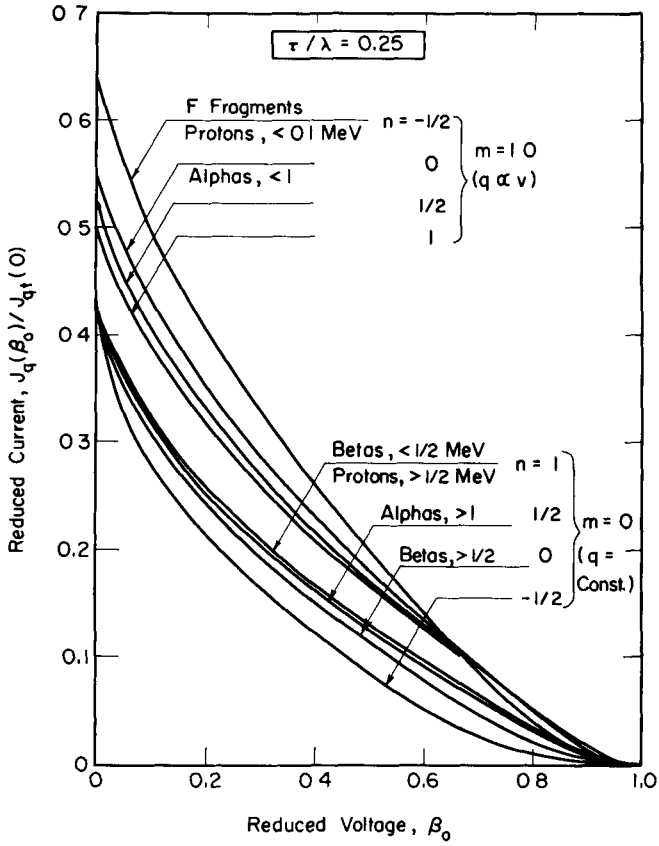

Fig. 4.11(a) — The charge-collection current density as a function of reduced voltage for a fuel-layer thickness of $\tau/\lambda = 0.25$.

(fixed energy loss), the curve for m = 0 always lies below that for m = 1 because the particle that loses charge (m = 1 corresponds to q ∝ v) has less trouble overcoming the potential barrier. On the other hand, if m is fixed, the curves with smaller values of n are lowest. This is best understood for m = 0, where charge losses do not enter. Then, according to the energy loss law, Eq. (3.27), as n decreases and goes negative, the energy loss per unit path dT/dr increases so the emerging particles simply possess less energy. This trend also occurs for the m = 1 curves, but here, the spread is not so large since the charge loss partly compensates for the increased energy loss.

The curves for $\tau/\lambda = 0.25$ and 0.5 show the same trends; however, in these cases, care must be taken in interpretation due to the variation of intercepts at $\beta_0 = 0$. For m = 0, since no charge loss occurs, all

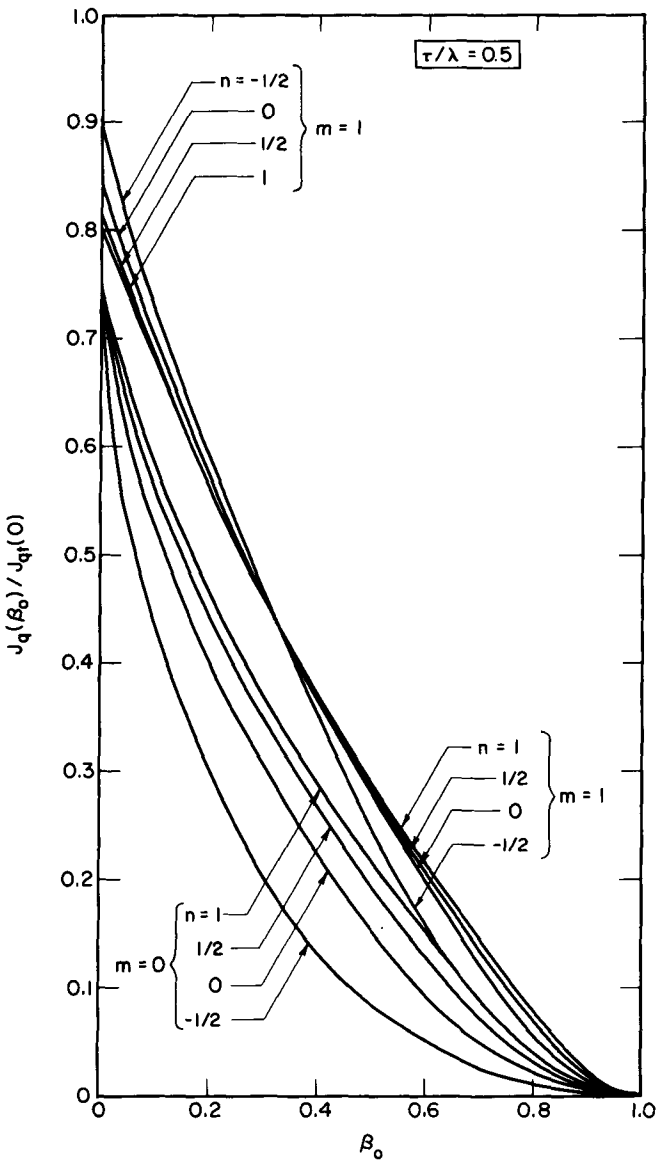

Fig. 4.11(b) — The charge-collection current density as a function of reduced voltage for a fuel-layer thickness of $\tau/\lambda = 0.5$.

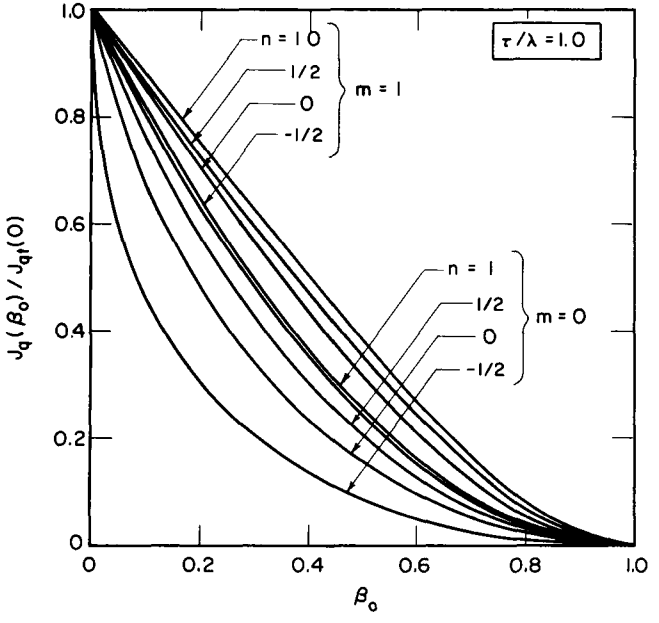

Fig. 4.11(c) —The charge-collection current density as a function of reduced voltage for a thick fuel layer.

the curves have a common intercept that depends only on the escape probability. It is easily shown from Sec. 4-1.4 that

$$\frac{J_q(0, \tau/\lambda)}{J_{qt}(0)} = 2\left(\frac{\tau}{\lambda}\right)\left(1 - \frac{\tau}{2\lambda}\right) \qquad (m = 0). \tag{4.83}$$

For m = 1, even for $\beta_0 = 0$, a charge loss occurs; consequently, the intercepts for m = 0 must be modified by the ratio of the charge loss for a plate thickness of τ/λ to that for a thick plate. For example, for $\tau/\lambda = 0.25$, Fig. 4.6 shows that with m = 1 and $n = -\frac{1}{2}$, $\langle q \rangle_\tau / q_0 = 0.73$ vs 0.5 for $\tau/\lambda = 1.0$. If the intercept for m = 0, $n = -\frac{1}{2}$ in Fig. 4.11(a) or (b) is multiplied by the ratio 0.73/0.50, the intercept for m = 1 is obtained, and a similar argument may be applied to the other curves. (While the $n = -\frac{1}{2}$ curve starts higher, it falls off more rapidly with voltage as argued earlier.)

As usual, if the source emits particles with a distributed energy and charge, a final integration over these spectra is required. To illustrate this, it is assumed that the source can be written as a product of functions depending on energy and charge such that

$$S(T_0, q_0) = N(T_0)\, Q(q_0). \tag{4.84}$$

Since the currents have been found as a function of β_0, it is also convenient to transform the source dependence to β_0, in which case by definition

$$S(\beta_0,q_0) = N(T_0)\, Q(q_0) \left|\frac{dT_0}{d\beta_0}\right|$$

$$= N\left(\frac{q_0V^+}{\beta_0}\right) Q(q_0)\, \frac{q_0V^+}{\beta_0^2}. \tag{4.85}$$

For example, the fission fragment spectrum of Eq. (3.35) would be

$$\frac{\beta_{0j}^2\, N_j(\beta_{0j})}{q_{0j}V^+} = \begin{cases} 0.685 \exp\left[-\alpha\left(\dfrac{q_{0j}V^+}{\beta_{0j}} - 67\right)^2\right] & (j = 1) \qquad (4.86a) \\ \exp\left[-\gamma\left(\dfrac{q_{0j}V^+}{\beta_{0j}} - 98\right)^2\right] & (j = 2). \qquad (4.86b) \end{cases}$$

The total current is then

$$J_q(V^+) = \int_{\beta_0=[V^+/(T_0/q_0)_{max}]}^{\infty} d\beta_0 \int_{q_0=0}^{\infty} dq_0\, J_q(\beta_0,q_0)\, S(\beta_0,q_0). \tag{4.87}$$

Note that, while the integration is over β_0, it is carried out with the voltage V^+ fixed, so J_q is a function of V^+. Care must be taken when evaluating this integral for thin plates since $J_q(\beta_0,q_0)$ involves μ_c [Eqs. (4.74) and (4.78)], which is itself a function of β_0, and this leads to a somewhat tedious problem for those cases where μ_c comes from a cubic or high-order algebraic equation.

4-3.3 Voltage—Current Analysis (Method B)

The arguments involved in evaluating the limits in Method A are straightforward but somewhat complex in detail. It may be helpful to consider a slightly different but entirely equivalent point of view. A thick plate will be used in this illustration in order to minimize the complexity. The extension to a thin plate requires that the integrations involved be divided into regions in the same fashion as in Method A.

We begin with the current from Eq. (4.2) derived for a point kernel and spherical coordinates, and, if we assume a uniform isotropic source, Eq. (4.2) becomes

$$J(\tau,\vec{\Omega};r,T_0) = \frac{S(T_0,q_0)}{4\pi}\, T(r,T_0)\, \mu\, d\mu\, d\phi\, dr. \tag{4.88}$$

The charge current density follows immediately by integration

$$J_q(\tau;T_0) = \frac{S(T_0,q_0)}{2} \int_{\mu^-}^{\mu^+} d\mu\, \mu \int_{r^-}^{r^+} q(r)\, dr \tag{4.89}$$

where the probability $T(r,T_0)$ has been replaced by appropriate evaluation of the limits on r. The lower limit on r is immediately seen to be

$$r^- = 0. \tag{4.90}$$

The maximum value of r comes from the energy balance given in Eq. (4.60)

$$T_{\tau z}^- = q_\tau V^+. \tag{4.91}$$

As discussed earlier, $T_{\tau z}^-$ specifies a minimum energy, and it corresponds to either a minimum speed for a fixed angle or a minimum angle for a fixed speed at the surface. Using the former point of view, we note that a minimum speed at the surface in turn specifies the maximum distance a particle can travel between its point of birth and the surface. This distance r^+ can be found by substituting the energy–range and charge–range relations into Eq. (4.91), and this gives

$$\mu^2 T_0 \left[1 - \frac{r^+}{\lambda(T_0)}\right]^{1/(n+1)} = q_0 \left[1 - \frac{r^+}{\lambda(T_0)}\right]^{m/2(1+n)} V^+ \tag{4.92a}$$

or

$$r^+ = \left[1 - \left(\frac{\beta_0}{\mu^2}\right)^{2[(1+n)/(2-m)]}\right] \lambda(T_0). \tag{4.92b}$$

The limits on μ are the same as found for Method A, i.e., for a thick plate

$$\mu^- = \sqrt{\beta_0}\,; \qquad \mu^+ = 1. \tag{4.93}$$

The charge current density integral is now completely specified, and, writing it out in detail, we obtain

$$J_q(\tau;T_0) = \frac{S(T_0,q_0)\, q_0}{2} \int_{\mu=\sqrt{\beta_0}}^{1} d\mu\, \mu \times \int_{r=0}^{\{1-(\beta_0/\mu^2)^{2[(1+n)/(2-m)]}\}\lambda(T_0)} \left[1 - \frac{r}{\lambda(T_0)}\right]^{m/2(1+n)} dr. \tag{4.94}$$

It is fairly straightforward to verify that these integrals lead to the same results as obtained earlier in Eqs. (4.82a) and (4.82b). This is most easily done by selecting specific values of m and n, e.g., n = m = 0 represents a particularly easy case, which immediately gives Eq. (4.82a). It may appear from the present treatment that Method B is considerably simpler than A, but this is somewhat misleading. Much of the complexity involved previously in Method A arose because we started with the thin plate analysis. While some labor is saved in Method B because the currents are not transformed to involve energy (r is retained as the variable throughout), this might even be a disadvantage in some situations—e.g., if the current energy spectrum is required for other purposes, Method A may be the easiest way to find it and the charge current density simultaneously.

4-3.4 Cell Efficiency Calculations

The cell efficiency, which follows directly from the definition given in Chap. 2 [Eq. (2.19)], is

$$\eta_c(\beta_0, \tau/\lambda) = \frac{\int_{\mu^-}^{\mu^+} d\mu \int_{T_z^-}^{T_z^+} dT_z\, J(\tau,\mu,T_z;T_0)\, q(T_z)\, V^+}{S(T_0,q_0)\,\tau T_0}$$

$$= \frac{\beta_0}{S(T_0,q_0)\,\tau q_0} J_q(\beta_0, \tau/\lambda) \qquad (4.95)$$

where $J_q(\beta_0, \tau/\lambda)$ can be taken from Eq. (4.78).

Cell efficiencies calculated from this result are shown in Figs. 4.12(a) to (c) for various m and n and for τ/λ = 0.25, 0.50, and 1.0. As might be expected, the efficiency is reduced as τ/λ increases, e.g., the maximum value for n = m = 1 at τ/λ = 0.25 is ≈6.7% vs ≈ 4% for τ/λ = 1.0. The explanation for differences observed for various values of n and m is the same as used in the discussion of the current–voltage behavior in Fig. 4.11. Note, in general, that the largest variation in efficiency is due to n, the results being much less sensitive to m. This can be explained on the following basis: As m is increased, a given particle will have less charge at the surface so it crosses the barrier more easily (increasing the current). At the same time, it is less "valuable" (i.e., less energy is converted when it is collected), and these effects tend to compensate each other.

For a fixed m, the largest efficiency always occurs for the largest n (n = 1 in these figures) corresponding to the minimum energy loss per unit path.

If the source has a distributed charge–energy spectrum, the final integration, which is analogous to Eq. (4.87), is

$$\eta_c(V^+, \tau/\lambda) = \int\int \eta_c(\beta_0, \tau/\lambda)\, S(\beta_0, q_0)\, d\beta_0\, dq_0. \tag{4.96}$$

A calculation of this type has been carried out by Miley[4] for fission fragments in connection with a study of the Fission-Electric Cell. He used Eq. (4.86) for the source energy spectrum and assumed a single charge was associated with each group so that the $Q(q_0)$ of Eq. (4.84) was simply

$$Q(q_0) = \delta(q_0 - 15e)\, \delta_{j=1} + \delta(q_0 - 16e)\, \delta_{j=2} \tag{4.97}$$

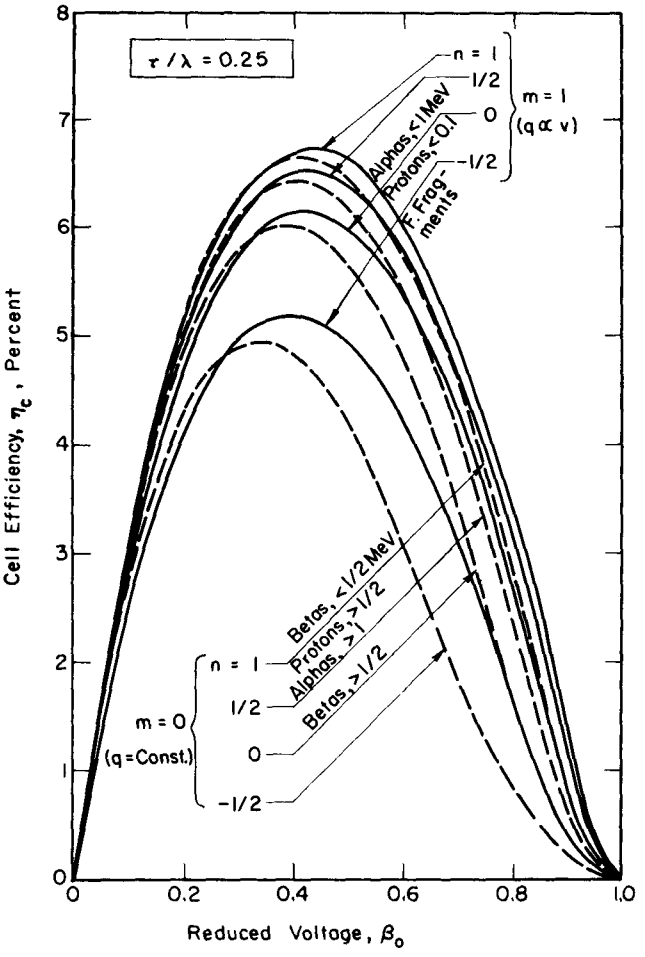

Fig. 4.12(a)—Cell efficiencies vs voltage for a fuel-layer thickness of τ/λ = 0.25.

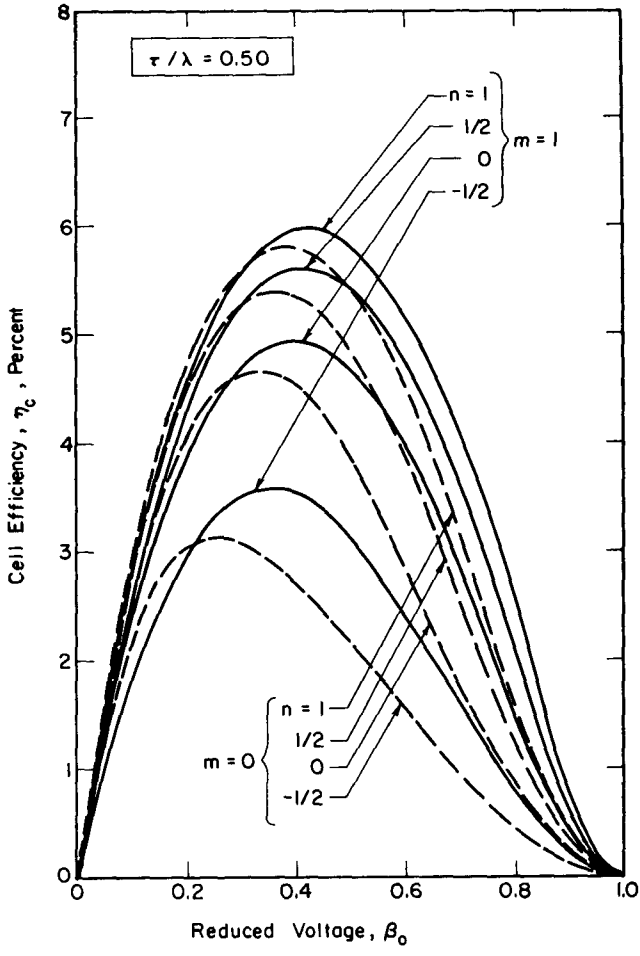

Fig. 4.12(b) —Cell efficiencies vs voltage for a fuel-layer thickness of $\tau/\lambda = 0.5$.

where the subscripts j = 1 and j = 2 refer to the heavy and light groups, respectively. Results for a thick plate are shown in Fig. 4.13, and the variation with fuel-layer thickness is illustrated in Fig. 4.14. As we found earlier, the curves with either $n_1 = n_2 = -\frac{1}{2}$ or $n_1 = -\frac{1}{2}$, $n_2 = -\frac{2}{3}$ with m = 1 (as opposed to m = 0) are expected to be reasonably accurate.

A 10.6-μ layer is essentially a thick plate, and a comparison of Fig. 4.13 with 4.12(c) (for $\tau/\lambda = 1.0$ and monoenergetic particles) indicates a close agreement. For example, curve E_2 peaks at $\approx$1.3% vs $\approx$1.5% for $n = -\frac{1}{2}$, m = 0 in the earlier figure. Likewise, E_3 predicts

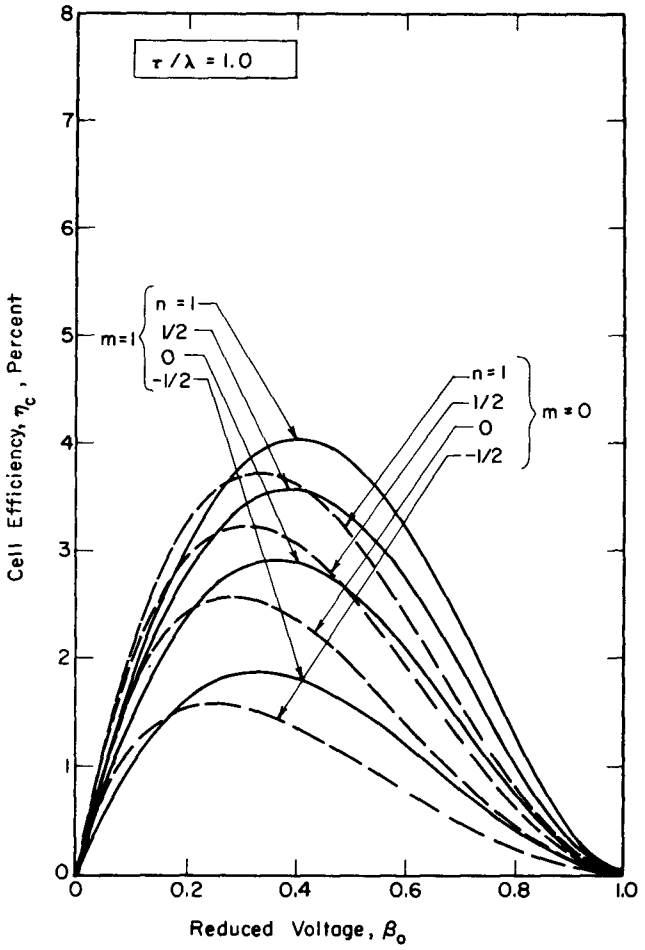

Fig. 4.12(c) — Cell efficiencies vs voltage for a thick fuel layer.

≈1.6% vs 1.8%. Thus, in this case, the use of the detailed spectrum and energy–range correlation only results in a 10 to 15% correction. Of course, the fragment energy spectrum is quite narrow within each group, so the correction would not have been expected to be large. Perhaps the most important problem is the proper selection of n (e.g., many early investigators used $n_1 = n_2 = 0$, which, as seen from these curves, results in considerable error).

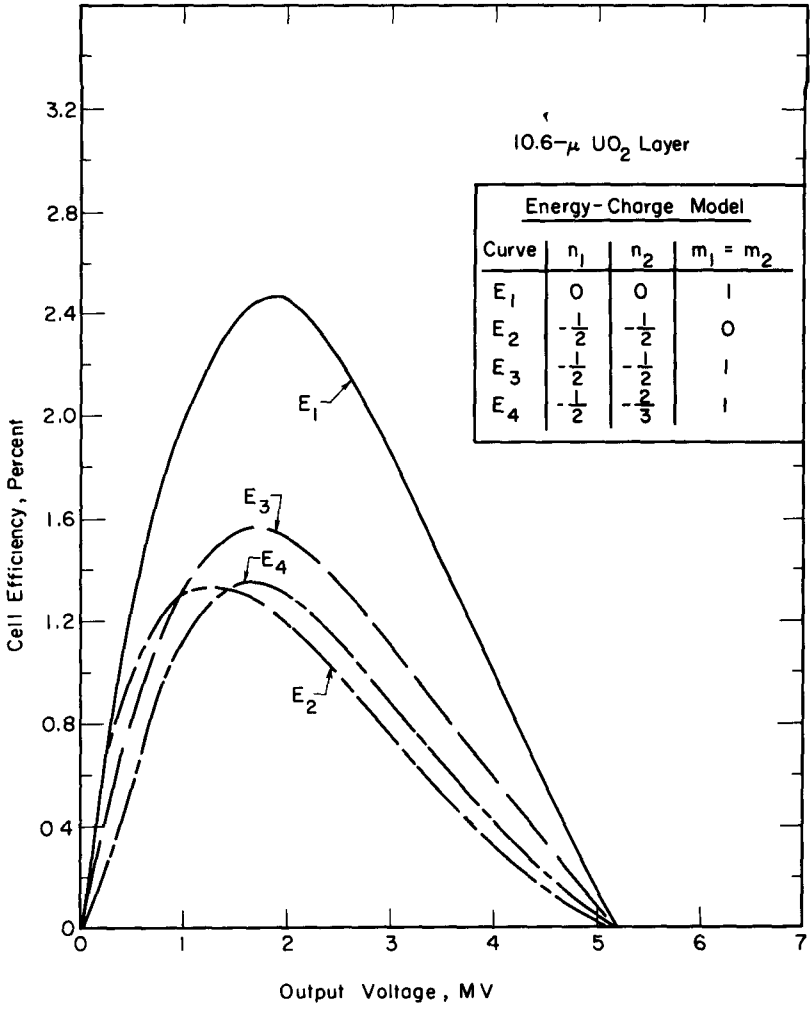

Fig. 4.13 — Efficiency calculations for a Fission-Electric Cell with a 10.6-μ UO_2 fuel layer (a thick fuel layer).

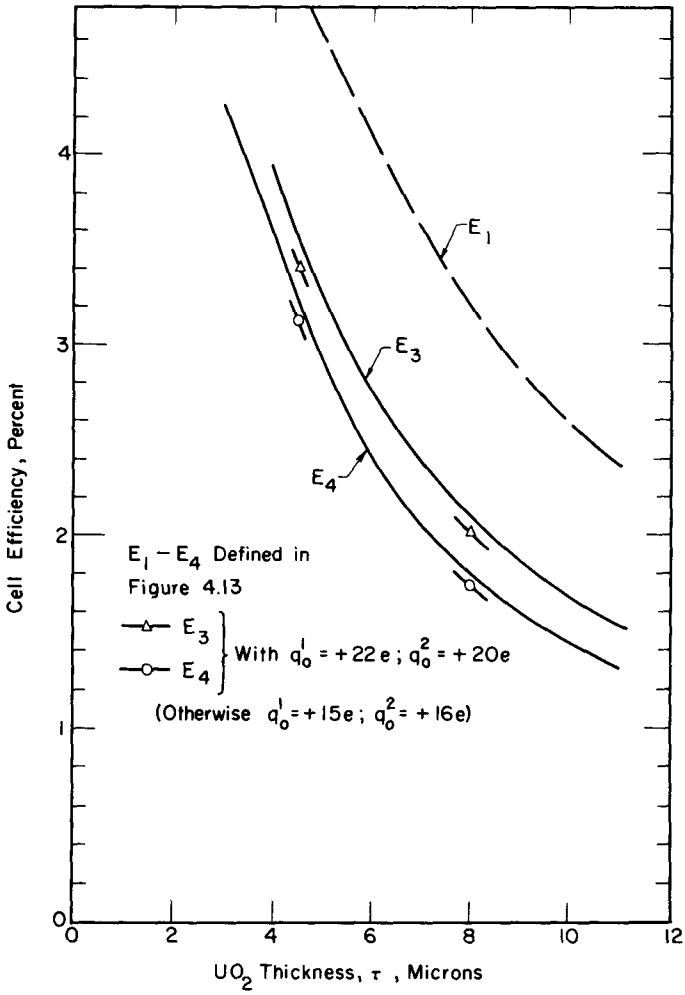

Fig. 4.14—Variation of the maximum cell efficiency with fuel-layer thickness. (Here, q_0^1 represents the initial charge for a heavy fragment while q_0^2 refers to a light fragment.)

4-4 THE TWO-REGION PROBLEM

In some instances, it is desirable to coat the fuel layer with a thin protective layer of material such as gold or stainless steel to prevent radioactive contamination of the system. This leads to a class of problems, called "two-region problems," illustrated in Fig. 4.15. Another important situation where such problems occur is in Interac-

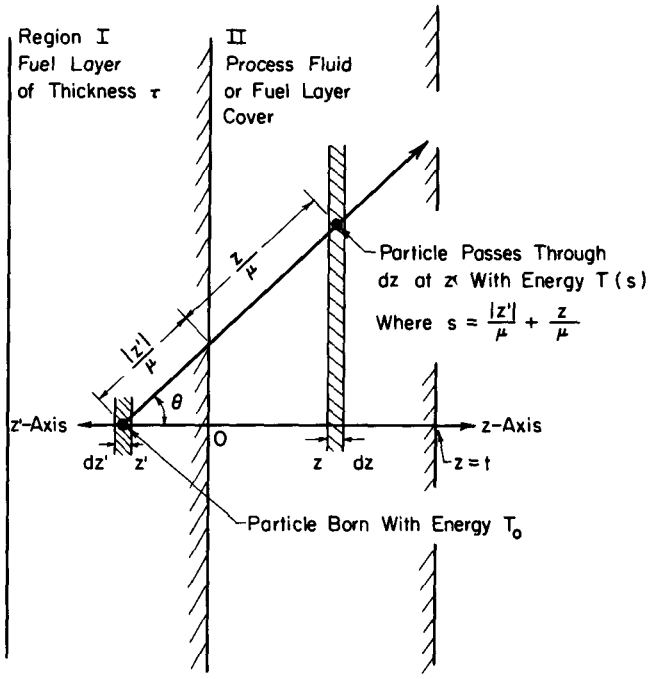

Fig. 4.15 — The two-region problem in planar geometry.

tion-Energy Cells (Chap. 1, Sec. 1-3.2), in which case the non-emitting layer, instead of being a coating, can be visualized as a gas or other material that is being irradiated by particles from the fuel.

Multilayer designs and numerous other geometries may also arise, but, to illustrate the basic principles involved in the analysis, we will restrict our attention to the simple planar geometry of Fig. 4.15. (The following is an abbreviation and slight modification of a derivation by Miley and Thiess[19].)

As before, the coating and fuel are assumed to be electrical conductors so, even when the cell is operating at a voltage, the electrical field in those two regions is zero. Subscripts I and II will be used with the various parameters required to indicate the region involved, e.g., $\lambda_I(T_0)$ is the range evaluated in Region I. The energy–range fitting parameter will also be subscripted for generality, although as stressed in Chap. 3, it is only weakly dependent on materials and particle energies so that to a first approximation $n_I \approx n_{II}$.

It is most convenient to carry out the derivation in terms of non-dimensional (reduced) parameters defined as

$$\epsilon \equiv T/T_0 \tag{4.98a}$$

and

$$z \equiv z/\lambda_{II}(T_0) = z/\lambda_{II}(1). \tag{4 98b}$$

(Since ϵ and z incorporate T_0, it will no longer be retained as an explicit parameter. Note that ϵ evaluated at T_0 is 1.)

The slowing model of Eq. (3.28) can be applied between any two points of the particle's path as long as they lie *within the same region* If s represents the distance between these points,

$$\frac{\epsilon}{\epsilon_1} = \left[1 - \frac{s}{\lambda_i(\epsilon_1)}\right]^{1/(n_i+1)} \qquad (i = \text{I or II}) \tag{4.99}$$

where the reduced energy ϵ_1 represents the energy of the particle at $s = 0$. When this relation is applied to Region I, $s = 0$ will be defined as the point of birth of the particle. Then, since particles are born with energy T_0, ϵ_1 is equal to 1.0 for Region I. However, for Region II, s will be defined as zero at the interface, and the corresponding value of ϵ_1 will be denoted ϵ', the prime being used to indicate the energy of the particle at the interface.

The energy dependence of the range must satisfy Eq. (3.29) in each region so that

$$\frac{\lambda_i(\epsilon)}{\lambda_i(\epsilon_1)} = \left(\frac{\epsilon}{\epsilon_1}\right)^{n_i+1} \qquad (i = \text{I or II}) \tag{4.100}$$

The current at the interface $J_I(0,\mu,\epsilon';1)$ is found by using specific values for $\lambda_I(1)$ and n_I in Eq. (4.12). Then, since J_I is known, the problem resolves into one of finding the resulting current $J_{II}(z,\mu,\epsilon)$ at some point z in Region II. Since Region II is source free, a transmission function method can be used, and we introduce $T(r, \epsilon' \rightarrow \epsilon)$ as the probability that a particle with energy ϵ' will have an energy ϵ per unit ϵ after traveling a distant r in Region II. This function is easily found by noting that the slowing law of Eq. (4.99) requires a unique relation between z and ϵ; hence T must be a delta function of the form

$$T(z/\mu, \epsilon' \rightarrow \epsilon) = \frac{\delta(\epsilon' - \epsilon_p)}{|d\epsilon/d\epsilon'|} \tag{4.101a}$$

Here, ϵ_p represents the particular energy that a particle starting with energy ϵ' has after traveling a distance z/μ, which according to the slowing law is given by

$$\epsilon_p = \left[\epsilon^{n_{II}+1} + \frac{z}{\mu}\right]^{1/(n_{II}+1)}. \tag{4.101b}$$

The Jacobian is included in Eq. (4.101a) to transform from the "per unit" ϵ' inherent in the delta function to the "per unit" ϵ required in the definition of T. It may be found by differentiation of Eq. (4.101b) with $\epsilon_p \equiv \epsilon'$, and this gives

$$\left|\frac{d\epsilon}{d\epsilon'}\right| = \left[\epsilon^{n_{II}+1} + \frac{z}{\mu}\right]^{n_{II}/(n_{II}+1)} \epsilon^{-n_{II}}. \tag{4.102}$$

Having determined T, we are in a position to find J_{II} in terms of the known interface current since by definition

$$J_{II}(z,\mu,\epsilon) = \int_{\epsilon'} J_I(0,\mu,\epsilon')\ T(z/\mu,\ \epsilon' \to \epsilon)\ d\epsilon'. \tag{4.103}$$

Substitution for T and integration yields

$$\frac{J_{II}(z,\mu,\epsilon)}{\tau\, S(1)} = \frac{n_I + 1}{2\tau/\lambda_I}\left[\epsilon^{n_{II}+1} + \frac{z}{\mu}\right]^{(n_I - n_{II})/(n_{II}+1)} \epsilon^{n_{II}}\,\mu \tag{4.104}$$

and $J_{II}(z)$ can then be found by subsequent integration over μ and ϵ using the limits of Table 4.2.

TABLE 4.2 — LIMITS FOR J_{II}

		μ_{min}	μ_{max}	
$0 < z < z_c$	$0 < \epsilon < \epsilon_c$	$\frac{z}{1-\epsilon^{n_{II}+1}}$	$\frac{\tau/\lambda_I + z}{1-\epsilon^{n+1}}$	(if $n = n_I = n_{II}$)
			Eq. 4.111a	(otherwise)
	$\epsilon_c < \epsilon < \epsilon_m$	$\frac{z}{1-\epsilon^{n_{II}+1}}$	1.0	
$z_c < z < 1.0$	$0 < \epsilon < \epsilon_m$			

where

$$z_c \equiv [1 - \tau/\lambda_I(1)]^{(n_{II}+1)/(n_I+1)} \qquad (\text{for } \tau/\lambda_I \leq 1)$$

$$\epsilon_m \equiv (1-z)^{1/(n_{II}+1)}$$

$$\epsilon_c = (z_c - z)^{1/(n_{II}+1)}$$

The limits are somewhat complicated and require explanation. They arise because, for fixed values of the reduced energy ϵ and position z, a unique range of direction cosines exists that allows a particle to reach z with the desired ϵ.

A critical value of z exists, labeled z_c, such that a particle born at the *back* face of the fuel layer and traveling straight forward ($\mu = 1.0$) will just reach z_c with zero energy. This occurs when the distance traveled in Region II equals the range corresponding to the interface energy ϵ' so that $z = \lambda_{II}(\epsilon')$; using Eqs. (4.99) and (4.100), we find

$$z_c = \frac{\lambda_{II}(\epsilon')}{\lambda_{II}(1)} = \begin{cases} [1 - \tau/\lambda_I(1)]^{(n_{II}+1)/(n_I+1)} & (\tau/\lambda_I \leq 1) \quad (4.105a) \\ 0 & (\tau/\lambda_I > 1). \quad (4.105b) \end{cases}$$

Now for $z_c < z < 1.0$, the reduced energy can vary between $0 < \epsilon < \epsilon_m$ where the upper limit ϵ_m occurs when a particle is born at the interface and travels straight ahead to z

$$\epsilon_m = (1 - z)^{1/(n_{II}+1)}. \quad (4.106)$$

Correspondingly, the direction cosine μ will vary between 1.0 and a minimum value defined by a particle born at the interface which leaves at a large angle such that it just arrives with energy ϵ at z, in which case

$$\epsilon = \left[1 - \frac{z}{\mu_{min}}\right]^{1/(n_{II}+1)}. \quad (4.107)$$

These results are illustrated schematically in Fig. 4.16(a). Particles born in the fuel layer over a surface shown by the solid line can reach z with the proper energy. The particle with the maximum angle is born at the interface, and, as the angle decreases, the reduced path length in Region II is compensated by starting deeper in the fuel layer until $\mu = 1.0$ at the deepest point of origin.

We next consider $0 < z < z_c$. This must be further subdivided depending on whether the energy is greater or less than a critical value ϵ_c corresponding to a particle born at the back surface of the fuel and traveling straight forward. Repeated application of Eqs. (4.99) and (4.100) to evaluate the interface energy ϵ' and to obtain $\lambda_{II}(\epsilon')$ in terms of $\lambda_{II}(1)$ gives

$$\epsilon_c = \left[1 - \frac{\tau}{\lambda_I(1)}\right]^{1/(n_I+1)} \left\{1 - \frac{z}{[1 - \tau/\lambda_I(1)]^{(n_{II}+1)/(n_I+1)}}\right\}^{1/(n_{II}+1)} \quad (4.108)$$

Now, if $\epsilon > \epsilon_c$, the particle must have originated somewhere inside the surface shown by a dashed line in Fig. 4.16(a). In this case, the limits for μ are identical to those already derived. However, if $\epsilon < \epsilon_c$, the surface of origin (birth) of the particle will intercept the

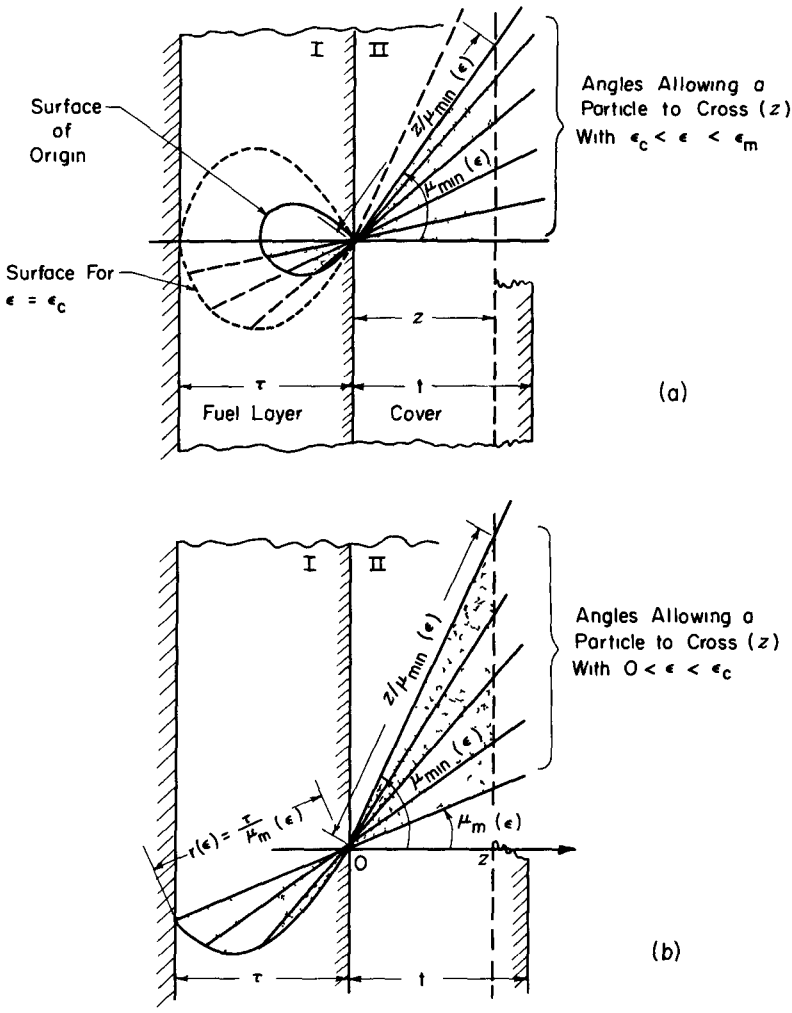

Fig. 4 16—Illustration of limits in the two-region problem. (a) Energies above ϵ_c (b) Energies below ϵ_c.

rear of the fuel layer as illustrated in Fig 4.16(b). This leads to a new limit for μ_{max}, which is

$$\mu_{max} = \frac{\tau}{r(\epsilon')} \tag{4.109}$$

where $r(\epsilon')$ is the distance from the intercept at the rear surface to the front interface. It is expressed as a function of the interface energy

by again using Eq. (4.99) to obtain

$$r(\epsilon') = \lambda_I(1)\left[1 - (\epsilon')^{n_I+1}\right] \tag{4.110}$$

where r is now understood to lie along μ_{max}. However, for the particle to reach z with a fixed ϵ, the value of ϵ' must also satisfy Eq. (4.99) for Region II. Using this relation, along with Eq. (4.100), to eliminate ϵ' in favor of ϵ and substituting into Eq. (4.109), we find

$$\mu_{max} = \frac{\tau/\lambda_I(1)}{1 - \left[\epsilon^{n_{II}+1} + z/\mu_{max}(\epsilon)\right]^{(n_I+1)/(n_{II}+1)}} . \tag{4.111a}$$

In general, this transcendental equation must be solved numerically for μ_{max}; however, for the special case where $n = n_I = n_{II}$ an analytic solution is easily obtained

$$\mu_{max} = \frac{\tau/\lambda_I(1) + z}{1 - \epsilon^{n+1}} . \tag{4.111b}$$

This completes the evaluation of the limits, and they, along with Eq. (4.104), are valid anywhere in the interior of Region II. For cell calculations, we are interested in the current at the surface of Region II, which then represents the plate facing the collector electrode. This is found by evaluating Eq. (4.104) at $z = t$ where t is the thickness of the cover layer. *This result can then be used in place of Eq. (4.57) to calculate cell performance following the methods developed in Sec. 4-3.2.* The limits in Table 4.2 can be used for short-circuit calculations, but limits for voltage operation must be derived as indicated in Sec. 4-3.2.

Calculations of this type are fairly complicated and have not been carried out to date. However, it is clear that the cover layer may have a significant effect, especially if it is fairly thick. Some indication of this can be gained from Fig. 4.17, where the total particle and energy currents are shown as a function of z for several specific values of n (zero voltage case). The total current corresponds to integration of Eq. (4.104) over all allowed μ and ϵ indicated in Table 4.2. This figure shows that even a thin coating with $z = 0.1$ over a thick fuel layer ($\tau/\lambda_I = 1.0$) reduces the particle current by almost 20% and the energy current by ≈35%.

The energy current is more drastically affected than the particle current due to the energy loss a particle suffers as it passes through the cover layer. The corresponding shift in energy is illustrated in Fig. 4.18, where various particle current energy spectra are shown for $z = 0.25$ for several fuel-layer thicknesses. These curves should

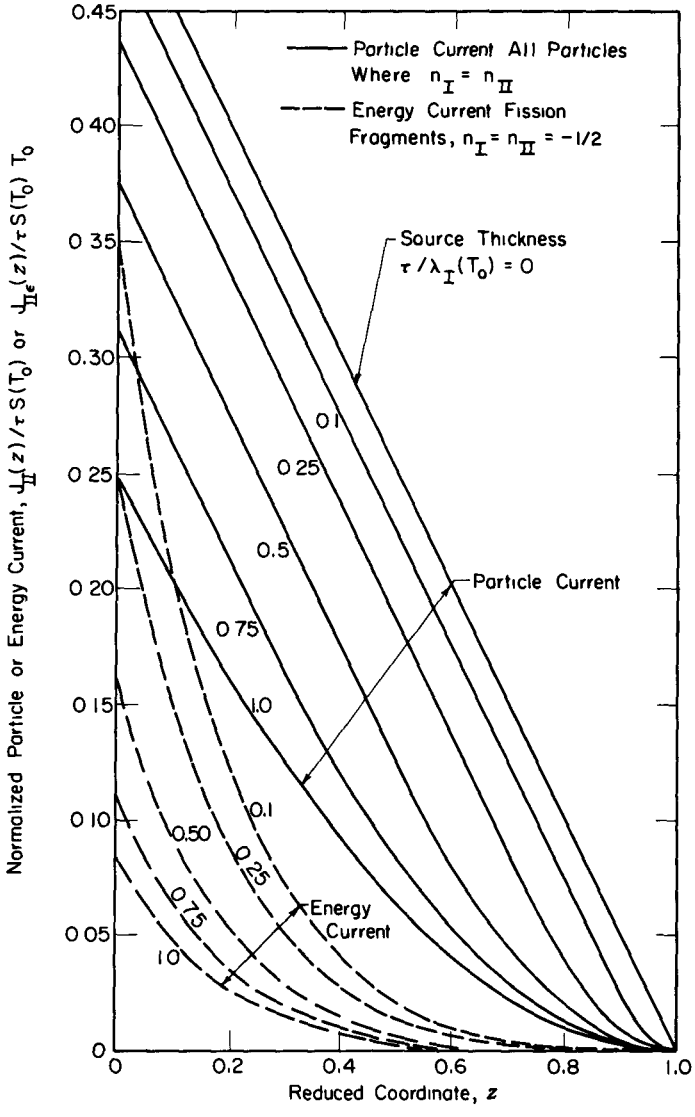

Fig. 4.17 — Spatial distribution of the energy and particle currents for various source thicknesses.

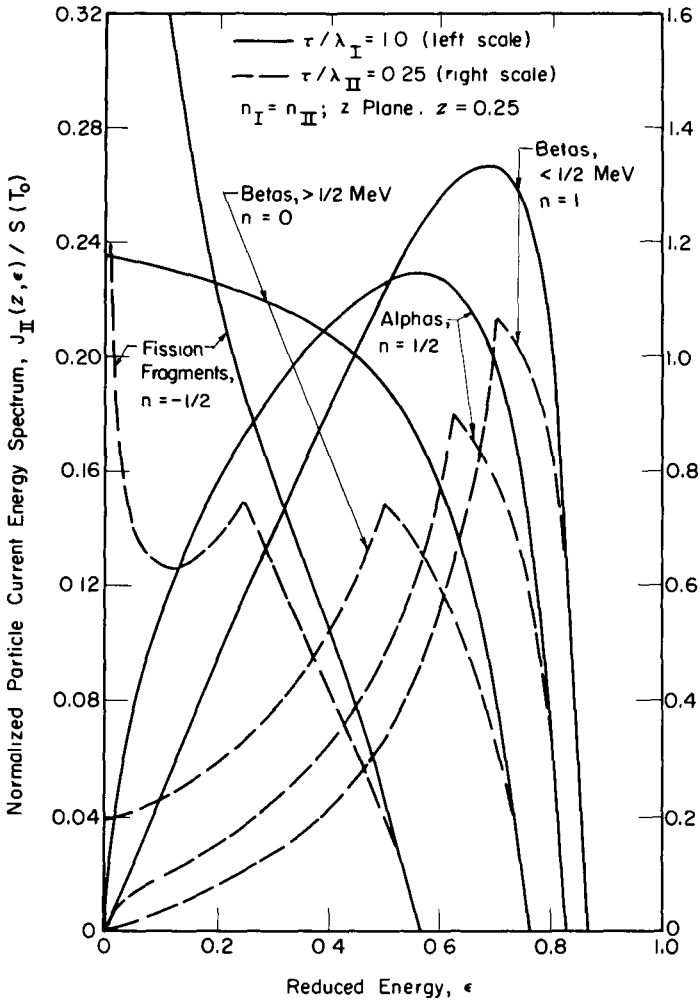

Fig. 4.18 — Particle current energy spectra at $z = 0.25$ for two fuel-layer thicknesses.

be compared to the earlier results shown in Fig. 4.3 for a bare fuel layer. The sharp break at the peak of the spectra for thin plates arises, because, as illustrated earlier in Fig. 4.18, a zone is created that does not contribute to the current. This peak and the associated concave shape at lower energies are smoothed out in passing to the thick plate ($\tau/\lambda_I = 1.0$). In contrast to the bare fuel results, the intercepts on the ϵ-axis are all less than 1.0, and this presents the energy lost by a particle traveling straight through ($\mu = 1.0$) the coating.

In addition to Direct-Collection Cell calculations, the two-region problem is of prime importance in Interaction-Energy Cells. Then, the ionization–excitation rate in a gas or fluid adjacent to a fuel region is of interest, so, if a bare fuel is assumed, Region II can be envisioned as the gas or fluid. As discussed in Sec. 4-1.3, since there is no source in Region II, the energy deposition rate per unit volume due to particles of energy ϵ (a generalization of the earlier energy independent result) is

$$L_\epsilon(z,\epsilon) = -\nabla \cdot \vec{J}_{II\epsilon}(z,\epsilon). \tag{4.112}$$

The energy current $J_{II\epsilon}$ required can be found by an integration involving J_{II} from Eq. (4.104)

$$J_{II\epsilon}(z,\epsilon) = \int_{\mu_{min}}^{\mu_{max}} [J_{II}(z,\mu,\epsilon)]\, \epsilon \, d\mu \tag{4.113}$$

where appropriate limits are to be taken from Table 4.2. If an energy dependent G value is known such that $G(\epsilon)$ represents the number of particular reaction products (e.g., ion pairs or excited states, etc.) formed per 100 eV of energy deposited by a primary particle of energy ϵ, the local product formation rate $R(z)$ is

$$R(z) = -\int_{\epsilon_{min}}^{\epsilon_{max}} \left[\frac{G(\epsilon)}{100} \frac{\partial}{\partial z} J_{II\epsilon}(z,\epsilon)\right] d\epsilon. \tag{4.114}$$

Now the limits are determined by either Table 4.2 or other energy requirements (like threshold energies) associated with the reaction, whichever is more restrictive. Often $G(\epsilon)$ is roughly constant and an average value is used, in which case Eq. (4.114) reduces to the simple form

$$R(z) \approx \frac{\langle G \rangle}{100} \left[-\frac{d}{dz} J_{II\epsilon}(z)\right]. \tag{4.115}$$

Calculations corresponding to Eq. (4.115) have been reported by Leffert et al.,[20] who were interested in space charge neutralization by fission fragment irradiation of noble gases in thermionic diodes. Also, Nguyen and Grossman[13] have published studies concerned with fission fragment ionization in a MHD channel. However, the techniques used in these studies were limited to the case of a constant G-value and fission fragments. Miley and Thiess[19], following the method outlined here, have reported results for various particles including protons, alpha particles, fission fragments, and electrons. They also considered the problem of excitation of helium by alpha particles, in which case the reaction rate exhibits a threshold energy and fairly strong energy dependence so that the generalized form of $R(z)$ given in Eq. (4.114)

was required. These calculations generally involved numerical evaluation of the integrals; however, analytic solutions are tabulated in Ref. 19 for $J_{II}(z,\epsilon)$ and $J_{II}(z)$ for the special cases where $n = n_I = n_{II}$ with $n = -\frac{1}{2}$, 0, $\frac{1}{2}$, or 1.

4-5 SLOWING IN THE PRESENCE OF AN ELECTRIC FIELD

The discussion to this point has assumed that charged particles slow in the solid medium purely by ionization–excitation energy losses. This is valid for passage through the fuel layer in a coated plate cell where the electrical conductivity of the fuel eliminates electric fields from inside the layer. Once the particle breaks the surface, it enters an electric field in the inter-electrode space, but then no ionization–excitation losses occur because this region is maintained under a vacuum.

A more complicated situation occurs where the two effects—ionization–excitation and electric fields—are present simultaneously. A most important illustration occurs in the DVE cell (Sec. 2-6.2), where charged particles originate in an electric field region in a dielectric. To demonstrate the analysis required, we will consider a specific DVE cell, the Gamma-Electric Cell, in which Compton electrons are assumed to contribute the dominant current.

The basic problem is that, as a particle moves through its trajectory, the orientation of the decelerating force due to ionization–excitation collisions continuously changes relative to the electric field force. However, if the energy loss model of Chap. 3 is adopted, it is possible to represent the electronic collisions as an effective force, which can be resolved into appropriate components so that an analytic solution is possible. To do this, Eq. (3.28) is first written in terms of speed v, giving

$$\left(\frac{v}{v_0}\right)^2 = \left[1 - \frac{r}{\lambda(T_0)}\right]^{1/(n+1)} \tag{4.116}$$

and this is differentiated to obtain the acceleration a. Using the identity that v equals dr/dt, we obtain

$$a \equiv \frac{dv}{dt} = -\frac{v_0^2}{2(n+1)\,\lambda(T_0)} \left(\frac{v}{v_0}\right)^{-2n} \tag{4.117}$$

which, based on Newton's law, defines a force $\vec{F}$ such that

$$|\vec{F}| = \frac{T_0}{(n+1)\,\lambda(T_0)} \left(\frac{T}{T_0}\right)^{-n} . \tag{4.118}$$

The magnitude of $\vec{F}$ represents an equivalent force that would produce an average deceleration equal to that caused by ionization–excitation losses. Its direction is taken to be exactly opposed to the velocity vector.

Now, consider as an example the planar geometry of Fig. 4.19. The collector potential gives rise to a retarding electric field E, which, for

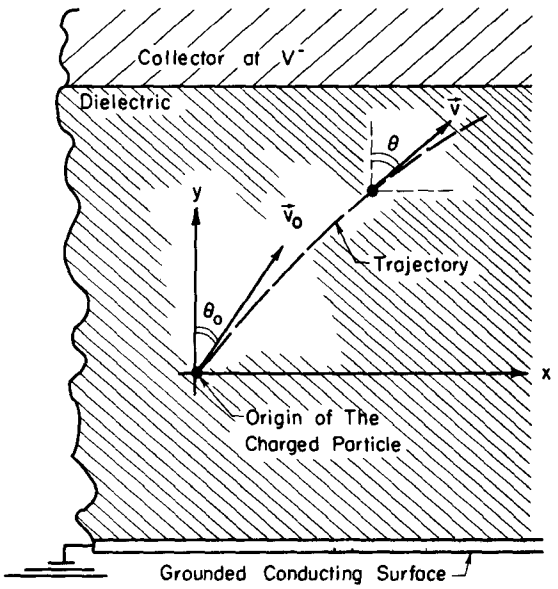

Fig. 4.19 — Emission from a dielectric volume in planar geometry.

simplicity, is assumed to be position independent. (This, in fact, corresponds to the linear potential of Fig. 2.25, which, as discussed earlier, is not a bad assumption for a Gamma-Electric Cell.) In this situation, the y-component of acceleration is due to a superposition of the electric field force with $\vec{F}$ from Eq. (4.118) and is given by

$$a_y \equiv \frac{d^2y}{dt^2} = -\left[\frac{eE}{m_e} + \frac{T_0/m_e}{(n+1)\,\lambda(T_0)}\left(\frac{T}{T_0}\right)^{-n}\cos\theta\right]. \tag{4.119}$$

The solution of this equation turns out to be a classic problem in particle dynamics related to the case where a projectile (e.g., a bullet from a rifle) is shot into the air so that its velocity is affected by both gravity (corresponds to E) and a drag force proportional to the velocity raised to an arbitrary power.[21]

The method of solution required depends on the value of n, which in the present case depends on the charged particle involved. Relative

to the algebra involved, by far the simplest situation is for $n = -1/2$, and this will be used here to illustrate the calculation. Actually, this corresponds to fission fragments, whereas electrons, which are of primary interest here, fall in the range $n = 0$ to 1.0 depending upon their energy (Table 3.4). Still, in addition to demonstrating the problem in a simple fashion, the present calculation is of interest since it, in effect, overestimates the energy loss that would be expected for electrons and, in this fashion, it represents a limiting case. (This assumes the other parameters like m_e and $\lambda(T_0)$ used in the calculation are evaluated for electrons.)

With $n = -1/2$, Eq. (4.119) becomes

$$-\frac{d^2y}{dt^2} = g - K\frac{dy}{dt} \tag{4.120}$$

where

$$g = \frac{eE}{m_e} \tag{4.121a}$$

$$K = \frac{2T_0}{m_e v_0 \lambda(T_0)} \tag{4.121b}$$

and the solution is immediately found to be

$$Ky = -gt + (v_0 \cos \theta_0 + g/K)(1 - e^{-Kt}). \tag{4.122}$$

A corresponding analysis of the x-component of acceleration gives

$$Kx = v_0 \sin \theta_0 (1 - e^{-Kt}) \tag{4.123}$$

so that the trajectory is completely defined. However, because we are mainly interested in those particles that are able to reach the collector, only the y-component of acceleration is required here. A critical condition in the trajectory is the "fall-back" point, which is defined by

$$v_y \equiv \frac{dy}{dt} = 0. \tag{4.124}$$

We define y^* and t^* as the vertical distance and the time, respectively, that a particle travels before "falling back." To find these quantities, Eq. (4.124) is solved with the use of Eq. (4.122), giving

$$t^* = \frac{1}{K} \ln \psi \tag{4.125a}$$

$$y^* = -\frac{g}{K^2} \ln \psi + \frac{L}{K} (\psi - 1) \tag{4.125b}$$

where

$$\psi \equiv 1 + \frac{v_0 \cos \theta_0}{L} \tag{4.126a}$$

$$L \equiv g/K . \tag{4.126b}$$

Equation (4.125b) is a key relation since it defines the maximum distance a particle with an initial velocity v_0 and direction cos θ_0 can be from the collector and still be able to reach the collector.

Further insight can be gained at this point by digressing a moment to consider the special case of zero field. Then, g = 0, and the equations of motion corresponding to (4.122) and (4.123) are

$$Ky = v_0 \cos \theta_0 (1 - e^{-Kt}) \tag{4.127a}$$

$$Kx = v_0 \sin \theta_0 (1 - e^{-Kt}) \tag{4.127b}$$

which, as expected, represent straight-line motion. Further, it is seen that the equation corresponding to Eq. (4.125b) is

$$y^* = \lambda(T_0) \cos \theta_0 . \tag{4.128}$$

The maximum distance *any* particle could be from the collector and still reach it occurs when cos θ_0 = 1; so the maximum value of y* is

$$y^*_{max} = \lambda(T_0) \qquad (E = 0) \tag{4.129}$$

and the maximum value of the initial angle θ_0 for a given value of y* is

$$[\theta_0]_{max} = \cos^{-1} \frac{y^*}{\lambda(T_0)} \qquad (E = 0). \tag{4.130}$$

These limits can now be used to evaluate the short-circuit-current density $J_q(0;T_0)$. It is most convenient to use the plane-kernel method developed in Appendix D, in which case the current is given by

$$J_q(0;T_0) = q_0 \int_{y^*=0}^{\lambda(T_0)} dy^* \int_{\mu_0=y^*/\lambda}^{1} d\mu_0 \, S(y^*, \mu_0, T_0) \tag{4.131}$$

where $S(y^*, \mu_0, T_0)$ is the source strength at y* per unit volume emitting particles with initial direction cosine μ_0 per unit cosine and energy T_0 per unit energy. [The notation $J(0;T_0)$ indicates a zero field and a

source of particles with initial energy T_0.] The charge q_0 associated with the particles is taken as a constant since electrons are of prime interest.

Equation (4.131) specifies the short-circuit charge current; however, the integral is quite involved if S represents Compton electron production. We will defer this problem until the general case of $E \neq 0$ is considered, but now we can verify the accuracy of Eq. (4.131) by assuming a simple, although unrealistic, isotropic source. If a uniform spatial distribution is also assumed, S becomes

$$S(y^*, \mu_0, T_0) \rightarrow \frac{S(T_0)}{2} \tag{4.132}$$

and carrying out the integrations in Eq. (4.131), we obtain

$$J_q(0;T_0) = q_0 \frac{S(T_0)\ \lambda(T_0)}{4} . \tag{4.133}$$

Since there is no field present, this is entirely analogous to the thick plate situation described by Eqs. (4.5) and (4.9), and the results agree, as they should. (The factor q_0 obtained here converts from a particle to a charge current.)

We now return to the original problem and extend the preceding analysis to the general case of a finite field E. Then, Eq. (4.125b) relates y^* and θ_0; so

$$y^*_{max} \equiv [y^*]_{\mu_0=1} = -\frac{g}{K^2} \ln\left(1 + \frac{Kv_0}{g}\right) + \frac{v_0}{K} . \tag{4.134}$$

The current $J_q(E;T_0)$ corresponding to the field E, is found by modifying the limits of Eq. (4.131) to obtain

$$J_q(E;T_0) = q_0 \int_{y^*=0}^{y^*_{max}} dy^* \int_{[\mu_0(y^*)]_{min}}^{1} d\mu_0\, S(y^*, \mu_0, T_0) \tag{4.135}$$

where y^*_{max} comes from Eq. (4.134) and $[\mu_0(y^*)]_{min}$ is found by solving Eq. (4.125b) for μ_0 as a function of y^*.

This result puts us in a position to carry out a practical calculation for the Gamma-Electric Cell, where the source term, corresponding to the production rate of Compton electrons, becomes

$$S(y^*, \mu_0, T_0) = N_e N_\gamma \frac{d\sigma}{d\mu_0}\ \delta[T(\mu_0) - T_0]. \tag{4.136}$$

Here N_e is the electron density in the dielectric, N_γ is the incident gamma flux intensity (neglecting attenuation), and $d\sigma/d\mu_0$ is the dif-

ferential Klein–Nishina cross section defined in detail later in Table 5.6, Chap. 5. The delta function appears because, in Compton scattering, the electron energy is uniquely related to the scattering angle (Table 5.6).

If this form is used for the source term in Eq. (4.135) and this equation is then integrated over T_0, we find

$$J_q(E) = \int J_q(E;T_0)\, dT_0 = N_e N_\gamma q_0 \int_{y^*=0}^{y^*_{max}(E)} dy^* \int_{[\mu_0(y^*)]_{min}}^{1} d\mu_0 \left(\frac{d\sigma}{d\mu_0}\right). \quad (4.137)$$

Note that $y^*_{max}(E)$ depends on both E and λ through Eq. (4.134). (The evaluation of λ in this limit requires special attention. As noted earlier, T_0 and μ_0 are uniquely related in Compton scattering, so that $\lambda(T_0)$ can be replaced by $\lambda(\mu_0)$. Then, since by definition y^*_{max} involves $\mu_0 = 1$, $[\lambda(\mu_0)]_{\mu_0=1}$ is used in Eq. (4.134) to evaluate y^*_{max}.)

Because of the complicated nature of $d\sigma/d\mu_0$, the integrations must be carried out numerically. Results assuming a polystyrene dielectric are shown in Fig. 4.20 where $J_q(E)$ is plotted as a function of E for

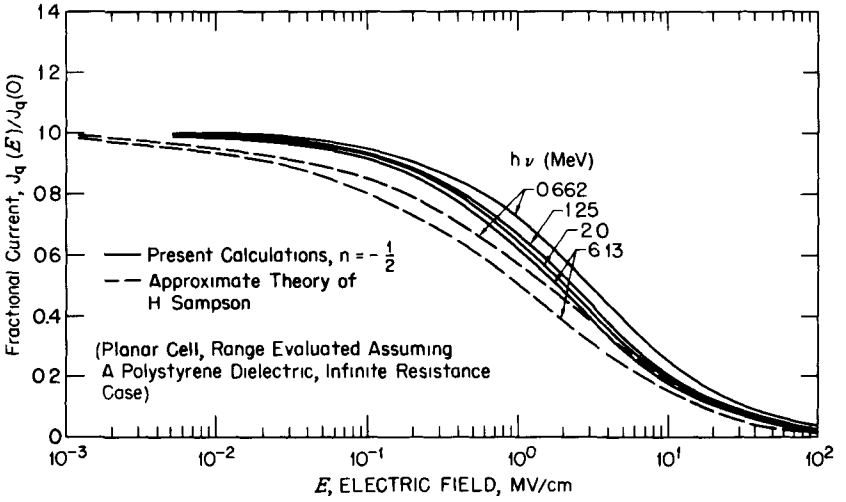

Fig. 4.20 — Forward Compton current reaching the collector vs the electric field.

several incident gamma-ray energies. For comparison, results from similar calculations reported by Sampson[22] are also included. He employed an approximate model where a straight-line energy loss calculation was superimposed on the curved trajectories calculated for the no-loss case. Thus, the differences between his results and the present calculations are not surprising; however, the general agreement in the shape of the curves lends confidence to the present method.

It is also interesting to compare these curves to the earlier plot for an ideal DVE cell (Fig. 2.29). Again, the general shapes are in good agreement; however, the ideal-cell results were presented as a function of the field U and its cut-off value U_M defined in Eqs. (2.70) and (2.72), respectively. It is seen from these definitions that

$$E = \left\langle \frac{eT_0}{\lambda_e} \right\rangle \frac{U}{U_M} \approx \frac{1}{2} \frac{U}{U_M} \qquad \text{(MV/cm)} \tag{4.138}$$

where the factor of $\frac{1}{2}$ is an estimated value assuming polystyrene. From this scale relationship, it is evident that the present curves do not decrease quite so rapidly with an increasing field as does the average cosine model. This is probably because Compton emission favors forward directions more strongly than indicated in the cosine model, and any error is aggravated because the forward scattered electrons are favored with larger energies. Still, the agreement is amazingly good considering the many assumptions inherent in the ideal DVE cell calculations.

Several other features of Fig. 4.20 should be noted. First, since gamma-ray attenuation has been neglected, the dielectric thickness corresponding to Fig. 4.20 is arbitrary; hence, for a fixed field E, the overall voltage can be made arbitrarily large by selecting a thick cell. This means that, as in the ideal case, the cell voltage can exceed the voltage equivalent of the Compton electron kinetic energy. As explained in connection with the ideal cell, this is possible because electrons are born throughout the dielectric so they face, on the average, a potential barrier that is less than the total potential difference between the electrodes. Also, leakage currents (e.g., ohmic leakage) that might prevent such high voltages have been neglected.

Another somewhat surprising feature of Fig. 4.20 is that the curves for lower gamma-ray energies fall above those for higher energies. As the gamma-ray energy is reduced, so are the initial energies of the Compton electrons, and this would be expected to reduce the number reaching the collector. However, it must be remembered that the curves in Fig. 4.20 are normalized to the short-circuit values $J_q(0)$, so variations with voltage and not absolute current are of interest. At zero voltage, particles reaching the collector originate from a volume defined by the range $\lambda(T_0)$, but as a voltage is applied, energy balance requirements gradually diminish this volume. Since $\lambda(T_0)$ decreases with decreasing gamma-ray energy, the collection volume for low-energy gamma rays lies closer to the collector electrode at zero voltage and remains so even as a voltage is applied. Thus, electrons born in this volume face, on the average, a smaller potential barrier (for a fixed gradient), and, as a result, a larger fraction is collected.

Another way of looking at this is to note that, as pointed out in the ideal-cell analysis, the break in the current–voltage curves occurs at about $U/U_M = 1$, or according to Eq. (4.138), at $E = \langle eT_0/\lambda \rangle$. However, λ is proportional to T_0^2 for electrons below ½ MeV [Eq. (3.60a)], so the break point in E will vary as T_0^{-1}. Thus, the break point increases with decreasing gamma-ray energy, and a curve with the break point at a higher E-value will automatically fall above one with a lower break point if, as in Fig. 4.20, all curves are normalized to the short-circuit current.

Returning to the analysis, we should note that solutions can be found in a similar fashion for other values of n. In some cases, the equations for y* and t* can be taken from analogous problems discussed in Ref. 21 and other literature dealing with classical particle dynamics; however, in general, a numerical analysis is required.

4-6 SUMMARY

This chapter was devoted to the development of techniques for charged-particle transport calculations of interest in cell designs. The generalized slowing model of Chap. 3 was used so that the methods are essentially independent of the specific type of particle involved.

The methods were illustrated using the special case of planar geometry, and, except for Sec. 4-5, isotropic emission was assumed. In theory, the extension to other geometries, emission distributions, etc., can be accomplished by a combination of the methods developed here and those of Chap. 2. It is clear, however, that such calculations may be quite tedious from an algebraic point of view.

The problem of escape and collection of particles emitted from a fuel layer in the absence of a voltage has received more attention in the literature than the voltage case, which is of ultimate interest here. Zero-voltage current spectra have been shown to compare favorably with experimental data for fission fragments (Figs. 4.4 and D.7), lending confidence to the theory. Unfortunately, reliable data are not available to check the voltage calculations.

Some of the more useful specific results obtained include:

- *Figures 4.5 and 4.6:* average charge and energy of particles leaving fuel layers of various thicknesses.
- *Figures 4.11 and 4.12:* current and efficiency vs voltage for a planar plate cell with isotropic emission.
- *Figure 4.17:* spatial distribution of currents in a fluid being irradiated by particles from a neighboring fuel layer of various thicknesses.
- *Figure 4.20:* Compton current collected vs electric field for a DVE cell.

• *Figures D 4 and D 6*· escape probabilities and average energy losses for slab, spherical, and cylindrical solids.

Figures 4.12 and 4.14 serve as reminders that the energy loss during transport through the fuel can seriously cut into efficiencies. (In this connection, it must be remembered that, as noted in Chap. 2, planar geometry is poor for use with isotropic emission—thus, the absolute efficiencies shown here are low.) There is a strong motivation to use very thin fuel-layer coatings; however, some compromise is obviously necessary to achieve a reasonable power level and/or power density.

As pointed out in Chap. 2, the DVE cell gets around the fuel-layer thickness problem, and the detailed calculations of Sec. 4-5 for a Gamma-Electric Cell confirm these earlier conclusions. However, as presently conceived, the overall cell efficiency is limited by poor energy coupling with the gamma beam and, as will be discussed in Chap. 6, by radiation effects on the dielectric.

Multiregion calculations were introduced in Sec. 4-4. While such problems may be important in some cell designs, their main significance probably lies with problems where escaping particles ionize and excite a surrounding fluid or gas.

REFERENCES

1. D Kamke, *The Energy Spectrum of Fission Particles Leaving a Fuel Sheet*, Tech. Release 34-249, Jet Propulsion Lab., January 1961.
2. E. E Lewis, "A Generalization of the Dirac Chord Method to Include Charged-Particle Phenomena," *Nucl Sci Eng., 25* 359 (1966).
3. E. E. Lewis and R. Pfeffer, "The Influence of Source Geometry on Fission Fragment Escape Probabilities," *Nucl Sci. Eng., 27* 581 (1967).
4. G. H. Miley, "Fission Fragment Transport Effects as Related to Fission-Electric-Cell Efficiencies," *Nucl. Sci. Eng., 24* 322 (1966).
5. S. Kahn, R. Harman, and V. Forgue, "Energy Distribution of Fission Fragments from Uranium Dioxide Films," *Nucl Sci. Eng., 23* 8 (1965).
6. R. F. Redmond, R. W. Klingensmith, and J N. Anno, "Energy Spectrum of Fission Fragments Emitted from Thin Layers of Uranium Dioxide," *J. Appl. Phys , 33* 3383 (1962).
7. G. Safonov, Direct Conversion of Fission to Electric Energy in Low Temperature Reactors, Rand Report RM-1870, Rand Research Corporation, January 1957
8. C. J. Heindl, Efficiency of Fission Electric Cells, Tech. Report 32-105, Jet Propulsion Lab., May 1961
9. A. Schock, A Direct Nuclear Electrogenerator—Analysis of Cylindrical Electrode Configuration, AFOSR-TN-59 590, 1959.
10. A. M Plummer, W. J. Gallagher, R. G. Matthews, and J. N. Anno, The Alpha-Cell Direct-Conversion Generator, NASA-CR-54256, Battelle Memorial Institute, Columbus, Ohio, November 1964.
11. A. J. Cohen, A Numerical Analysis of Direct Nuclear Electrogenerator Cells that Use Cerium-144 Beta-Emitting Radioisotope Sources, Report NASA-TN-D-2070, NASA Lewis Research Center, November 1963.

12 G. H. Miley and H. T. Sampson, "Gamma-Electric Cell Theory and Experiment," *Proc. Intern Conf on Energetics, University of Rochester, 1965*, published by the Am. Soc. Mech. Eng , New York, N. Y., pp. 238-251, 1965.
13. D. H. Nguyen and L. M. Grossman, "Ionization by Fission Fragments Escaping from a Source Medium," *Nucl. Sci. Eng., 30* 233 (1967).
14. H. Faraggi and A. Garin-Bonnet, *Experimental Measurement of Fission Fragment Paths in Uranium, Gold, Molybdenum, Zirconium, and Silicon*, CEA-966, 1958.
15. R. V. Meghreblian and D. K. Holmes, *Reactor Analysis*, McGraw-Hill Book Company, New York, 1960.
16. M. Abramowitz and I. A. Stegun (Eds.), *Handbook of Mathematical Functions*, Nat. Bureau of Standards, Appl. Math Series 55, 1964.
17. P.A.M. Dirac, Approximate Rate of Neutron Multiplication of a Solid of Arbitrary Shape and Uniform Density, British Report MS-D-5, Part I, 1943 (declassified).
18. K. M. Case, F. deHoffmann, and G. Placzek, *Introduction to the Theory of Neutron Diffusion*, Vol. I, Los Alamos Scientific Laboratory, Los Alamos, June 1953.
19. G. H. Miley and P. E. Thiess, "A Unified Approach to Two-Region Ionization-Excitation Density Calculations," *Nucl. Appl., 6* 434 (1969).
20. C. B. Leffert, D. B. Rees, and F. E. Jamerson, "Noble Gas Plasma Produced by Fission Fragments," *J. Appl Phys., 37*, 1 133 (1966).
21. E. J. Routh, *A Treatise on Dynamics of a Particle*, Chap. 3 (A reproduction of a work published by Cambridge University in 1898), Dover Publications, Inc., New York, 1960
22. H. T. Sampson, "A Theoretical and Experimental Analysis of the Gamma-Electric Cell," Ph. D. Thesis, Nuclear Engineering Program, Univ. of Illinois, 1967.

5

Secondary-Electron Emission

5-1 INTRODUCTION

Secondary electrons are liberated whenever ionizing radiation bombards a solid surface, and the number produced may be considerably larger than the number of primary particles hitting the surface; e.g., 300 to 600 electrons/fragment are emitted in bombardment of a thin UO_2 layer by fission fragments, and a yield of $\approx$10 electrons/ion is obtained for alpha particle bombardment of gold foil. Thus, the net charge leaving the surface with the secondary electrons can well be larger than the net charge entering via primaries, in which case secondary electron emission can dominate the current in a Direct-Collection Cell. Some radiation detection devices like the Semirad detector (discussed in Chap. 7) actually operate on this principle. However, the energy associated with the secondary electrons is generally only a fraction of that associated with the primary particles; therefore, for efficient power conversion, secondary emission must be suppressed in cells using positive particles (e.g., Fission- and Alpha-Electric Cells), otherwise the collector potential may actually be negative and small rather than positive (and large) as desired.

In the present chapter, we will develop a basic description of the production of secondary electrons while their effect on cell operation and possible suppression methods are considered in Chap. 6. Secondary emission is discussed in a number of general references[1–7], but the treatment is largely restricted to bombardment by electrons and select low-q ions in the low- and medium-energy region (<10 keV). Cell applications, however, are often concerned with highly charged ions such as alpha particles and fission fragments with energies extending into the MeV region, and unfortunately very little information is available for such cases[8,9].

In the following sections, we first consider the "low-energy" component or secondaries with energies below 50 eV. This is generally the dominant component relative to numbers of electrons involved.

Next, the "high-energy" component (secondaries with energies >50 eV) is discussed. This component is of particular interest because a high-voltage, low-power cell (e.g., the plate-type Gamma-Electric Cell

discussed in Chap. 7) can be constructed using it as the charging current.

Finally, electron backscattering, due to its intimate relation to secondary emission, is discussed in some detail.

The main intent of the analysis presented here is to provide a conceptual understanding, and simplified models are used where possible. The reader should be warned, however, that even more elaborate theories leave much to be desired; e.g., Kaminsky and others have stressed that "none of the professed theories of the kinetic-emission mechanism have been generally successful" (Ref. 5, p. 332), and Dekker explains: "The main reason for this state of affairs is the complexity of the problem, which becomes evident when one considers qualitatively what happens in the secondary emission process" (Ref. 1, p. 252). It might be added that these remarks are generally directed toward the treatment of the low-energy component. The high-energy component simply has not received sufficient study to allow a definitive evaluation.

5-2 CLASSIFICATION

5-2.1 Kinetic and Potential Emission

Electron emission requires that sufficient energy be transferred to an electron in a solid to raise it into the kinetic energy continuum above the surface barrier, and this energy must come from the bombarding particle. In the case of bombardment by heavy ions, the energy transferred can originate with either the kinetic energy or with the internal potential energy (ionized or excited states) of the ion—the processes being called *kinetic* emission (or ejection) and *potential* emission, respectively[5,6]. Because of the high energies of the ions involved in nuclear cells, kinetic emission generally dominates, and we will immediately confine our discussion to it. This is implied in the following sections, although the process is simply referred to as secondary emission. In fact, for the special case of beta or electron bombardment, kinetic emission is the only mechanism possible since, ignoring relativistic effects, internal energy storage is not permitted.

Secondary emissions due to gamma-ray interactions are also important in many cells; however, it is conventional to refer to the electrons produced in this manner as photoelectric or Compton currents although both correspond to kinetic emission as defined above.

5-2.2 Energy Components of the Secondaries

Secondary electrons are traditionally divided into two energy groups where 50 eV is defined as the dividing energy between the low-energy (or soft) component and the high-energy component (e.g., see Ref. 1,

p. 253, and Ref. 9, p. 36). This division is quite arbitrary; it arises because, as illustrated by Rudberg's measurements[10] in Fig. 5.1, the bulk of the secondaries created by low- or medium-energy bombardment fall into a Maxwellian-like distribution that lies well below 50 eV.

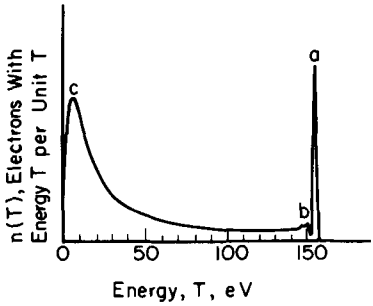

Fig. 5.1 — Energy distribution of secondary electrons emitted during the bombardment of Ag by 155-eV electrons. (After Dekker, Ref. 1; based on data by Rudberg, Ref. 10. The peak at "c" is associated with the soft secondary component while "a" and "b" correspond to elastic and inelastic reflection of the primary electrons, respectively.)

The low-energy component is generally thought to represent electrons initially liberated in the track of the primary, which then slow in the solid, diffuse to the surface, and finally escape. These electrons have received the most attention in studies to date, and, in fact, the high-energy component is often neglected in computations of the secondary yield. This is implied although not often stated in much of the literature. It is a valid concept for bombardment energies up to the keV range; however, the higher energy component becomes quite significant for high-energy bombardment. This point is illustrated in Figs. 5.2(a) and (b), which show data by Miller and Porter[11] and by Trump and Van de Graaff[12], respectively, for electron bombardment. Similar behavior has been observed by Kronenberg et al.[13] in proton bombardment experiments, and a typical result is shown in Fig. 5.3, where a detailed energy spectrum of the high-energy component is given for various angles of incident (relative to the surface normal) for the proton beam. Note that the number of electrons decreases quite rapidly with energy. The contribution due to these electrons (between 100 eV and 2 keV) was about 25% of the total secondary yield. The increase in yield for smaller angles of incidence is expected since secondaries are more likely to escape if the primary follows a path almost parallel to the surface.

The available data seem to confirm that the high-energy secondary component is mainly due to coulomb scattering; e.g., the 2-keV end point of the data in Fig. 5.3 corresponds closely to the maximum energy

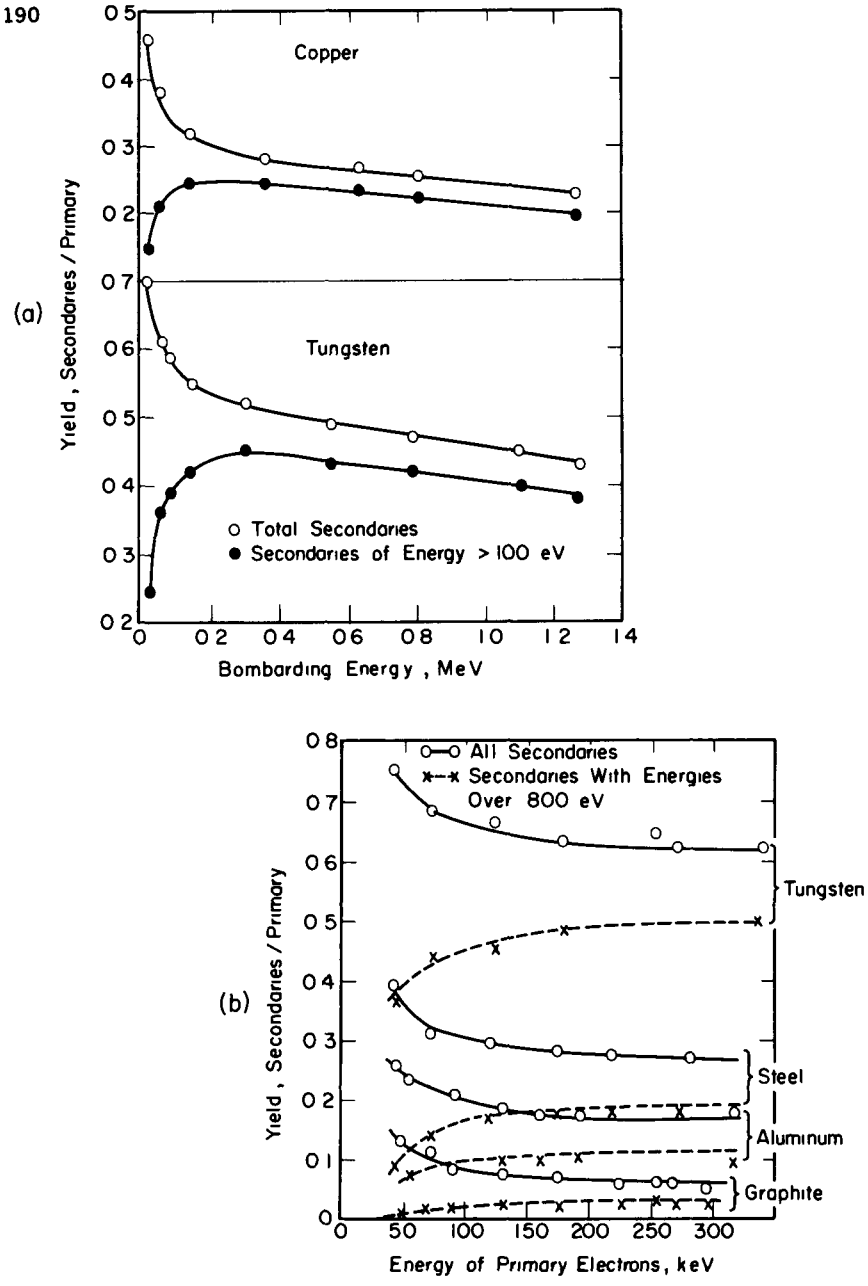

Fig. 5.2—Effect of bombardment energy on the high-energy secondary component. (a) Secondary yield vs bombardment energy for electrons incident on copper and tungsten. (From Kronenberg, Ref. 9, based on data by Miller and Porter, Ref. 11.) (b) Yield data for secondaries above 800 eV due to electron bombardment. (From Kronenberg, Ref. 9, based on data by Trump and Van de Graaff, Ref. 12.)

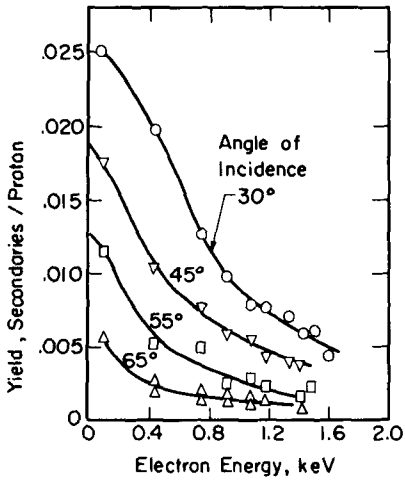

Fig. 5.3 — High-energy secondary electron yield for 0.96-MeV proton bombardment of aluminum. (From Kronenberg et al., Ref. 13.)

a 1-MeV proton can deliver to an electron through coulomb scattering. This is not surprising, since ion slowing can be envisioned as involving two "types" of collision processes[14]. In one, referred to as a "distant collision," the field associated with the ion weakly interacts with the atoms so that only small amounts of energy are transferred in each collision, creating low-energy secondaries. The second process is, in effect, a free collision between the ion and an atomic electron where large amounts of energy can be transferred, and the resulting "knock-on" electrons, often called δ-rays, may have energies extending into the keV region. These δ-rays in turn create additional secondaries as they slow. The δ-rays themselves ultimately stop in the solid or escape across the surface, in which case, depending on their residual energy, they may add to either the high- or the low-energy component.

According to Bohr[15], the total energy loss of high-energy ions is roughly divided equally between these two collision processes; thus, a significant fraction of the energy will be carried off by the high-energy component. However, because each carries such high energy, there will be generally far fewer δ-rays than "soft" secondaries.

5-3 MODELS FOR THE LOW-ENERGY COMPONENT DUE TO HIGH-ENERGY BOMBARDMENT

The bombarding particles in radiation cells may have a spread in energies ranging from the MeV region down to quite low energies. We will first consider methods for predicting yields due to bombardment

by the high-energy particles, and their use will be illustrated through some typical calculations in following sections. Then, it is shown in Sec. 5-5 how the analysis can be modified to apply to low-energy bombardment.

5-3.1 The Thermionic Model

A number of theories have been advanced to explain low-energy secondary emission, but two of the best known are the "Thermionic" and the "Ionization–Diffusion" theories. In the Thermionic model, first suggested by Kapitza[16], secondary electrons are assumed to originate from a microscopic zone of elevated temperature around the track of the bombarding particle. The temperature is calculated from the energy lost by the incoming particle, and the emission is then found from the Richardson equation for thermionic emission. The resulting expression for the secondary yield due to a normally incident ion is[8]

$$\Delta = \frac{1.23A_R\ (dT/dx)^2}{8\pi K C_v \rho e} \tag{5.1}$$

where (dT/dx) is the energy loss per unit path for the incident particle; K, the thermal conductivity; C_v, the specific heat; and ρ, the density of the target material. The Richardson constant A_R is $\approx$120 A/(cm^2 deg^2) neglecting reflection, and the yield Δ is defined as the total number of low-energy secondaries emitted per incident particle. Yields calculated from Eq. (5.1) are in reasonable agreement with experiment; however, there are indications that the factor (dT/dx) should appear as the first power instead of being squared. This is commonly attributed to some fundamental difficulties inherent in the derivation (Ref. 5, p. 332; Ref. 8, p. 6). The concepts of the thermal constants K and C_v have meaning only in the sense of a statistical mean, and their use here is questionable in light of the non-equilibrium energy distribution of electrons and ions created in the track of the bombarding particle. For this same reason, the use of the Richardson equation, which assumes an equilibrium distribution of electron velocities, is also questionable. Anno[8] has suggested that a correlation of the thermal constants K and C_v with (dT/dx) might improve the accuracy of the model, but this has not been done to date, and, because of these difficulties, we will not pursue this model further here.

5-3.2 The Ionization–Diffusion Model

The "Ionization–Diffusion" model has been studied in various forms by a number of investigators. A general review of this model is presented in several references (Ref. 1, p. 263; Ref. 5, p. 333), and the

present treatment is largely based on the well-known study by Sternglass[17] combined with the slowing model developed in Chap. 3. The resulting model turns out to be fairly similar to the "semiempirical" theory discussed by Dekker (Ref. 1, pp. 264-272).

As the name implies, the Ionization–Diffusion model assumes a two-step process: In the first, high-energy "secondary electrons" are produced along the track of the primary particle as it slows and produces ionization in the solid. Next, as is illustrated in Fig. 5.4, these electrons undergo a diffusion process, and a certain fraction produced near the surface escape giving rise to the secondary emission current. Additional secondary electrons produced by the energetic δ-rays can also contribute to the emission current.

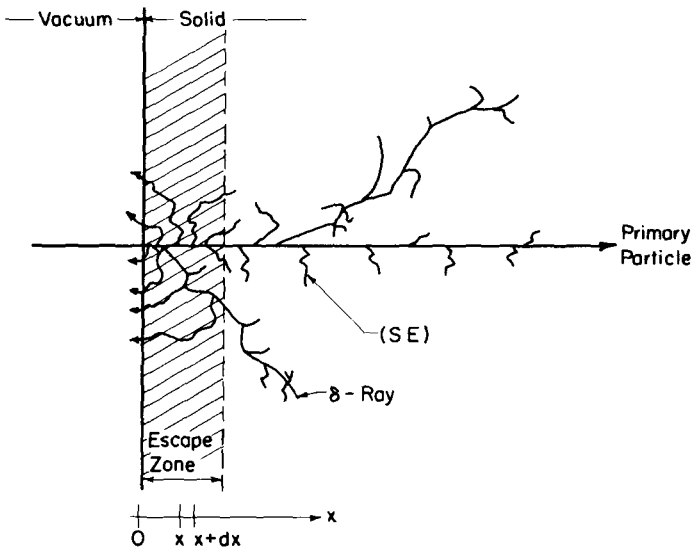

Fig. 5.4 — Formation of secondary electrons (SE) and δ-rays by a high-energy charged particle. (The shaded area indicates the escape depth or zone for secondary electrons.)

Before proceeding, it is instructive to consider some of the particle ranges involved. As discussed in Chap. 3, primary particles having energies of order of 1 MeV penetrate to depths of 10^{-3} cm or more. The low-energy secondary component has energies of the order of 10 eV, and in metals this corresponds to an electron range of 10^{-6} to 10^{-7} cm. Finally, the range of the δ-rays will be intermediate between these extremes; e.g., assuming coulomb type scattering, the most energetic (≈4.4 keV) δ-ray from 2-MeV proton bombardment will have a range of about 2×10^{-5} cm in Al.

This suggests the concept of an "escape zone" or volume where secondaries can be born and still escape (Fig. 5.4). The depth of this zone will be of the order of the secondary range, or only 10 to 100 Å below the surface. It follows that the energy of a high-energy primary particle will remain essentially constant over this distance, and to a good approximation, it can be evaluated at the entering energy.

We are now in a position to calculate the secondary yield for normal incidence of high-energy bombarding particles as illustrated in Fig. 5.4. The production of internal secondaries in a thickness dx at x consists two parts: One corresponds to direct formation due to "distant" (soft) collisions of the primary particle, while the second is due to similar collisions involving the δ-rays. If E_{se} is defined as the mean energy required per internal secondary formed, the number of secondaries produced per unit volume at x due to an incident particle of energy T_i is

$$n_s(x,T_1) = \frac{1}{E_{se}}\left[\left\langle\frac{dT_1}{dx}\right\rangle^{(1)} + \int_0^\infty g(x;x',T_1)\left\langle\frac{dT_1(x')}{dx'}\right\rangle^{(2)} dx'\right]. \tag{5.2}$$

The superscripts (1) and (2) indicate energy losses due to distant collisions and δ-ray formation, respectively. The function $g(x;x',T_1)$ represents the fraction of the energy going into δ-ray production at x′ that is deposited and available for secondary production at x per unit volume.

It is convenient to define an auxiliary function $f(x;T_1)$ such that

$$n_s(x;T_1) = \frac{1}{E_{se}}\left[\left\langle\frac{dT_1}{dx}\right\rangle^{(1)} + f(x;T_1)\left\langle\frac{dT_1}{dx}\right\rangle^{(2)}\right] \tag{5.3}$$

so by definition

$$f(x;T_1) = \frac{\int_0^\infty g(x;x',T_i)\,\langle dT_i/dx'\rangle^{(2)}\,dx'}{\langle dT_1/dx\rangle^{(2)}}. \tag{5.4}$$

Thus, $f(x;T_1)$ represents the ratio of the energy deposited per unit volume at x by δ-rays to the energy that goes into δ-ray formation in the volume, and it is termed the "fractional δ-ray energy return." However, it must be remembered that the energy is "returned" to the volume at x for the most part by δ-rays that are both outside of this volume. (An explicit expression for $f(x,T_1)$ is derived in Appendix E, and this is discussed further in following sections.)

Since, as already noted, for high-energy bombardment the primary particle energy is essentially constant across the escape zone and also the energy losses due to distance collisions and δ-ray production are roughly equal, we will assume that

$$\left\langle \frac{dT_1}{dx} \right\rangle^{(1)} \approx \left\langle \frac{dT_1}{dx} \right\rangle^{(2)} \approx \frac{1}{2} \left\langle \frac{dT_1}{dx} \right\rangle_{x=0} \tag{5.5}$$

where $\langle dT_1/dx \rangle_{x=0}$ represents the total energy loss per centimeter for the bombarding particle evaluated at the surface $x = 0$.

Substitution into Eq. (5.3) gives

$$n_s(x;T_1) \approx \frac{1}{2E_{se}} \left\langle \frac{dT}{dx} \right\rangle_{x=0} [1 + f(x;T_1)] \tag{5.6}$$

which is the desired working relation for the internal secondary electron production rate.

Next, it is necessary to consider the diffusion and possible escape of these internal secondaries. Two types of energy-loss mechanisms occur in the diffusion process—namely, elastic and inelastic collisions. Inelastic collisions effectively raise other electrons to various excited levels and correspond to relatively large energy transfers per collision, whereas elastic collisions involve smaller amounts of energy transfer to the thermal vibrational modes of the lattice. In metals in particular, inelastic collisions dominate, and only a few collisions are sufficient to lower the electron's energy below that required to escape across potential barrier at the surface. In fact, Sternglass[17] points out that a typical secondary of 2 to 15 eV suffers on the average 2 to 5 collisions before losing its ability to escape. Thus, the actual process appears to lie somewhere between a straight-line motion and a diffusion process. In both cases, however, the secondary flux will essentially decrease exponentially with distance from an isotropic source. Thus, as originally suggested by Sternglass, we will assume that $P(x)\,dx$, the probability that a particle born in the volume dx at x will escape across the surface, is of the form

$$P(x)\,dx = A_s P_s \exp\left(-\frac{x}{L_s}\right) dx \tag{5.7}$$

where A_s is a source normalization factor, L_s is the characteristic diffusion length for secondaries, and P_s is the surface transmission factor or the probability that an electron reaching the surface can escape across the surface potential barrier.

The secondary yield $\Delta(T_1)$, defined as the number of secondaries escaping per incident particle of energy T_1, can then be written as an integral over the internal production rate times the probability of getting to and escaping across the surface, or

$$\Delta(T_i) = \int_0^\infty n_s(x';T_i)\, P(x')\, dx'$$
$$\approx \frac{P_s A_s}{2E_{se}} \left\langle \frac{dT_i}{dx} \right\rangle_{x=0} \int_0^\infty [1 + f(x';T_i)] \exp\left(-\frac{x'}{L_s}\right) dx'. \qquad (5.8)$$

The upper limit on the integral is extended to infinity although the escape zone and secondary range concepts suggest a finite upper limit. However, the exponential involved becomes so small for distances greater than L_s that the difference is not significant. (This ambiguity arises because we have combined two different concepts—a mean range model and diffusion theory.)

Before Eq. (5.8) can be used, the various parameters must be evaluated. This is discussed in some detail in Appendix E, and suggested values of the parameters are summarized in Table 5.1. Also,

Table 5.1—SUMMARY OF PARAMETERS FOR METALS FOR EQ. (5.8)

Description	Approximate value
Source normalization	$A_s = \frac{1}{2}$
Surface transmission function	$P_s = 0.9$
Effective diffusion length (cm)*	$L_s = 10^{16}/(0.4Z^{\frac{1}{3}}N)$
Energy required per secondary (eV)	$E_{se} = (20-30)$

*Z and N are the atomic number and atomic density (atoms/cm^3), respectively, of the target.

it is shown in the appendix that an approximate form for the δ-ray energy-return fraction $f(x;T_i)$ is

$$f(x;T_i) = \begin{cases} 1 - \left[\left(1 - \frac{x}{L_\delta}\right)^{\frac{1}{2}} \Big/ \left(1 - \frac{L_B}{2L_\delta}\right)\right] & \left(\frac{x}{L_\delta} < 1\right) \qquad (5.9a) \\ 1 & \left(\frac{x}{L_\delta} > 1\right) \qquad (5.9b) \end{cases}$$

where

$$L_\delta = \bar{\mu}_\delta \lambda_\delta(\overline{T_{\delta 0}}) \qquad (5.10a)$$

$$L_B = (2L_\delta)\left(\frac{r\bar{\bar{K}}}{1 - r\bar{\bar{K}}}\right). \qquad (5.10b)$$

The significance of the characteristic lengths L_δ and L_B can be visualized with the aid of Fig. 5.5, which illustrates the basic processes assumed in the derivation of the present form of the energy-return fraction. As shown, δ-rays traveling in roughly straight-line motion in the

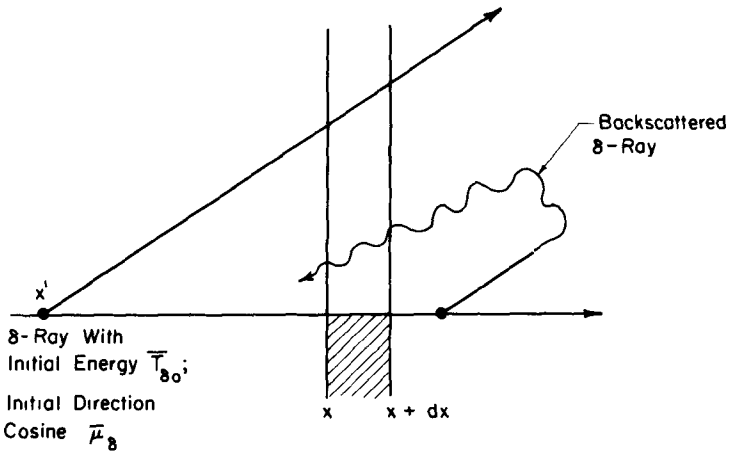

Fig. 5.5 — Schematic illustration of two processes involved in δ-ray energy return.

forward direction will lose energy as they pass through the reference volume at x. This process is characterized by L_δ, which represents the average distance of travel by a δ-ray in the forward direction, i.e., the projection of its range λ_δ on the x-axis. [The average initial direction cosine and energy of the δ-ray ($\overline{\mu}_\delta$ and $\overline{T}_{\delta\,0}$) required to evaluate L_δ can be determined using the Rutherford scattering relations discussed in Sec. 5-6. The range itself can then be evaluated using the Katz–Penfold relation of Chap. 3.]

The length L_B enters as a correction for δ-rays that suffer large angle collisions and then, as illustrated in Fig. 5.5, deposit energy in the volume as a result of this backscattering process. It involves the backscattering coefficient r and also $\overline{K}$, the fractional energy associated with backscattered electrons. (Methods for evaluation of both of these parameters are given in Sec. 5-7.)

It might be noted that Eq. (5.9) is based on the slowing theory of Chaps. 3 and 4; whereas, in his original study, Sternglass assumed a diffusion theory model that leads to a slightly different result. The differences do not appear to be large, however, and we will use Eq. (5.9) in succeeding sections. It is a natural extension of the earlier development, and the slowing model should provide closer approximation of the physical processes involved in δ-ray transport than would diffusion theory.

We are now in a position to evaluate the integral involved in Eq. (5.8), but first it is convenient to separate the contributions due to soft secondaries and those due to δ-rays. This results in

$$\Delta(T_1) = \Delta_0(T_1)\,[1 + F(T_1)] \tag{5.11}$$

where $\Delta_0(T_i)$, the yield exclusive of δ-ray contributions, is given by

$$\Delta_0(T_i) = \frac{L_s P_s A_s}{2E_{se}} \left\langle \frac{dT_i}{dx} \right\rangle_{x=0}. \tag{5.12}$$

The function $F(T_i)$ now incorporates the fractional energy return $f(x;T_i)$, and a form that will be useful for later expansions is

$$F(T_i) = 1 - L_s^{-1} \int_0^\infty \phi(x;T_i) \exp\left[-\left(\frac{x}{L_s}\right)\right] dx \tag{5.13a}$$

where

$$\phi(x;T_i) \equiv 1 - f(x;T_i). \tag{5.13b}$$

If the present result for $f(x;T_i)$, namely Eq. 5.9, is used to evaluate $F(T_i)$, we find

$$F(T_i) = 1 - \left(1 + \frac{L_B}{2L_\delta}\right)^{-1} U\left(\frac{L_\delta}{L_s}\right) \tag{5.14a}$$

where the function U is defined by

$$U(x) = \frac{\exp(-x)}{x^{1/2}} \int_0^x \sqrt{y} \exp y \, dy. \tag{5.14b}$$

This is the most general result for $F(T_i)$; however, for the case of high-energy ion bombardment, an approximate form can be derived as follows: The principle contribution to the integral in Eq. (5.13a) comes from the region before the exponential term becomes too small—i.e., $x/L_s < 1$. However, as noted earlier, the range for δ-rays produced by high-energy ion bombardment (hence L_δ) is as much as an order of magnitude larger than the secondary electron diffusion length L_s. Thus, the region of the dominant contribution corresponds to $x/L_\delta < 1$, and it follows that ϕ, defined in Eq. (5.13b), can be expanded as

$$\phi(x_i;T_i) \approx \left(1 + \frac{L_B}{2L_\delta}\right)^{-1} \left(1 - \frac{x}{2L_\delta}\right) \tag{5.15}$$

in which case $F(T_i)$ reduces to

$$F(T_i) \approx 1 - \left(1 + \frac{L_B}{2L_\delta}\right)^{-1} \left(1 - \frac{L_s}{2L_\delta}\right). \tag{5.16}$$

Generally, as discussed in Sec. 5-7, backscattering is not too important for low-Z targets, in which case, $L_B/L_\delta \approx 0$, and

$$F(T_1) \approx \frac{L_s}{2L_\delta}. \tag{5.17}$$

For situations of interest here, L_s/L_δ will generally be of order of 0.1 to 0.3, so the δ-ray contribution to the yield will typically be less than $\frac{1}{3}$ of the total contribution—the dominant contribution being from "distant collisions" represented by $\Delta_0(T_1)$ in Eq. (5.11). (This conclusion applies only to high-energy ions. Gamma photons do not undergo distant collisions in the sense used here, and they represent an important exception discussed in later sections.)

5-4 LOW-ENERGY COMPONENT YIELD DUE TO HIGH-ENERGY ION AND ELECTRON BOMBARDMENT

In this case, $\langle dT_1/dx\rangle_{x=0}$ can be evaluated using the slowing model of Chap. 3; consequently, substitution of Eqs. (3.27) and (5.16) into the yield relation of Eq. (5.11) gives

$$\Delta(T_1) = \frac{L_s P_s A_s}{E_{se}} \frac{T_1}{(n+1)\,\lambda_1(T_1)} \left[1 - \frac{1}{2}\frac{1-(L_s/2L_\delta)}{1+(L_B/2L_\delta)}\right] \tag{5.18}$$

where the slowing parameter n and range λ_1 refer to the bombarding ion and are evaluated at its entering energy T_1.

This result is quite general and can be applied to a variety of particles, including protons, alpha particles, fission fragments, and electrons in the high keV or MeV region.

5-4.1 High-Energy Ion and Electron Bombardment

The most extensive data available are from electron and proton beam studies, and we will review some of the latter to illustrate the use of Eq. (5.18).

Yields based on this equation are compared in Fig. 5.6 with data collected by Sternglass[17] for bombardment of various materials by 0.1- to 2-MeV protons. Curve 1 represents a simplified form of Eq. (5.18), where the δ-ray contribution $F(T_1)$ is neglected, and as discussed in Chap. 3, n = 0.8 is selected to represent protons. The proton range was evaluated at 1 MeV by using the nomograph of Fig. 3.6. Both this range and the secondary diffusion length L_s were calculated assuming an aluminum target; however, the result is quite insensitive to the specific target material as is confirmed by the experimental data

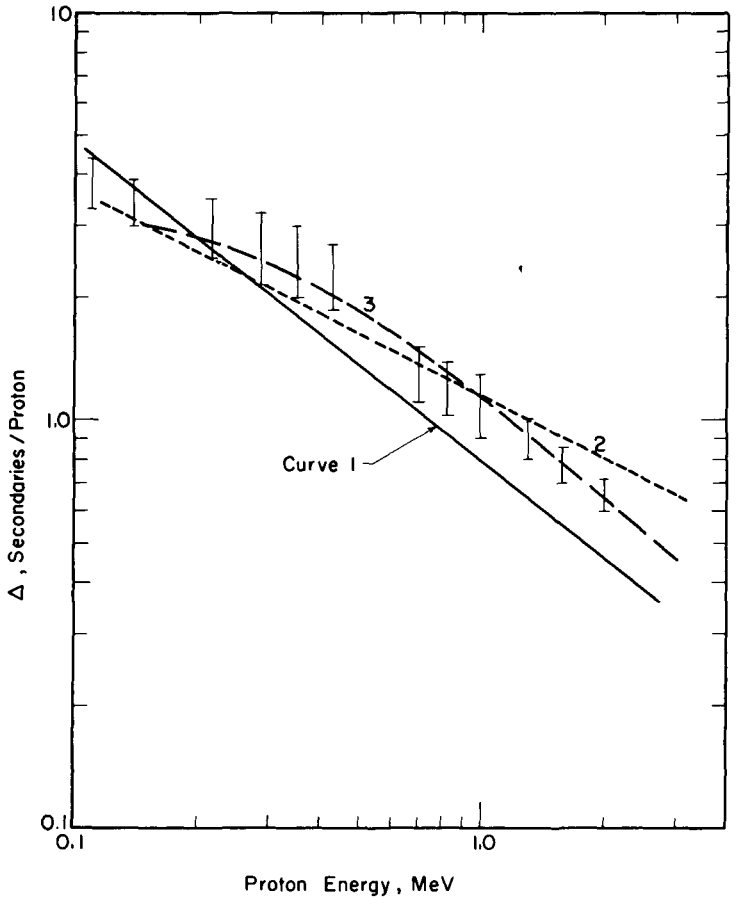

Fig. 5.6—Comparison of calculated and measured secondary yields for proton bombardment. [The bars represent the range of various data collected by Sternglass (Ref. 17) for Al, Mg, Fe, Ni, Cu, Mo, Au, and Pb targets. Curve 1 represents Eq. (5.18) with λ_i from Fig. 3.6, n = 0.80, and $F(T_i) = 0$; curve 2, Eq. (5.20); and curve 3, calculations by Sternglass including $F(T_i)$ and using Eqs. (3.4) and (3.8) for (dT/dx).]

shown in Fig. 5.6. The reason for this can be best understood by substituting the range in the form given in Eq. (3.26) into Eq. (5.18) along with the explicit form of L_s given in Table 5.1.

If, as before, $F(E_i)$ is neglected, this gives

$$\Delta(T_i) \approx \frac{P_s A_s}{2E_{se}} \left(\frac{10^{16}}{0.4 Z^{1/3} N} \right) \frac{C_i}{T_i^n} \tag{5.19}$$

where C_i, the constant in the range relation, is given by either Eq. (3.17)

or (3.20) depending on the energy of the particle If the intermediate energy form is used [Eq. (3 20)], the yield may be written as

$$\Delta(T_1) \approx \frac{10^{16} P_s A_s}{0\ 8 E_{se}} \frac{16\pi q^2 \hbar}{m_e} \sqrt{\frac{M}{2}}\, T_1^{-1/2}$$

$$= (2.68 \times 10^{-2}) \sqrt{\frac{M}{m_e}} \left(\frac{q}{e}\right)^2 T_1^{-1/2} \qquad (5.20)$$

with T_1 expressed in MeV. It will be noted that the dependence on N and Z has canceled out, demonstrating the insensitivity to the nature of the target. (A similar argument was originally proposed by Sternglass[17].) Here, n = 0.5 has been used as indicated in Eq. (3.19) to be consistent with this form for C_1 This result is shown as curve 2 in Fig. 5 6, and fairly good agreement is observed in the region below 1 MeV. However, at higher energies, the slope appears to be in error. This is to be expected since, as discussed in Chap. 3, 0.8 (not 0.5) is the preferred value for n at higher energies.

If curve 1 were renormalized to the measured yield at 1 MeV, it would give an excellent fit in the region above 0.5 MeV. The error in amplitude can be attributed to possible inaccuracies in the range used and also the neglect of $F(T_1)$, but it fails to show the curvature indicated by the data bars at lower energies. The curvature is the result of two effects As seen from Fig. 3.5, the parameter n changes fairly drastically for protons below 0.5 MeV, and this is in a direction to cause a marked decrease in the yield. Concurrently, the reduced bombardment energy leads to softer δ-rays, which are more likely to create secondaries near the surface that are in a favorable position to escape. As a result, $F(T_1)$, and hence the yield, will increase, and this partly compensates for the first effect but not enough to prevent the curvature observed in the yield curve. Both effects have been included in a detailed calculation by Sternglass[17] shown as curve 3 in Fig. 5.6, and the agreement with the data bars is excellent. [His calculation is essentially the equivalent of retaining the full form of Eq. (5.18).]

Considering the many approximations made in these calculations, we find the agreement surprisingly good, and this lends considerable confidence to the Ionization–Diffusion model used here.

5-4.2 Fission-Fragment and Alpha-Particle Yields

Fission fragments and alpha particles are frequently encountered in radiation cells, and secondary yields are important in both instances since they are generally much larger than unity.

In some cases R_Δ, the ratio of the yields for the two different types of particles, is of interest. This ratio may be found directly from Eq. (5.18), which, if we neglect $F(T_1)$, gives

$$R_\Delta \equiv \frac{\Delta^f(T_f)}{\Delta^\alpha(T_\alpha)} = \left(\frac{n_\alpha + 1}{n_f + 1}\right)\left(\frac{T_f}{T_\alpha}\right)\frac{\lambda_\alpha(T_\alpha)}{\lambda_f(T_f)} \tag{5.21}$$

where the quantities labeled f and α pertain to fission fragments and alpha particles, respectively. The ratio of the ranges required here can be taken from the specific correlations indicated in Chap. 3; however, it is perhaps more instructive to use the expression derived by Bohr [Eq. (3.47)], in which case we find

$$R_\Delta = \frac{2}{7}\frac{n_\alpha + 1}{n_f + 1}\frac{Z_f^{2/3}\hbar^2}{A_f M_f e^4}\left(\frac{M_f}{M_\alpha}\right)^{n_\alpha+1}\left(\frac{T_\alpha}{T_f}\right)^{n_\alpha} T_f \cdot \tag{5.22}$$

Inserting average numerical values ($n_\alpha \approx 0.5$; $n_f \approx -0.5$; $A_f \approx M_f \approx 120$; $Z_f \approx 50$); we obtain

$$R_\Delta = 3.1\left(\frac{T_\alpha}{T_f}\right)^{1/2} T_f \tag{5.23}$$

where the energies are in MeV. This gives the desired yield ratio, and the fission fragment yield can also be found directly from R_Δ by using Eq. (5.20) to represent the alpha yield. In doing this, we assume that the alpha-particle energy is sufficiently large so that $q_\alpha \approx 2e$, then

$$\Delta^f(T_f) = R_\Delta \Delta^\alpha = 44(T_f)^{1/2} \tag{5.24}$$

Only a few experiments have been carried out with alpha particles and fission fragments, and recent data by Anno[18] and Jamerson et al.[19] are summarized in Table 5.2 along with some earlier values by Stein and Leachman[20]. An important point to note is that there are considerable differences in the geometries involved in the various experiments. As indicated, some measurements were made on the exit side of a foil as the particles passed through it. In the case of the uranium materials, the fragments were born in the foil and created secondaries as they escaped through the surface. Except for the data of Stein and Leachman, the bombarding particle directions were almost random or isotropic, rather than perpendicular to the surface as assumed in the calculations considered thus far. Because of this, considerable care must be taken in using the data of Table 5.2. Some methods for making geometric corrections are considered in the following sections; however, for the moment, we note that Anno[18] has applied geometric corrections to the data for fission fragments merging from UO_2 and alphas from Au, and he reports a yield ratio corresponding to normal incidence of $R_\Delta \approx 21$ to 22 (vs about 40 to 60 for the raw data of Table 5.3). Corresponding to these data, Eq. (5.23) gives $R_\Delta \approx 50$ for $T_\alpha = 3$ MeV and $T_f = 80$ MeV; i.e., it overestimates the yield by roughly a factor of 2. (Anno reports a calcu-

Table 5.2 — YIELD MEASUREMENTS FOR ALPHA PARTICLES AND FISSION FRAGMENTS

Particle	Foil	Direction*	Source†	Yield, Δ (secondary electrons/ primary particle)	Charge Ratio (secondaries/ primary particle)	Ref.
Fission fragments	0.6 mg/cm^2 Ni (thin)	E	B	70 ± 7		20
	0.6 mg/cm^2 Ni (thin)	I	B	40		20
	15.5-μ U–Ni alloy (thick)	E	F	207 ± 10		19
	0.1- to 3-μ UO_2 (thin)‡	E	F	572 ± 58 to 299 ± 45, respectively	28 to 21	18
Alpha particles						
^{210}Po (≈3 MeV)	100-μ Au (thin)‡	E	B	9.21 ± 0.75 (5.5)§	4 95 ± 0 16	18
4.8 MeV	0 6 mg/cm^2 Ni (thin)	E	B	2		20

*E: emerging from the foil; I: entering.
†B: external beam; F: internal fission.
‡λ_f is ≈9 μ in UO_2 and λ_α is ≈300 μ in Au.
§Estimated value for normal incidence.

Table 5.3 — CALCULATED AND EXPERIMENTAL YIELDS

Target	Particle	Yield (normal incidence)		
		Measured*	I–D Model†	Thermionic Model‡
Au	Alpha (≈3 MeV)	5.5	5.7§ 8 8¶	5.8
UO_2	Fission fragment	118	800§ 440¶	7.7×10^4

*Corrected for geometry, Δ^f obtained from Δ^α using $R_\Delta = 21\ 3$ (Ref. 18, p 58).

†Equation (5 8)

‡Calculations by Anno[18] using the following constants

	Au	UO_2
C_v [cal/(g °C)]	0.32	0.078
K [cal/(sec cm °C)]	0 71	0.0063
ρ (g/cm^3)	19 3	10.1
$\langle dT/dx \rangle$ (cal/cm)	$2\ 6 \times 10^{-10}$	3.4×10^{-9}

§Values reported by Anno[18] based on $\langle dT_1/dx \rangle$ given above and $\bar{I} = 690$ eV for Au.

¶Based on Eqs. (5.20) and (5.23).

lated value of $R_\Delta \approx 22.7$, but, instead of using Bohr's relation for the range ratio, he used experimental values.)

These data provide an interesting test for the Ionization–Diffusion and the Thermionic models. Anno has compared both models with his experimental data, and his results along with additional calculations based on the equations derived here are summarized in Table 5.3. Both models show reasonable agreement for alpha particles; however, for fission fragments, the thermionic model completely breaks down. He attributes this to the fact that it predicts a yield proportional to the square of the energy loss rate [Eq. (5.1)] rather than the first power as in the Ionization–Diffusion model. Noting that $\langle dT/dx \rangle$ is proportional to q^2 (the square of the ionic charge), he argues that this is particularly important for fission fragments where q is so large.

Because of their significance to nuclear cells, some additional measurements by Anno should be noted. A plot of the yield for fragments vs UO_2 coating thickness is shown in Fig. 5.7. The yield is seen to decrease with increasing coating thickness, and Anno predicts an asymptotic value of ≈ 100. This behavior can be explained qualitatively by noting that, as the coating thickness increases, the average particle energy near the surface decreases, and, as discussed in connection with Eq. (5.24), the yield for fragments will decrease with decreasing energy. A similar plot for the ratio of the charge carried by the secondaries to that of the fragments is shown in Fig. 5.8. This ratio is almost independent of the coating thickness since the average fragment

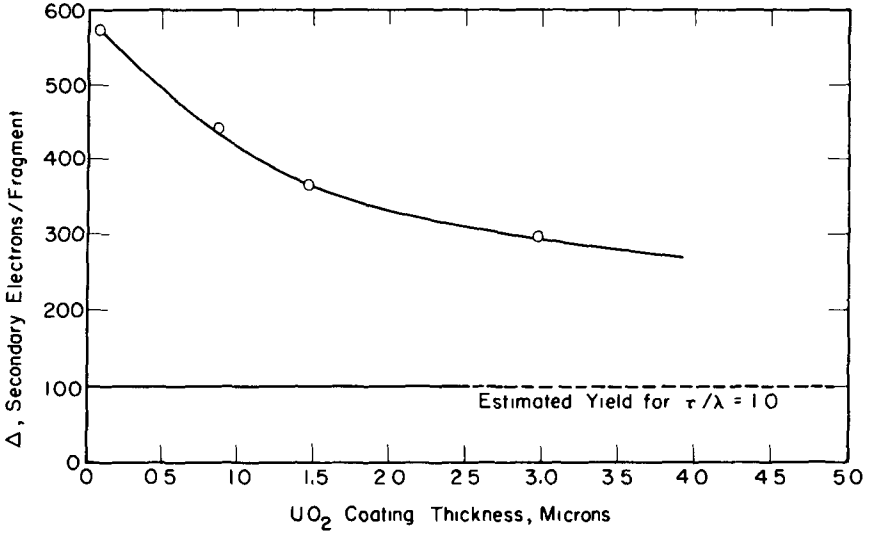

Fig. 5.7 — Secondary yield for fission fragments born in a UO_2 coating vs coating thickness. (From Anno, Ref. 18.)

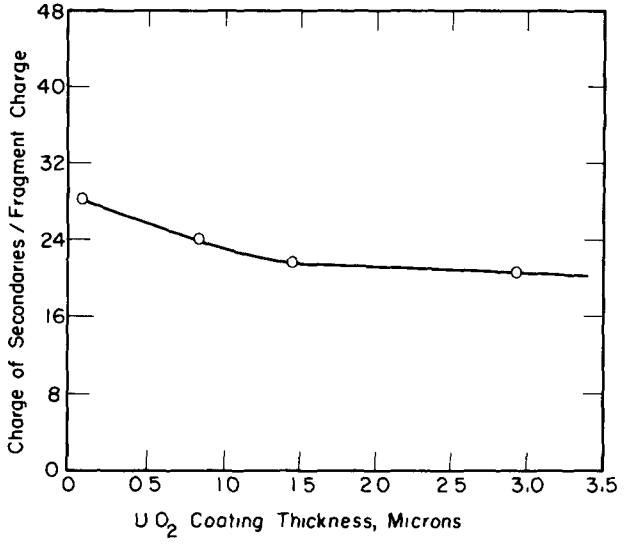

Fig. 5.8 — Ratio of the charge carried by secondaries to that for fragments vs UO_2 coating thickness. (From Anno, Ref. 18.)

charge also decreases with coating thickness (Fig. 4.6), and this compensates for the decreased yield.

5-4.3 Gamma-Radiation Bombardment

Gamma radiation is frequently present in nuclear cells, so the secondary yield due to gamma-photon bombardment is of concern and some modification of the preceding analysis is required for this case.

Consider a beam of j photons/(cm^2 sec) each having energy $h\nu_0$ normally incident upon the target: The energy current I associated with this beam is

$$I = j \times (h\nu_0) \quad \text{MeV}/(\text{cm}^2 \text{ sec}) \tag{5.25}$$

and, if the binding energy for photoelectric production and rest mass energy for pair production are neglected, the expression for energy absorption is

$$\frac{dI}{dx} = \mu_a I. \tag{5.26}$$

The cross section μ_a is termed the energy absorption linear attenuation coefficient, and its listings are given in several places, e.g., Ref. 21. (The energy absorption mass attenuation coefficient μ_a/ρ is often tabulated rather than μ_a.) This cross section accounts for energy going into Compton electrons, photoelectrons, and pair production, and, if μ_{ce}, μ_{pe}, and μ_{pp}, respectively, represent cross sections for each of these processes, then

$$\mu_a = \mu_{ce} + \mu_{pe} + \mu_{pp} \quad \text{cm}^{-1}. \tag{5.27}$$

It is also often convenient to work with the cross section per atom σ defined as μ/N, where N represents the number of target atoms per cubic centimeter and the same subscript nomenclature will be used for σ as in Eq. (5.27).

Since photons do not carry a charge, "distant collisions" do not occur in the same fashion as for ions. While "soft" primary electrons can be produced by other mechanisms in gamma interactions, their production is not favored. Electrons produced by Compton and pair production, and even the photoelectric effect, generally exceed 50 eV for the high-energy gamma rays of interest here. In fact, Stevens and Artuso[22] have shown that less than 6% of all electrons emitted during ^{60}Co gamma irradiation of Al, C, Fe, and W foils have energies less than 50 eV. This represents an upper limit for the production of soft internal secondaries since it also includes those produced by the hard

electrons. On this basis, it appears reasonable to neglect the term representing distant collisions in the yield relation. This amounts to neglecting $\langle dT_i/dx \rangle^{(1)}$ in Eq. (5.3) and setting $\langle dT_i/dx \rangle^{(2)}$ equal to $(1/j)(dI/dx)$; thus, the resulting expression for the yield of secondary electrons per photon of energy $h\nu_0$ is

$$\frac{\Delta(h\nu_0)}{(L_s P_s A_s/E_{se})\,\mu_a h\nu_0} = \begin{cases} F(h\nu_0) & [F(h\nu_0) < 1] \quad (5.28a) \\ 1 & [F(h\nu_0) > 1]. \quad (5.28b) \end{cases}$$

Further insight can be gained by inserting parameters from Table 5.1 and by using the asymptotic high energy form of $F(h\nu_0)$ without backscattering [Eq. (5.17)], in which case the yield reduces to

$$\Delta(h\nu_0) = \frac{6 \times 10^{36}}{Z^{2/3}N} \frac{(\sigma_a)h\nu_0}{\langle \mu_\delta \lambda_\delta(h\nu_0) \rangle} \qquad [F(h\nu_0) < 1] \tag{5.29}$$

where $h\nu_0$ is in MeV. As a first approximation, it can be assumed that

$$\langle \mu_\delta \lambda_\delta(h\nu_0) \rangle \propto \frac{A}{\rho Z} h\nu_0 \tag{5.30}$$

where the proportionality of the range and $h\nu_0$ is roughly demonstrated in Fig. 3.14, and the quantity $(A/\rho Z)$ corrects for the variation of electron range with material as discussed in Sec. 3-5. This gives

$$\Delta(h\nu_0) \propto \Delta(h\nu_0) \propto Z^{1/3}\,\sigma_a \tag{5.31}$$

which indicates that the energy dependence of Δ will roughly follow that of the cross section σ_a. Some feeling for this can be gained from Fig. 5.9. Although this particular graph is for aluminum, it is fairly typical. At lower photon energies, the photoelectric effect dominates, and σ_a increases with decreasing photon energy, indicating a strong increase in yield at low gamma-ray energies. On the other hand, at higher energies where the Compton process and pair production dominate, σ_a does not vary greatly, so the yield should not be strongly influenced by the photon energy.

Equation (5.31) can also be used to gain some indication of the variation of yield with material; however, this is complicated because the Z dependence of the cross section σ_a depends on the photon energy. Some indication of this can be obtained from the approximate dependence of the various components of σ_a (Ref. 14, pp. 672-743):

(Compton) $\sigma_{ce} \propto Z$ (5.32a)

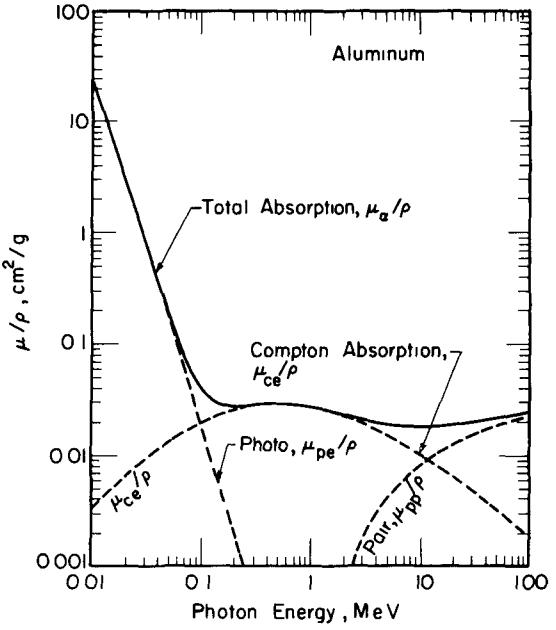

Fig 5.9 — Variation of the energy absorption mass coefficient μ_a/ρ with energy for aluminum. (From Evans, p. 715, Ref. 14. The individual curves were computed by Evans from tables of atomic cross sections prepared by G. R. White. The corresponding linear coefficients for aluminum may be obtained by multiplying all curves by $\rho_{Al} = 2.70$ g/cm³.)

$$\text{(Photoelectric)} \qquad \sigma_{pe} \propto (Z)^{4 \text{ to } 5} \tag{5.32b}$$

$$\text{(Pair)} \qquad \sigma_{pp} \propto Z^2. \tag{5.32c}$$

Since $A \approx 2Z$, we see that, aside from density effects, the yield will tend to increase with Z at low energies where the photoelectric effect dominates but will be less dependent on or even decrease with Z at higher energies.

Insufficient experimental data are available to assess the accuracy of Eq. (5.28), but a rough check can be made by comparison with the yields reported by Stevens and Artuso shown in Table 5.4. Because of the geometry involved, it is difficult to evaluate $F(h\nu_0)$; however, since the values shown are for gammas *emerging* from a "thick" foil (thick relative to the electron, not the gamma range), one might expect $F(h\nu_0)$ to approach 1.0. (This will be discussed in more detail in Sec. 5-4.4.) In this case, the yields calculated from Eq. (5.28) and using σ_a for Fe from Ref. 21 are found to be 1.7×10^{-4} and 4.6×10^{-4} electrons/photon for $h\nu_0 = 0.15$ and 1.25 MeV, respectively. This shows the correct en-

Table 5.4— YIELD MEASUREMENTS FOR GAMMA RAYS EMERGING FROM THICK FOILS*

Source	Foil	Yield, $\Delta(h\nu_0)$ (secondary electrons/photon)
0.15- to 1.33-MeV gammas	Fe	5.4×10^{-5} to 2.4×10^{-4}
^{60}Co gammas†	Fe	2.4×10^{-4}
	Al	3.1×10^{-4}
	W	2.9×10^{-4}

*After Stevens and Artuso[22]. These measurements used a collimated beam with a target inserted at ≈45°.

†Calculated from Tables 4 and 7 and Fig. 29 of Ref. 22 using the relation Δ = V (50 eV) × (quantum efficiency)

ergy dependence, but the measured values in Table 5.4 increase somewhat more rapidly with energy.* The use of 1.0 for $F(h\nu_0)$ is no doubt partly responsible for the discrepancy Aside from the energy dependence, the variation with material does not turn out so well. Values of 2.68, 4.6, and 12.0×10^{-4} are predicted for Al, Fe, and W, respectively, while the data of Table 5.4 indicate much less variation The reason for this discrepancy is not clear

5-4.4 Geometric and Angular Effects

The preceding development assumed normal incidence of high-energy bombarding particles on a flat target surface. Appropriate corrections must be applied if the geometry or angle of incidence is different. Most workers[4, 9, 13] have assumed that the angular dependence of the yield for high-energy bombardment is given by

$$\Delta(\mu, T_1) = \frac{\Delta(T_1)}{\mu} \tag{5.33}$$

where μ is the direction cosine relative to the normal to the surface, $\Delta(T_1)$ is the yield for normal incidence, and $\Delta(\mu, T_1)$ is the yield for a current of bombarding particles having a direction defined by μ. This expression is based on the intuitive argument that the yield is proportional to the track length of the primary particles within the escape

*Note from Fig. 5.9 that this energy range falls around the knee of the cross-section curve. Thus the slight increase in yield with energy does not violate the earlier suggestion that energy variations will roughly follow the cross section. Energies well below 0.1 MeV would be required to enter the region where photoelectric interactions cause a considerable increase in the yield.

zone. There are, however, several difficulties with this formulation. One is that the energy of the primary particle is assumed to be constant across the escape zone in the derivative of $\Delta(T_1)$, and even though the escape zone is quite thin (order of 10 Å or so), this assumption will break down at large angles (small μ). Data are lacking for $\mu < 0.34$ (or $\theta > 70°$), where this effect might appear[8]; however, a number of experiments[4, 9, 13] in the range $0.34 < \mu < 1$ have demonstrated good agreement with Eq. (5.33), and a typical comparison is shown in Fig. 5.10. In fact,

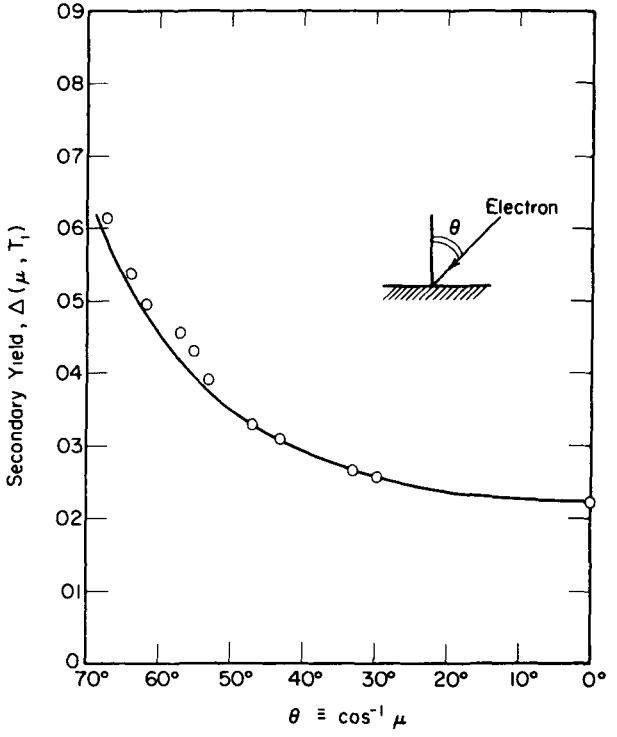

Fig 5.10 — Dependence of the secondary yield on angle of incidence for bombardment of aluminum by 1 3-MeV electrons. [From Kronenberg, Ref. 9, data from Shats et al., the solid curve is based on Eq (5.33)]

the accuracy of the correlation is better than anticipated since two additional effects can occur. Both the secondary source normalization factor A_s and the energy return fraction $f(x;T_1)$ might be expected to depend on μ, but apparently these effects are partially compensating, weak, or both.

A detailed derivation of the yield for non-normal incidence would be valuable in understanding these problems, however, this has not

been worked out to date, and, to avoid undue complexity, we will use Eq. (5.33) while keeping in mind the aforementioned reservations.

Consider a bombarding particle angular current of $J(\mu, T)$ particles per second per unit energy and unit μ and per square centimeter of surface. Then, the total yield Δ_T based on Eq. (5.33) is

$$\Delta_T = \frac{\iint \Delta(T)\, J(\mu, T)\, dT\, d\mu/\mu}{\iint J(\mu, T)\, dT\, d\mu}. \tag{5.34}$$

Some specific cases will illustrate the significance of this result:

(a) Monoenergetic, Isotropic Incident Flux

The angular current is related to the angular flux by Eq. (4.41), which in the present case reduces to

$$J(\mu, T) = \mu\, \phi(\mu, T) \equiv \mu B\, \delta(T - T_0) \tag{5.35}$$

where B is a normalization constant related to the scalar flux ϕ_T by

$$\phi_T = \int \int \phi(\mu, T)\, d\mu\, dT \equiv B. \tag{5.36}$$

Substitution into Eq. (5.34) then gives

$$\Delta_T = 2\Delta(T_0). \tag{5.37}$$

In other words, the yield for an isotropic incident flux is twice that for normal incidence. (This result has also been derived by Kronenberg[9].)

(b) Monoenergetic, Isotropic Incident Current

For this case, by definition, the angular current is

$$J(\mu, T) = H\, \delta(T - T_0) \tag{5.38}$$

where H is a normalization constant. Then, Eq. (5.34) reduces to

$$\Delta_T = \Delta(T_0)\, \ln\, (1/\mu_{min}). \tag{5.39}$$

In the earlier calculation we set $\mu_{min} = 0$; however, more care is required here since the yield goes to infinity as $\mu_{min} \to 0$. One way to avoid this difficulty is to note that there is a natural "break point" in the cosine corresponding to

$$\mu_c \approx t_E/\lambda_i \tag{5.40}$$

where t_E is the secondary escape zone thickness and λ_1 is the range of the bombarding particle. Particles with a direction cosine in the region $0 < \mu < \mu_c$ will remain inside the escape zone throughout their entire trajectory. Thus, they travel a distance λ_1 in this zone, and, if we continue to assume that the yield is proportional to the track length inside the escape zone, we obtain

$$\Delta(\mu, T_1) = \Delta(T_1) \frac{\lambda_1}{t_E} \qquad (0 < \mu < \mu_c). \tag{5 41}$$

One problem with this relation is that the bombarding particle energy will clearly vary along its track, so it would seem more sensible to use an energy averaged value of the normal yield. However, as shown below, the contribution to the total yield from this term is small; consequently, the error introduced by neglecting the energy variation is not too important, and a correction will not be attempted here.

The integral of Eq. (5.34) can then be broken into two parts, where Eq. (5.41) is used for $\mu < \mu_c$ and Eq. (5.33) is used for $\mu > \mu_c$. Then, the yield becomes

$$\Delta_T = \Delta(T_0) [\ln (1/\mu_c) + 1]. \tag{5.42}$$

Typical values of interest here are $t_E \approx 10$ Å and $\lambda_1 \approx 10^{-3}$ cm, so that μ_c may be of order of 10^{-5} giving $\Delta_T \approx 13\Delta(T_0)$. This result is only approximate since it stresses large angles where the yield angular correlation is not expected to be too accurate. Still, it effectively demonstrates that the yield for an isotropic current may be an order of magnitude larger than that for normal incidence.

(c) Incident vs Exit Yields

At this point we turn our attention to another question: How does the yield compare for particles incident on the surface of a foil as opposed to particles emerging from within a target? The latter case is important since it is often encountered with radioactive sources, and also, a bombarding particle may pass completely through a thin foil, in which case, both situations occur simultaneously.

As illustrated in Fig. 5.11, the main difference between entrance and exit yields can be traced to the δ-ray contribution. A primary particle is shown passing through a foil that is thick relative to the escape zone thickness but thin relative to the primary particle's range. Since δ-rays are preferentially driven forward, the fractional energy return $f(x;T_1)$ will increase roughly in the fashion indicated. The resulting contribution to $F(T_1)$ involves an integration over $f(x;T_1)$ as indicated in

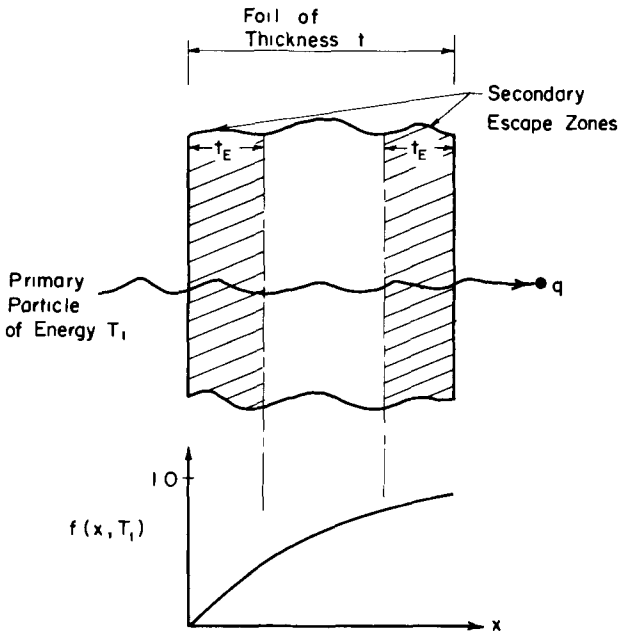

Fig. 5.11 — Comparison of incident and exit δ-ray contributions.

Eqs. (5.11) and (5.13), and we have shown [Eq. (5.17)] that, on the entrance side, if backscattering is neglected

$$F_{in}(T_1) \approx \frac{L_s}{2L_\delta} \ll 1. \tag{5.43}$$

If the foil thickness is comparable to the characteristic δ-ray length L_δ (a reasonable assumption for $t \gg t_E$), Eq. (5.9b) shows that $f(x;T_1) \to 1.0$, and, as a result, according to Eq. (5.13)

$$F_{exit}(T_1) \approx 1.0. \tag{5.44}$$

Thus, the δ-ray contribution is much larger on the exit side, and, based on Eq. (5.11), we find that

$$\Delta_{exit}(T_1) \approx 2\Delta_{in}(T_1) \qquad (\lambda_i \gg t \gtrsim L_\delta) \tag{5.45}$$

where $\Delta_{in}(T_1)$ is the conventional yield for normal incident. This result is consistent with studies by Anno and Jung[23] and also with measurements by Stein and Leachman[20] given in Table 5.2 (p. 203), which show that the yields differ by a factor of about 1.8.

On the other hand, if the foil is so thin that $t \approx 2t_E$ and $t/L_\delta \ll 1$, $f(x;T_1)$ will not differ greatly across the two zones, and the yields will be approximately equal, or

$$\Delta_{exit}(T_1) \approx \Delta_{in}(T_1) \qquad (t \approx t_E). \tag{5 46}$$

Calculations for intermediate thicknesses require a detailed consideration of $f(x,T_1)$.

(d) Applications to Radioactive Layers

The application of the preceding results is illustrated by two situations often encountered with radioactive sources. (These situations have also been considered by Anno[8], but the following presentation differs from his in several respects.)

(1) Monoenergetic, Isotropic Emitter with a Non-emitting Coating. This represents the situation commonly encountered where a cladding is applied over an emitting material. We will restrict our attention to two extreme cases: a very thin cladding vs a thick one that approaches the range of the source particle. An idealized plane source is assumed, and the geometry is illustrated in Fig. 5 12. First, consider the case

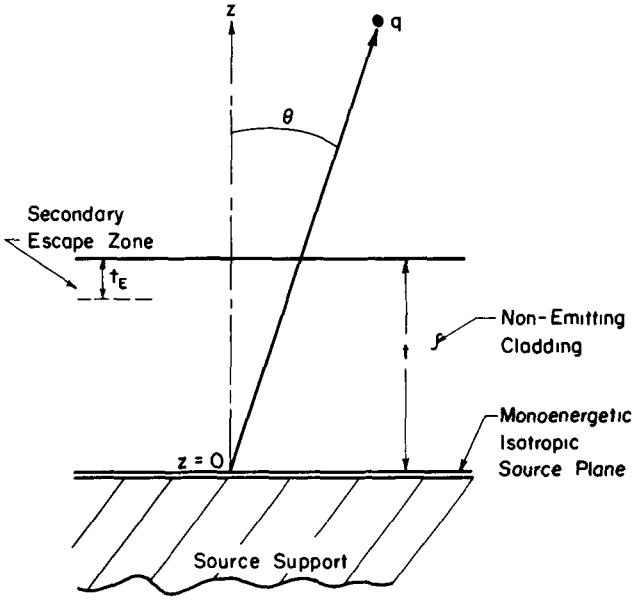

Fig 5.12—Geometry for coated emitter calculations.

where the cladding is so thin that it approaches the escape zone thickness. Since the source is an isotropic emitter, we use

$$[J(\mu,T)]_{z=0} = S(\mu,E) = \frac{S_0}{2}\,\delta(T-T_0) \tag{5 47}$$

Under these conditions, Eqs (5 42) and (5 46) are valid, and

$$\Delta_{exit}(T_0) \approx \Delta_{in}(T_0) \approx \Delta(T_0)\left[\ln\left(\frac{\lambda_1}{t_E}\right)+1\right] \tag{5 48}$$

so, as before, $\Delta_{exit}(T_0)$ may be an order of magnitude larger than the yield for normal incidence.

Next, consider a thick cladding where $t \to \lambda_1$ (t cannot exceed λ_1 or no particles would escape) Now, although the source is monoenergetic, the particles come off at various angles, consequently, they will lose varying amounts of energy as they traverse the cladding prior to entering the escape zone. We will again neglect the energy loss in crossing the zone itself and assume that the particle angle–energy spectrum entering this zone is the same as at the surface.

The surface current can be found by introducing a transfer function $T(s,T_0 \to T)$ representing the probability that a particle with initial energy T_0 will have an energy T per unit after traveling a distance s [this concept was used earlier in Eq. (4 101)]. Then, the current is simply related to the source by

$$\begin{aligned} J(t,\mu,T) &= S(z',\mu,T_0)\; T(t/\mu,\; T_0 \to T) \\ &= \frac{S_0}{2}\,\delta(T-T^*) \end{aligned} \tag{5.49}$$

where the property of an isotropic uniform source has been used Also it has been recognized that, since the slowing model represented by Eq. (3.28) specifies a unique relation between T and the distance traveled, T can be written as a delta function with

$$T^* = \left[T_0\left(1-\frac{t}{\mu\lambda_1}\right)\right]^{1/(n+1)} \tag{5.50}$$

Use of this expression in Eq. (5.34) gives a yield of

$$\Delta_{exit} = \frac{2(n+1)\,\Delta(T_0)}{V}\int_0^{V^{1/(n+1)}} \frac{dy}{1-y^{n+1}} \tag{5 51a}$$

where

$$V \equiv 1 - \frac{t}{\lambda_1}. \tag{5.51b}$$

It has been assumed that the δ-ray contribution $F(T_i)$ is about 1.0, and that the yield $\Delta(T)$ is equal to $[\Delta(T_0)/(T/T_0)^n]$ as indicated by Eq. (5.19). The integral can be evaluated for specific values of the primary particle energy loss parameter n; for example, if n = 1 (typical of electrons below ½ MeV)

$$\Delta_{exit} = \Delta(T_0)\left[\frac{2}{V}\ln\left(\frac{1+V^{1/2}}{1-V^{1/2}}\right)\right]. \tag{5.52}$$

Note that if $t/\lambda_1 \approx 1$ and $V \ll 1$, then Δ_{exit} may again be several orders of magnitude larger than the normal incident value. Physically, it might be envisioned that, in the limit as t/λ_1 just exceeds unity, the primary particle could conceivably stop *in* the escape zone. Thus, it would not cross the surface; yet, it would produce secondaries that might escape, and, with the yield defined as secondaries *per primary*, this corresponds to an infinite yield! This is not entirely realistic, since in fact, straggling effects would make it difficult to stop a significant fraction of the particles in the small thickness represented by the escape zone.

Alternately, it should be noted that the assumption that $\Delta(T)$ varies as $1/T^n$ introduces a singularity since for low-q ions or electrons where the slowing-down parameter n is positive this expression approaches infinity as $T \to 0$. The energy at the surface approaches zero as $t/\lambda_1 \to 1$, and the yield Δ_{exit} goes to infinity in this limit. (This is a result of the present approximate model, which does not account for the fact pointed out in Chap. 3 that n will change sign near the end of the charged particle track.)

For these reasons, Eqs. (5.51) and (5.52) should be considered only a first approximation. Away from the singularity at V = 0, they should provide order of magnitude results, and this should be valuable in studying trends.

(2) Bare Monoenergetic, Isotropic Emitter Layer. Another common situation involves a bare emitter layer deposited on a support plate as pictured in Fig. 5.13. Again, for uniform monoenergetic, isotropic emission the source is given as

$$S(z',\mu,T) = \frac{S_0}{2}\,\delta(T - T_0). \tag{5.53}$$

Consider the source plane at z': To escape, a particle emitted at z' must pass through a remaining thickness of material equal to $(\tau - z')$. Thus, the problem is similar to the previous case, but with two differences: If τ is large, the thickness of material above the source will vary from thin ($\approx t_E$) to thick, i.e., between the two extreme cases already considered. In addition, particles can be born in the escape zone itself.

These problems make this a difficult situation to handle precisely without extensive numerical work. To avoid this, we will employ several assumptions leading to a simplified solution that should somewhat overestimate the yield. If $\Delta(z',\mu,T')$ is defined as the yield due to particles born at z' with direction cosine μ and energy T', the total yield can be expressed as

$$\Delta \equiv \frac{\iiint \Delta(z',\mu,T')\, S(z',\mu,T')\, dT'\, d\mu\, dz'}{J(\tau)} . \tag{5.54}$$

In the spirit of the preceding analysis, it is assumed that $\Delta(z',\mu,T')$ can be represented region-wise with the escape zone forming one region, and the remainder of the layer forming the other (Regions I and II, respectively—*see* Fig. 5.13). This suggests that

$$\frac{\Delta(z',\mu,T')}{\Delta_0(T')} = \begin{cases} \dfrac{\tau - z'}{\mu\, t_E} & (\mu > \mu^*) \\ \dfrac{\lambda_i}{t_E} & (\mu < \mu^*) \end{cases} \quad \text{Region I} \quad [(\tau - t_E) < z' < \tau] \tag{5.55a, 5.55b}$$

$$\frac{2}{\mu}\, J(\tau,\mu,T;z',T') \quad \text{Region II} \quad [0 < z' < (\tau - t_E)] \tag{5.55c}$$

where the dividing direction cosine μ^* defines the direction such that a particle born at a depth $(\tau - z')$ in Region I will just reach the surface after traveling a distance λ_i, or

$$\mu^* = \frac{\tau - z'}{\lambda_i} . \tag{5.56}$$

Particles with $\mu < \mu^*$ will stop inside the escape zone after traveling a distance λ_i, and this accounts for Eq. (5.55b). The yield for particles born in Region II is evaluated from Eq. (5.33) by again assuming that the current through the escape zone is essentially equal to the surface current. This is similar to the approach used to derive Eq. (5.51a), and, in fact, $J(\tau,\mu,T;z',T')$ can be found from Eq. (5.49) with T_0 replaced by T' and the definition of T^* modified such that

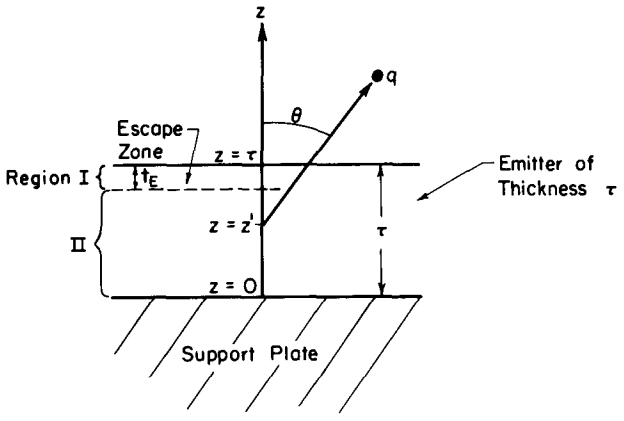

Fig. 5.13 — Geometry for bare emitter calculations.

$$T^* = T' \left[1 - \frac{\tau - z'}{\mu \lambda_i}\right]^{1/(n+1)} . \tag{5.57}$$

[Finally, note that the factor of 2 appears in Eq. (5.55c) to represent the δ-ray contribution because it is again assumed that $F(T_1) = 1$.]

Then, if Eqs. (5.55a to c) are inserted in Eq. (5.54) and the integration carried out over the appropriate ranges indicated, we find

$$\Delta = \Delta_1 + \Delta_2 \tag{5.58}$$

where Δ_1 represents the contribution from Region I and is

$$\Delta_1 = \frac{\Delta(T_0)}{2[1 - t_E/2\lambda_i]} \left[1 + \frac{1}{2}\left(\frac{\lambda_1}{t_E}\right)^2\right] . \tag{5.59}$$

The yield Δ_2 represents the contribution from Region II, and it is

$$\Delta_2 = \frac{2(n+1)\,\Delta(T_0)\,\lambda_i}{(\tau - t_E)[1 - (1/2\lambda_1)(\tau + t_E)]} \int_{1-\tau/\lambda_i}^{1-t_E/\lambda_1} d\mu \times \int_0^{\mu^{[1/(n+1)]}} \frac{dy}{1 - y^{n+1}} \qquad (\tau/\lambda_1 \gtrsim 1) \tag{5.60}$$

which can be evaluated once n and τ/λ_i are specified.

Note that both Δ_1 and Δ_2 have been normalized by the surface currents due to particles originating in the respective regions. These cur-

rents were found by integration of the plane kernel of Eq. (D.6) of Appendix D, using the appropriate limits indicated in Eqs. (5.55a to c).

Inspection of these results shows that the yield for this case may again be an order of magnitude or so larger than the value for normal incidence.

5-4.5 The Energy Spectrum and Angular Dependence of Secondaries

The theory presented here permits calculation of the secondary yield, but it does not give the energy spectrum or angular distribution of the secondaries. Investigations of this problem are reviewed in several references (e.g., pp. 286-297 of Dekker[1]). The theory most compatible with the present development is that of Baroody[24] who neglects binding effects in the calculation of the production of internal secondary electrons but includes an interaction with the target lattice in calculating their escape. (Otherwise, it turns out that conservation of energy and momentum would make escape impossible.) Further, he assumes a priori that the incident particles only interact with conduction electrons, which are described by a degenerate Fermi model. The energy distribution n(p) of escaping electrons predicted by this model for electron bombardment is of the form

$$n(p) = C(p_0)\frac{p - p_0}{p(p^2 - 1)^2} \tag{5.61}$$

where p is a function of the electron energy T defined as

$$p = \left(1 + \frac{\phi + T}{E_f}\right)^{1/2} = [p_0^2 + \epsilon\,(p_0^2 - 1)]^{1/2}. \tag{5.62}$$

Here ϕ and E_f are the work function and Fermi energy, respectively, of the target, and the reduced energy $\epsilon \equiv T/E_f$ has been introduced. The parameter $C(p_0)$ is a weak function of p_0, the latter being defined as

$$p_0 = p|_{T=0} = \left(1 + \frac{\phi}{E_f}\right)^{1/2}. \tag{5.63}$$

Thus both $C(p_0)$ and p_0 are fairly insensitive to the target material, and, over a reasonable range of p_0, Eq. (5.61) predicts a maximum in the distribution at $T \approx 0.7\,\phi$.

Baroody has compared this result with data for electron bombardment of various metals and, as shown in Fig. 5.14, he finds reasonably good agreement. More recently, Stevens and Artuso[22] compared the Baroody theory with measurements for gamma irradiation of iron, and

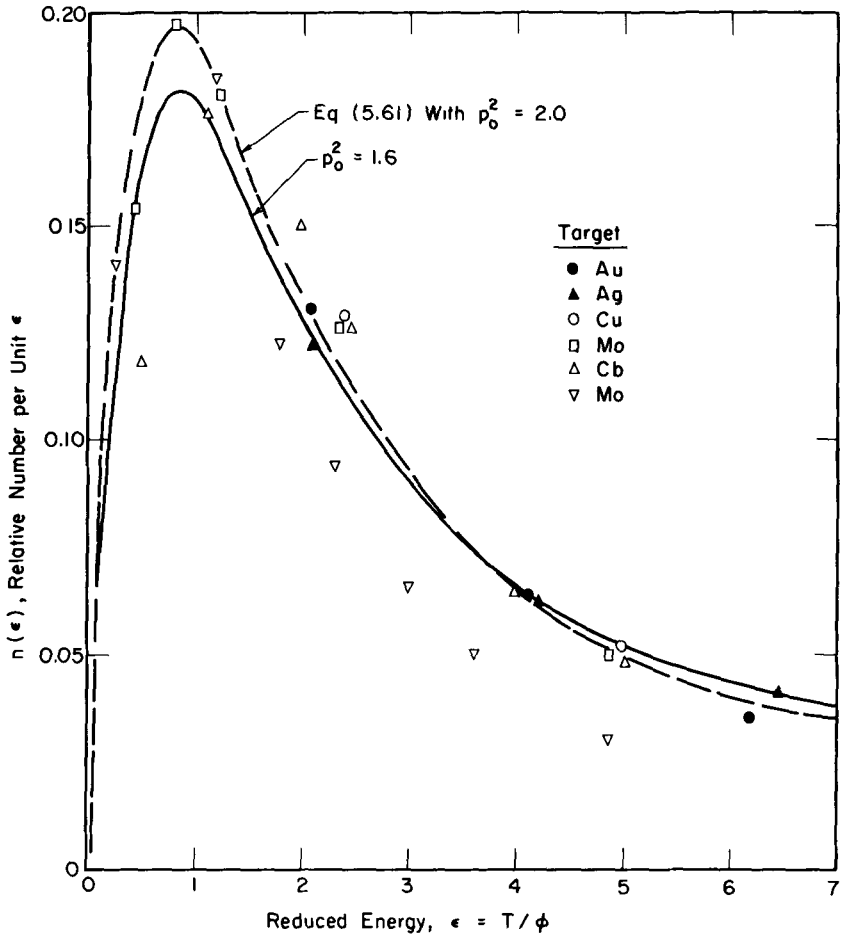

Fig. 5.14—Comparison of predicted and experimental secondary electron energy spectra for electron bombardment. (From calculations by Baroody, Ref. 24. The experimental data were collected from various workers by Baroody.)

rough agreement was found as illustrated by the typical results shown in Fig. 5.15.

Baroody's theory can also be used to find the angular distribution of the secondaries. The number emerging per unit angle $n(\theta)$ turns out to be of the form

$$n(\theta) \propto [\cos\theta\ (1 + 0.28\ \sin^2\theta + 0.14\ \sin^4\theta + \ldots)]. \tag{5.64}$$

The coefficients in the expansion are a slowly varying function of p_0 (those shown are for $p_0^2 = 1.6$). Experimental data for the angular dis-

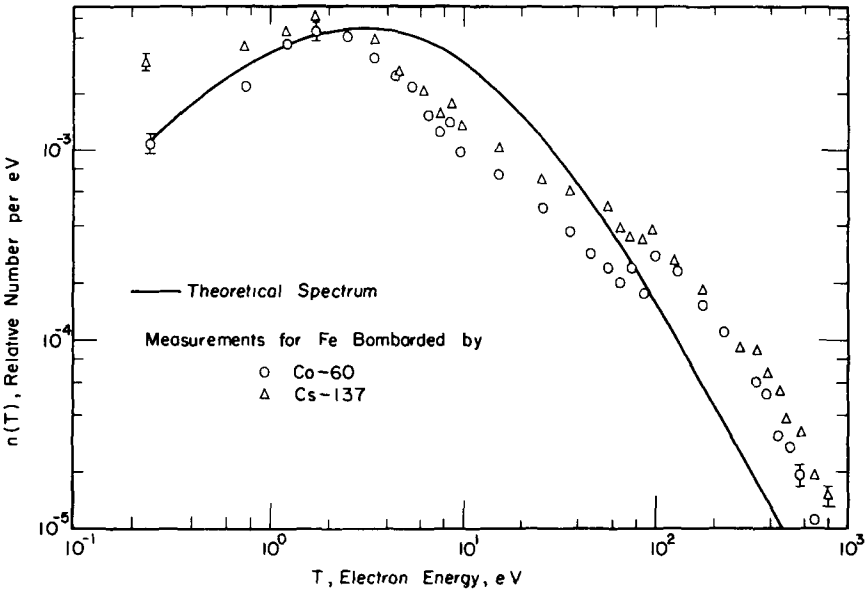

Fig. 5.15 — Comparison of calculated and experimental secondary energy spectra for iron bombarded by ^{60}Co and ^{137}Cs gamma rays. (From Stevens and Artuso, Ref. 22.)

tribution are limited, but a cosine distribution is commonly accepted as a first approximation.

5-4.6 The Effect of Temperature and Electric Fields

Possible changes in secondary yields due to the elevated temperatures and large electric fields encountered in radiation cells represent an important concern. Unfortunately, information of this type is skimpy, and what does exist is often contradictory. This is partly because the effects are small, so measurements are difficult. This is, in fact, consistent with the yield model presented earlier. Variations in both temperature and electric field might be expected to result principally in changes of the work function, but, as stressed in Appendix E, the work function plays a relatively minor role in the escape of secondaries.

Temperature effects have been reviewed most recently by Sternglass[17], Dekker[1], and Anno[8]. Sternglass argues that the primary influence is to change the secondary diffusion length L_s, and he suggests, by analogy with the effects on electrical conductivity, that the resulting temperature (T) dependence of the yield should be of the form

$$\Delta \propto (1 + \beta T)^{-1} \tag{5.65}$$

where β is a constant roughly equal to 2.5×10^{-3} per °K. This predicts, then, a small but detectable decrease in yield with increasing temperature. The accuracy of this result is not clear, however, since as Anno points out, recent measurements with well-cleaned surfaces show little or no variation up to 450°C.

Early measurements also indicated that emission is independent of electric field, but more recent studies by Anno and Jung[23] show a small effect, and plots of their results for both alpha particles and fission fragments are shown in Fig. 5.16. Changes in the yield of the order of

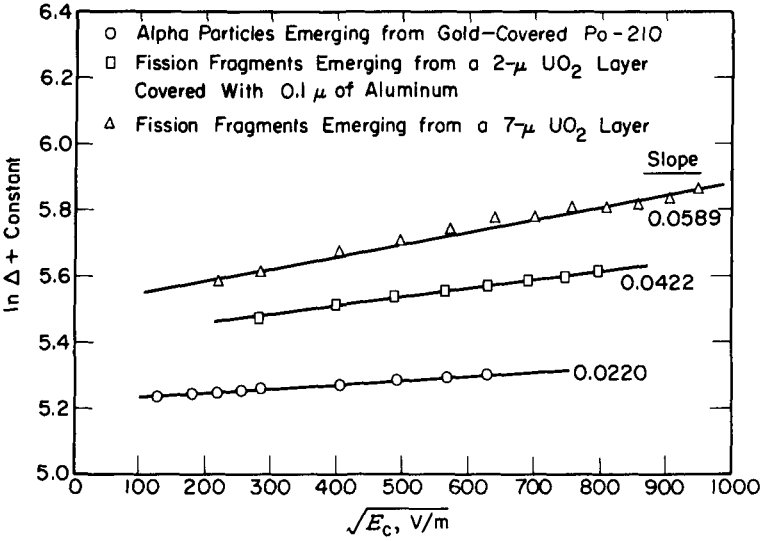

Fig. 5.16 — The influence of an electric field on secondary production. (From Anno, Ref. 8.)

10^{-5}%/(V/m) occur, and the authors suggest that this is primarily caused by the Schottky effect, which would reduce the surface work function according to

$$\Delta\phi \approx \left(\frac{e E_c}{4\pi\epsilon_0}\right)^{1/2} \tag{5.66}$$

where E_c is the electric field at the surface and ϵ_0 is the dielectric constant for a vacuum. (This explains the selection of $E_c^{1/2}$ for the axis in Fig. 5.16.)

A change in ϕ of order of 0.02 eV is predicted by Eq. (5.66) for the maximum voltages in Fig. 5.16. However, it is not clear that this is sufficient to account for the indicated change in yield within the context of

the surface transmission theory of Appendix E. In fact, Anno admits that "a portion of the secondary yield might be due to local heating effects and hence the small electric field dependency might be interpreted as a Schottky effect associated with thermionic emission, but the evidence is rather indirect and inconclusive."

5-4.7 The Yield for Insulators

The preceding theory has been specifically concerned with emission from metal targets. Metals are commonly used for the electrode and grid structures in radiation cells; however, electrical insulators must also be used for various parts in the cells, and it is important to consider how the theory should be extended to include them.

Typical values of the maximum yield Δ_m for electron bombardment for metals, semiconductors, and insulators are given in Table 5.5.

Table 5.5—TYPICAL PARAMETERS FOR ELECTRON BOMBARDMENT*

	Δ_m	T_{im} (keV)†	L_s (Å)	$E_{se}/P_s A_s$ (eV)
		Metals		
Li	0.5	0.09		
Fe	1.3	≈0.4		
Pt	1.8	0.7	20	160
Pb	1.1	0.5		
		Semiconductors		
Si	1.1	0.25		
Ge	1.15	0.4	35	143
		Insulators (Single Crystals)		
MgO	24	1.2	230	20.5
NaCl	≈8			

*Selected values from Dekker[1]. The values of L_s and $E_{se}/P_s A_s$ are estimates based on fitting a yield model to experimental data.

†T_{im} is the bombarding energy corresponding to the maximum yield.

Values for metals and semiconductors are generally of order of unity, but insulators have considerably larger yields. This is commonly attributed[1] to two factors: The secondary diffusion length is larger in insulators, and the energy requirement per internal secondary produced is smaller. Both effects can be traced, at least qualitatively, to differences in the energy level structure. As illustrated in Fig. 5.17, insulators exhibit a characteristic forbidden region of order of 10 eV as opposed to a continuum for metals and a forbidden region of only 1 eV or so in semiconductors. In the case of an insulator, internal

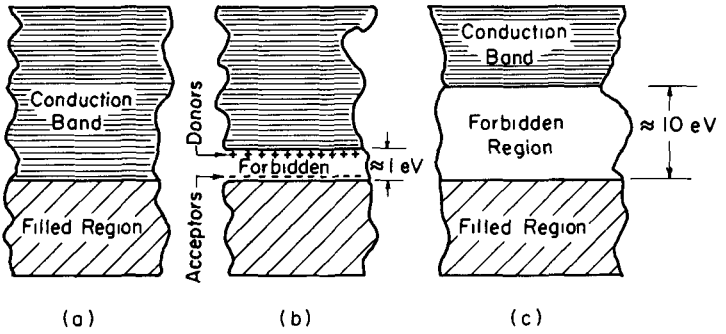

Fig. 5.17—Schematic energy level diagrams. (a) Metals. (b) Semiconductors. (c) Insulators.

secondaries must be created with sufficient energy to place them in the conduction band. However, once there, they cannot transfer energy to electrons in the filled band after their energy drops below ≈10 eV (the forbidden band width). The only allowed interaction then is in the form of phonon formation, and this is a relatively weak interaction. Consequently, these electrons migrate over relatively large distances until their energy drops to about 1 eV, at which point they can finally fall back into a level in the "filled" band. Because of this, the diffusion length L_s is large for insulators as compared to metals, where interactions with bound electrons can occur throughout the slowing process. For example, Table 5.5 indicates that L_s is almost an order of magnitude larger for MgO than for metals or semiconductors. Note that the gap for a semiconductor like Ge is so narrow that its L_s is of the same magnitude as that of a metal.

The second effect is also illustrated in Table 5.5, where it is seen that E_{se}, the energy required to produce an internal secondary, is about a factor of 5 less for MgO than for metals. The reason for this is more subtle, and Dekker[1] attributes it to differences in the cascade process involved in internal electron production in insulators. (The values of $(E_{se}/P_s A_s)$ in Table 5.5 are all considerably higher than those recommended by Sternglass. This appears to be partly due to the model used to fit the experimental data; however, they still illustrate relative trends.)

If L_s and E_{se} are corrected in this fashion, the previous theory can be applied to insulators.

In conclusion, it should be noted that, because of the differences in the governing mechanisms, the diffusion length is more strongly affected by temperature in insulators than metals. Thus, the yield also depends more critically on temperature, and to a first approximation[1], it varies as $[1/T(°K)]$ for typical insulators.

5-5 THE LOW-ENERGY COMPONENT DUE TO LOW-ENERGY BOMBARDMENT

In general, direct collection devices will involve a spread of charged particle energies, and both low- and high-energy bombardment must be considered.

The theory developed in previous sections assumed that the bombarding particle energy was sufficient to make its range much larger than the secondary escape zone thickness. Thus, $\langle dT_1/dx \rangle$ was treated as a constant across this zone, and its value at the surface was used in evaluating the yield. However, this is no longer valid for low-energy bombardment, where the primary particle range may be comparable with or even less than the escape zone thickness. Then the spatial dependence of $\langle dT_1/dx \rangle$ must be retained under the integral in Eq. (5.8), and the yield assumes the form

$$\Delta(T_1) = \frac{P_s A_s}{E_{se}} \int_0^{\lambda_1(T_1)} \langle dT_1/dx \rangle \exp\left(-\frac{x}{L_s}\right) dx \tag{5 67}$$

The δ-ray contribution $F(T_1)$ has been set equal to 1.0 since δ-rays produced will be fairly soft and thus will lose most of their energy within the escape zone. Also, the upper limit of the integral is now identified as the range of the primary particle since $\langle dT_1/dx \rangle$ is zero for x larger than this.

Using the energy loss model of Chap. 3 [Eq. (3 27)] to evaluate $\langle dT_1/dx \rangle$, we find after some algebra that

$$\Delta(T_1) = Y_0 G_{n+1}(r) \tag{5.68}$$

with the parameter Y_0 given by

$$Y_0 = \frac{P_s A_s T_1}{E_{se}} \left(\frac{L_s}{\lambda_1(T_1)}\right)^{1/(n+1)} = \frac{P_s A_s}{E_{se}} [(n+1) C_1 L_s]^{1/(n+1)} \tag{5.69a}$$

where the constant C_1 has been introduced by use of Eq. (3 26) for the range, and n again represents the slowing parameter for the bombarding particle The other function in Eq (5.68) involves the integral

$$G_j(r) = \exp(-r^j) \int_0^r \exp(y^j)\, dy \qquad (j = 1, 2, 3, \ldots) \tag{5.69b}$$

with

$$r = \left[\frac{\lambda_1(T_1)}{L_s}\right]^{1/(n+1)}. \tag{5 69c}$$

It is known as Dawson's integral and is tabulated in Ref. 25 for various values of j.

This form of Eq. (5.68) was selected deliberately so that only the function $G_j(r)$ depends on the energy of the primary particle. The intermediate form of Y_0 in Eq. (5.69a) appears to involve T_i, but when Eq. (3.26) is used to evaluate λ_i, the energy dependence cancels out as indicated. (This form for the yield equation has been obtained by several workers, e.g., see Dekker[1].)

In practice, it is often useful to recast Eq. (5.68) in terms of dimensionless variables, and this form is often called a "universal" yield equation since it turns out to depend only weakly on the target material. To do this, we introduce r_m and T_{im} as the values of these parameters corresponding to the maximum yield Δ_m. First, Eq. (5.68) is differentiated with respect to r and set equal to zero, which gives

$$G_{n+1}(r_m) = \frac{1}{(n+1)r_m^n} \tag{5.70}$$

as the defining relation for r_m.

Substitution of this result into Eq. (5.68) gives the maximum yield in terms of r_m as

$$\Delta_m = Y_0 \frac{1}{(n+1)r_m^n}. \tag{5.71}$$

This is then used to form the reduced yield which is defined as

$$\Delta(T_i)/\Delta_m = (n+1)r_m^n G_{n+1}(r). \tag{5.72}$$

The argument of G can be expressed in terms of the energy ratio T_i/T_{im} by noting that

$$\frac{r^{n+1}}{r_m^{n+1}} = \frac{\lambda_i(T_i)}{\lambda_i(T_{im})} = \left(\frac{T_i}{T_{im}}\right)^{n+1} \tag{5.73}$$

where Eq. (3.26) has again been used to evaluate the range ratio. Thus the r-dependence of G can be replaced by $(r_m T_i/T_{im})$ and the reduced yield becomes

$$\Delta(T_i)/\Delta_m = (n+1)r_m^n G_{n+1}(r_m T_i/T_{im}). \tag{5.74}$$

Recalling that r_m is defined by Eq. (5.70), we see that it is only a function of the energy loss parameter n, which, for a given type of bombarding particle, is relatively insensitive to the target material. Thus, a plot of $\Delta(T_i)/\Delta_m$ vs T_i/T_{im} should yield a "universal" curve, i.e., one

that is essentially independent of the target material. A plot of this type is shown in Fig. 5.18, and indeed, the experimental data—in this case for electron bombardment—indicate a fairly systematic correlation despite the variety of materials involved.

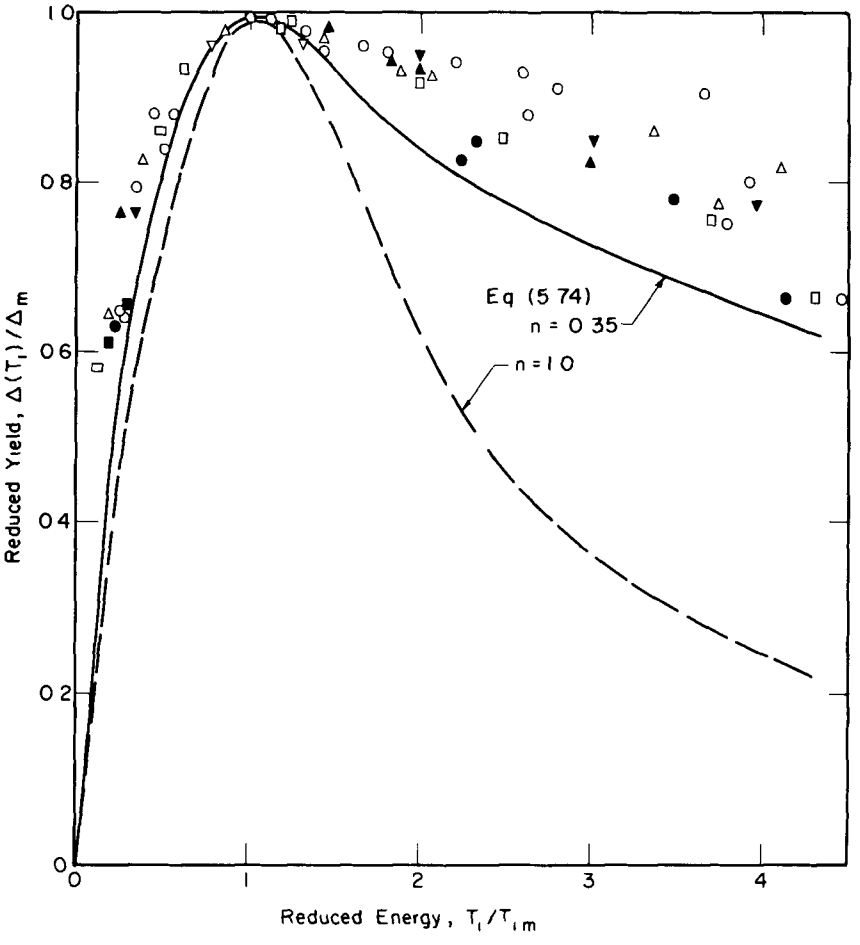

Fig. 5.18—Comparison of the "universal" yield curve and experimental data for electron bombardment. (After Dekker, Ref. 1. The data points are from various workers as reported by Baroody, Ref 24.)

The solid curve (n = 0.35), reported by Dekker[1], gives a better fit to the data points for higher energies than the dashed curve, which is for n = 1 0. The latter is equivalent to early calculations reported by Baroody[24], who derived an expression comparable to Eq. (5 74) with n = 1 0 directly from the free electron model noted in Sec 5-4.5.

Considerable speculation[1] resulted about the cause of the failure of n = 1.0 for electron bombardment, largely because earlier workers expected this exponent to agree with the Thomson–Whiddington Law. However, as discussed in Chap. 3, this would only be valid for quite low electron bombardment energies. In fact, as seen from Fig. 3.12, n starts to decrease at ≈ 50 keV, approaching zero at 1 MeV. (Recall that the exponent on the energy variation of λ corresponds to n + 1. The breakpoint of ½ MeV noted in Table 3.4 is simply the center energy of this transition region.) Thus the improvement in the fit achieved at higher energies in Fig. 5.18 through the use of n = 0.35, i.e., lying between the extreme values of 0 and 1.0, would appear to be consistent with our transport model. A further test of the universal curve against data for other bombarding particles having different n values should shed more light on this, but such a comparison has not been reported to date.

The shape of this yield curve has a simple physical explanation in terms of the escape zone concept. At very low energies $[(T_i/T_{im}) < 1]$, the range of the bombarding particle is less than the zone thickness. As the bombarding particle energy is increased, its range increases and more energy is deposited in the escape zone, causing an increase in the yield. Once the primary particle range exceeds the escape zone thickness, the energy deposited in this zone is proportional to $\langle dT_i/dx \rangle$, which, for low-q ions and electrons, decreases with increasing energy, so that ultimately the yield decreases with increasing energy. In fact, the latter portion of the curve corresponds to high-energy bombardment and the decreasing yield is consistent with Fig. 5.6.

Asymptotic expressions are easily obtained for extreme energies. For low-energy bombardment, λ_i/L_s will be small, and an expansion of the exponential in Eq. (5.68) gives

$$\Delta(T_i) \approx \frac{P_s A_s}{E_{se}} \left[1 - \left(\frac{n+1}{n+2} \right) \frac{\lambda_i}{L_s} + \dots \right] T_i \,. \tag{5.75}$$

In other words, $\Delta(T_i)$ is roughly proportional to T_i, which agrees with the preceding argument. Also note that this implies that the bombarding particle is completely stopped in the escape zone, which means that all its energy T_i becomes available for secondary electron production in this zone. As a result, the factor $P_s A_s/E_{se}$ must account for the number of secondaries formed and for their escape probability, and this is consistent with the earlier definition of these parameters.

An asymptotic expression can be obtained for high energies by simply evaluating $\langle dT_i/dx \rangle$ at the surface as was done earlier. Alternatively, we can achieve the same result directly by using an expansion of $G_{n+1}(r)$ for large r. It is convenient to specialize to n = 1, in which

case an expansion[26] for Dawson's integral is readily available, namely

$$G_{n+1}(r) \approx \frac{1}{2r} + \frac{1}{4r^3} + \frac{1 \cdot 3}{8r^5} + \ldots \qquad (r \gg 2). \tag{5.76}$$

Now, if only the first term of this expansion is retained, the yield becomes

$$\Delta(T_1) \rightarrow \frac{Y_0}{2r} = \frac{P_s A_s L_s}{E_{se}} \left(\frac{C_1}{T_1}\right) = 2\Delta_0(T_1) \tag{5.77}$$

where $\Delta_0(T_1)$ corresponds to the yield derived earlier for high-energy bombardment [Eq. (5.12)] neglecting the δ-ray contribution. The factor of 2 that appears here occurs because, as stressed in formulating Eq. (5.68), the δ-ray contribution $F(T_1)$ was set equal to 1.0. This is not valid at higher energies, and to be consistent, $F(T_1)$ should be evaluated explicitly as was done in earlier sections. (This point has not been stressed in the literature with the result that the "universal" curve based on Eq. (5.68) has frequently been improperly extended to high energies.)

5-6 HIGH-ENERGY COMPONENT YIELDS

In contrast to low-energy yields, the emission of high-energy electrons (>50 eV) has received relatively little attention.

High-energy emission is important in radiation cell concepts for several reasons. If it is necessary to suppress secondary currents, the grid voltages or magnetic field strength must be selected in order to stop all or a part of the high-energy component. Alternately, devices designed to operate on the secondary electron current (e.g., the Compton diode described in Chap. 7) can achieve high voltages by collecting the high-energy component. Other cells, such as the Semirad detector (Chap. 7), mainly operate by collecting the low-energy emission component. Still their response to the energy spectrum of the incoming radiation depends on the variation of the low-energy/high-energy electron yield ratio with the energy of the bombarding particle.

Also, in cases where an external radiation source is used to create ionization in a gas or liquid, secondary emission from the walls of the container may represent an important source of ionizing radiation. Then, despite the relatively low yield for the high-energy component, the large energy per particle can result in the deposition of a significant amount of energy in the medium.

5-6.1 A Model

Recent theoretical studies by Sawyer and Van Lint[27] and combined theoretical–experimental studies by Stevens and Artuso[22] and Ebert and Lauzon[28] have considered high-energy emission due to gamma-radiation and electron bombardment. Other measurements by Miller and Porter[11] and Kronenberg[9], involving electron and proton bombardment, respectively, were noted earlier. However, studies of heavy-ion bombardment are notably lacking, although some related work directed at establishing the charge of heavy nuclei in cosmic radiation has been reported (Ref. 29, p. 252).

High-energy emission simply represents δ-rays that escape from the surface and, thus, is directly related to the calculation of the δ-ray contribution to low-energy secondary production discussed earlier. As an illustration of the problem, consider a metallic foil of thickness τ as shown in Fig. 5.19. (Note the similarity to the δ-ray energy return cal-

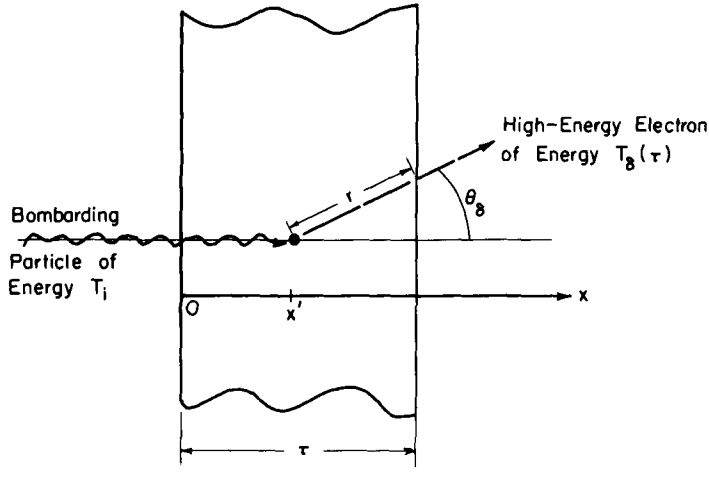

Fig. 5.19—Geometry for high-energy electron emission calculations.

culation involving Fig. 5.5. Averaged parameters were used in the earlier calculations [Eq. (5.10)], but we are now interested in more detail and will elect to use the transport methods developed in Chaps. 3 and 4. In effect, this will answer the question of how to find appropriate averages for the earlier calculations.)

The current can be calculated by either the point- or plane-kernel methods of Chap. 4. The plane kernel is a natural choice where the energy of the bombarding particle varies significantly across the plate so that the electron source rate is not uniform in the x direction. However, to illustrate the basic concepts with a minimum of algebra, we will as-

sume a "thin" foil, so the energy of the bombarding particle T_1 remains approximately constant in transversing the foil, in which case the point-kernel method is somewhat simpler to use. We will describe δ-ray transport by the straight-line mean-range approximation of Chap. 3, which, because of the high energies involved, should be reasonably accurate. However, it should be noted that this automatically neglects the contribution of large-angle electron–electron scattering whereby the primary electron might produce another high-energy electron. In other words, the secondaries produced during the δ-ray slowing process are assumed to be soft enough so that, by the time they reach the surface, they contribute to the low-energy rather than the high-energy yield. Then the angular current at the surface follows directly from Eq. (4.5): (A subscript δ is used throughout to distinguish parameters related to the high-energy electrons from those associated with the bombarding ion.)

$$J_\delta(\tau,\mu_\delta;r,T_{\delta 0}) = S_\delta(\mu_\delta,T_{\delta 0})\, T(r,T_{\delta 0}) \tag{5.78}$$

where $T(r,T_{\delta 0})$, defined by Eq. (4.3), represents the probability that an electron of initial energy $T_{\delta 0}$ can travel a distance r without stopping (The other notation used here follows the convention of Chap. 4.)

The evaluation of Eq. (5.78) is complicated because the source is generally non-isotropic, and the precise angular distribution depends on the type of bombarding particle involved. This is illustrated in Table 5.6, which lists the differential cross sections for electron production due to ion, electron, and photon bombardment. Expressed in terms of the differential cross section, the electron source rate becomes

$$S_\delta(\mu_\delta,T_{\delta 0}) = NZ \left(\frac{d\sigma}{d\mu_\delta}\right) \delta[T_{\delta 0}(\mu_\delta) - T_{\delta 0}] \tag{5 79}$$

where NZ, the number of electrons per target atom, is included because the differential cross section is on a per electron basis. The delta function appears because of the unique initial energy–angle relation represented by $T_{\delta 0}(\mu_\delta)$, which is to be taken from Table 5.6. (This relation arises because of energy and momentum conservation requirements.)

To calculate the current due to a bombarding particle of energy T_1, it is necessary to insert this source into Eq. (5.78) and integrate over all allowed δ-ray energies, i.e., over all $T_{\delta 0}$. Because of the delta function, we immediately obtain

$$J_\delta(\tau,\mu_\delta;r,T_1) = NZ \left(\frac{d\sigma}{d\mu_\delta}\right) T[r,T_{\delta 0}(\mu_\delta)]\ \mu_\delta \tag{5.80}$$

which after integration over r gives

Table 5 6 — RELATIONS FOR HIGH-ENERGY ELECTRON PRODUCTION

Bombarding Particle	Differential Cross Section/Electron, $d\sigma/d\mu_\delta$	Initial Energy, $T_{\delta 0}(\mu_\delta)$	Nomenclature
Ions, Rutherford scattering (p. 251, Ref 29)	$\frac{d\sigma}{d\mu_\delta} = \left(\frac{M}{m_e}\right)^2 \frac{\pi e^4 Z^2}{2T_1^2 \mu_\delta^3}$	$T_{\delta 0} = \frac{4m_e}{M} T_1 \mu_\delta^2$	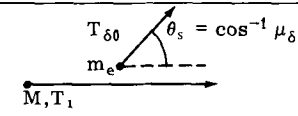
Relativistic electrons, Moller's approximation (p. 277, Ref 29)	$\frac{d\sigma}{d\mu_\delta} = \frac{4\pi e^4}{m_0 c^2}\left[\frac{(m_0c^2)^2}{T_1(T_1+2m_0c^2)}+1\right]\left[1+\frac{T_{\delta 0}}{2m_0c^2}\right] \times \left[\frac{1}{T_1^2} - \frac{1}{T_{\delta 0}(T_1 - T_{\delta 0})}\frac{m_0c^2(2T_1+m_0c^2)}{(T_1+m_0c^2)^2} + \frac{1}{(T_1-T_{\delta 0})^2} + \frac{1}{(T_1+m_0c^2)^2}\right]\frac{T_{\delta 0}}{\mu}$	$T_{\delta 0} = \frac{T_1\mu_\delta^2}{1+(T_1/2m_0c^2)(1-\mu_\delta^2)}$ where m_0 is the electron rest mass	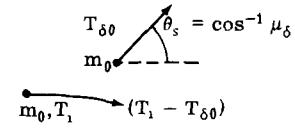
Photons, Klein-Nishina cross section (p. 318, Ref 29)	$\frac{d\sigma}{d\mu_\delta} = \frac{\pi r_0^2}{\mu_\delta^2}\left[\frac{2(\alpha+1)\mu_\delta^2}{(\alpha+1)^2-\mu_\delta^2\alpha^2}\right]^2 \times \left\{1+\left[\frac{(\alpha+1)^2(1-\mu_\delta^2)-\mu_\delta^2}{(\alpha+1)^2-\mu_\delta^2\alpha(\alpha+2)}\right]^2 + \left[\frac{4\alpha^2\mu_\delta^4}{[(\alpha+1)^2-\mu_\delta^2\alpha(\alpha+2)][(\alpha+1)^2-\mu_\delta^2\alpha^2]}\right]\right\}$ where $r_0 = \frac{e^2}{m_0c^2} = 2.818 \times 10^{-13}$ cm, $\alpha = h\nu_0/m_0c^2$	$T_{\delta 0} = \frac{2m_0c^2\mu_\delta^2}{A-\mu_\delta^2}$, $A = \left(1+\frac{m_0c^2}{h\nu_0}\right)^2$	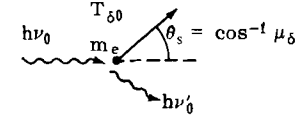

$$\frac{J_\delta(\tau,\mu_\delta;T_1)}{NZ\,(d\sigma/d\mu_\delta)\,\mu_\delta} = \begin{cases} \lambda_\delta[T_{\delta 0}(\mu_\delta)] & (0 < \mu_\delta < \tau/\lambda_\delta) \quad (5.81a) \\ \tau/\mu_\delta & (\tau/\lambda_\delta < \mu_\delta < 1). \quad (5.81b) \end{cases}$$

Note that Eq. (5.81a) covers the entire range of μ_δ in the limit of a thick plate; otherwise, both solutions must be retained.

5-6.2 Ion Bombardment

To proceed further, we must select a specific bombarding particle. For ion bombardment, the Rutherford scattering relations of Table 5.6 can be used. If the electron range is written as a function of angle using Eq. (3.26) and the initial-energy–angle relation of Table 5.6, we obtain

$$\lambda_\delta(\mu_\delta) \approx C_\delta^1 T_1^{(n_\delta+1)}\,\mu_\delta^{2(n_\delta+1)} \quad (5.82)$$

where

$$C_\delta^1 \equiv \frac{1}{C_\delta(n_\delta+1)}\left(\frac{4m_e}{M}\right)^{n_\delta+1}. \quad (5.83)$$

The constant C_δ corresponds to the constant C in Eq. (3.26) as applied to the high-energy electrons (δ-rays). The energy loss parameter n_δ should be evaluated for electrons (Table 3.4).

Substitution of this relation for the range into Eq. 5.81 gives the final form for the angular dependent current at the surface

$$\frac{J_\delta(\tau,\mu_\delta;T_1)}{\pi NZ^3e^4M^2/2m_e^2} = \begin{cases} C_\delta^1 T_1^{(n_\delta-1)}\,\mu^{2n_\delta} & (0 \le \mu_\delta \le \mu_\delta^*) \quad (5.84a) \\ \tau/(T_1^2\mu_\delta^3) & (\mu_\delta^* \le \mu_\delta \le 1) \quad (5.84b) \end{cases}$$

where

$$\mu_\delta^* = \tau/\lambda_\delta(\mu_\delta^*). \quad (5.85)$$

An explicit expression for the limit μ_δ^* can be found by use of Eq. (5.82) to represent $\lambda_\delta(\mu_\delta^*)$ in Eq. (5.85), which, upon solving for μ_δ^*, gives

$$\mu_\delta^* = \begin{cases} \chi^{1/(2n_\delta+3)} & (0 \le \chi \le 1) \quad (5.86a) \\ 1 & (\chi > 1) \quad (5.86b) \end{cases}$$

where the parameter χ, defined as

$$\chi \equiv \frac{\tau}{C_\delta^1 T_1^{(n_\delta+1)}} = \frac{\tau}{[\lambda_\delta]_{\mu_\delta=1}} \quad (5.87)$$

gives the ratio of the plate thickness to the maximum range of a δ-ray. In other words, $\chi \geq 1$ represents a "thick" plate relative to δ-ray production. (Since in general $\lambda_\delta \ll \lambda_i$, the plate can still be "thin" relative to the range of the bombarding ion as assumed at the start of the derivation. The terminology "thick" and "thin" in succeeding paragraphs will always refer to the δ-ray and its range.)

Written in terms of the parameter χ, Eqs. (5.84a and b) become

$$J_N \equiv \frac{J_\delta(\tau,\mu_\delta;T_i)}{J_\delta(\tau,1;T_i)} = \begin{cases} \dfrac{\mu_\delta^2}{\chi} & (0 \leq \mu_\delta \leq \chi^{1/(2n_\delta+3)}) \qquad (5.88a) \\ \mu_\delta^{-3} & (\chi^{1/(2n_\delta+3)} \leq \mu_\delta \leq 1) \qquad (5.88b) \end{cases}$$

where the "reduced" angular current J_N has been normalized to the current evaluated at $\mu_\delta = 1.0$.

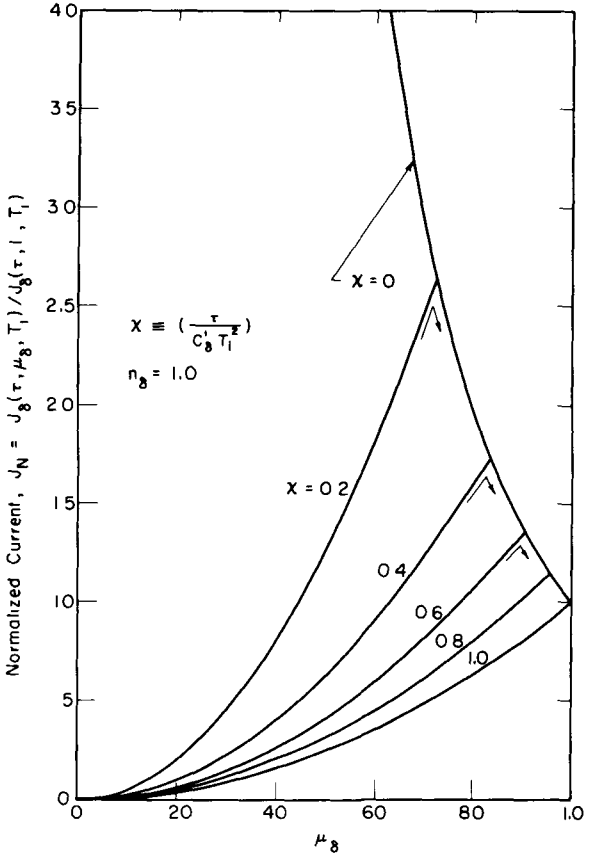

Fig. 5.20 — Angular dependence of the high-energy component of secondary emission due to low-q ion bombardment.

This result is illustrated for various values of χ in Fig. 5.20. The curves shown are for $n_\delta = 1.0$, which corresponds to δ-rays below 0.5 MeV. This should be quite realistic for ion energies of interest here; e.g., the maximum δ-ray energy $(4m_e/M)T_i$ (see Table 5.6) falls in the keV range for 1- to 10-MeV ions. [If higher energy ions are of interest, a second δ-ray energy group above 0.5 MeV might be added with $n_\delta = 0$; however, this makes the analysis more complicated since Eq. (5.84) must be divided into additional angular regions due to the δ-ray energy–angle dependence.]

Figure 5.20 has several important features. Note for a thick plate ($\chi \geq 1.0$) that forward directions are strongly favored. This is because δ-rays born with $\mu_\delta \approx 1.0$ have the largest energy, and for a thick plate, many of these δ-rays are able to escape even if they are born deep in the plate while those with lower energy ($\mu_\delta \ll 1$) are stopped. As the plate thickness is reduced, the volume contributing high-energy δ-rays decreases while the low-energy component electrons are essentially unaffected since they are born so close to the surface anyway. Thus, as χ is reduced below 1.0, the curves peak for $\mu_\delta < 1.0$ and are in a sense "depleted" at larger values of μ_δ. (The amplitudes of the peaks in Fig. 5.20 increase with decreasing χ because of the normalization employed—the actual magnitude of the current decreases.) In the extreme case of a very thin plate ($\chi \approx 0$), the angular dependence of the current reduces to that of the Rutherford cross section which varies as μ_δ^{-3} (Table 5.6).

The yield Δ_δ found by integration of the angular current over all allowed angles is

$$\Delta_\delta(T_i) \equiv \int J_\delta(\tau,\mu_\delta;T_i)\, d\mu_\delta$$

$$= \begin{cases} K_1\chi \left\{ \left[\dfrac{2(C_\delta^1)^2}{(2n_\delta+1)} + 1 \right] \chi^{-[2/(2n_\delta+3)]} - 1 \right\} T_i^{(n_\delta-1)} & (\chi \leq 1) \quad (5.89a) \\ \dfrac{2K_1(C_\delta^1)^2}{(2n_\delta+1)} T_i^{(n_\delta-1)} & (\chi \geq 1) \quad (5.89b) \end{cases}$$

where

$$K_1 \equiv \frac{\pi N Z^3 e^4 M^2}{4C_\delta^1 m_e^2}. \qquad (5.90)$$

It is seen from Eq. (5.89b) that in the limit of the "thick" plate the yield is independent of the energy of the bombarding particle (T_i) provided that $n_\delta = 1.0$ as argued earlier. However, this is not true for very thin plates since χ in Eq. (5.89a) is itself a function of (T_i). In the limit where $\chi \ll 1$, Eq. (5.89a) can be expanded to give

$$[\Delta_\delta(T_i)]_{\chi \ll 1} \approx 2K_1(C_\delta^1)^{(2n_\delta+5)/(2n_\delta+3)}\, \tau^{(2n_\delta+1)/(2n_\delta+3)}\, T_i^{-[1/(2n_\delta+1)]} \tag{5.91}$$

Thus, in this limit, for any reasonable value of n_δ, the yield always decreases with increasing bombardment energy. This is explained physically by noting that the yield is proportional to the energy deposited in the volume where the escaping δ-rays originate. For a thin plate this volume is the full thickness τ so the energy deposited, $[\langle dT_i/dx\rangle\tau]$, decreases with increasing ion energy because of the decrease in $\langle dT_i/dx\rangle$. In contrast, the escape depth for a thick plate is λ_δ, so the energy deposited is $[\langle dT_i/dx\rangle\lambda_\delta]$. Now the increase in λ_δ with ion energy tends to compensate for the decrease in $\langle dT_i/dx\rangle$, and according to Eq. (5.89b), if $n_\delta = 1.0$, these effects just cancel.

The energy spectrum of the escaping current is also often of interest. This can be calculated using the method developed in Sec. 4-1.2, Chap. 4. Corresponding to Eqs. (4.11) and (5.78), we write

$$J_\delta(\tau,\mu_\delta,T_\delta;T_{\delta 0}) = \frac{S_\delta(\mu_\delta,T_{\delta 0})\, T(r,T_{\delta 0})\, \mu_\delta}{|dT_\delta/dr|}. \tag{5.92}$$

If the energy loss law for δ-ray slowing,

$$T_\delta = T_{\delta 0}\left[1 - \frac{r}{\lambda(T_{\delta 0})}\right]^{1/(n_\delta+1)} \tag{5.93}$$

is used to evaluate $|dT_\delta/dr|$ and Eq. (5.79) is used for the source, the integration over all allowed initial energies can be carried out, and the current due to bombarding particle of energy T_i is found to be

$$J_\delta(\tau,\mu_\delta,T_\delta;T_i) = \frac{(n_\delta+1)\,\lambda(T_{\delta 0})\,NZ}{T_{\delta 0}}\left[\frac{T_\delta}{T_{\delta 0}}\right]^{n_\delta}\left(\frac{d\sigma}{d\mu_\delta}\right)\mu_\delta\,. \tag{5.94}$$

As in Eq. (4.12), the probability $T(r,T_{\delta 0})$ has been replaced with the requirement that $T_\delta > 0$. (It must be remembered when using this result that $T_{\delta 0}$ is a function of μ_δ.) The energy spectrum, found by integration over μ_δ, is then

$$\begin{aligned} J_\delta(\tau,T_\delta;T_i) &= \int J_\delta(\tau,\mu_\delta,T_\delta;T_i)\, d\mu_\delta \\ &= K_E\, T_\delta^{n_\delta} \int_{\mu_\delta}^{\mu_\delta^+} (d\mu_\delta/\mu_\delta^2) \end{aligned} \tag{5.95}$$

where

$$K_E \equiv \frac{\pi NZ^3e^4}{2C_\delta T_i^2}\left(\frac{M}{m_e}\right)^2 \tag{5.96}$$

and Eq. (5.82) has been used to evaluate $\lambda(T_{\delta 0})$, and the Rutherford cross section from Table 5.6 has been inserted for $(d\sigma/d\mu_\delta)$. Some care is required in evaluating the limits on μ_δ: The maximum value is simply $\mu_\delta^+ = 1$, but the minimum is more complex. The initial energy of the δ-ray $T_{\delta 0}$ must be equal to or larger than the energy of interest, T_δ. This requirement, combined with the angular dependence of initial energies from Table 5.6, defines the maximum angle of emission (minimum direction cosine), which we write as

$$T_\delta = T_{\delta 0}(\mu_\delta^-) = (\mu^-)^2 T_{\delta 0}^* \tag{5.97a}$$

or

$$\mu_\delta^- = \sqrt{T_\delta / T_{\delta 0}^*} \tag{5.97b}$$

where

$$T_{\delta 0}^* = \frac{4m_e}{M} T_i = [T_{\delta 0}]_{\mu_\delta = 1}. \tag{5.98}$$

Here, $T_{\delta 0}^*$ represents the maximum energy transferred to a δ-ray, and it becomes a convenient normalization for energy scales in the following equations.

These limits are sufficient for a thick foil, but, if it is thin in the sense that $\tau < \lambda_\delta$, the integration must be further split into two parts. This reasoning is entirely analogous to the situation encountered in Eqs. (4.12) and (4.17), and the critical angle is again given by $\mu_c = \tau/r$. Then integration of Eq. (5.95) gives

$$\frac{J_\delta(\tau, T_\delta; T_i)}{K_E T_\delta^{n_\delta}} = \begin{cases} \left(\sqrt{T_{\delta 0}^*/T_\delta} - 1\right) & (T_{\delta\tau} \le T \le T_{\delta 0}^*) \qquad (5.99a) \\ \left(\sqrt{T_{\delta 0}^*/T_\delta} - \dfrac{\tau}{r}\right) & (0 \le T \le T_{\delta\tau}) \qquad (5.99b) \end{cases}$$

where the dividing energy $T_{\delta\tau}$, defined as the energy at the surface for a δ-ray passing through the foil at $\mu_\delta = 1$, is given by

$$\frac{T_{\delta\tau}}{T_{\delta 0}^*} = \left[1 - \frac{\tau}{\lambda(T_{\delta 0}^*)}\right]^{1/(n_\delta + 1)} \tag{5.100}$$

The distance r appearing in Eq. (5.99b) must be eliminated by use of the energy loss law [Eq. (5.93)]. In doing this, we must take care to evaluate any angles involved at the critical value μ_c, in which case we find

$$r = \lambda[T_{\delta 0}(\mu_c)]\left\{1 - \left[\frac{T_\delta}{T_{\delta 0}(\mu_c)}\right]^{n_\delta+1}\right\}. \tag{5.101}$$

However, this is more complicated than previous calculations in Chap. 4 because $T_{\delta 0}$ now involves μ_c, which is itself a function of r. If τ/r is substituted for μ_c, we find after some algebra that

$$\left[\frac{r}{\lambda(T^*_{\delta 0})}\right]^{2(n_\delta+1)+1} + \left(\frac{T_\delta}{T^*_{\delta 0}}\right)^{n_\delta+1}\left[\frac{r}{\lambda(T^*_{\delta 0})}\right]^{2(n_\delta+1)} = \left[\frac{\tau}{\lambda(T^*_{\delta 0})}\right]^{2(n_\delta+1)} \tag{5.102}$$

where use has been made of the relations

$$(n_\delta + 1)C_\delta = \frac{(T^*_{\delta 0})^{n_\delta+1}}{\lambda(T^*_{\delta 0})}. \tag{5.103}$$

The latter follows from Eq. (3.26) and is simply a statement of the energy dependence of the range as evaluated at the maximum energy $T^*_{\delta 0}$. Since $\lambda(T^*_{\delta 0})$ and τ are fixed, the solution of Eq. (5.102) gives r as a function of T_δ, and substitution of this result back into (5.99b) gives the current as an explicit function of T_δ. The algebra is tedious, however, since even for $n_\delta = 0$ Eq. (5.102) reduces to a cubic equation, and $n_\delta = 1$ results in a fifth-order equation, so its roots are best found numerically.

Calculations of the current from Eq. (5.99) are shown in Fig. 5.21 as a function of the reduced energy $T_\delta/T^*_{\delta 0}$, for $n_\delta = 0$ and 1, and for several values of the plate thickness. For convenience a normalized current, defined as $J_\delta/K_E(T^*_{\delta 0})^{n_\delta}$, is plotted. Since, for most cases of interest here, a majority of the δ-rays have energies below ½ MeV, the results from $n_\delta = 1$ are of most practical importance.

The characteristics displayed by these curves deserve some explanation: Since $T^*_{\delta 0}$ represents the maximum δ-ray energy, all curves pass through $T_\delta/T^*_{\delta 0} = 1.0$. For both values of n_δ, low energies dominate; however, this is accentuated for $n_\delta = 0$, which favors larger energy losses early in the track so that the average electron leaves the plate with a smaller energy. This trend is consistent with the spectrum calculations shown earlier in Fig. 4.3 (cf. n = 0 and 1.0 curves) for a monoenergetic source; however, low energies are now even more strongly weighted (note the logarithmic scale of Fig. 5.21) because the Rutherford cross section favors low energies. This also explains the relatively weak dependence on plate thickness (τ/λ) observed in Fig. 5.21. As seen from Eq. (5.102), the range λ used is evaluated at the maximum δ-ray energy, and this is considerably larger than the range for the soft electrons. Thus, even when $\tau/\lambda = 0.25$, the plate is essentially "thick" for a bulk of the electrons leaving its surface.

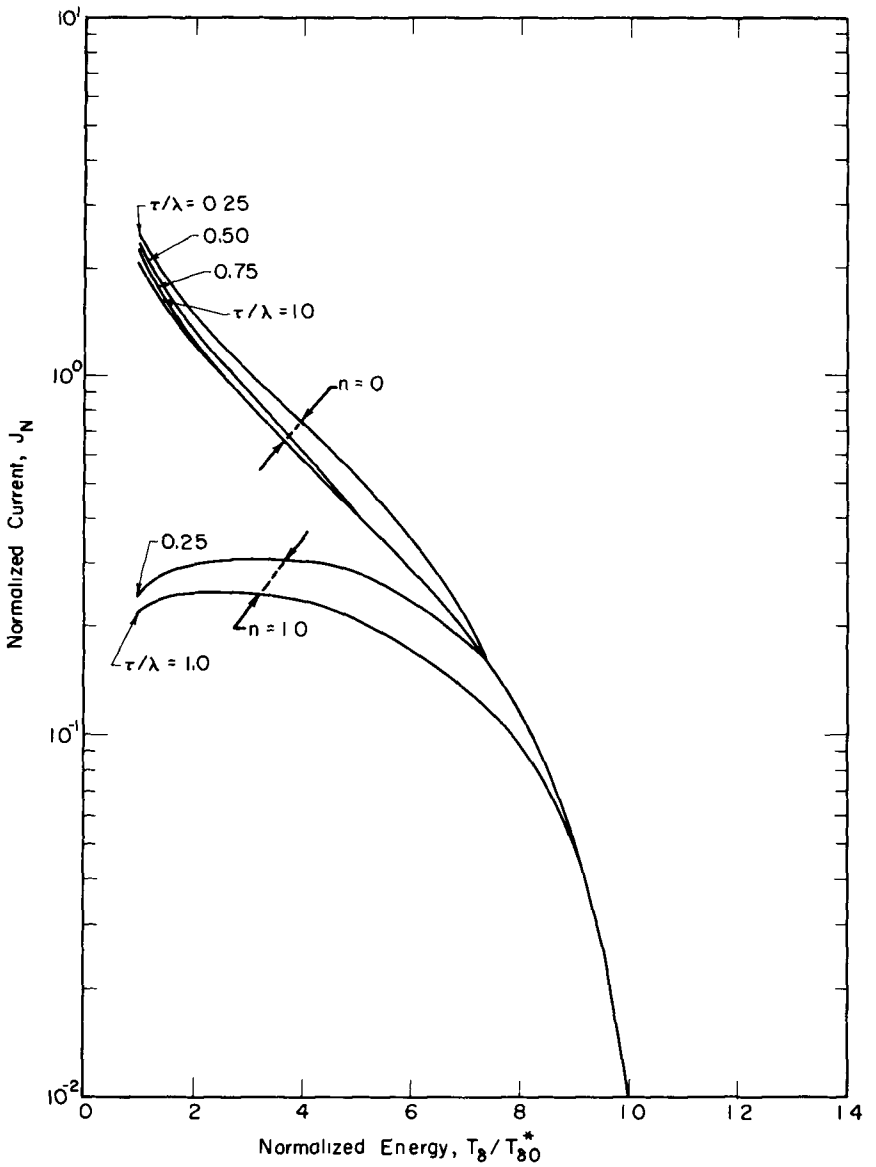

Fig. 5.21 — Energy spectra of the high-energy component due to low-q ion bombardment.

At this point, since it may be necessary to use a plane kernel in some problems, it is constructive to see how it might be applied to the preceding calculations. Consider the angular current calculation: Equation (5.78) is replaced by

$$J_\delta(\tau,\mu_\delta;x',T_{\delta 0}) = S_\delta(x',\mu_\delta,T_{\delta 0})\ T[(\tau-x')/\mu_\delta,\ T_{\delta 0}] \tag{5.104}$$

where $S_\delta(x', \mu_\delta, T_{\delta 0})\ dx'$ represents the δ-ray source rate per square centimeter at x' having directions corresponding to μ_δ per unit direction cosine and energy $T_{\delta 0}$ per unit energy (cf. Fig. 5.19). The probability $T[(\tau-x')/\mu_\delta,\ T_{\delta 0}]$ follows the same definition as earlier. As before, the integration over $T_{\delta 0}$ can be carried out immediately and corresponds to replacing $T_{\delta 0}$ with its value for a given direction [i.e., $T_{\delta 0}(\mu_\delta)$]. Then integration over x' gives the desired current

$$J_\delta(\tau,\mu_\delta;T_i) = NZ \int_0^\tau dx' \left(\frac{d\sigma}{d\mu_\delta}\right)\left\{1 - \int_0^{(\tau-x')/\mu_\delta} dy\ \delta[y-\lambda_\delta(T_i,\mu_\delta)]\right\}. \tag{5.105}$$

The major advantage of this formulation occurs when it is necessary to include the primary particle energy loss. Since both $d\sigma/d\mu_\delta$ and λ_δ depend on the energy T_i, they will be dependent on x' if T_i varies with x'.

It is easily shown that Eq. (5.105) reduces to the earlier result given in Eqs. (5.84a and b) for the case where T_i is independent of x'. The integration over the delta function in Eq. (5.105) can be evaluated by using Eq. (5.82) to represent λ_δ. The value of this integral changes from zero to one when

$$\frac{\tau-x'}{\mu_\delta} = C_\delta^1\, T_i^{(n_\delta+1)}\ \mu_\delta^{2(n_\delta+1)} \tag{5.106}$$

and this defines a lower limit on x' so that Eq. (5.105) can be written as

$$J_\delta(\tau,\mu_\delta;T_i) = NZ \int_{\tau-\gamma}^{\tau} \left(\frac{d\sigma}{d\mu_\delta}\right) dx' \qquad [(\tau-\gamma) \geq 0] \tag{5.107}$$

where

$$\gamma \equiv C_\delta^1\, T_i^{(n_\delta+1)}\ \mu_\delta^{(2n_\delta+3)}. \tag{5.108}$$

The requirement that $(\tau - \gamma)$ must be positive represents the division between a thin and thick plate. The break point occurs when $(\tau - \gamma)$ equals zero, so, using the definition for γ and solving for μ_δ, we find

$$\mu_\delta = \left[\frac{\tau}{C_\delta^1 T_i^{(n_\delta+1)}}\right]^{1/(2n_\delta+3)} \tag{5.109}$$

which is identical to Eq. (5.87) obtained earlier in the point-kernel calculation. Now, if the integration indicated in Eq. (5.107) is carried out with the Rutherford cross section, the same result as given in Eqs. (5.99a and b) is again obtained as expected.

5-6.3 Electron and Photon Bombardment

The extension of the preceding methods to electron or photon bombardment can be accomplished with the aid of the cross sections and energy–angle relations summarized in Table 5.6. However, these relations are somewhat complex, so numerical integrations are most expedient. A few calculations of this type have appeared in the literature. Sawyer and Van Lint[27] have considered both electron and photon bombardment, but, while their basic method of calculation is similar to the one presented here, there are some minor differences in the definition of ranges, etc. One point relative to electron bombardment deserves note: The bombarding particles cannot be distinguished from the emitted electrons in this case, and these authors define the secondary electron somewhat arbitrarily as the one leaving a collision with the lesser energy, so the cross section given in Table 5.6 is restricted to values of $T_{\delta 0} \leq (T_i/2)$.

Some of the results by Sawyer and Van Lint are shown in Figs. 5.22 to 5.25. The first illustrates that the high-energy yield increases with target thickness until the attenuation of the incident beam ultimately reserves this trend. The maximum value of 8% shown for 25-MeV electrons is in "general agreement" with unpublished experimental data by Poll and Van Lint noted in Ref. 27. Otherwise, no experimental comparisons with the calculations shown in this and the following three figures are available.

The next figure (5.23) shows that the most probable energy of escape is ≈ 0.15 MeV for bombardment by prompt fission gamma rays and 25-MeV electrons. The 600 kV x-ray spectrum does not reach a maximum on the scale shown and was not reported. The angular distribution of the high-energy secondaries for 25-MeV electron bombardment is shown in Fig. 5.24, and the final plot (Fig. 5.25) is of value for quick current estimates. The use of the latter is illustrated by Sawyer and Van Lint for a target of thickness 0.01 g/cm^2 exposed to a prompt fission gamma-ray field of 7×10^9 rads/sec. A high-energy secondary current of ≈ 1 mA/cm^2 is indicated; thus, if it is desired to study this effect in the laboratory, one could, according to the graph, use a 25-MeV electron accelerator capable of a dose rate of 3×10^{10} rads/sec or alternately a 600 kV x-ray source of 2.5×10^9 rads/sec.

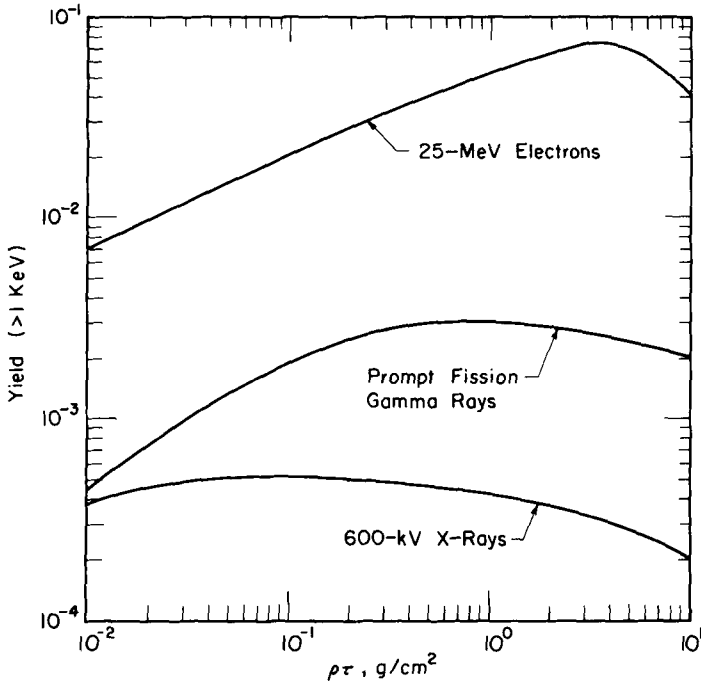

Fig. 5.22 — Variation of the high-energy yield with target thickness for electron and photon bombardment of aluminum. (From Sawyer and Van Lint, Ref. 27.)

Stevens and Artuso[22] have considered bombardment by gamma rays from ^{60}Co, ^{137}Cs, and ^{24}Na, and their calculations are again similar to those described earlier except for several details. (One point is of special interest: Instead of using a mean range concept, they used the Mar transmission function described in Chap. 3 [Eq. (3.65)] to provide a correction for straggling.)

Some of their results are presented in Figs. 5.26 and 5.27. The first figure shows the calculated angular current emitted from three different target materials bombarded by ^{60}Co gamma rays. The target thickness was chosen to be just equal to the range of the most energetic Compton electron produced in it. A maximum is predicted at about 10° as contrasted to about 30° for the 25-MeV electron bombardment discussed earlier, probably because the Compton scattering process is more peaked in the forward direction. However, in this case some experimental data are available — reported by Ebert and Lauzon[28] for an aluminum target — and, as seen from the figure, these data indicate the maximum occurs at a much larger angle. The cause of this discrepancy is not known. In this regard, Stevens and Artuso note that,

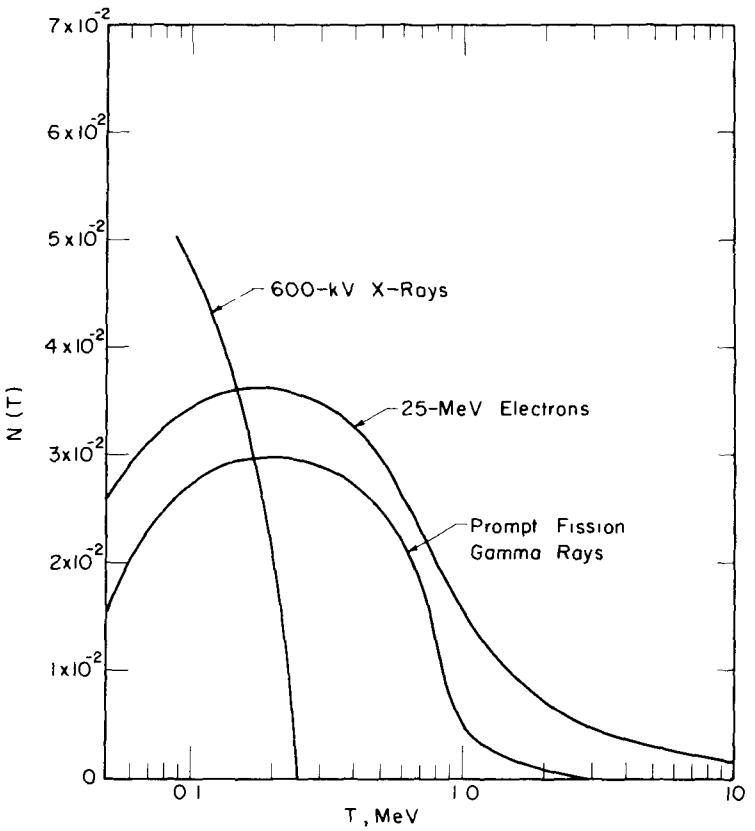

Fig 5.23 — High-energy component energy spectrum for electron and photon bombardment [From Sawyer and Van Lint, Ref. 27. A 1 g/cm^2 aluminum target is assumed The ordinate N(T) represents the number of high-energy (>1 keV) secondary electrons escaping with energy T, per MeV energy interval, per incident particle.]

despite the large differences in the precise angular distribution, the total yield they calculate agrees with the measured value within 10%.

The calculated energy spectrum is compared with measurements by Oda and Suzuki[30] in Fig 5.27. Both curves peak at about 0.8 MeV; however, the calculated values are several orders of magnitude lower than the experimental data at low energies. Again, the cause of this discrepancy is uncertain. It is possibly due to the neglect of knock-on electrons produced by the primary Compton electrons in the calculations. Indeed these electrons might be expected to enhance the spectrum in the 10 to 100-keV range.

In conclusion, it appears that continued experimental and theoretical efforts are warranted to resolve the differences observed and to extend the range of comparisons.

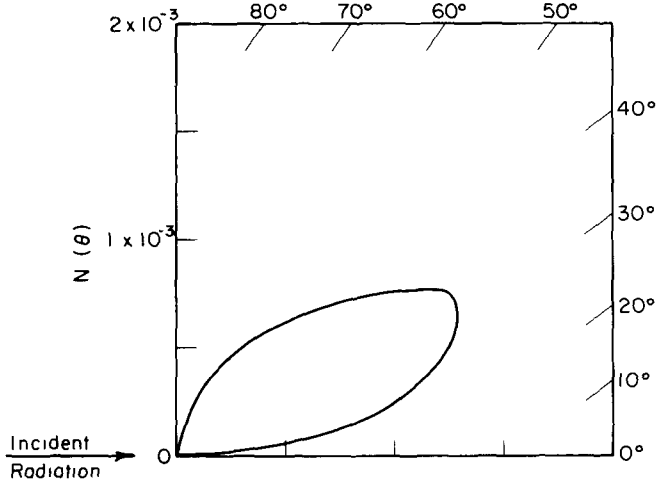

Fig. 5.24—Angular distribution of the high-energy component for 25-MeV electron bombardment of a 1 g/cm^2 aluminum target. [After Sawyer and Van Lint, Ref. 27. N(θ) is the emission angular spectrum for secondary electrons >1 keV, per degree, per incident particle.]

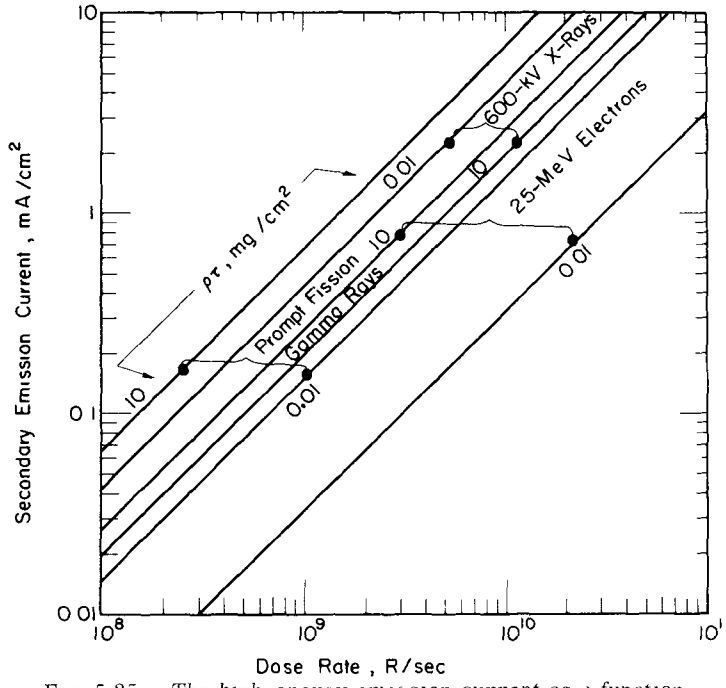

Fig. 5.25—The high-energy emission current as a function of dose rate for various aluminum thicknesses and various sources. (After Sawyer and Van Lint, Ref. 27.)

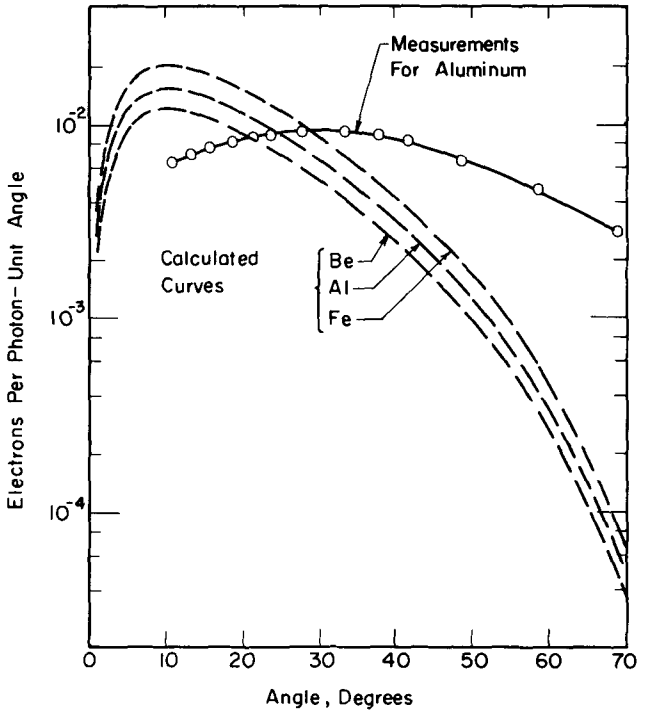

Fig. 5.26 — Comparison of measured and calculated angular distribution of high-energy electrons emitted by ^{60}Co gamma-ray bombardment. (The calculated curves are from Stevens and Artuso, Ref. 22; the data points are based on measurements by Ebert and Lauzon, Ref. 28.)

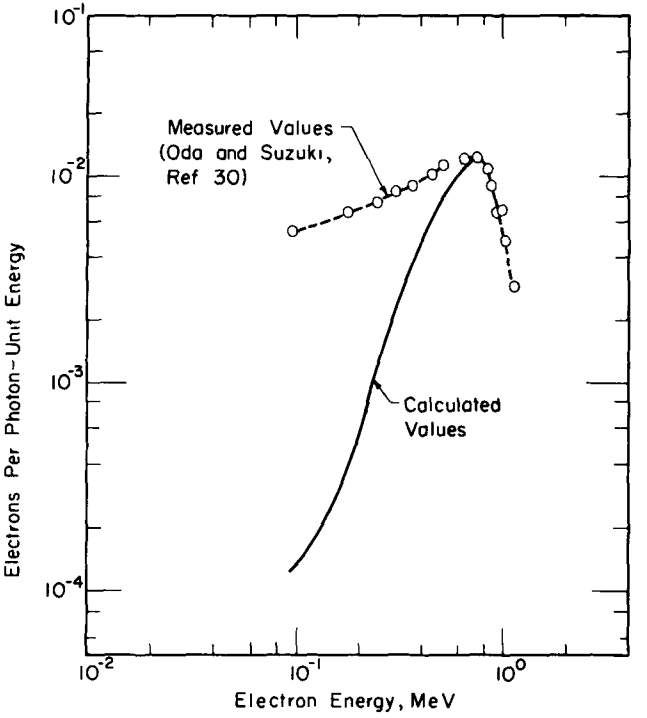

Fig. 5.27 — Comparison of measured and calculated energy spectrum for high-energy electrons emitted from iron bombarded by ^{60}Co gamma rays. (From Stevens and Artuso, Ref. 22.)

5-7 ELECTRON BACKSCATTERING

During electron bombardment, the emission current at the bombarded surface consists of reflected primary electrons, commonly termed "backscattered electrons," as well as secondary electrons. Experimentally, it is not possible to distinguish unambiguously a reflected primary from a secondary, but, as discussed earlier, secondaries are arbitrarily identified as the component with energies < 50 eV, so backscattered electrons are generally defined as those having higher energies. It is recognized that "true" primaries may end up being counted as secondaries and vice versa, but this provides a working definition.

Backscattering is obviously closely related to secondary emission, and it is an important phenomenon in its own right in Beta and also Secondary-Emission Cells. Backscattered electrons from the collector in these cells can represent an important loss in both current and efficiency.

Experimental studies of backscattering were reported as early as 1923 by Schonland[31], and the well-known work of Sternglass[32] was carried out in 1954. Some of the more recent studies are indicated in Refs. 33 to 37; the work of Cohen and Koral[37] is of particular interest because it grew out of Beta Cell studies.

Some theoretical studies are indicated in Refs. 38 to 42; however, Everhart[39] pointed out in 1960: "It is somewhat surprising that little theoretical consideration has been given to the reflected electrons." While there has been some additional work since then, this observation is still appropriate.

Bethe's original approach[38] assumed that the primary electron travels straight into the target and then, at a certain point, undergoes a uniform diffusion process. This approach neglects the possibility of reflection by single, large-angle scattering events. Taking the opposite point of view, Everhart[39] neglected multiple collisions and assumed reflection is entirely due to large-angle scattering. Later, Archard[40] attempted to combine these two extremes, and his theory was developed further by Tomlin[41]. Noting that these approximations have met "with only limited success," Dashen[42] has developed an "exact" integral equation; however, the solution of this equation requires fairly elaborate numerical methods unless simplifying assumptions are made.

In the present development, we rely heavily on the approximate treatments of Everhart[39] and Archard[40]. They fit in nicely with the previous development of electron transport and give fairly accurate results.

First, consider large-angle scattering due to elastic collisions between electrons and the target nuclei: An idealized planar target with

perpendicular incidence is illustrated in Fig. 5.28. Everhart shows that Rutherford's scattering formula is reasonably accurate for electrons even at fairly low energies; e.g., >170 eV for Al, >1900 eV for Au. Then, assuming Rutherford scattering dominates, the probability of an electron of mass m and speed v(x) in a volume dx at x scattering

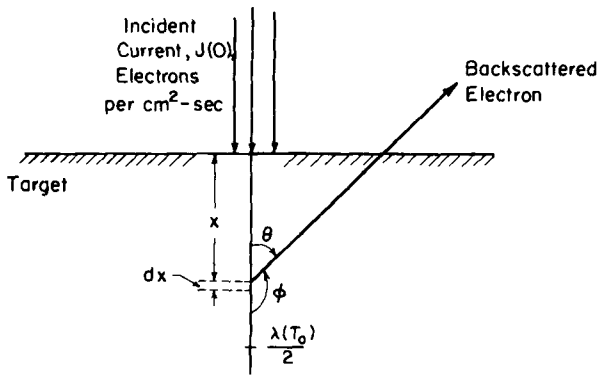

Fig. 5.28—Geometry for backscattering calculations.

through an angle ϕ per unit angle in a target which consists of N nuclei per cubic centimeter of atomic number Z is[14,39]

$$N\left(\frac{d\sigma}{d\phi}\right) dx = \frac{NZ^2e^4}{4m^2[v(x)]^4} \sin^{-4}\left(\frac{\phi}{2}\right) dx \tag{5.110}$$

where e is the electronic charge. The speed v(x) can be evaluated using the energy loss model of Chap. 3, which in terms of speed is simply

$$\left[\frac{v(x)}{v_0}\right]^2 = \left[1 - \frac{x}{\lambda(v_0)}\right]^{1/(n+1)} \tag{5.111}$$

where v_0 is the incident speed and x is the distance of penetration into the target (Fig. 5.29). Combining these relations, we find the differential current of electrons deflected through an angle θ per unit angle at a normalized depth Y is

$$J(Y,\theta) = \frac{NZ^2e^4\,\lambda(v_0)}{4mv_0^4 \cos^4(\theta/2)} \frac{J(Y)\sin\theta}{(1-Y)^{[2/(n+1)]}} \tag{5.112a}$$

where J(Y) is the total electron current reaching a depth Y in the target; the angles involved are related by (Fig. 5.28)

$$\theta = \pi - \phi \tag{5.112b}$$

and the reduced dimension Y is defined as

$$Y = x/\lambda(v_0). \tag{5.112c}$$

Following arguments originally advanced by Everhart, we will assume that any electron suffering a deflection through an angle greater than 90° is lost to the lower layers but that those deflected at smaller angles effectively continue straight ahead; thus

$$J(Y) \approx J(0) - \int_0^Y dY' \int_0^{\pi/2} J(Y',\theta)\, d\theta. \tag{5.113}$$

Archard[40] has pointed out that some improvement can be made by further assuming that half the electrons deflected at small angles are also lost since a second collision occurring after an average deflection of 45° is equally likely to cause the electron to reverse its direction or continue forward. His approximation would replace Eq. (5.113) with

$$J(Y) \approx J(0) - \int_0^Y dY' \left[\int_0^{\pi/2} J(Y',\theta)\, d\theta + \frac{1}{2} \int_{\pi/2}^{3\pi/4} J(Y',\theta)\, d\theta \right]. \tag{5.114}$$

However, in interest of simplicity, we will neglect this correction in the present development. Then, after the angular integration, we find from Eq. (5.113) that

$$J(Y) = J(0) - g \int_0^Y \frac{J(Y')\, dY'}{(1 - Y')^{2/(n+1)}} \tag{5.115}$$

where

$$g = \frac{\pi N Z^2 e^4 \lambda(v_0)}{m^2 v_0^4} \tag{5.116}$$

(Note that since $NZ^2 \propto Z^2/A$ where A is the atomic weight of the target to a first approximation, $g \propto Z$.) This integral equation for J(Y) may be converted to a differential equation by differentiation with respect to Y, which gives

$$\frac{dJ(Y)}{J(Y)} = -g \frac{dY}{(1-Y)^{2/(n+1)}}. \tag{5.117}$$

For electrons, n = 1 and n = 0 are of interest, representing energies below and above ½ MeV, respectively (Table 3.4), and the corresponding solutions of Eq. (5.117) are

$$\frac{J(Y)}{J(0)} = \begin{cases} (1-Y)^g & (n = 1) \quad (5.118a) \\ \exp\left(\frac{gY}{Y-1}\right) & (n = 0) \cdot \quad (5.118b) \end{cases}$$

These results, when substituted back into Eq. (5.112), complete the evaluation of the differential current $J(Y,\theta)$, and this may in turn be used to find the differential reflection coefficient $r(Y,\theta)$ defined as

$$r(Y,\theta) = \frac{J(Y,\theta)}{J(0)}. \quad (5.119)$$

The total reflection coefficient r is found by integration over all allowed values of Y and θ, which, as seen from Fig. 5.28, are

$$0 < \theta < \theta_m \quad (5.120a)$$

$$0 < Y < \tfrac{1}{2} \quad (5.120b)$$

where θ_m is defined by

$$Y(1 + \sec \theta_m) = 1. \quad (5.121)$$

Integration of Eq. (5.119) using these limits gives

$$r = \begin{cases} (g - 1 + 0.5^g)/(g + 1)g & (n = 1) \quad (5.122a) \\ (2 - e^{-g}) - (1 + 2g)e^g \ln 2 \\ -g + \sum_{j=2}^{\infty} [(-1)^j(2^j - 1)g^j]/j \cdot j! \end{cases} \quad (n = 0) \quad (5.122b)$$

where e is the base of the natural logarithm.

The result for n = 1 is essentially the same as that obtained earlier by Everhart, who based his derivation on the Thomson–Whiddington Law for electron slowing, and his calculations (solid curves) are compared with experimental data in Fig. 5.29. The lower curve corresponds to an independent evaluation of the parameter "g" based on Terrill's measurements[43], and Everhart found it necessary to empirically adjust "g" in order to obtain the upper curve, which represents a better fit to the data. He attributed this problem to the neglect

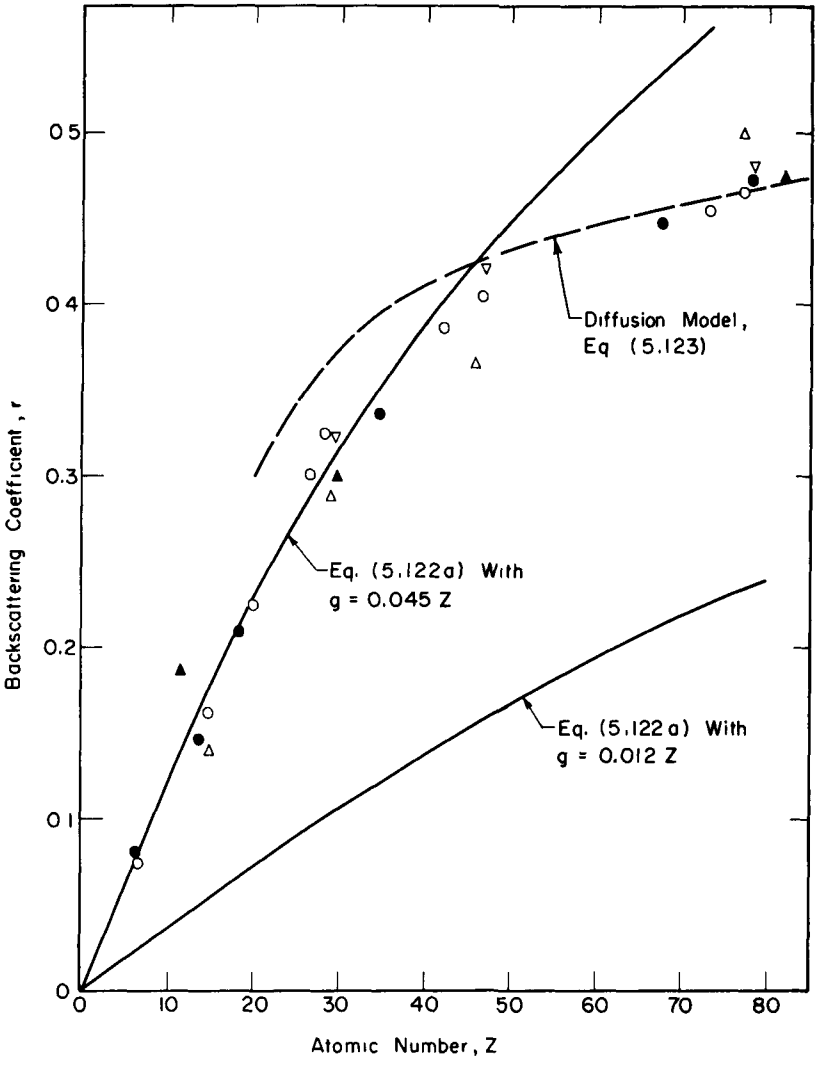

Fig. 5.29 — Comparison of calculated and experimental reflection coefficients. (After Everhart, Ref. 39, and Archard, Ref. 40, including data collected by them from various workers for bombardment in the range 10 to 100 keV.)

of multiple scattering; however, more recent studies by Archard indicate that much of the discrepancy is eliminated if Eq. (5.114) is used to evaluate J(Y) instead of Eq. (5.113). While this correction, or alternately the adjustment of "g", permits a good fit to experimental data for $Z < 40$, the experimental data remain consistently lower than predicted for higher Z (Fig. 5.29). This appears to indicate a fundamental weakness in the model which Archard has attributed to the increased importance of diffusion-like transport for high-Z materials. Using a diffusion model, he shows that

$$r \approx \frac{7Z-80}{14Z-80} \tag{5.123}$$

which is included as a dashed line in Fig. 5.29. This gives much better agreement at high Z, and a combination of the two theories affords a reasonably accurate simple model for backscattering.

The data in Fig. 5.29 include a range of bombarding energies. This might be questioned since r depends on the incoming energy through g, which is a function of v_0 [Eq. (5.116)]. However, the resulting variation in r, as indicated in Fig. 5.30, is gradual for many materials and can be taken as essentially constant over rather broad energy regions.

The preceding development can also be used to evaluate the energy returned by backscattered electrons. According to Fig. 5.28, a reflected electron will travel a total distance $x(1 + \sec\theta)$, and, if this is substituted for the distance in Eq. (5.111), we find that K, the ratio of the energy of the reflected electron to its entering energy, is

$$K = [1 - Y(1 + \sec\theta)]^{1/(n+1)}. \tag{5.124}$$

The mean fractional energy return $\bar{K}$ is then given by

$$\bar{K} = \frac{\int dY \int K\, J(Y,\theta)\, d\theta}{\int dY \int J(Y,\theta)\, d\theta} \tag{5.125}$$

where $J(Y,\theta)$ can now be taken from Eq. (5.112) and the integration limits are given in Eqs. (5.120a and b). (Note that $\bar{K}$ is defined per backscattered electron; thus, the actual fraction of the incident energy that is returned is $(r\bar{K})$, where r is the reflection coefficient.)

Everhart has computed $\bar{K}$ assuming $n = 1$, and a comparison with some experimental data is shown in Fig. 5.31. The data he used were for a small $\Delta\theta$ about a fixed angle, so the angular integration indicated in Eq. (5.125) was omitted in evaluating the curves in this figure. As is seen, the agreement with the data is not too good; however, the data are not internally consistent, and further studies are required before the

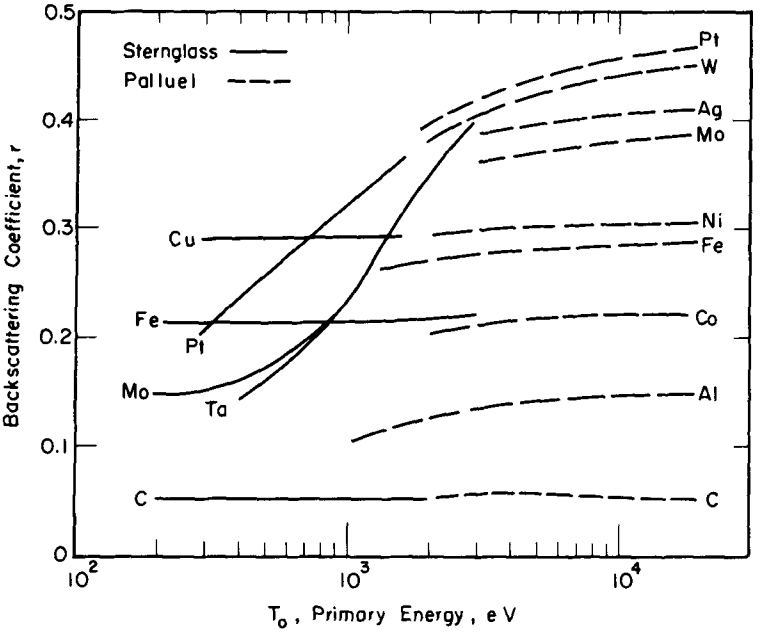

Fig. 5.30 — Variation of the backscattering coefficient with energy of the primary electron for various materials. (From Dekker, Ref. 1, based on data from Sternglass and Palluel.)

accuracy of the model can be fully assessed. (Note that much better agreement is obtained with the several data points for 15° and 75° that were taken by a single worker as opposed to the other data at 8° and 45° from two other studies.)

Some further trends are illustrated in Fig. 5.32 which show the energy spectrum of backscattered electrons from various targets due to bombardment at ≈2 keV and 0.68 MeV. As indicated, the mean value $\overline{K}$ lies between 0.4 and 0.6 for 2 keV bombardment, and, while it is not reported, $\overline{K}$ for the 0.68-MeV case is obviously shifted to higher values (≈0.6 to 0.8).

While the relations developed above give some insight into the mechanisms involved, from a practical point of view it is worthwhile to note some recent empirical correlations reported by Koral and Cohen[44]. These correlations, based on their own experiments[37], offer good accuracy over a range of variables and for primary energies from 0.6 to 1.8 MeV corresponding to typical beta-particle energies.

They define r_m as the maximum backscattering ratio for normal incidence, which occurs in the limit where the target thickness equals or exceeds $[\lambda(v_0)/2]$ (Fig. 5.28). Noting that r/r_m is essentially independent of the primary electron energy, they have correlated this ratio

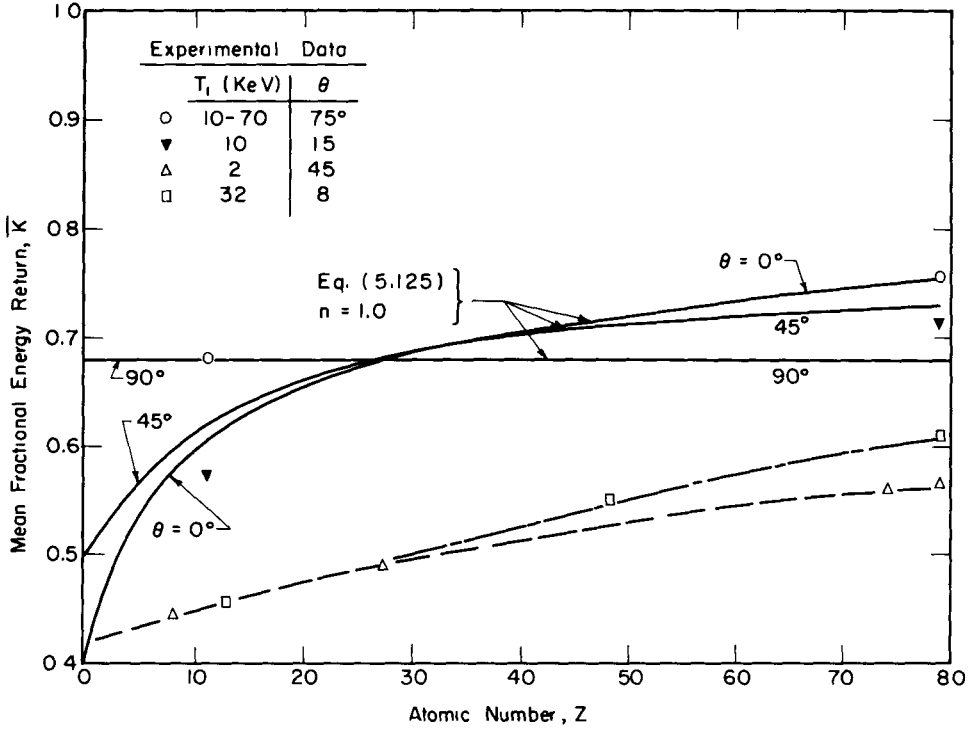

Fig 5 31 — A comparison of calculated and measured values of the mean fractional energy of reflected electrons vs Z (After Everhart, Ref 39)

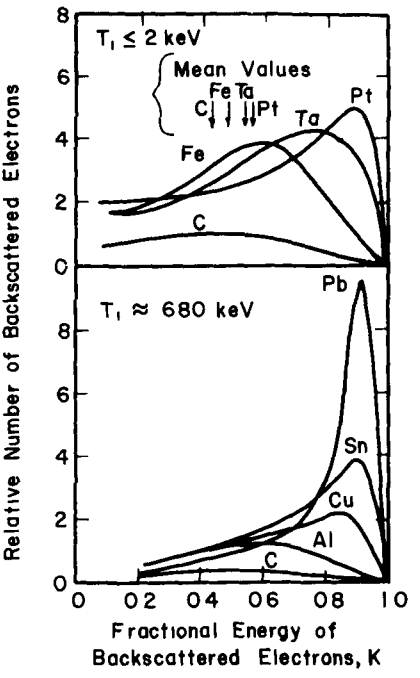

Fig 5.32 — Fractional energy of backscattered electrons for two different primary electron energies (From Dekker, Ref. 1, based on data by Sternglass and Bothe)

with target thickness, and for normal incidence they suggest

$$\frac{r}{r_m} - 1 - \exp\left[-\alpha(2\tau/\lambda)\right]^b + f \tag{5 126}$$

where α and b, the principal fitting parameters, are defined as

$$\alpha = 0.760Z^{0\ 55} \tag{5.127a}$$

$$b = 2.32 - (8.40 \times 10^{-3})Z \tag{5.127b}$$

and f is a small non-systematic correction factor. These three parameters are listed in Table 5.7 for seven elements.

Koral and Cohen have also studied the dependence on the angle of incidence. They find that the reflection coefficient r_ψ for electrons incident at an angle ψ (relative to the surface normal) can be correlated with τ by using a slightly modified version of Eq. (5.126), namely

$$\frac{r_\psi}{r_{m\psi}} = 1 - \exp\left[-\alpha\left(\frac{2\tau}{\lambda}\right)^{bC_\psi}\right] + f \tag{5.128}$$

Table 5.7 — TYPICAL PARAMETERS FOR THE KORAL AND COHEN CORRELATION[44]

(a) The Parameters α, b, and f for Various Materials

Material	Atomic Number, Z	α	b	f
Aluminum	13	3.13	2.21	0.05
Iron	26	4.81	2.11	0.015
Nickel	28	4.90	2.08	0.015
Molybdenum	42	6.05	1.94	0.005
Silver	47	6.82	1.92	0.005
Tantalum	73	8.41	1.70	≈ 0
Gold	79	8.58	1.65	≈ 0

(b) The Parameter B for Aluminum, Molybdenum, and Gold

Material	Energy (MeV)	Range, λ (mg/cm^2)	B (10^{-2}/deg)
Aluminum	0.8	309.0	3.10
	1.2	517.2	3.32
	1.8	838.4	3.63
Molybdenum	0.8	340.2	1.77
	1.2	569.0	1.88
	1.8	922.2	2.07
Gold	0.8	371.0	1.29
	1.2	620.6	1.38
	1.8	1006.0	1.51

(c) The Parameter C_ψ for Molybdenum

Angle of Incidence, ψ (deg)	C_ψ
0	1.00
30	0.825
45	0.716
60	0.551

where $r_{m\psi}$ represents the variation of r_m with ψ which is found to be of the form

$$\frac{r_{m\psi}}{r_m} = \cosh(B\psi) \tag{5.129a}$$

and

$$B = Z^{-1/2}\,[0.333 \times 10^{-4}\,\lambda + 0.103] \tag{5.129b}$$

with λ in milligrams per square centimeter. For convenience, typical values of B are also given in Table 5.7. The other new function introduced here, C_ψ, essentially represents an angular dependent correction to the parameter b. Unfortunately, a correlation for C_ψ is not available, and the only values reported (Table 5.7) are from a fit to experimental data for molybdenum.

5-8 SUMMARY

The important process of secondary electron production has been developed using an Ionization–Diffusion model to calculate low-energy yields and a hard collision–δ-ray transport model to calculate high-energy yields. Although similar to earlier calculations for electron bombardment, the present results offer considerably more flexibility in that the extension to other bombarding particles, e.g., alpha particles, protons, fission fragments, etc., is simply accomplished by substitution of appropriate values of the range λ and slowing parameter n.

Calculated low-energy yields for bombardment by high-energy, low-q ions were shown to be in reasonable agreement with experimental data; however, the agreement for bombardment by fission fragments or gamma radiation is only approximate.

The effects of geometry, angle of incidence, temperature, and electric fields on the low-energy yield were reviewed. Geometry and incidence angle in particular were found to be extremely important; e.g., the yield for an isotropic incident flux was found to be roughly twice that for normal incidence. Likewise the yield for the exit side of a thin plate was approximately double that for the side where the ion beam enters. It was also noted that, because of their relatively large diffusion length, the yield for insulators is considerably larger than for metals or semiconductors.

High-energy emission has received less attention in the literature. While a theory for ion bombardment is developed here, little or no experimental data is available for comparison. Some comparisons of similar calculations for gamma-ray bombardment have been reported, and, while the total yields seem to agree fairly well, there is poor agreement with the measured energy and angular distributions.

Because of its intimate relation to secondary production and its importance in cell operation, electron backscattering was also considered. A simplified theory incorporating the slowing law of Chap. 3 predicts reflection coefficients with fair accuracy but gives the fractional energy of the reflected electrons with less confidence.

In conclusion, these methods should be of value in the design of high-power cells where it is desired to suppress secondaries, and also in special cells or instrumentation concepts that operate on the current produced by secondary emission.

REFERENCES

1. A. J. Dekker, "Secondary Electron Emission," in *Solid State Physics*, Advances in Research and Applications, F. Seitz and D. Turnbull (Eds.), Vol. 6, pp. 251-311, Academic Press, New York, 1958.
2. H. Bruining, *Physics and Applications of Secondary Electron Emission*, Pergamon Press Ltd., London, 1954.
3. O. Hachenberg and W. Brauer, "Secondary Electron Emission from Solids," in *Advances in Electronics and Electron Physics*, Vol. XI, pp. 413-499, Academic Press, New York, 1959.
4. H. S. W. Massey and E. H. S. Burhop, *Electronic and Ionic Impact Phenomena*, Chaps. V and IX, Oxford at the Clarendon Press, 1952.
5. M. Kaminsky, *Atomic and Ionic Impact Phenomena on Metal Surfaces*, Chap. 14, Academic Press, New York, 1965.
6. E. W. McDaniel, *Collision Phenomena in Ionized Gases*, Chap. 13, John Wiley & Sons, New York, 1964.
7. S. C. Brown, *Introduction to Electrical Discharges*, Chap. VII, John Wiley & Sons, New York, 1966.
8. J. N. Anno, "Secondary Electron Production from Alpha Particles and Fission Fragments," Ph. D. Thesis, Physics and Astronomy Depts., Ohio State University, Columbus, Ohio, 1965.
9. S. Kronenberg, "High-Intensity Radiation Dosimetry with Semirad," U. S. Army Research and Development Monograph Series, No. 3, Chap. 6, U.S.A. Electronics Command, Fort Monmouth, New Jersey, 1966.
10. E. Rudberg, "Inelastic Scattering of Electrons from Solids," *Phys. Rev., 50:* 138 (1936).
11. L. Miller and W. C. Porter, "Secondary-Electron Emission by Primary Electrons in the Energy Range of 20 keV to 1.3 MeV," *J. Franklin Inst., 260:* 31 (July–December 1955).
12. J. G. Trump and R. J. Van de Graaff, "The Secondary Emission of Electrons by High Energy Electrons," *Phys. Rev., 75* 1 (1949).
13. S. Kronenberg, K. Nilson, and M. Basso, "Emission of Secondary Electrons from Metals by 1-MeV Protons," *Phys. Rev., 124:* 1709 (1961).
14. R. D. Evans, *The Atomic Nucleus*, pp. 574-581, McGraw-Hill, New York, 1955.
15. N. Bohr, "The Penetration of Atomic Particles through Matter," *Kgl. danske Vidensk Selsk., mat fysiske, 18:* 8 (1948).
16. P. L. Kapitza, "On the Theory of δ-Radiation," *Philos. Mag., 45:* 989 (1923).
17. E. J. Sternglass, "The Theory of Secondary Electron Emission by High Speed Ions," *Phys. Rev., 108:* 1 (1957).
18. J. N. Anno, "Secondary Electron Production from Fission Fragments Emerging from Thin Layers of Uranium Dioxide," *J. Appl. Phys., 33:* 1678 (1962).
19. F. E. Jamerson, C. B. Leffert, and D. B. Rees, "Secondary Electron Yield from Fission Fragments," *J. Appl. Phys., 36:* 355 (1965).
20. W. E. Stein and R. B. Leachman, "Fast Detector of Heavy Particles," *Rev. Sci. Inst., 27·* 1049 (1956).
21. H. Etherington (Ed.), *Nuclear Engineering Handbook*, p. 7-63, McGraw-Hill, New York, 1958.
22. J. Stevens and J. F. Artuso, "Nuclear Studies of the Compton Diode, Fiscal Year 1966," Tech. Report No. S-349-R, EGG-1183-2110, the EG&G Company, Santa Barbara, Calif., November 1966.
23. J. N. Anno and R. G. Jung, "Comparison of Secondary Electron Yield from Emerging from and Impinging upon a Thin Layer of Uranium Dioxide," *J. Appl. Phys., 36:* 3949 (1965).
24. E. M. Baroody, "A Theory of Secondary Electron Emission from Metals," *Phys. Rev., 78:* 780 (1950).

25. M. Abramowitz and I. A Stegun (Eds.), "Handbook of Mathematical Functions," Nat. Bureau of Standards, *Appl. Math Ser., 55* (1964).
26. J. B. Rosser, *Theory and Application of* $\int_0^z e^{-x^2} dx$ and $\int_0^\tau e^{-\psi^2 y^2} dy \int_0^y e^{-x^2} dx$, Mapleton House, Brooklyn, New York, 1948.
27. J. A. Sawyer and V. A. J. van Lint, "Calculation of High-Energy Secondary Electron Emission," *J Appl Phys , 35* 1706 (1964).
28 P. J. Ebert and A. F. Lauzon, "Measurement of Gamma-Ray Induced Secondary Electron Current from Various Elements," UCRL-14270, Lawrence Radiation Laboratory, September 1965.
29. H. Bethe and J. Askin, "Passage of Radiations Through Matter," in *Experimental Nuclear Physics,* Vol. 1, pp. 166-358, E. Segrè (Ed.), John Wiley & Sons, New York, 1953.
30. N. Oda and H. Suzuki, "Energy Spectra of Secondary Electrons in Various Material Irradiated by Gamma Rays from Co-60 and Cs-137," *J Phys Soc. of Japan, 15* 2365 (1960).
31. B. F. J. Schonland, "The Passage of Cathode Rays Through Matter," *Proc Roy Soc (London), A104* 235 (1923). See also *Proc Roy Soc (London), A108* 187 (1925).
32. E. J Sternglass, "Backscattering of Kilovolt Electrons from Solids,", *Phys. Rev , 95* 345 (1954).
33. J. E. Holliday and E. J. Sternglass, "Backscattering of 5–20 keV Electrons from Insulators and Metals," *J Appl Phys , 28* 1189 (1957).
34. H. Kanter, "Zur Rückstreuung von Elektronen im Energiebereich von 10 bis 100 keV," *Annalen der Physik, Series 6, 20* 144 (1957).
35. T. L. Matskevich, "Investigation of Electron-Reflection by Dielectrics," *Soviet Phys.–Tech. Phys., 2* 255 (1957).
36. K. Wright and J. Trump, "Back-scattering of Megavolt Electrons from Thick Targets," *J Appl Phys , 33* 687 (1962).
37. A. J. Cohen and K. F. Koral, "Backscattering and Secondary-Electron Emission from Metal Targets of Various Thicknesses," NASA-TN-D-2782, NASA Lewis Research Center, April 1965.
38. H. Bethe, "Zur Theorie des Durchgangs Schneller Korpuskularstrahlen durch Materie," *Annalen der Physik, Series 5, 5* 325 (1930).
39. T. E. Everhart, "Simple Theory Concerning the Reflection of Electrons from Solids," *J. Appl. Phys., 31* 1483 (1960).
40. G. Archard, "Backscattering of Electrons," *J Appl Phys , 32* 1505 (1961).
41. S. G. Tomlin, "The Back-Scattering of Electrons from Solids," *Proc Phys. Soc , 82* 465 (1963).
42. R. F. Dashen, "Theory of Electron Backscattering," *Phys Rev , 134* A1025 (1964).
43. H. M. Terrill, "Loss of Velocity of Cathode Rays in Matter," *Phys Rev , 22* 101 (1923).
44. K. F. Koral and A. J. Cohen, "Empirical Equations for Electron Backscattering Coefficients," NASA-TN-D-2909, NASA Lewis Research Center, July 1965.

6

Leakage Currents

The performance of a Direct-Collection Cell is strongly influenced by various leakage currents. Currents due to finite insulator resistances, secondary electron emission, and sputtering are considered in this chapter, along with voltage breakdown, which is included as the limiting or extreme case. Both leakage and breakdown can be affected by the phenomenon of radiation-induced space charge in dielectrics, and this is also discussed.

Secondary emission, space charge, and sputtering effects are all caused by charged particles passing through or bombarding a surface; thus, they are directly related to the transport of the primary charged particles. Ohmic-leakage currents and voltage breakdown are problems associated with any high-voltage device; however, even these effects are not entirely independent of the charged-particle currents and associated radiation fields. For example, the insulator resistance, which determines ohmic leakage, will generally have a radiation-induced component. Also, there is evidence that high-voltage breakdown may be affected by radiation, especially for solid insulators.

The performance of the various cell designs studied to date has always, ultimately, been limited by one or more of these leakage currents. Unfortunately, the present understanding of the underlying mechanisms is, at the best, fragmentary, and it would appear that studies of basic mechanisms should be one of the major objectives of future research.

6-1 OHMIC-LEAKAGE CURRENTS

Any actual cell will fall short of the ideal of having an infinite resistance between the emitter and collector. Even if a hard vacuum is maintained between the plates, some solid supports or separators must also be used, and ohmic leakage through the separator structure is likely to be significant at high voltages. This is particularly true for volume-emitter cells that rely entirely on a solid insulator.

It is assumed, in the following analysis, that the resistance of the insulator is known, and it is simply designated as R_I. Several points should be stressed in this regard: First, leakage along the surface of

the insulator often may be equal to, or be larger than, the leakage through its volume. While such currents can be reduced significantly by maintaining a low humidity, or by designing grooved surfaces to lengthen the current path, etc., they are difficult to eliminate. Second, both the primary charged-particle current and associated nuclear radiations from the source may cause an instantaneous increase in the insulator's conductivity (radiation-induced conductivity) as well as a long-term change due to a gradual deterioration of the insulator (radiation damage).

In the present analysis, we will ignore long-term radiation damage, but we will assume that the value of R_I includes a correction for radiation-induced conductivity. (Methods are discussed in Sec. 6-4.1.)

6-1.1 The Equivalent Circuit

The equivalent circuit concept is an attempt to represent the cell by a network composed of conventional electrical elements (resistors, capacitors, etc.). Its selection is to some extent arbitrary since several circuits, differing somewhat in detail, may still mock up critical resistance and time constant values. The validity of any circuit must ultimately rest on how accurately it predicts experimental voltage–current (V-I) characteristics, and for new designs, this may well involve fitting some parameters to selected test results.

Both circuits shown in Fig. 6.1 have been used in previous studies. Circuit A has commonly been used in "Nuclear Battery" studies[1–3], and Circuit B was used by Plummer et al.[4] to analyze Alpha Cell experiments. However, these studies have been restricted to the low-voltage range, where a linear analysis is applicable. In the present development we will consider the more general case of high-voltage operation where both circuits must contain nonlinear elements.

In Circuit A, the current from the "current source" can be thought of as representing the net current reaching the collector. A path for ohmic-leakage currents through the insulator between the plates is provided by the resistance R_I. Note that these currents bypass the load resistance. Since the cell configuration resembles a capacitor, an equivalent capacitance C_c is included. Based on this logic, Circuit A must have one or possibly two nonlinear elements. The source current, since it represents the net collector current, is by definition a nonlinear function of voltage as shown in Chaps. 2 and 4 [e.g., see Eq. (2.13)]. A second nonlinearity may enter if the insulator resistance R_I is strongly affected by radiation as discussed earlier.*

*Consider, for example, a Gamma-Electric Cell. One way to change the current output is to vary the intensity of the input gamma radiation, and this, in turn, will cause a change in R_I.

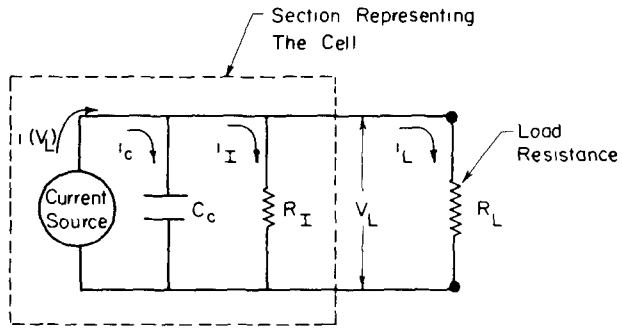

Circuit A

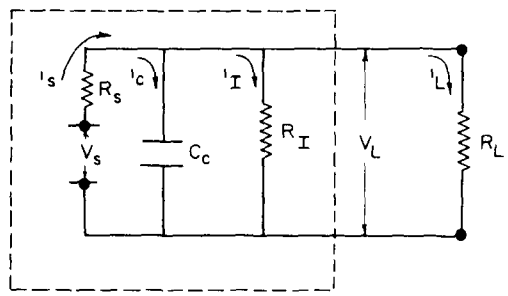

Circuit B

Fig 6 1—Two equivalent circuits

Circuit B differs from A in that the current source has been replaced by the voltage–resistance pair V and R This is useful where it is desirable to assign an impedance to the source, and R_s is termed the "source impedance."

It is seen that Circuits A and B are equivalent if the source impedance is defined as

$$R = \frac{V_s}{i_s} \equiv \frac{V_0}{i(V_L)} = \frac{T_0/q_0}{i(V_L)} \tag{6.1}$$

The symbol $i(V_L)$ is used as a reminder that the current through the load is a function of the voltage drop across the load V_L. Also, V_s is identified as the equivalent voltage V_0 associated with the initial energy T_0 and charge q_0 of the particle used in the cell. Then, under a short-circuit condition the voltage drop across R_s will just balance V_0 But,

if a finite load resistor is added, the current $i(V_L)$ will decrease so that, according to Eq. (6.1), R_s must increase. Thus, R_s depends on V_L and is then, by definition, a "nonlinear element."*

The source impedance corresponding to a short-circuit condition frequently enters the analysis, and we will assign it the symbol R_0, i.e.,

$$R_0 \equiv [R_s]_{V_L=0} = \frac{V_0}{i(0)} \tag{6.2}$$

6-1.2 Steady-State Current Analysis

Consider Circuit A in Fig. 6 1. The capacitor does not enter the calculation of steady-state currents so the load voltage V_L is equal to the voltage across the cell plates, and the current is simply

$$i(V_L) = i(\beta_0) = A_c J_q(\beta_0) \tag{6.3}$$

where A_c is the cell collector area and $J_q(\beta_0)$ is the charge current density such as given by Eq. (2.13) or (4.63) as a function of the reduced voltage β_0. It is assumed that consistent units are applied so that i is expressed in amperes

Kirkoff's relations for Circuit A require that

$$i(\beta_0) = i_I + i_L \tag{6.4}$$

and

$$V_L = i_L R_L = i_I R_I \tag{6.5}$$

from which we find that

$$i_L = \frac{i(\beta_0)}{1 + (R_L/R_I)} \tag{6.6}$$

---

*Note that the definition of R_s is not unique. From a practical point of view, it represents the impedance as "seen" by instrumentation connected across the load terminals (the position of R_L in Fig. 6.1) However, a combination of the two resistances R_s and R_I is always involved, and either or both could be defined as nonlinear as long as the combination yields the correct V-I characteristic

For example, an alternate selection might define the source impedance as a constant equal to the short circuit value R_0. Then, R_I would be assigned an appropriate voltage dependency so that the V-I characteristic of Circuit B would remain the same as for Circuit A. However, this is rather awkward, and it will not be used here.

The form for $i(\beta_0)$ must be specified: To illustrate the problem with a minimum of complexity, we will use the non-relativistic result for an ideal parallel-plate cell with isotropic emission given in Eq. (2.13a). The extension to other geometries, including a finite fuel-layer thickness, is straightforward but tedious. Substitution of Eqs. (2.13a) and (6.3) into Eq. (6.6) gives

$$i_L = \frac{i(0)\ (1 - \sqrt{\beta_0})}{1 + (R_L/R_I)} \ . \tag{6.7}$$

However, the reduced voltage β_0 is by definition a function of i_L since

$$\beta_0 = \frac{q_0 V_L}{T_0} = \frac{V_L}{V_0} = \frac{i_L R_L}{V_0} \ . \tag{6.8}$$

Equations (6.7) and (6.8) involve the load current i_L, the load voltage V_L, and the load resistance R_L. Any one of these may be eliminated between the two equations so that three basic plots are possible: i_L vs V_L; i_L vs R_L; and V_L vs R_L. The first two are considered in some detail in the following sections, and a $V_L - R_L$ plot is presented in Appendix F.

(a) *Current–Voltage Curves*

Current–voltage curves may be constructed by eliminating R_L between Eqs. (6.7) and (6.8). This gives

$$\frac{i_L}{i(0)} = 1 - \sqrt{\beta_0} - \frac{\beta_0}{\rho_c} \tag{6.9}$$

where

$$\rho_c = \frac{R_I\, i(0)}{V_0} = \frac{R_I}{R_0} \ . \tag{6.10}$$

As indicated by Eq. (6.10), ρ_c may be interpreted as the ratio of the insulator resistance R_I to the short-circuit source impedance R_0. This parameter appears frequently, and we will term it the "cell characteristic" since it depends only on the cell design; i.e., on the geometry, the insulator involved, the charged particle used, and the source strength. The larger the value of ρ_c, the closer the cell approaches the ideal of having a perfect insulator and, hence, minimum ohmic-leakage currents. Thus, ρ_c is a measure of the "goodness" of the cell design relative to ohmic-leakage losses.

For a perfect insulator, R_I approaches infinity, giving an infinite value of the cell characteristic, and Eq. (6.9) reduces to the ideal-cell

case [Eq. (2.13a)]. On the other hand, as ρ_c decreases, the current corresponding to a fixed voltage is reduced due to ohmic leakage. These observations are illustrated in Fig. 6.2, where $i_L/i(0)$ vs β_0 is shown for various ρ_c.

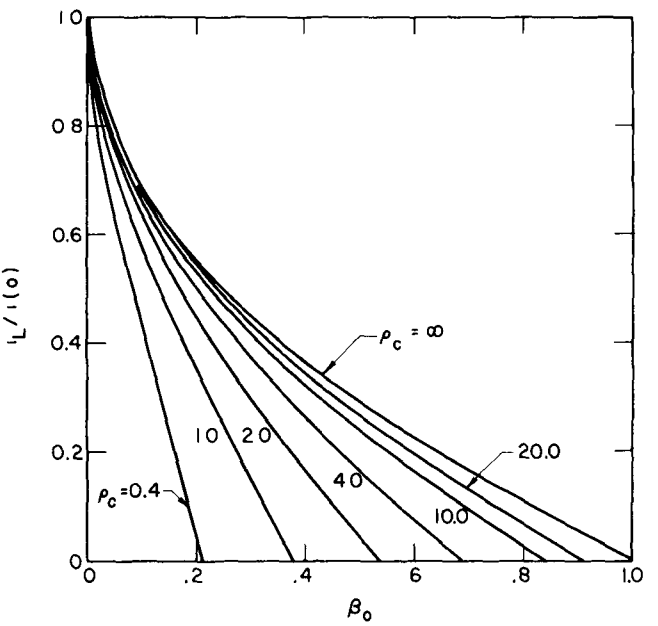

Fig. 6.2 — Current–voltage curves for various values of the cell characteristic. (Parallel-plate cell, isotropic emitter, zero fuel-layer thickness.)

A finite insulator resistance also limits the maximum obtainable load voltage. Note in Fig. 6.2 that, except for $\rho_c = \infty$, the current goes to zero at $\beta_0 < 1.0$. This occurs because the open-circuit voltage is no longer equal to V_0, as in an ideal cell, but is fixed by the voltage drop caused by the leakage current flow across the internal resistance R_I. The dependence of the maximum voltage on ρ_c can be found by setting $i_L = 0$ in Eq. (6.9) and solving for β_0. This gives

$$\beta_{0M} \equiv [\beta_0]_{max} = \frac{\rho_c^2}{4}\left(\sqrt{1+\frac{4}{\rho_c}} - 1\right)^2. \tag{6.11}$$

A plot of this relation is shown in Fig. 6.3. As expected, β_{0M} decreases as ρ_c decreases, and, in fact, for small values of ρ_c, Eq. (6.11) can be expanded to obtain

$$\beta_{0M} \approx \rho_c(1 - \sqrt{\rho_c}) \qquad (\rho_c < 0.1). \tag{6.12}$$

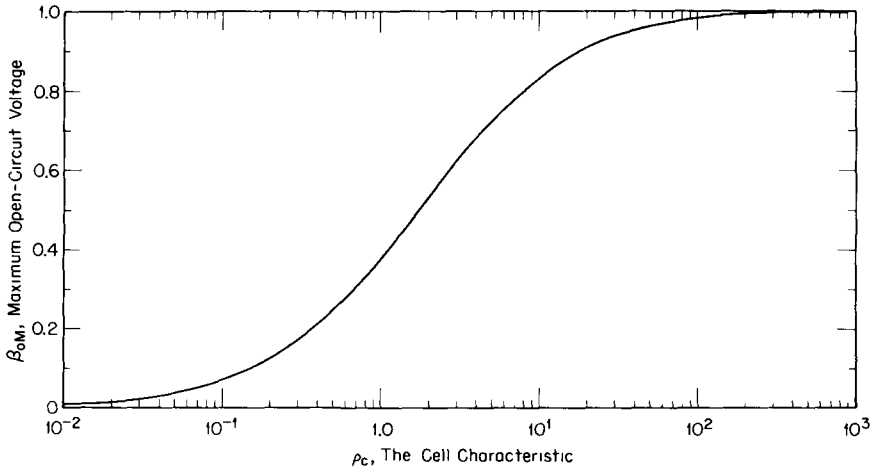

Fig. 6.3 — Variation of the maximum voltage with the cell characteristic. (Parallel-plate cell, isotropic emitter, zero fuel-layer thickness.)

The other extreme ($\rho_c \to \infty$) corresponds to the limit for an ideal cell and $\beta_{0M} \to 1$.

(b) *Current–Load Curves*

The load resistance is often specified in cell applications. If so, the corresponding current can be found by trial and error from current–voltage curves such as shown in Fig. 6.2. The voltage is estimated, and i_L read from the graph. This value should agree with V_L/R_L based on the estimated V_L and the known R_L. If not, the process is repeated, and so on. This is not too convenient, so it is useful to construct current–load curves directly from Eqs. (6.7) and (6.8). To do this, V_L is eliminated between these equations, which gives

$$i_L = i_e \left[1 + \frac{\gamma}{2}\left(1 - \sqrt{1 + \frac{4}{\gamma}}\right)\right] \tag{6.13}$$

with

$$i_e = \frac{i(0)}{1 + R_L/R_I} = i(0)\,\frac{R}{R_L} \tag{6.14a}$$

and

$$\gamma = \frac{i_e R_L}{V_0} = \frac{R}{R_0} = \rho_c \frac{i_e}{i(0)}\,\frac{R_L}{R_I}\,. \tag{6.14b}$$

The cell characteristic ρ_c [Eq. (6.10)] again appears, and R, the equivalent resistance for a parallel circuit containing R_L and R_I, is defined as

$$R = \frac{R_I R_L}{R_I + R_L} . \tag{6.14c}$$

In this analysis, γ, the ratio of the equivalent resistance R to the short-circuit source impedance R_0 [Eq. (6.14b)], plays a role similar to the cell characteristic. However, γ retains a dependence on the load resistance through R, and hence it is not an independent parameter in the same manner as ρ_c. (As stressed previously, ρ_c depends only on the cell design and source strength.)

The parametric groups of Eq. (6.13) were selected for convenience in a graphical presentation such as shown in Fig. 6.4. This plot may be

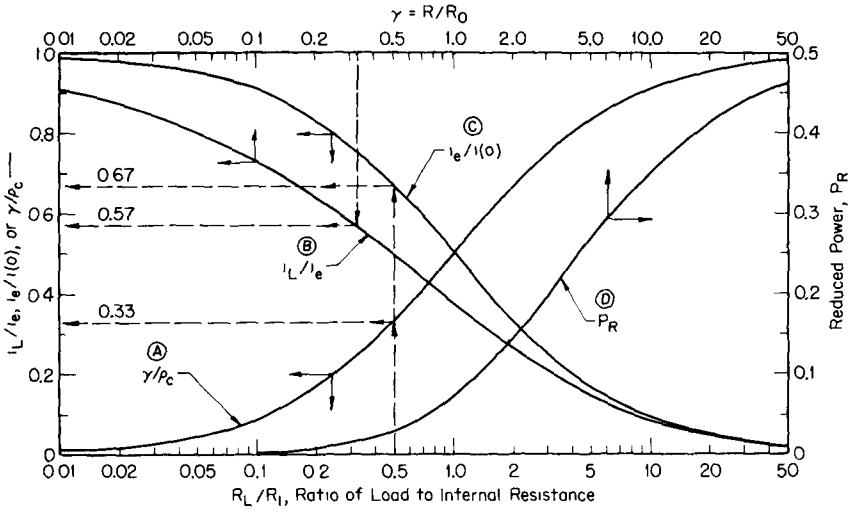

Fig. 6.4—Normalized current and power vs R_L/R_I. (For a zero fuel-layer thickness, isotropic emitter, parallel-plate cell.)

used as follows: First, the load resistance R_L is selected, and this fixes the ratio R_L/R_I so that γ/ρ_c can be found from curve A. Assuming the cell characteristic ρ_c is known, we can define γ, which can then be used along with curve B to find i_L/i_e. Finally, i_e is eliminated by use of curve C and the resistance ratio R_L/R_I.

For example, consider a cell with a cell characteristic $\rho_c = 1.0$ and a resistance ratio of $R_L/R_I = 0.5$. From curve A, we read $\gamma/\rho_c = 0.33$, so that $\gamma = 0.33\ (1.0) = 0.33$. Then, $i_L/i_e = 0.57$ is read from curve B. Also, $i_e/i(0) = 0.67$ is read from curve C. This gives $i_L/i(0) = (i_L/i_e)[i_e/i(0)] = 0.38$, and, since the short-circuit current i(0) is a

characteristic of the cell, this gives a unique solution for the load current i_L.

This result can also be used to determine the cell voltage from the current–voltage curves presented earlier in Fig. 6.2. For $i_L/i(0) = 0.38$ and $\rho_c = 1.0$, a reduced voltage of 0.19 is read.*

Equation (6.13) can also lead to some useful limiting approximations. First, consider an ideal cell where by definition $R_I = \infty$. Then Eqs. (6.14a and b) reduce to

$$i_e \rightarrow i(0) \qquad \gamma \rightarrow R_L/R_0 \tag{6.15}$$

and substitution into Eq. (6.13) gives

$$i_L = i(0)\left[1 + \frac{R_L}{2R_0}\left(1 - \sqrt{1 + \frac{4R_0}{R_L}}\right)\right]. \tag{6.16}$$

Typically, V_0 is of the order of 10^6 V (Table 1.1), and the current i(0) ranges from 10^{-9} to 1A, in which case, $R_0 > 1$ MΩ. Thus, as long as the load resistance is in the hundred or thousand ohm range, we can assume that $R_L/R_0 \ll 1$, which gives

$$i_L \approx i(0)\left(1 - \sqrt{\frac{R_L}{R_0}}\right) \approx i(0). \tag{6.17}$$

This shows that the current remains quite constant even if the load resistance varies over several orders of magnitude *so long as it falls well below the megohm range.* Loads of this type are common where a maximum power output is not important, e.g., in nuclear instrumentation, timing circuits, etc., and for this reason, radiation cells (or nuclear batteries) are often called "constant current sources"[1–3]. However this nomenclature is dangerous since the current will depend on the load resistance in the useful power range where megohm resistances are required. Then, the complete form of Eq. (6.13) must be retained; in fact, at the extreme where the load resistance is so large that $R_L/R_I \gg 1$, we find that

$$\frac{i_e}{i(0)} \rightarrow \frac{R_I}{R_L} \qquad \gamma \rightarrow \rho_c \tag{6.18}$$

---

*A check of the internal consistency of the two figures can be made by noting that this gives a ratio of ρ_c/β_0 of (1.0/0.19) or 5.2. Alternately, $\rho_c/\beta_0 = (R/R_0)(V_0/V_L) = (R_I/R_L)(i(0)/i_L)$, and this can be evaluated using $R_L/R_I = 0.5$ as specified in the original determination of $i_L/i(0)$ from Fig. 6.4. This gives a ratio of (1/0.5)(1/0.38) or 5.2, which checks the first result.

in which case Eq. (6.13) reduces to

$$i_L \approx i(0)\,\psi(\rho_c)\,\frac{R_I}{R_L} \tag{6.19}$$

with

$$\psi(\rho_c) = 1 + \frac{\rho_c}{2}\left(1 - \sqrt{1 + \frac{4}{\rho_c}}\right). \tag{6.20}$$

Since for a given cell, ρ_c, $i(0)$, and R_I will be fixed, Eq. (6.19) shows that in this limit i_L varies inversely with R_L.

(c) *Power Output*

The power produced across the load resistor is by definition

$$P_L \equiv i_L^2 R_L = [i_L/i(0)]^2\, P_0 \tag{6.21}$$

where

$$P_0 = i^2(0)\, R_L. \tag{6.22}$$

One method of determining P_L is as follows: For a given resistance ratio R_L/R_I, the voltage β_0 can be read from Fig. F.1, Appendix F. Then, with this value of β_0, $i_L/i(0)$ can be read from Fig. 6.2 and used in Eq. (6.21) to find P_L. (Note that P_0 is known once R_L is selected since the short-circuit current $i(0)$ is determined solely by the cell design and source strength.)

Alternately, once R_L/R_I is selected, i_L/i_e and γ/ρ_c can be read from Fig. 6.4, and γ can then be determined since ρ_c has a fixed value for a given cell. Finally, with this value of γ, the ratio $i_e/i(0)$ is read from Fig. 6.4. The power can then be determined from Eq. (6.21) since $i_L/i(0)$ is identically equal to the product of the two current ratios found above.

The results of such calculations are included in Fig. 6.4 (curve D) where the reduced power P_R, defined as

$$P_R \equiv \frac{P_L}{P^*}\left(\frac{\rho_c R_L}{R_I}\right) = \frac{\gamma^2}{2}\left[1 + \frac{\gamma}{2}\left(1 - \sqrt{1 + \frac{4}{\gamma}}\right)\right]^2 \tag{6.23}$$

is plotted as a function of the parameter γ. Use has been made of Eqs. (6.13) through (6.14c), and the normalizing power P^* is given by

$$P^* = i(0)\, V_0 = \frac{i_L}{i(0)}\,\frac{P_0}{\beta_0}. \tag{6.24a}$$

(This presentation was selected rather than plotting P_L directly against R_L/R_I since the latter would involve curves with both ρ_c and i(0) as parameters.) The power P* is a useful quantity for later calculations. As the product of the charged-particle current and the voltage equivalent of their kinetic energy, it effectively represents the input power associated with the particle current leaving the source plate. Since the exit current is equal to the escape fraction E [Eq. (4.45)] times the total source birth rate, P* is related to the total input (or source) power P_S by

$$P^* = P_S \cdot E \,. \tag{6.24b}$$

For the ideal cells treated in the present examples, absorption in the fuel layer is omitted, but E is typically identified as 1/2 to account for absorption in the support plate, i.e., one-sided emission as discussed in Chap. 2.

While the presentation of Fig. 6.4 is useful, a direct power–voltage plot leads to an easier visualization of cell performance. Substitution of $i_L/i(0)$ from Eq. (6.9) into Eq. (6.21) gives

$$P_L = P_0\left(1 - \sqrt{\beta_0} - \frac{\beta_0}{\rho_c}\right)^2 = P^*\,\beta_0\left(1 - \sqrt{\beta_0} - \frac{\beta_0}{\rho_c}\right). \tag{6.25}$$

This relation is illustrated in Fig. 6.5, where for convenience, the maximum power P_{max} and voltage β_{0M} have been used to normalize the scales. In contrast to the earlier presentations, such as Fig. 6.2, the normalization by β_{0M} forces all the curves to pass through 1.0 on the abscissa. (This causes some problems; e.g., at first glance it might appear that the current ratio decreases with increasing values of ρ_c. This is because, as seen from Eq. 6.11, the normalizing factor β_{0M} also depends on ρ_c.)

An analytic expression for the maximum power can be determined by differentiation of Eq. (6.25). The voltage β_0^{PM} corresponding to the maximum power is found to be

$$\beta_0^{PM} = \frac{9}{16}\,\phi(\rho_c) \tag{6.26}$$

where

$$\phi(\rho_c) = \frac{\rho_c^2}{4}\left(\sqrt{1 + \frac{32}{9\rho_c}} - 1\right)^2. \tag{6.27}$$

The maximum power, obtained by substituting this result back into Eq. (6.25), is then found to be

$$\frac{P_{max}}{P^*} = \frac{9}{16}\left[\frac{1}{\phi} - \frac{3}{4}\left(\frac{1}{\sqrt{\phi}} + \frac{3}{4\rho_c}\right)\right]\phi^2. \tag{6.28}$$

These relations are shown in Fig. 6.6. As expected, both the maximum power and the voltage at which it occurs increase with ρ_c. In the limit as $\rho_c \to \infty$, the radical in Eq. (6.27) can be expanded to obtain

$$\beta_0^{PM} \to 4/9 \tag{6.29}$$

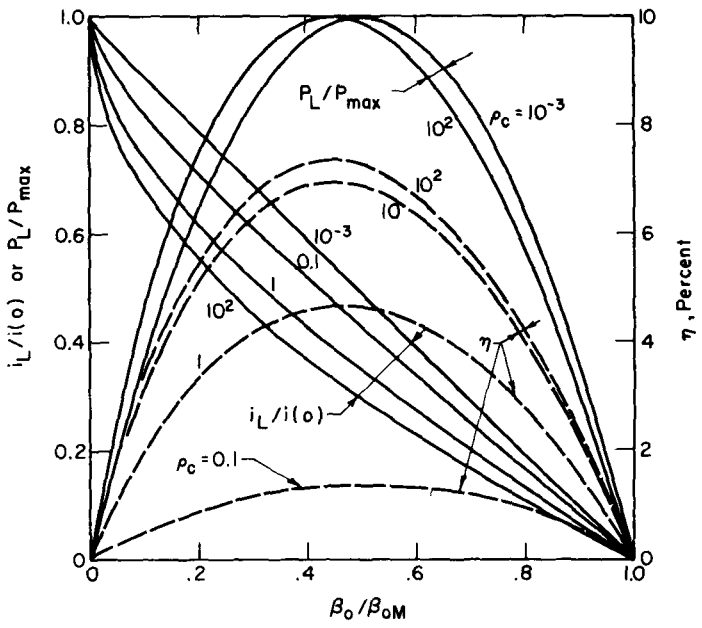

Fig. 6.5 — Cell current, power, and efficiency vs voltage for various values of the cell characteristic. (For a zero fuel-layer thickness, isotropic emitter, parallel-plate cell.)

which agrees with the maximum efficiency (or power) point found in Chap. 2 for an ideal planar cell with isotropic emission. The corresponding power is

$$P_{max} = 4P^*/27 \tag{6.30}$$

which is consistent with the maximum ideal-cell efficiency calculated in Chap. 2. This is demonstrated by noting that the maximum efficiency is, by definition, equal to P_{max} divided by the total source power P_S.

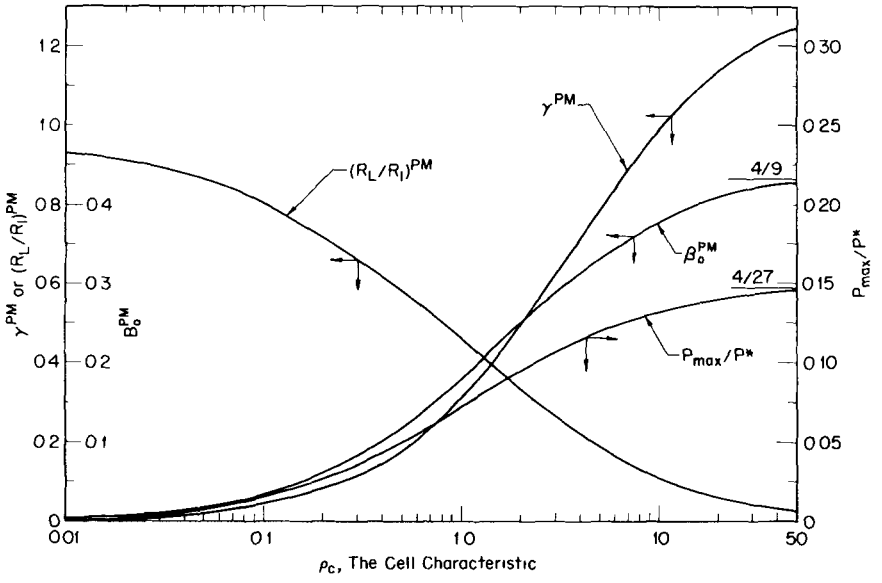

Fig 6.6—Maximum power and corresponding values of γ^{PM}, the reduced voltage (β_0^{PM}), and resistance ratio $[(R_L/R_I)^{PM}]$ vs the cell characteristic. (For planar geometry, isotropic emission, with zero fuel-layer thickness.)

Hence, Eqs. (6.30) and (6.24b) are used with an escape fraction of 1/2, and

$$[\eta_c^*]_{max} = \frac{P_{max}}{P_S} = \frac{P_{max}}{2P^*} = 0.074 \tag{6.31}$$

which agrees with Table 2.3.

Operation at the maximum power point can be achieved by proper selection of the load resistance R_L. Once the voltage B_0^{PM} corresponding to this point is known, R_L (actually the ratio R_L/R_I) can be selected from the voltage–load curves of Fig. F.1 (Appendix F). Alternately, the required value of R_L can be found by using Eq (F.1) to evaluate B_0^{PM} in Eq. (6.26). This gives

$$\frac{(\gamma^{PM})^2}{2}\left(1 + \frac{2}{\gamma^{PM}} - \sqrt{1 + \frac{4}{\gamma^{PM}}}\right) = \frac{9}{16}\,\phi(\rho_c) \tag{6.32}$$

where γ^{PM} is the value of this parameter, defined in Eq. (6.14b), which leads to a maximum power. In turn, γ^{PM} can be related to the resistance ratio $(R_L/R_I)^{PM}$ required for maximum power by combining Eqs.

(6.10 and 6.14b), which gives

$$\gamma^{PM} = \rho_c \frac{(R_L/R_I)^{PM}}{1 + (R_L/R_I)^{PM}} \tag{6.33}$$

and for convenience, a plot of this relation is included in Fig. 6.6. This curve requires some explanation. Although γ^{PM} increases with increasing ρ_c, the ratio γ^{PM}/ρ_c decreases, and as a result the corresponding resistance ratio $(R_L/R_I)^{PM}$ shown in Fig. 6.6 also decreases. This should not, however, be interpreted to mean that a smaller load is required to achieve a maximum power as the cell approaches the ideal case ($\rho_c = \infty$). The point is that R_I also increases with increasing ρ_c such that the absolute value of R_L^{PM} increases although the ratio $(R_L/R_I)^{PM}$ decreases. This can be seen by observing that the product of $(R_L/R_I)^{PM}$ and ρ_c [which gives $(R_L/R_0)^{PM}$ and thus removes the dependence on R_I] increases with increasing ρ_c. In fact, in the limit where $\rho_c = \infty$, it is easily shown using Eq. (6.29) for an ideal isotropic planar cell that R_L^{PM} corresponds to $(4/3)R_0$ where, as defined earlier, R_0 is the short-circuit source impedance. (This violates the traditional rule of thumb that a maximum output occurs when the load and source impedances are matched. The reason is that, as stressed previously, the nuclear cell is inherently nonlinear.)

(d) *Efficiencies*

Two efficiencies are of interest in radiation cell analysis. The first, the *collection efficiency*, is a measure of the conversion of kinetic energy to potential energy for charged particles reaching the collector relative to the initial kinetic energy of all particles emitted. This is equivalent to the ideal-cell efficiency η_c^* of Eq. (2.19). However, in a real cell, as shown by the equivalent circuit, some of the particles reaching the collector leak back to the emitter due to the finite internal resistance. Thus the energy converted when these particles are collected never appears at the load, and this suggests the use of a second efficiency, the *actual cell efficiency* η_c, to indicate the power that actually appears across the load relative to the input power associated with the particle kinetic energy. Then it is, by definition, given as

$$\eta_c = \frac{\text{(power out)}}{\text{(initial power associated with the particles)}} = \frac{P_L}{P_S} \tag{6.34}$$

where

$$P_S = S_0 T_0 \mathcal{T} = P^*/E \,. \tag{6.35}$$

Here, S_0 is the emission rate per unit volume of particles with initial kinetic energy T_0 from a fuel layer of volume τ. The relation to P* follows from Eq (6.24b).

For example, for the ideal (isotropic) planar cell, Eq. (6.25) can be used to evaluate P_L, and the actual cell efficiency is found to be

$$\eta_c = \frac{\beta_0}{2}\left(1 - \sqrt{\beta_0} - \frac{\beta_0}{\rho_c}\right) \tag{6.36}$$

where E has again been identified as 1/2 to account for one-sided emission.

Equation (6.36) shows that η_c depends strongly on the cell characteristic ρ_c. If $\rho_c \to \infty$, the ideal-cell efficiency is recovered [cf Eq. (2.22a)]. Thus the ratio η_c/η_c^* represents a figure of merit for the efficiency of a particular cell, and a plot of this ratio is shown in Fig. 6.7 for the isotropic planar cell. The efficiency ratio is of course smaller the smaller the cell characteristic; further, this ratio decreases with increasing voltage because the larger potentials enhance leakage currents. The zero intercept occurs at the maximum voltage point [β_{0M} of Eq. (6.11)] because the actual load current goes to zero at

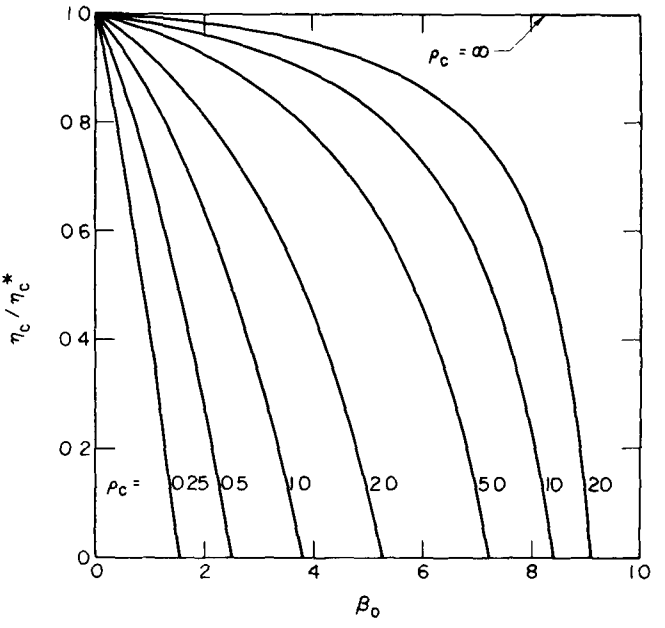

Fig 6.7 — Ratio of the actual cell efficiency to the collection (ideal) efficiency as a function of voltage and cell characteristic (For planar geometry, isotropic emission, zero fuel-layer thickness.)

this point whereas particles continue to reach the collector (ideal-cell current) until β_0 equals 1.0.

Another difference between these two efficiencies is that their maximum values occur at different voltages. For example, for the isotropic planar cell, the maximum value of the ideal-cell efficiency occurs at $\beta_0 = 4/9$; whereas, the maximum value of the actual cell efficiency coincides with β_0^{PM}, defined in Eq. (6.26). As seen from the plot of β_0^{PM} in Fig. 6.6, the voltage leading to the maximum actual efficiency always lies *below* the value for a maximum collection efficiency. (Note that $[\eta_c]_{max}$ corresponding to β_0^{PM} can be read directly from Fig. 6.6 by dividing values from the P_{max}/P^* curve by two.)

6-1.3 Other Results

Three additional equivalent circuit results of interest are included in Appendix F: Another possible representation, the voltage–load curve, is presented; the extension of the results to other geometries is illustrated; and the effects of leakage currents on charging times are discussed.

6-2 SECONDARY-ELECTRON CURRENTS

Although cells can be designed that actually operate on secondary-electron currents, in most designs, as is illustrated in Figs. 6.8 and 6.9, secondary emission represents a leakage current. Sketch (a) of Fig. 6.8 shows a cell using a positive primary particle. To operate properly, this cell should build up a positive collector potential; however, secondary electrons from the emitter layer will then be attracted to the collector, causing a leakage current that tends to neutralize the desired positive charge. Secondaries will also be emitted from the collector as the primary hits it, but they will mainly be attracted back to the collector, and any that are energetic enough to reach the emitter will, in effect, aid positive charge build-up at the collector.

As pointed out in Chap. 5, the charge carried by secondaries may well be larger than that of the primary current. If so, this may ultimately cause the collector potential to switch from positive to negative as illustrated in Fig. 6.8(b). Since secondaries have a relatively low kinetic energy, this potential will not be large. Further, the positive particle energy cannot be converted, and if, as occurs in the Fission-Electric Cell, the major portion of the kinetic energy is carried by positive primaries, this mode of operation will have a poor conversion efficiency.

Secondary emission may also be important in cells using negative primary particles, e.g., a Beta Cell. As illustrated in Fig. 6.8(c), the

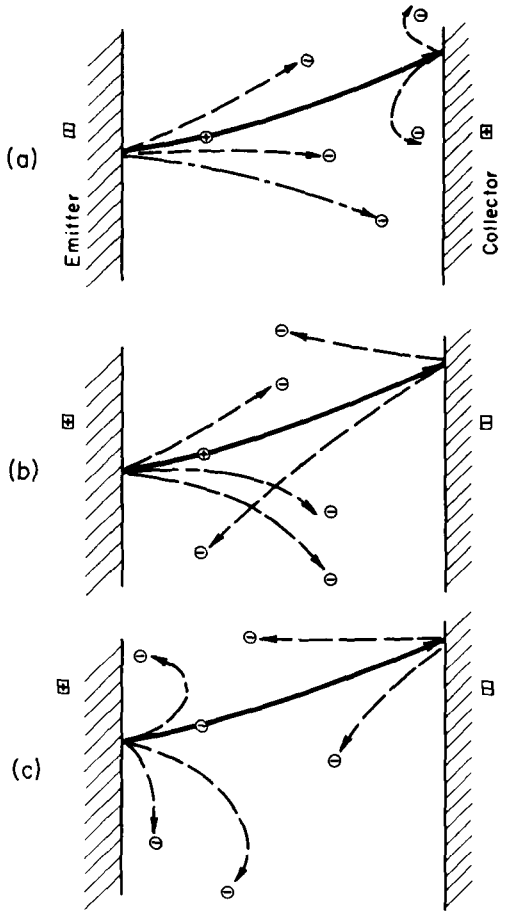

Fig. 6.8—Schematic representation of secondary electron leakage currents in positive- and negative-particle coated-plate cells. (a) Positive primary particle, positive collector. (b) Positive primary particle, negative collector. (c) Negative primary particle.

secondary current produced at the emitter tends to cancel itself, but secondaries from the collector represent a leakage. This current could prevent an adequate voltage build-up, but it is difficult to envision it causing a switch in the collector potential.

Secondary currents can also arise in other ways—a common one is the transmission of primary particles through the collector as illustrated in Fig. 6.9. In Fig. 6.9(a), secondary electrons are lost from the back face of the collector of a Gamma-Electric Cell as gamma radiation passes through the collector. It is possible to reduce or eliminate this current by using a thicker collector, but this adds to the

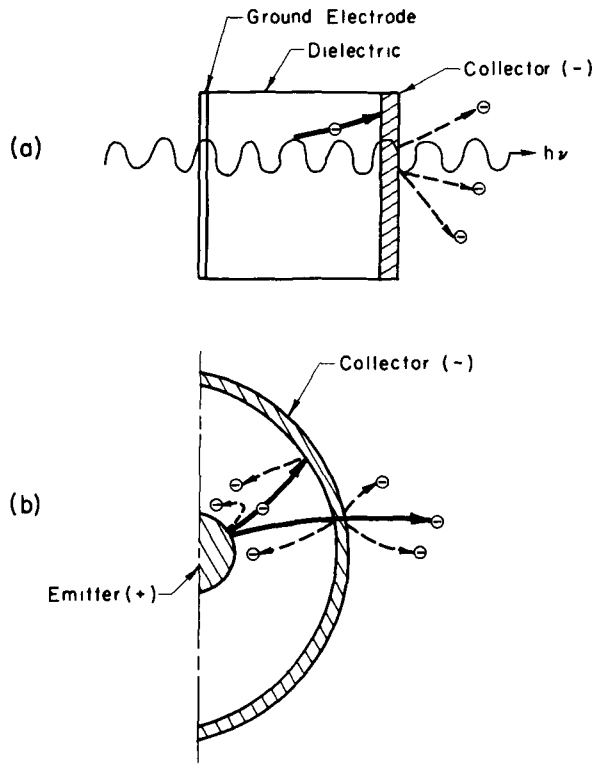

Fig. 6.9 — Schematic representation of leakage currents associated with transmission through the collector. (a) Secondary emission from the back face of the collector electrode in a Gamma-Electric Cell. (b) Secondary emission due to transmission through the collector in a Beta-Electric Cell with spherical geometry.

weight of the cell. This may be undesirable in some applications, and frequently a compromise between leakage and weight is sought. Such a situation is illustrated in Figure 6.9(b), where a spherical Beta-Electric Cell, representative of a typical design for space applications (discussed later in Chap. 7), is shown. Here, the collector area is large, and, if it is made thick enough to stop all of the beta particles hitting it, the unit becomes intolerably heavy.

6-2.1 Secondary-Beta and Other Leakage Currents

Electron leakage currents can arise through mechanisms other than secondary emission. For example, consider a Fission-Electric Cell in which fission fragments produced by neutron induced fission in a uranium fuel layer are collected. Fission fragments are radioactive

and decay, predominantly through beta emission. Thus, beta particles will be produced by fragments stopped in both the fuel layer and the collector. The resulting currents are similar to secondary-electron currents in effect, but there are two major differences: First, the average beta energy will in general be larger, and second, the magnitude of the beta currents will depend on the fragment concentration on the plate rather than the bombardment rate. (During extended steady state operation, an equilibrium between the fragment concentration and arrival rate may be achieved, but this will not be true in general.)

Because of the specialized nature of currents such as this, we will not analyze them in detail here. However, the following discussion of secondary emission can be extended to these situations without too much effort. (A further discussion of beta currents in the Fission-Electric Cell may be found in Refs. 5 and 6.)

6-2.2 Suppression of Secondary Currents

Since the average energy of secondary electrons is less than that of the primary particles, it is possible to use either a magnetic or electric field to "filter out" secondaries preferentially. Both methods have been used: Safonov[5] first considered the use of grid suppression in a Fission-Electric Cell, although at the time he was primarily concerned with the beta current suppression. Several of the experimental cells tested by Krieve[6] at the Jet Propulsion Laboratory (JPL) had grid suppressors, and the Alpha-Electric Cell experiments at the Battelle Memorial Institute (BMI) by Plummer et al.[4] also used a grid. Because the grid effectively adds a third plate structure, these cells have often been called a Fission-Electric "Triode" or Alpha "Triode."

The use of a magnetic field to suppress the beta current in a Fission-Electric Cell was first considered in detail by Schock[7], and magnetic suppression was used with success in later experiments at JPL[6]. It was considered as an alternative in the BMI Alpha Cell experiments[4], but the magnet weight and associated power losses for a practical cell were thought to be "prohibitive."

To date, no other method of suppression has been developed. Methods have been used to reduce secondaries; e.g., a specially prepared carbon collector was used in tritium batteries manufactured by Radiation Research Corporation[8], and Linder and Christian[9] used an aluminum liner on a copper collector in their Beta Cell studies (Sec. 7-4.2). However, while care in the selection of materials, surface treatment, and geometry will help, it does not seem possible to eliminate emission currents by these means.

Of course, secondary suppression is not required in all cells: Preliminary studies of a large ^{144}Ce Beta Cell (similar to the one

pictured in Fig. 7.23) indicate that secondary currents will only cause moderate efficiency losses[10]. Also, a number of smaller Beta Cells (nuclear batteries) using fuels like ^{3}H, ^{85}Kr, and ^{90}Sr have operated successfully without grids[11].

In short, secondary currents are important in all cell designs, but they are extremely crucial in positive-particle cells. This has been demonstrated quite vividly since, apparently, a combination of secondary emission and sputtering effects prevented voltage build-up in a number of early Fission-Electric Cell experiments[6]. Also, Plummer et al.[4] state "the most critical element in the operation of the Alpha Cell is the grid."

Because of their importance, we will consider grid and magnetic suppression units in some detail. This is a complicated problem; consequently, as in previous sections, the basic principles will be illustrated using simple geometries. Still, in practice, considerable effort should be devoted to optimizing the design for a specific cell and cell geometry.

Many of the problems involved are similar to those in electron tube design, discussed in Refs. 12 to 15. However, there are differences due to the higher energy of the particles involved here as well as the high operating voltages, and care should be exercised in any analogy.

6-2.3 Electric-Field Suppression Using Grids

In principle, the secondary emission currents illustrated in Fig. 6.8 can be suppressed by the grid designs illustrated in Fig. 6.10. The corresponding potential diagrams are sketched in Fig. 6.11. (The grids shown in these figures are only intended as schematic representations. In practice, a number of designs[12–15] such as the traditional squirrel cage, window screen, etc., might be used.)

The grid shown in Fig. 6.10(a) creates a retarding potential for negative particles in the region of the emitter, and, with proper selection of the grid potential, the low-energy secondaries can be preferentially repelled [see Fig. 6.11(a)].

The collector–grid shown in Fig. 6.10(b) may be useful in cells using negative primary particles, but it has a limitation. As seen from the figure, the grid represents the maximum potential barrier for the primaries, and, if a large grid potential is required, it may cause a significant reduction in the primary current. As a result, this design is not as satisfactory as is the emitter–grid, but fortunately, as stressed earlier, secondary emission currents are not as serious in negative-particle cells where it might be used.

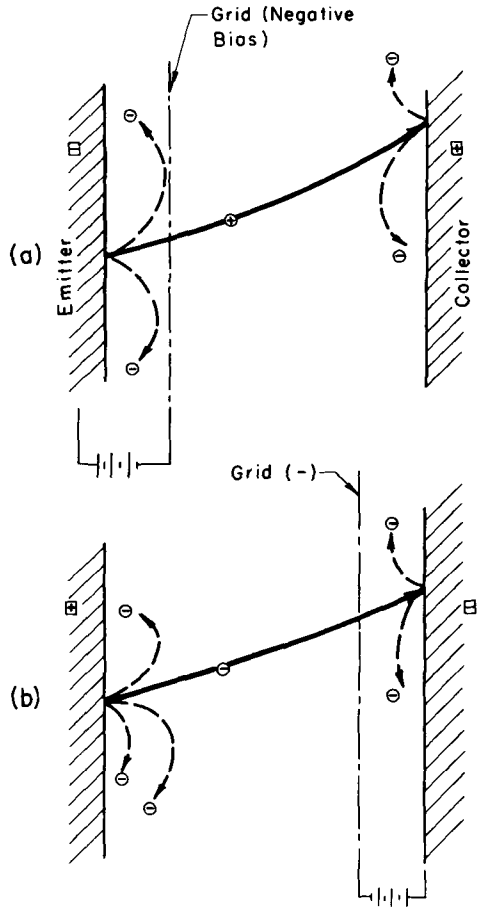

Fig. 6.10 — Secondary-electron current suppression by grids. (a) Suppression of secondaries produced at the emitter. (b) Suppression of secondaries produced at the collector in a negative-particle cell.

(a) *Grid Losses and the Equivalent Circuit*

A perfect grid would simply suppress all secondary-electron currents and would not itself introduce leakage currents. In practice, however, several effects occur:

- The grid intercepts a certain fraction of the primary particles and, thus, prevents their collection.
- Particles striking the grid produce additional secondaries, some of which escape and continue to the collector.

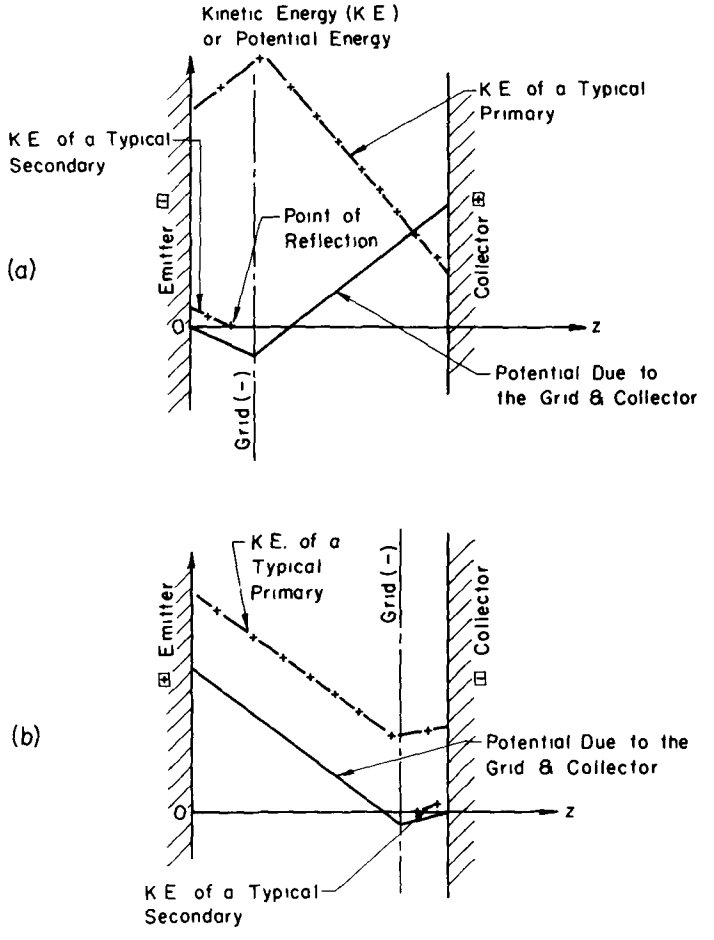

Fig. 6.11 — Schematic potential diagrams for the grids illustrated in Fig. 6.10. (a) Emitter–grid geometry. (b) Collector–grid geometry.

- Depending on the grid voltage selected, some of the high-energy secondaries may still be transmitted.

These effects will be illustrated for the gridded positive-particle cell of Fig. 6.10(a). A simple modification of the equivalent circuit is used as shown in Fig. 6.12. The *net* current from the emitter is divided — part (transmitted component) goes to the collector as usual, but part is intercepted by the grid. The latter is in effect a loss, so in Fig. 6.12(b), the transmitted component (i_a) replaces the charging current $[i(V_L)]$ in the equivalent circuit (cf. Fig. 6.1).

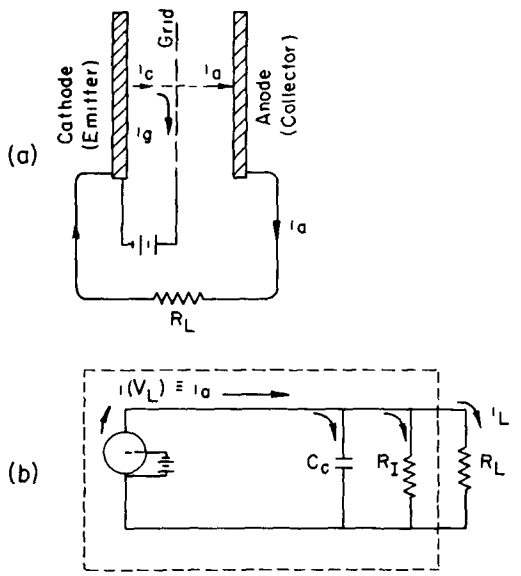

Fig. 6 12 — The inclusion of grid effects in the equivalent circuit. (a) A schematic representation of an ideal gridded cell (Note $i_c = i_a + i_g$.) (b) The corresponding equivalent circuit. (The inclusion of a finite internal resistance R_I now allows part of the anode current to leak back to the collector without passing through the load.)

However, the transmitted component is more complex than this indicates. Conceptually, it may be viewed as consisting of the various currents illustrated in Fig. 6.13, and four basic parameters are required to define the fate of the primary current from the emitter

- f Fraction of the primaries intercepted by the grid (alternately labeled the attenuation factor or the f-factor).
- η_g Ratio of the charge associated with secondary electrons produced at the grid to that associated with the intercepted primaries
- x Fraction of the secondary electrons produced at the grid that leave it with the same direction as the bombarding current.
- $f(\beta_0)$ Fraction of the primaries transmitted through the grid with sufficient energy to reach the anode held at a voltage V_L or reduced voltage β_0.

As indicated, a fall-back current of primaries equal to $i(0)[1 - f] \times [1 - f(\beta_0)]$ will occur, which passes back through the grid. Because of variations in both energy and angular distribution, the grid parameters f', η_g', and x' associated with this current may differ in magnitude from the unprimed parameters, but their basic definitions remain unchanged.

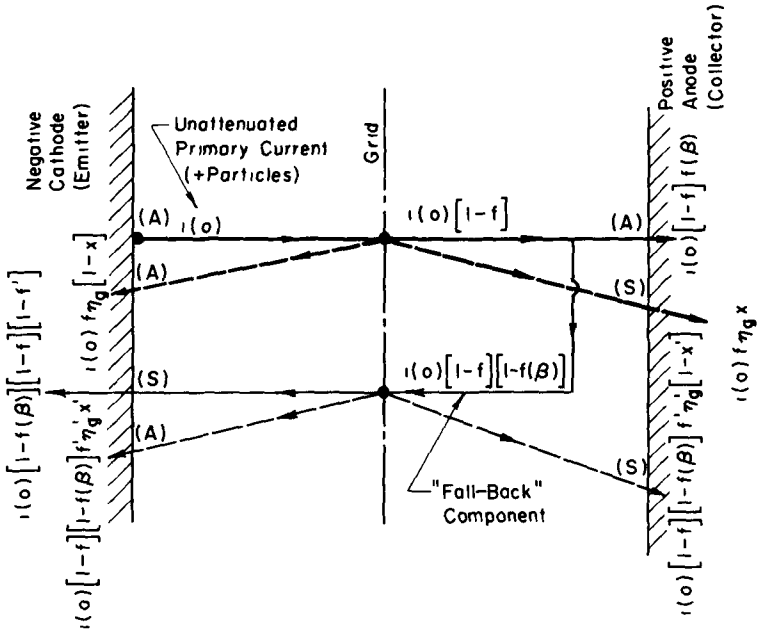

Fig. 6.13 — Schematic representation of internal currents in a gridded cell. (Solid lines indicate an ion current, dashed lines represent secondary electrons. The (A) or (S) by each current indicates whether it adds or subtracts from the respective plate current.)

Addition of the components, shown in Fig. 6.13, with careful attention to use the proper signs, then gives the net cathode, anode, and grid currents. The anode current is of immediate interest and is found to be

$$\frac{i_a}{i(0)} = k_1 \{1 - k_2 [1 - f(\beta_0)]\} \tag{6.37a}$$

where

$$k_1 = 1 - f\ (1 + \eta_g x) \tag{6.37b}$$

and

$$k_2 = \frac{(1 - f)\ [1 + f' \eta'_g\ (1 - x')]}{1 - f\ (1 + \eta_g x)} . \tag{6.37c}$$

Now the current to the load can be computed by substitution of $i_a/i(0)$ from Eq. (6.37a) into Eq. (F.3), and this gives

$$\frac{i_L}{i(0)} = k_1 \{1 - k_2 [1 - f(\beta_0)]\} - \frac{\beta_0}{\rho_c} . \tag{6.38}$$

The collection fraction $f(\beta_0)$ required here corresponds to the current ratio $i(\beta_0)/i(0)$ for a cell with an infinite internal resistance R_I; hence, it can be taken directly from the current calculations of Chaps. 2 and 4; e.g., Eq. (2.13) would be used for a planar cell.

As an illustration, results for isotropic emission in a planar cell and for two extreme values of the cell characteristic (ρ_c = 1.0 and ∞) are shown in Fig. 6.14. Methods to evaluate the various parameters, f, η_g, x, etc., will be discussed in the next section; however, this figure is based on the measured values in Table 6.1 which were reported by Plummer et al.[4] for several Alpha-Cell experiments. Their experiments used cylindrical geometry, but these parameters should still be representative of values possible with plane geometry. The fall-back parameters (primed) were not reported, so calculations for two cases are included: where the primed parameters are zero and also where they are equal to forward (unprimed) values.

Several points will be noted. The currents (and hence the efficiencies) for the gridded cells are significantly reduced below that for an "ideal grid" (curve 1), and the maximum attainable voltage is also reduced. The forward (unprimed) parameters essentially serve as a normalization for the curves since they mainly enter through k_1, which is a constant multiplier in Eq. (6.37). The slope of a curve is most strongly influenced by the factor k_2 (cf. curves 6 and 7). While f is involved, k_2 is most strongly dependent upon the fall-back (primed) parameters. If, as in curve 7, these parameters result in a large value for k_2, the curve decreases quite rapidly with voltage. This occurs because the number of fall-back particles increases at higher voltages, and their interaction with the grid becomes increasingly important.

(b) *Grid Design*

The ideal grid would be one with 100% transmission (f = 0) and would return all secondaries without requiring an excessive grid bias. These characteristics involve two parameters: the attenuation or f-factor; and the amplification or μ-factor. Since these are key factors in grid design, they are considered first.

• *The f-factor.* As defined earlier, the f-factor gives the fraction of the primary particles that are intercepted by the grid. Thus, to a first approximation, it is simply given by an area ratio

$$f \approx \frac{\text{(area "blocked" by the grid wires on surface passing through them)}}{\text{(total surface area)}} \tag{6.39a}$$

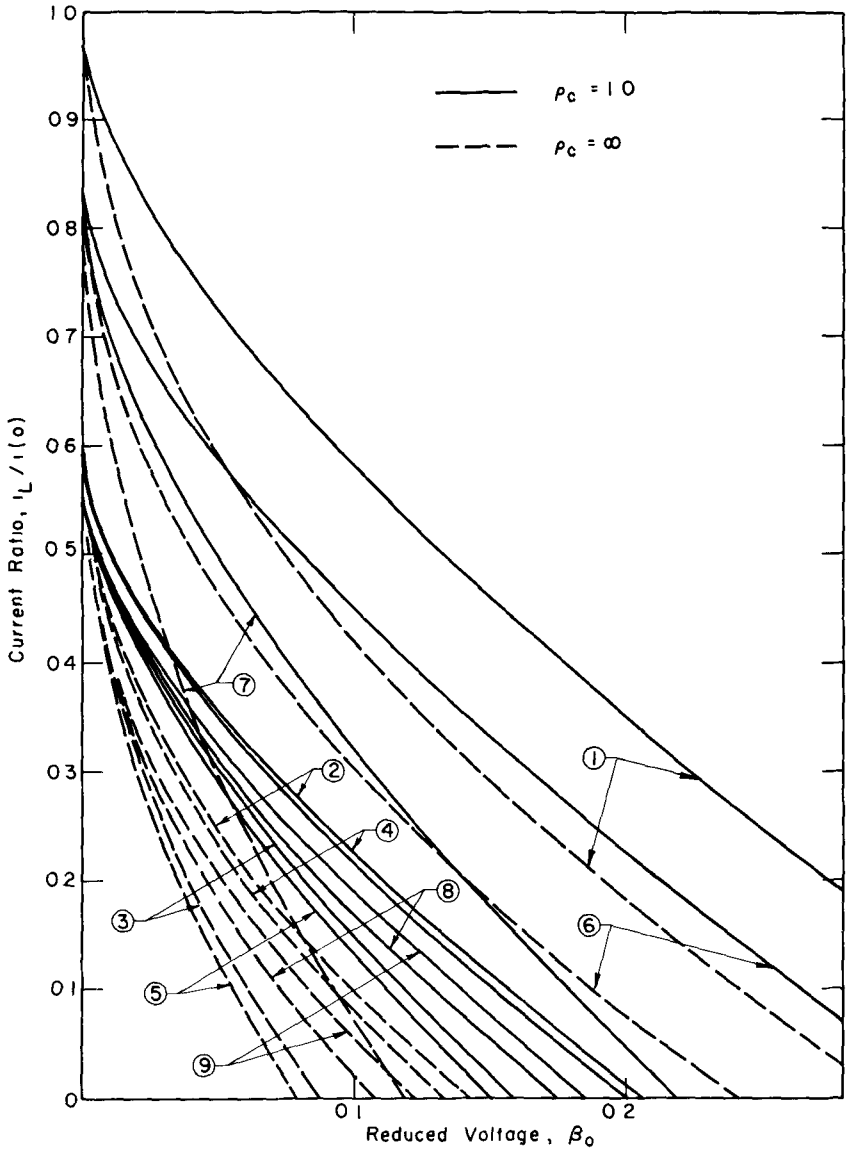

Fig. 6.14—Grid effects, parallel-plate cell (Curve numbers refer to grid parameters listed in Table 6 1) To use the $\rho_c = \infty$ curves, multiply the voltage scale by 3 33

$$f = 2r_g/a \qquad \text{(plane geometry)} \tag{6.39b}$$

$$= Nr_g/\pi c \qquad \text{(cylindrical geometry)} \tag{6.39c}$$

where r_g is the grid wire radius, a is the spacing between grid wires, N is the number of grid wires, and c is the radius of the grid cage circle in cylindrical geometry. This area ratio is also frequently termed the screening fraction of the grid. Its use for the f-factor is only approximate, since this neglects effects due to the angular distribution

Table 6.1—GRID PARAMETERS USED IN CURRENT CALCULATIONS

Curve No.*	f	η_g	x	f′	η_g'	(1−x)	k_1	k_2
1†	0			0			1.0	1.0
2	0.12	2.96	0.772	0	0	0	0.606	1.45
3	0.12	2.96	0.772	0.12	2.96	0.772	0.606	1.85
4	0.096	6.84	0.458	0	0	0	0 606	1.49
5	0 096	6.84	0.458	0.096	6.84	0.458	0 606	1.94
6	0.1	5	0.1	0.1	5	0.1	0.85	1.11
7	0.1	5	0.1	1.0	5	0.1	0.85	1.58
8	0.096	7.01	0.489	0.096	7.01	0 489	0.57	1.66
9	0.096	7.01	0.489	0	0	0	0.57	1.56

*The parameters f, η_g, and x for curves 2,3 and 4,5 correspond to measured results reported by Plummer et al.[4] for a 1¼-in.-diam. grid circle (shown later in Fig. 7.17) using clean and oxidized grid wires, respectively. Curves 8,9 correspond to a 2-in.-diam. circle. No values were reported for f , η_g', and x′, hence, two extremes are included in each case. Curves 6 and 7 are included to demonstrate the influence of f .

†Corresponds to an ideal grid.

and trajectory of the emitted particles. As pointed out by Plummer et al.[4], a more refined analysis may give values of order of 6% larger for grids in a typical Alpha Cell.

Another effect, not included in this estimate of the f-factor, is the influence of the attractive force of the negative grid on positive particles. However, the operating voltage of the grid will normally be in the kilovolt range, so this will be a small effect for high-energy particles of interest here. In fact, the Plummer work shows that an approximate correction for attraction is given by

$$f_V \approx f\sqrt{1 + \frac{qV_g}{T_0}} \tag{6.40}$$

where f is to be taken from Eq. (6.39), q and T_0 are the energy and charge of the particle, and V_g is the grid voltage. Since T_0/q is typi-

cally of the order of 1 MV, V_g would have to be 10^5 V or more for this correction to be important.

- *The μ-factor.* The μ- (or amplification) factor is defined as

$$\mu = [-V_a/V_g]_{\text{cut-off}} \tag{6.41}$$

where V_a and V_g are the anode and grid voltages, respectively, corresponding to a "cut-off" condition where the grid prevents any secondary electrons from reaching the anode. (This assumes a positive anode, negative grid.)

The μ-factor does not appear explicitly in the preceding leakage calculation; however, it represents an important aspect of any grid design. Normally it is desirable to maintain low grid voltages (to prevent breakdown to the cathode, minimize power supply requirements, etc.), and this suggests that the grid should be designed with a large μ-factor. However, as shown in the following analysis, this places certain restrictions on plate and grid spacings, grid wire sizes, etc., so that a compromise with other parameters is often necessary.

The μ-factor concept originated in vacuum-tube design calculations[12–15] where the initial energy of the electrons is neglected. This is not a good assumption for secondaries from charged particle bombardment, but the few cells designed to date that used grids have relied on vacuum-tube data for a first estimate of the μ-factor.

The traditional form[12] for the μ-factor for plane geometry with equally placed grid wires of radius r_g, separated by a distance "a," and located a distance "c" from the cathode and "b" from the anode (plate) is

$$\mu = \frac{2\pi b/a - \ln \cosh 2\pi r_g/a}{\ln \coth 2\pi r_g/a} \approx \frac{2\pi b/a}{\ln \coth 2\pi r_g/a} . \tag{6.42}$$

A plot of this relation is shown in Fig. 6.15(a). An equivalent form can be obtained for cylindrical geometry by applying conformal transformation techniques to Eq. (6.42). The result is[4,12]

$$\mu \approx \frac{-N \ln b/c}{\ln Nr_g/c} = \frac{N \ln b/c}{\ln 1/\pi f} \tag{6.43}$$

where now b is the radius of the anode, c is the radius of the grid cage, and N represents the number of wires. The geometry and this relation are shown in Fig. 6.15(b).

These figures demonstrate an important aspect of the grid design. It is seen that the μ-factor can be increased by increasing the screening fraction (essentially equal to the f-factor). But, as pointed out previously, a low screening fraction is desirable. The only alternate way to

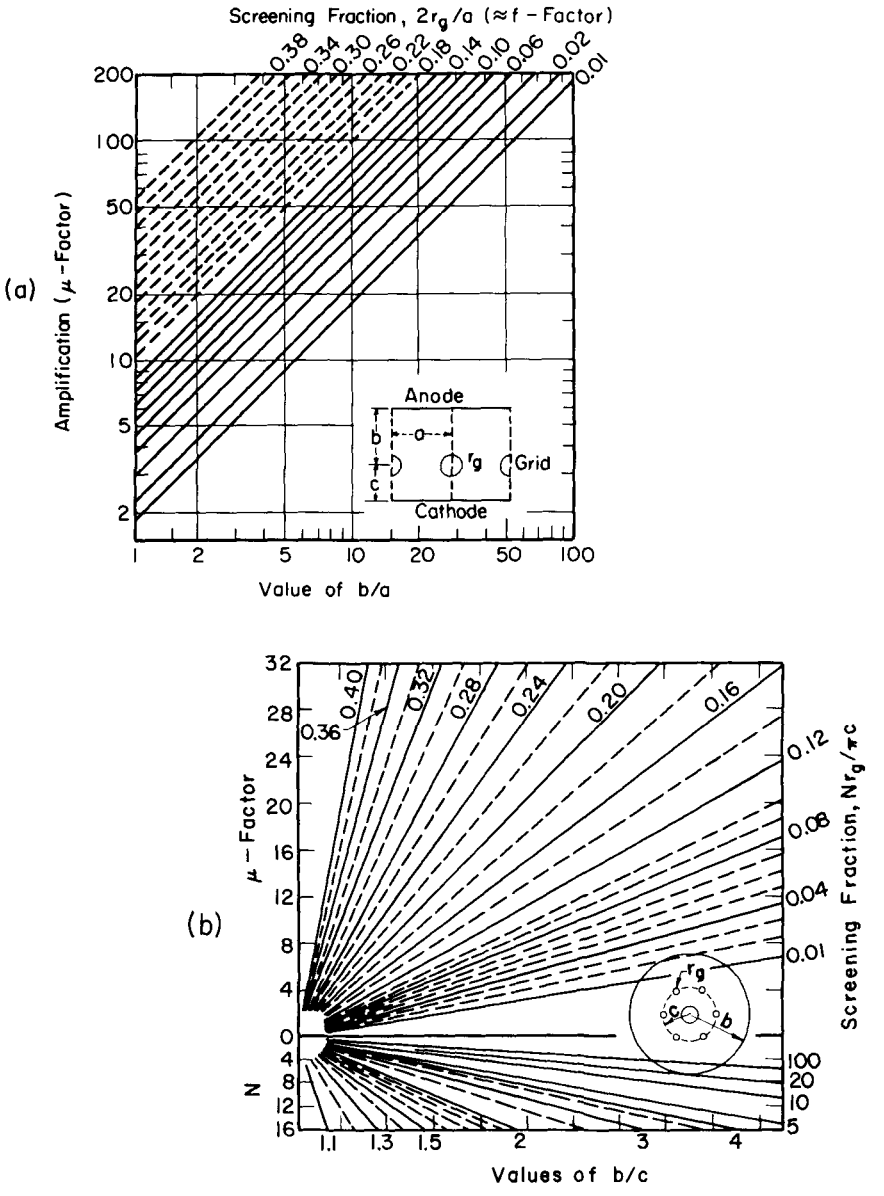

Fig. 6.15 — Amplification factor (μ-factor) for plane and cylindrical geometry. (Adapted from Spangenber, Ref. 13. The initial electron energy and relativistic effects are neglected in these plots.) (a) Plane geometry. To use, enter the appropriate b/a value, go vertically to the corresponding screening fraction, and read the μ-factor. (b) Cylindrical geometry. To use, enter the number of grid wires N, go horizontally to the b/c value, vertically to the screening fraction, and read the corresponding μ-factor.

obtain a large μ-factor is to increase the distance b (grid-anode separation for the plane case, or the anode radius for cylindrical geometry). However, this leads to a larger cell volume and a large anode area, hence weight — consequences that may not always be compatible with the design criteria. Practical designs will generally involve a compromise or optimization of these factors.

Also, note that the grid wire must not be too close to the anode or voltage breakdown will occur. The minimum spacing is, in effect, fixed by breakdown criteria discussed in following sections.

The approximate nature of the present evaluation of the μ-factor has been stressed. In practice, however, this approach seems to be reasonably satisfactory; for example, Plummer and his associates have used similar correlations in an Alpha Cell design with good results. Specifically, a $1\frac{1}{4}$-in. grid circle (see Chap. 7, Fig. 7.17) was designed to have a μ-factor of 41, and a value of 50 was measured; a 2-in. circle was designed for 48.5, and 40 was measured. A similar analysis was used by Krieve[6] in the design of a gridded Fission-Electric Cell experiment. Although a specific comparison with experimental measurements was not given, the cell appears to have met the design critieria of $\mu \approx 20$ fairly well.

• *The η_g, x, and "Fall-back" Parameters.* The charge ratio η_g and the escape fraction x are other important quantities required in the grid analysis. The charge ratio η_g could be evaluated directly from the secondary yield using methods developed in Chap. 5; however, such an analysis has not been carried out to date. It is complicated because the yield will depend on the direction of travel and the actual point on the wire that the impingent particle strikes. This determines the cord length and proximity to the surface for the particle track in the wire, and, as stressed earlier, the yield is strongly dependent on these factors.

The same difficulty is inherent in the calculation of the x-factor. In fact, Alpha Cell experiments that will be described in Sec. 7-3 indicate an unexpectedly large x-factor that has been attributed to grazing collisions, which release electrons on the anode side of the grid.

The factors f′, η_g', and x′ associated with "fall-back" particles are even more difficult to evaluate. As a first estimate, they might be set equal to their unprimed counterparts; however, this will be somewhat in error because of the differences in both the energy and angular distributions for "fall-back" particles relative to the primary current from the emitter.

• *Other considerations.* Plummer et al.[4] stress two additional factors to be considered in the grid design: (1) *Structural strength.* The minimum grid wire diameter is generally selected to prevent exces-

sive bowing due to electrostatic attraction between the anode and the grid. Additional supports may be required in extreme cases. (2) *Secondary yield.* The grid material should be selected with care to reduce the secondary yield at the grid. In addition to adding to leakage currents, secondary electrons escaping the grid may have sufficient energy after acceleration by the anode potential to cause a strong source of bremsstrahlung at the anode. This could require extra shielding for personnel safety.

Several points deserve consideration in any attempt to reduce secondary emission at the grid. Field emission effects on the side exposed to the anode may increase the yield, and, as a result, it might be desirable to stagger the grid wires to obtain partial shielding[4]. Also, in cells with high gamma-radiation intensities, gamma-induced secondaries may add to the yield, and this should be considered in the design.

6-2.4 Magnetic Suppression

Instead of a grid, a vertical or axial magnetic field might be considered for planar or cylindrical geometries to suppress secondary electrons. This approach has the immediate advantage that the grid losses just discussed are avoided; however, it generally turns out that the field strength required is large, and the magnet system is bulky and heavy.

The determination of the required magnetic field strength involves a straightforward extension of the energy and momentum balances of Chap. 2 to include the magnetic field. This analysis has been developed in several references in connection with "magnetron oscillators" where a similar situation is encountered[16–18].

The magnetic field strength that just prevents all electrons from reaching the anode is called the "magnetic cut-off." In the case of planar geometry, if relativistic effects and the initial electron energy are neglected, the field B_c required for cut-off is[16]

$$B_c = \frac{1}{d}\sqrt{\frac{2mV^+}{q}} \tag{6.44}$$

where m and q are the electron mass and charge, V^+ is the anode voltage, and d is the plate spacing. Characteristically, the critical field decreases in proportion to the spacing but increases with the square root of the anode voltage.

A more general relation, which was derived by Schock[7] for cylindrical geometry and both includes relativistic effects and allows for an initial electron energy T_1, is

$$B_c = \frac{4T_0/cq}{b\left[1-(a/b)^2\right]}\left\{\left[\left(\frac{T_i + qV^+}{T_0}+1\right)^2 - 1\right]^{1/2} + \frac{a}{b}\left[\left(\frac{T_i}{T_0}+1\right)^2 - 1\right]^{1/2}\right\} \quad (6.45)$$

where T_0 is the electron rest mass energy; c, the speed of light; b, the diameter of the outer electrode (anode); and a, the cathode diameter. In the limit of zero initial energy, this reduces to the expression derived in Ref. 18, and further, for non-relativistic cases (low V^+), it reduces to the standard magnetron cut-off relation derived in Refs. 16 and 17. (Eq. 6.45 assumes a uniform field density across the cell, but it can be extended to include a radial dependence following the methods of Ref. 18.)

Approximate field requirements for cells operating at lower voltages (<100 kV) can be found from the nomograph of Fig. 6.16. It is valid only where corrections for relativistic effects and initial velocities

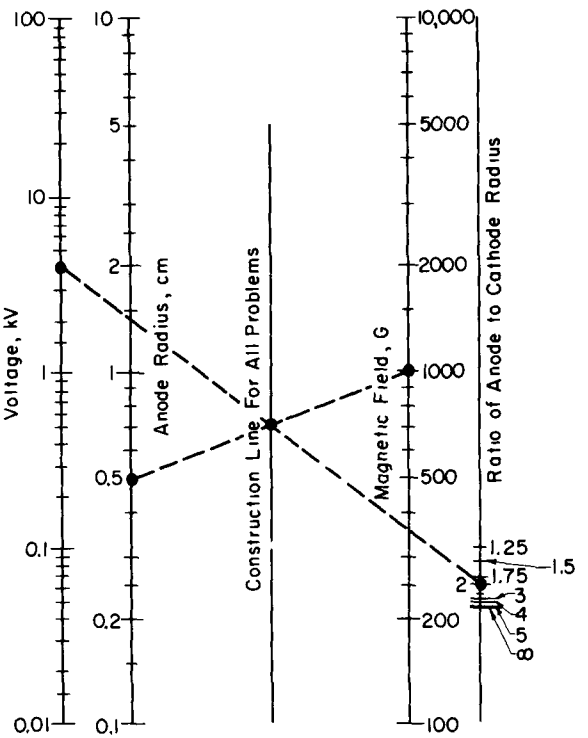

Fig. 6.16—Nomographic chart of the magnetic cut-off relation for cylindrical geometry. (After K. R. Spangenber, Ref. 17. Neglects relativistic effect and initial electron energies.)

are not required. This is reasonable if one is interested in suppression of the low-energy component of secondary electrons (<50 eV) in low-voltage cells. However, if megavolt potentials are involved or if the high-energy secondary component or beta particles are of interest, Eq. 6.45 should be used in its full form.

Some typical calculations are shown in Fig. 6.17. Plummer et al.[4] were chiefly concerned with low-energy secondaries since this ac-

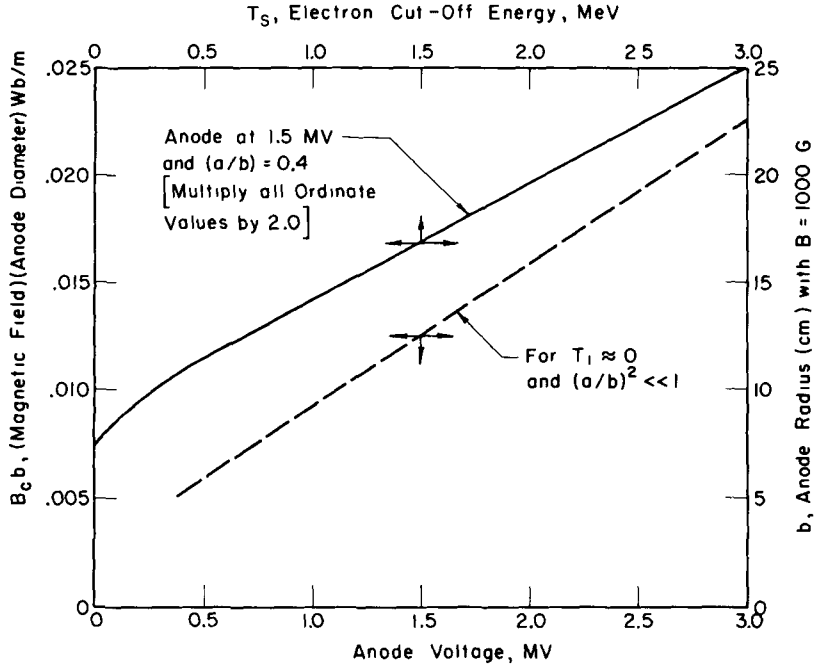

Fig. 6.17 — Magnetic field requirements. (The solid curve is from calculations by Schock, Ref. 7, where all electrons having energies $< T_s$ are cut-off. The dashed curve was calculated by Plummer et al., Ref. 4, for suppression of low-energy secondaries in an Alpha Cell.)

counts for the bulk of the secondary production. Thus, the initial electron energy T_i was neglected in calculating this curve (solid line), and, because a large outer-to-inner diameter ratio was involved, the factor $(a/b)^2$ was neglected relative to 1.0. As seen from the figure, to obtain 1-MV operation, a field-diameter product of ≈ 0.01 Wb/m is required corresponding to a field of 0.05 Wb/m^2 or 500 G for the 20-cm diameter cell.

Plummer's group felt this approach was impractical because of magnet weight and power losses involved in maintaining a field of this strength over the relatively large cell volume. However, their con-

clusion was based on a specific application with certain weight and size requirements, and magnetic suppression, despite the relatively large field requirement, may be of advantage in some cases. It is particularly attractive in experimental cells where a clean geometry is desired; for example, in his Fission-Electric Cell experiments, Krieve[6] used magnetic suppression with average fields of order of 1000 G (Chap. 7, Fig. 7.11). His experiments, however, brought out an important problem: If a low-energy electron from the cathode suffers energy losses via collisions, as can happen if a vapor pressure develops in the inter-electrode space owing to sputtering of the electrodes, it may be energetically impossible for the electron to return to the cathode despite the magnetic field. As a result, electrons may be "trapped" in the inter-electrode space, and their density can increase to the point where a leakage current will develop as they drift or diffuse to the anode while ions formed in the collisions drift to the cathode. This effect was observed by Krieve, and a major design change was required to overcome it (see Fig. 7.10 and the related discussion).

Returning to Fig. 6.17, we see that the magnetic field strength requirement increases rapidly for higher energy electrons (solid curve). For example, with the anode fixed at 1.5 MV, suppression of all electrons having energies up to 500 keV ($T_s = 0.5$) requires $B_c b = 0.023$ Wb/m as opposed to 0.015 Wb/m for suppression of the low-energy secondaries alone; i.e., for $T_s = 0$. (A corresponding value of 0.0125 Wb/m is read from the dashed curve for 1.5 MV. The difference is apparently due to the assumption by Plummer's group that $(a/b)^2 \ll 1$, and their neglect of relativistic effects as the electrons are accelerated across the 1.5-MV potential.) In practice, one would probably settle for a magnetic field strong enough to suppress soft secondaries and simply suffer a high-energy leakage current, which is hopefully small.

This figure also reminds us that an alternative to increasing the field strength is to increase the outer electrode radius. Whether or not this is a suitable approach depends on power density requirements and possible effects associated with the increased void fraction: e.g., increased uranium inventory requirements in a nuclear reactor involving Fission-Electric Cells.

6-3 VOLTAGE BREAKDOWN*

As stressed in Chap. 1, the fate of radiation cells as high-power devices depends, to a large part, on the development of designs that can

*The reader's attention is also called to an excellent recent text devoted to the varied technological problems associated with the use of high voltages, namely L. L Alston (Ed.), *High-Voltage Technology*, Oxford University Press, London, 1968.

maintain voltages of the order of a million volts without resorting to excessive plate spacings. As was shown in Table 1.4, such designs have not been achieved to date, and, to progress toward this goal, a better understanding of voltage breakdown would appear necessary. The present section reviews current theories for the two most common situations encountered in cells: Breakdowns in vacuum and in solid dielectrics. Some information is available for liquids; however, few cells have used liquid dielectrics to date, so for this material the reader is referred to Ref. 19.

In addition to the development of basic concepts, some of the breakdown criteria presented here may be of immediate value in design evaluation. However, there is one problem: Most all definitive studies have involved breakdown outside a radiation field. No doubt the cell radiations will affect breakdown—but a precise evaluation is an important problem that must be studied in the future. In fact, such studies may play a key role in the long-range cell development.

6-3.1 Breakdown in Vacuum

Alpert et al.[20] have reviewed the following four basic theories proposed at various times to explain the initiation of breakdown in vacuum:

(1) Surface-regeneration processes.[21–23]
(2) Electron-beam effects.[24–26]
(3) The clump hypothesis.[27,28]
(4) Field emission.[29–36]

The surface-regeneration theory assumes breakdown is initiated by the interchange of charged atomic particles between the electrodes. Particles from one electrode produce particles of the opposite sign upon impact on the other electrode[21], and breakdown occurs when the regeneration coefficient for this process exceeds unity.

This mechanism is not currently believed important in actual breakdown because experiments indicate the regeneration coefficients are generally too small[20]; however, it is thought to be associated with prebreakdown current flows. Arnal[22] and Mansfield[23] have shown that such flows occur under certain conditions, particularly under poor vacuum. These currents have been termed "microdischarges" by Arnal because they characteristically occur as self-extinguishing pulses of about a millisecond duration. Microdischarging causes a drain on the power supply, but in general does not lead to a destructive discharge. (As will be discussed in Sec. 7-3, microdischarging has been observed in an Alpha Cell.)

A related mechanism, the electron-beam effect, was first proposed by Bennett[24], who suggested that an electron beam originating by field

emission from point projections on the electrode is confined to a very narrow column as a consequence of a magnetic self-focusing (pinch) effect. The returning ions would likewise be localized, and they would initiate the arc.

Later studies[25,26] ascribe breakdown to localized heating of the anode by the impinging electron beam; however, calculations by Maitland[26] indicate space charge effects in the beam will cause spreading so that the maximum power density occurs at a current density of $\approx 10^4$ A/cm^2 for typical spacings. On the other hand, measurements indicate currents of the order of 10^7 A/cm^2 occur at breakdown, so there is considerable doubt that localized anode heating plays a major role in the initiation of breakdown.

The clump hypothesis, originally proposed by Cranberg[27], resulted from his observation that data from a large number of experiments seem to follow a square root law variation of breakdown voltage V_b with gap spacing d; i.e.,

$$V_b = (Cd)^{1/2} \tag{6.46}$$

where C is a proportionality constant that, based on a variety of data, he found to be about 0.1 (MV)^2/cm.

Equation (6.46) can be explained quite simply in terms of the clump theory by assuming that breakdown is due to detachment by electrostatic repulsion of a clump of material (loosely adhering to one electrode, but in electrical contact with it) that then traverses the vacuum gap and strikes the other electrode, which is at lower potential[27]. Assume breakdown occurs when the energy per square centimeter delivered to the target electrode exceeds a value C′, which is a characteristic of the electrode. This energy is given by the product of the gap voltage V and the charge density on the clump, and, if the charge density is assumed to be proportional to the field E at the electrode of origin, the breakdown criterion is

$$VE \geq \kappa C' \equiv C \tag{6.47}$$

where κ represents some numerical factors to account for effects such as field inhomogeneities. For parallel-plate electrodes the field is given by

$$E = V/d \tag{6.48}$$

and use of this in Eq. (6.47) gives Eq. (6.46).

More recent studies have resulted in some modifications of Cranberg's criterion based on other assumptions as to the details of the clump initiating process[28]. However, Alpert et al.[20] point out, "In

the ranges of voltages and gap spacings of typical interest, there is little direct evidence for the Cranberg mechanism." They note that attempts to measure transit times for the clumps have given negative results. To explain the correlation with gap spacing, they suggest that the electric field on the electrode where the clump originates will be strongly affected by the projection of the clump out of the surface and it is this enhancement factor that varies with the gap spacing. This explanation is, in fact, currently accepted as most realistic. It represents an extension of the field-emission theory originally pursued by Fowler and Nordheim[29] and later by Dyke and co-workers[30–32] and by Alpert, Lee, Lyman, and Tomaschke[20, 33–36].

A more quantitative understanding of this mechanism can be gained from Fig. 6.18, which shows the field enhancement factor β_F as a func-

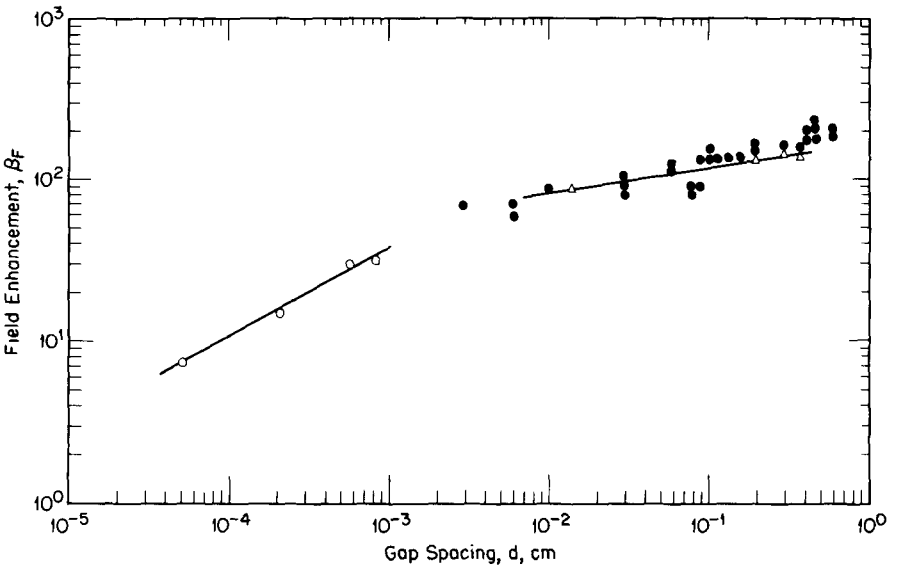

Fig. 6.18 — Variation of the field enhancement factor with spacing. (After Alpert et al., Ref. 20. Combines data from prebreakdown tests as well as cases where full breakdown occurred.)

tion of gap spacing. More precisely, β_F is defined as the ratio of the electric field at the emission site to the average field. Note that values of β_F as high as 10^2 are obtained at a spacing of about 10^{-1} cm. The data shown in this figure are for tungsten electrodes, and it was found[20] that, if the measured breakdown field was corrected for enhancement (multiplied by β_F), a "true" field of about 7×10^7 V/cm is obtained, independent of the gap spacing, over the range indicated from 10^{-4} to

1 cm. This result lends considerable confidence to the enhancement theory.

An alternate presentation of these data is shown in Fig. 6.19, where the measured breakdown voltage is plotted against the gap spacing. If no correction is made, the points cluster around a line whose slope is ≈ 0.7. (See the curve labeled V_b vs d, which is similar to Cranberg's correlation but with a slightly different slope.) To account for enhance-

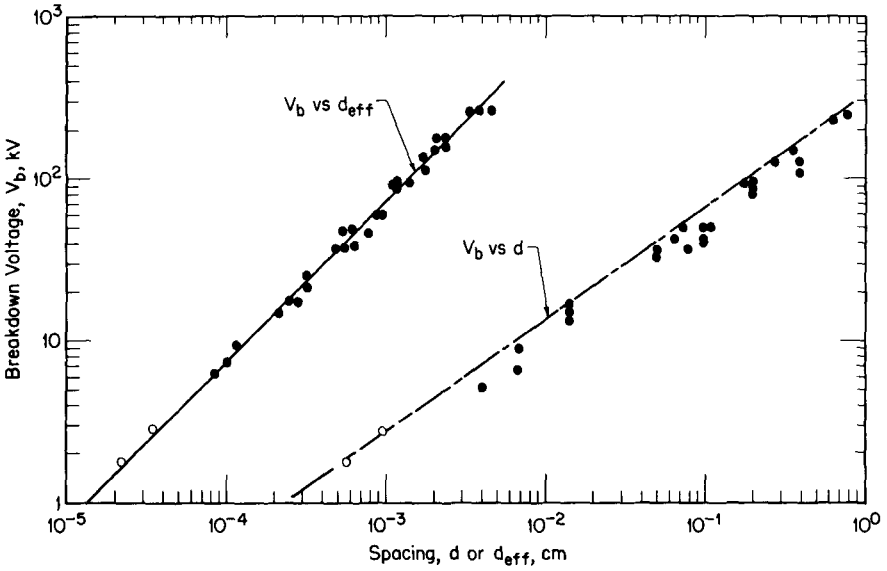

Fig. 6.19—Breakdown voltage and spacing correlations. (After Alpert et al., Ref. 20.)

ment, the breakdown voltage is replotted as a function of an "effective" gap spacing d_{eff} that is defined as

$$d_{eff} \equiv d/\beta_F . \tag{6.49}$$

This gives a line of slope 1.0, which is in agreement with the existence of a constant field value at breakdown.

The variation of β_F with d can be interpreted as the combination of two effects. For small spacing, the dominant effect is associated with an enhancement due to microscopic projections (whiskers) on the cathode. At larger spacings, macroscopic changes in the electric field distribution become important.

One question initially raised about the mechanism concerned the understanding of how a multiplicity of points on a large-area cathode, each of different height and enhancement, could be consistent with the

simple field and voltage correlations already noted. Recent calculations by Tomaschke and Alpert[36] have shown, however, that the correlation can indeed be explained in terms of the average behavior of a multiplicity of points.

Modified field-emission microscope studies have added direct evidence that whisker growth plays a fundamental role in breakdown[35]. These observations as well as back calculations from β_F data indicate that, for tungsten, the whiskers can be roughly pictured as projections $\approx$1-μ long with a pencil-like shape and a diameter about $^1/_{10}$ their height. A dynamic picture of their growth and destruction emerges; e.g., as breakdown begins, some projections may be destroyed while new ones are created.

A summary of recent values for the "true" breakdown field for various electrode materials is given in Table 6.2. It is interesting that the critical field varies only slightly from metal to metal, and, as Alpert[37] points out, "... in round numbers the critical field for breakdown for any metal and any geometry is approximately the same, i.e., 10^8 V/cm or one volt per angstrom."

Table 6.2—CRITICAL FIELD VALUES FOR VARIOUS METALS*

Metal	Work Function (eV)	E_b (V/cm)	Standard Deviation
W	4.5	6.40×10^7	1.00×10^7
Au	4.8	6.36×10^7	0.63×10^7
Cu	4.6	14.80×10^7	2.40×10^7
Cr	4.6	5.32×10^7	0.10×10^7
Mo	4.2	5.58×10^7	0.63×10^7
Ni	4.6	10.40×10^7	1.30×10^7

*Includes data by I. Brodie and also by Alpert as reported by Alpert[37].

Another important contribution from this theory is that it provides some insight into the effect of gas on the breakdown process. As pointed out later in Chap. 7, both Alpha and Beta Cell experiments have shown that the voltage-holding capability reaches a maximum at a gas pressure of about 10^{-4} Torr (Figs. 7.20 and 7.21). This is essentially independent of the nature of the gas; e.g., the effect has been observed for noble gases such as argon and also for attaching gases such as nitrogen. Because of the importance of obtaining high voltages, this phenomenon has held considerable interest. In 1967, Alpert et al.[38] showed it could be explained in terms of the whisker process. As illustrated schematically in Fig. 6.20, they propose that a selective sputtering by ions partly destroys the whiskers. Because of the high fields near the whisker tip, virtually every neutral in this region will be ionized by electron colli-

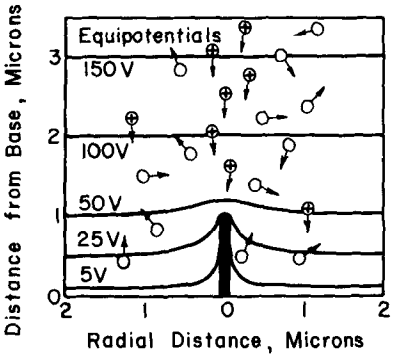

Fig. 6.20 — Schematic representation of selective ion bombardment of a whisker. (After Alpert et al., Ref. 38. Calculated equipotentials shown are for an average electric field of 5×10^5 V/cm.)

sion when the current reaches about 10^5 A/cm^2 (somewhat below the breakdown point). Thus, the whiskers are bombarded by a large number of ions having energies of order of 100 eV. This is quite sufficient to cause selective sputtering or similar dislocation damage to the emitting whisker, which in turn can reduce the enhancement coefficient β_F by a factor of 20 to 100.

In conclusion, the whisker theory gives an important physical picture for the initiation of electrical breakdown between metallic electrodes in high vacuum. It is interesting to speculate on how this picture might be affected by a radiation field, especially one composed of heavy, high-energy charged particles such as encountered in Fission and Alpha Cells. Unfortunately, this must remain speculation since definitive experiments have not been performed.

6-3.2 Breakdown in Solids and over Solid Surfaces

Radiation cells frequently involve the use of a solid insulator, and some cells, such as the solid-state Beta Battery and the Gamma-Electric Cell (described further in Chap. 7), use a dielectric material between the electrodes. Also, insulators must be used in all vacuum-type cells for positioning the plates apart, and, in some designs, an insulator is also used for the vacuum chamber wall. Thus, voltage breakdown in the insulator or across its surface becomes an important consideration.

Such breakdown has been observed in several instances: Sampson and Miley[39] have reported dielectric breakdown in high-voltage Gamma-Electric Cell studies using lucite and silicone; Plummer et al.[4] were concerned about possible flashover or arcing across the anode-insulator for their Alpha Cell; and the Leesona Moos ^{85}Kr battery typically discharges at 7 to 9 kV by arcing across the insulator separating the electrodes. (Further discussion of these observations is deferred until Chap. 7.) Breakdown has not been encountered more

frequently simply because leakage currents in many designs studied have prevented achievement of breakdown potentials. If high-voltage operation receives more stress in the future, such breakdown will certainly be a key problem.

The theory of breakdown in solids has been reviewed by a number of authors[40–47] and will not be discussed here in any detail. While investigations of the phenomena have followed a scientific basis since the early work of von Hippel[48] and Frohlich[49] in 1937, there are still many unanswered questions about the prebreakdown mechanisms that initiate the final instability. The problem is greatly complicated by the variety of ways the breakdown can occur: e.g., thermal instability, electrochemical decomposition, electromechanical forces, erosion by partial discharges, electron impact ionization, phase change, etc. (These and the following comments draw heavily upon the excellent reviews by Darveniza[46] and Whitehead[41].)

With careful control and design, it is possible to exclude thermal and other miscellaneous breakdown processes, and the limiting condition is then called *intrinsic* breakdown. It is characterized by two features: (1) Once the critical voltage is exceeded, breakdown occurs in less than 10^{-6} sec; thus, it is independent of the duration of the applied voltage. (2) Within wide limits, the critical electric field for breakdown is independent of the size and shape of the dielectric or the material of the electrodes. (An exception occurs for the one special case of "avalanche" breakdown where the critical field value does vary somewhat with the dielectric thickness.)

For insulators of interest here, the intrinsic breakdown field strength is generally above 10^6 V/cm, and some typical measurements are indicated in Fig. 6.21. As seen from drawing (a), both theory and experiment are in reasonable agreement for the case of glass; however, the situation is not so clear for other materials, so experimental data are desirable where good accuracy is necessary. Note that, as illustrated in part (b), a marked decrease in the breakdown strength occurs with increasing temperature, and this suggests that care must be taken to cool radiation cells if a maximum voltage is desired. (Materials like polymethyl methacrylate and polythene shown here have received considerable use in cells where radiation levels are not so high as to cause radiation damage.)

Modern theories generally propose an electronic process for breakdown, and this suggests that there are two principal aspects of the mechanism: (1) A source of initiatory electrons in the conduction band (unoccupied in a perfect insulator) where acceleration is allowed. (2) An inbalance between the acceleration of electrons by the field and their retardation by collisions.

Two sources of initiatory electrons are generally considered; namely thermal activation from defect levels just below the conduction

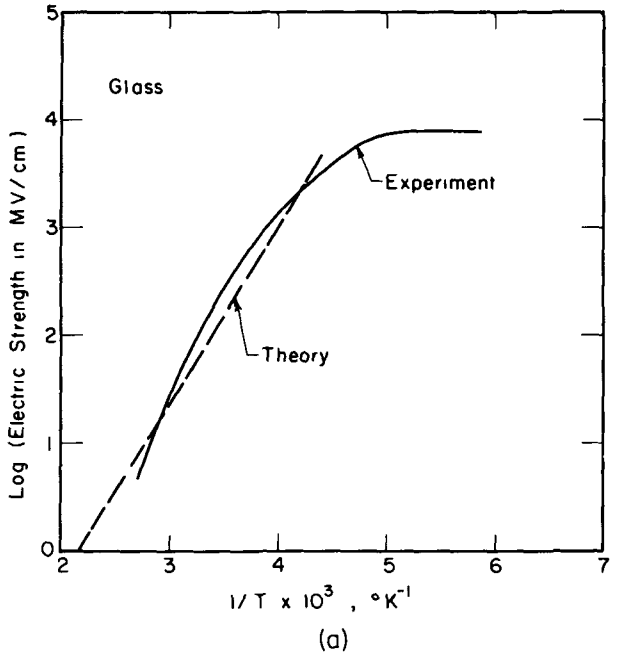

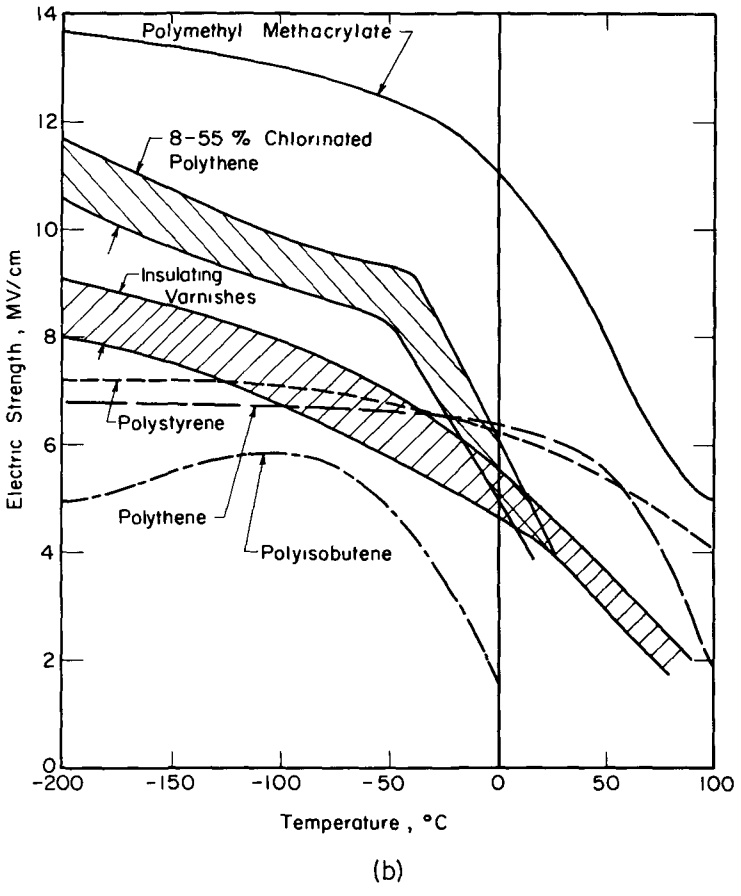

Fig. 6.21 — Variation of the intrinsic electric field strength with temperature for some representative materials. (Adapted from Whitehead, Ref. 41. Includes data by Oakes and also by Thomas and Griffith, as reported by Whitehead.) (a) Comparison of Frohlich's theory with experiments on glass. (b) Curves for some typical materials.

band and field activation. Another mechanism, which has not been studied in any detail to date but may be very important in radiation cells, is that nuclear radiations may excite electrons into the conduction band. Black and Charlesby[43] point out that, indeed, available data, while meager, do indicate a decrease in the breakdown voltage for polymers in a radiation field. This is also consistent with observations reported by Sampson and Miley[39] for the Gamma-Electric Cell experiments noted earlier. They report discharges and nonlinear effects (during irradiation) at electric field strengths as much as an order of magnitude lower than normal breakdown values. However, it is possible that space charge effects may have been involved also.

Another important phenomenon that may cause discharge of a high-voltage cell is breakdown over the insulator surface, often called "flashover." In many cases (e.g., the insertion of a smooth insulating surface across an air gap), the critical value of the electric field for flashover turns out to be lower than that for breakdown of either air alone or the insulator itself. Unfortunately, few fundamental studies of the processes have been reported, so it is only possible to review ad hoc data.

Darveniza[46] comments on five such types of data:

- *Smooth surfaces in otherwise uniform fields* Most information is available for a smooth surface such as glass or porcelain in air. At atmospheric pressure, the flashover voltage for a 1-cm gap is about half of the breakdown voltage for air alone, and it falls to about one third at 10 cm. At lower pressures, or when the pressure–gap-spacing product is less than 20 Torr-cm, the flashover and breakdown voltages are substantially the same.
- *Smooth surfaces in non-uniform fields* If, in addition to the parallel component, the electric field has a component normal to the insulator, flashover will depend on the relative dielectric constant of the insulator. Measurements in air have shown that the flashover voltage may increase by as much as a factor of two as this constant decreases from 10 to 1.
- *Corrugated surfaces*. In all cases, corrugation of a solid surface increases the flashover voltage. With care, it is sometimes possible to achieve a design where flashover is no longer the limiting condition.
- *Contaminated surfaces* Contamination invariably reduces the flashover voltage, sometimes drastically. Hygroscopic materials (e.g., glass, porcelain, etc.) are particularly prone to surface condensation of moisture, even under conditions of fairly low humidity. Measurements have shown a reduction of flashover voltage by as much as 15% in such cases.

- *Other factors*. In addition to humidity, surface roughness, dust, surface charges, non-uniform leakage currents, and uneven contact with electrodes are all known to affect flashover.

While the detailed mechanisms associated with flashover are not well understood, there appear to be two broad categories: clean surfaces and those that are heavily contaminated. For clean surfaces, suitably shaped to provide a surface path that is long compared to the shortest air path, the breakdown is thought to be a gas discharge in which the electric field is distorted by the presence of the insulator. Such discharges may start as a corona and then develop into a glow discharge, spark, and arc—each distinguished by a progressively larger current density[40, 41, 47]. Since the corona is frequently (but not always) the first step in this process, the recent review of the subject by Loeb[47] is of particular interest. At the other extreme, when surfaces are heavily coated with moisture or similar contamination, ionic-leakage currents flow, and Darveniza[46] has proposed that breakdown results from thermal ignition due to this flow and associated high current density predischarges.

Again, it is quite reasonable to suspect that both of these mechanisms may be enhanced by the additional ionization due to the intense radiation fields encountered in Direct-Collection Cells. Some data for a reduced flashover voltage have been reported for polymers[43], but a quantitative understanding or correlation is not available.

6-4 OTHER RADIATION EFFECTS

The radiation environment of a radiation cell introduces a number of problems that affect its performance. The possible effects on voltage breakdown and secondary electron currents have already been discussed, and other important possible effects include: mechanical deterioration by radiation damage; induced conductivity; induced space charge; and sputtering.

The general theory of radiation damage is treated in several standard texts, e.g., Refs. 50 to 53, and general problems related to electronic systems have been reviewed by Olesen[54]. Organic plastics are frequently used as a dielectric material in cells, and radiation damage to such materials is discussed in Refs. 55 to 59.

However, the aforementioned references deal primarily with "permanent" damage in the sense that it is measured after the sample is removed from the radiation field. This includes changes in such physical properties as tensile strength, hardness, elasticity, and electrical resistivity. Such damage is certainly important in cell design, particularly relative to lifetime; however, since the subject is complex and has been discussed at length in the references, it will not be treated

here. Rather, we will consider several important "in-field" effects that occur *during* irradiation. These include induced conductivity, space charge, and sputtering. Less information is available about these, and yet each has been found to be a limiting feature in certain cell experiments.

6-4.1 Radiation-Induced Conductivity

In general, the conductivity of an insulator placed in a radiation field will increase, the change being a function of the radiation intensity. This is an extremely important effect in high-voltage cell operation, because, as was shown in Sec. 6-1, the insulator conductivity generally determines the maximum voltage and power output for radiation cells (as pointed out in Sec. 6-1, R_I is assumed to include a correction for the induced conductivity).

Most of the studies of radiation-induced conductivity reported to date have involved plastics[60–68], principally polyethylene, while only a few inorganic materials such as tantalum oxide, magnesium oxide, and mica have been studied[65,68].

Based on Ohm's law, the conductivity σ is defined as

$$\sigma = \left(\frac{L}{A}\right)\frac{i}{V} \qquad (\Omega\text{-cm})^{-1} \tag{6.50}$$

where i is the current through a sample with cross section A and length L due to an applied voltage V. It may be related to mobilities of the charge carriers through

$$\sigma = \sum_j e_j n_j \mu_j \tag{6.51}$$

where e_j, n_j, and μ_j are the charge, density, and mobility of the j*th* type carrier. The summation is extended over all carriers involved in the current flow, which, for solids, are electrons and holes. However, for simplicity in the following analysis, we will assume that the electron mobility dominates so the summation will be dropped, it being understood that unsubscripted parameters then refer to electrons.

The conductivity during irradiation, defined here as σ^*, is frequently correlated with the absorbed radiation dose rate R using a form originally suggested by Mayburg and Lawrence[60]

$$\sigma^* - \sigma = \sigma_0 \left(\frac{R}{R_0}\right)^{\Delta} \tag{6.52}$$

where σ is the conductivity without radiation present, Δ is a fitting parameter, and R_0 is a reference dose rate that corresponds to a difference in conductivity equal to σ_0.

Early experiments by Mayburg and Lawrence[60], Fowler[62], and Winslow and Alger[63] showed that the exponent Δ generally ranges from 0.5 to 1.0. Fowler has carried out one of the most comprehensive studies, and his values for Δ and σ_0 are summarized in Table 6.3. However, care must be exercised in using these data. As seen from the polystyrene data, considerable variation may occur due to slight dif-

Table 6.3 — RADIATION-INDUCED CONDUCTIVITY PARAMETERS*

Material	Δ	σ_0 $[(\Omega\text{-cm})^{-1}]$
Moulded amber	1.0	1×10^{-17}
Natural amber	1.0	1×10^{-18}
PMMA plasticized†	1.0	3×10^{-18}
Mica	0.95	1×10^{-17}
PMMA red '400'	0.93	2×10^{-17}
Polyethylene terephthalate	0.83	6×10^{-20}
Polyethylene	0.81	9×10^{-17}
Polystyrene‡	0.65 to 0.75	1 to 2×10^{-18}
PTFE†	0.63	8×10^{-17}
PMMA unplasticized†	0.5	2×10^{-18}

*Measured by Fowler, Ref. 62. All values are for R_0 = 8 R/min at a temperature of 20°C and are based on measurements using dose rates from 10^{-3} to 1 R/h and a maximum dose of 5×10^6 R.

†PMMA = polymethylmethacrylate; PTFE = polytetrafluoroethylene.

‡The ranges indicate differences between British and U. S. samples.

ferences between the compositions of materials produced by various manufacturers (or even in different lots). Also, studies by Yahagi and Danno[64] indicate that the parameters for higher dose rates (>10^2 R/h) may differ somewhat.

The basic mechanism involved in induced conductivity remains debatable. Mayburg and Lawrence originally proposed the H^+ ion (proton) as a charge carrier in polyethylene. However, Fowler contradicts this and suggests a trapping model where electronic conduction dominates. Yahagi and Danno support Fowler's general conclusion, but point out some discrepancies. In particular, they propose that molecular motion in the polyethylene chain may be important in some cases, and they also suggest that the interaction of Compton electrons as well as δ-rays with trapped electrons may be significant.

More recently Harrison[66] suggested that a "hopping model," attributed to unpublished studies by S. H. Glarum, is more suitable than the conduction band model. Coppage and Peterson[67] claim they avoid the

use of a model "as much as possible in the belief that insufficient knowledge exists concerning the transport properties of polymeric materials to warrant use of any 'conventional' models."

Despite these problems, it is instructive to consider Fowler's model in some detail. Besides giving some "feeling" for the phenomenon, it provides a qualitative prediction of many features.

Many of the materials of interest here (e.g., polystyrene) are completely amorphous. Others like polyethylene have crystalline regions randomly embedded in an amorphous mass. While the existence of an energy-band structure is not obvious in such cases, Fowler's model is based on the assumption of an equivalent structure. He notes that if an electron is given sufficient energy by ionizing radiation, it becomes free to move and may be visualized as existing in an "effective" conduction level.

As illustrated in Fig. 6.22, traps can arise in several ways—a conventional trap-energy level structure is shown in sketch (a), whereas

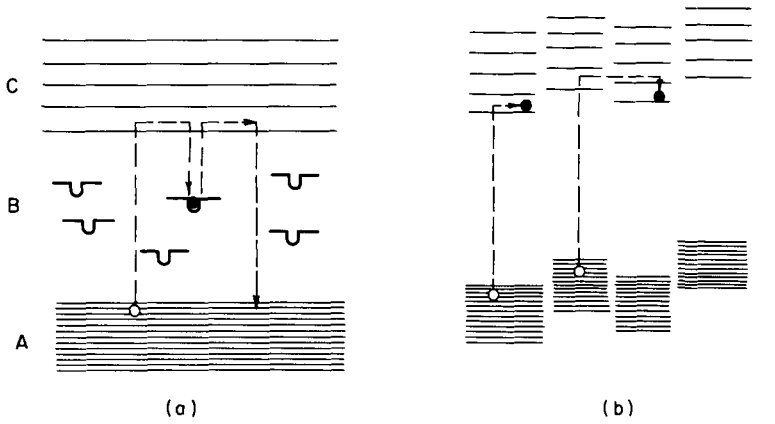

Fig. 6.22—Trapping concepts. (After Fowler, Ref. 62.) (a) Energy-level diagram for a single group of atoms. [Energy represented vertically, distance horizontally. A: Normally full (valence) levels. B: Normally forbidden levels, with metastable trapping levels for electrons. C: Conduction levels (normally empty).] (b) Energy-level diagram for a material with a disordered structure. (Shows schematically how the conduction levels for one group of atoms may be the trapping levels for a neighboring group.)

trapping due to a disordered structure is shown in (b). The traps compete with holes for electron capture, and thus they reduce the available number of conduction electrons.

Fowler points out that, to explain "dark" conductivities (no radiation present) of the order of 10^{-20} $(\Omega\text{-cm})^{-1}$ for insulators that typically have a thermal activation energy of only 1 to 1.5 eV, trap densities

must be quite large, ranging from 10^{13} to 10^{20} traps/cm^3. The discrete energy-band picture suggests that the trapped electron must receive sufficient energy to reach a higher energy level before it can escape; thus, it is assumed, as illustrated in Fig. 6.22, that all trapped electrons must pass through the conduction band in order to be released. Also, since relatively few electrons will receive just the right amount of energy to be lifted from the valence level to a trap, it is assumed that electrons pass through the conduction band *prior* to being trapped. In this sense, trapped electrons can only communicate with the conduction band, and a key assumption generally made is that the trapped electron density is in *thermal* equilibrium with the conduction electron density. This is generally justified because of the relatively small energy gap between the traps and the conduction band. This suggests that, under steady state irradiation conditions, there is a dynamic equilibrium between the rate at which electrons enter the conduction band from traps and the rate of loss to traps. It further implies that the dominant loss rate of conduction electrons is due to recombination with holes, so that the source-loss rate balance for the conduction electron density n is simply

$$\frac{R}{\xi} = bn(n + m) \tag{6.53a}$$

where

$$b = qv \qquad (\text{cm}^3/\text{sec}) . \tag{6.53b}$$

As before, R is the absorbed radiation dose rate; ξ, the energy required to produce an electron-hole pair; m, the trapped electron density; and the recombination coefficient b represents the product of the electron-hole recombination cross section q and the conduction electron speed v. Since an electron in either the conduction band or a trap leaves a hole in the valence band, the quantity (n + m) gives the number of holes, and the recombination rate is taken to be proportional to this times the density n.

This type of relation is consistent with models suggested by Kittel and also Rose[69] for the analysis of photoconductivity in insulating crystals.

To illustrate the significance of Eq. (6.53), we will consider the extreme cases where the conduction electron density greatly exceeds the trapped electron density (n + m), and vice versa. Then, substitution of Eq. (6.53) for n in the definition of the conductivity [Eq. (6.51)] gives

$$\frac{\sigma^*}{e\mu} = \begin{cases} (R/\xi b)^{0.5} & (n \gg m) \qquad (6.54a) \\ (R/\xi bm)^{1.0} & (m \gg n) \qquad (6.54b) \end{cases}$$

which shows the plausibility that the exponent in Eq. (6.52) varies between 0.5 to 1, depending on the relative magnitudes of n and m. (For simplicity, we have omitted the dark current contribution, i.e., assumed $\sigma^* \gg \sigma$.)

However, this argument ignores the earlier assumption that trapped and conduction electrons exist in thermal equilibrium—then, since the traps are at lower energies, the trapped density m will always exceed n as long as sufficient trap sites are available. This suggests that Eq. (6.54b) should be used; however, m can not be viewed as a constant but, in fact, depends on n. To analyze this case, it is necessary to describe the distribution of the trapping sites in energy, and this will in turn determine both the exponent Δ and the temperature dependence of the conductivity. As a simple illustration, consider the extreme case where all of the traps are located at a single depth T_1 below the conduction band, such that the energy distribution for the traps M(T) becomes a delta function given by

$$M(T)\, dT = \delta(T_1 - T)\, dT . \tag{6.55}$$

Then, for thermal equilibrium at temperature T, the electron density ratio becomes

$$n/m \approx \exp\,(-T_1/kT) \tag{6.56}$$

where k is the Boltzmann constant. For reasonable values of T_1, $m \gg n$, and combining Eqs. (6.53) and (6.56) and using the definition of σ [Eq. (6.51)], we find

$$\sigma^* = \left[\frac{e\mu}{\sqrt{\xi}\, qv} \exp\left(-\frac{T_1}{2kT}\right)\right] R^{1/2} \qquad (\sigma^* \gg \sigma) . \tag{6.57}$$

Comparison with Eq. (6.52) shows that, in this case, $\Delta = 1/2$ and the bracketed quantity corresponds to (σ_0/R_0^{Δ}). The quantity $(T_1/2)$ in the exponential temperature dependence can be viewed as an activation energy.

While this result demonstrates some of the main features of the model, a more realistic trap distribution should be used in practice. Fowler[62] has considered two important cases: (1) A constant distribution, i.e., M(T) = constant. (2) An exponential distribution, i.e., $M(T) \propto \exp(-T/kT_1)$, where (kT_1) is a characteristic energy of the material. He shows in the first case that $\Delta = 0.97$ and, in the case of the exponential, that $\Delta = kT_1/(T + kT_1)$; in the limit of a very steep exponential distribution, $kT_1 \to T$ and $\Delta \to 1/2$, which is in agreement with Eq. (6.57). (The delta function can be viewed as the limiting case for a steep exponential.) In these instances, the actual temperature dependence of

σ^* does not turn out to be a pure exponential, but over a reasonable range of temperatures the difference is negligible.

Using these results and assuming a mobility of $\mu = 10^{-3}$ cm^2/(V-sec) and an average speed of $v = 10^7$ cm/sec, Fowler has back-calculated the recombination cross sections q, which, along with typical activation energies, are shown in Table 6.4. The other important parameter involved in Eq. (6.53), the energy absorbed per carrier ξ, has been estimated by Coppage and Peterson[67] to be $\approx 3 \times 10^3$ eV for polystyrene. However, they point out that estimates by various persons vary by as much as an order of magnitude.

While there are some exceptions, the general trend is for an increasing activation energy as $\Delta \to 0.5$ (cf. Tables 6.3 and 6.4), and this is in agreement with Fowler's analysis.

Table 6.4 — TYPICAL PARAMETERS*

	Recombination Cross Section, q (cm^2)	Activation Energy, $T_1/2$ (eV)
Moulded amber	4×10^{-15}	0.06
Polyethylene	1×10^{-16}	0.35
Polystyrene (U. S. sample)	3×10^{-15}	0.18
Polytetrafluoroethylene	1×10^{-17}	0.5

*From Fowler, Ref. 62.

More recently, Yahagi and Danno[64] have studied the temperature dependence of polyethylene and teflon over a wider range of temperatures. Their results, shown in Fig. 6.23 and Table 6.5, indicate that the activation energy, as well as Δ, change abruptly at about $-40°$C. Below $-40°$C the induced current is constant or increases slightly, and they suggest that, at these low temperatures, the rate of release of trapped electrons is controlled by radiation interaction with them, rather than by thermal activation as assumed earlier.

The values of Δ in Table 6.5 are somewhat smaller than those noted earlier from Fowler's measurements, and Yahagi and Danno suggest this may be due to the higher dose rates they used and/or a difference in the crystallinity between their samples and those used by Fowler.

The decay of the induced conductivity immediately following an irradiation can also be determined with the trap model: The rate of decay of conduction electrons is equal to the difference between the rate of release of trapped electrons and the recombination rate. (Note that, since the radiation is "off," the source term R/ξ does not appear.) If a dot is used for the time derivate, the balance is

$$\dot{n} \approx -\dot{m} - bnm \tag{6.58}$$

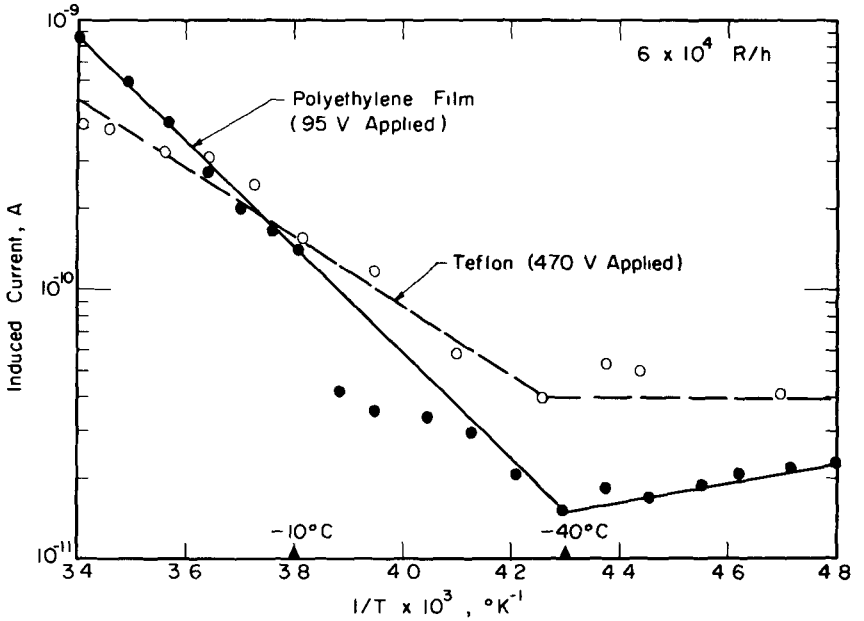

Fig. 6.23—Variation of current with temperature for polyethylene and teflon films. (For irradiation at 6×10^4 R/h with the polyethylene and teflon samples biased externally at 96 and 470 V, respectively. After Yahagi and Danno, Ref. 64.)

Table 6.5—EFFECT OF TEMPERATURE ON INDUCED CONDUCTIVITY PARAMETERS*

	Temp. (°C)	Δ	Activation Energy, $T_i/2$ (eV)
Polyethylene film	+9 to −20	0.61	0.34
(0.1 mm thick)	−54 to −75	0.83	≈ 0
Polyethylene cable	(room)	0.68	
Teflon film	+9 to −40	0.83	0.32
(0.5 mm thick)	−50 to −61	0.97	≈ 0

*By Yahagi and Danno, Ref. 64. Dose rate range, 10^3 to 10^5 R/h (^{60}Co source). Maximum dose, 5×10^5 R.

where b is the recombination coefficient defined in Eq. (6.53b). Following Fowler, we assume that the rate of release from traps is rapid enough to keep pace with recombination. Then, an approximate thermal equilibrium will be maintained so that Eq. (6.56) may be used to eliminate m and $\dot{m}$, and the solution of the resulting equation is

$$\frac{n(t)}{n(0)} = [1 + n(0)C_1 t]^{-1} \tag{6.59}$$

with

$$C_1 = b\left[\exp\left(-\frac{T_1}{kT} + 1\right)\right] \qquad (\delta\text{-trap distribution}) . \tag{6.60a}$$

Here n(0) is the conduction electron density at the time the radiation is "turned-off." Fowler has shown that a more realistic exponential trap distribution leads to this same result for n(t)/n(0), but with C_1 defined as

$$C_1 = bT_1/T \qquad \text{(exponential distribution)} \tag{6.60b}$$

where T_1 is the characteristic temperature which defines the trap distribution as discussed earlier.

Fowler has checked both the hyperbolic time dependence and temperature behavior predicted by Eqs. (6.59) and (6.60b), and he reports quite good agreement for polyethylene cable at moderate temperatures and dose rates. Some typical values of $n(0)C_1$ that he found from plots of n(t)/n(0) are given in Table 6.6. The values of n(0) listed were calculated using values of q from Table 6.4.

Two points should be noted: (1) The trap densities suggested earlier of 10^{13} to 10^{20} traps/cm^3 are considerably larger than n(0), so the assumption that $m \gg n$ should be valid even at quite large dose rates. (2) The time constants show considerable spread, and compari-

Table 6.6—DECAY PARAMETERS AND CONDUCTION ELECTRON DENSITIES*

Material	$[n(0)C_1]^{-1}$ (min)	n(0) (electrons/cm^3)
Moulded amber	8.4×10^{-3}	6×10^4
Polyethylene	7.5	6×10^5
Polystyrene (U. S. sample)	7.8×10^2	1.2×10^4
Polytetrafluoroethylene	1.1×10^3	5×10^5

* After Fowler, Ref. 62. For an initial irradiation at 8 R/min at 20°C.

son with Table 6.3 indicates that the time constant increases with decreasing Δ, i.e., with the shift from a constant to a steeply exponential trap distribution.

More recent data effectively demonstrate that the situation is more complex than indicated by the simple model used here. Harrison[66] has shown the decay of the conductivity for six organic materials irradiated by a pulsed 1000-Ci ^{60}Co source can be correlated with an expression of the form

$$\frac{\sigma(t)}{\sigma(0)} = \sum_{i=1}^{4} K_i \exp(-t/\tau_i) \tag{6.61}$$

where K_i and the time constant τ_i serve as fitting parameters. Because of their practical importance, average parameters are given in Table 6.7. Harrison justifies this correlation on the basis of a conduction-trapping model that allows two classes of traps: The "α-traps," close to the conduction band, can return electrons to the conduction band by thermal excitation; "β-traps," lying much deeper, are generally filled, and their electrons have a large probability of recombining to the ground state directly. In contrast to the earlier development that assumed a thermal equilibrium during decay, Harrison neglects release to the conduction band, and he determines the decay rate of conduction electrons by a sum of rates due to recombination with holes and trapping into various unfilled α-trap levels. The time constants in Eq. (6.61) are viewed as characterizing each of these rates.

The seeming conflict between Eq. (6.61) and the hyperbolic behavior found by Fowler can be rationalized as follows. From Table 6.7, we note that there is generally one dominant time constant τ_d — the other components essentially represent initial transients. Thus, after these transients disappear, but before time t is large compared to the dominant constant, the time variation of the conductivity is given approximately by

$$\frac{\sigma(t)}{\sigma(0)} = \exp\left(-\frac{t}{\tau_d}\right) \approx \left(1 + \frac{t}{\tau_d}\right)^{-1} \qquad \left(\frac{t}{\tau_d} \ll 1\right) . \tag{6.62}$$

Comparison with Eq. (6.59) shows that τ_d^{-1} plays the role of $n(0)C_1$ in this approximation. Fowler, in fact, neglected initial transients in his analysis, and, while he did include data for times longer than would be valid for the above expansion, he stopped measurements fairly quickly due to the small currents involved. Thus, the two interpretations of the decay data are not too surprising, and actually, the general trends of the time constants for polyethylene and polystyrene in Tables 6.6 and 6.7 are similar. However, there are significant differences be-

Table 6.7 — AVERAGE DECAY PARAMETERS*

Material	$\sigma(0)$ $[10^{-16}\ (\Omega\text{-cm})^{-1}]$	Initial Dose Rate (R/sec)	Time Constants (sec)				Weighting Factors			
			τ_1	τ_2	τ_3	τ_4	K_1	K_2	K_3	K_4
Teflon	7	3.3	0.43	2.01	16.5	226	0.38	0.30	0.26	0.06
Polyethylene	5	1.7	2.2	13	173		0.48	0.30	0.22	
Polyvinyl-chloride	0.76	3.3	1.5	250			0.62	0.38		
Kel-F	1.6	6.7	1.4	$>10^3$			0.35	0.65		
Polystyrene	1.0	6.7	0.47	875			0.80	0.20		
Nylon	1.94	3.3	2.1	$>10^3$			0.18	0.82		

*By Harrison, Ref. 66.

Notes: 1. Sample thicknesses ranged from 0.04 to 0.08 cm. Applied fields from 3 to 40 kV/cm were used.
2. Temperatures were 60 to 80°C except for polyethylene (43°C) and nylon (30°C).
3. Exposure times generally 60 to 120 sec.
4. All commercial grade materials.

tween absolute values, even if corrections are made for the dose rate differences.

Unfortunately, Harrison does not present results for different dose rates for a single sample. This would clear up the obvious question of whether or not τ_d depends on n(0).

The discussion to this point has centered on gamma-induced conductivity. Since nuclear cell applications may involve reactors, it is significant to note that Coppage et al.[65] have correlated results from mixed neutron–gamma irradiations with a form similar to Eq. (6.52), namely

$$\sigma^* = A_n R_n^{\Delta} + A_\gamma R_\gamma^{\Delta} \tag{6.63}$$

where the subscripts n and γ represent neutron and gamma parameters, respectively. They show that for a wide variety of dielectrics

$$0.06 \leq (A_n/A_\gamma) \leq 0.55 \, . \tag{6.64}$$

Thus, in general, neutrons are less effective, per unit absorbed dose rate, in inducing a conductivity.

Finally, several results from nuclear cell studies deserve note. Sampson[70] has used Fowler's model in his analysis of voltage operation of a Gamma-Electric Cell with good results; however, this does not represent a sensitive test of the model. Coleman and Bohm[8,61] report an interesting effect observed in studies of solid-dielectric Beta Batteries where the conductivity for some materials was actually found to decrease with long time irradiation. For example, beta irradiation of polystyrene resulted in an initial increase of conductivity from 10^{-16} to about 10^{-15} $(\Omega\text{-cm})^{-1}$, but, after one day of continued irradiation, the conductivity began to decrease with approximately the square root of time. This decrease has been observed to continue for polystyrene for irradiation periods as long as a year. In this case, the ultimate conductivity was less than that for an unirradiated sample. A similar effect was noted for teflon and Kel-F, but these materials became brittle in a matter of weeks and were prone to breakdown. Radiation damage also appeared to reverse the trend in polyethylene after a week or so. No explanation has been given for this effect. While the results noted are for beta-particle irradiation, similar effects might be expected for gammas; however, this has not been verified experimentally and further studies have not been reported to date.

6-4.2 Radiation-Induced Space Charge in Dielectrics

Experiments have demonstrated that significant space-charge and polarization effects may occur during bombardment of dielectrics by

electrons from direct electron irradiation, from Compton scattering by gamma- or x-rays, or from δ-ray electrons produced by heavy-ion bombardment.

Gross[71] has published a bibliographical review of some studies through 1963, and the present development is largely based on this and later publications by Gross and his co-workers, especially Refs. 72 to 75.

Some terminology is noted first. A dielectric containing a permanent volume polarization, due to its similarity to a magnet, is called an "electret" (according to Gross, this terminology can be traced back to O. Heaviside). A prefix often indicates the method used to introduce the polarization; e.g., electrets prepared by combined electric and thermal treatment are called "thermoelectrets," those prepared by light excitation are "photoelectrets," and those prepared by penetrating radiation, "radioelectrets." The last are of primary interest here.

The formation of a space charge can be visualized as follows: High-energy electrons are frequently trapped at the end of their range in the dielectric. The detailed trapping mechanism is not entirely clear; however, there is ample experimental evidence to show the trapping efficiency may be quite high in some materials, even approaching 100%. If the dielectric is sufficiently thick, continued exposure can lead to a space charge so large that it will actually produce electrical breakdown. This was first observed in 1959–1962, when a number of radiation shielding windows in hot caves were shattered before preventive steps were taken[76–78]. Breakdown in glasses and polymers may occur spontaneously or by induced field enhancement obtained when a pointed metal rod is pressed to the surface of the dielectric. Lichtenberg figures have been obtained in this manner from electron bombardment. Charge storage has been determined in several studies that use an electrometric method or alternately measure the charge released by heat treatment or exposure to ultraviolet radiation[71]. In some cases, the actual spatial distribution of the charge has been determined by sectioning the target, and this technique has been used to measure electron ranges[72].

Some important aspects of space-charge storage can be illustrated through a simple analytic model. Let us first consider gamma irradiation of a dielectric of thickness d as illustrated in Fig. 6.24. As noted earlier, the Compton electrons are preferentially scattered forward, and L_δ is defined as their average displacement along the x-axis [Eq. (5.10a)].

Two basic assumptions are made: (1) The holes are taken as immobile, and recombination or neutralization of the hole, once formed, is neglected. (2) All electrons are assumed to be trapped at the end of their track.

These assumptions are equivalent to postulating that the dielectric is a perfect insulator in which charged-particle mobilities are zero. At first thought, in light of radiation-induced conductivity, this may appear to be a poor assumption. However, for the dielectrics of interest here (i.e., polymers, glass, etc.), barring breakdown, conductivity effectively sets an upper limit on the electric field build-up. Thus, this idealized model provides a fairly realistic representation of initial space-charge effects *prior* to the development of large fields or breakdown.

If the radiation intensity is assumed to be constant during the irradiation period, the rate of growth of holes in a volume element dx, designated as $[dn_+(x)/dt]\,dx$, is

$$\frac{d}{dt}[n_+(x)\,dx] \approx \frac{\mu_{ce} I_\gamma(x)}{\langle T_c \rangle}\,dx = \mu_c \frac{I_\gamma(0)}{\langle h\nu \rangle} \exp(-\mu_a x)\,dx \tag{6.65}$$

where $I_\gamma(x)$ is the gamma energy current [MeV/(cm^{2}sec)] at x, $\langle T_c \rangle$ is the average Compton electron energy, μ_c and μ_{ce} are the Compton linear attenuation and absorption coefficients, respectively, and μ_a is the total linear absorption coefficient (as defined in Sec. 5-4.3).*

The growth of trapped electrons $[dn_-(x)/dt]\,dx$ is displaced from the point where the electron originates by L_δ; thus

$$\frac{d}{dt}[n_-(x)\,dx] \approx \begin{cases} \dfrac{\mu_c I_\gamma(0)}{\langle h\nu \rangle} \exp[-\mu_a(x - L_\delta)]\,dx & (x \geq L_\delta) \quad (6.66a) \\ 0 & (x < L_\delta)\,. \quad (6.66b) \end{cases}$$

With the present average path model, no electrons stop between 0 and L_δ, whereas in reality a few would. (The dielectric is assumed to be thicker than L_δ, which is not uncommon, since L_δ is generally of order of 0.1 cm or so in dielectrics of interest.)

*This formulation includes a contribution from scattered photons. Compton production is found by dividing the energy absorbed in dx by the average Compton electron energy [identified as $\langle h\nu \rangle$ (μ_{ce}/μ_c)]. An alternate approach, used some in the literature, evaluates Compton interactions due to the attenuated primary beam. This amounts to substituting the total linear *attenuation* coefficient μ_0 for the absorption coefficient μ_a in Eq. (6.65). The point is that $\mu_0 > \mu_a$ because μ_0 includes a scattering coefficient, and in essence this states that any scattered photons are removed from the beam. In fact, high-energy scattered photons will contribute to Compton production, and the present approach makes an allowance for this. Due to angular effects and the fact that $\langle h\nu \rangle$ should be an average over both the primary and the scattered components, i.e., be a function of x, this treatment probably overestimates hole production. Still it should be of sufficient accuracy for present purposes.

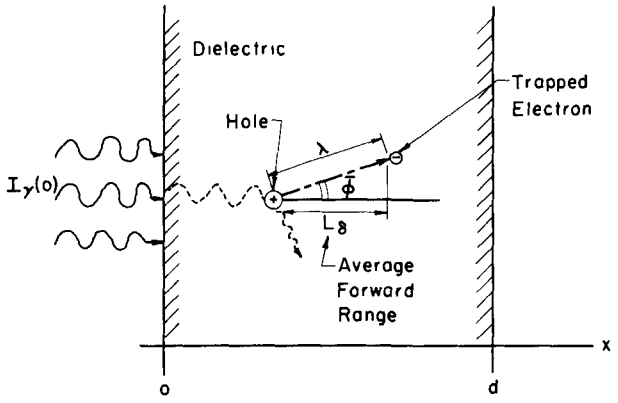

Fig. 6.24 — Hole-electron production in the dielectric.

Since the gamma intensity is assumed to be independent of time, the space charge $\rho(x)$ due to an irradiation of length t seconds is found immediately to be

$$\rho(x) = \int_0^t \frac{d}{dt}[e(n_+ - n_-)] = \begin{cases} At \exp(-\mu_a x) & (x < L_\delta) \quad (6.67a) \\ -\mu_a L_\delta At \exp(-\mu_a x) & (x \geq L_\delta) \quad (6.67b) \end{cases}$$

where

$$A \equiv \frac{e\mu_c I_\gamma(0)}{\langle h\nu \rangle} . \qquad (6.68)$$

The exponential involving $\mu_a L_\delta$ has been expanded as $(1 + \mu_a L_\delta)$ in the derivative since in general $\mu_a L_\delta \ll 1$.

This result is shown schematically in Fig. 6.25. The space charge, which is positive near the surface being bombarded, changes sign at $x \approx L_\delta$ and then gradually decreases. Since $\mu_a L_\delta \ll 1$, the amplitude of the negative charge region is considerably less than for the positive region. This is consistent with the concept of gamma–electron equilibrium discussed in connection with the Gamma-Electric Cell in Secs. 2-6.2 and 4-5, where the space charge was neglected altogether. However, it is now apparent that this is not valid for long irradiations since the space charge will continue to increase with time, until, depending on the material, either breakdown or charge leakage takes place.

The general characteristics of Fig. 6.25 have, in fact, been verified by Murphy and Gross[73]. As illustrated in Fig. 6.26, they sectioned a Carnauba wax sample following irradiation with ^{60}Co gamma rays and

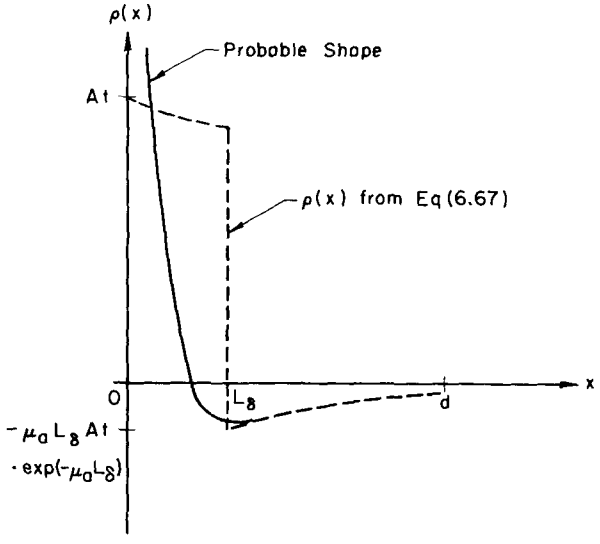

Fig. 6.25 — Spatial distribution of gamma-induced space charge.

then measured the charge released from each section using thermo-depolarization (heating) methods. A positive current in this figure indicates a negative space charge. Note from curve D that a positive space charge was present in a 1-mm section near the surface, whereas the net charge over the entire sample (curve A) was negative.

An interesting observation brought out by these curves is that the rate of charge release is surprisingly slow compared to the rate of storage: For example, the charging rate for negative space charge is seen from Eq. (6.67) to be $L_\delta A$, or $\approx 10^{-15}$ C/(cm^2 sec) per R/h for typical materials. For the irradiation of Fig. 6.26, this is equivalent to about 2×10^{-12} C/(cm^2 sec), whereas the discharge rate is seen to be approximately 3×10^{-15} C/(cm^2 sec), or three orders of magnitude less. A similar result has been noted by Gross[74] for plexiglass.

Care must be taken in analyzing the discharge of a sample: Consider the situation shown in Fig. 6.27, where a low-impedance ammeter is connected across the samples' faces, which are coated with a thin conducting layer such as Aquadag (similar to a Gamma Cell configuration). The space charge will induce surface charges δQ_0 and δQ_d on the faces as illustrated. When these charges are released (by heating, uv treatment, etc.), the total charge release per square centimeter of surface measured by the ammeter will be

$$Q = -\int i\, dt = \int_0^d (\delta Q_0 - \delta Q_d)\, dx = \int_0^d \left(\frac{d - 2x}{d}\right) \rho(x)\, dx . \qquad (6.69)$$

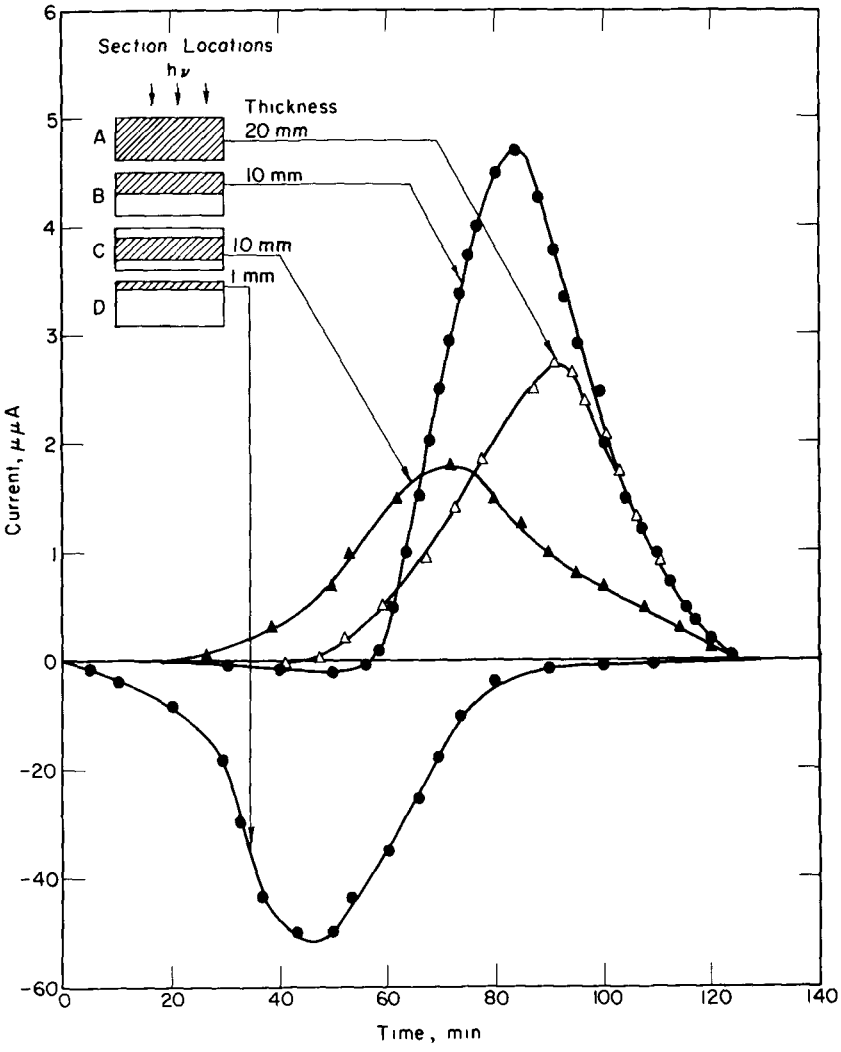

Fig. 6.26 — Thermodepolarization currents from sections of Carnauba wax. (From data by Murphy and Gross, Ref. 73. For 28-cm^2 samples with a ^{60}Co gamma radiation dose rate of 2×10^3 R/h.)

The integral may be evaluated by using Eq. (6.67) for $\rho(x)$. The result, if we again assume $\mu_a L_\delta \ll 1$ and expand the exponential terms, is

$$Q = L_\delta A t \left\{ \exp(-\mu_a d) - \frac{2L_\delta}{d} - \frac{2}{\mu_a d}\left[(\mu_a d + 1)\exp(-\mu_a d) - 1\right] \right\}. \qquad (6.70)$$

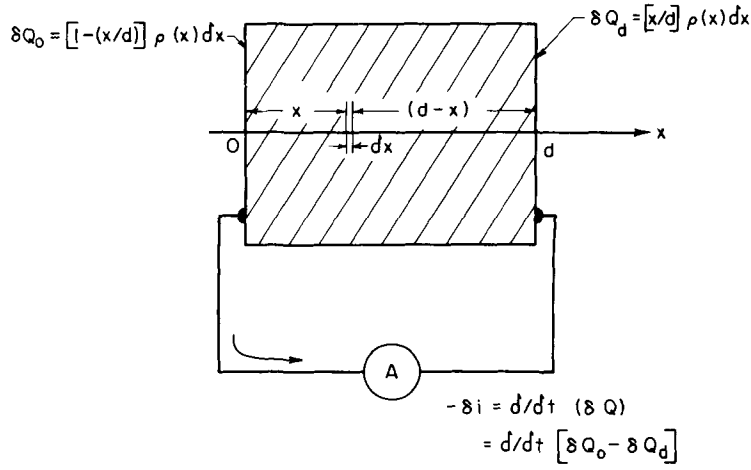

Fig. 6.27—Currents involved in discharge of the space charge. [The induced surface charges, δQ_d and δQ_0, are due to the space charge in the volume element dx. The total current then requires a final integration over the volume of the dielectric, i.e., over dx as indicated in Eq. (6.69).]

(Note that the time t is the irradiation time and not the discharge time.) It is obvious that the charge measured here is somewhat different from the actual charge stored Q_s, which is simply

$$Q_s = \int_0^d \rho(x)\, dx \,. \tag{6.71}$$

Comparison of this expression and Eq. (6.69) shows that the measured value Q is generally less than Q_s.

In an effort to explain the large value of the discharge time noted above, Gross[74] has proposed that part of the stored space charge is compensated by a bound polarization charge. As illustrated in Fig. 6.28, it is assumed that, after an initial discharge at time t_s, the bound (persistent) polarization remains but slowly decays giving rise to a net electric field. This theory is consistent with the experimental observation that not all the space charge is released in a single breakdown. The most dramatic example of this is reported by Hardtke and Ferguson[78], who observed spontaneous light flashes for several hours after the initial breakdown of heavily irradiated glass samples. Also, they were able to trigger discharges two or three times by striking a sharp instrument on the glass surface.

In his analysis, Gross assumes, for slow variations in the electric field, that the electric displacement $\vec{D}$ has two components given by

$$\vec{D} = \epsilon^* \vec{E} \equiv (\epsilon \vec{E} + \epsilon' \vec{E}) = \epsilon \vec{E} + \vec{P} \,. \tag{6.72}$$

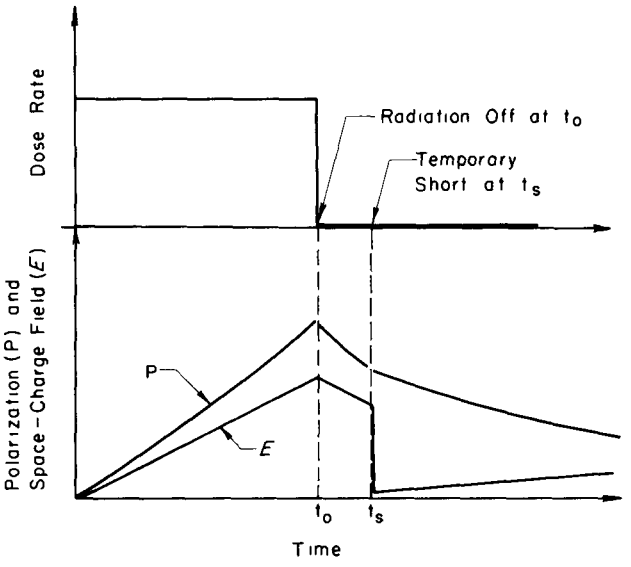

Fig. 6.28 — Explanation of repeated discharge in terms of bound polarization. [After Gross, Ref. 74. The dose rate is constant prior to t_0, zero afterwards, and the faces of the sample are temporarily shorted at time t_s. The corresponding polarization (P) and space charge fields (E) produced by the Compton current are illustrated for a thick sample. During the irradiation period E increases, then decreases slightly following t_0, and falls to zero at the time t_s; it then increases afterwards due to renewed charge build-up. Concurrently P increases during the irradiation period, decreases slightly between t_0 and t_s, and decreases slowly afterwards.]

Thus, the dielectric constant ϵ^* has two components: ϵ, which is in phase (in a time varying sense) with the field, and ϵ', which describes the persistent polarization $\vec{P}$ and is generally out of phase with $\vec{E}$.

Before analyzing the resulting discharge characteristics, it is of interest to see how this affects charging currents. If the dielectric is placed between two conductors as is done in the Gamma-Electric Cell, the current density J(x,t) due to gamma irradiation at time t and the electric field E (external plus space charge field) can be visualized as a sum of four components given by

$$J(x,t) = \sigma E(x,t) + g(x,t) + \epsilon \frac{\partial E(x,t)}{\partial t} + \frac{\partial P(x,t)}{\partial t} \tag{6.73}$$

Here, σ is the dielectric conductivity (so σE is the ohmic-conduction current), g represents the Compton current (i.e., the current calculated in Sec. 4-5), and the remaining currents account for charge storage associated with the electric field and polarization, respectively. The

parameters σ, ϵ, and ϵ' are assumed to be independent of position x For short-circuit operation of a cell of length d, we require that

$$\int_0^d E(x,t)dx = 0 \tag{6 74a}$$

Therefore operation termwise on Eq (6.73) by $\int_0^d dx \ldots$ and use of Eq. (6.72) yield

$$J_N(t) \equiv \frac{1}{d}\int_0^d J(x,t)\,dx \xrightarrow[V=0]{} \frac{1}{d}\int_0^d g(x,t)\,dx = \langle g \rangle \tag{6.74b}$$

where $J_N(t)$ represents the average* net current observed in the external circuit [This identification is possible since the flow of charge J(x,t) through an incremental distance dx results in an *induced* current J(x,t)(dx/d) in the electrodes, so the integration over the cell volume gives the total contribution to the external current due to all of these motions.] This result shows that, under the assumptions inherent in derivation (σ and ϵ independent of x), the *short-circuit* current depends only on the Compton current, even during transient operation As originally noted by Gross, it is "this property which allows the Gamma Cell to be used as a radiation detector with a response directly proportional to radiation flux irrespective of radiation induced changes of conductivity."

It is worthwhile to digress at this point and consider several important aspects of Eq. (6.74b), e.g., it can be used to give a better understanding of the range of validity of the collector-balance method for current calculations used for the Gamma Cell in Chap. 2 †

Consider a highly idealized case (steady state) where all the gamma radiation entering at x = 0 is absorbed in the cell This results in a Compton current $g_1(x)$ that, for simplicity, we will take to be an extreme case where g_1 is constant between x = 0 and x = d_1 where $d_1 < d$. Then from Eq. (6.74b), the external current observed is

---

*Average in the sense that transients induced in the plates due to the motion of individual electrons are omitted. It may be viewed then, as a time integral over an interval Δt corresponding to the time of flight, or alternately as the average over a large electron population as implied by the use of a current in the integral

†The necessity for caution in use of the balance method has been stressed by J. G Kelly[79], who states "The early analysis [by Gross, cf. Eq. (6.74b)] . apparently left some users of these devices with misconceptions about how the Compton currents are correlated with the current which flows in the lead of the measuring electrode. For example, .. incorrectly assumed that a knowledge of the net current across the electrode boundary is all that is required ... the displacement current must be considered also "

$(d_1/d)g_1$, *even though no Compton electrons flow across the dielectric-collector interface.* This is not surprising since it simply represents the induced current created on the plates by movement of the charge over a distance d_1 between them. However, it is disturbing that this might seem to imply that the collector-balance technique used in Chap. 2 to calculate currents is restricted not only to steady state operation as discussed there but also to cases where the gamma field is spatially uniform. That the latter restriction is not necessary can be seen by considering the example further. At the start of the irradiation, a negative space charge will rapidly accumulate as electrons are trapped at d_1, and the build-up will continue until the associated electric fields reach a point where they can drive, via ohmic leakage, sufficient currents away from d_1 to balance the Compton current input. Envision, then, an idealized space-charge sheet at d_1 causing a potential $-V_1$. With both plates grounded (short-circuit), electrons from this sheet will gradually leak to *both* electrodes. The current to the collector will be $\sigma V_1/(d - d_1)$ and to the emitter $\sigma V_1/d_1$. However, the net contribution to the external current requires a path-length weighting, i.e., $(d - d_1)/d$ and d_1/d, respectively. As a result, both contribute $(\sigma V_1/d)$, but since they are oppositely directed, the net effect on the external current cancels [in agreement with the absence of such a term in Eq. (6.74b)]. Still, if a balance is considered around the collector, it will contain the ohmic current $\sigma V_1/(d - d_1)$. Further, the sum of the leakage currents must equal the Compton input or

$$\frac{\sigma V_1}{(d - d_1)} + \frac{\sigma V_1}{d_1} = g_1. \tag{6.75a}$$

so that

$$\sigma V_1 = \frac{d_1(d - d_1)}{d} g_1. \tag{6.75b}$$

Substitution back into the expression for the ohmic-leakage current at the collector gives

$$J = \frac{\sigma V_1}{d - d_1} = \frac{d_1}{d} g_1 \tag{6.75c}$$

which agrees with the previous result from Eq. (6.74b).

In conclusion, this demonstrates that the electrode-balance technique is valid as long as leakage currents are properly included and a *true* steady state condition is reached in the sense that the internal space-charge and polarization fields have reached an equilibrium. The

latter is, of course, more demanding than simply requiring a constant gamma flux since some time may elapse after changes in the gamma intensity before an internal balance is achieved. Prior to equilibrium, Eq. (6.74b) must be employed, or under voltage conditions the analysis must begin with Eq. (6.73), in which case, both the ohmic and displacement current terms will explicitly survive. [A detailed analysis of an actual device including such terms has not been reported to date. It would involve a calculation of the time-dependent space-charge field, such as is done later to obtain Eq. (6.92), combined with an evaluation of the resultant induced charge on the electrodes. With respect to the latter, Kelly[79] has derived Green's functions for induced charges in several geometries of interest, including the cylindrical chamber (both end-on and side-on), the spherical chamber, and a pancake cell.]

Now returning to the problem of the calculation of space-charge discharge characteristics, we note from Poisson's equation that

$$\nabla \cdot \epsilon^* E = \nabla \cdot \epsilon E + \nabla \cdot \mathbf{P} = \rho_d + \rho' = \rho_T \tag{6.76}$$

where ρ_d is the uncompensated charge density, ρ' is the charge density associated with the persistent polarization, and ρ_T is the total of these. During discharge, only the uncompensated component will be released: i.e.,

$$\rho_d = \rho_T - \rho' = \rho_T - \nabla \cdot \mathbf{P} \, . \tag{6.77}$$

The charge collected upon breakdown can be determined from Fig. 6.29. If breakdown is assumed to occur to the plate at $x = 0$, the charge at this plate is neutralized, and this releases δQ_d, which flows through the ammeter. Thus, the measured charge per square centimeter of surface will be

$$Q = \int_0^d \frac{x}{d} \, \rho_d(x) \, dx \, . \tag{6.78}$$

We determined the total space charge distribution earlier [Eq. (6.67)]; however, now we want to find the uncompensated component of the space charge. Also, the earlier calculation did not allow for ohmic leakage, which has been added to Eq. (6.73), so we must start from scratch to find $\rho_d(x)$.

During the irradiation, conservation of charge requires that the total charge density ρ_T must satisfy the continuity equation

$$\frac{\partial \rho_T}{\partial t} + \nabla \cdot \mathbf{J}_c = \frac{\partial \rho_T}{\partial t} + (\sigma \nabla \cdot E + \nabla \cdot g) = 0 \tag{6.79}$$

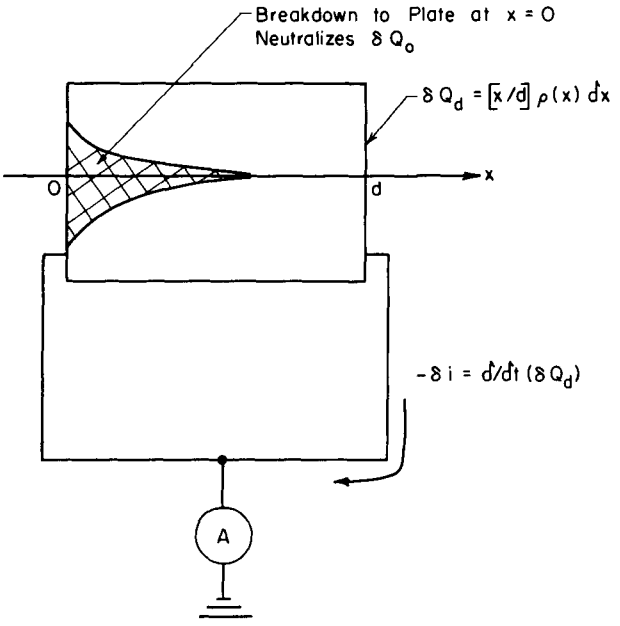

Fig. 6.29 — Schematic representation of charge neutralization during breakdown. (As in Fig. 6.27, the surface charge is due to a space charge in a volume element dx.)

where J_c is the total conduction current (ohmic plus Compton) defined as

$$J_c(x,t) \equiv \sigma E(x,t) + g(x,t). \tag{6.80}$$

But using Eq. (6.76) (i.e., Poisson's equation), we can eliminate E, and this gives

$$\frac{\partial \rho_T}{\partial t} + \frac{\sigma}{\epsilon^*} \rho_T = -\nabla \cdot g. \tag{6.81}$$

If a steady-state irradiation is assumed so that g is independent of time,* we obtain

$$\rho_T = -\tau \left[1 - \exp\left(-t/\tau\right)\right] \nabla \cdot g \tag{6.82}$$

*The assumption of a time independent g is even more demanding than it may appear at first thought. It implies short-circuit or low-voltage operation such that the plate potentials do not increase and interfere with Compton transmission. Likewise, the internal space-charge fields must not grow to the point where they interfere.

where the time constant τ is

$$\tau = \epsilon^*/\sigma . \tag{6.83}$$

The uncompensated charge density ρ_d can now be found by noting from Eq. (6.76) that, since $\nabla \cdot \epsilon^* E = \rho_T$ and $\nabla \cdot \epsilon E = \rho_d$,

$$\rho_d = \epsilon \rho_T / \epsilon^* . \tag{6.84}$$

If this result and Eq. (6.82) are used for $\rho_d(x)$, the solution to Eq. (6.78) is then found to be

$$Q = G\, F(d) [\, 1 - \exp\, (-t/\tau)\,] \tag{6.85}$$

where

$$G = \frac{\epsilon\, g(0)}{\mu_a d \epsilon^*}\, \tau \tag{6.86a}$$

$$F(d) = [1 - (1 + \mu_a d)\, \exp\, (-\mu_a d)]. \tag{6.86b}$$

The Compton current has been assumed to be in equilibrium with the gamma radiation, and hence, by comparison with Eq. (6.65), it has been assigned a spatial variation of the form

$$g(x) = g(0)\, \exp\, (-\mu_a x) . \tag{6.87}$$

Two limits are of interest: for short irradiation times, i.e., as $t \to 0$,

$$Q \approx \frac{Gt}{\tau}\, F(d) \tag{6.88a}$$

and, for extended irradiations such that $t \to \infty$,

$$Q \approx GF(d) = \frac{\epsilon\, g(0)}{\mu_a\, \sigma d}\, F(d). \tag{6.88b}$$

Note that in the last case ϵ^* cancels out, which shows that the final value of Q is independent of polarization effects. [Unlike Q, the actual charge stored Q_s, given by $\int_0^d \rho_T(x)\, dx$, is increased by a factor ϵ^*/ϵ.]

However, since the time constant τ is proportional to ϵ^* [i.e., to $\epsilon\,(1 + \rho'/\rho_d)$], it is increased by polarization, and this, in effect, reduces the rate of build-up of the total space charge ρ_T and also ρ_d.

To obtain some feeling for the factors involved, we note that Hardtke and Ferguson[78] found that the charging of glass (Pittsburgh Plate No. 4966 and 6792, 10 cm thick) irradiated with 5.2×10^5 R/h could be correlated by

$$Q \approx 4.4 \times 10^{-7} \left[1 - \exp\left(-t/2.3 \times 10^5\right)\right] \quad C/cm^2 \tag{6.89}$$

where t is in seconds. Comparison with Eq. (6.85) shows that the time constant is 2.3×10^5 sec. Gross[74] further points out that numerical evaluation of Eq. (6.88a) for this sample gives

$$Q \approx 7.9 \times 10^{-11} \left(\epsilon/\epsilon^*\right) t. \tag{6.90}$$

The comparable short-time expansion of Eq. (6.89) is

$$Q \approx 1.9 \times 10^{-12} t \tag{6.91}$$

and comparison of these two equations indicates that $\epsilon^*/\epsilon \approx 41$ for this glass. The handbook value of ϵ is 5.2×10^{-13} F/cm, and substitution of these results, along with τ found above, into Eq. (6.83) gives $\sigma \approx 10^{-16}$ $(\Omega\text{-cm})^{-1}$, which is about 20 times the normal value for Pittsburgh Plate glass outside of a radiation field. This would, indeed, appear to be a reasonable magnitude for the radiation conductivity.

In addition to this change in conductivity, as suggested in Sec. 6-3.2, radiation would be expected to reduce the dielectric strength. In fact, Gross[74] has noted that the intrinsic dielectric strength of Pittsburgh Plate glass is 5×10^6 V/cm, while data by Ernsberger and McGary[78] for electron bombardment indicate a breakdown value of 1.2 to 2.7×10^6 V/cm.

Aside from discharge characteristics, the preceding analysis can be used to demonstrate the calculation of the time evolution of the electric field in the dielectric. To do this, we use Eq. (6.82) for ρ_t in Poisson's equation and integrate; this yields

$$E(x,t) = E(0,t) + \frac{1}{\sigma}\left[1 - \exp\left(-t/\tau\right)\right]\left[g(0) - g(x)\right]. \tag{6.92a}$$

As indicated earlier, the time independent form of g used here implies that the fields developed do not become large enough to interfere with the Compton current. If, consistent with this, a short-circuit condition is assumed, $E(0,t)$ can be evaluated through use of Eq. (6.74a). This gives

$$E(x,t) = \frac{1}{\sigma}\left[1 - \exp\left(-t/\tau\right)\right]\left[J_N - g(x)\right] \tag{6.92b}$$

where J_N is the net current as defined by Eq. (6.74b).

We saw in the earlier model [Eq. (6.67)], which neglected ohmic leakage, that $E(x,\infty) = \infty$; however, now a finite limit of $[J_N - g(x)]/\sigma$ is reached, indicating a balance between the charging and leakage currents. In other words, unless breakdown occurs first, ohmic leakage will eventually limit the field.

While this conclusion remains valid, in many cases the field due to a long-term irradiation may well be large enough to affect the Compton current, in which case the analysis must be modified. Gross and Nablo[75] have considered this situation, and, in fact, they show that potentials can develop that actually exceed the voltage equivalent to the incident electron energy. While this result may seem surprising at first, they stress that it is not a violation of energy conservation. A majority of the electrons are trapped in a region of lower potential, but some are trapped in a location where the potential gradually increases with irradiation time to a value above their equivalent energy.

6-4.3 Sputtering

Heavy neutral or charged particles incident on a surface will cause the ejection of heavy particles in addition to the secondary electrons discussed in Chap. 5. Following the original observations of Grove in 1852, this phenomenon has been termed *sputtering*. It can be viewed essentially as the erosion or evaporation of a surface under heavy-particle bombardment. This is undesirable in many situations: e.g., the bombardment by residual gas ions can drastically reduce cathode life in vacuum tubes; bombardment of surfaces in space vehicles by solar wind particles may cause deterioration; and contamination of the plasma in thermonuclear devices due to sputtering of vessel walls has an undesired cooling effect. On the other hand, a number of important applications have developed in recent years, which include thin film deposition, cleaning of semiconductor surfaces, and ion getter pumps. (For further details see Refs. 80 to 84.)

In view of the particle currents involved, sputtering is likely to be important in radiation cells. Two undesirable effects are possible: If the sputtered material is metallic, deposits could build up on insulating surfaces allowing leakage currents or even electrical breakdown. In addition, the sputtered particles themselves, if charged, may form a leakage current. Even sputtered neutrals may be ionized by collisions with other sputtered particles and/or electrons in the inter-electrode space. The latter situation has in fact been observed in Fission-Electric Cell experiments using magnetic secondary suppression where trapping in the magnetic field resulted in high electron densities (further details are given in Sec. 7-2).

While this is the only experimental observation of sputtering in a radiation cell reported to date, such effects are likely to be encountered

more frequently as experience is gained with higher power cells designed for long-term operation.

As with secondary production, sputtering represents an extremely complex phenomenon. Increasing amounts of experimental and theoretical information have become available in recent years, but many aspects still remain unexplained, and there are gaps in available data.

A detailed treatment will not be attempted here, and the reader interested in further depth should consult review articles such as Refs. 80 to 84. The present section will be confined to some introductory concepts, followed by a discussion of data for fission fragment bombardment, which represents a regime of particle charge and energy not covered in most reviews.

We will confine our attention to *physical* sputtering which results from momentum transfer from incident particles to the target atoms. (Another type of sputtering, classed as *chemical* sputtering, occurs when bombarding and target particles form a chemically reactive species or a volatile compound.)

Sputtered particles may be either neutral or charged, and they may be single atoms or clumps of material. The *sputtering* yield for a particular species is defined as the number of particles of that species ejected per incident particle. The *total* yield is based on the total number of atoms ejected regardless of their nature.

Sputtering, like secondary-electron emission, was originally thought to occur through a local heating or hot spot mechanism. However, most current treatments are based on a detailed collision model, and some feeling for the processes involved can be gained from the schematic diagram of Fig. 6.30. The incident particle may undergo a number of hard collisions in the target, wherein sufficient energy is transferred

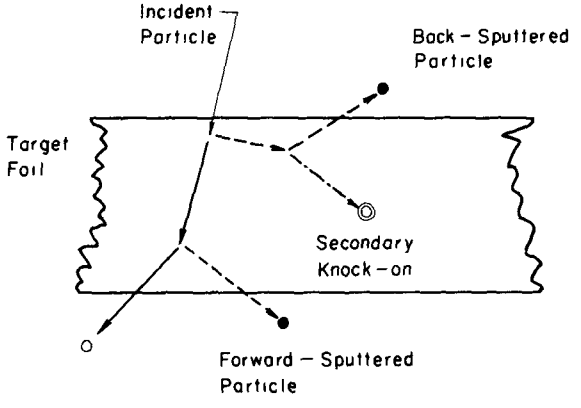

Fig. 6.30 — Schematic diagram of sputtering. (As illustrated, for thin targets, both forward and backward sputtering may occur.)

to the target atom to cause its displacement. The latter then travels through the target until it slows down and stops, or alternately until it escapes across the surface. Its travel, like the primary, is characterized by electronic interactions (straight-line path) and a few hard collisions (large-angle collisions). This picture is quite similar to the description of secondary electron production in Chap. 5, but of course the energies and ranges of the displaced ions are considerably different from those for secondary electrons.

While, as illustrated, both "forward" and "backward" sputtering can occur, the following remarks are generally limited to the backwards case, which has been studied in most experiments. (The fission fragment studies, to be described later, represent a major exception where forward yields are generally reported.)

Total yields may be surprisingly large, e.g., as shown in Fig. 6.31 20- to 50-keV xenon or krypton incident on copper will eject 10 to 20

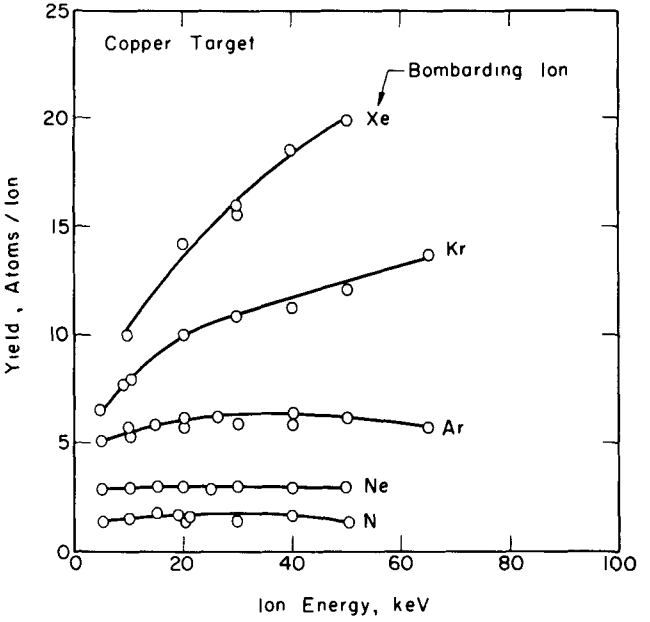

Fig. 6.31 — Sputtering yields for copper bombarded by keV ions. (From McDaniel, Ref. 84, based on data by O. Almen and G. Bruce as reported by McDaniel.)

atoms/incident ion. (Most experimental data are for ion bombardment since energetic ion beams are so conveniently obtained with accelerators.)

As might be expected, the yield depends on a number of parameters including the energy and type of bombarding particle, the angle of inci-

dence, the type and temperature of the target and its structure (crystalline, etc.), as well as the cleanliness and nature of the surface. General correlations are not readily available, but several general observations may be of value here.

Yields generally increase with atomic number of both the bombarding ion and the target, within ranges or periods defined by sharp dips near atomic numbers of 13, 21, 40, and 60. The increase with atomic number of the bombarding ion is evident from Fig. 6.31, and a characteristic energy dependence is also observed. A threshold energy exists (not discernable in the figure since it usually occurs at 8 to 25 eV), followed by a gradual increase in yield with energy, a saturation, and finally decreasing yields. The decreasing yield occurs at higher energies because these particles penetrate so deeply before suffering a hard collision that the displaced particles have difficulty escaping. Thus, the "escape zone" concept developed for secondary electron emission in Chap. 5 can also be applied here, and this allows a rationalization of other features of sputtering data. For example, larger yields are obtained for bombardment at oblique angles since more collisions occur in the escape zone. Also the point of saturation occurs at lower energies for small ions like H^+, which can penetrate the solid more readily.

One bit of evidence that supports the momentum transfer picture of sputtering is the observation that single-crystal targets primarily emit in the nearest-neighbor directions. This is consistent with the assumption that the recoil of the target atoms displaced by the primary produces a collision cascade in the target. These cascades would be expected to travel most readily in the nearest-neighbor (close packed) directions with sputtering occurring when the cascade reaches the surface.

A realistic theoretical model must include a careful treatment of the collisions illustrated in Fig. 6.30. (This differs somewhat from the treatment of charged-particle transport developed in Chap. 3. There the stress was placed on electronic interactions, and hard collisions were ignored or averaged over the track. Now the hard collisions must be stressed.) As pointed out by Kaminsky[83], there are three important energy regimes:

- Particles with high energies interact through Coulombic repulsion between their own and the target atom's nuclear charges (Rutherford collision region).
- At medium energies, the electron cloud causes a partial screening so a weakly-screened Coulombic collision model is appropriate.

- At low energies, little penetration of the electron cloud occurs, suggesting a hard-sphere collision model.

The dividing energies are defined more precisely by Kaminsky[83], and some feeling for magnitudes can be obtained from Table 6.8.

Note that the energy T_1 lies in the kilovolt range and may be several hundred keV for heavier ions. Energies below T_1 correspond to the hard-sphere region, and much of the available experimental data falls in this classification. Kaminsky reviews several theoretical studies

Table 6.8— LIMITING ENERGIES FOR IONIC COLLISIONS*

Hard-sphere region $T < T_1$
Weak screening region $T_1 < T < T_2$
Rutherford region $T > T_2$
All data for a copper target

	Ion Energy (keV)	
Bombarding Ion	T_1	T_2
H^+	2.6	4.1
He^+	5.6	69.1
N^+	24.4	$3\,5 \times 10^3$
Ne^+	39.0	11.1×10^3
Ar^+	93.4	82.6×10^3
Xe^+	632	353×10^3

*After Kaminsky, Ref. 83

for this range, and he points out the model of Rol, Fluit, and Kistemaker, while quite simple, has been fairly successful. It is instructive to consider their model since it stresses several concepts. They assume that only the first hard collision of the incident particle contributes to sputtering, and they neglect contributions due to secondary knock-ons by the displaced particles or due to the cascading effect noted previously. They assume that the energy transferred in the first collision is roughly proportional to the maximum energy transfer T_{max} while the collision probability is inversely proportional to the mean free path $\lambda(T)$. Hence, to a first approximation, the yield S is proportional to $T_{max}/\lambda(T)$; i.e.,

$$S = K \frac{T_{max}}{\lambda(T)} \tag{6.93}$$

where the constant of proportionality K is found by a fit to experimental data.

From an energy and momentum balance, it is found that

$$T_{max} = \frac{mM}{m + M} T \tag{6.94}$$

where m and M are the incoming and target particle masses, respectively, and T is the bombarding energy. (This neglects other energy losses prior to the collision itself.) For hard-sphere collisions, it can be shown[83] that

$$\lambda(T) = \frac{1}{\pi R^2 N_0} \tag{6.95}$$

where the radius R, which represents the distance of closest approach, can be found from a transcendental equation, namely

$$R(T) = \frac{0.57 \times 10^{-8}}{(Z_1^{2/3} + Z_2^{2/3})^{1/2}} \ln \frac{Z_1 Z_2 e^2 (m + M)}{4 \pi R(T)\, MT} . \tag{6.96}$$

Here, N_0 is the number of target atoms per cubic centimeter, Z_1 and Z_2 are the atomic numbers of the incident particle and the target atom, respectively, and e is the unit of electron charge. Combining these equations, we find

$$S = \pi N_0 K \frac{mM}{m + M} T R^2(T) . \tag{6.97}$$

Since R(T) is only weakly dependent upon T, this predicts that S varies with T in an approximately linear fashion. This result has been compared to several sets of experimental data, and agreement within 20% is reported[83] in the range from 5 to 20 keV.

Estimates of sputtering yields in radiation cells involve several complicating factors. Forward sputtering will occur at the emitter coupled with backward sputtering at the collector. Other surfaces, such as grids and side walls, will also be involved. Both the energy and angle distributions of the primary particles are complicated and vary with operating voltage. Very few data are available for the high energies (MeV range) involved in many decay sources. Further, what does exist is often conflicting. The situation can be illustrated by considering the special case of fission fragments. They represent an interesting regime of high energy and charge not covered in the general literature. (Further, it is not clear how to extrapolate available data and models to this regime.)

The status of measurements for fragments by Ershler and Lapteva[85], Rogers and co-workers[86–89], Nilsson[90–92], Lepscky et al.[93],

and Ferrari and Segre[94] is summarized in Table 6.9, and several points become apparent: The yields show quite wide variations and are extremely dependent on the target material and the state of its surface. Some yields reported are very large—of the order of 10^4 or more.

These experiments, in contrast to normal sputtering studies using accelerator beams, involved fission foils encapsulated with a catcher foil and irradiated in a neutron field. This is not an ideal set-up—there are a number of open questions in interpretation of the data, which, no doubt, add to the spread in the results reported.

The mechanisms involved appear to be more complex than those discussed earlier for low-energy low-q ions. For example, Rogers[88] found from electron microscope examinations that vaporization, rather than knock-on effects, appeared to dominate. In addition, there is other evidence that the sputtered particles may be quite large clumps of atoms.

It may be concluded that fragment sputtering can be quite significant. However, continued studies are required before a precise evaluation or understanding of the yield is possible. It would be possible to extend the earlier equivalent circuit concepts to include sputtering effects in the analysis of radiation cells. However, the yields involved are so uncertain that this calculation would not be meaningful at this time.

6-5 SUMMARY

It has been demonstrated that cell operating characteristics are most conveniently represented through the use of an "equivalent circuit." To study high-voltage operation, the present analysis extends the analysis reported previously in the literature to include the nonlinear cell current–voltage character. It is shown that the cell characteristic ρ_c defined in Eq. (6.10) as the ratio of the internal resistance to the short-circuit source impedance must be large for efficient operation.

For the equivalent circuit analysis to be meaningful, all possible sources of leakage currents and voltage limitations must be considered. Unfortunately, the various problems which may arise are quite complex, and a variety of different mechanisms are involved.

Secondary-electron emission currents are quite significant in positive-particle cells (Fission and Alpha Cells, etc.) and their inclusion in the equivalent circuit has been discussed along with possible suppression via grids or magnetic fields. A grid introduces additional currents that must be incorporated in the equivalent circuit as indicated in Eq. (6.38). Magnetic suppression, since it does not require internal structures, is free of this complication; however, the size and weight of the magnets make their use in practical devices questionable.

Table 6.9— FISSION FRAGMENT SPUTTERING DATA

Investigators and Date	Target	State of Surface	Forward Sputtering Yield	Comments
Ershler and Lapteva[85], 1956	^{233}U	Oxidized, but organics removed	24	Not corrected for refission or sputtering at catcher foil.
	^{233}U	Oxidation removed by polishing	1,200	
	^{239}Pu	Oxidation removed by polishing	3,500	Alpha sputtering yield of ^{239}Pu reported as 0.02.
Rogers and Adam[86], 1962	93% enriched ^{235}U	0.0005-in.-thick foil, rolled and polished	2,000	Corrected for refission at catcher, but not for sputtering or sticking fraction.
Rogers[87], 1964	93% enriched ^{235}U	Very thin foil	1,000	Added geometric corrections in evaluation. Used multiple collectors to obtain dose.
Rogers[88], 1964	93% enriched ^{235}U	Thick emitter	630	Electron microscope examination indicates a vaporization process as opposed to knock-ons.
		Saturated collector alone	10,000	

Rogers[89], 1965	UO_2 film on ^{235}U	Vacuum deposited 400-Å UO_2 film, 50-Å grain sites	≈50,000	Grain size grew to 180 Å during irradiation.
Nilsson[90], 1964	UO_2	0.5- to 1-mm-thick coating on quartz ampoules. 7- to 8-Å grain size	5 to 9	Not corrected for refission or sputtering at catcher since saturation not obtained.
Nilsson[91,92], 1966	UO_2	Sintered and irradiated in air at 760 mm	≈150	Higher yield in air attributed to radiation oxidation.
	UO_2	At 10^{-5} mm, sintered	9	
	Nat. U	At 10^{-5} mm, electro-polished	43	
Lepscky et al.[93], 1965	25% enriched UO_2	Sintered pellets, 9-mm dia. and 0.4- to 0.7-mm thick, 10^{-3} torr	0.24 to 27,000	Smallest yield for 14-μ grain size, largest for 1250 μ.
Ferrari and Segre[94], 1967	25% enriched UO_2	Sintered pellets, 20-mm dia. and 4-mm thick, 10^{-3} torr, grains >1μ	7,000 to 50,000	Large yields attributed to microcracks or agglomeration.

Another radiation-induced current discussed here is sputtering. As pointed out, some problems in voltage build-up in Fission-Electric Cells using magnetic suppression have been traced to subsequent ionization of sputtered materials. This represents a special circumstance, but even if sputtering currents are not critical *per se*, they can also lead to serious contamination of the system. For example, electrode material may be plated out on insulating surfaces, causing a reduction in resistivity, or even breakdown.

The internal resistance used in the equivalent circuit analysis should be corrected for radiation-induced conductivity. While a general theory describing this effect is not available, a reasonable representation can be obtained using Eq. (6.52) with parameters listed in Table 6.3. The possibility of a radiation-induced space charge in insulating materials must also be considered, and this is particularly important in solid-state cells such as the Gamma-Electric Cell. Not only may the space charge interfere with charged-particle passage, but actual voltage breakdown may result.

Voltage breakdown, as has been repeatedly stressed, has limited the voltage output of cells constructed to date to values well below optimum. A thorough understanding of mechanisms involved in vacuum breakdown is just beginning to emerge, and some aspects of this theory have been presented. In practice Fig. 6.19 can be used as a breakdown criterion for a radiation-free environment. However, some allowance for a reduced breakdown voltage in radiation fields should be included.

Breakdown in solids can proceed through a variety of mechanisms, making it difficult to present a generalized correlation. Materials of interest typically have intrinsic strengths greater than 10^6 V/cm, and some typical data are presented in Fig 6.21

The reader should remain alert to the possible existence of additional leakage current phenomena since much remains to be learned in this area. Obviously, the basic understanding of even those currents considered here is poor. Each is of sufficient complexity to require an entire book for complete coverage, however, the scarcity of information presently available would prevent this. Further insight will not be gained easily, but hopefully this situation will gradually improve with continued research.

REFERENCES

1. J H. Coleman, "Radioisotopic High-Potential Low Current Sources," *Nucleonics, 11* 42 (1953).
2. W Shorr, "Nuclear Batteries—A Survey," *Proc Intern Conf. on Peaceful Uses of Atomic Energy,* 15, p 310, United Nations, New York, 1956
3. A B Garrett, *Batteries of Today,* Chap IX, Research Press, Inc., Dayton, Ohio, 1957

4. A M. Plummer, W. J. Gallagher, R. C. Matthews, and J. N. Anno, *The Alpha-Cell Direct-Conversion Generator,* NASA Report CR-54256, Battelle Memorial Institute, Columbus, Ohio, November, 1964.
5. G. Safonov, *Direct Conversion of Fission to Electrical Energy in Low Radiation Temperature Reactors,* Report RM-1870, The Rand Corporation, Santa Monica, Calif., January 8, 1957.
6. W. F. Krieve, *JPL Fission-Electric Cell Experiment,* Tech. Report No. 32-981, Jet Propulsion Laboratory, Calif. Inst. of Tech., Pasadena, Calif., November 15, 1966.
7. A. Schock, *A Direct Nuclear Electrogenerator,* Report AFOSR TN-59-590, Fairchild Aircraft Company, Engine Division, Deer Park, New York, June 15, 1959.
8. J. H. Coleman, "Nuclear Batteries," *Proc. Tenth Annual Battery R and D Conf* , Power Sources Division, Ft. Monmouth, New Jersey, pp 56-59, May 1956.
9. E. G. Linder and S. M. Christian, "Use of Radioactive Material for Generation of High Voltage," *J Appl Phys., 23* 1213 (1952).
10. A. J. Cohen, *A Numerical Analysis of Direct Nuclear Electrogenerator Cells That Use Cerium 144 Beta-Emitting Radioisotope Sources,* NASA-TN-D-2070, Lewis Research Center, Cleveland, Ohio, November, 1963.
11. W. R. Corliss and D. G. Harvey, *Radioisotopic Power Generation,* Chap. 9, pp. 236-253, Prentice Hall, Inc., Englewood Cliffs, New Jersey, 1964.
12. W. G. Dow, *Fundamentals of Engineering Electronics,* 2nd ed , Chap. II, pp. 25-59, Chap. IV, pp. 81-123, Chap. VI, pp. 174-193, John Wiley and Sons, New York, 1952.
13. K. R Spangenber, *Vacuum Tubes,* 1st ed., Chap. 6, pp. 97-124, Chap. 7, pp. 125-167, Chap. 9, pp. 201-237, McGraw-Hill, New York, 1948.
14. W. R. Smythe, *Static and Dynamic Electricity* 2nd ed., Chap. V, pp. 111-217, Chap. XVI, pp. 560-584, McGraw-Hill, New York, 1950.
15. J. Millman and S. Seely, *Electronics,* 2nd ed., Chap. 16, pp. 476-493, Chap. 17, pp. 496-538, McGraw-Hill, New York, 1951.
16. W. G. Dow, *Fundamentals of Engineering Electronics,* 2nd ed., pp. 48-60, John Wiley and Sons, New York, 1952
17. K. R. Spangenber, *Vacuum Tubes,* 1st ed , pp. 621-674, McGraw-Hill, New York, 1948.
18. W. R. Smythe, *Static and Dynamic Electricity,* 2nd ed., pp. 560-569, McGraw-Hill, New York, 1950.
19. Ignacy Adamczewski, *Ionization, Conductivity and Breakdown in Dielectric Liquids,* Taylor & Francis, Ltd., London (1969). Also see J. A. Kok, *Electrical Breakdown of Insulating Liquids,* Interscience Publishers, Inc., New York, 1961.
20. D. Alpert, D. A. Lee, E. M. Lyman, and H. E. Tomaschke, "Initiation of Electrical Breakdown in Ultra-high Vacuum," *J. Vacuum Sci. Tech., 1* No 2, 35 (Nov./Dec 1964).
21. L. C. Van Atta, R. J. Van de Graaff, and H. A. Barton, "A New Design for a High-Voltage Discharge Tube," *Phys Rev , 43* 158 (1933).
22. R. Arnal, "Les 'Microdécharges' Électriques dans le Vide Dynamique," *Ann. Physik, 12* 830 (1955), in French, English Translation, USAEC TR-2837, Office of Technical Services, Department of Commerce, Washington, D. C.
23. W. K. Mansfield, "Pre-breakdown Conduction in Continuously Pumped Vacuum Systems," *Brit. J. Appl. Phys., 11* 454 (1960).
24. W. H. Bennett, "Magnetically Self-Focusing Streams," *Phys. Rev., 45* 890 (1934).
25. W. S. Boyle, P. Kisliuk, and L. H. Germer, "Electrical Breakdown in High Vacuum," *J. Appl. Phys., 26* 720 (1955).
26. A. Maitland, "New Derivation of the Vacuum Breakdown Equation Relating

Breakdown Voltage and Electrode Separation," *J. Appl. Phys., 32* 2399 (1961).
27. L. Cranberg, "The Initiation of Electrical Breakdown in Vacuum," *J. Appl. Phys., 23* 518 (1952).
28. D. Alpert and D. Lee, *Electrical Breakdown in High Vacuum,* Report R-129, Coordinated Sci. Lab., University of Illinois, Urbana, June 7, 1962.
29. R. H. Fowler and L. Nordheim, "Electron Emission in Intense Electric Fields," *Proc. Roy. Soc. (London), A119* 173 (1928).
30. W P. Dyke and J. K. Trolan, "Field Emission Large Current Densities, Space Charge, and the Vacuum Arc," *Phys. Rev., 89* 799 (1953).
31. W. P. Dyke, J. K. Trolan, E. E. Martin, and J. P. Barbour, "The Field Emission Initiated Vacuum Arc. I. Experiments on Arc Initiation," *Phys Rev., 91* 1043 (1953).
32. W. W. Dolan, W. P. Dyke, and J. K. Trolan, "The Field Emission Initiated Vacuum Arc. II. The Resistively Heated Emitter," *Phys Rev., 91* 1054 (1953).
33. H. E. Tomaschke, *A Study of the Projections on Electrodes and Their Effect on Electrical Breakdown in Vacuum,* Report R-192, Coordinated Sci. Lab., University of Illinois, Urbana, January 1964.
34. D. A. Lee, *Calculations Concerning Electrical Breakdown Induced by the Melting of Microscopic Projections,* Report R-280, Coordinated Sci. Lab., University of Illinois, Urbana, January 1966.
35. E. M. Lyman, *Studies Relevant to the Electrical Vacuum Gyro Program of Electrical Breakdown in Ultrahigh Vacuum,* Report R-334, Coordinated Sci. Lab., University of Illinois, Urbana, January 1967.
36. H. Tomaschke and D. Alpert, "Field Emission from a Multiplicity of Emitters on a Broad-Area Cathode," *J. Appl. Phys., 38* 881 (1967).
37. D. Alpert, University of Illinois, private communication.
38. D. Alpert, D. Lee, E. M. Lyman, and H E. Tomaschke, "Effect of Gas Pressure on Electrical Breakdown and Field Emission," *J. Appl. Phys., 38* 880 (1967).
39. H. T. Sampson and G. H. Miley, "High Voltage Gamma-Electric Cell Operations," *Nucl. Appl., 5* 145 (1968).
40. F. W. Peek, Jr., *Dielectric Phenomena in High-Voltage Engineering,* 3rd ed., McGraw-Hill, New York, 1929.
41. S. Whitehead, *Dielectric Breakdown in Solids,* Oxford University Press, London, 1950.
42. J. H. Mann, "Dielectric Breakdown in Solid Insulation," in *Progress in Dielectrics,* Vol. 1, J. B. Birks and J. H. Schulman (Eds.), Heywood and Co., Ltd., London, 1959.
43 R. M. Black and A. Charlesby, "Irradiated Polymers," in *Progress in Dielectrics,* Vol. 2, pp. 77-111, J. B. Birks and J. H. Schulman (Eds.), Heywood and Co., Ltd., London, 1960.
44. R. Stratton, "The Theory of Dielectric Breakdown in Solids," in *Progress in Dielectrics,* Vol. 3, J. B. Birks and J. Hart (Eds.), Heywood and Co., Ltd., London, 1961.
45. J. J. O'Dwyer, *The Theory of Dielectric Breakdown of Solids,* Oxford University Press, London, 1964.
46. M. Darveniza, "Electrical Breakdown in Solids and Over Solid Surfaces," Chap. 9 in S. C. Haydon, *Discharge and Plasma Physics,* University of New England, Armidale, N.S.W. Australia, 1964.
47. L. B. Loeb, *Electrical Coronas, Their Basic Physical Mechanisms,* University of California Press, Berkeley and Los Angeles, 1965.
48. A. von Hippel, "Electrical Breakdown of Solid and Liquid Insulators," *J. Appl. Phys., 8* 815 (1937).
49. H. Frohlich, "Electrical Breakdown in Ionic Crystals," *Proc. Roy Soc (London), A160* 230 (1937).

50. G. J Dienes and G. H Vineyard, *Radiation Effects in Solids*, Interscience Publishers, Inc., New York, 1957.
51. P. S. Billington and J. H. Crawford, Jr., *Radiation Damage in Solids*, Princeton University Press, Princeton, New Jersey, 1961.
52. B. T. Kelley, *Irradiation Damage to Solids*, Pergamon Press, New York, 1966.
53. J. P. Howe and S. Siegel, "Radiation Damage in Solids," in *Nuclear Engineering Handbook*, H Etherington (Ed.), pp. 10-83 to 10-125, McGraw-Hill, New York, 1958.
54. H. L. Olesen, *Radiation Effects on Electronic Systems*, Plenum Press, New York, 1966.
55. O. Sisman and C. D. Bopp, "Physical Properties of Irradiated Plastics," ORNL-928, USAEC Tech. Inf. Service, Oak Ridge, Tenn., June 29, 1951. See also ORNL-1373, a supplement to ORNL-928.
56. V. P. Calkins, "Radiation Effects on Reactor Materials: Nonmetals," *Nucleonics, 12* 9 (September 1954).
57. A E. Javitz, "Impact of High Energy Radiation on Dielectrics," *Elect. Mfg., 55* 86 (June 1955).
58. C. G Collins and V. P. Calkins, *Radiation Damage to Elastomers, Organic Liquids, and Plastics*, APEX-261, Office of Tech. Service, Dept. of Commerce, Washington, D. C., September 1956.
59. V. P. Calkins, "Radiation Damage to Liquids and Organic Materials," in *Nuclear Engineering Handbook*, H. Etherington (Ed.), pp. 10-126 to 10-148, McGraw-Hill, New York, 1958.
60. S Mayburg and W. L. Lawrence, "The Conductivity Change in Polyethylene During γ-Irradiation," *J. Appl. Phys., 23* 1006 (1952).
61. J. H. Coleman and D. Bohm, "A Method for Increasing the Electrical Resistivity of Insulators Under Ionizing Radiation," *J. Appl. Phys., 24* 497 (1953).
62. J. F. Fowler, "X-Ray Induced Conductivity in Insulating Materials," *Proc. Roy Soc. (London), A236* 464 (1956).
63. J. W. Winslow and R. S. Alger, *Radiation-Induced Currents in Solid Organic Insulators*, USNRDL-TR-325, USN Radiation Defense Laboratory, San Francisco, Calif., 1959.
64. K. Yahagi and A. Danno, "Gamma-Ray Induced Conductivity in Polyethylene and Teflon Under Radiation at High Dose Rate," *J. Appl. Phys., 34* 804 (1963).
65. F. N Coppage, A. W Snyder, and F. C Peterson, *Neutron Effectiveness in Producing Photoconductivity in Dielectric Materials*, Report SCR-670, Sandia Corp., Albuquerque, New Mexico, June 1963.
66. S. E. Harrison, *Gamma-Ray Photoconductivity Decay in Organic Dielectric Materials*, Report SCR-671, Sandia Corp., Albuquerque, New Mexico, June 1963.
67. F. N Coppage and F. C Peterson, *Some Properties of Conductivity Induced in Polystyrene by Pulsed Gamma Rays*, Report SCR-65-943, Sandia Corp., Albuquerque, New Mexico, June 1965.
68. V. A. J. van Lint, "Ionization-Induced Conductivity in MgO," GA-8138, General Atomics, San Diego, Calif., August 1967. Also see D. K. Nichols and V. A. J. van Lint, "Theory of Transient Electrical Effects in Irradiated Insulators," GA-7228, July, 1966.
69. Charles Kittel, *Introduction to Solid-State Physics*, 2nd ed., pp. 512-529, John Wiley and Sons, New York, 1956. Also see A. Rose, "An Outline of Some Photoconductive Processes," *RCA Review, 12* 362 (1951).
70. H. T. Sampson, "A Theoretical and Experimental Analysis of the Gamma-Electric Cell," pp. 104-107, Ph. D. Thesis, Nuclear Engineering Program, University of Illinois, Urbana, 1967.
71. B. Gross, *Charge Storage in Solid Dielectrics—A Bibliographical Review*

on the Electret and Related Effects, pp. 134-143, Elsevier Publishing Co., New York, 1964.
72. B. Gross and R. J. de Moraes, "Gamma Irradiation Effects on Electrets," *Phys Rev , 126* 930 (1962).
73. P. V. Murphy and B. Gross, "Polarization of Dielectrics by Nuclear Radiation. II. Gamma-Ray Induced Polarization," *J. Appl. Phys., 35* 171 (1963).
74. B. Gross, "Compton Current and Polarization in Gamma-Irradiated Dielectrics," *J. Appl. Phys., 36* 1635 (1965).
75. B. Gross and S. V. Nablo, "High Potentials in Electron-Irradiated Dielectrics," *J. Appl Phys , 38* 2272 (1967).
76. V. Culler, "Gamma-Ray Induced Electrical Discharge in Radiation Shielding Window," *Proc. Seventh Hot Lab. and Equip. Conf.*, p. 120, Cleveland, Ohio, American Nuclear Society, Hinsdale, Ill , 1959.
77. T. M. Proctor, "X-Ray Induced Electrical Polarization in Glass," *Phys. Rev. Letters, 3* 575 (1959).
78. F. C. Hardtke and K. R. Ferguson, "The Fracture by Electrical Discharge of Gamma-Irradiated Shielded Window Glass," *Proc. 11th Hot Lab. and Equip. Conf.*, New York, p. 369, American Nuclear Society, Hinsdale, Ill., 1963. Also see F. M. Ernsberger and T. E. McGary, "Gamma-Radiation-Induced Conductivity in Nuclear Shielding Glasses as Determined by Space Charge Decay," p. 383.
79. J. G. Kelly, "Compton Diodes Theory and Conjectures," SC-RR-67-855, Sandia Corp., Albuquerque, N. Mex., March 1968.
80. G. K. Wehner, "Sputtering by Ion Bombardment,"*Advan Electron Electron Phys , 7* 239 (1955).
81. G. Carter and J. S. Colligon, *Ion Bombardment of Solids*, American Elsevier Publishing Co., New York, 1968.
82. R. Behrisch, "Feslköperzerstaubung durch Ionenbeschn β," *Ergebnisse der Exacten Naturwissenschaften, 35* 295 (1964).
83. Manfred Kaminsky, *Atomic and Ionic Impact Phenomena on Metal Surfaces*, pp. 142-232, Academic Press, Inc., New York, 1965.
84. E. W. McDaniel, *Collision Phenomena in Ionized Gases*, pp. 649-658, John Wiley and Sons, New York, 1964.
85. B. V. Ershler and F. S. Lapteva, "The Evaporation of Metals by Fission Fragments," *J. Nucl. Energy II, 4* 471 (1957). [Translated by S. F. Pugh from *Atomnaya Energiya, 1* No. 4, 63 (1956).]
86. M. D. Rogers and J. Adam, "Ejection of Atoms from Uranium by Fission Fragments," *J. Nucl. Materials, 6* 182 (1962).
87. M. D. Rogers, *Dynamic Equilibrium Between Ejection and Re-ejection of Uranium by Fission Fragments*, AERE-R4519, U. K. Atomic Energy Authority, Harwell, Berkshire, 1964.
88. M. D. Rogers, *Mass Transport of Uranium by Fission Fragments*, AERE-R-4639, U. K. Atomic Energy Authority, Harwell, Berkshire, 1964.
89. M. D. Rogers, *Mass Transport and Grain Growth by Fission Fragments in Thin Films of Uranium Oxide*, AERE-R-4793, U. K. Atomic Energy Authority, Harwell, Berkshire, 1965.
90. Gösta Nilsson, *Ejection of Uranium Atoms from UO_2 by Fission Fragments*, AE-136, Aktiebolaget Atomenergi, Stockholm, Sweden, 1964.
91. Gosta Nilsson, "Ejection of Uranium Atoms from Electropolished Foils of Uranium Metal by Fission Fragments," *J. Nucl. Materials, 20* 231 (1966).
92. Gösta Nilsson, "Ejection of Uranium Atoms from Sintered UO_2 by Fission Fragments in Different Gases and at Different Gas Pressures, *J. Nucl. Mater., 20* 215 (1966)
93. C. Lepscky, G. Segre, C. Cesarano, S. Ferrari, and L. Giaquinto, "Uranium and Fission Products Release from Uranium Dioxide," RT/CHI(65)27, Comitato Nazionale Energia Nucleare, Rome, Italy, 1965.
94. S. Ferrari and G. J. Segre, "Experiments on the Uranium Emission from Sintered Uranium Oxide Pellets," *J. Nucl. Materials, 24* 150 (1967).

7

Specific Applications

7-1 INTRODUCTION

A number of review articles[1–12] concerned with the direct conversion of radiation into electrical power have appeared in recent years; however, they have generally focused on "nuclear batteries" and most frequently on those using a beta-emitter source. The Fission-Electric Cell and high-power Alpha and Beta Cells have not been discussed in detail. Also the Gamma-Electric and Secondary-Emission Cells have received little notice, and it is only in recent months that a fairly detailed study of a Thermonuclear-Electric Cell was reported; hence, these various concepts will be given special attention here. Before proceeding, however, some points of philosophy may serve to clarify the review.

The present coverage is restricted to direct-collection concepts. This includes any device that operates on charged particles associated with nuclear radiation by either converting their "natural" kinetic energy to potential energy or using it as the "driving force" for collection. No distinction is made between primary and secondary particles in this definition. Under it a Gamma-Electric Cell is a perfectly good direct-collection device even though it collects Compton electrons rather than the primary photons.

This rules out devices like the Ionization-Electric Cell (Chap. 1) in which the radiation energy is used to produce ionization and some force other than the "natural" kinetic energy is used to separate and collect the charge. It also rules out "Tertiary Nuclear Batteries,"[8] which generally use a double-conversion technique; e.g., a solar cell is used to convert light energy released by radiation entering a phosphor. Such techniques may be important in some applications; however, the earlier chapters were designed as a foundation for understanding direct collection and space does not permit inclusion of the multitude of hybrid conversion schemes that may be possible.

At this stage in the development of direct-collection concepts, it would seem to be a mistake to concentrate solely on large power

uses. From a mechanistic point of view, many of the problems are the same whether one is designing a cell for use as a power source or as a nuclear-radiation detector. There certainly must be a shift in emphasis; e.g., high-voltage vs short-circuit operation, efficiency vs linear response, etc. But still, an understanding of cells for both applications should produce a healthful cross-fertilization of ideas, and the entire spectrum of applications is considered in the present review.

In the preceding chapters, direct-collection concepts were classified as Plate-Emitter or Volume-Emitter Cells. In theory at least, either can be designed to operate with any type of charged-particle source. However, in practice, certain sources are better suited to a certain type cell, and specific problems are closely related to this selection. For this reason, the following discussion will be organized according to the radiation source and will include: the Fission-Electric Cell (FEC); Alpha-Electric Cell (AEC); Beta-Electric Cell (BEC); Gamma-Electric Cell (GEC); Secondary-Emission Cell (SEC); and Thermonuclear-Electric Cell (TEC). For convenience the abbreviations indicated in parenthesis will frequently be employed.

7-2 THE FISSION-ELECTRIC CELL

The Fission-Electric Cell (FEC) is a classic example of the coated-plate converter, and the analysis presented in the preceding chapters is directly applicable to it. Uranium, used as the coating, undergoes neutron-induced fission, and the resulting primary current of fission fragments carries a high energy and positive charge.

The FEC holds a prime place in the conversion of energy released during nuclear fission. As discussed in Chap. 3, about 80% of this energy initially resides as kinetic energy of the fission fragments; *thus, any scheme designed to utilize this energy without passing through a heat cycle must involve the fragments.* The FEC represents the most concrete, if not the only concept, that has been advanced to do this. Unfortunately, as presently conceived, it does not appear to be competitive except for highly specialized applications or as a topping unit. Still considerable effort was devoted to both conceptual designs and experiments in the period from 1957 to 1966, and the achievement of high-voltage build-up in 1966 (described later) after years of frustration represents a deep satisfaction.

However, the FEC-reactor concept represents one of the most complex of all of the direct-collection systems. One must deal not only with the effects of various parameters on the collection efficiency

but also with their effect on criticality. Unfortunately, these two (cell operation and criticality) are strongly interdependent; e.g., the surface-to-volume ratio, void volume, and fuel-coating thickness affect both the particle collection efficiency and neutronic characteristics.

G. Safonov[13,14] carried out the first definitive study of the FEC in 1957, and he attributes the first suggestion of the principle to comments by E. P. Wigner[15] as early as 1944. Apparently, the concept was not pursued seriously because it was thought that the large void volume required would lead to prohibitive reactor sizes and fuel inventories. However, Safonov was concerned with cavity reactor design in the middle 1950s,* and he first pointed out that this concept might reduce the size and fuel inventory of a FEC-reactor to a reasonable magnitude.

Safonov's 1957 report presents current, efficiency, electrode heating, and charging time curves for parallel-plate cells, and in addition, he brought out the following points:

> The non-thermal nature of direct collection might be exploited by designing a low-temperature reactor system. This would make it possible to use structural materials that have exceptionally low thermal neutron absorption cross sections (like magnesium and aluminum) but that, because of strength limitations, cannot be used in high-temperature systems. As an illustration, Safonov proposed a design for a 200-MW cavity reactor, shown in Fig. 7.1, that employed magnesium construction, a graphite reflector, and D_2O coolant. The cavity concept plus low parasitic neutron losses lead to a reasonable size and ^{235}U inventory. With a D_2O flow rate of ≈ 5 m/sec, the highest temperature in the system is estimated to be about 120°C. An electrical current of about 16 A would be delivered under short-circuit conditions and about 7 A at 1 MV.
>
> The absence of steam turbines and electric generators, combined with reduced construction costs for low-temperature operation, should reduce the capital investment in the reactor system. This is significant since capital investment represents a major factor in nuclear plant economics. However, part of the savings might be offset by the rather intricate cell fabrication requirements.
>
> Calculations indicate that the cavity reactor FEC design might be adapted to a breeder system with a high conversion ratio.
>
> The unique high-voltage output, coupled with the periodic discharge capability, could be of special interest in certain applications,

*The basic geometry of a "cavity reactor" is simply a cavity filled with dilute fissionable fuel surrounded by a relatively thick moderator–reflector region. For a general discussion see Ref. 16.

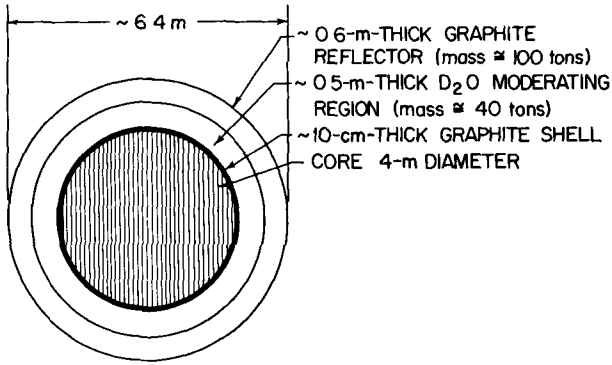

Fig. 7.1 — Schematic diagram of a low-temperature FEC–cavity reactor. [After *Safonov*, Ref. 13. The 4-m-diam. vacuum region contains 20 positive and 20 negative electrodes alternately spaced with 10-cm vacuum gaps. Negative electrodes are coated with 2.4×10^{-3} g/cm^2 ^{235}U. Electrodes may be laminar or concentric cylinders. All electrodes are internally cooled by D_2O. Calculations indicate a critical mass of 8-kg ^{235}U and a reactor power of 200 Mw(th).]

e.g., for a coupled reactor–Van de Graaff accelerator system, for the initiation of fusion reactions, etc. (As pointed out in Appendix A-1, the FEC develops high voltages with currents several orders of magnitude larger than conventional Van de Graaff techniques.)

Refueling is an important problem, and several unique methods were considered: One was to electroplate the fuel on the surfaces using a solution technique. Another involved continuous refueling by injecting small amounts of gaseous $^{235}UF_6$ into the vacuum space between electrodes. When ionized, the positive $^{235}UF_6$ molecule would be accelerated to the cathode thus replacing depleted fuel.

A multiple-layer collector using a "honeycomb" type structure might result in a gain in efficiency by as much as 30% over single-plate collectors, but the added complexity would seem to offset this advantage.

The efficiency is reduced several percent if fission betas are not suppressed. On the other hand, if the cell were operated on betas alone, a maximum efficiency of only about ½% at 0.5 MV is predicted.

Safonov concludes his report with the comment: "It seems meaningless to forecast the applications and implications ... prior to first complete demonstrations of technical feasibility." To this end he eventually turned his attention to experiments using a beam port of the

GE Vallecitos reactor,[17] and the Jet Propulsion Lab experiments described later grew out of this effort.

The next major study involved a detailed treatment of a cylindrical electrode configuration by A. Schock.[18] In addition to a quantitative proof of the improved collection efficiencies attainable with cylindrical geometry, he considered the problem of heat removal and magnetic

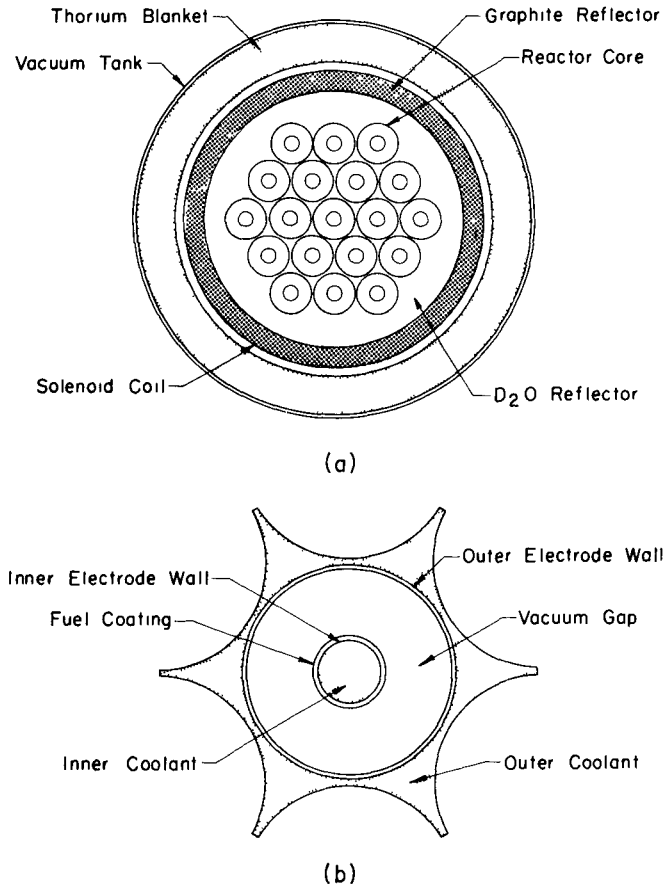

Fig. 7.2—Schematic sketch of the reactor proposed by Schock. (From Ref. 18.) (a) Schematic view of the reactor cross-section. (b) Detailed view of an electrode cell.

suppression of fission betas in some detail. The reactor and cell are shown in Fig. 7.2, and the influence of Safonov's low-temperature concept is evident. Beryllium electrodes with a ^{233}U coating and D_2O coolant at about 60°C were assumed, and the reactor included a fertile breeding blanket containing thorium, along with a large, high-current

solenoid coil for suppressing the beta particles. Some results from Schock's analysis include:

Conversion efficiencies up to 13%, electric power densities up to 4.5 MW/m^3 of core, and neutron multiplication factors up to 2.1 were found for inner-electrode temperatures ranging up to 350°C. However, as illustrated in Figs. 7.3(a) and (b), these characteristics were shown to be interdependent, so the maximum values noted above cannot all be obtained simultaneously. The selection of an operating point represents a compromise between these characteristics, which must be based upon the intended application.

Relativistic corrections are important in beta suppression calculations, since even electrons starting at zero energy will reach relativistic speeds in the large accelerating potentials involved. In the reactor study he selected a beta cut-off energy of ≈ 1 MeV, and the magnetic field was limited to 2000 G on the basis of current engineering feasibility. These requirements fixed the cell diameter ratio. Schock considers this "one of the most questionable points of (his) analysis," and he suggests that a better design might have been achieved if more freedom in the diameter ratio were allowed. (In retrospect, it appears that he may have been overly concerned with beta suppression. The effect is not that large; the first concern probably should be to suppress secondary electrons, and since they are less energetic, smaller fields are required.)

A "finger" design for the inner electrode was considered, which would allow refueling by immersion in an electropolating solution.

Internal fins in the coolant channels of the inner electrode were considered to improve heat transfer and allow higher power densities.

It was suggested that subcooled boiling might be exploited to achieve high heat fluxes at relative low temperatures and pressures.

In addition to the uses noted earlier, Schock introduced the thought that the high potentials might be attractive for electrical space propulsion. He also noted that, as suggested in Chap. 1, the FEC could be used in a conventional plant as a topping unit.

In the early 1960s, as Safonov began his FEC experiments, two major laboratories [Cal Tech's Jet Propulsion Lab (JPL) and Battelle Memorial Institute (BMI)] launched theoretical and experimental studies.

At JPL, Kamke[19] carried out a more detailed analysis of fragment transport through the fuel layer, and Heindl[20,21] made a thorough comparison of the efficiencies obtained for parallel-plate, concentric-

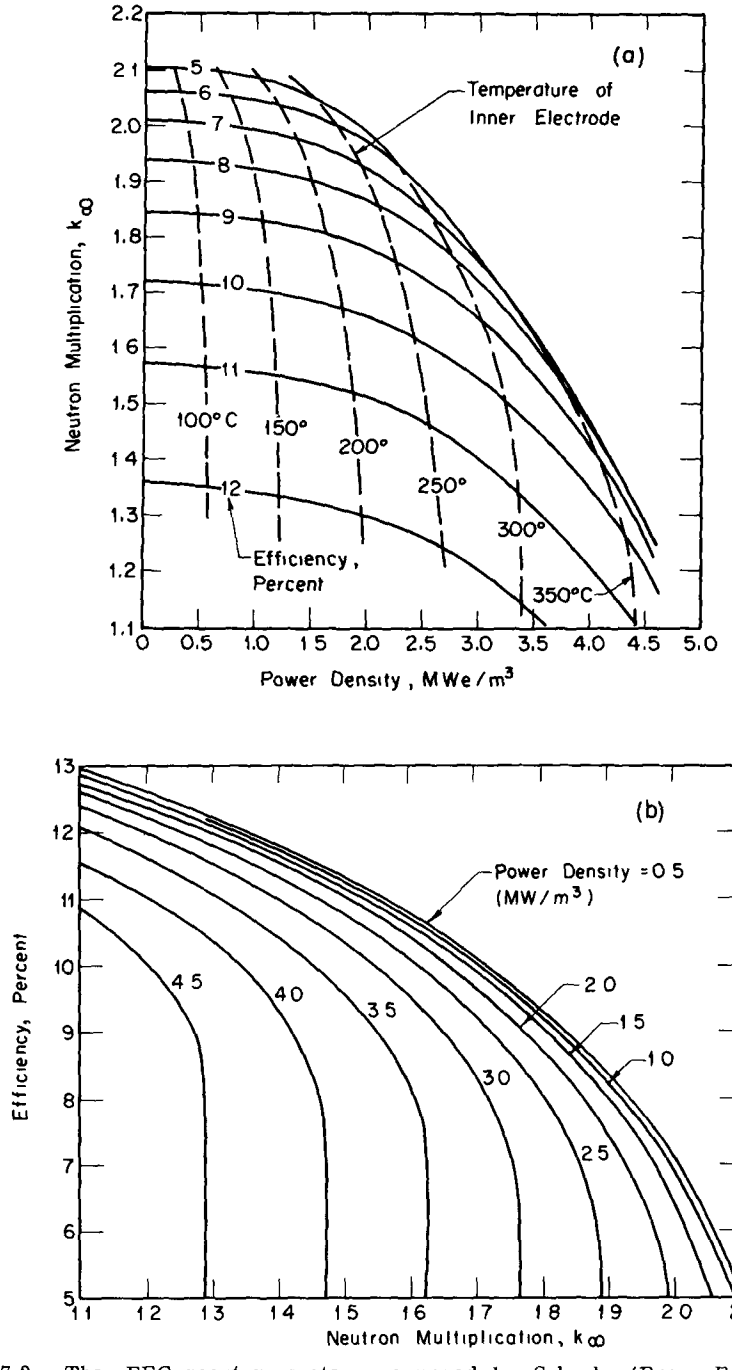

Fig. 7.3—The FEC-reactor system proposed by Schock. (From Ref. 18.) (a) The effect of power density, efficiency, and neutron multiplication on the inner-electrode temperature. (b) Interdependence of efficiency, power density, and neutron multiplication.

sphere, and concentric-cylinder geometries. While confirming the increases in efficiencies in going from plane to cylindrical to spherical electrodes, Heindl observed that this progression of geometries is accompanied by a decreasing ratio of fuel surface to void volume. And he showed that, if the fuel volume is held constant, the increased fuel-thickness requirement results in a loss in overall efficiency, which to a large extent offsets the gain in collection efficiency. Because of this, he concluded that the choice of geometry for space application will be largely determined by the overall power-to-weight ratio and engineering practicability of the design.

A general review of the JPL program, published by Heindl et al.[22] in 1963, discussed their interest in space applications (e.g., electric propulsion), and a schematic illustration of a combined reactor–waste-heat radiator system for this purpose is shown in Fig. 7.4. In

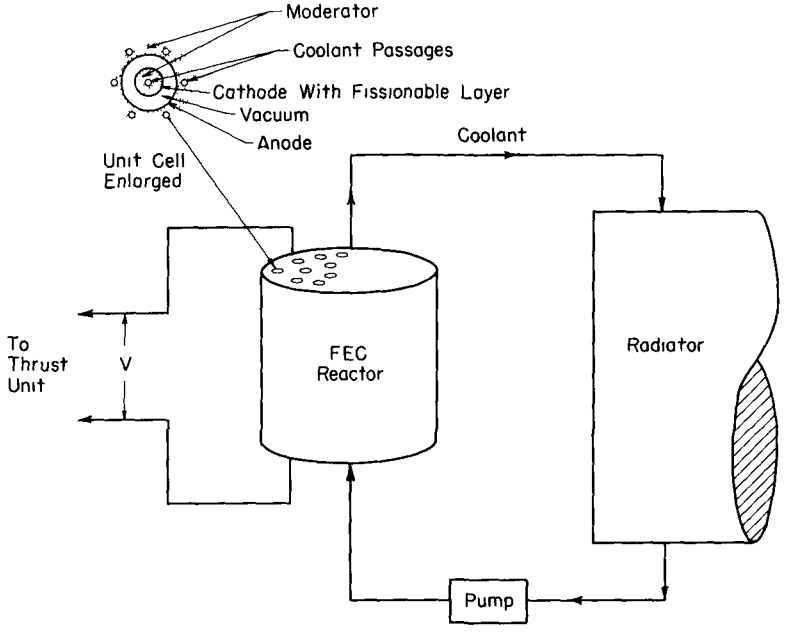

Fig. 7.4—Schematic diagram of a FEC-reactor system for electric propulsion in space. (After Heindl et al., Ref. 22.)

sharp contrast to the low-temperature systems promoted by the previous studies, the space system was viewed as a high-temperature unit. Using the same argument (that the FEC does not operate on a heat cycle) the authors noted that a minimum-temperature differential could be maintained between the core and the waste-heat radiator without loss of efficiency. This permitted a sharp reduction in the radiator

size and weight, which is quite significant in the typical space power unit Calculations assumed a 1-MWe reactor with a radiator operating at 2000°F

However, because of the low fuel inventory and vacuum gaps, the concept tends toward a large, relatively heavy, thermal reactor The need for secondary-electron suppression is also a complication, and three important additional developmental problems were outlined (1) Experimental demonstration of voltage operation (2) Proof that relatively high fuel burnup levels can be used without serious damage to cell performance. (3) Development of a means of handling very high voltages in the reactor, power transmission system, and propulsion units. This same report describes the JPL experimental program prior to 1963. In-core tests at the GE Vallecitos reactor used the experimental cell configuration shown in Fig. 7.5. While magnetic field suppression is indicated, some capsules used electrostatic grids. All

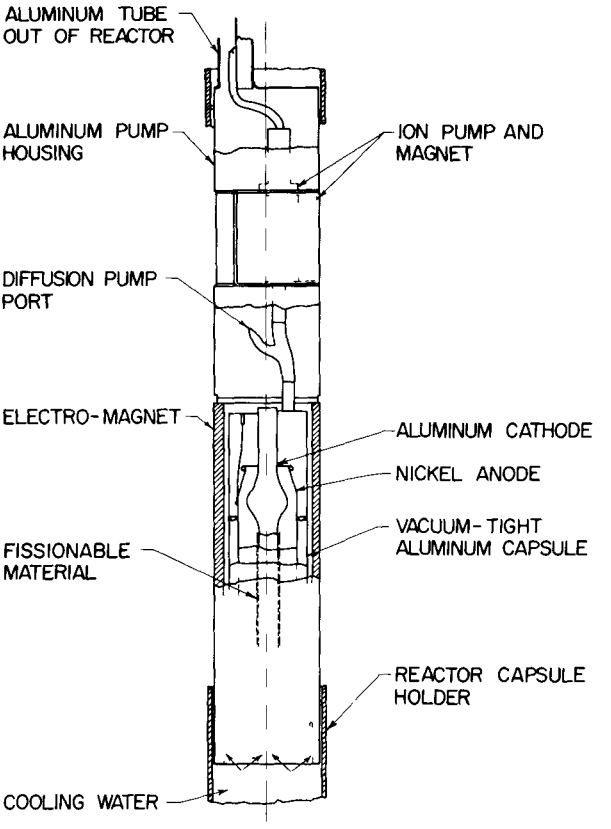

Fig 7.5—A typical JPL–FEC experimental capsule (After Heindl et al., Ref 22.)

structural components were aluminum except for the anode (nickel) and the grids (molybdenum and platinum). A maximum magnetic field corresponding to 370 G in the center of the cathode and 890 G near the ends was used. The first tests indicated a surprisingly large background current of 0.3 to 0.9 μA in the same direction as the fission fragment current that was attributed to a Compton current.

Output currents in these tests started out at about 8 to 10 times background but generally decreased to about half of this value after extended operation. This effect was attributed to outgassing of the system by radiation, the build-up of beta decaying fragments on the anode, and the accumulation of uranium on the anode. A graphic demonstration of the importance of electron suppression is shown in Fig. 7.6, where the current is shown as a function of the magnetic coil current. Reverse currents (negative sign) were obtained for field coil currents below ≈ 4 A.

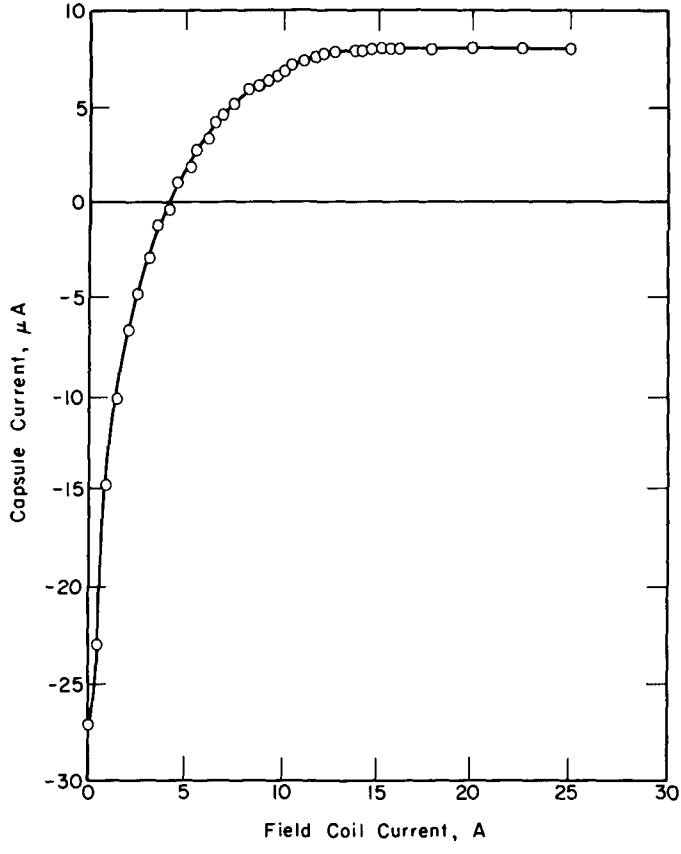

Fig. 7.6—Measured cell currents with magnetic field suppression. (After Heindl et al., Ref. 22.)

Attempts at voltage build-up were erratic—only the order of 11 to 810 V was obtained. Leakage currents were suspected, but tests performed in cells without the fissioning layer failed to verify this. Several other reasons were postulated but, as it is developed, frustrating years of attempts to generate voltages ensued before the problem was finally isolated. Before continuing the discussion of the JPL work, however, let us skip to the Battelle program, which was developing simultaneously.

The Battelle studies originated in 1958 and extended through the early 1960s,[23–25] when the FEC was dropped in favor of the Alpha-Electric Cell studies described in the next section. The BMI group chose to concentrate on the development of a "squirrel-cage" grid assembly, which they termed the "triode concept," and an illustration of a typical cell is shown in Fig. 7.7. It had a 40-wire squirrel-cage grid–cathode assembly composed of 5-mil-diam. stainless steel wires on a $1^1/_4$-in.-diam. grid circle. The cathode was an 18-in.-long ×

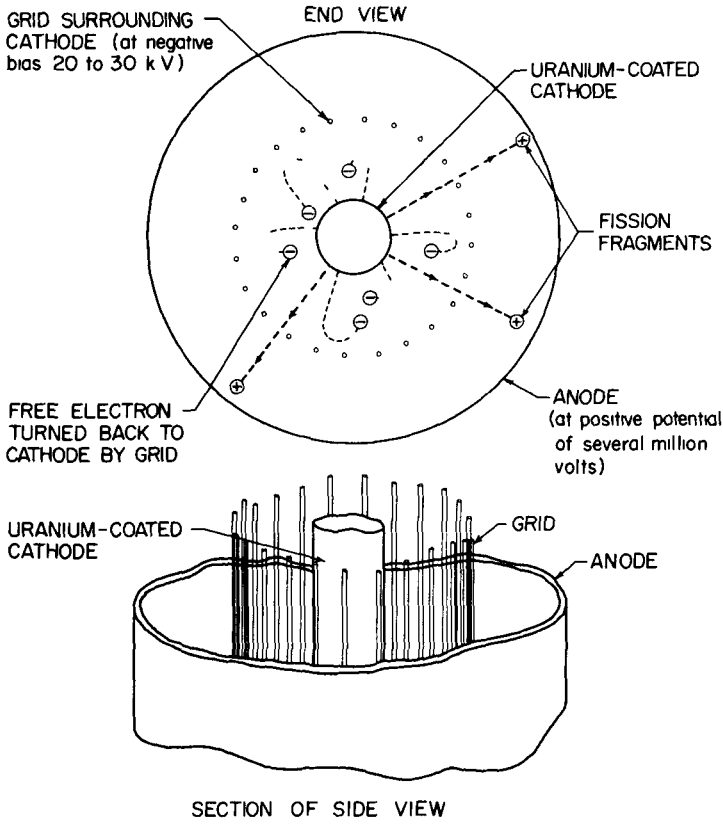

Fig. 7.7—A schematic illustration of the Battelle triode (After Anno, Ref. 23.)

$^1/_2$-in.-diam. molybdenum tube coated with 2 μ of UO_2. A number of variations of this design were also studied, involving over 100 in-pile experiments. Unfortunately, a detailed report of this work was never published. Some results are summarized in Ref. 23, and other data have been obtained from Ref. 25. Points to be noted include:

Short-circuit currents in approximate agreement with calculations were obtained.

Currents were found to be insensitive to pressures below 10^{-4} mm Hg. (Measurements were made to 10^{-8} mm Hg.)

A 100-V negative grid bias was found effective for suppressing most of the true secondaries, but an additional bias was required to stop the high-energy component. An additional leakage attributed to gamma reactions with the fuel coating was observed but could not be suppressed. It represented a loss of $\approx 10\%$ in the net current from the cell.

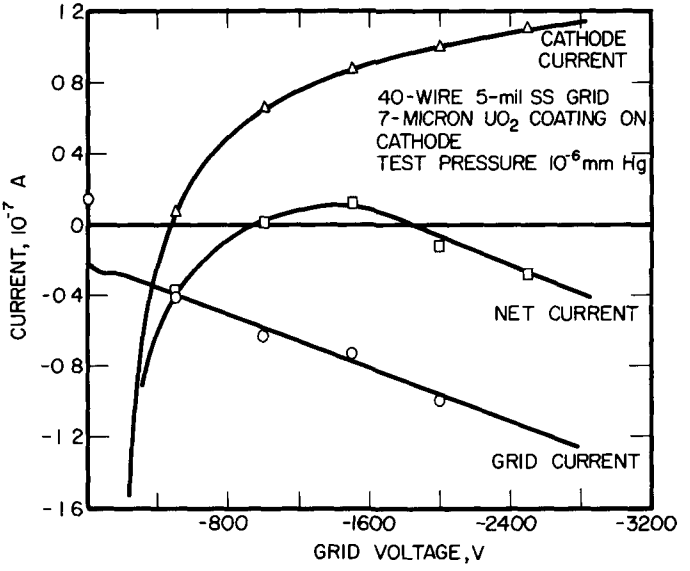

Fig. 7.8 — Typical current behavior of the Battelle triode. (After Anno, Ref. 25.)

A typical test result is shown in Fig. 7.8. The desired positive net current was only achieved over a limited range of grid voltages. An anomalous leakage current at larger grid voltages actually caused the net current to reverse signs, and this limited initial tests to less than 100 V. Results from later tests have not been

reported, but apparently a satisfactory voltage build-up was not achieved. These problems motivated the companion studies of secondary-electron emission due to fragment bombardment discussed earlier in Chap. 5.

In addition to the actual experiments, several associated studies and design concepts deserve note:

Anno and Fawcett[23] have suggested that an ac output might be obtained by oscillating the grid voltage.

One study considered a "vacuum-tube" reactor for use as a low-temperature central-station power plant. The reactor had 2-million Triode Cells and CO_2 cooling. The cells, being spherical, capitalized on the high efficiency for this geometry, and the authors felt that the tubes could be produced at costs comparable to ordinary vacuum tubes.

The major emphasis centered on space-power systems. Conceptual designs for both low- (1–3 kWe) and high-power (1 MWe) systems were carried out. The most promising low-power systems used graphite rods with a thin plutonium carbide emitter surface spaced throughout a canned lithium hydroxide moderator. With the fuel temperature limited to 3400°F and the LiOH to 1400°F, the reactor was critical with 300 Triode Cells giving a core diameter of 122 cm and a height of 47.3 cm. Waste-heat removal was by axial conduction along the graphite rods and subsequent radiation to outer space. The inter-electrode volume (at 1-cm spacing) was vented directly to space to produce the necessary vacuum. The specific weight of this system was about 200 lb/kWe at 6 kV/cm. Several concepts using other moderators, a central driver region surrounded by FECs, and a liquid-metal coolant loop were also studied; however, these appeared to be only marginally competitive with the system described above.

Several 1-MWe systems were considered. Because of the higher power levels, forced convection cooling was required, but the inter-electrode volume was still vented to space. Ranges of parameters studied were: core diameter, 4 to 9 ft; core length-to-diameter ratio, 1.0; void fractions, 0.2 to 0.7; reflector thickness, 0 to 6 in.; fuel materials, UO_2, UC, PuO_2; moderator and reflector materials, BeO, C, Be_2C; coolant, lithium. The radiator inlet temperature was set at 2400°F. The radiator tubes and structure were made of columbium surrounded by graphite fins and a meteoroid barrier. Limiting potentials of 3 and 6 kV at 1 cm were assumed. The general trends of these calculations are summarized in Fig. 7.9. It was stressed that these were preliminary

studies and the situation could drastically change, if for example, improved techniques were developed to permit higher voltages, two-sided emission, etc.

Thus, though extensive experiments had been performed at both JPL and BMI, a satisfactory voltage build-up had not been achieved by 1964. Further, the cause of this failure had not been clearly identified. Battelle became increasingly involved in Alpha Cell work at this time, so the main experimental effort continued at JPL.

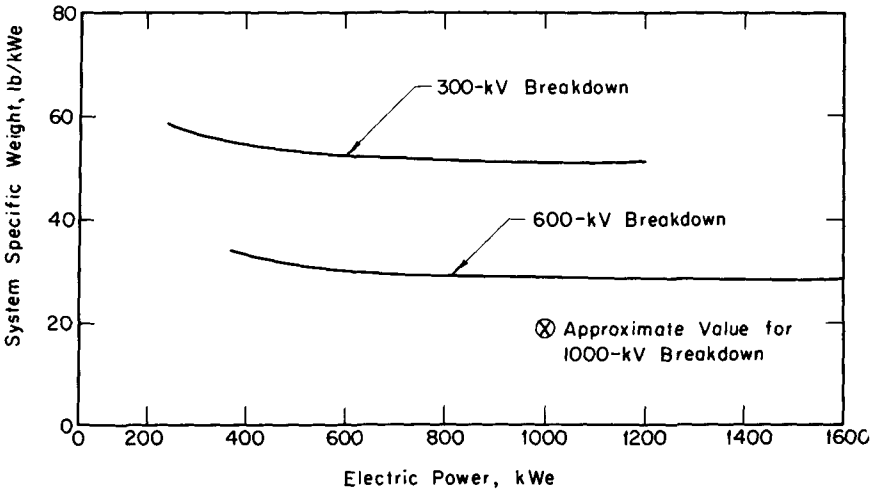

Fig. 7.9 — Specific weight estimates for a high-power triode space power plant. (After Anno, Ref. 25. Conditions assumed include: sufficient fuel for 1-year life; UO_2-Be_2C bare reactor; optimum cylindrical geometry; and the weight includes both the reactor and radiator system.)

During this period, several improvements in the theory were reported: Shapiro[26] developed a two-group model to treat fragment transport through the fuel layer. The effect of fragment charge neutralization during the slowing process, neglected in earlier studies, was incorporated into this model. Concurrently, Miley[27] reported a detailed study of the effect of fragment transport on cell efficiency. Reference to this was made earlier in Chap. 4, and many of the techniques discussed in that chapter evolved from this study.

A milestone in FEC development was achieved when Krieve[28] reported in 1966 that 21-kV potentials had finally been obtained in the JPL experiments. (Actually stable outputs were lower — about 4 kV.) Although these voltages are not large when compared to the 1 MV or so theoretically possible, they are significant in that this indicated some understanding of the leakage effect had been achieved.

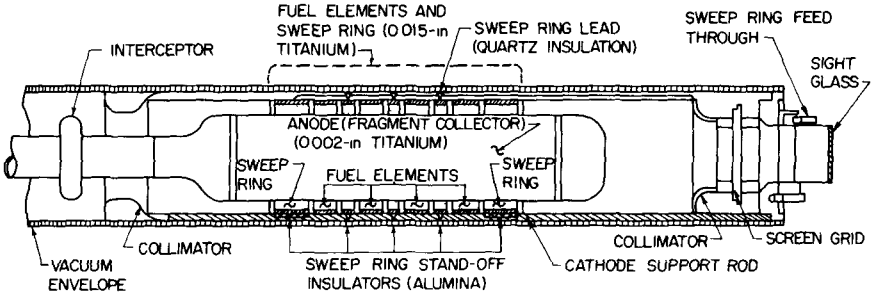

Fig. 7.10—Cylindrical cell for the modified FEC capsule used in voltage buildup experiments at JPL. (After Krieve, Ref. 28.)

The experimental cell is illustrated in Fig. 7.10. Comparison with the earlier cell (Fig. 7.5) indicates that considerable modifications were made following the initial tests—the revised design was based on the following arguments:

> The leakage currents in earlier cells were attributed to the build-up of high electron concentrations in the inter-electrode space. Normally, the magnetic field would return secondary electrons to the emitter (cathode); however, it was argued that these electrons may suffer ionizing collisions with neutral atoms sputtered from the cathode, and this has two effects: Because of its reduced energy, the original electron is prevented from returning to the cathode and will eventually drift to the anode. The electron produced in the ionization event will also go to the anode, and these two electron currents represent a leakage. The process may also be aggravated by the ions produced since they can acquire sufficient energy to cause additional sputtering as they strike the cathode. In the extreme, this process could develop a full glow discharge, and such discharges were, in fact, observed.

The modified cell had two features designed to reduce electron accumulation. As seen from Fig. 7.10, the cathode was designed to surround the anode (the reverse of the original design). This reduces the electron path-length and thus reduces collisions. Also the fuel elements on the cathode were alternated with nonfueled rings. These rings were maintained at a positive potential relative to the fuel, and they served to sweep electrons out of the inter-electrode space that would ordinarily have insufficient energy to return to the fuel surface. Figure 7.11 shows the experimental data obtained with this cell and includes for comparison a series of magnetron-limit curves.

With a sweep ring potential of 2.5 kV, a peak output of $\approx$ 21 kV was developed with 60-A field current. However, it was not reproducible

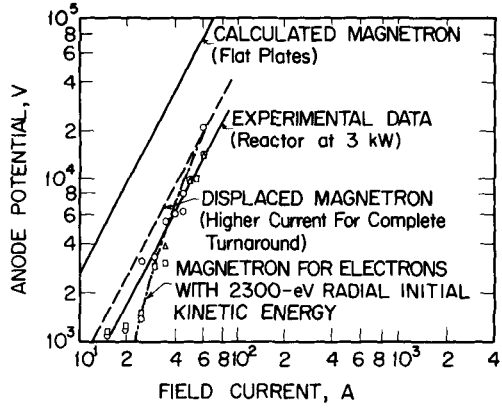

Fig. 7.11 — Open-circuit voltage vs magnetic field current for the modified JPL cell. (After Krieve, Ref. 28. The magnetic field was ≈10 G/A.)

and the largest consistent output was 13.5 kV. Some fluctuations still occurred until the field current was reduced to 35 A, giving a potential of 3.8 kV. Additional observations include:

As shown in Fig. 7.11, the potentials attained were below the calculated magnetron-limit values. This was attributed to end effects. (The calculations shown were based on an infinite flat plate approximation.) Since the experimental points follow a line parallel to the calculated values, it is believed that higher voltages could have been obtained if a larger magnetic field strength had been available.

The charging of the cell was cyclic rather than steady as expected. This was attributed to an electron build-up prior to achieving the magnetron limit. It was postulated that this could be overcome by proper load matching, but this was not attempted.

It was noted that the volume where the ionization probability is largest decreases with increasing voltage. Thus sweep rings might not be needed at large voltages.

Based on these experiments, Krieve listed the following as major problem areas remaining in FEC development:

- Handling of high voltages, with particular emphasis on insulators in radiation fields.
- Electron and ion behavior in $\vec{E} \times \vec{B}$ fields including the effects of sweep rings and end effects.
- Sputtering by fragments.

•Fuel element material including surface treatment before and after deposition.

Finally, two recent conceptual design studies are of interest: One by Shapiro[29,30] and another by Mokski.[31] Shapiro has reported a study of a graphite-moderated FEC-reactor typical of those of interest at JPL. The total size, temperature, and total thermal power of the reactor were fixed, and the remaining parameters were optimized. Some results are illustrated in Fig. 7.12. As noted earlier by Heindl, these curves illustrate that, while the collection efficiency increases with larger radii ratio R_2/R_1, the increased fuel-layer thickness required offsets this gain and the overall efficiency actually decreases. For the system studied, the optimum efficiency occurred for R_2/R_1 between 1.1 and 1.65.

The voltage-breakdown curves determine the optimum operating point, and this occurs well below 1 MV, where there is little difference in the various breakdown criteria. [The range shown at higher voltages

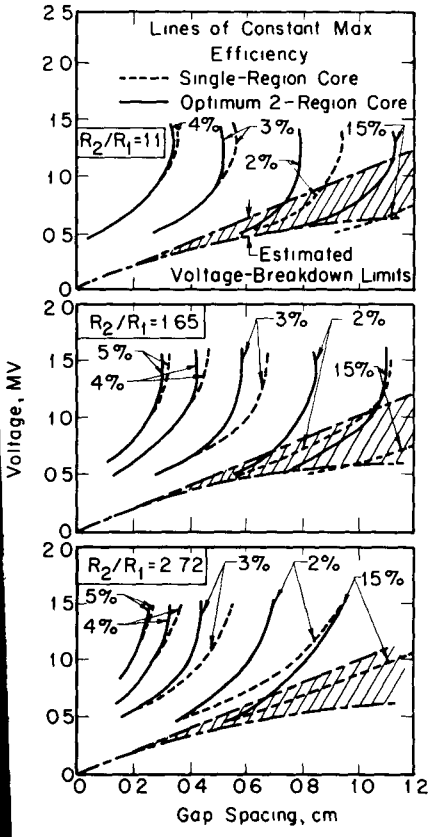

Fig. 7.12—Efficiency curves for a graphite-moderated FEC reactor. (After Shapiro, Ref. 30. The single-region core used cylindrical geometry. The 2-region design used a compact, central region without cells. Escaping neutrons from this region entered surrounding FEC's, which can be designed with an optimum fuel-layer thickness.)

represents approximate uncertainty limits Shapiro assigned to the extrapolation of Alpert's and Lee's data (Fig. 6.19).]

If the fuel mass required were reduced by $\frac{1}{2}$ or $\frac{1}{3}$ in some fashion (better design, improved calculations, etc.), the efficiency curves of Fig. 7.12 could be adjusted by dividing the spacing by 2 or 3, etc. Shapiro notes as an example that the maximum efficiency for $R_2/R_1 = 1.65$ is $\approx 2\%$ at 500 kV, but this is increased to $\approx 3.5\%$ at 650 kV if the fuel loading is halved.

In summarizing this study, Shapiro stresses that the optimum operating voltage is shifted downward from that calculated without criticality considerations. Thus, he concludes, "The criticality requirement may be a more severe limitation on efficiency than the effect of voltage breakdown."

Finally, it is instructive to note that this study follows a pattern that stresses three distinct and basic areas of a FEC-reactor design: neutronics, fission fragment physics, and voltage breakdown.

The companion study by Mokski[31] considers the fluid systems aspects of FEC space reactor designs. He selected gas cooling for a detailed study on the basis that:

- The FEC-reactor is inherently a low-power-density device and hence ideally mated to gas cooling.
- Significantly higher temperatures would appear possible with gas-cooled reactors than with a liquid-metal system.
- Problems of two-phase condenser–radiators and corrosion by liquid metals are avoided.
- Gas-cooled systems are notably trouble free.
- Thick meteoroid armor permits a high radiator gas pressure without a further weight penalty.

Mokski assumed a 10-ft diam. × 10-ft reactor with cylindrical cells operating at 1 MW with 1-cm gaps. A total power of 500 MW(th) and a minimum of 25 MWe were selected, along with a moderator to total volume ratio of 0.5. This represents a scale-up of the 200-MW(th) (1-MWe) reactor considered by Shapiro.

Results indicate an overall specific weight of about 6.9 to 13 lb/kWe (not including shields), corresponding to conversion efficiencies of 5% and 10%, respectively. (However, in view of Shapiro's results, these efficiencies seem rather optimistic.) As illustrated in Fig. 7.13, the largest and heaviest single component in the system was the radiator, and the high temperatures allowed by the FEC resulted in a 50 to 80% reduction in radiative area relative to conventional designs. It is noted that, on a specific weight basis, the overall FEC system with a 5% efficiency is competitive with space power plants using a liquid metal

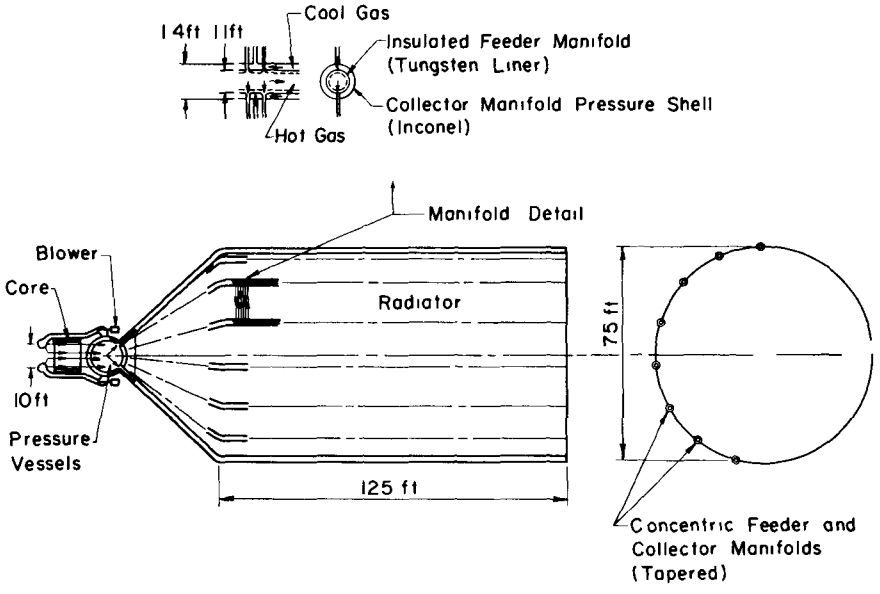

Fig. 7.13—The gas-cooled FEC reactor and radiator system considered by Mokski (Ref. 31). (For a 25-MWe gas-cooled reactor and radiator concept assuming 5% fission-electric conversion efficiency and a 0.375-in.-o.d. radiator tube. For 10% conversion efficiency the radiator area required would be approximately half of the area shown in the above sketch and would be equivalent to a cylinder of 60-ft diam. and 100-ft length.)

vapor Rankine cycle with an efficiency of 15%, and in addition, the FEC system would be smaller in size. An FEC system with 10% efficiency would have a decided advantage in both respects, and plants as large as 25 MWe could conceivably be put into earth orbit in a single launch.

7-3 THE ALPHA-ELECTRIC CELL

The conventional Alpha-Electric Cell (AEC), like the FEC, represents a Plate-Emitter Cell. Particles originate in a fuel layer (or coating on the plate) that is commonly envisioned as an alpha-emitting radioisotope such as polonium-210, curium-242, curium-244, or plutonium-238, although a cell might be designed to operate in a reactor based on an (n-α) reaction using a coating like boron-10.

The first reference to an Alpha Cell appears to be due to P. H. Miller.[32] In 1946, he suggested a spherical cell fueled with ^{210}Po. He envisioned using stages (i.e., cells connected in series to obtain higher voltages), and he estimated that about 1 g of ^{210}Po per stage would give a 25-μA current and 2 MV per stage. He noted that the selection of a

fuel-layer thickness of the order of the alpha-particle range ($\approx 5 \times 10^{-5}$ cm) combined with the 1 g/stage fuel loading, fixes the emitter radius of a spherical cell at ≈ 15 cm.

The first extensive study of the concept was reported in 1962 by J. Anno[33] of BMI. He was the first to recognize the key point that high-energy alpha particles, like fission fragments, give a secondary yield well above unity. Thus, suppression of the secondaries represents a critical problem in reducing the concept to practice. (Miller and others who considered the Alpha Cell earlier were apparently unaware of the necessity of suppression.)

Anno explained the motivation for the Battelle studies by pointing out five advantages of the Alpha Cell relative to the more common Beta Cell:

> Secondary suppression may actually offer a direct, fairly efficient means of converting the high-voltage dc output to a low-voltage ac current. Oscillation of the grid voltage would give an ac output which might then be "stepped-down" to lower voltages. Because of the lower secondary yields, this method does not appear feasible for use with a Beta Cell. [This concept has not been proved experimentally, and several developmental problems remain. A special transformer such as a piezoelectric transducer (discussed later, see Fig. 7.22) would be required to match the very high cell impedance. Also, the grid oscillator requires a special design because of the large voltage swings involved.]
>
> Alpha decay provides an essentially monoenergetic source, whereas beta decay leads to a continuous energy spectrum. Thus, as noted in Chap. 2, it should be possible to select an unique operating voltage to obtain an optimum efficiency. In contrast, for the Beta Cell, an optimum voltage based on one energy will be "off-optimum" for others represented in the source spectrum. (In retrospect, it might be added that, thus far, the major inefficiencies in actual cells have come from leakage currents, and this is especially important in an Alpha Cell, where the source energies are relatively high.)
>
> Higher power densities are available from alpha than from beta emitters in the half-life range of interest.
>
> Alpha decays are not generally accompanied by the troublesome high-energy gamma rays associated with most beta decays, and also bremsstrahlung is less. Still, spontaneous fission and/or secondary reactions associated with alphas from sources such as ^{210}Po, ^{242}Cm, and ^{238}Pu result in neutron emissions which require some shielding.
>
> The alpha-particle range is considerably less than that for betas; e.g., a 2-MeV beta will penetrate 0.15 in. of aluminum vs about

0.001 in. for a 5-MeV alpha. Thus, a thin-walled collector can be used, and this reduces the cell weight considerably. (However, a thin fuel layer and large emitter surface areas are implied so the overall cell size may suffer.)

The experimental Alpha Cell studies at Battelle extended over approximately a 3-year period and produced a wealth of information.[34–37] Initial experiments used a triode design similar to that shown earlier in Fig. 7.7. Five curies of ^{210}Po were distributed on a $\frac{1}{2}$-in.-diam. by 12-in.-long cathode (emitter) with a squirrel-cage grid of 40 stainless-steel 0.010-in.-diam. wires on a 1.25-in.-diam. grid circle. The grid–cathode assembly was installed into a concentric 4-in.-i.d. anode cylinder electrically insulated by a quartz tripod.

A $^{144}Ce/^{144}Pr$ beta source was inserted initially to test voltage characteristics. A grid bias was not required, and a maximum voltage of 50 KV was achieved. At this point microdischarging began and prevented further build-up.

The microdischarging phenomenon appeared to be consistent with Arnal's "clump theory" (Sec. 6-3.1), and it was estimated that each discharge (clump) consisted of roughly 10^{10} electrons. As illustrated in Fig. 7.14, it was consistently initiated at a threshold of about 50 kV,

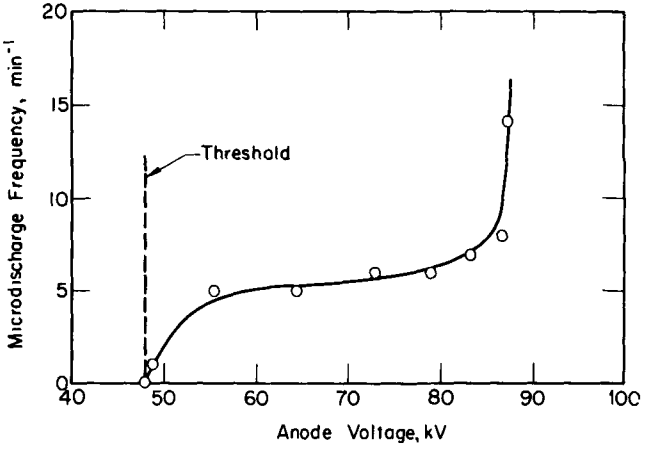

Fig. 7.14 — Microdischarge frequency vs the anode (collector) voltage. (Initial experiments with Cell No. 1 using a beta source. From Plummer et al., Ref. 37.)

and the discharge frequency increased with voltage but was typically of the order of 5 clumps/min in the beta source experiment. This did not cause a complete discharge of the cell, since as illustrated by Fig. 7.15, the discharging essentially balanced the charging current so that voltage build-up simply stopped. A number of experiments were carried

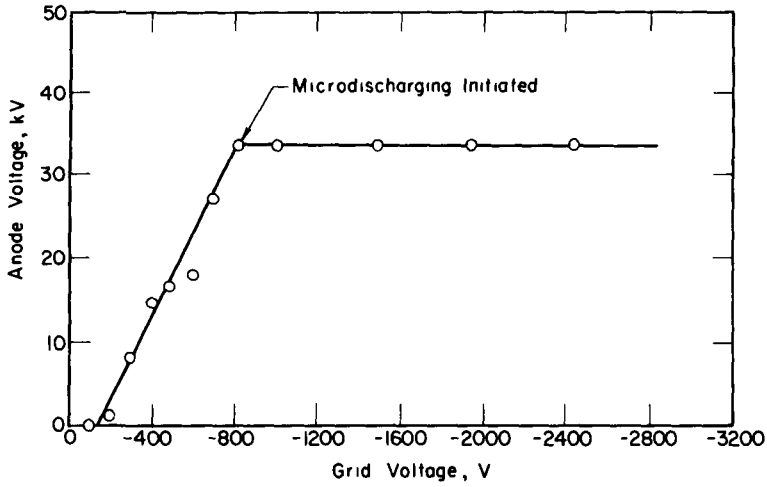

Fig. 7.15 — Effect of microdischarging on voltage build-up. (Experiments with Cell No. 1 using ^{210}Po. From Plummer et al., Ref. 37.)

out using the ^{210}Po alpha source under different grid voltages, etc. The maximum potential obtained was 50 kV with a grid bias of −800 V, at which point microdischarging again limited further build-up as is shown in Fig. 7.15.

A modified cell (Cell No. 2, Fig. 7.16) was built in an effort to overcome the microdischarge limitation. One major change involved replacement of the simple tripod anode insulator with the composite aluminum−quartz structure of Fig. 7.16. This was based on two points:

Microdischarging was thought to be associated with preferential emission of electrons and negative ions near the anode−insulator junction. To reduce the high electric fields in this region, the junction at the bottom of the anode was formed with an undercut recess, and epoxy resin was used to attach the insulating glass. Also the voltage "grading" along the insulator provided a more uniform electric field and prevented a local flashover.

Other properties of the insulator (e.g., surface resistivity) were not considered to be as important as the insulator junction phenomenon. However, since the junction effect decreases with increasing dielectric constant of the insulator, quartz was selected in preference to a glazed ceramic. This structure was designed to sustain 400 to 500 kV.

In addition, the overall dimensions of the electrodes were enlarged as indicated in Fig. 7.17 to reduce local electric fields. A thin steel

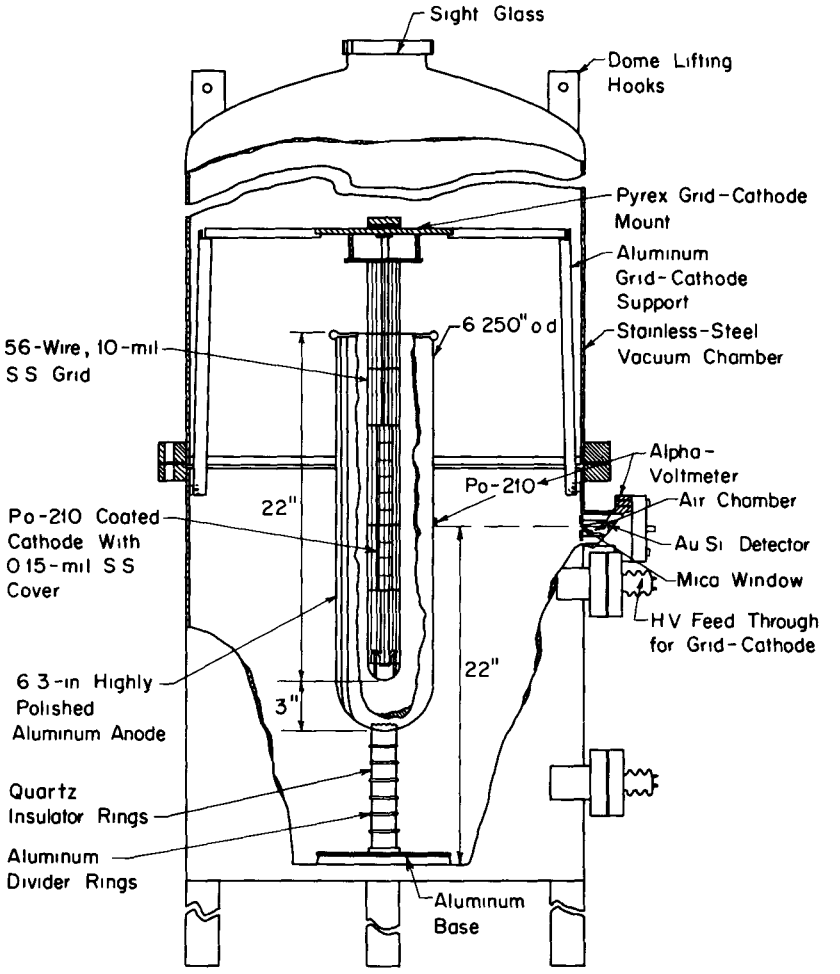

Fig. 7.16—Arrangement of the modified Battelle Alpha Cell experiment—Cell No 2 (After Plummer et al , Refs 36 and 37.)

coating was placed over the fuel layer to reduce polonium migration and contamination of the apparatus (gold was used in the first cell). The new grid was designed with an amplification factor of ≈ 50 to allow control of 500 kV with a grid voltage of 10 kV. The principal results from the modified cell experiments were

> Initial voltage build-up studies achieved 100 kV with approximately −2 kV on the grid, at which point microdischarging again occurred. After several hours of operation, the maximum voltage and microdischarging dropped back and stabilized at 40 or 50 kV The

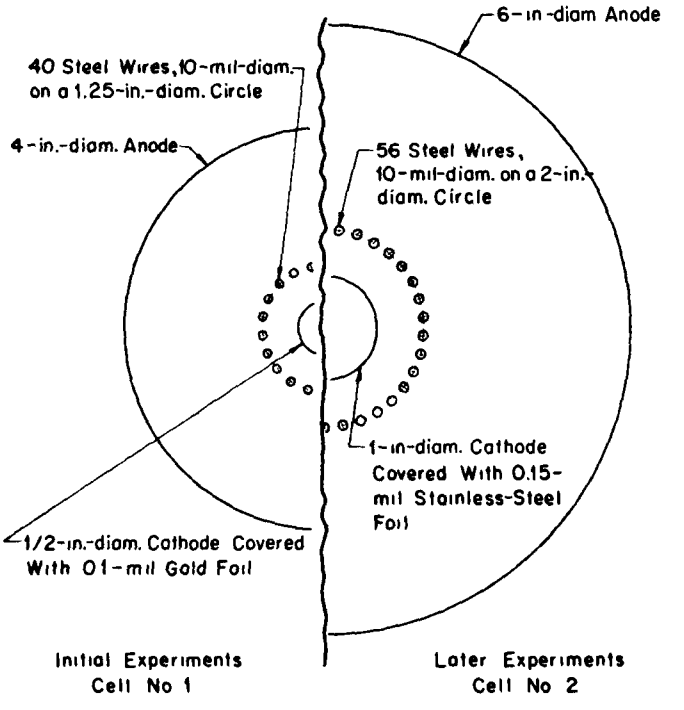

Fig. 7.17—A comparison of the two cell geometries. (From Plummer et al., Ref. 37.)

reason for this is not known. Typical voltage behavior in later runs is shown in Fig. 7.18. The collector voltage–grid voltage data confirm that the grid amplification factor was about equal to the design value of 50. The voltage–time curve shows a constant charging current up to about 30 kV as expected. The change in slope at that point was attributed to a voltage dependency of the grid x-factor (Sec. 6-2.3), i.e., the fraction of secondaries produced at the grid escaping to the collector.

From these data, it appears that the change in x-factor might be the next limiting phenomenon if microdischarging were overcome. This stresses the importance of a highly transparent grid so few secondaries are formed at the grid in the first place. Plummer et al. suggest that new designs—e.g., a grid with staggered wires such that some of the wires would suppress secondaries released from the others—might help overcome the problem.

The microdischarge effect itself seemed to be quite similar to that observed in the first cell. A frequency of roughly 90 dis-

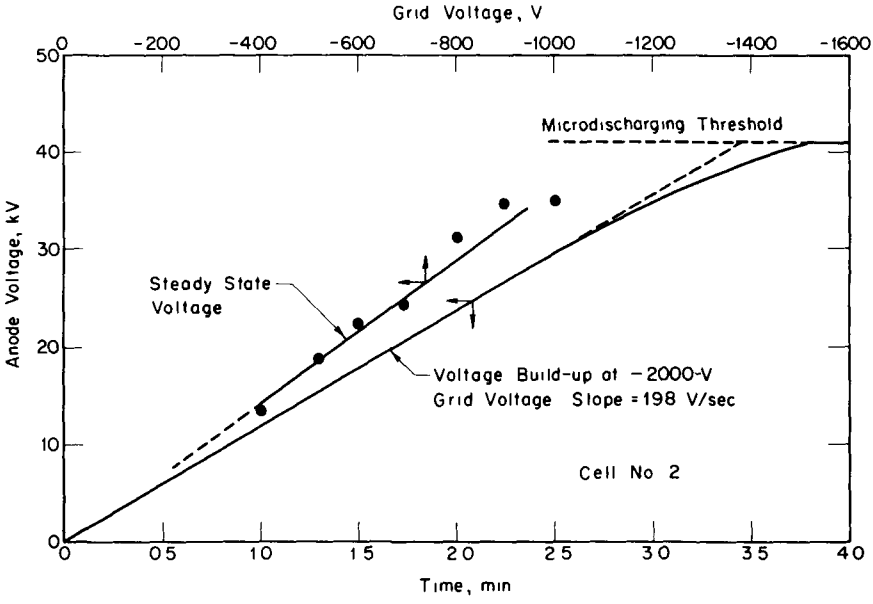

Fig. 7.18 — Variation of collector voltage with grid voltage and a typical voltage build-up with time. (After Plummer et al., Ref. 37.)

charges/min was found with approximately 3×10^{10} electrons/discharge.

Several successful extended tests were conducted maintaining a voltage just below the microdischarge limit for periods up to 60 hours.

Aside from microdischarging and a pressure effect described in following sections, the bulk of the data obtained from these experiments was in fair agreement with initial design predictions, and this confirms a reasonable understanding of basic cell and grid design principles. The short-circuit currents were in good agreement with predictions, and the secondary-electron current, found from the difference in grid currents in going from large positive to large negative grid voltages, was $\approx 10^{-7}$ A as expected. The alpha current at large negative grid voltage was $\approx 10^{-8}$ A, or an order of magnitude less than the secondary current in agreement with secondary yield predictions of ≈ 10.

Grid parameters were summarized earlier in Table 6.1. Although based on a combination of calculated and measured characteristics, they are thought to be reasonably accurate. Several points are of particular interest: The large alpha/secondary

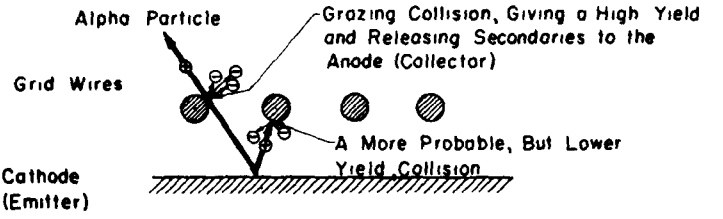

Fig. 7.19—A possible mechanism for electron escape from the grid–emitter assembly. (After Plummer et al., Ref. 37. The unexpectedly large x-factor measured in Alpha Cell experiments is attributed to the high-yield grazing collisions.)

charge ratio for the grid of the second cell was attributed to the unintentional use of partially oxidized grid wires. The large value of η_g for Cell No. 2 was off-set by a reduced x-factor such that the grid–cathode current for the two cells turned out to be similar.

The grid x-factor appears to represent the major uncertainty in grid design. Neither the large size of the x-factor nor the difference between the cells indicated in Table 6.1 was expected. A high rate of grazing collisions illustrated in Fig. 7.19 was proposed as a possible explanation.

The charge ratio η_g was found to be about the same for the two cells, although a gold covering was used in the first one and steel in the second. This is consistent with the observation in Chap. 5 that the secondary yield is not strongly dependent on materials. The yield at the emitter did vary some with grid voltage (Schottky effect), but in contrast, the yield at the grid itself appeared to be independent of voltage. This might be related to a difference between particles emerging from, as opposed to impinging on, the surface; but this situation is not clear. An apparent Schottky effect was observed at the grid in the earlier Fission Cell experiments (Sec. 7-2), and this was one of the early explanations suggested for the anomalous leakage currents in those experiments.[35]

The experiments discussed to this point were all carried out with the cell under a vacuum of 10^{-5} Torr or better. Most interesting results were obtained from pressure effect studies.

Data in Fig. 7.20 for Cell No. 1 display similar features for both the beta and the alpha source. Below 10^{-4} mm Hg, the voltage is independent of pressure, but above 10^{-4}, a sharp decrease occurs followed by a region around 10^{-3} where higher voltages are obtained. At still higher pressures, the cell voltage decreases rapidly.

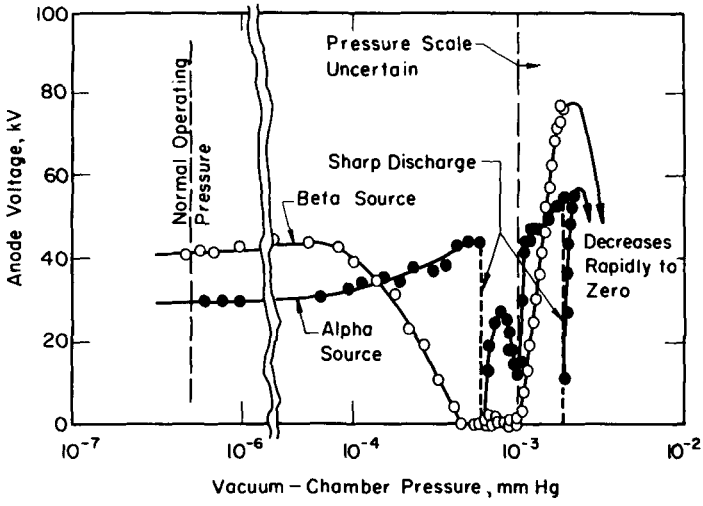

Fig. 7.20 — Voltage–pressure plot for Cell No. 1 with both a beta and an alpha source. (Based on data by Plummer et al., Ref. 37.)

An anomalous voltage peak at about 10^{-3} mm Hg had been reported earlier by Linder and Christian,[38] and for comparison, their data from Beta Battery studies are shown in Fig. 7.21. As discussed in Sec. 6-3.1 in connection with vacuum breakdown, the peak at about 10^{-3} mm Hg appears to be due to destruction of surface whiskers by ion bombardment, while the ultimate decrease in voltage at higher pressures is apparently due to ionization of the gas and the resulting leakage currents.

Surprisingly, Cell No. 2 did not exhibit the anomalous peak although a number of gas conditions were tried as well as a 4-in.-diam. emitter (the same size as used in Cell No. 1). Since the general cell designs were similar, the effect was thought to be quite sensitive to the detailed geometry. (This explanation does not seem too reasonable, and the whole situation deserves further investigation. It is not clear that it would be desirable to operate a cell at this point, but at least this may represent a way of bypassing microdischarging to obtain data at higher voltages.)

In addition to results pertaining directly to cell operation, the Battelle studies included several other aspects of interest:

Plummer et al.[37] estimate a magnetic field-collector diameter product of Bb = 0.02 Wb/m would be required for the Alpha Cell (Fig. 6.17). This indicates an axial field of order of 1000 G for a typical 20-cm collector diameter. They felt that maintaining such

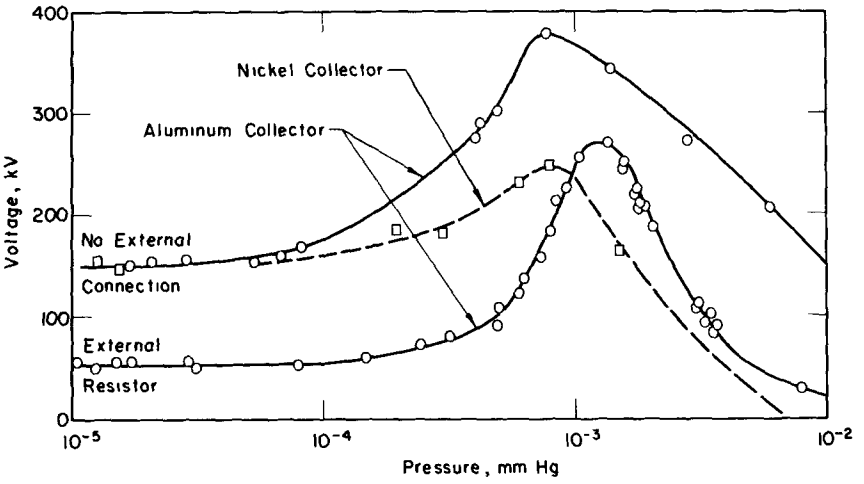

Fig. 7.21 — Original measurements of the anomalous pressure effect by Linder and Christian (Ref. 38). (Obtained with the ^{90}Sr battery of Fig. 7.26.)

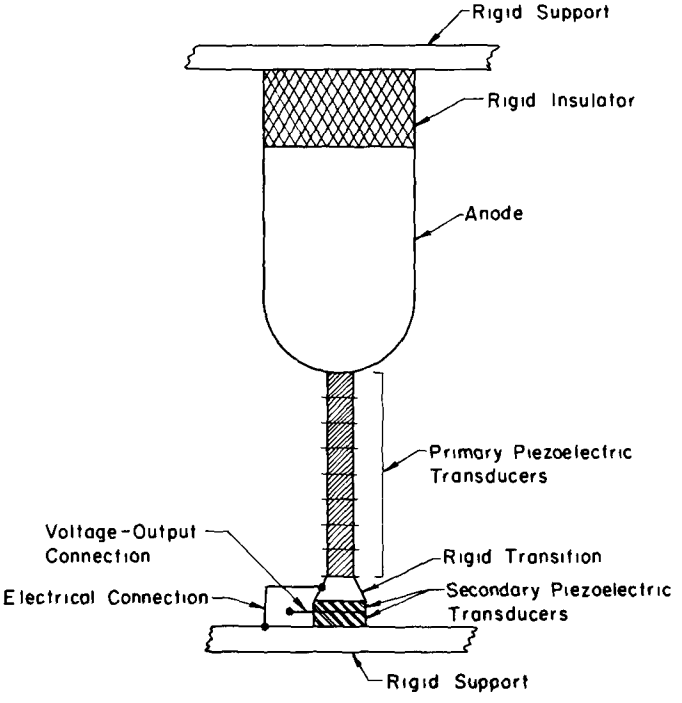

Fig. 7.22 — Schematic arrangement of the piezoelectric transducer proposed by Plummer et al. (Ref. 37).

a field over the volume involved would be prohibitive because of magnet weight and power losses. For this reason, gridded cells were studied exclusively. (The magnets used in the JPL Fission Cell studies were indeed of this order of magnitude. This is satisfactory in the lab and in some respects gives a cleaner experiment; however, the problems of weight, etc., must be faced eventually, and in some applications, grids may be mandatory.)

Voltage measurements require a very high impedance voltmeter due to the large impedance of the cell. A "generating voltmeter" was used in the JPL studies, but even then the 3×10^{-11} A drawn by this unit was, as Krieve points out, "not insignificant." An "alpha-voltmeter," originally described by Bettenhausen and Gallagher,[39] was used in the Battelle studies. This involved mounting an auxiliary ^{210}Po alpha source outside the anode wall with a thin-window air chamber between the source and a surface barrier detector (Fig. 7.16). The electric field, caused by the voltage build-up on the anode, retarded the alpha-particle motion. The resulting change in range as they passed through the air chamber was measured with the detector, and this was correlated with the voltage. This method completely avoids the problem of leakage currents through the meter. It works best for high voltages, and tests from 30 to 50 kV demonstrated excellent accuracy in this region.

The problem of conversion of the high-voltage dc output, mentioned briefly at the beginning of this section, was considered in some detail from two points of view:

(1) *Ballistic methods* which in some fashion control the cell charging current, e.g., the use of internal deflectors to focus the alpha current alternately on one collector and then another.

(2) *External circuit methods* such as using a piezoelectric transformer, or series charging and parallel discharging of a bank of capacitors, etc.

It was concluded that the method best meeting Battelle's specific requirements was the piezoelectric transformer. This scheme is illustrated in Fig. 7.22. The voltage across the primary transducers produces a strain, which is in turn transmitted to the secondary transducers, thereby inducing a voltage across the secondary. In this study, which was not necessarily optimized, primary voltage oscillations (driven by grid oscillations) were presumed to vary between 1.3 and 2 MV, producing −5.2 and 3.7 kV in the secondary. The output power was 773 W corresponding to an electrical-power-conversion efficiency of 9.5%.

One important aspect of the piezoelectric transducer should be noted. This circuit appears as a capacitor to the voltage source; thus, the source must provide both charging and discharging capability. The Triode Cell with grid control is one of the few power sources that can be operated as an oscillating positive and negative voltage source.

7-4 THE BETA-ELECTRIC CELL

As noted previously, most of the "nuclear batteries" manufactured to date have used a beta source. There is not a clear distinction between a "cell" and a "battery," and the direct-collection devices discussed here could be called either in good conscience—in fact, both terminologies have been used in the literature. However, since the term "battery" tends to carry a connotation of lower-power output, we will arbitrarily restrict this term to devices operating in the fractional-watt range.

7-4.1 High-Powered Beta-Electric Cells

Commercial nuclear batteries generally have outputs in the microwatt range. Several proposals[8] have been presented to scale up these concepts to the kilowatt range or above, and there seems to be no fundamental obstacle to this. However, a number of factors (e.g., heat removal, size, etc.) have not been considered in sufficient detail to determine the practicality of simple scaled-up designs. The only detailed study of a high-power cell now available is by Cohen, Low, and Michelsen[40–43] of the NASA Lewis Laboratory made in connection with a power source for use in an electrostatic propulsion system. Their studies were primarily analytic; some experimental electron backscattering investigations have been reported, but no cell studies *per se*. A Beta-Electric Cell (BEC) was selected in preference to an Alpha-Cell for four main reasons:[40,42]

A larger fuel thickness can be used giving a smaller overall cell size.

Lower operating voltages are required for efficient operation of a beta-emitter such as ^{144}Ce ($\langle T_\beta \rangle \approx 0.2$ to 0.3 MeV) as opposed to ^{210}Po ($T_\alpha \approx 5.3$ MeV), and this lessens the problem of high-voltage breakdown.

Since the high-voltage dc output is mated to the propulsion requirement, the ability to use a grid to produce ac output is not important. The BEC, by avoiding the grid, is simpler to construct.

A suitable beta emitter such as $^{144}Ce/^{144}Pr$ is more available than ^{210}Po.

The design concept is illustrated in Fig. 7.23a. Both spherical and cylindrical configurations were considered in the 10- to 50-kWe range, and 100- to 500-kWe cells were envisioned by 1980 depending upon the availability of ^{144}Ce. The choice of ^{144}Ce from among those isotopes that offer suitable power densities, half-lives, etc., was in fact largely dictated by the anticipated availability. Typical results are reproduced in Table 7.1, and some comments should be noted:

The weight per unit power is perhaps the most important criterion for space power of this type; however, efficiency has a direct bearing on economic feasibility because the fuel is very expensive.

The specific weight increases monotonically with both the fuel support and collector thickness so that, from this point of view, the ideal would be a zero thickness for both.

The collector, representing the largest area, is the most important single weight factor. As seen from Table 7.1, designs having sufficient thickness to stop all the beta particles (≈ 1 g/cm^2 aluminum) result in unreasonable specific weights, and undesirably high collector temperatures. For these reasons, the thick collector approach was abandoned. Fortunately, the current requirement for propulsion thrusters is so low that a partially transparent collector can be used (represented by 20 and 5 mg/cm^2). Then, to maintain neutrality, betas passing through the collector must be compensated for by expelling positive ions. As illustrated in Fig. 7.23a, this requires an ion-gun unit, but fortunately, it is not too heavy.

The effect of varying the radius ratio is illustrated in Fig. 7.23b. The optimum occurs at a ratio of roughly 2.0, and this value was used in most cases in Table 7.1.

The emitter temperature for the spherical configuration was satisfactory for all fuel-layer thicknesses considered. However, the thicknesses must be < 70 mg/cm^2 in the cylindrical case to prevent melting of the metallic fuel. Increasing the radius ratio also lowers the temperature some, but the weight penalty makes this undesirable.

The cells were intended for 700-kV operation, so including a safety factor, a 1-MV "design" point was used in voltage breakdown estimates. Based on Cranberg's breakdown criterion, a minimum gap thickness was calculated, and this in turn led to the minimum emitter radii listed in Table 7.1, where a fixed-radius

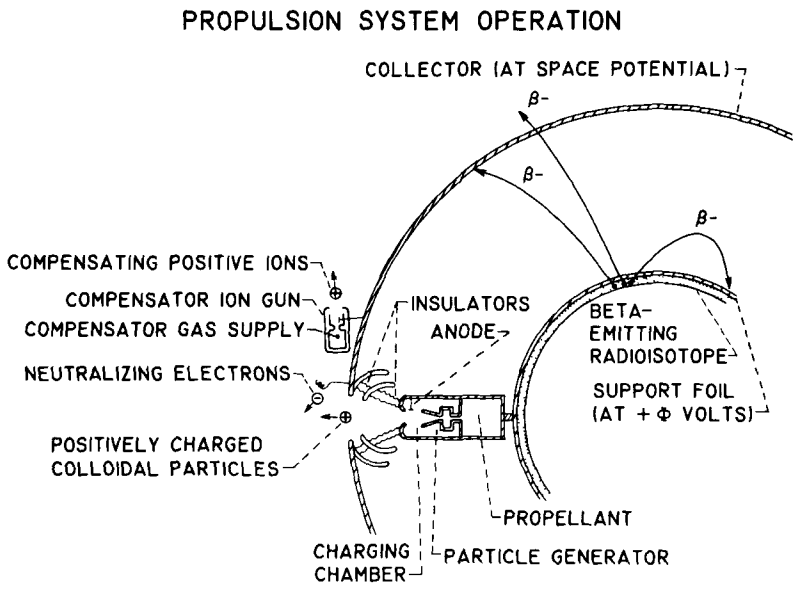

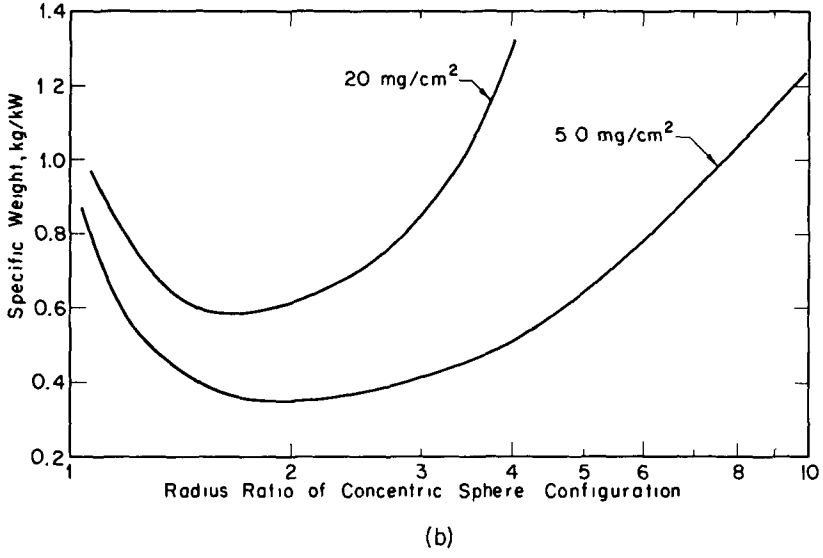

Fig. 7.23 — Electrostatic propulsion system based on the Beta Cell concept. (From Refs. 40 to 42.) (a) Proposed lay-out for spherical geometry. (b) Effect of radius ratio on specific weight. (Spherical electrodes with a fuel-layer thickness of 35 mg/cm^2, a support thickness of 25.9 mg/cm^2, and two different collector thicknesses as indicated.)

Table 7.1—PARAMETERS FOR VARIOUS SPHERICAL AND CYLINDRICAL BEC DESIGNS*

Parameter	Spherical cells				Cylindrical cells			
	A	B	C	D	A′	B′	C′	D′
Fuel-layer thickness, mg/cm^2	0.875	17.5	70.0	350	0.875	17.5	70.0	350
Support layer thickness, mg/cm^2	25.9	25.9	25.9	51.8	25.9	25.9	25.9	51.8
Radius ratio	2.0	2.0	2.0	1.5	2.0	2.0	2.0	1.5
Efficiency, percent	30.0	29.5	23.6	8.35	17.0	16.8	14.6	6.05
Operating voltage, kV	740	710	690	530	580	580	570	440
Weight per unit power, kg/kW, at various aluminum collector thicknesses:								
1.0 g/cm^2	627	32.4	10.0	3.68	555	28.3	8.37	3.68
20.0 mg/cm^2	16.6	0.975	0.435	0.625	18.4	1.15	0.544	0.834
5.0 mg/cm^2	7.28	0.503	0.287	0.577	10.1	0.743	0.424	0.788
Temperature of emitter, °C	−36	237	466	1,027	−6	295	549	1,090
Temperature of collector, °C	−116	65	217	689	−74	151	341	780
Minimum size† at 1-MV breakdown voltage:								
Inner rad., cm	20.0	20.0	20.0	30.0	14.4	14.4	14.4	24.5
Outer diam., cm	80.0	80.0	80.0	90.0	57.8	57.8	57.8	73.8
Power, W	32.7	634	2050	11,300	92.2	1890	6550	29,400
Current, mA	0.0442	0.894	2.93	21.3	0.159	3.26	11.5	66.8
Size for 100-kW generator:								
Inner diam., m	22.2	5.00	2.79	1.79	9.50	2.09	1.17	.653
Outer diam., m	44.3	10.0	5.58	2.69	19.0	4.18	2.34	1.36
Length, m					95.0	20.9	11.7	6.53

*From Ref. 40.

†Length of cylinder in this case is taken as five times the outer diameter.

ratio of 2.0 is assumed. Aside from this point, the cells shown scale linearly in total power output with respect to the emitter area. The powers represented by the minimum emitter radii are the order of a few kilowatts, which is consistent with the propulsion requirement. In this case, lower powers require a thinner fuel layer, which results in an increased specific weight.

Although the cylindrical configuration does not match the efficiency or specific weight predicted for spherical cell, some practical advantages involved with the mechanical design, etc., may still lead to its use.

A total gamma radiation of 0.05 MeV/decay is emitted from ^{144}Ce. The resulting unshielded dose rates are fairly high, and a lead or concrete shield would be required prior to launching, but in flight, a boom could be used to reduce the effect on the payload. It is estimated that a 200-day Mars probe would result in a total dose of $\approx 2 \times 10^7$ R at the payload (below the maximum exposure specified for most materials). This poses more of a problem, however, if manned interplanetary flight is considered, but massive components like solar flare shelters and/or propellant might be located to provide partial shielding.

A 6200-lb payload could be delivered to the 500-mile Mars orbit in 260 days with a 100-kW radioisotope electrostatic spacecraft weighing 8000-lb and boosted by a Centaur. In contrast an all-chemical Centaur system could only deliver an 1100-lb payload. A similar superiority is demonstrated for longer missions.

7-4.2 Beta Batteries

Various nuclear batteries and, in particular, Beta Batteries are reviewed in some detail in several references;[1–8] so we will only concentrate on points of interest to the present development here.

The first operating Direct-Collection Cell was in fact a Beta Battery built by Moseley[44] in 1913. While it appears that the concept can be traced to work by R. J. Strutt in 1902, Moseley's experiment was the first to achieve a voltage build-up. His cell, illustrated in Fig. 7.24, attained potentials near 150 kV with a 20-mCi radon source. The wall thickness of the quartz bulb source holder was selected so that it would absorb alphas but transmit the more penetrating beta particles from the radon. The maximum voltage was limited by an internal flashover which discharged the device.

In recent years, Beta Batteries using emitters like tritium, $^{90}Sr/^{90}Y$, ^{85}Kr, etc., have become fairly common. This is partly because of the availability of these isotopes and partly because the

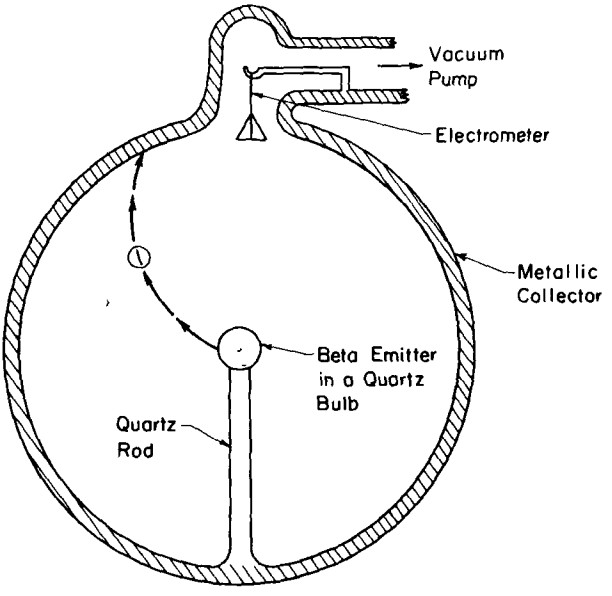

Fig. 7.24 — Moseley's first nuclear battery. (From Ref. 44.)

larger range of beta particles (vs alphas particles) simplifies the source design, and as described later, makes use of a solid dielectric insulator possible.

Such batteries are, in fact, the only direct-collection devices, other than radiation-detection instrumentation, that are presently produced commercially. Manufacturers include Radiation Research Corp., Tracerlabs, Leesona Moos Labs, and General Radioisotope Processing Corp. However, as stressed by Shorr,[4] the nuclear battery should not be viewed as a general replacement for the common chemical battery. This is because of safety aspects related to the radioactivity involved and also, at present, the price. Thus, nuclear batteries are generally reserved for situations where one or more of the following characteristics can be exploited:

- Compact and portable size.
- Simple, rugged construction.
- Insensitivity to external conditions (pressure, temperature, moderate E&M fields).
- Very long life.
- Constant current over a relatively large range of voltages.

Typical applications have involved dosimeter chargers, delay timers, and electric-detonator power sources. To match the high cell impedance (discussed in Chap. 6), high-impedance external circuits are required, and three examples discussed by Windle[7] are illustrated in Fig. 7.25. The battery is used in Circuit A to charge a capacitor (C).

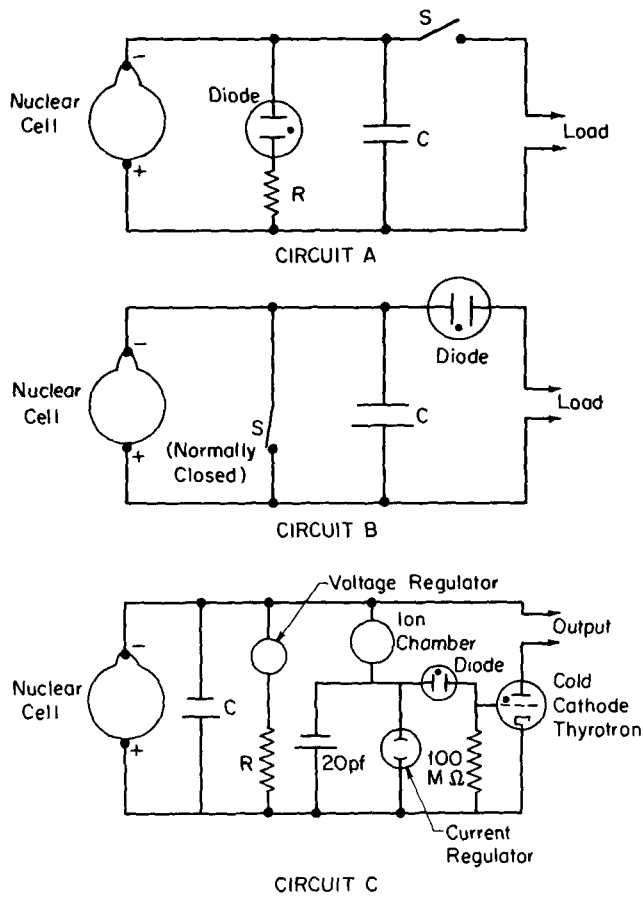

Fig. 7.25 — Typical circuits utilizing Beta Batteries. Circuit A: pulsed voltage source. (Courtesy of Leesona Moos Laboratories.) Circuit B: time delay circuit. (Courtesy of Leesona Moos Laboratories.) Circuit C: gas-density-sensor circuit (from Ref. 7.)

Once a preset voltage level is achieved, the regulating diode (D) becomes conducting such that this voltage level is maintained. Closing the switch (S) discharges the circuit through the load, which provides a pulse source for the operation of relays, detonators, etc.

In Circuit B, the constant charging characteristic of the cell over a fairly large range of voltages is used as the basis for a time delay. A cold-cathode diode is inserted between the battery and the load. The size of the capacitor and the diode breakdown voltage are selected to give the desired delay between the opening of the switch (S) and the time when the capacitor is discharged through the diode to the load.

Circuit C is used to measure gas density. The resistance of the open ion chamber depends on the density of the air or gas involved; i.e., the chamber acts as a variable resistor in the circuit. Accuracies of about 3% at 1 Torr have been reported for this method. Other types of transducers can be built with the same circuit by replacing the ion chamber with some other resistance which depends on the quantity to be measured.

Beta Batteries in use today are generally either of the plate-emitter or the conducting-volume-emitter type (Chap. 2). The insulation required in the plate cell has been achieved with either a vacuum or a solid dielectric. The volume emitter commonly uses a radioisotope in gaseous form and a solid insulator. We shall consider each in turn.

(a) Solid Emitter–Vacuum-Type Beta Batteries

Moseley's experiment, described in the preceding section, was the first study of a vacuum-type Beta Battery. Further studies did not occur until 1947, when Linder began his, and he was later joined by Christian[38] to undertake detailed experiments with a vacuum cell. These studies are especially significant since, to the author's knowledge, the Linder–Christian cell produced the highest voltage (365 kV) and the highest measured conversion efficiency (20%) reported to date (except for TEC simulation, see p. 431). A nominal 250 mCi of ^{90}Sr was used (Fig. 7.26), which was evaporated from an aqueous solution of

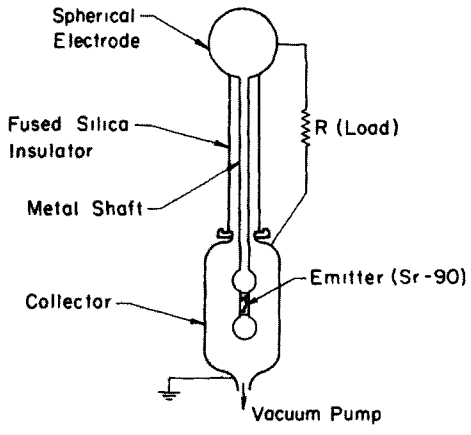

Fig. 7.26—A simplified sketch of the Linder–Christian vacuum-type Beta Battery. (Adapted from Ref. 38.)

strontium nitrate onto the inner surface of the cylindrical emitter (0.80-in.-diam. × 1.5-in. nickel). Two field-reducing spheres were added at the ends of the emitter, and the copper collector was lined with aluminum to reduce secondary-electron emission and bremsstrahlung. Fused silica with a surface resistance of $2 \times 10^{15}\Omega$ at 25% humidity was used for the insulator.

A short-circuit current of about 10^{-9} A was obtained. A complete current–voltage curve was not reported; however, the calculated curve of Fig. 7.27 was presented. As illustrated by the source energy spectrum also shown in Fig. 7.27, this calculation assumed that electrons with equivalent energies above the operating voltage could be collected (shaded portion of the spectrum).* As expected, the shapes of the V-I characteristic and the source spectrum curves are quite similar. The load line of Fig. 7.27 corresponds to the surface resistance of the insulator, and the intersection gives a theoretical maximum

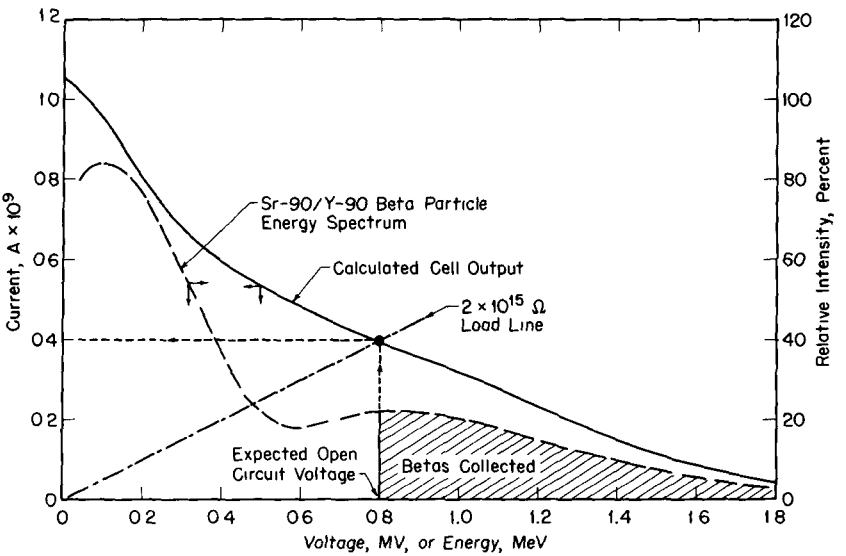

Fig. 7.27—Beta energy spectra and calculated current–voltage curves for the Linder–Christian Beta Battery. (From Ref. 38.)

*This method of calculation is only approximate. As shown in Chap. 2, detailed energy and momentum balances indicate that not even all of these electrons can reach the collector. The Linder–Christian calculation effectively corresponds to the limit of a spherical geometry with zero emitter radius. Actually the cell was not too far from this ideal, so the error introduced should not be overly serious.

potential of 800 kV, which is about twice the value actually obtained (365 kV) (As indicated earlier this maximum voltage was obtained via the anomalous pressure effect illustrated in Fig. 7.21.) Higher voltages were prevented by internal breakdown through the vacuum space between the emitter and collector. This breakdown involved current pulses and was apparently similar to the microdischarging discussed in Sec. 7-3 in connection with the Battelle Alpha-Cell experiments. It was thought to involve a current build-up due to secondary electrons emitted from the anode by ion bombardment and positive ions given off from the emitter by electron bombardment (the "surface regeneration theory" of Sec. 6-3.1). If correct, the type of surfaces involved should be important, and, as seen in Fig. 7.21, there was indeed considerable difference between results with an aluminum vs a nickel collector for pressures above 10^{-4} mm Hg. However, it is not clear why this was not also true at lower pressures.

A voltage build-up curve was also reported (Fig. 7 28), and initial slope was found to agree quite well with calculations based on the assumption of a constant charging current independent of voltage (valid

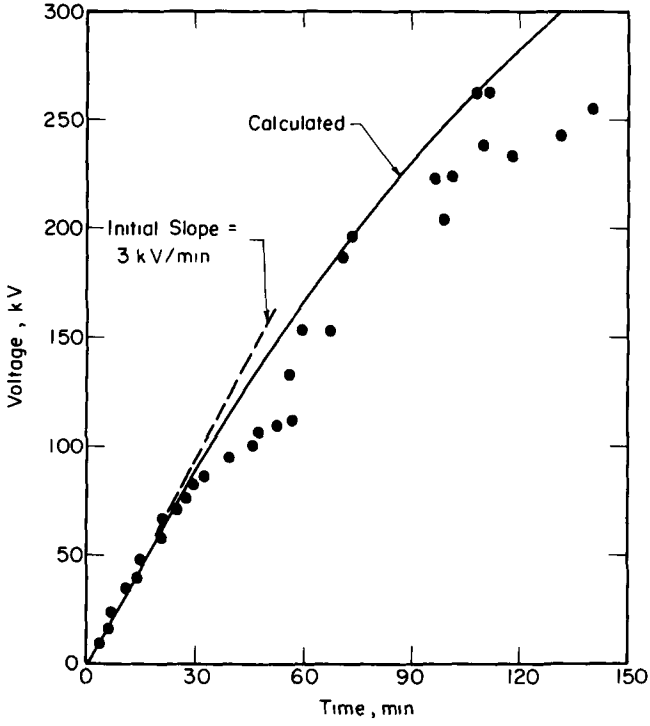

Fig 7.28—Charging curve for the Linder–Christian Beta Battery. (From Ref. 38.)

for $\beta < 0.2$ as seen from Fig. F.3, Appendix F. However, as might be expected, some nonlinear effects are noticeable at higher voltages.

In summary, Linder and Christian concluded that the insulation problem, argumented by the small charging currents, represents the chief limitation to obtaining both high and stable voltages.

The power range was restricted by the limited availability and high cost of radioisotopes at the time of the experiments; however, they predicted that this situation would improve, as indeed it has. Major advantages of such batteries include a long life, small weight and size, and insensitivity to external conditions.

Vacuum-type Beta Batteries have been produced commercially by the Radiation Research Corporation,[45–47] which elected to use either tritium or krypton-85 for microwatt output. As described in the following paragraphs, a polystyrene dielectric was used with krypton-85;

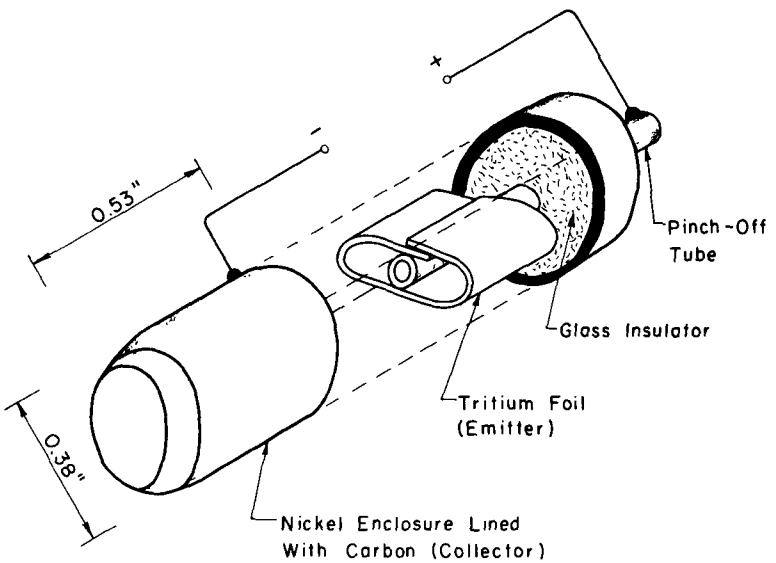

Fig. 7.29 — Exploded view of the Model R-1A vacuum-type tritium battery manufactured by Radiation Research Corporation. (From Refs. 46 and 47.)

however, the range of tritium betas in polystyrene is too short to permit the use of commercial (≈ 0.5 mil) polystyrene sheet. Some thin-film techniques were tried, but they were not found to be satisfactory; consequently, the vacuum design shown in Fig. 7.29 was developed. The original model used a $\frac{1}{5}$-Ci source and produced about 50 $\mu\mu$A at 400 V (Fig. 7.30). (Figure 7.30 also demonstrates the problem of attempting to use a solid polystyrene insulator. In this case

output voltages were limited to < 50 V.) Later models were scaled up to produce 1000 $\mu\mu$A at 1 kV.

Several problems encountered in these designs are of interest: The source foil in the original battery had tritium gas absorbed in a thin layer of zirconium. A low output current per unit area was obtained, so finally a special source production unit was designed to use the same chamber for evaporation of the thin zirconium foil and reaction with the tritium. About 35 square inches of foil containing 50 Ci were produced per run, and the foil was then cut into 250 pieces of about $\frac{1}{8}$ square inch each. It was wrapped around the filament to maximize its surface to volume ratio.

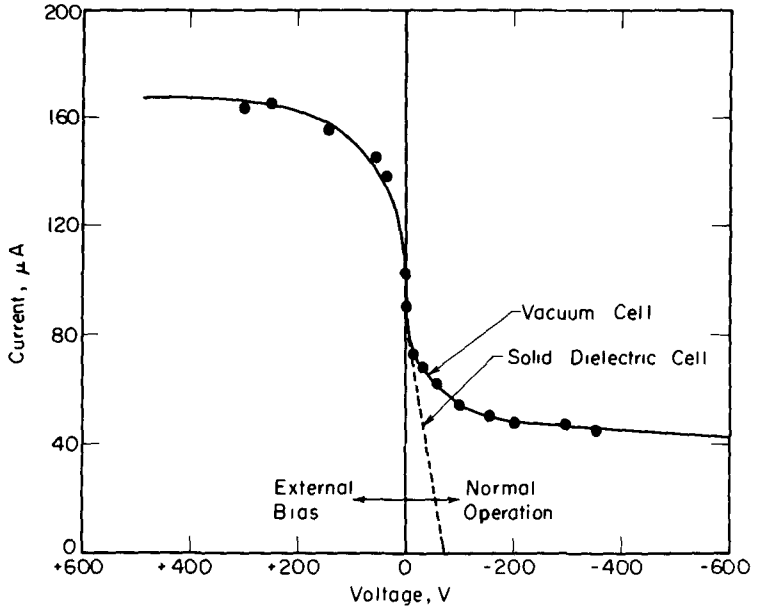

Fig. 7.30 — Current–voltage characteristic of the Model R-1A battery shown in Fig. 7.29 and a solid dielectric type battery. (Adapted from data by Coleman, Ref. 46.)

Considerable study was devoted to the collector design.[45] The secondary-electron yield was found to be 50% or more for all surfaces tested. A carbon disc gave the lowest yield, but it had the disadvantage of being brittle and required a fairly thick wall. As a result, the deposition of a colloidal graphite-binder mixture onto a metal support was investigated. The secondary-electron yield was found to depend on the size of the graphite particles — the best results being obtained with an extra fine carbon powder and a decomposable nitrocellulose binder.

Gas evolution from the coating caused some problems. The original batteries were assembled and then baked at 150°C while degassing. This rather low temperature was selected to avoid evolution of tritium from the source; however, battery performance was found to decrease gradually as the graphite degassed under radiation. To avoid this, the collector was baked at 1000°C in a vacuum jar, while suspended over the source. It was then lowered onto the source and brazed in place by remote control without breaking the vacuum. This technique produced batteries which maintained a pressure below 0.1 μ Hg for the cell's life, and, at these pressures, currents from ionization of residual gases were found to be negligible.

(b) Solid Emitter–Solid Dielectric Type Beta Batteries (a CVE Cell)

The use of a solid insulator instead of a vacuum offers several advantages:

- Construction is simplified.
- Very compact, rugged cells are feasible, and the danger of leaks is eliminated.
- Secondary-electron currents are reduced since most low-energy secondaries will be absorbed in the dielectric.
- In addition to solid-state sources, a gaseous source can be used.

There are, however, some disadvantages:

- Primary particles lose energy and some are absorbed in passing through the dielectric.
- Ohmic leakage through the dielectric, especially under irradiation conditions, may be serious at high voltages.
- The ultimate voltage breakdown point is typically lower for solid dielectrics than for vacuum.
- Radiation damage to the dielectric may impose a lifetime limitation.

In general, the application will determine which of these factors is most important and will, in turn, dictate the choice of a solid insulator or vacuum.

A solid dielectric design, illustrated in Fig. 7.31, was investigated by Rappaport and Linder[48] in 1953. They built two batteries, the first used 2 mCi and the second 54 mCi of $^{90}Sr/^{90}Y$. Both used a polystyrene dielectric. These cells produced short-circuit currents of 10^{-11} and 2.5×10^{-10} A and open-circuit potentials of 3.7 and 6.6 kV, respectively. These results showed a resistivity for the polystyrene of 0.5 to 7 $\times$

10^{15} Ω-cm, which indicated a bombardment-induced conductivity since normal values of resistivity for polystyrene ranges from 10^{18} to 10^{22} Ω-cm. The lower value was found for the 54-mCi cell, and this was attributed to the larger current; however, it is interesting that the resistance decreased only by a factor of 14 while the current increased by a factor of 25 in going from the 2- to the 54-mCi cell.

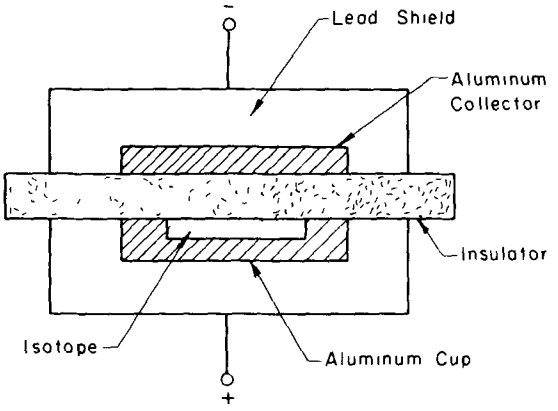

Fig. 7.31—An early solid emitter, solid insulator Beta Battery. (After Coleman, Ref. 49.)

It was found that an optimum dielectric thickness existed that yielded a maximum charging rate (the specific thickness was not reported). This is to be expected since increasing the thickness decreases the ohmic and secondary-electron leakage currents, but it also decreases the primary current.

Charging rates and voltages were found to be affected by earlier operation, and this was termed "charge soakage." This phenomenon was not explained, but it appears to be associated with trapped space charge effects (Sec. 6-4.2) as well as radiation-induced conductivity changes in the insulator (Sec. 6-4.1).

Linder and Rappaport concluded that, in addition to a simple, rugged, long-lived power source, batteries of this type offered a new and relatively simple means of studying basic radiation effects on solids.

J. H. Coleman[49] of Radiation Research Corporation has carried out extensive studies of solid dielectric cells. He was the first to point out that polystyrene offers two major advantages as the dielectric: After an initial decrease, its electrical resistance actually increases with moderate radiation dosages (Sec. 6-4.1), and radiation damage (e.g., embrittlement, voltage breakdown, etc.) is not generally a problem.

This led to the development of a $^{90}Sr/^{90}Y$ fueled, polystyrene battery at Radiation Research called Model D-50. (See Fig. 7.32.) The predecessor to this design used a source of 10 mCi of $^{90}Sr/^{90}Y$ welded between two strips of 0.0005-in.-thick gold foil. Roughly 60% of the betas were lost due to absorption in the foil, and this problem was eliminated in Model D-50 by forming the insulator in a cup shape, which could contain the radioisotope. Electrical contact was through a 0.005-in.-diam. Monel wire, which passed through a polystyrene insulator to reduce surface leakage.

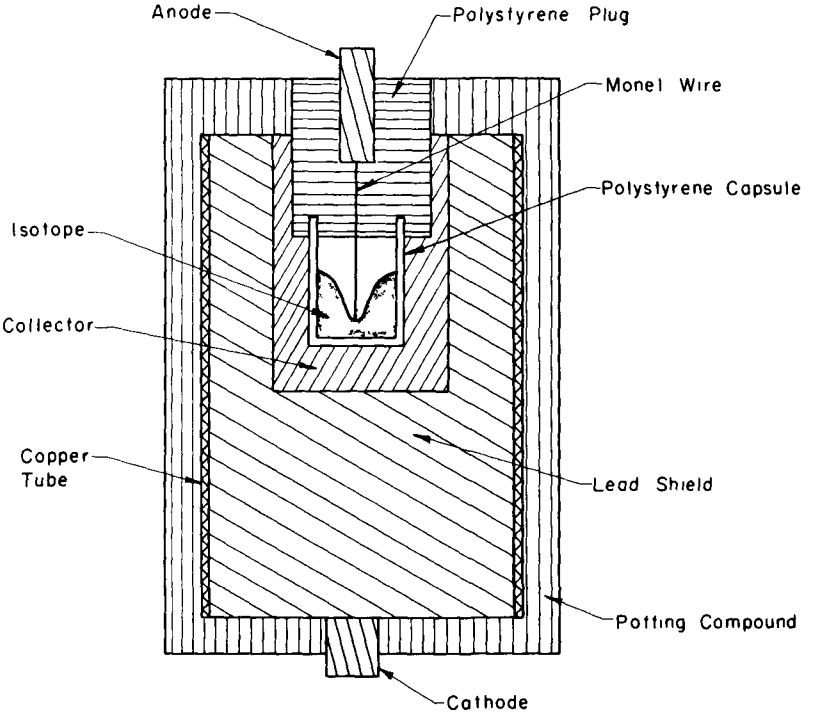

Fig. 7.32—The Radiation Research $^{90}Sr/^{90}Y$ solid emitter, polystyrene dielectric battery. (After Coleman, Ref. 49.)

A short-circuit current of 40 $\mu\mu$A was obtained while the maximum voltage increased from hundreds to 7000 V after 2 weeks. A $^1/_{32}$-in.-thick polystyrene insulator was used to achieve high voltages, but this absorbed about 67% of the betas.

(c) Volume (Gaseous) Emitter—Solid Dielectric Beta Batteries

An important feature of a solid dielectric insulator is that the use of a radioisotope in the gaseous form becomes feasible. The radiation

will partially ionize the gas so a reasonable electrical conduction may be expected; thus, these devices are normally classified as Conducting-Volume-Emitter (CVE) Cells, such as discussed in Chap. 2. Krypton-85 has been used widely as the source because it has reasonable availability, a relatively high-power density, and the lowest toxicity of any isotope.

The Radiation Research Model K-2 Krypton Battery[47] has a thin (ten 0.001-in. layers) polystyrene insulator and an aluminum collector in a case similar to that used in the tritium battery shown earlier. It is somewhat heavier, however, since krypton requires some shielding.

Another design, shown in Fig. 7.33, has been described by W. Windle[7] of the Sandia Corporation in some detail. A glass bulb, having volume

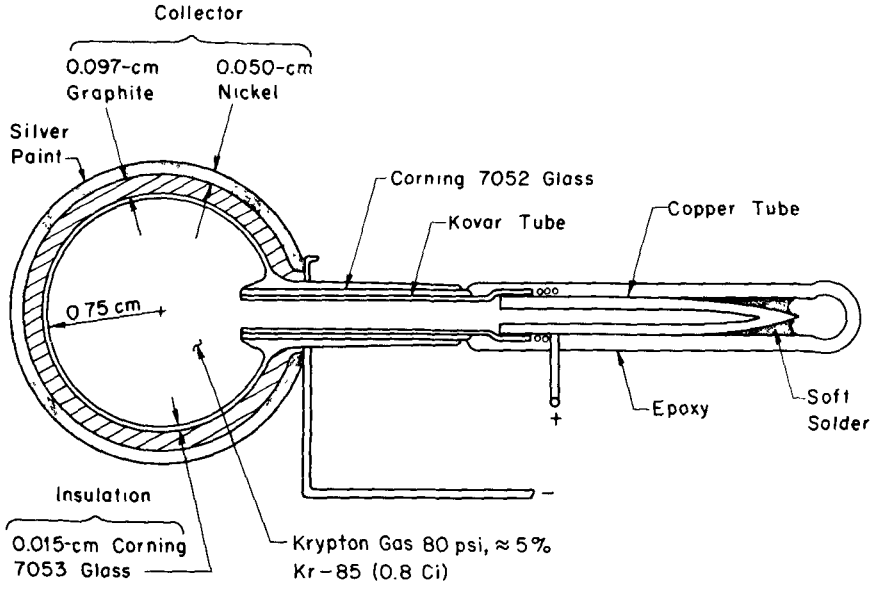

Fig. 7.33 — Design of the Sandia Corporation ^{85}Kr battery. (After Windle, Ref. 7.)

of ≈ 1.6 cm^3 with a 0.015-cm wall, is blown on a Kovar tube using a graded glass-to-metal seal giving an equivalent resistance of $\approx 5 \times 10^{13}\,\Omega$. (Corning 7059 glass was used for the bulb in later designs to prevent radiation-induced cracking frequently encountered in the model shown in Fig. 7.33 after operation for a year or so.) To minimize bremsstrahlung, the bulb is spray coated with graphite to a thickness of 0.1 cm, and a silver coating is then painted onto the graphite to serve as a conductor for the nickel-plating process. The 0.05-cm nickel layer serves as a physical support and also as the negative terminal.

The ionized gas represents the positive electrode, and the Kovar-copper fill tube provides a conducting path to it.

The bulb is generally filled to about 80 psi corresponding to 0.8 Ci of ^{85}Kr. The cell is capable of voltages well above 20 kV, and some typical current–voltage curves are shown in Fig. 7.34. The increased slope of the 165° curve is attributed to a decrease in the glass resistance at elevated temperature. As seen, the effect is small for low-voltage operation ($\approx$ 2 to 3 kV).

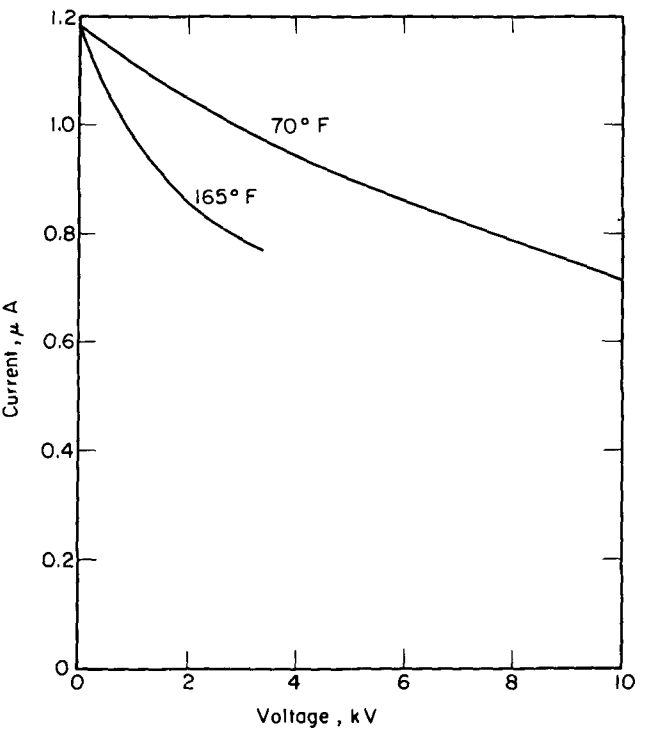

Fig. 7.34 — Current–voltage characteristics of the Sandia Corporation Battery for two different temperatures. (Adapted from Ref. 7.)

The Leesona Moos Model 300 Battery[50] has a similar design, and measurements using this battery reported by Guyot and Miley[51] also indicate a slight temperature dependence. The maximum voltage they obtained was 7 to 9 kV, where a discharge occurred due to arcing across the insulator.

(d) Self-Powered Neutron Detectors: A Special Beta Battery

Self-powered neutron detectors, only recently developed, have assumed an important role as in-core nuclear reactor monitors[52–54] and a

typical design is shown in Fig. 7.35. The emitter is formed of some material that undergoes neutron capture, producing either capture gamma rays or beta particles during decay. In the latter case, the device is simply a special type of Beta Battery. Generally, a solid

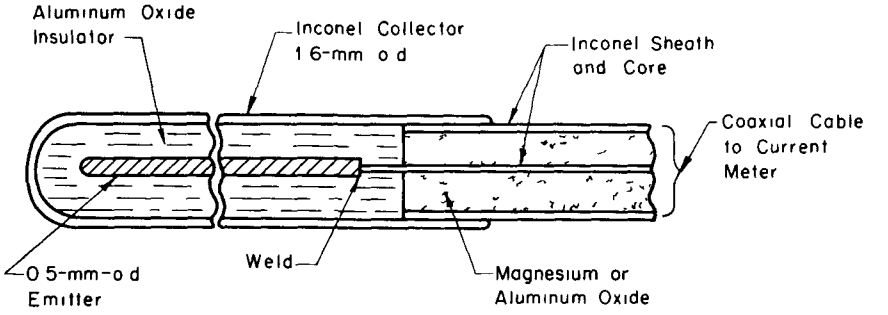

Fig. 7 35—A self-powered neutron detector. (From Ref. 52.)

insulating material is used, and the metal oxides (MgO, Al_2O_3, and BeO) are typically selected because of the need for a high resistivity and reactor compatibility. Low manganese content Inconel 600 has been used for the collector-sheath It has good corrosion properties, and the probability of neutron activations leading to beta decay (an unwanted background) is lower than for most stainless steels

Some possible emitter materials are presented in Table 7.2 along with some comments about their performance. Emitters producing

Table 7.2—EMITTER MATERIALS*

Material	Reaction	Neutron Sensitivity† [A/(nv cm)]	Comments
Rhodium-103	$n\beta$	1.2×10^{-21}	Highest sensitivity
Vanadium-51	$n\beta$	7.7×10^{-23}	1/v detector
Cadmium	$n\gamma$	1.6×10^{-22}	250°C max. temp.
Cobalt-59	$n\gamma$	1.7×10^{-23}	Long life

*From Ref. 52.

†Values are for a 0.02-in.-diam. emitter in a 0 0625-in.-o.d detector and are per centimeter of emitter length.

capture gammas operate mainly by collection of Compton electrons, and thus, as described in Sec. 7-5, they are essentially Gamma-Electric Cells.

Advantages of these detectors include low cost, simplicity of operation and read-out instrumentation, continuous operating capability in high flux, high-temperature environment, and small size.

7-5 THE GAMMA-ELECTRIC CELL

The Gamma-Electric Cell (GEC) operates by direct collection of electrons produced by gamma-ray interactions through the photoelectric effect, Compton scattering, and pair production. For typical dielectrics and photon energies of interest, the Compton effect dominates and is particularly efficient because it favors forward electron scattering.[55,56] Thus, the GEC has generally been designed to collect Compton electrons, and in fact, they have frequently been termed "Compton Diodes," "Compton Elements," or "Compton Batteries."

There are two common designs: one uses a solid dielectric insulator, and the other, a vacuum space insulator. In the former type, the dielectric serves both as an insulator and as the source of Compton electrons. In the terminology of Chap. 2, it is a Dielectric-Volume-Emitter (DVE) Cell. The vacuum-type GEC, on the other hand, is a simple plate cell (Fig. 2.1), and we will consider each type separately.

7-5.1 The Solid-Dielectric Type Gamma-Electric Cell

While discussions of Compton currents and associated effects appeared earlier, the first serious study of the possibility of using these currents in a power producing device was reported in 1955 by Kloepper and Madsen[57] who were concerned with a vacuum-type cell. Then in 1959, B. Gross[58] proposed a cell that utilized a dielectric insulator–Compton scatterer, and in 1964, he was granted a patent for a dosimeter based on this concept.[59] He and his associates have reported extensive investigations of the GEC[60–64] and related effects, including beta-particle transmission through dielectrics[65] and radiation-induced space charge effects (Chap. 6).

Gross was primarily concerned with using the GEC as a gamma-ray dosimeter, and one of his early designs is shown in Fig. 7.36. Radiation impinging on the top electrode enters the dielectric, where Compton scattering takes place. Compton electrons produced in the dielectric are scattered preferentially forward in the direction of the collector electrode, and they, in effect, set up an electric current. However, the dielectric is typically thin relative to the photon mean free path in it, so a significant fraction of the photons may pass through it and strike the collector (bottom) electrode. Gross originally noted that these photons will scatter Compton electrons out of the collector and create a leakage current. To prevent this, he used a thick electrode; however, this only represents a partial solution since photons absorbed in the collector do not contribute to the Compton current, and the energy associated with them is ultimately converted to waste heat. Another approach is to increase the dielectric thickness in order to

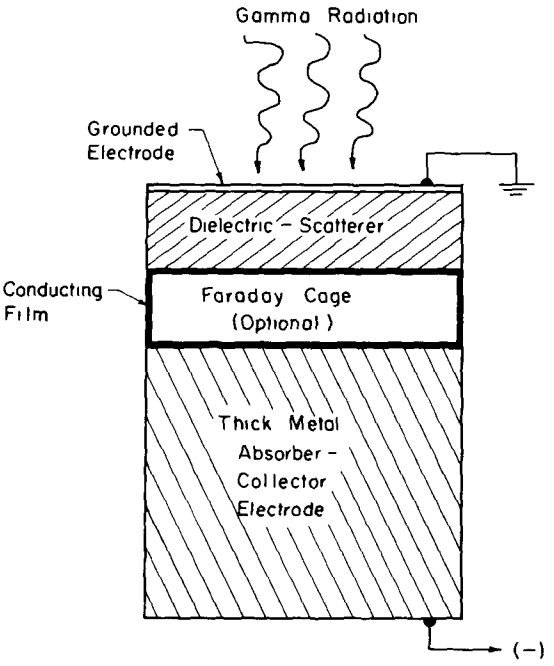

Fig. 7 36—Schematic arrangement of the GEC proposed by Gross (Adapted from Ref 61. The Faraday cage, designed to minimize backscattering effects, was not used in early cells)

operate at a higher voltage, but there is an optimum thickness that should not be exceeded. This occurs when the photon attenuation in the dielectric becomes so large that it seriously reduces the photon intensity in the region near the collector. Then the Compton current is also reduced in this region and a reduced electrical output results Thus, a dielectric thickness is typically selected that is of the order of the photon mean free path, and this thickness is inevitably much larger than the Compton electron range

This brings up another important concept. With the dielectric considerably thicker than the Compton range, the electrons may be viewed as stepping through the dielectric much as illustrated earlier in Fig 2.25. As Gross described it, an "equilibrium" is established between the Compton and gamma-ray currents, and the resulting electron balance (Chap. 2) prevents the formation of a space-charge region—at least in the interior of the dielectric

Gross also pointed out that leakage currents could arise due to backscattering of electrons and/or photons from the collector, and he suggested the solid Faraday cage (Fig. 7 36) to minimize these effects.

In this design, the collector consists of two pieces: The top block is a dielectric of low atomic number covered on all surfaces by a thin conducting film such as Aquadag; and the lower block is lead or some other suitable gamma absorber. The coated dielectric behaves electrically as if it were a metal, and it operates in the same manner as the conventional Faraday cage. Electrons stopped in the dielectric set up field lines that terminate at the coating so that, independent of the internal space charge distribution, an effective electric charge of the same sign as that inside appears at the surface. In effect this is equivalent to using a metallic collector of low atomic number, and this reduces electron backscattering.

In addition, the cage serves to absorb back-scattered gamma radiation from the lead block before it can reenter the main dielectric. Since the energy of such gammas will be fairly low, the cage can effectively attenuate them without requiring an excessive thickness.

While proposing these designs, Gross also developed a theoretical treatment of the Compton current, i.e., the short-circuit output current for a GEC. Basically, he showed that this current is equal to the Compton electron production rate per unit volume times the average forward travel of each electron, and he derived an expression of the form*

$$J \approx e\,[\mu_c N_\gamma]\lambda_{eff}\,\cos\bar{\phi} \qquad (A/cm^2) \tag{7.1}$$

The product of μ_c, the gamma-ray attenuation coefficient due to Compton reactions (cm^{-1}), and N_γ, the photon incident photon current [photons/(cm^2 sec)], give the Compton source per unit volume, assuming the gamma intensity is essentially constant across the cell. The product of the "effective" range of these electrons λ_{eff} and the cosine of the average scattering angle $\bar{\phi}$ gives an effective forward travel. This is similar to L_δ used in Chap. 5 [Eq. (5.10a)]; however, Gross defined the parameters involved somewhat differently. Based on an inspection of various experimental data, he evaluated λ_{eff} as two-thirds the practical range given by the Katz–Penfold relation. In addition, he took the average angle to be approximately equal to the angle corresponding to the average electron energy.

Calculated currents based on this theory are shown in Fig. 7.37 for various absorber thicknesses and gamma-ray energies. The parameters do not vary greatly for low-Z materials, and these curves assume a typical low-Z dielectric. Gross inferred from these results that the energy response could be flattened or alternately that it is possible to discriminate against either high- or low-energy photons by

*This has been shown[56,66] to be in approximate agreement with the zero voltage limit of Eq. (4.137). Alternately, the similarity to Eq. (2.78) is obvious.

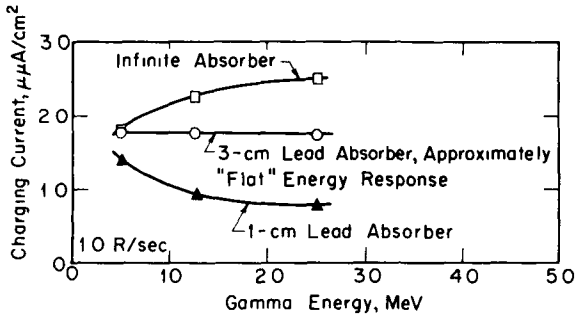

Fig. 7.37—Calculated Compton currents for a typical low-Z dielectric and several absorber thicknesses. (After Gross and Murphy, Ref. 62.)

proper selection of the absorber thickness. Such tailoring of the response is important for many dosimeter applications.

To test his theory, Gross constructed a cell similar to the design shown in Fig. 7.36. It had a 12 × 12 × 12-cm lead block covered by a plexiglass Faraday cage with the same base size and a height of 2.5 cm. The dielectric was a 2.5-cm-thick sheet of plexiglass. A current of 8.8×10^{-11} A was measured using a ^{60}Co source giving an incident energy flux of 1.7×10^5 ergs/sec over a 64-cm^2 area. Calculations based on Eq. (7.1) predicted 7.65×10^{-11} A, which indicates reasonable agreement with the experiment.

Gross also built a portable receiver[63] shown in Fig. 7.38. It had a disc-shaped central electrode (lead) with a 10-cm diam. and a 1-cm

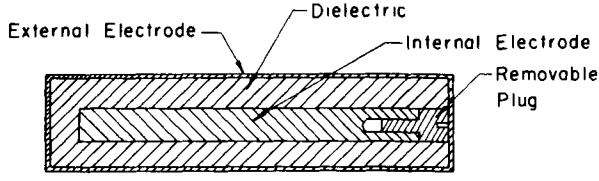

Fig. 7.38—A portable GEC dosimeter designed by Gross. (From Refs. 61 and 63. A cross section of the cylindrical cell is shown.)

thickness surrounded by a 1-cm-thick Lucite insulator covered by a conductive coating and a thin metallic foil housing. The Compton current developed during irradiation charges the measuring electrode so a potential is created between it and ground. After irradiation, the plug shown in the figure is removed and the voltage is recorded, giving a measure of the total radiation dose. A sensitivity of ≈ 1 V/R is reported.

Later studies[62,63] involved measurements with a cylindrical detector having a 4-cm-diam. × 12-cm lead absorber rod surrounded by

paraffin and a 7.5-cm-diam. × 22-cm thin-walled aluminum tube outer electrode. An average current of 1.5 $\mu\mu A/cm^2$ per R/sec was measured using a ^{60}Co source, which is in rough agreement with Fig. 7.37. Subsequent irradiation in a gamma field from a nuclear reactor gave 1.6 $\mu\mu A/cm^2$ per R/sec. Since the reactor gamma-energy spectrum covers a broad range, the close agreement with the ^{60}Co measurement verifies the rather flat energy response of the cell.

The cell designs noted thus far have all utilized an external source of gamma radiation. Experimental data are not available, but Gross has also proposed using a self-contained source. As illustrated in Fig. 7.39, a gamma-emitting radioisotope could simply be surrounded by an insulator having a conducting coating. An important aspect of this design is that a thick absorber electrode is unnecessary. The outer conducting film can be grounded, and a positive potential build-up will develop between ground and the radioisotope source. Since the outer electrode is grounded, the Compton and secondary electrons leaving this surface with the transmitted gammas will not affect the operation.*

In 1963, Gross[64] reported studies using a GEC with a teflon insulator and interchangeable teflon and lead absorbers. Current–time

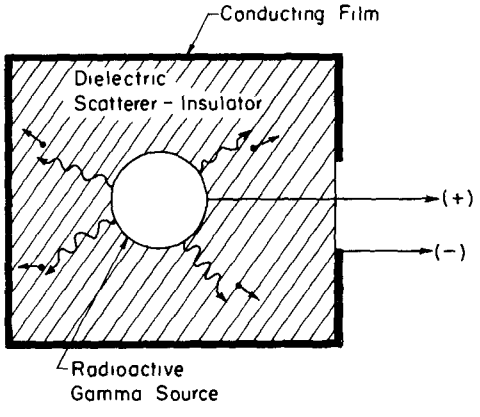

Fig. 7.39—A GEC with an internal source (After Gross, Ref. 63. Compton electrons derived from gammas from the source at center move preferentially outward. The source then assumes a positive potential relative to the outer-conducting film)

*It appears that the same technique might be used in the standard plate-external source cell However positive space charge build-up in front of the emitter electrode might be a critical problem. In the conventional cell, even a small conductivity permits a flow of sufficient electrons from the grounded emitter to limit the space charge build-up immediately in front of it. But, if the emitter is floating, this flow is retarded, and the resulting space charge may cause breakdown. However, to the author's knowledge, experimental verification of this effect has not been reported to date.

measurements shown in Fig. 7.40 exhibit a characteristic drop in the current at the start of an irradiation followed by a partial recovery, and Gross attributes this behavior to polarization effects in the dielectric. A small current was still detected immediately after removal of the teflon absorber cell from the radiation field This current had a reverse direction relative to the forward Compton current, but it was several orders of magnitude smaller. Results from similar experiments using the teflon–lead absorber cell are also shown. In this case the reverse current (after removal from the radiation field) was

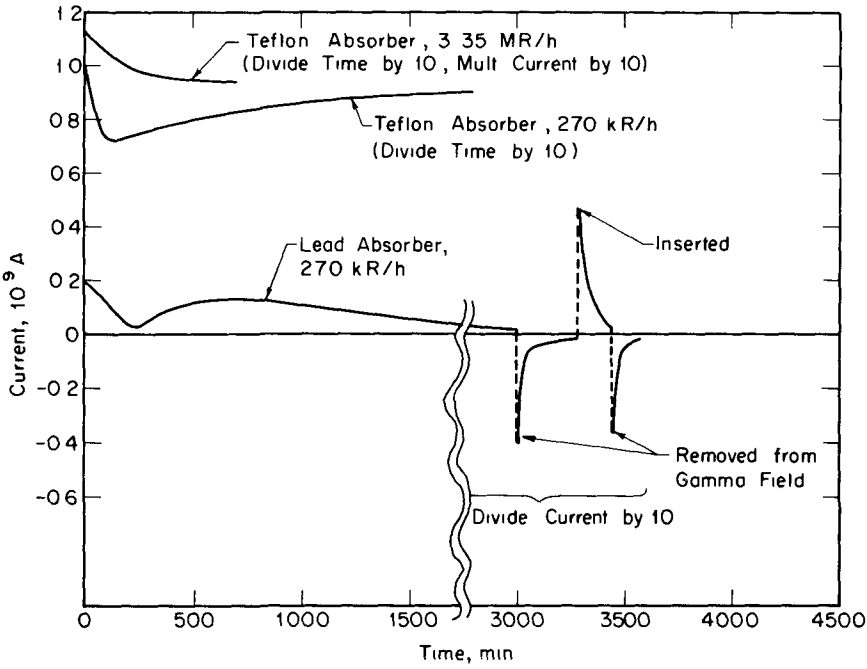

Fig. 7 40 — Current–time curves for the teflon GEC with teflon and lead absorbers. (After Gross, Ref 64.)

initially of the same order of magnitude as the Compton current, and renewed irradiation resulted in another transient in the Compton current. Such behavior is analogous to the case where a dielectric is first polarized with an external voltage and then short-circuited. Gross attributed the increased reverse current to an enhancement of polarization by backscattered gamma and x-radiation from the lead absorber Since its energy will be low, this radiation will be more rapidly attenuated in the dielectric, and an equilibrium electron current may not be achieved.

In 1963, B. Raab[67] suggested using nuclear cells in a power-producing shield for space reactors. He pointed out that radiations carry away up to 10% of the total power produced and that an "active" shield could reclaim part of this waste energy. This, he noted, could be a valuable supplement to the primary power, particularly when relatively small quantities of high-voltage dc power are needed for special purposes, e.g., in connection with electric propulsion schemes.

Raab proposed a composite design (Fig. 7.41) in order to convert both neutron and gamma-radiation energy. Thermal neutron absorption in the anode results in a beta-decaying isotope with a short half-life, and the betas are then collected as shown. Fast-neutron conversion is accomplished by collecting protons scattered out a hydrogenous elec-

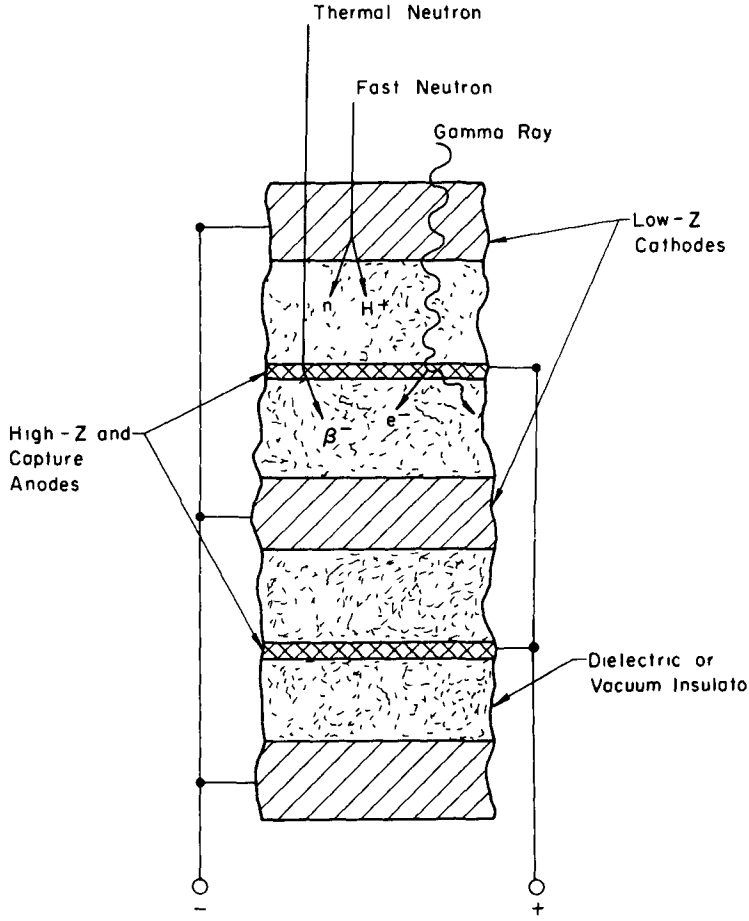

Fig. 7.41 — The power-producing shield concept proposed by Raab. (From Ref. 67.)

trode. Gamma conversion depends on the difference in Compton currents resulting from the use of alternate high- and low-Z (atomic number) electrodes. He suggested ^{238}U would be suitable for the anode because it combines a high-Z and relatively high thermal neutron cross section. The ^{239}U produced by the absorption in turn provides an additional beta-particle source, since it decays via beta emission with a 23.5-min half-life. Other possible choices for this electrode include ^{152}Eu and ^{165}Dy. Lithium hydride or a conducting hydrocarbon plastic was suggested for the cathode if fast-neutron conversion is desired; if not, a beryllium plate might be used.

Raab estimated that, if one-third of the SNAP-2 reactor shield were constructed in this fashion, this portion would weigh 100 lb and produce 35 W at 200 kV—roughly 1% of the total system electric power. He also considered the possibility of both vacuum and solid dielectric cells, but felt the latter would have a decided advantage because of the simplicity of construction and ruggedness. However, problems such as radiation-induced space charge, induced conductivity, radiation damage, heating effects, etc., must be examined in more detail before the value of this concept can be fully assessed. Despite this, the active shield concept represents an important contribution by providing added motivation for the development of Direct-Collection Cells

In 1965-1966, GEC studies were reported by L. W. Nelms[68 69] of General Dynamics, and an important series of progress reports[70–73] became available from a coordinated program at Los Alamos Scientific Laboratory (LASL) and Edgerton, Germeshausen, and Grier (EG&G) of Las Vegas. (The Santa Barbara branch of EG&G and the Lawrence Radiation Laboratory[74–77] were simultaneously studying vacuum-type devices as part of this program.)

Nelms considered a fundamental question: Are Compton effects really the dominant mechanism in the GEC? In addition to Compton and photoelectric scattering, he considered the possibility of photovoltages excited in a manner analogous to those generated in light-sensitive semiconductor devices. To study this, he designed a series of ^{60}Co irradiation experiments using cells such as shown in Fig. 7.42, and the results from these measurements are given in Table 7.3.

The unique feature of this cell is that the ^{60}Co rods can be located either in the center, as shown in Fig. 7.42, or alternately in a circle on the outside. This allowed Nelms to study the variation of the output with the direction of the gamma radiation. The $1 \times 10^9\ \Omega$ load resistance used in the voltage measurements was purposely fixed lower than the internal cell resistance to minimize the influence of the latter. Nelms noted that Compton currents, in contrast to photovoltaic effects, have a direction determined by the radiation field and are essentially independent of temperature. Both points are confirmed by the results shown

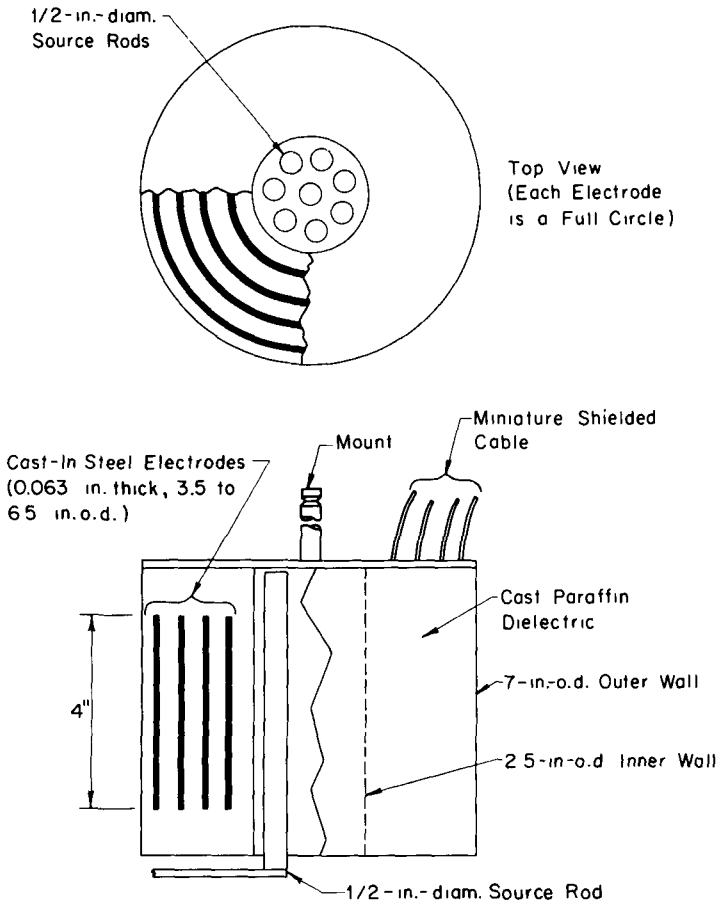

Fig. 7.42—The GEC design used by Nelms. (Based on Ref. 68.)

Table 7.3—TEMPERATURE AND RADIATION FIELD DIRECTION EFFECTS ON A GEC*

Radiation Field Direction†	Potential‡ (V)	Temperature (°C)
Inside to outside	−5.4	80
Inside to outside	−5.4	37
Inside to outside	−5.4	146
Outside to inside	+1.4	80

*From Ref. 68.

†The inside to outside direction was obtained with source rods in the center holes of the cell shown in Fig. 7.42.

‡All data for a 1×10^9 Ω load resistor.

in Table 7.3; thus, he concluded that the photovoltaic effect, if present, was small.

Nelms also appears to have been unaware of the earlier work by Gross, and, using an independent approach, he derived the following expression to predict the Compton current for short-circuit conditions

$$J \approx e[N\ \mu] \cdot \frac{1}{\Sigma_c} \qquad (A/cm^2) \tag{7.2}$$

As defined in Eq. (7.1), N_γ represents the incident photon current while μ represents the gamma-ray attenuation coefficient. Nelms defined Σ_c as an absorption coefficient for the Compton electrons, and he suggested that it could be evaluated from measurements of beta-ray attenuation. A comparison with Eq. (7.1) shows that Σ_c^{-1} in effect replaces $\bar{\lambda}_{eff} \cos \bar{\phi}$; i.e., it represents the average forward travel of the Compton electrons. (The identification of Σ_c with beta-ray attenuation is an expedient that would not appear necessary since specific range–energy correlations are available.)

The basic difference between this and the earlier derivation by Gross is that Nelms essentially performed a balance around the collector electrode to determine the number of electrons reaching it. This approach is quite similar to the one used in Sec. 2-6.2, and Nelms termed this the *critical thickness* concept. Gross, on the other hand, based his calculations on the charge induced on the collector due to electron displacement motion in the dielectric. As discussed in Chap. 2, the two approaches are equivalent for steady state calculations, but the induced charge method must be used for transient analysis.*

The LASL–EG&G studies[70–73] were apparently motivated by the possible use of GECs as gamma detectors in high-intensity fields such as encountered in pulsed reactor and also bomb experiments. Tolman[71] has described the development of a spherical "Dielectric Compton Detector" with a sensitivity of 1×10^{-10} A per R/h for use in the weapons test program. This detector, shown in Fig. 7.43 and designated

*As stressed in Chap. 6, leakage currents are extremely important at high voltages, and they are included in an approximate fashion later in Eq. (7.5). However, as pointed out in Sec. 6-4.2, in the case of the GEC, leakage currents can occur even under steady-state, short-circuit operation. This is due to space charge effects (Sec. 6-4.2) and gamma absorption in the dielectric which result in internal electric fields and a spatially dependent Compton electron source, respectively. Such effects were ignored in the preceding analyses and in the earlier ideal cell calculations, but fortunately experiments bear out that this is reasonable for typical low-voltage, short-term irradiations. In general, however, leakage currents (and displacement currents in transient studies) should be included.

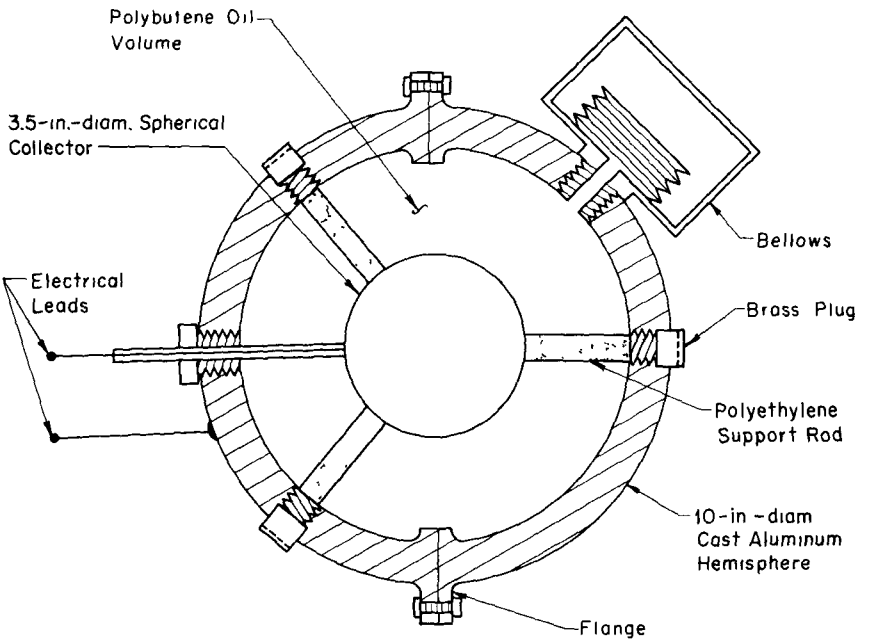

Fig. 7.43 — Sketch of the O(S) S-10 spherical detector using a polybutene oil insulator. (Based on information by Tolman, Ref. 71.)

O(S) S-10, has a spherical stainless-steel collector supported by four evenly spaced polyethylene rods. It is unique in that a liquid (grade 32X Polybutene oil) is used as the dielectric. While this detector is normally used as a gamma monitor, it is also sensitive to neutrons, which interact with the oil driving protons into the collector. (Note: The neutron-induced current has a reverse direction relative to the Compton current.) Tolman concluded this detector meets all standard requirements including sensitivity, ease of calibration, assembly, reliability, and in addition, the cost is less than other types of detectors.

Pigg[70] has reported the use of five different types of GEC detectors in the nuclear rocket study program. He lists six distinct advantages for them:

- Dynamic range-linearity. Can be obtained within several percent over seven decades or more.
- Durability ruggedness. There are no breakable parts; the weakest feature is the electrical lead at the collector.
- External power supply. None is required.
- Size. Smaller and lighter than conventional detectors.

- Fast time response. Units with rise time of order of 1 nsec have been tested.
- Cost. Cheaper than other types of units.

An interesting facet of these detectors is that, to insure a stable, reproducible output, they are routinely given an initial exposure or "bake-in" of about 4×10^3 R from ^{60}Co. A machined polyethylene dielectric is used, and, during assembly, a rather high static charge is thought to be formed on its surface. If so, the radiation exposure would serve to discharge this field. It also appears that some polarization effects are involved since the cells must be rotated to expose both faces during the "bake-in."

The LASL–EG&G groups have examined the variation of the cell response with gamma-ray energy in some detail. Pigg[72,73] reported the results shown in Table 7.4 for a teflon–aluminum cell consisting of a

Table 7.4— ENERGY RESPONSE OF A TEFLON DETECTOR*

Source	Photon Energy (MeV)	Sensitivity (A per R/sec)	
		Measured	Calculated
^{137}Cs	0.662	2.1×10^{-11}	1.85×10^{-11}
^{60}Co	1.17, 1.33	4.27×10^{-11}	3.77×10^{-11}

*Reported by J. L. Pigg, Refs. 72 and 73.

3.34-in.-diam. × 1.5-in.-thick aluminum collector encased in teflon. The sensitivity for 0.66-MeV gamma radiation is about a factor of two lower than for 1.17 to 1.33 MeV. Calculations reported for both energies were about 12% too low. (These calculations appeared to be quite thorough, but details were not given in the report.) For this design, the aluminum collector transmits part of the gammas, so the net current involves a difference between those electrons driven from the teflon into the collector and those driven out of the back face of the cell. The back face current appears to have been about 60% of the collector current, so errors in the calculation of both currents become important and the small discrepancy noted is not too surprising.

Detectors, such as this, that involve a difference in Compton currents generated in two materials can have quite an unexpected dependence on the energy of the incident radiation. The LASL–EG&G "ON" type detectors (Fig. 7.44) are an excellent example.[73–74] A 32X polybutene oil is used as the dielectric, and a nickel collector is centered with polyethylene supports in an aluminum case.

The energy response is shown in Fig. 7.45, where some measured and calculated data are presented. Interestingly, the calculated current

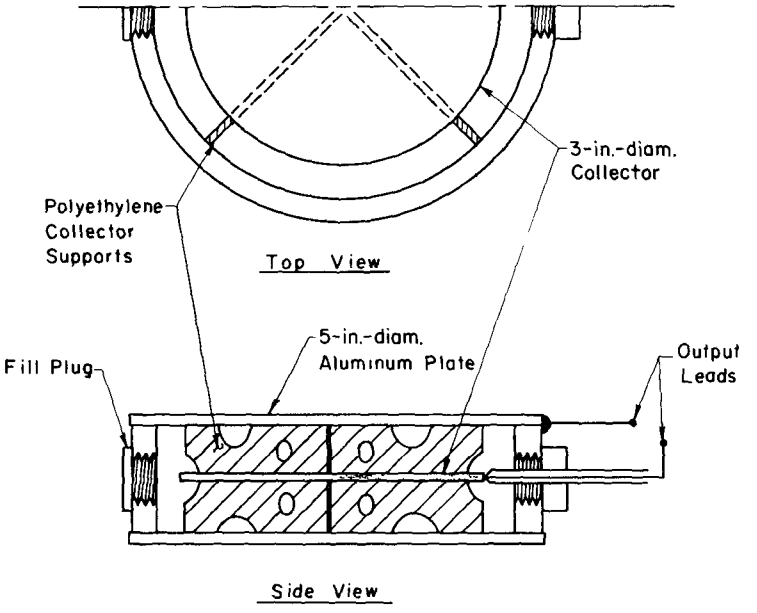

Fig. 7.44—A schematic layout of the ON-11 detector. (A polybutene oil is used to fill the cell. Based on data by Pigg, Ref. 73.)

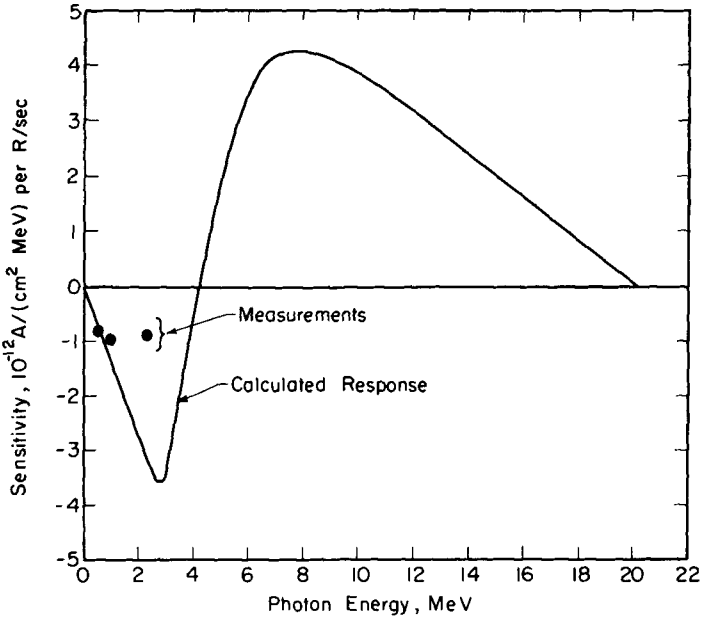

Fig. 7.45—Sensitivity of ON-11 detector vs photon energy. (From data by Pigg, Ref. 73.)

actually changes signs at about 4 MeV. This "cross-over" point occurs when the electron current driven out of the nickel collector exceeds that driven into it. Calculations indicate it corresponds to an energy where ≈10% of the incident Compton electrons are transmitted through the nickel without being collected.

Calculations for 1.25-MeV gammas indicate the current collected from the oil is 11.26×10^{-6} electrons/(R cm^2) while the current from the nickel plate is 10.09×10^{-6} electrons/(R cm^2). The net current is then the difference or 1.17×10^{-6} electrons/(R cm^2). Note that an error in the calculation of either current will result in a larger percentage error in the net current.

The experimental points in Fig. 7.45 are for ^{137}Cs, ^{60}Co, and ^{24}Na irradiations. Higher energy isotope sources were not available, so to verify the change in sign of the output, Anderson and Hocker[74] exposed the cell to bremsstrahlung produced by electron bombardment of a gold–tungsten target. The results shown in Fig. 7.46 clearly demonstrate the sign change. It occurs for an electron energy of 10 MeV, which corresponds to a fairly broad photon energy spread between 1–7 MeV with a peak at roughly 4 MeV; i.e., this is in qualitative agreement with Fig. 7.45.

An interesting auxiliary experiment involved a comparison of lead and aluminum collectors. Since the electron backscattering coefficient for lead is nearly three times that of aluminum, a change in current was expected; however, none was observed, which contradicts the concept, discussed earlier, that electron backscattering at the collector is important in such cells. This result has since been corroborated by independent experiments at LASL, but a full explanation for the lack of backscattering effect has not been reported.

P. V. Murphy, a co-worker with Gross in the original GEC studies, recently discussed a dielectric-type detector under development at Thermo Electron Engineering Corporation[78,79]. This cell, named the "Solid Compton Recoil Electron Detector" (SCRED) and illustrated in Fig. 7.47, features a built-in solid-state electrometer. The cell itself is quite similar in concept to the early design in Fig. 7.36. One added feature is the external scatterer. The dielectric insulator itself is relatively thin; thus, the external scatterer ensures sufficient scattering volume to obtain an equilibrium electron current. This is important to ensure a linear dose rate dependence over a large range. Also, by proper selection of the scatterer material, it is possible to adjust the dependence on photon energy. Tests of various scatterers are presented in Table 7.5, and it is observed that polyethylene resulted in the least variation between 0.65 and 1.3 MeV.

Murphy also investigated the effect of the absorber thickness and composition. The SCRED design uses a coated plastic Faraday cage in back of the high-Z absorber as well as in front of it (Fig. 7.47). The

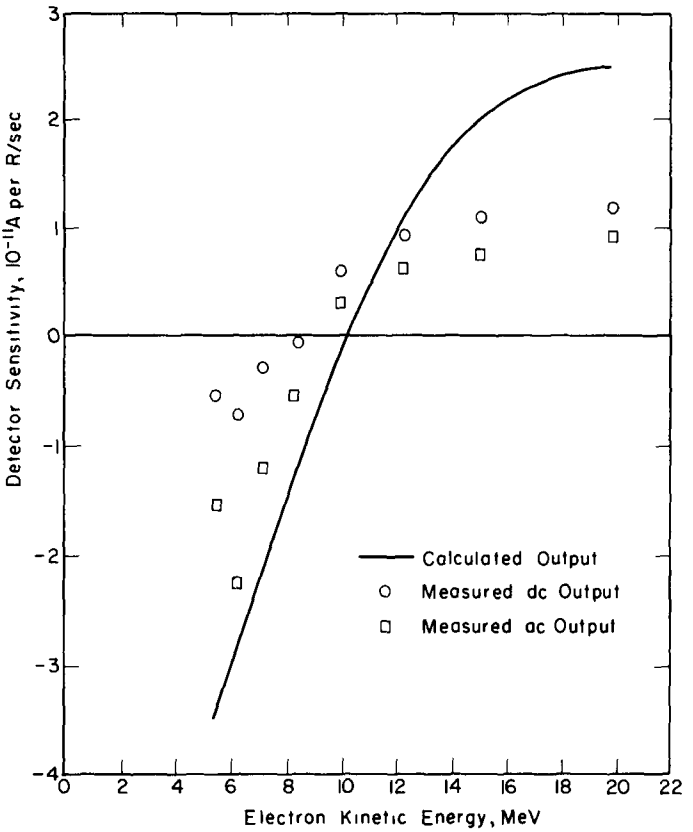

Fig. 7.46—Sensitivity of ON-11 detector for bremsstrahlung due to various energy electrons incident on a gold target. (From Anderson and Hocker, Ref. 74.)

front cage reduces backscatter as discussed earlier, and the cage behind the absorber operates in a similar fashion to reduce electron scattering out of the back face due to gammas transmitted through the absorber. Thus, a minimum absorber thickness and weight can be used.

To optimize the SCRED design, Murphy considered the effect of varying the dimensions of the absorber as well as the scatterers. He found that, in either case, the sensitivity increases with increasing thickness until a maximum or equilibrium value is obtained as indicated in Table 7.6.

The dependence on incident radiation angle was found to fall between an isotropic response and the cosine behavior predicted by simple theories. For comparison, another cell was tested having a 10.8-cm-diam. hemispherical lead absorber, a matching plastic backscatter shield, and a plastic external absorber. It did not show much

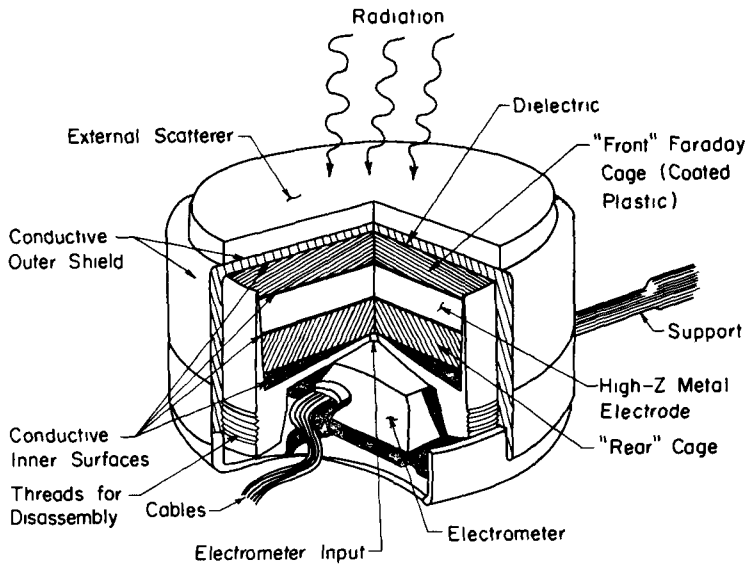

Fig. 7 47 — The SCRED cell design by Murphy. (From Refs. 78 and 79.)

Table 7.5—VARIATION OF ENERGY RESPONSE WITH EXTERNAL SCATTERERS*

External Scatterer	Sensitivity (mA per 10^6 R/sec) ^{137}Cs (≈ 0.65 MeV)	^{60}Co (≈ 1.25 MeV)
0.016-in. Pb	93	58
0.032-in. Sn	76	53
0.032-in. Cu	73	49
0.032-in. Ni	73	49
0.394-in. Polyethylene	80–85	74

*From Ref. 79, for the SCRED Cell of Fig. 7.47.

improvement; consequently, Murphy concluded, if a true isotropic response is imperative, a full spherical detector must be employed.

Murphy did not encounter polarization effects in these studies, but he did observe a troublesome transient voltage that he attributed to mechanical strains created during cell assembly. He found that the transients were reduced if the insulator was applied in layers using a fluidized bed encapsulation technique, thus reducing strains. (In retrospect, it would appear that this problem is associated with those dis-

Table 7.6—SCRED COMPONENT THICKNESS REQUIREMENTS FOR EQUILIBRIUM SENSITIVITY*

Source	Component	Thickness for Equilibrium Sensitivity (cm)
^{60}Co	Lead absorber	6 to 4
^{60}Co	Tungsten absorber	4
^{137}Cs	Lead absorber	3 to 4
^{137}Cs	Tungsten absorber	2 to 3
^{60}Co	External plastic scatterer (1-cm lead absorber)	0.3
^{60}Co	Conductive plastic backscatterer (1-cm lead absorber)	0.2

*From Ref. 79.

cussed earlier in connection with the LASL–EG&G cells where a "bake-in" period was found necessary.)

Several interesting GEC studies have been reported by Japanese investigators: Hirakawa and Mizumachi[80] have carried out detailed calculations of the short-circuit current starting with the relations*

$$J(\vec{r}) = e \sum_i \int G(\vec{r}, T') N_i D_i(T') dT' \qquad (A/cm^2) \tag{7.3}$$

$$D_i(T') = \int \int \frac{d\sigma_i(T,\beta;T')}{d\Omega_\beta} \overline{\lambda(T)} \cos\beta \, d\Omega_\beta \, dT \tag{7.4}$$

where $G(\vec{r},T')$ represents the gamma current per unit area at $\vec{r}$ with energy T' per unit energy, $d\sigma_i/d\Omega_\beta$ is the differential cross section for the scattering of an electron through an angle β (giving it an energy T) due to an incident gamma ray of energy T', and $\overline{\lambda(T)}$ is the mean range of electrons of energy T. The summation over i allows for various processes: In this instance, Compton scattering and photoelectron emission were both included. Their calculations predict a current of $7.6 \times 10^{-12} S/r^2$ (A/cm^2 per R/min) for ^{60}Co irradiation of polymethylmethacrylate (PMMA) as opposed to a measured value of 5.9×10^{-12} S/r^2. (S is the source strength in curies, and r is the distance from the source in centimeters.) A comparison was also made with measurements using electron bremsstrahlung impinging on paraffin. In this case, the observed currents were roughly a factor of two smaller than predicted, and the reason for this is not understood.

E. Hiraoka[81] has studied two cells similar to the design shown in Fig. 7.36 with cross sections (perpendicular to the incoming radiation)

*Again, these equations appear to be consistent with the zero voltage limit of Eq. (4.137). However, there is insufficient information available to check the detailed parameters used in the calculation.

measuring 5 × 5 and 10 × 10 cm and arranged so that various dielectric and absorber thicknesses could be used. Either PMMA or paraffin could be employed as the dielectric with lead as the absorber. Glass dielectrics were also tried, but they were discarded because of polarization effects.

Paraffin dielectric cells were selected to detect the total (time integrated) dose by measuring their voltage build-up. (Hiraoka felt that paraffin was best for suppression of leakage currents, which are important in voltage operation.) A linear response was found up to 250 V and a total dose of 6000 R; however, a fairly strong directional sensitivity with "half intensity" angle of $\approx 30°$ was observed.

Hiraoka used a PMMA dielectric cell to measure dose rates, and in this case, he measured the short-circuit current and tested the cell's linearity with dose rate using bremsstrahlung from a gold target bombarded by electrons from a 15-MeV Linac. A linear response was obtained for average dose rates up to 500 R/min (corresponding to a peak intensity of 10^7 to 10^8 R/min during the Linac pulses). In comparison, a Victoreen ion chamber was found to saturate and display a nonlinear response in the same field.

Finally, Hiraoka attempted to design a cell that would be fairly insensitive to the gamma energy. First, he measured the effect of varying the dielectric and lead thicknesses separately. As seen from Fig. 7.48, the cell output was found to decrease with increasing photon energies for a dielectric thickness below 17 to 22 mm, and vice versa above 22 mm. Also, a minimum absorption (hence minimum cell output) in the lead was found for a gamma energy of about 8 MeV. Based on this information, Hiraoka showed (Fig. 7.49) that a 25-mm dielectric and a 70-mm lead absorber should give a flat response since the increase in output with energy for this dielectric thickness is just balanced by the decreased absorption in the lead. (This is similar to the method proposed by Gross, illustrated in Fig. 7.37, but now the importance of the dielectric thickness becomes apparent.) The energy response of this cell was studied experimentally, again using bremsstrahlung from a gold target bombarded in the 15-MeV Linac. Hiraoka noted that with a constant target current the bremsstrahlung intensity in the forward direction (toward the cell) should be proportional to the third power of its energy. The GEC was found to follow this law nicely between 5 and 15 MeV, whereas the Victoreen chamber again showed some deviations.

The GEC studies described to this point have concentrated on short-circuit operation. Sampson and Miley[56,66,82] have reported a series of high-voltage studies in which three different cells were studied: The MOD I Cell (Fig. 7.50) used concentric cylindrical electrodes in addition to a collector plate; the MOD II Cell (Fig. 7.51) used multiplate planar collectors; and a MOD III Cell, which used a simple

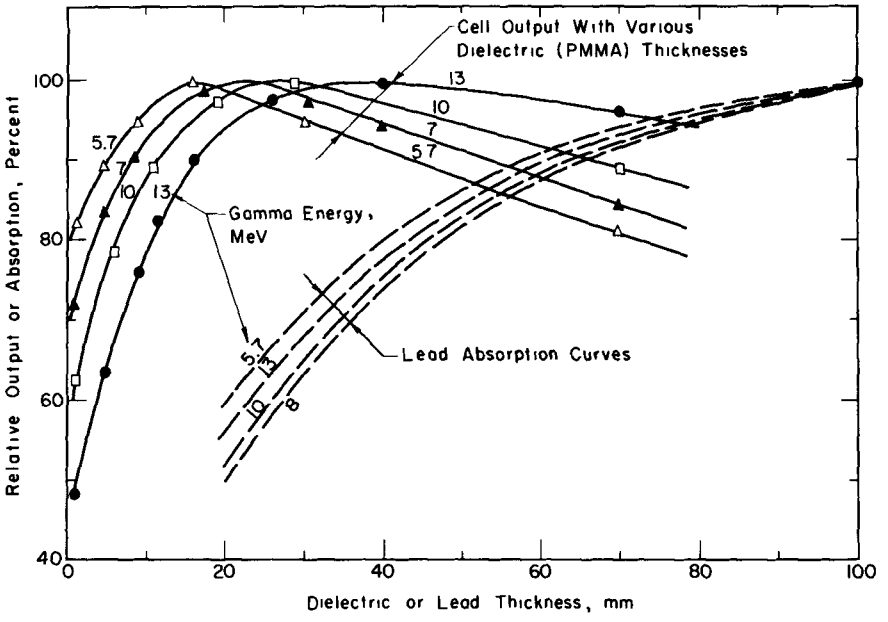

Fig. 7.48 — The effect of varying the dielectric and lead absorber thicknesses. (From Measurements by Hiraoka, Ref. 81.)

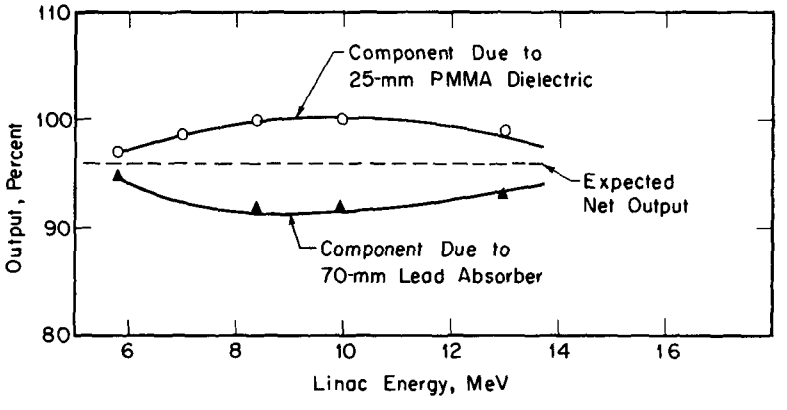

Fig. 7.49 — The effect of combining the curves from Fig. 7.48 for a 25-mm dielectric and a 70-mm lead absorber. (The dotted line is the expected value. After Hiraoka, Ref. 81.)

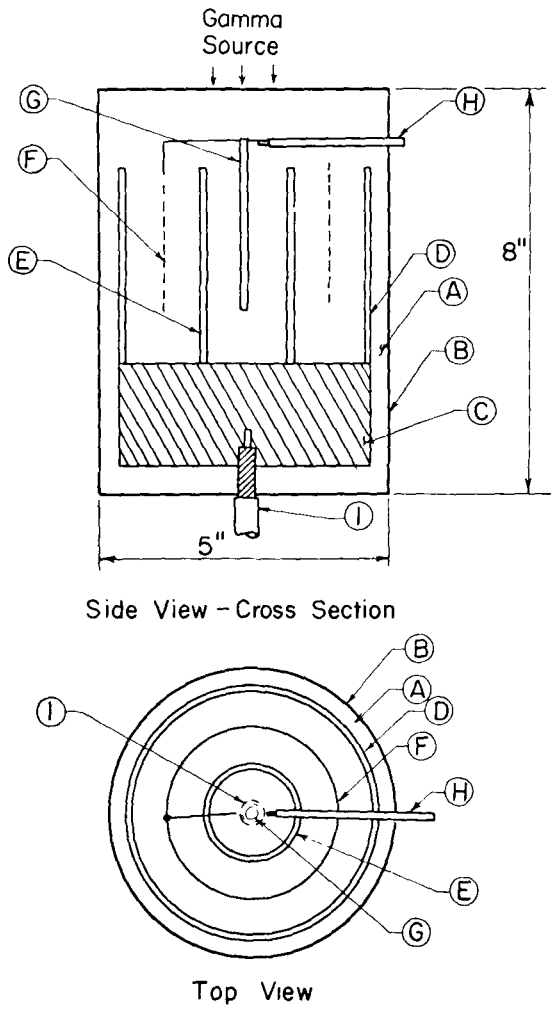

Fig. 7.50—Illustrative sketch of a MOD I type Gamma-Electric Cell showing: (A) dielectric; (B) outer container; (C) lead collector; (D) outer cylindrical collector; (E) inner cylindrical collector; (F) ground electrode; (G) ground electrode; (H) and (I) output cables. (From Sampson and Miley, Ref. 66.)

planar emitter–collector–absorber construction. (The multiplate cells were designed to increase the collection area, i.e., to increase currents.) Polystyrene, silicone, and also a modified epoxy resin were tested for use as the dielectric. All cells were completely encapsulated in an effort to eliminate surface leakage currents.

The MOD I and MOD II Cells produced short-circuit currents of 3.3×10^{-17} and 4.7×10^{-17} A/cm^2 per R/h, respectively. These cur-

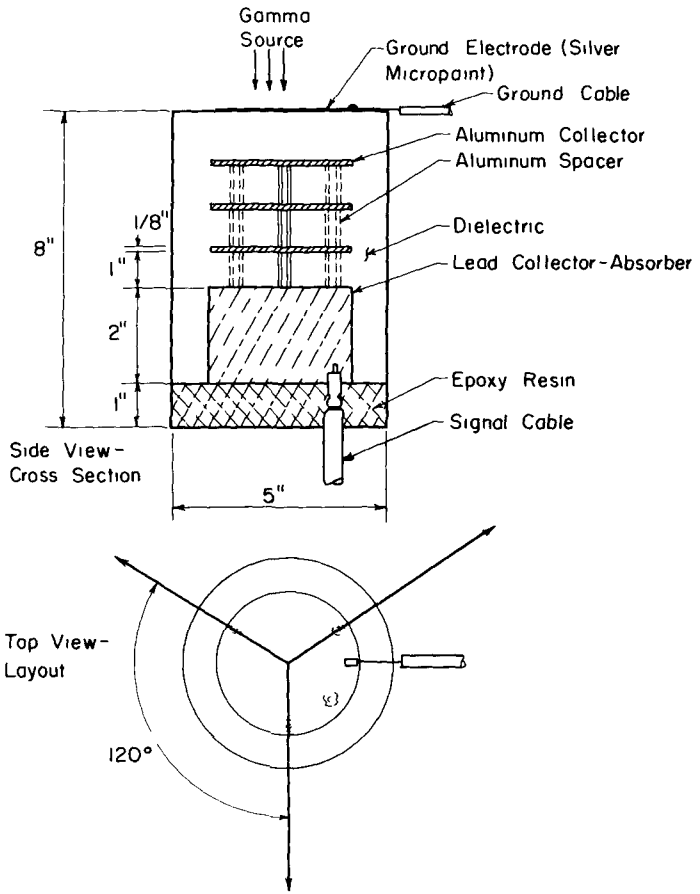

Fig. 7.51 —Illustrative sketch of the MOD II type Gamma-Electric Cell (From Sampson and Miley, Ref. 66)

rents were found to be essentially independent of the type of dielectric material used and to vary linearly with the gamma dose rate.

Typical voltage build-up curves for MOD I Cells using polystyrene and silicone dielectrics are shown in Fig. 7.52 for irradiations in a TRIGA nuclear reactor. The slow voltage decay at 10^6 R/h was attributed to radiation-induced changes in the electrical properties of the dielectric. This effect was not observed at lower radiation intensities as illustrated by the curve for 2.5×10^5 R/h. Similar results were found for epoxy cells (not shown).

A voltage breakdown occurred in several MOD I Cells with a silicone or Lucite dielectric, and a post-mortem examination revealed

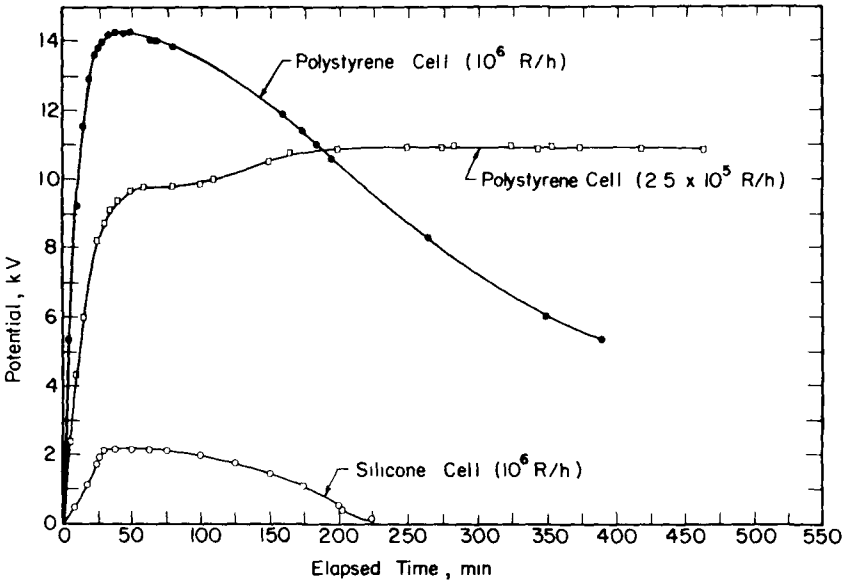

Fig. 7.52 — Voltage output curves for MOD I cells. (From Sampson and Miley, Ref. 66.)

cracks in the dielectric extending radially between the high voltage and ground electrodes. This was attributed to space-charge storage effects, but interestingly, no failures were observed for polystyrene or epoxy cells.

The voltage build-up curves for an epoxy MOD II cell, shown in Fig. 7.53, represent the highest potentials reported to date ($\approx$ 19 kV). As seen, quite stable outputs were obtained at the lower radiation intensities, but again a slow decay occurred at 10^6 R/h.

In summary, these results verify that kilovolt potentials can be generated with GEC's. Of the materials studied, epoxy and polystyrene appear to be best suited for voltage operation, while silicone and Lucite are restricted to low voltages.

Because of the complex geometry involved, the MOD I and II cell results are not easily compared to theory, so the planar MOD III cell was constructed explicitly to provide a clean comparison. Experiments with this cell used a ^{60}Co source and demonstrated four points:

Current densities strongly depend on the gamma beam-to-collector area ratio. Comparisons with theory are best made by an extrapolation to a zero ratio.

Current–voltage measurements using a bias voltage technique agreed with theory to about 10 kV/in., where nonlinear effects

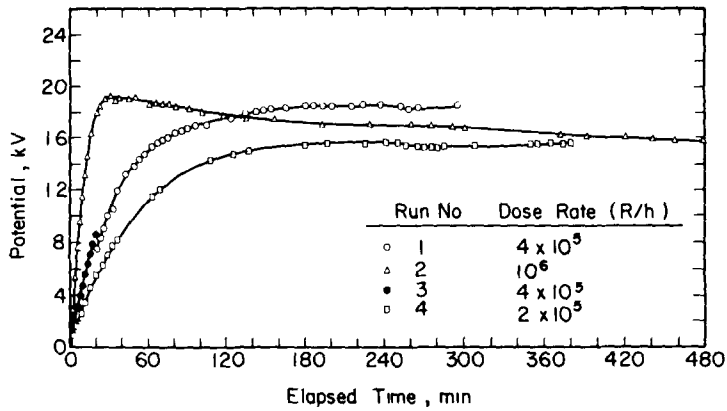

Fig. 7.53 — Voltage output curves for MOD II cells with an epoxy dielectric. (From Sampson, Ref. 56.)

were observed, possibly indicating the on-set of voltage breakdown. Breakdown at such a low voltage gradient, a factor of 50 below the intrinsic strength of polystyrene, was attributed to radiation effects and possible internal electric fields due to space charge storage.

Differences observed between increasing and decreasing voltage measurements, as well as a transient in the short-circuit voltage, were attributed to space charge storage effects.

Currents were not affected by changing from lead to a graphite collector, indicating that electron backscattering effects are small. This agrees with the results by Pigg noted earlier, but contradicts the measurements by Murphy.

In addition to these experiments, Sampson and Miley also considered the theoretical analysis of high-voltage GEC operation in some detail. Since, as discussed in Chap. 2, the Compton current is a function of the voltage gradient (V/d) rather than V alone, they rearranged Eq. (F.3) to obtain

$$\frac{i_L}{i(0)} = \frac{i_c(V/d)}{i(0)} - \frac{V}{d}\Lambda \tag{7.5a}$$

where i is the total current (the current density J times the cross-sectional area of the cell A_c), the subscripts are as defined earlier, and the parameter Λ is a reduced electrical conductivity given by

$$\Lambda = \sigma^* A_c / i(0). \tag{7.5b}$$

The conductivity σ^* has an asterisk as a reminder that it includes radiation-induced conductivity. Note that $\Lambda = 0$ represents an "ideal" dielectric that stops all leakage currents, whereas presently available materials generally fall in the range of 10^{-5} to 10^{-6}.

The current $i_c(V/d)$ is the "forward" Compton current, and it may be calculated as indicated in Chap. 4, pp. 177–184.

Results of calculations based on Eq. (7.5), with $i_c(V/d)$ evaluated by Eq. (4.137), are shown in Fig. 7.54 for various values of conductivity

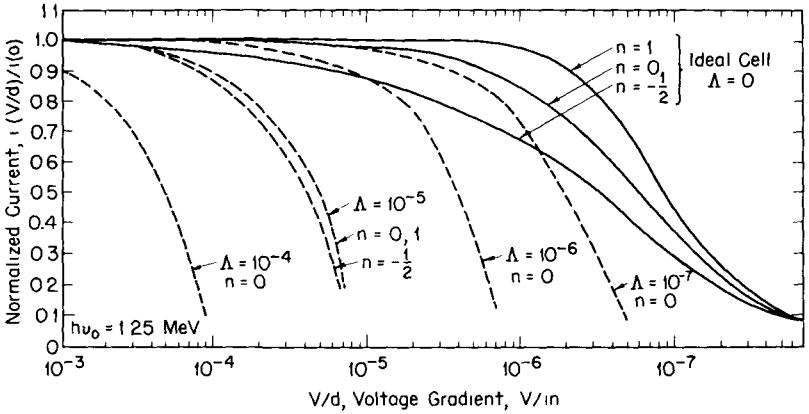

Fig. 7.54—Current–voltage gradient plots for a Gamma-Electric Cell. (After Sampson and Miley, Ref. 66.)

and typical values of the slowing parameter n for electrons. (Note that the $\Lambda = 0$ curves are similar to those shown earlier in Fig. 4.20.) Clearly the leakage currents due to a finite Λ strongly affect operation. This is, of course, similar to the leakage current effect illustrated in Figs. 6.2 and F.2.

Sampson and Miley[66] show that a useful approximation to these current characteristics is given by

$$\frac{i_L}{i(0)} \approx \begin{cases} 1 - \dfrac{V}{d}\Lambda & \left(\dfrac{V}{d} \begin{cases} \ll T_0/e\lambda(T_0) \\ \leq 1/\Lambda \end{cases}\right) \qquad (7.6a) \\ \dfrac{T_0 d}{eV\,\lambda(T_0)} - \dfrac{V}{d}\Lambda & \left(\dfrac{T_0}{e\lambda\,(T_0)} \ll \dfrac{V}{d} \leq \sqrt{\dfrac{T_0}{\lambda(T_0)\,e\Lambda}}\right). \qquad (7.6b) \end{cases}$$

Here T_0 and $\lambda(T_0)$ refer to the average initial energy and range of the Compton electrons, respectively, and e is the electronic charge. As stressed in Chaps. 2 and 4, these relations (and the curves of Fig. 7.54) show that the ideal-cell current ($\Lambda = 0$) goes to zero asymptotically as

$V/d \to \infty$. However, in practice, leakage currents set an upper limit on the achievable voltage gradient, and this is represented by the limits assigned to V/d in Eqs. (7.6a) and (7.6b).

These equations also illustrate another characteristic noted in Chaps. 2 and 4: The maximum output voltage can be increased by simply increasing d, the length of the cell. A limit occurs, however, since gamma attenuation, neglected here, will eventually become large enough to reverse this trend.

Based on Eq. (7.6), Sampson and Miley show that the maximum power for a cell of fixed length d is approximately

$$\frac{P_{max}}{i(0)} \approx \text{min.} \begin{cases} \dfrac{d}{4\Lambda} & \left(\dfrac{V}{d} \approx \dfrac{1}{2\Lambda}\right) \quad (7.7a) \\ \dfrac{T_0 d}{e\,\lambda(T_0)} & \left(\dfrac{V}{d} \geq \dfrac{T_0}{e\,\lambda(T_0)}\right). \quad (7.7b) \end{cases}$$

The value given in Eq. (7.7a) corresponds to large Λ, where the maximum open-circuit voltage gradient is less than twice the value of the break point in the $\Lambda = 0$ curve of Fig. 7.54. Again, in this region, the power can be increased by making d larger, until one of two things happen: gamma attenuation dominates, or the limit of Eq. (7.7b) is achieved. Equation (7.7b) corresponds to the power at the breakpoint of the $\Lambda = 0$ curve, which in turn corresponds to the maximum power for an ideal cell.

In summary, these studies of high-voltage operation indicate that the GEC may be of value in special purpose applications requiring kilovolt operation with low currents. However, a number of questions need further study—e.g., lifetime, long-term radiation damage effects, and a criterion for optimum multiplate designs.

7-5.2 Vacuum Type Gamma-Electric Cells

The vacuum GEC concept is illustrated in Fig. 7.55. In contrast to the dielectric type GEC, the Compton electrons are produced in an emitter plate, and as the name implies, a vacuum is used to insulate the electrodes. Also, the emitter is typically metallic so the Compton electrons are produced in a region that is free from potential gradient. As a result, the vacuum GEC can be viewed simply as a Plate-Emitter Cell (Sec. 2-2.1). Thus, the analysis developed for these cells in Chaps. 2 and 4 is valid, provided the Klein–Nishina cross section is used to represent the angular distribution of the source as was done in Sec. 4-5. The thick collector shown in Fig. 7.55 represents the conventional method of preventing gamma-induced secondary-electron emission from the back side of the collector. An alternate possibility

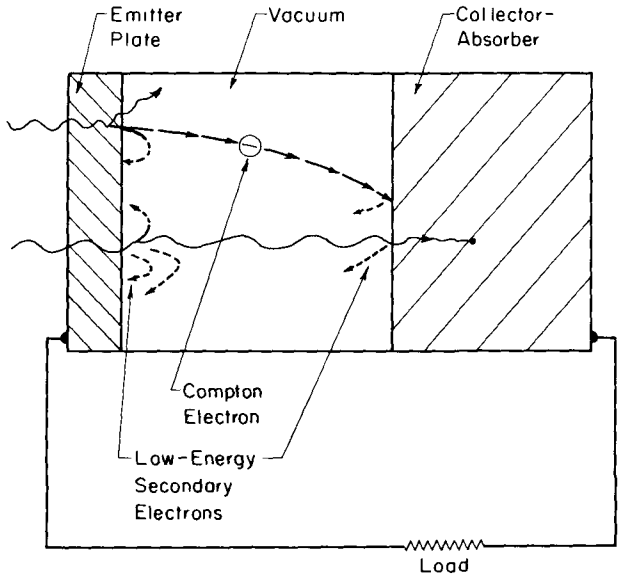

Fig. 7.55 — Illustration of a vacuum-type GEC.

is to create a net current by the difference in electron emission from a low-Z collector and a high-Z emitter.

It is apparent that secondary-electron currents, typical of all vacuum-type cells, will occur here. As explained in Chap. 5, "secondary electrons" are, by definition, the low-energy component of emitted electrons, whereas forward Compton electrons correspond to the high-energy component. (Secondaries, it will be noted, can originate from the Compton electrons themselves as well as from the gammas.) Fortunately, as shown in measurements to be discussed shortly, secondary yields are low enough so that grid or magnetic suppression is not necessary.

Most applications of these cells to date have been for radiation detection, in which case the load in Fig. 7.55 is replaced by a bias voltage supply. Two modes of operation are possible:

(1) *Positive collector bias.* With a positive bias, both the primary Comptons and secondaries from the emitter reach the collector. The secondaries thus collected serve to multiply the current, which is desirable in some measurement situations. Such devices are commonly called Semirad detectors[83] (Secondary-Electron Mixed-Radiation Dosimeters). While the difference is not great, we will classify these devices as Secondary-Emission Cells, rather than GECs, and they are discussed further in the next section.

(2) *Negative collector bias.* The collector will normally develop a negative potential in the absence of a bias voltage. However, for detectors, it is simpler to use a bias voltage supply in lieu of the thick collector that would be required to ensure a voltage build-up. The bias voltage suppresses secondaries, leaving Compton electrons as the primary forward current. Hence, such devices are included in the GEC discussion.

As noted earlier, the first detailed discussion of a GEC by Kloepper and Madsen[57] was concerned with a vacuum-type cell. This cell, shown in Fig. 7.56, had a 0.064-in.-thick aluminum plate emitter and a thick lead collector. A beam from a 0.52-Ci ^{60}Co source passed through a $1\frac{1}{4}$-in. collimator before hitting the emitter, and bar magnets, providing a central field of ≈ 90 G-cm (225 G) could be inserted to suppress secondaries.

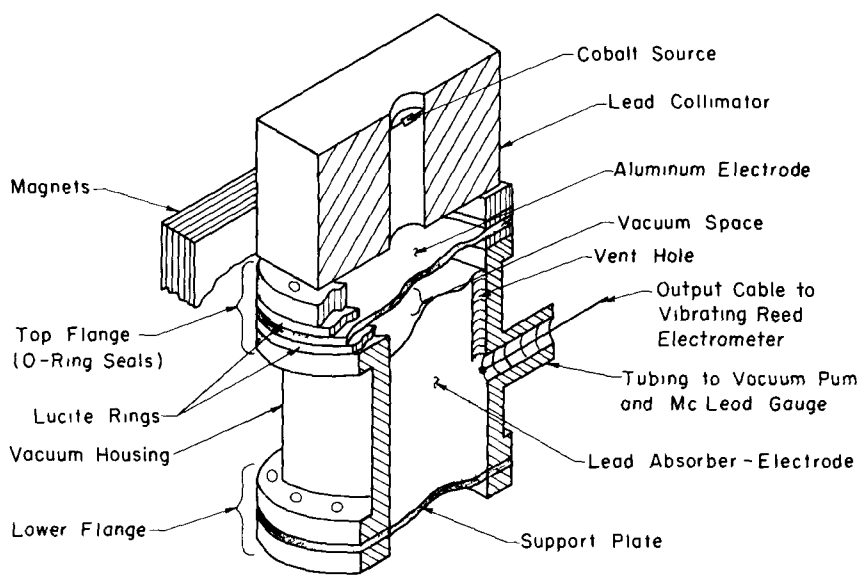

Fig. 7.56—Isometric view of the cell used by Kloepper and Madsen. (Adapted from Ref. 57.)

Typical results from the Kloepper–Madsen measurements are presented in Fig. 7.57. The collected current has been divided into two components: I_V, a voltage and polarity sensitive portion attributed to secondaries; and I_C, which, because it is independent of voltage (up to the 33 V, maximum), is attributed to Compton electrons. This identification was further verified since the magnetic field mainly affected I_V, indicating it consists mostly of low-energy secondaries.

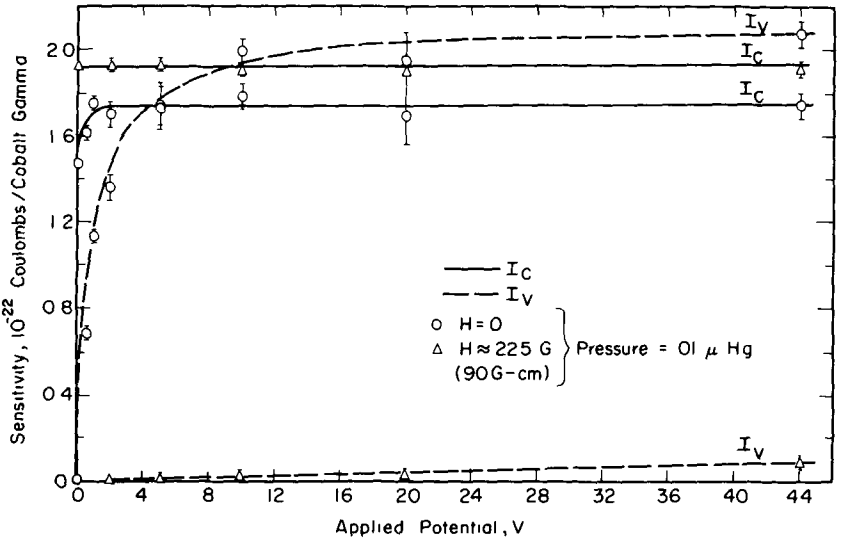

Fig. 7.57 — Sensitivity of the cell of Fig. 7.56 vs collector bias voltage and magnetic field strength. (From Kloepper and Madsen, Ref. 57.)

[Equation (6.44) indicates that this field should have cut off any electrons below about 800 eV.]

Similar experiments at a higher pressure (≈ 7 μ Hg) showed a decrease in I_V with voltage with the 225-G field present. This was attributed to electrons created by ionization of the gas in a region too close to the collector to be suppressed by the magnetic field They calculated a sensitivity of 5.6×10^{-3} electron/photon, including an allowance for 17% transmission of gammas through the collector. While a factor of 4.6 lower than measured, this was considered to represent a reasonable agreement. The difference was attributed to two major assumptions in the theory: straight-line electron paths in the plate, and the neglect of secondary and photoelectric emission by low-energy scattered gammas from the front surface of the collector.

Kloepper and Madsen discussed the desirability of avoiding the thick collector. They pointed out that, since Compton production goes roughly as Z/A (which is fairly constant from material to material), it is difficult to achieve a significant net current merely by selection of different plate materials. A very thin collector with high gamma transmission was considered but discarded because Compton transmission would also occur, leading to a difficult optimization problem. Another scheme mentioned was the use of a hole in the collecting plate the size of the incoming gamma beam (assumed small relative to the plate areas). Compton electrons emitted at an angle would still be col-

lected. This design was discarded because electron leakage through the hole appeared to be serious and also because of possible difficulties in designing an insulated outer container to provide a vacuum enclosure.

Apparently unaware of Kloepper's and Madsen's work, Hosemann and Warrikhoff[84] reported the development of a dosimeter, shown in Fig. 7.58, which is based on the same concept, and they called it a

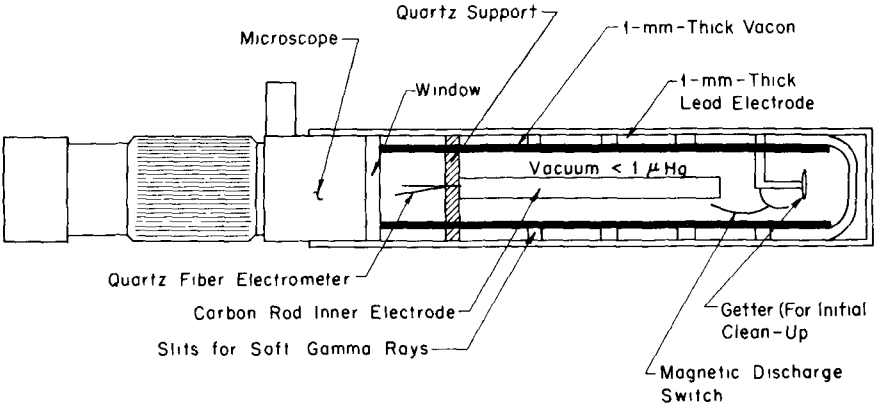

Fig. 7.58 — The "self-powered dosimeter" developed by Hosemann and Warrikhoff. (From Ref. 84. The dosimeter is a cylindrical cell made up of an inner graphite electrode and an outer electrode. The dose is read from an internal quartz-fiber electrometer.)

"roentgen element" or a "self-powered" dosimeter. Instead of using a thick collector, this device operates by differential emission from a high-Z emitter and low-Z collector. Voltage build-up to about 100 V was recorded with the special quartz fiber electrometer. They reported an energy dependence of only ±8% between 80 keV to 1.2 MeV and a sensitivity of 0.5 V/R.

The 1-mm-thick lead emitter was coated with a Vacon layer, which provided a vacuum-tight seal and also helped flatten the energy dependence. Its thickness was chosen such that it transmitted most of the electrons produced in the lead by high-energy gammas, but it stopped the soft electrons produced by low-energy gammas. The Vacon, in effect, serves as an emitter for the low-energy secondaries that are released as the low-energy gammas pass through it. (The slits in the lead electrode shown in Fig. 7.58 allow very soft gammas to pass through to the Vacon.) Because of the low Z of the Vacon, the low energy yield is reduced to a value roughly equal to the high energy yield due to the combined emission from the Vacon and the lead. This lessens the dependence on the gamma-ray energy, and the technique

is termed "electron filtering" by Hosemann and Warrikhoff. For vacuum cells, then, this technique is equivalent to the variable absorber thickness used by Gross or the external scatterer used by Murphy in dielectric type designs.

Hosemann and Warrikhoff cite a number of advantages for such a dosimeter. In comparison to Semirad detectors (next section) no auxiliary power supply is required. As with the Semirad and dielectric GEC, it has a fast response and can be used in very high dose rates without saturation. Better insulating materials can be used than in the normal ionization type dosimeter, and this gives a higher RC time constant and a lower charge leakage rate ($\approx 0.02\%$ per week depending on the measured dose).*

Aside from actual device studies, several investigations have been designed to obtain a better understanding of Compton currents emitted from plates of various materials, and this is, of course, the basic mechanism involved in the vacuum GEC. The studies of Sawyer and Van Lint, Stevens and Artuso, and Oda and Suzuki were discussed in Sec. 5-5 in connection with the theory of high-energy secondary emission Another study along these lines by Almond and Schmidt[85] reports currents from single plates of various metals, graphite, and polyethylene as well as various combinations of these plates separated by a $\frac{1}{8}$-in. air gap They used gammas from a pulsed reactor (KUKLA).

7-6 THE SECONDARY-EMISSION CELL

The Secondary-Emission Cell (SEC) is closely related to the vacuum-type GEC; however, we distinguish between the two on the following basis· the principal current carriers in the GEC are the high-energy Compton electrons, whereas low-energy secondaries form the main current in the SEC.

As illustrated in Fig. 7 55, during high-voltage operation, the vacuum-type GEC rejects the low-energy secondaries simply because they cannot overcome the potential barrier. However, during short-circuit or low-voltage operation, because of their larger yield, the low-energy secondaries from the emitter will be the main charge carrier. Cells restricted to this mode of operation are then termed SEC's. While subtle, the difference is nevertheless important. As stressed in Chap. 1, the bulk of the energy released by nuclear sources is carried by high-energy particles. Thus, the SEC concept sacrifices

*The extension of the self-powered detector concept to neutron detection was discussed earlier in connection with Fig. 7.35. However, in contrast to the Hosemann–Warrikhoff detector, a solid metal oxide insulator has normally been used

much of the energy associated with primaries *in exchange for current multiplication* via the larger yield of the low-energy secondaries.

Since the SEC must operate at very low voltages, it is inherently restricted to lower power densities than the GEC. (In fact, for radiation-detection applications, a bias voltage is generally used so that a net power input is required.) Still the SEC has important advantages for radiation detection, and the possibility remains open for using it as a low-power topping unit on a heat cycle.

The concept was apparently first proposed by Schwartz[86, 87], who in 1954 obtained a patent for a SEC design illustrated in Fig. 7.59. A

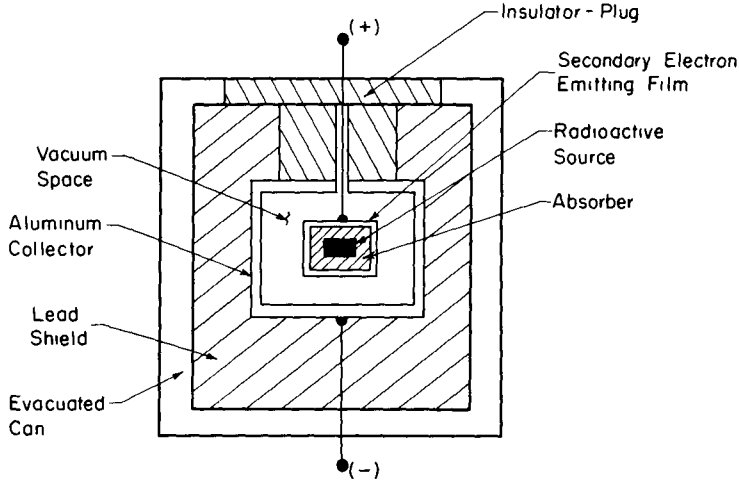

Fig 7.59 — The secondary-electron-emission battery proposed by Schwartz (From Refs. 86 and 87)

thin film of high-Z material on the emitter was used to enhance secondary production. The "absorber" is designed to slow the primary particles so they enter the emitter film with low energies, enhancing the secondary yield (As stressed earlier, much of the energy of the primaries from the source will be lost in the "absorber.") However, performance data for such a device are not available, and it is not clear that the "absorber" would completely eliminate the high-energy secondary component. If not, operation under high impedance loads (approaching open-circuit conditions) would revert to collection of Compton electrons for a gamma-emitting source, or δ-rays for ion or beta emitters.

The most important application of the SEC concept has been its use for radiation detection. Then, a reverse bias is applied, and the device is commonly called a Semirad detector. Considerable research

and development has been devoted to the Semirad by the U. S. Army Electronics Command (Refs. 83 and 88 to 90).

The term "mixed radiation dosimeter" is used since, by proper selection of the emitting film, it is possible to detect specific types of radiation selectively (e.g., fast neutrons, slow neutrons, gamma rays, or x-rays) in a mixed radiation environment. Mechanisms for detection of gamma rays and neutrons are illustrated in Fig. 7.60. Gamma detection follows the earlier discussion, whereas fast-neutron detection relies on secondary emission associated with the recoil proton. Slow or thermal neutrons can be detected with a boron (secondary emission due to the alpha produced) or ^{235}U coating (secondary emission due to the fission fragments produced).

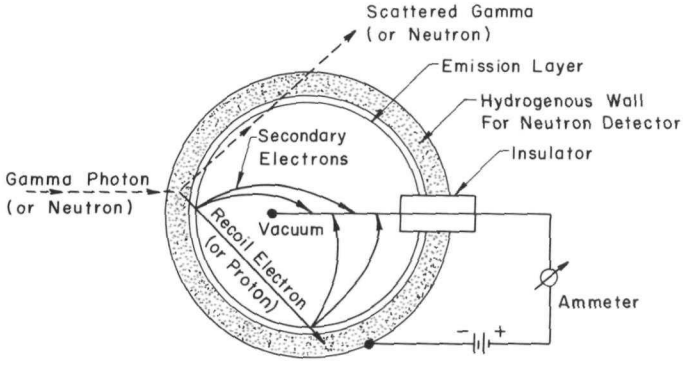

Fig. 7.60 — Semirad concepts. (After Kronenberg, Ref. 83.)

It is then possible to combine these concepts into a single device such as illustrated in Fig. 7.61, which favors the detection of one type of radiation. With the biasing arrangement shown, the current that is associated with the gammas (Compton electrons) and collected on the center plate is essentially canceled by the one collected on the bottom plate. However, the neutron-induced current produced at the center plate does not cancel. This, then, is the counterpart of a compensated ion chamber.

The Semirad detector has received wide usage, chiefly because its response to radiation is linear over a wide range of intensities. It is particularly useful in high-intensity fields such as encountered in pulsed reactors, nuclear explosions, etc. The collection times involved are less than for an ionization chamber since the diffusion of charged particles in a gas is avoided. Thus, the Semirad has an excellent frequency response — for example, microsecond and better resolution has been demonstrated in fields involving megarads per second[88].

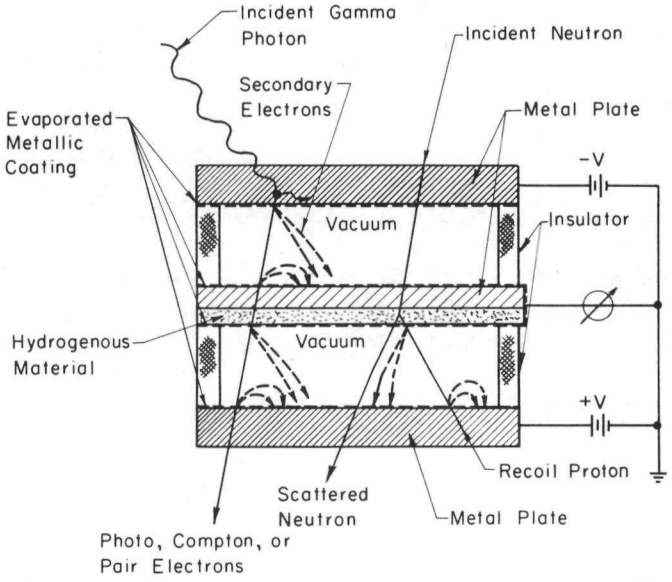

Fig. 7.61 — Principle of the gamma-compensated fast-neutron Semirad detector. (After Kronenberg, Ref. 83.)

Considerable technology has developed relative to the Semirad concept, and a number of variations of the basic design have been considered. However, further discussion will not be included here because of the excellent coverage in the monograph by Kronenberg[83].

7-7 THE THERMONUCLEAR-ELECTRIC CELL

The coupling of a Direct-Collection Cell to a thermonuclear (fusion) reactor represents a most significant potential application for these cells. Further, as will become evident from the following discussion, the Thermonuclear-Electric Cell (TEC) development represents a less formidable challenge than its counterpart, the Fission-Electric Cell. Efficient operation at lower voltages is feasible, and charged particles can be extracted from the confining magnetic field region of the fusion reactor, making an external collector practical (as opposed to the internal collector arrangement envisioned for fission reactors).

The fundamentals related to the generation and confinement of a hot plasma suitable for energy generation via fusion reactions are presented in several books, such as Refs. 91 and 92. Problems related to stable confinement are still formidable, but experiments with several approaches have progressed to the point that serious thought

is currently being put into the engineering problems related to a full-scale reactor and the associated energy-conversion components[93,94]. Besides the sheer technological challenge involved, the original motivation for fusion research was that it represents a practically inexhaustive source of energy. While recent advances in the development of breeder-type fission reactors have somewhat reduced the urgency associated with this goal, it has become evident that other factors may be of even more immediate significance

The inherent safety of a fusion system with a minimum potential for radioactive contamination eases siting problems. Other attributes, including potential for low electrical costs and reduced thermal pollution revolve around the energy-conversion system and its efficiency To understand this better, we recall the primary reactions that may be involved in the reactor

$$(D-D)\qquad {}^{2}_{1}H + {}^{2}_{1}H \rightarrow \begin{cases} {}^{3}_{2}He + {}^{1}_{0}n & (0.8\ MeV)\ \ (2.5\ MeV) \\ {}^{3}_{1}H + {}^{1}_{1}H & (1.0\ MeV)\ \ (3.1\ MeV) \end{cases}$$

$$(D-T)\qquad {}^{2}_{1}H + {}^{3}_{1}H \rightarrow {}^{4}_{2}He + {}^{1}_{0}n \qquad (3.5\ MeV)\ \ (14.1\ MeV)$$

$$(D-{}^{3}He)\qquad {}^{2}_{1}H + {}^{3}_{2}He \rightarrow {}^{4}_{2}He + {}^{1}_{1}H \qquad (3.6\ MeV)\ \ (14.7\ MeV)$$

The kinetic energy associated with the reaction products in the early fusion reactors will probably be processed through a conventional heat cycle–turbogenerator to produce electricity If liquid metals are used to capitalize on the high plasma temperature, conversion efficiencies of the order of 60% can be anticipated Still, as Eastlund and Gough[93] succinctly point out, "This is not an optimum match . . such converters require the fusion energy .. at over 50,000,000°C to be degraded to temperatures less than 2000°C because of materials' limitations."* The alternative, as has been recognized for some time (e.g., see pp. 4 and 15, Ref. 92), is to couple an energy converter directly to the charged particles. However, except for the D–^{3}He reaction, a significant fraction of the energy released will be associated

*In addition to electrical energy output, Eastlund and Gough discuss two other important energy conversions possible with a fusion device. In one, the "fusion torch" is used to reduce any material to its basic elements for separation The other would use the resulting radiation field for process heating or chemical processing in the body of a fluid.

with neutrons. Although a cell might be devised to transfer the energy of the neutrons to charged particles [by fission, (n,α) reactions, proton recoil, etc.], it is generally envisioned that the neutron energy, along with x-radiation energy, etc., would be processed through a conventional heat cycle.

Referring back to the reactions, we see that the D–D cycle releases 8.4 MeV in charged particles out of a total of 25 MeV; i.e., about 33%. (This assumes that because of its fast reaction rate all the tritium produced reacts in a D–T cycle but that the slowly reacting ^{3}He remains unreacted[92].) Since this would be the maximum fraction of the energy release that would be processed by the direct conversion scheme, it might, in a sense, be viewed as a topping cycle in the D–D reactor. Still, as will be seen, its efficiency and low cost make this approach quite attractive. At the other extreme, a D–^{3}He reactor could conceivably operate primarily on a direct conversion cycle since both reaction products are charged. Unfortunately, however, it appears that the first generation of fusion reactors will probably operate on a D–T cycle because it offers a fast reaction rate and a lower "ignition" temperature[91,92]. (In addition to direct conversion considerations, this cycle has the disadvantage of requiring tritium, which will probably be produced or "bred" by neutron reactions in a lithium blanket surrounding the reactor. Thus lithium becomes, in effect, a fuel, and natural reserves again become important. Although reasonably plentiful, lithium supplies fall well short of the ideal of deuterium. The D–^{3}He cycle represents a similar problem, but, in this case, ^{3}He is bred in a D–D reactor or through the decay, albeit a 12-year half-life, of tritium.)

Despite the general recognition of the possibility of direct conversion in connection with the fusion reactor, little thought had been put into specific concepts until recently. At the 1969 Culham conference three fairly detailed proposals were presented: Peschka and Kelm[95] discussed an inductive magneto-plasma-dynamic converter; Oliphant[96] outlined a method using an expansion of the plasma against the magnetic field; and Post[97] described a direct-collection scheme.

At this stage, it is not clear which, if any, of these concepts may receive ultimate application. However, because of the possible importance of this application, and because it is based on concepts discussed here, we will review Post's scheme in some detail. The following is based largely on Ref. 97, and it should be stressed that, since it *represents a first exploration of the concept*, continued modification and revision may well take place.

Post and his colleagues at Lawrence Radiation Laboratory have been strongly involved in the mirror approach to fusion containment illustrated in Fig. 7.62 (see Chap. 15, Ref. 91, or Chap. IX, Ref. 92). In contrast to closed systems such as toroids or stellarators, the

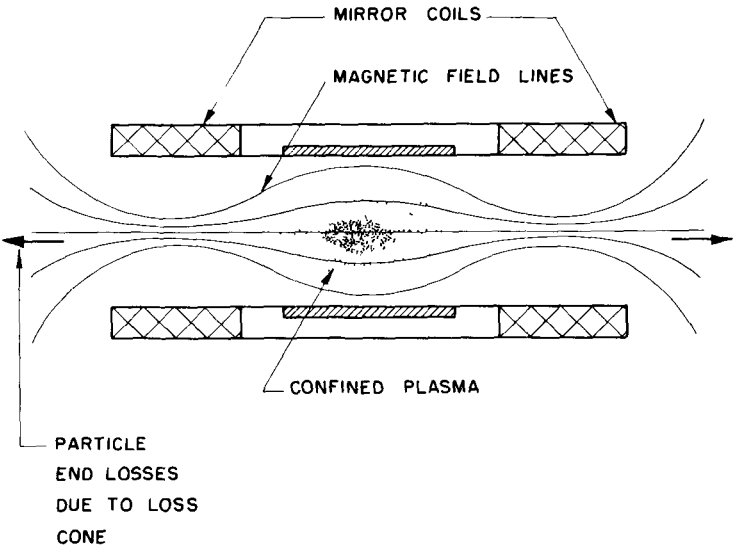

Fig. 7.62 — Schematic illustration of the mirror confinement scheme.

mirror is an open system in that plasma particles can always leak out of the ends of the mirrors due to the so-called loss cone. Thus, although recent experimental results are encouraging relative to the possibility of achieving containment with a mirror-type device, engineering projections indicate that the resulting Q-value, defined as the ratio of the net energy production to energy injected, may be disappointingly low because of these losses. Post then proposes to capitalize on this feature by using a Direct-Collection Cell to recover the energy associated with the particles leaking through the loss cone. This was suggested in Chap. 1, but, as stressed there, such an approach is complicated by the energy spread of the charged particles so that a multiplate collector like that illustrated in Fig. 1.9(d) represents the key to efficient operation. However, before the collector is discussed, it is important to recognize that two additional steps are necessary to "prepare" the beam, namely, expansion and separation.

The expansion step involves passing the escaping plasma beam through a region where the magnetic field strength is reduced (expanded). This serves two functions: It creates a well-defined directed motion by converting perpendicular particle velocities to parallel,*

*Parallel and perpendicular directions are defined relative to the magnetic field lines in the mirror region of the device in Fig. 7.62. Thus, if a collector cup is placed at the end of the mirror, the kinetic energy associated with the parallel component can be converted to potential, but, as pointed out in Chap. 2, the perpendicular component is not converted.

and it reduces the plasma density so that ion–electron separation is easier.

An expansion chamber such as that envisioned by Post is shown in Fig. 7.63. His design was coupled to a quadrupole magnetic well or "disk" mirror machine so that the fringing magnetic field of the mirror links with a radial field in the large doughnut-shaped chamber. (As discussed later, the reactor would probably run with fairly high average ion energies, roughly 100 keV.) Fields of the order of 150 kG in the mirror are thus gradually weakened to a few hundred gauss; the initial bundle of flux lines are transformed to a flat fan-shaped pattern. The conversion from perpendicular to parallel velocity can be estimated simply by the well-known adiabatic mirror law[92,97]. Using this law plus an estimate for nonadiabatic effects for typical conditions, Post found that the perpendicular-energy component of the ions can be reduced to less than 1% of the mean energy of the exit stream (≈3 keV for a mean stream energy of 500 keV). This accomplishment is equivalent to establishing an almost ideal parallel-beam ion source, and the high efficiency of the conversion to the parallel component is a key factor leading to a high cell efficiency.

The stream density leaving the expander should be relatively low, about 10^6 particles/cm^3 in Post's example, so that space charge problems are minimal and the separation of electrons from the ion stream is easily carried out.

The separation step is also illustrated in Fig. 7.63, where the magnetic field lines are simply diverted outwardly near the exit of the expander. The lighter electrons will essentially follow the lines, whereas the heavy, high-energy ions will cross them with only a small deflection.

While the electron energy could conceivably be recovered, this step is probably unnecessary. Plasma electrons are electrostatically confined in mirror systems; thus, upon escape, their energy is reduced by the plasma potential, and, as a result, the energy associated with the electron stream is only a small fraction of that carried by ions.

In summary, a directed beam of energetic ions is obtained from the expander–separator section. The beam density may typically have a density of the order of 10^6 ions/cm^3 with an average energy of 500 to 800 keV but with an energy spread ranging from the plasma potential (≈100 to 200 keV) up to the quite high values corresponding to the tail of the plasma distribution (MeV range). As stressed earlier, the key problem then revolves around the efficient collection of this polyenergetic beam. Post suggests the possible use of a modified, somewhat more sophisticated version of the multiplate collector concept suggested in Chap. 1. He envisions "a series of electrostatic lenses in the form of hollow electrodes of progressively increasing positive potential through which each ion is guided until it is diverted

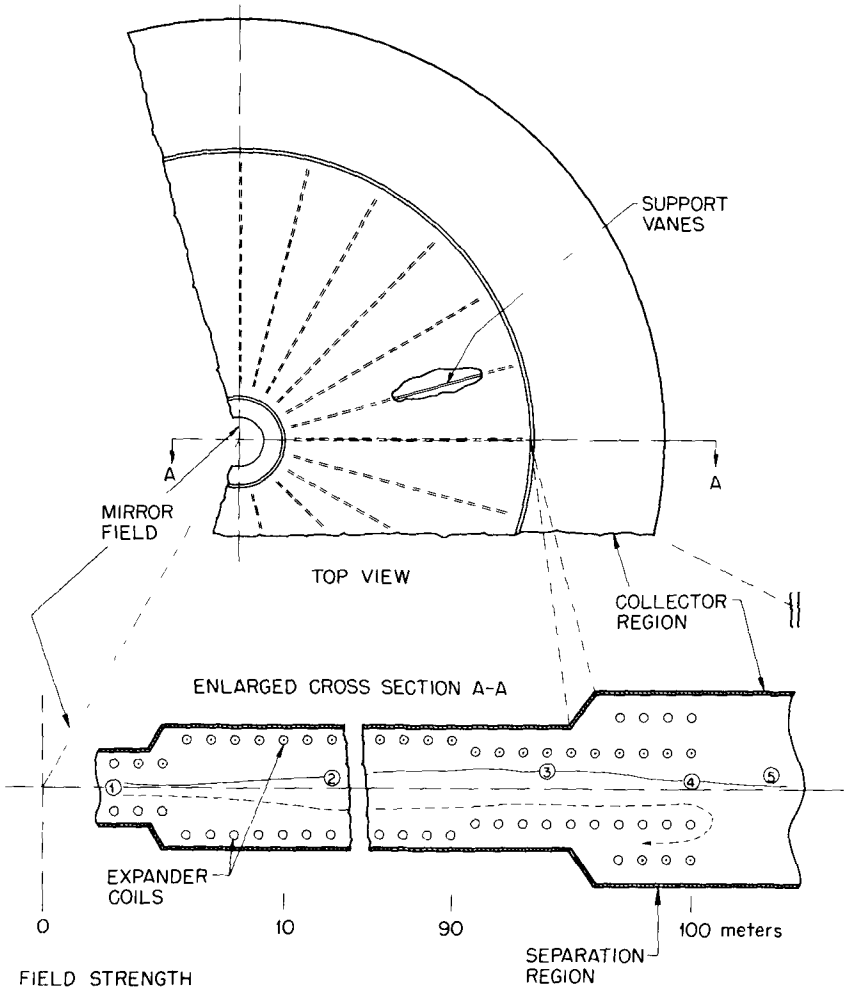

Fig. 7.63 — A possible expander–separator arrangement adapted from Post[97]. The large size — almost 200 m in diameter — of the expander section dwarfs the "disk"-type mirror machine. Detailed calculations indicate that the deuteron trajectory shown here results in the conversion of 478 keV out of an initial 500 keV into the desired parallel energy component. The rapid reversal of field lines at the end of the expander section effectively affords 100% separation of ions and electrons. Collector plates, not shown here, lie to the right of position 5.

and collected at that electrode whose potential lies nearest below the ion's initial energy." Once the specific ion energy distribution is known, the efficiency of such an arrangement can be easily analyzed by using methods developed in earlier chapters. Post shows that, for a reasonably large number of collectors (>10) and for typical mirror energy distributions, the ideal conversion efficiency of such an arrangement is approximately equal to $(1 - 1/N)$ where N is the number of collectors. His design used 25 collectors, giving an ideal efficiency of about 96%. In practice, this value will certainly be reduced by various losses neglected in the calculation, but it appears feasible to expect efficiencies of this order of magnitude. It is this high efficiency that makes the concept so attractive. (Such a high efficiency is not inconsistent with the earlier Coated-Plate Cell calculations. In contrast to, say, the Fission-Electric Cell, the present case offers the ideal of a parallel-beam source. Further, the disastrous losses associated with particle transport through a fuel layer are avoided.)

Instead of the magnetic-analyzer system illustrated earlier in Fig. 1.9(d) to separate the ion stream into discrete energy groups, Post suggests the use of a charge-exchange system or, alternately, a system that overfocuses the magnetic lenses. The former would take advantage of the rapid decrease with energy of the charge-exchange cross section of certain metal vapors like magnesium at energies higher than about 5 keV. Metallic-vapor streams would be maintained within the hollow collector electrodes so that any ion slowing to 5 keV would undergo charge exchange. The residual energy of the neutralized ion would be lost with the neutral particle; however, the low-energy positive ion would complete the current loop, giving a net conversion of the kinetic energy associated with the deceleration of the original ion from its initial energy (hundreds of kiloelectron volts) to 5 keV.

The alternate approach of overfocusing would utilize the energy-sensitive focusing characteristic of periodic electrostatic lenses. Low-energy particles would be overfocused, deflected sideways, and subsequently collected in the hollow electrodes.

It is important to note that the potentials involved in the collector are in the range of hundreds of kilovolts. This, along with the ability to use large-size units (high power densities are not a primary goal), should lessen voltage breakdown problems relative to many of the other cells discussed here where megavolt potentials and small spacings are involved.

Rather than attempt to transform to an ac output, Post suggests that an attractive approach would be to convert to a common dc potential for direct connection to a high-voltage dc transmission line. This is illustrated schematically in Fig. 7.64, where inverters are used to diminish all potentials from collectors above the desired value $\overline{V}$ and

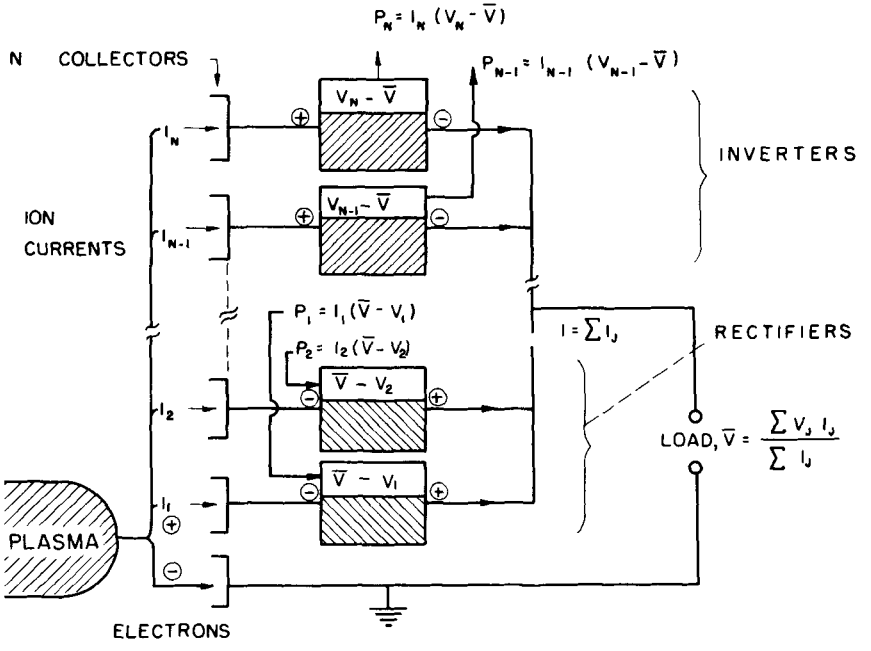

Fig. 7.64 — Schematic diagram of the rectifier–inverter circuitry proposed by Post[97]. The various collector voltages, V_N, V_{N-1}, ... V_1, are brought to an average value $\bar{V}$ through the inverter–rectifier bank. The power outputs P_N, P_{N-1}, ... from the inverters serve as the inputs (P_1, P_2, ..., etc.) to the rectifiers. As indicated, the resulting currents are summed prior to passing through the load at voltage $\bar{V}$. The result is high-voltage dc output.

rectifiers are employed to raise potentials from collectors below this value. The resulting currents are summed. If $\bar{V}$ is taken as the mean voltage of the collector system, the ac power from the inverters will be just sufficient to power the rectifiers. It is expected that such a system can be highly efficient, approaching 99%.

The various component efficiencies are summarized in Table 7.7. Although these values are probably optimistic, Post asserts that an overall efficiency in the range 90 to 95% should be feasible. The effect on overall plant efficiency can be seen from a topping cycle analysis similar to that of Appendix A-3.* If the 33% associated with charged particles in a D–D reactor is passed through a direct-collection unit of 90% efficiency and the remaining energy is processed through a 60% efficient thermal cycle, the overall plant efficiency is 70%, which

*The analysis of Appendix A-3 must be modified since, in contrast to Fig. 1.8, only a part of the energy flow Q now passes through the topping unit.

Table 7 7—SUMMARY OF ESTIMATED LOSSES FOR THE TEC*

	Losses
Expander	1%
Collector	3%
Inverter–rectifier	< 1%
Total	≈ 5%
Overall efficiency, 95%	

*From Post, Ref 97

represents an improvement of more than 16% over the all-thermal case. Even larger gains would be possible with a D–^{3}He reactor, where, as noted earlier, both reaction products are charged. Post has considered such a cycle in some detail, and he finds Q-values in the range of 4 to 19 for a 1000-MWe reactor.* (He also shows that satisfactory Q-values ranging from 5 to 15 are obtainable with direct conversion coupled with a D–T cycle that employs a breeding blanket and neutron-capture reactions to "multiply" the neutron energy; Q-values from 4 to 9 are found for a D–D cycle with reinjection of tritium from the D–D reaction and neutron-energy multiplication.)

Some important additional points made by Post are summarized as follows:

As repeatedly stressed here, unlike thermal plants, the efficiency of the Direct-Collection Cycle would depend on practical and economic factors rather than thermodynamic limits.

The large physical size of the expander and collector, combined with the high conversion efficiency, result in an extremely low heat dissipation per unit area. Thus, space charge, rather than heat removal, limits the maximum output power density.

A 1000-MWe reactor would typically involve an 800-keV ion current density of 400 μA/cm^2 at the expander exit, giving a charge density $\approx 2.6 \times 10^6$ ions/cm^3. This density would result in an average space-charge field of over 100 V/cm in the collector, leading to a several-kV potential difference between the midplane and edge of the ion stream. This space charge can be controlled by electrostatic focusing; however, difficulties will be encountered if it is necessary to operate on lower ion energies unless lower

*Although there is no general agreement as to the minimum Q-value that will lead to an economically competitive system, values well over 5 are generally sought.

power densities are also used. In some cases it might be advantageous to subdivide the magnetic flux in the expander so that "stacked" collector structures of reduced aperture could be used. Post shows that each subdivision results in roughly a fourfold increase in space-charge power-handling capacity. Alternately, operation of reactors below the 100-keV ion energy considered here would become more practical.*

Reactor operation at the relatively high ion energy (100 keV) assumed here requires a high β (plasma/magnetic pressure). Fortunately β values of 0.5 or higher appear feasible for mirror systems. Since the nuclear power density scales roughly as β/T_i, operation at $\beta = 0.5$ and $T_i = 300$ keV is roughly equivalent to $\beta = 0.05$ and $T_i = 30$ keV, which are typical for low β toroidal systems.

At the 1000-MWe reactor level, capital costs of about $11.50/kWe are estimated for the entire direct converter system including the inverter–rectifier units. This is quite low, reinforcing interest in the concept. In some cases it may be possible to reduce costs even further by using one (or two) direct converters to serve many individual mirror reactors.

The dominant elements in the cost are the large fan-shaped vacuum chamber enclosing the expander–collector structure, the coil system required to maintain the 500-G field through the expander, and the operation of the inverter–rectifier system.

In summary, it appears that application to a thermonuclear reactor may be quite important, but considerably more study is required to determine the most suitable system and all the ramifications. As Post concludes: "... adequately favorable power balances and potentially highly favorable capital costs should be possible for a fusion reactor system based on the combination of injection-fed mirror confinement zones coupled to a direct converter system. Depending on the fuel cycle chosen, the direct converter plays either a primary or a secondary role. In any event, efficient direct conversion would have a major favorable impact on the overall power balance situation for mirror systems."

*Because the charged particle densities involved in the other cells considered in this book are well below the space-charge limit, previous calculations and discussions neglected this effect. Thus application of these results to the TEC must be made with this limitation in mind.

7-8 SUMMARY

With the conclusion of this review, we are in a better position to appreciate the comments about the status of cell development introduced in Sec. 1-5.

It is clear that the direct-collection concept has had a significant impact in the areas of instrumentation and batteries. Six different types of radiation-detection cells, which are available commercially, were summarized in Table 1.4, and their applications are expected to expand, along with continued significant R&D programs, at several laboratories.

Batteries are also available commercially. Although this application represents a volume market, as indicated in Table 1.4, the features commonly stressed are not very demanding on actual cell performance. Simplicity, ruggedness, temperature independence, etc., imply mechanical requirements but have not forced an intensive research program. In fact, instrumentation requirements such as linearity, selective compensation against certain radiations, maximum sensitivity, etc., demand a more detailed understanding of basic processes. Thus, although battery applications would seem to be a logical springboard for research that might ultimately result in higher power devices, little momentum seems to be gathering through this route.

However, there are some bright points in battery applications: Both useful power production and high voltages have been successfully demonstrated. Further, the Linder–Christian battery demonstrated the ability to obtain good efficiencies (order of 20%) in actual devices.

This brings us to high-power devices. It is certainly risky to anticipate applications for such cells at this time. While single-cell applications have some unique advantages, the importance of possible combination cycles or topping units (Sec. 1-3.4) should not be overlooked. As summarized in Table 1.5, fairly detailed conceptual designs for Fission, Alpha, and Beta Cells have been encouraging, particularly for special applications like space propulsion, but attempts at experimental verification have only been partially successful. This appears to be a situation similar to that in other fields of endeavor (e.g., controlled thermonuclear reactors) where demanding technological advances are attempted in short periods of time. The first attempts to construct high-power devices were of a demonstration type. However, the rather serious problems encountered in this approach have made it necessary to fall back and concentrate on various fundamental aspects of the concept—the hope being that the information thus obtained can eventually be synthesized into a high-performance device.

The potential gain from using direct-collection methods with open-ended thermonuclear reactors has resulted in considerable interest and

effort in this direction. In fact, the USAEC has reported (CTR office *Newsletter* of Feb. 1970, released after composition of the "highlights" table in Chap. 1) that its Livermore group has measured efficiencies exceeding 90% in small-scale experiments. Of course, the ultimate fate of this cell and the time scale for its development are directly related to progress in overcoming confinement instabilities in the fusion device itself, and predictions are difficult to make for this. As stressed in Sec. 7-7, due to basic differences between the fusion reactor and other charged-particle sources, the Thermonuclear Cell will probably differ in many respects from other cells discussed here. Thus it is not clear how much "cross-fertilization" will occur during the development of these various cells, but success in one area may aid the others.

Finally, another aspect of the cells should be noted. The characteristic high-voltage, dc output has been a cause of some concern. However, an ac and dc high-voltage technology is slowly emerging in the power-engineering field. Thus, given an operational cell, the technology required to develop a useful power system is to some extent available.

In conclusion, we repeat again the comment that these concepts are only in their infancy. Most certainly their development will continue. The only question is How much and how fast? The present monograph is dedicated to assisting in the resolution of some of the problems facing the program.

REFERENCES

1. A Thomas, "Nuclear Batteries Types and Possible Uses, *Nucleonics, 13* 11, 129 (1955).
2. C. B Amphlett, "The Production of Electrical Power from Separated Fission-Products, *J Nuclear Energy, 1* 173 (1955).
3. E. G Linder, P. Rappaport, and J J. Lofershi, "The Direct Conversion of Radiation into Electrical Power, ' *Proc Internat Conf Peaceful Uses of Atomic Energy, 15,* pp 283-290, United Nations, New York, 1956.
4. W. Shorr, "Nuclear Batteries—A Survey, ' *Proc Internat Conf Peaceful Uses of Atomic Energy, 15,* pp. 310-316, United Nations, New York, 1956.
5. A. B Garrett, *Batteries of Today,* Chap. IX, Research Press, Inc , Dayton, Ohio, 1957.
6. C. K. Morehouse, R. Glicksman, and G. S. Lozier, "Batteries," *Proc of the IRE, 46* 8, 358 (1958).
7. W F. Windle, "Microwatt Radioisotope Energy Converters," *IEEE Transactions on Aerospace, 2* 2, 646 (1964).
8. W R. Corliss and D. G. Harvey, *Radioisotopic Power Generation,* Chap. 9, pp. 236-253, Prentice-Hall, Inc , Englewood Cliffs, N. J. (1964).
9. K. Von Schretzmann, "Uber die Direktumevandlung der Kinetischen Energie van Spaltbruchstrucken in Elektrische Energie," *Kerntechnik, 5* 9, 377 (1963)
10. J. Von Euler and A. Scharmann, "Die Erzeujung Elektrischer Energie mit Radionklidbatterien," *Kerntechnik, 5* 9, 385 (1963).
11. L E. Brownell, *Radiation Uses in Industry and Science,* pp. 145-156, USAEC, U. S Government Printing Office, Washington, D. C 1961.

12 S. W. Angrist, *Direct Energy Conversion,* pp. 395-402, Allyn and Bacon, Inc., Boston, 1965.
13. G. Safonov, "Direct Conversion of Fission to Electric Energy in Low Temperature Reactors," Rand Report RM-1870, The Rand Corp , Santa Monica, Calif., January 8, 1957
14. G. Safonov, "Direct Power Conversion, Part II, The Fission-Electric Reactor," ASTIA Document No. AD 14430, December 12, 1957.
15. E. P. Wigner, Chicago Memorandum N-1729, May 5, 1944.
16. R. W. Bussard and R. D. DeLauer, *Nuclear Rocket Propulsion,* Chap. 6, McGraw Hill, Inc., New York, 1958.
17. G. Safonov, "The Fission-Electric Cell Project (A Report on 1963 Operations), Final Report," USAEC Report TID-20575, March 1964.
18. A. Schock, "A Direct Nuclear Electrogenerator—Analysis of Cylindrical Electrode Configuration," Report AFOSR-TN-59-590, Fairchild Aircraft Corp , Engine Division, Deer Park, N. Y , June 15, 1959.
19. D. Kamke, "The Energy Spectrum of Fission Particles Leaving a Fuel Sheet," JPL Tech. Release No. 34-249, Jet Prop. Lab., Pasadena, Calif., January 9, 1961.
20. C. J. Heindl, "Comparison of Fission Electric Cell Geometries," JPL Tech. Report No. 32-101, Jet Prop. Lab., Pasadena, Calif., September 1, 1961.
21. C. J. Heindl, "Efficiency of Fission Electric Cells," JPL Tech. Report No. 32-105, Jet Prop. Lab., Pasadena, Calif., May 25, 1961.
22. C. J. Heindl, W. F. Krieve, and R. V. Meghreblian, "The Fission-Electric Cell Reactor Concept," *Nucleonics, 21* 4, 80 (1963).
23. J. N. Anno and S. L. Fawcett, "The Triode Concept of Direct Conversion," *Battelle Tech. Review,* p. 3 (Oct. 1962).
24. J. N. Anno, "A New Concept For Direct Conversion," *Proceedings, S W. Ohio Section, Vol. 1,* Am. Nucl. Soc., Hinsdale, Ill., September 1962.
25. J. N. Anno, "The Triode Concept of Converting Nuclear Energy Directly to Electrical Energy," Unpublished internal report, Battelle Memorial Inst., Columbus, Ohio, 1962.
26. J. L. Shapiro, "Improved Efficiency Calculations for the Fission-Electric Cell," JPL Space Prog Summary No. 37-27, Vol. IV, p. 138, Jet Prop. Lab., Pasadena, Calif., June 30, 1964, also No. 37-28, Vol. IV, p. 128, Aug. 31, 1964.
27. G. H Miley, "Fission-Fragment Transport Effects as Related to Fission-Electric-Cell Efficiencies," *Nucl. Sci. and Eng., 24* 322 (1966).
28. W. F. Krieve, "JPL Fission-Electric Cell Experiment," JPL Tech. Report No 32-981, Jet Prop. Lab., Pasadena, Calif., November 15, 1966.
29. J L. Shapiro, "The Two Region Fission-Electric Cell Reactor," JPL Tech. Report No. 32-685, Jet Prop. Lab., Pasadena, Calif., February 15, 1965.
30 J. L. Shapiro, "Design Study of a Fission-Electric Cell Reactor," JPL Tech. Report No 32-741, Jet Prop. Lab , Pasadena, Calif., August 1, 1965.
31. D. J. Mokski, "Fluid Systems Design Concept for a Large Gas-Cooled Fission-Electric Cell Reactor Space Power Plant," JPL Tech. Report No. 33-283, Jet Prop Lab., Pasadena, Calif., February 1, 1967.
32 P. H Miller, Jr., "A New Type of Electrostatic Generator," *Phys Rev , 69* 11 and 12, 666 (1946).
33. J. N. Anno, "A Direct-Energy Conversion Device Using Alpha Particles," *Nuclear News,* p 3 (December 1962).
34. A. M Plummer and J. N. Anno, "Battelle Studies on the Triode Concept of Direct Energy Conversion," *Proceedings, 1963 ASEE–AEC Summer Inst. on Direct Conversion,* P. Thiess (Ed.), Nucl. Eng Prog., University of Illinois, Urbana, Ill., January 1964.
35. A. M Plummer and J. N. Anno, "Conversion of Alpha Particle Kinetic Energy into Electricity," in Proceedings, AMU–ANL Conf. on Direct

Energy Conversion, November 1963, Report ANL-6802, pp. 170-180, Argonne Nat. Lab., Argonne, Ill., December 1963.
36. A. M. Plummer, W. J. Gallagher, R. G. Matthews, and J. N. Anno, "Alpha-Cell Direct-Conversion Generator," Report No. CR-54162, Battelle Memorial Inst., Columbus, Ohio, August 19, 1964.
37. A. M. Plummer, W J. Gallagher, R. G. Matthews, and J. N. Anno, "Alpha-Cell Direct-Conversion Generator," Report NASA-CR-54256, Battelle Memorial Inst., Columbus, Ohio, November 30, 1964. (Final Report for Contract NAS 3-2797.)
38. E G. Linder and S. M. Christian, "Use of Radioactive Material for Generation of High Voltage," *J. Appl. Phys , 23* 1, 65 (1953).
39. L. H. Bettenhausen and W. J. Gallagher, "An Alpha-Particle Voltmeter," *Nucleonics, 22* 6, 70 (1964).
40. A. J. Cohen and C. A. Low, Jr., "A Parametric Study of Direct Nuclear Electrogenerator Cells Using a Beta Emitting Source," Paper 63048-B, AIAA Electric Propulsion Conference, Colorado Springs, Colorado, March 1963.
41. W. R Michelsen and G. A Low, Jr., "Potentialities of the Radioisotope Electrostatic Propulsion System," Paper 63048-A, AIAA Electric Propulsion Conference, Colorado Springs, Colorado, March 1963.
42. W. R. Michelsen and C. A. Low, Jr., "Potentials of Radioisotope Electrostatic Propulsion," *Astronautics and Aerospace Eng.*, p. 52, (October 1963).
43. A. J. Cohen, "A Numerical Analysis of Direct Nuclear Electrogenerators Cells That Use Cerium-144 Beta-Emitting Radioisotope Sources," Report NASA-TN-D-2070, Lewis Research Center, Cleveland, Ohio, November 1963.
44. H. G. J. Moseley and J. Harling, "The Attainment of High Potentials by the Use of Radium," *Proc. Royal Soc. (London) A, 88* 471 (1913).
45. J. H. Coleman, "Nuclear Batteries," *Proc., Tenth Annual Battery R. and D. Conf.*, pp. 56-59, Power Sources Div., Ft Monmouth, N. J., May 1956.
46. J. H. Coleman, "Constant Current Charging Type Nuclear Batteries," *Proc., Eleventh Battery R. and D. Conf.*, pp. 106-108, Power Sources Div., Ft. Monmouth, N. J., May 1957.
47. J H. Coleman, "Nuclear Energy Sources," *Proc., 12th Annual Battery R. and D. Conf.*, pp. 108-110, Power Sources Div., Ft. Monmouth, N. J., May 1958.
48. P. Rappaport and E. G. Linder, "Radioactive Charging Effects With Dielectrics," *J. Appl. Phys., 24* 9 (1953).
49. J H. Coleman, "Radioisotopic High-Potential Low-Current Sources," *Nucleonics, 11* 12, 42 (1953).
50. *Raypak,* catalogue by Leesona Moos Laboratories, Jamaica, New York.
51. J. C. Guyot and G H. Miley, "Kr-85 Battery Experiment," in *Proc., 1963 ASEE–AEC Summer Inst. on Direct Conversion,* P. Thiess (Ed.), Nucl. Eng. Prog , University of Illinois, Urbana, Illinois, January 1964.
52. *Self-Powered Flux Detectors,* catalogue by Reuter–Stokes of Canada, Ltd., Preston, Ontario
53. J. W. Hilborn, "Self-Powered Neutron Detectors for Reactor Flux Monitoring," *Nucleonics, 22* 2, 69 (1964).
54. C. N. Jackson, Jr., "^{11}B Beta Current Thermal Neutron Flux Detector," Report BNWL-395, Battelle-Northwest, Richland, Washington, April 1967.
55. R. D. Evans, *The Atomic Nucleus,* Chaps. 23 to 25, McGraw-Hill, Inc., New York, 1955.
56 H. T. Sampson, "A Theoretical and Experimental Analysis of the Gamma-Electric Cell," Ph. D. Thesis, Nucl. Eng. Prog., University of Illinois, Urbana, Ill., August 1967.

57. I. M. Kloepper and V. A. Madsen, "Sensitivity of a Compton Detector," Report LA-1990, Los Alamos Sci. Lab., Los Alamos, New Mexico, September 1955.
58. B. Gross, "The Compton Current," *Zeitschrist fur Physik, 155* 479 (1959).
59. B. Gross, "Method and Apparatus for Measuring the Dosage of X-Rays and Gamma Rays," U. S. Patent 3,122,640, February 25, 1964.
60. B. Gross and P. V Murphy, "Electrical Irradiation Effects in Solid Electronics," *Nukleonik, 2* 7, 279 (1961).
61. B. Gross, "Compton Dosimeter for Measurement of Penetrating X-Rays and Gamma Rays," *Radiation Research, 14* 117 (1961)
62. B Gross and P. Murphy, "Solid-State Neutron–Gamma Dosimeter," in *Selected Topics in Radiation Dosimetry,* IAEA, Vienna, 1961.
63. B. Gross and P. Murphy, "Currents from Gammas Make Detectors and Batteries," *Nucleonics, 19* 3, 86 (1961).
64. B. Gross, "Gamma Radiation Induced Currents in Teflon," *Nukleonik, 6* 20 (1964).
65. B. Gross, A. Bradley, and A. P Pinkerton, "Beta Particle Transmission Currents in Solid Dielectrics," *J. Appl. Phys , 31* 6, 1035 (1960).
66 H. T Sampson and G. H Miley, "High Voltage Gamma-Electric Cell Operation," *Nuclear Applications, 5* 145 (1968).
67. B. Raab, "Power Producing Shield for Space Reactors," *Nucleonics, 21* 2, 46 (1963).
68. L. W. Nelms, "Induced-Voltage Studies in a Cobalt-60 Gamma Irradiator," Tech. Report WL-TR-64-149, Air Force Weapons Lab., Kirtland AFB, New Mexico, February 1965.
69. L. W. Nelms, "Study of Voltages Induced with 1300-Curie Cobalt-60 Irradiation and a 3-MW Nuclear Reactor," Tech. Report AFWL-TR-65-22, Air Force Weapons Lab., Kirtland AFB, New Mexico, March 1966.
70. J. L. Pigg, "Status Report on the Rover Dielectric Detector Program," EG&G Tech. Bulletin, Edgerton, Germeshausen and Grier, Inc., Las Vegas, Nevada, Oct. 1963. (Unpublished.)
71. E. L. Tolman, "O(s) S-10 Dielectric Compton Detector Development Report," EGG-1183-1174, Report No L-740, Edgerton, Germeshausen and Grier, Inc., Las Vegas, Nevada, October 15, 1965.
72. J. L. Pigg, "Energy Response of Dielectric Compton Detector," EG&G Tech. Bulletin TDS-T-001, April 26, 1966, Edgerton, Germeshausen and Grier, Inc., Las Vegas, Nevada, 1966.
73. P. L. Pigg, "Energy Response and Efficiency of Compton and Photoelectric Conversion Detectors," Tech. Memo L-161, EGG-1183-1252, Edgerton, Germeshausen and Grier, Inc., Las Vegas, Nevada, July 26, 1966.
74. W. C. Anderson and L. P. Hocker, "Preliminary Report, Photon Energy Response of the ON-11 Dielectric Detector," Edgerton, Germeshausen and Grier, Inc., Santa Barbara, California, 1966. (Unpublished.)
75. J. F. Artuso, "Accomplishments of Compton Studies Program, Fiscal Year 1965," EGG Tech. Report 1183-2043, No. S-295-R, Edgerton, Germeshausen and Grier, Santa Barbara, California, September 1965.
76. J. L. Pigg, "Reactor Compton Diode Detector," Report 6-105-01, Quarterly Progress Report, 2nd Quarter, Fiscal Year 1965, Edgerton, Germeshausen and Grier, Inc., Las Vegas, Nevada, 1965.
77. J. Stevens and J. F. Artuso, "Nuclear Studies of the Compton Diode, Fiscal Year 1966," Tech. Report No. S-349-R, EGG 1183-2110, Edgerton, Germeshausen and Grier, Santa Barbara, California, November 1966.
78. P. V. Murphy, "High Level Passive Radiation Monitor — The Solid Compton Recoil Electron Detector," First Quarterly Progress Report, U. S. Naval Radiological Defense Laboratory, Contract N0022866CO562, 15 April to 15 July 1966. Thermo Electron Eng. Corp., Waltham, Mass.

79. P V. Murphy, "High Level Passive Radiation Monitor — The Solid Compton Recoil Electron Detector," Second Quarterly Progress Report, U. S. Naval Radiological Defense Laboratory, Contract N0022866CO562, 15 July to 15 September 1966. Thermo Electron Eng. Corp., Waltham, Mass.
80. H. Hirakawa and Y. Mizumachi, "Electric Current due to γ-ray Irradiation," *Japanese J. Appl Phys., 5* 4, 305 (1966).
81. E. Hiraoka, "High Dose Detector for Gamma and X-Radiation Using Compton Scattered Electron," *Japanese J. Appl. Phys., 5* 4, 299 (1966).
82. G. H. Miley and H. T. Sampson, "Gamma-Electric Cell Theory and Experiment," *Proc., Internat. Conf on Energetics, University of Rochester, August 1965*, pp. 238-251, Am. Soc. Mech. Eng., New York, 1965.
83. S. Kronenberg, "High-Intensity Radiation Dosimetry with Semirad (Secondary-Electron Mixed-Radiation Dosimeters)," U. S. Army R and D Monograph Series No. 3, Ft. Monmouth, N. J., September 1966.
84. R. Hosemann and H. F. H. Warrikhoff, "Self-Powered Dosimeter for Gamma and X-Radiation," *Nucleonics, 22* 3, 51 (1964)
85. H. B. Almond and V. H Schmidt, "Electron Production and Transport in Electronic Materials in a Pulsed Nuclear Environment," Research Report D2-9878-3, Boeing Aircraft Corp., June 22, 1962
86. E Schwartz, "Secondary Emission Nuclear Battery," U. S. Pat. App , Ser. No. 434,095, June 2, 1954.
87. E. Schwartz, "Secondary-Emission Nuclear Battery," Report AD-66176, 1955. Also see p. 250, Ref. 8.
88. R. G. Saelens, "Tiny Gamma Detector for High-Intensity Radiation, Gamma Fields," *Nucleonics, 21* 3, 78 (1963).
89. S. Kronenberg, "Measuring Fast-Neutron Fluxes in Mixed Neutron–Gamma Fields," *Nucleonics, 21* 3, 78 (1963).
90. H M. Murphy, "Summary of Semirad Technical Aspects," Internal Report, Air Force Weapons Lab , Research and Technology Division, Biophysics Branch, Kirtland AFB, New Mexico, February 14, 1964.
91 D J Rose and M. Clark, Jr., *Plasmas and Controlled Fusion*, The M.I.T. Press, Cambridge, Mass., 1961.
92. S. Glasstone and R. H. Lovberg, *Controlled Thermonuclear Reactions*, D. Van Nostrand Company, Inc., Princeton, N. J., 1960.
93. B. J. Eastlund and W. C. Gough, "The Fusion Torch," USAEC Report WASH-1132, Division of Research, U. S. Atomic Energy Commission, U. S. Government Printing Office, Washington, D. C., May 15, 1969.
94. R. L. Hirsch (Ed.), "Perspectives on Controlled Thermonuclear Research," USAEC Report TID-24804, October 1968.
95. W. Peschka and S. Kelm, "High Temperature Energy Systems with Plasma Reactors and Inductive Magnetoplasmadynamic Converters," in *Electricity from MHD*, Symposium Proceedings, Warsaw, July 24–30, 1968, Vol. II, pp. 1133-1150, International Atomic Energy Agency, Vienna, 1968 (STI/PUB/191).
96. Thomas A. Oliphant, "Fuel Burnup and Direct Conversion of Energy in a D–T Plasma," *International Conference on Nuclear Fusion Reactors, Culham Laboratory, England, Sept 17–19, 1969*
97. R. F. Post, "Mirror Systems Fuel Cycles, Loss Reduction and Energy Recovery," *International Conference on Nuclear Fusion Reactors, Culham Laboratory, England, Sept. 17–19, 1969.* See also USAEC Report UCRL-71753, Lawrence Radiation Laboratory, Livermore, Calif., September 1969.

Blank Page

Appendix A

A-1 CURRENT AND POWER DENSITY ESTIMATES FOR DIRECT-COLLECTION CELLS

A-1.1 Fission-Electric Cell

The electrical current density J(V) in A/cm^2 of collector surface during operation at voltage V is:

$$J(V) = J_f \, q \, f_p(V) \tag{A.1}$$

where J_f is the fragment current [in particles/(cm^2 sec)] leaving the emitter and q is their charge (in coulombs) in multiples of the electronic charge e, cf. Eq. (3.2). The fraction of these fragments that overcome the potential barrier and reach the collector is denoted by $f_P(V)$.

$$J_f = (S_f \tau) \, f_r f_s = 2\bar{\Sigma}_f \phi_{th} \tau f_r f_s \approx 48.2 \, \phi_{th} \, \tau f_r f_s \tag{A.2}$$

where S_f represents the number of fragments born per cubic centimeter per second in the fuel layer of thickness τ and f_r and f_s give the fraction that escape capture in the fuel layer and support structure, respectively. The production rate S_f is simply twice the fission rate given by the fission cross section $\bar{\Sigma}_f$ times the thermal neutron flux ϕ_{th} [in neutrons/(cm^2 sec)]. The factor 2 enters because two fragments are emitted per fission. The other numerical values assume thermal fission of ^{235}U.

The thickness τ is a key variable. Clearly it should not be larger than the maximum range of the charged particle in the layer or particles born deep in the fuel will not be able to escape, and their kinetic energy will be converted to heat, which, in these cells, represents an energy loss. At the other extreme, as $\tau \to 0$, all particles escape the fuel layer and the efficiency is maximized, but the current and power densities approach zero. Thus, a compromise is required, and the optimum thickness will generally be smaller than the particle range. For the purposes of the present estimate, τ will arbitrarily be set equal to the range—about 10 μ for fission fragments in uranium metal. (Precise range correlations are presented in Chap. 3.) This gives an upper limit for current and power densities.

Using this τ in Eq. (A.2) and noting that $q \approx 20e$ for fission fragments (neglects charge neutralization, cf. Sec. 4-1.4), we find that

$$J(V) \approx 1.6 \times 10^{-19} \phi_{th} \; F(V) \tag{A.3}$$

where all three factors leading to particle losses have been lumped together into F(V), i.e.,

$$F(V) \equiv f_\tau f_s f_P(V). \tag{A.4}$$

A precise evaluation of F(V) depends on the cell geometry and operating voltage, but for the present calculation, an order of magnitude estimate is achieved by assuming infinite plane electrodes and an operating voltage of roughly 2×10^6 V. (This voltage selection follows the argument that an optimum efficiency will occur for a barrier about equal to half of the maximum value.)

Calculations in Appendix D (Fig. D.4) show that roughly 1/3 to 1/2 of the particles emitted from a fuel layer of thickness equal to the range will escape, i.e., $f_\tau \approx 1/3$. Since fission fragments are emitted isotropically, half the fragments will be emitted in the direction of the support plate, and, due to their short range, they will be stopped in it, which gives $f_s \approx 1/2$. It is shown in Chap. 2 that, of the remaining particles, approximately 1/3 will be able to overcome the 2-MV barrier and reach the collector (see Fig. 2.3), so that $f_P(V) \approx 1/3$. Combining these factors gives an approximate value for F(V) of 1/18.*

The thermal neutron flux will depend on the reactor power level (the cell is assumed to be a part of a nuclear reactor). For the present purposes an upper limit of 10^{14} neutrons/(cm^2 sec) will be used, and Eq. (A.3) then gives

$$[J(V)]_{V=2MV} \approx 0.8 \mu A/cm^2. \tag{A.5}$$

---

*This result is consistent with the calculation of the ideal-cell efficiency developed in Chap. 2, although the connection may not be obvious at first. This value of F(V) can be used to calculate a cell efficiency directly, in which case

$$\eta_c = \frac{(JV)_{out}}{(JV)_{in}} = \frac{V}{V_{max}} F(V) \approx 2.8\% . \tag{A.4a}$$

Alternately, Fig. 2.6 shows the ideal-cell efficiency η_c^* for isotropic emission to be $\approx 7.4\%$, and if this is corrected for fuel-layer losses using f_τ above, we obtain

$$\eta_c = f_\tau \eta_c^* \approx 2\ 5\% \tag{A.4b}$$

The difference between the results is simply due to the approximate values used here for f_τ and F(V).

This may appear to be an exceedingly low current density. Values quoted for nuclear–thermionic systems, for example, fall in the range of 1 to 10 A/cm^2 However, again it must be remembered that the Fission-Electric Cell produces millions of volts, whereas thermionic and similar devices produce only a few volts per unit.

These currents are, in fact, quite impressive relative to other high-voltage sources. This point is more obvious in terms of the total current that might be obtained from a typical reactor. The thermal power level P for a reactor is given by

$$P = C\,(\bar{\Sigma}_f \phi_{th})\,(A_s \tau) \tag{A.6}$$

where C represents the energy released per fission ($\approx$190 MeV), A_s is the fuel-layer surface area, and the other symbols have been defined previously.

Solving this equation for $\bar{\Sigma}_f \phi_{th} \tau$, substituting into Eq. (A.2), and using appropriate numerical values, we find

$$J(V) \approx 0.21 \left(\frac{P}{A_s}\right) F(V) \qquad A/cm^2 \tag{A.7}$$

where the power P is in megawatts thermal. Thus the total current is

$$i(V) \equiv J(V)\, A_s \approx 0.21 P\, F(V) \qquad A. \tag{A.8}$$

Again using $F(V) \approx 1/18$ and assuming a 100-MWt reactor (an average size power plant) gives $\approx$1.1 A. A current of this magnitude at 2×10^6 V is impressive, e g., it is several orders of magnitude larger than currents developed in conventional high-voltage sources such as the Van de Graaff generator.

The cell power density can now be evaluated. Assume that a gap spacing d on the order of 1 to 2 cm and a support plate thickness of 1 cm can be used. (The gap spacing requirement remains an open question. As discussed in Chaps. 6 and 7, these values are consistent with standard voltage breakdown correlations, but there is no information available about the possible effect of radiation on breakdown.) The resulting power density is then

$$[P]_{V \text{ cMV}} = \frac{J(V)\, V}{3 \text{ cm}} \approx \frac{1}{2} \qquad We/cm^3 \tag{A.9}$$

which is slightly lower than that obtained in conventional power reactors. For example, the pressurized-water Yankee power station[1] is rated at 136,000 kWe and has a 75.4-in.-diam. by 91.9-in -high core, equivalent to 5.2 We/cm^3.

However, the preceding calculation ignores one important aspect of the problem. Since the void fraction is large, the reactor will inherently have a large neutron leakage fraction, and a relatively large overall core volume will be necessary to achieve criticality. This requirement may, in fact, determine the power density, and then the calculations discussed in Chap. 7 predict power densities as much as an order of magnitude less than Eq. (A.9). This is still quite respectable, and, lest we become too concerned with these details, it is well to remember that there are many other aspects of the cell to be considered before its attractiveness can be fully evaluated; e.g., "Can the high-voltage low-current dc output be used effectively? Is it possible to capitalize on the non-thermal character of the cell and the fact that its efficiency is independent of temperature? Will radiation damage or gaseous fission product build-up limit the cell lifetime? What are overall system weights, efficiencies, etc.?" Such questions are discussed further in other chapters.

A-1.2 Radioisotopic Fueled Cells

The wide variations in decay rates, particle charge, energy, and range among various radioisotopes might lead one to expect correspondingly wide variations in cell characteristics for different fuels. While this is true for voltages, it turns out that current and power densities do not vary greatly. To illustrate this, two common isotopes, ^{90}Sr and ^{210}Po, which differ considerably in basic properties, are considered here.

Strontium-90 was the first fission product (yield $\approx 5.8\%$) available in a quantity sufficient for use in power sources. It was used in the SNAP-7 radioisotopic generator series, and more power has been delivered to date using it than from any other isotope[2]. It decays with a 28-year half-life via beta emission characterized by a maximum energy of 0.54 MeV. The daughter product, ^{90}Y, in turn decays by beta emission with $T_{max} = 2.26$ MeV and a 64.2-h half life. (The symbol T is used here and in succeeding sections to represent the kinetic energy associated with the various nuclear particles.) Thus the chain is

$$[^{90}Sr] \xrightarrow{28\ \text{years}} [^{90}Y] \xrightarrow{64.2\ \text{h}} [^{90}Zr]. \tag{A.10}$$

Since the ^{90}Y half-life is so short relative to that for ^{90}Sr, a "secular" equilibrium will occur[3]. That is, the decay rate of ^{90}Sr represents the limiting decay rate so that

$$\left(\frac{dN}{dt}\right)_{^{90}Y} \approx \left(\frac{dN}{dt}\right)_{^{90}Sr} = N_{Sr}\,\lambda_{Sr} \tag{A.11}$$

where N represents the number of atoms per cubic centimeter and λ is the decay constant (sec^{-1})

For optimum efficiency, the cell should operate at a voltage equal to $\approx 1/2$ of the maximum determined by the high energy ^{90}Y beta, i.e., at roughly 1/2 of (2.26), or 1 13 MV Then beta particles from the ^{90}Sr itself will have energy too low to reach the collector and only ^{90}Y will contribute to the conversion process. Its specific power can be found immediately because, with secular equilibrium*

$$P_{SP}(^{90}Y) \approx K \left(\frac{dN}{dt}\right)_{^{90}Sr} \langle T \rangle_{^{90}Y}$$

$$= \frac{(2.12 \times 10^3)(0.9)}{90(28)} = 0.76 \text{ W/g} \qquad \text{(A.12)}$$

where the average energy has been evaluated assuming that it is ≈ 0.4 T_{max} (Ref 3, p 537).

---

*Specific power, a term used in connection with radioisotopic generator design, is defined as power per unit weight due to radiations absorbed in a fuel layer composed of the pure radioisotope. Numerically it is related to the decay rate (dN/dt) by

$$P_{SP} = K \left(\frac{dN}{dt}\right) \langle T \rangle = \frac{2\ 12 \times 10^3 \langle T \rangle}{A T_{1/2}} \qquad \text{(A.11a)}$$

where K is a conversion factor to give proper units, $\langle T \rangle$ is the average energy (MeV) absorbed in the fuel per disintegration, $T_{1/2}$ is the half-life (years), and A is the atomic mass (g/mole) It is conventional to assume that 1/2 of the gammas emitted escape the fuel, so tabulations such as those given by Corliss and Harvey[2] use

$$\langle T \rangle = n_\alpha T_\alpha + n_\beta \langle T_\beta \rangle + \frac{1}{2} n_\gamma T_\gamma \qquad \text{(A.11b)}$$

where n_i gives the number of i*th* type particles emitted with energy T_i per disintegration. Beta emission involves an energy distribution, and hence an average value is used as indicated by the brackets.

We are not interested in the energy absorbed but rather the number of particles of a given type emitted, however, since P_{SP} is tabulated, it is often convenient to use it to calculate the emission rate given as

$$S_i = (P_{SP}\rho) \frac{n_i}{\langle T \rangle} \quad [i\text{*th* particles/(cm}^3 \text{ sec)}] \qquad \text{(A 11c)}$$

where ρ is the density of the isotope. In the present case, most of the energy is from beta emission so that

$$S_\beta \approx (P_{SP}\rho) \frac{1}{\langle T_\beta \rangle} \qquad \text{(A 11d)}$$

Next it is necessary to determine the particle range in the fuel layer since this will fix the fuel-layer thickness. A rough estimate, based on T_{max} and using the Katz–Penfold correlation (Fig. 3.12) discussed in Chap. 3 is

$$\lambda \approx \frac{1.3 \text{ g/cm}^2}{2.7 \text{ g/cm}^3} = 0.48 \text{ cm}. \tag{A.13}$$

The output current density can now be found; assuming a fuel-layer thickness equal to the range and using Eqs. (A.1), (A.11d), and (A.12), we find

$$J(V) \approx \frac{P_{SP}}{\langle T_\beta \rangle} (q\rho\lambda)\ F(V) = 0.06\ \mu\text{A/cm}^2 \tag{A.14}$$

where once again F(V) has arbitrarily been assigned a value of 1/18.

Since the operating voltage has been assumed to be 1.13 MV, the output power per square centimeter of emitter is

$$P_A = (6 \times 10^{-8})(1.13 \times 10^6) = 0.07 \text{ We/cm}^2. \tag{A.15}$$

Thus, a 2-cm plate separation with a 1-cm-thick support plate for the fuel layer would lead to a power density of about 2.3×10^{-2} We/cm^3.

While this output is an order of magnitude less than that calculated earlier for the Fission Cell, it is still quite respectable for radioisotopic generators. For example, the strontium titanate fueled SNAP-7A generator produced a maximum output of ≈ 12 W at 5 V via a lead telluride thermoelectric converter system[2]. The fuel-converter unit, shielding neglected, formed a cylinder approximately 23 cm in diameter by 20 cm high, which gives a power density of about 10^{-3} We/cm^3.

As a second example of a radioisotopic cell, consider one using ^{210}Po. This alpha emitter (5 MeV) is practically free of gamma emission and is characterized by a high specific power (141 W/g), a relatively short life (0.38 year), and a density of 9.4 g/cm^3. It was used[2] to fuel SNAP-3B, but has not found wide application because of its short half-life, expense, and relatively low melting point (254°C). Based on Fig. 3.6 of Chap. 3, the range of a 5-MeV alpha particle in polonium metal is found to be $\approx 10\ \mu$, and an analysis similar to that for ^{90}Sr gives a current density of $\approx 0.03\ \mu$A/cm^2 and a power density of about 2.5×10^{-2} We/cm^3 at 2.5×10^6 V, roughly the same order of magnitude as obtained for the ^{90}Sr cell. The seeming advantage of the larger power density is lost because the short alpha-particle range limits the fuel thickness. Note also that the particle energy dictates a somewhat higher voltage for efficient operation of the alpha cell vs the ^{90}Sr cell (2 vs 1.1 MV; other common β sources lead to even lower voltages, cf. Table 1.1)

Finally, it should be stressed that these calculations, as well as those for the Fission-Electric Cell, are only intended as order of magnitude estimates. There are many possible variations in geometry and construction that can result in either higher or lower outputs for a specific design. Also, as discussed in Ref. 2, there are various other isotopes that might be considered for fuel.

A-2 CURRENT AND POWER DENSITY ESTIMATES FOR A REACTOR—IONIZATION-ELECTRIC CELL

The cell current density involves the product of three factors: the fragment current, the number of ion pairs produced per fragment, and the net fraction of the ion pairs originally formed that are successfully separated and reach the proper collection electrodes; thus, the output current density $J(V_L)$[A/cm^2] for a cell with operating load voltage V_L is given by

$$J(V_L) \approx (J_f q) \frac{\langle T_f \rangle}{Wq/e} f_c(V_L)$$

$$\equiv (i_f)\,(M_f)\, f_c(V_L) \qquad A/cm^2 . \tag{A.16}$$

Here, J_f represents the fragment particle current leaving the uranium fuel. Multiplication of it by the charge q (coulombs) gives the equivalent fragment electrical-current density i_f (A/cm^2). The average fragment energy $\langle T_f \rangle$ divided by the average energy requirement per ion pair W and by the units of fragment charge q/e gives the multiplication of the fragment current due to ion pair production. This is denoted as M_f. Finally, $f_c(V_L)$ represents the fraction of ion pairs produced that contribute to the output current. It corrects for losses such as recombination or diffusion to the wrong electrode or out the sides of the cell. Such losses are strongly dependent on the operating voltage V_L and the inherent potential $\Delta\phi$, which determine the internal electric field. The internal field sets the rate at which charged particles can be "swept out" of the gas volume: The larger this rate, the shorter the residence time; hence, the lower the recombination probability, and vice versa.

If the fission fragment current selected earlier for the Fission-Electric Cell calculations [8×10^{11} fragments/(cm^2 sec)] is used, Eq. (A.16) predicts a current density equal to

$$J(V_L) \approx (2.6 \times 10^{-6})(1.33 \times 10^5)\, f_c(V_L) = 0.35\, f_c(V_L) \qquad A/cm^2 . \tag{A.17}$$

The current multiplication is seen to be considerable, and, in fact, if perfect separation and collection of the ion pairs could be achieved

$[f_c(V_L) = 1.0]$, a surprisingly large current density (0.35 A/cm^2) would be obtained. Since work function differences of the order of 1 V are obtainable,* the power density from a cell having 1-cm-thick electrodes with an 11-cm spacing would be a respectable 2.7×10^{-2} We/cm^3. Two obvious questions arise: Will $f_c(V_L)$ approach unity in practice? Why not increase the power density by simply increasing the gas pressure? Actually, both points reduce to questions about recombination and diffusion losses, and a crude estimate of $f_c(V_L)$ will illustrate this.

Neglecting diffusion due to concentration differences and assuming that the current can be described solely by a mobility of the ions and electrons in the internal electric field, the net ion current through the gas is given by[6] (for singly ionized species so q = e)

$$J^+(V_L) \approx [n^+ \mu^+ E(V_L)]e \tag{A.18}$$

where n^+ is the ion density (ions/cm^3), μ^+ is the ion mobility [cm^2/(V sec)], and $E(V_L)$ is the electric field present during operation at voltage V_L. A similar expression can be written for electrons; however, the ions move much more slowly, and the ability to sweep them out of the gas generally limits the current that can be drawn so that

$$J(V_L) \approx J^+(V_L). \tag{A.19}$$

The pressures assumed here should result in relatively low diffusion losses so that the dominant loss mechanism for ions will be recombination. Then, if we assume a neutral plasma ($n^+ \approx n^-$), the ion loss–source balance is simply

$$\alpha_c (n^+)^2 = S_V \approx J_f \frac{\langle T_f \rangle}{Wd} \tag{A.20}$$

where α_c is the volume recombination coefficient and S_V, the ion pair source rate [pairs/(cm^3 sec)], has been estimated from the fragment current J_f. A uniform energy loss across the gap d is assumed.

Next, $E(V_L)$ must be related to V_L. This raises some involved questions about space charge and sheath effects. For the moment, we will ignore these problems and simply assume a linear potential variation across the entire inter-electrode space, in which case

*For example, Ohmart[4] used an Al_2O_3 negative electrode and obtained $\Delta\phi$ = 1.34 V with a positive electrode having PbO_2 plated on gold, 0.98 V with oxidized copper, 0.67 V with silver, etc. Thomas and Ragosine[5] report $\Delta\phi \approx 1.6$ V for an aluminum and a platinum-sputtered aluminum combination.

$$E(V_L) \approx \frac{\Delta\phi - V_L}{d} . \tag{A.21}$$

Now, combining Eqs. (A.19) through (A.21) gives

$$J(V_L) \approx eS_V d \left[\frac{\mu^+}{\sqrt{\alpha_c S_V}}\left(\frac{\Delta\phi - V_L}{d^2}\right)\right]$$
$$\equiv (eS_V d)\, f_c(V_L) \tag{A.22}$$

where $f_c(V_L)$ is identified with the bracketed quantity by comparison with Eq. (A.16). Alternately, note that $(eS_V d)$ is simply the charge associated with the ion production rate over the total volume, so the remaining factor must represent the fraction of these ions that actually contributes to the current.

If, for the helium cell, rough values for μ^+, α_c, and $\Delta\phi - V_L$ of 10 $cm^2/(V\ sec)$, 10^{-9} cm^3/sec, and 1 V, respectively,[7] are inserted in Eq. (A.22), $f_c(V_L)$ turns out to be about 1.4×10^{-5}, indicating that the original current and power density calculations should be reduced by five orders of magnitude.*

Several methods might be considered in an attempt to reduce recombination losses. The selection of the gas is obviously of prime importance, and optimization of the pressure, temperature, ion production rate, and plate spacing might also be considered.

Some insight into pressure effects can be obtained by noting that to a first approximation $\mu^+ \propto p^{-1}$, $S_V \propto p$, $\alpha_c \propto p$, and, assuming the spacing is maintained at the source particle range,† $d \propto \lambda_q \propto p^{-1}$. Insertion of these relations in Eq. (A.22) predicts that $f_c(V_L)$ should be independent of pressure.

The pressure dependence of the parameters assumed here is only approximate, as is Eq. (A.22) itself In reality, $f_c(V_L)$ may vary some-

*This result will not be surprising to those who are familiar with ion chamber operation. Chambers are designed to avoid recombination so that their response will be linearly dependent on S_V, which is in turn proportional to neutron flux. This is accomplished by using a battery to obtain sweeping voltages as high as 1 kV over several centimeters. Even so, most ion chambers turn out to be nonlinear in the high fluxes assumed in this example, and it is clear that the few-volt internal fields in the Ionization-Electric Cell are far too low to prevent recombination. However, as argued earlier, an external bias voltage cannot be used since this results in a net input of energy, and this presents a dilemma

†The present discussion assumes that particles originate at one electrode and then enter the gas volume. An alternate possibility, which would give more freedom in the selection of plate spacing, would be to locate the source on a portion of the insulator separating the electrodes This would be particularly attractive if an external source were used, in which case we would be, in effect, considering parallel vs perpendicular incidence relative to the electrodes.

what with pressure, but this effect would not appear to be large enough to solve the problem. Thus, the pressure would probably be selected so that a reasonably small spacing could be used without significantly reducing the fraction of the incident radiation absorbed.

Temperature effects might be considered next, but they are more difficult to evaluate. Actually, the easiest solution is to reduce the ion pair production rate by reducing the radiation source intensity. This lowers the ion–electron concentrations and, thus, reduces the recombination rate; e.g., if, in the present helium cell example, S_V is decreased by a factor of 10^9 [corresponding to $\phi \approx 10^5$ neutrons/(cm^2 sec)], Eq. (A.22) predicts $f_c(V_L) \approx 0.4$. (It might appear that further reduction in S_V could lead to values of $f_c(V_L) > 1.0$, but this is obviously not allowed. At very low ion–electron densities, the assumption that recombination losses dominate is no longer valid; thus, Eq. (A.22) fails.)

While this reduction of S_V appears to solve the recombination problem (diffusion losses must still be considered), the obvious disadvantage is that the output current is drastically reduced. In the present example, according to Eq. (A.22), $J(V_L)$ drops to $\approx 1.4 \times 10^{-10}$ A/cm^2, and it is clear that the improved efficiency is obtained at the expense of the current and power density.

The specific values calculated here should not be taken too seriously since many rough estimates and approximations have been used and no attempt was made to optimize the design. Still, this does illustrate some of the significant parameters, and, at the same time, it vividly illustrates how the ability to separate and collect the ion pairs represents a serious limitation for Ionization-Electric Cell operation.

A-3 TOPPING CYCLE EFFICIENCIES

As an example of topping cycle efficiencies, consider the use of a nuclear cell of efficiency η_0 as a topping unit on a turbogenerator unit of efficiency η_{23} (this nomenclature follows Fig. 1.8). The resulting overall efficiency η follows directly from the flows indicated in Fig. 1.8 and is

$$\eta = \frac{Q(1 - H_{23} H_0)}{Q} = \eta_0 + \eta_{23} (1 - \eta_0). \tag{A.23}$$

Thus the ratio of this efficiency to that for the turbogenerator alone is

$$\frac{\eta}{\eta_{23}} = 1 + \eta_0 \left(\frac{1}{\eta_{23}} - 1 \right). \tag{A.24}$$

A plot of η/η_{23} is shown in Fig A.1. It is interesting to note that as long as the conventional turbogenerator–steam plant efficiency is below 50%, the increase in plant efficiency is greater than the efficiency of the topping plant alone. For example, a PWR nuclear–steam cycle is about 35% efficient, so a 10% efficient nuclear–direct topping unit will increase the overall plan efficiency by 19%—almost double the efficiency of the topping unit. (Note, however, that the efficiencies are not additive; e.g., in this case the overall efficiency with topping is

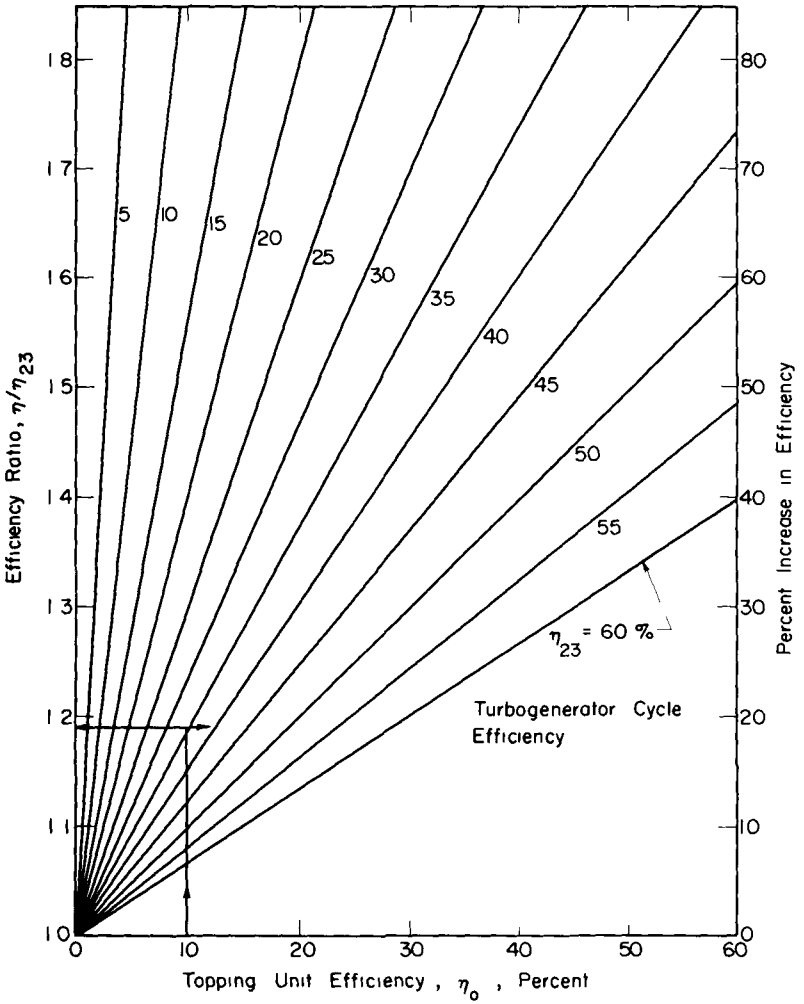

Fig. A 1—Increased efficiency due to topping.

1.19×35 or 41.6%, whereas the sum of the individual unit efficiencies is 45%.)

However, the full significance of a topping unit is best understood if we consider the practical situation where the output-power demand is set at a fixed level, which must be supplied by either the turbogenerator unit or the combination topping plant.

To study this situation, we need to rearrange Eq. (A.23) somewhat. Since generally

$$Q = \frac{\text{energy output}}{\eta} \tag{A.25}$$

if the output is fixed, the fractional reduction in input energy due to the addition of a topping unit is simply

$$\frac{Q_{23} - Q}{Q_{23}} = 1 - \frac{\eta_{23}}{\eta}. \tag{A.26}$$

Here Q is subscripted to indicate that it will be different in the two cases; i.e., Q_{23} represents the input for the turbogenerator alone, whereas Q is for the combination unit. For the previous PWR example, the addition of a 10% topping unit reduces the energy input requirement by $\approx 16\%$, possibly representing significant savings in fuel charges. Again, the effect of the topper is magnified if $\eta_{23} \gtrsim 50\%$ ($\eta_0 \gtrsim 20\%$).

Finally, consider the heat dump. The fractional reduction in heat rejection for the fixed output is

$$\frac{Q_{23}H_{23} - QH_{23}H_0}{Q_{23}H_{23}} = 1 - \frac{\eta_{23}}{\eta}(1 - \eta_0). \tag{A.27}$$

This result is shown in Fig. A.2 for various steam cycle efficiencies. Again, using the example of a PWR, the reduction in the heat that must be rejected is 24% with a 10% efficient topping unit. Advantage may be taken of this to reduce the condenser or cooling tower load, or if the heated exhaust goes directly into a stream or lake, the possibility of thermal pollution[8] would be reduced.

In summary, direct topping has a significant effect on the heat rejection and on fixed costs of turbo machinery and condensers. These two factors coupled with the reduction in fuel inventory may make such devices attractive, not only for space applications but also for central power stations.

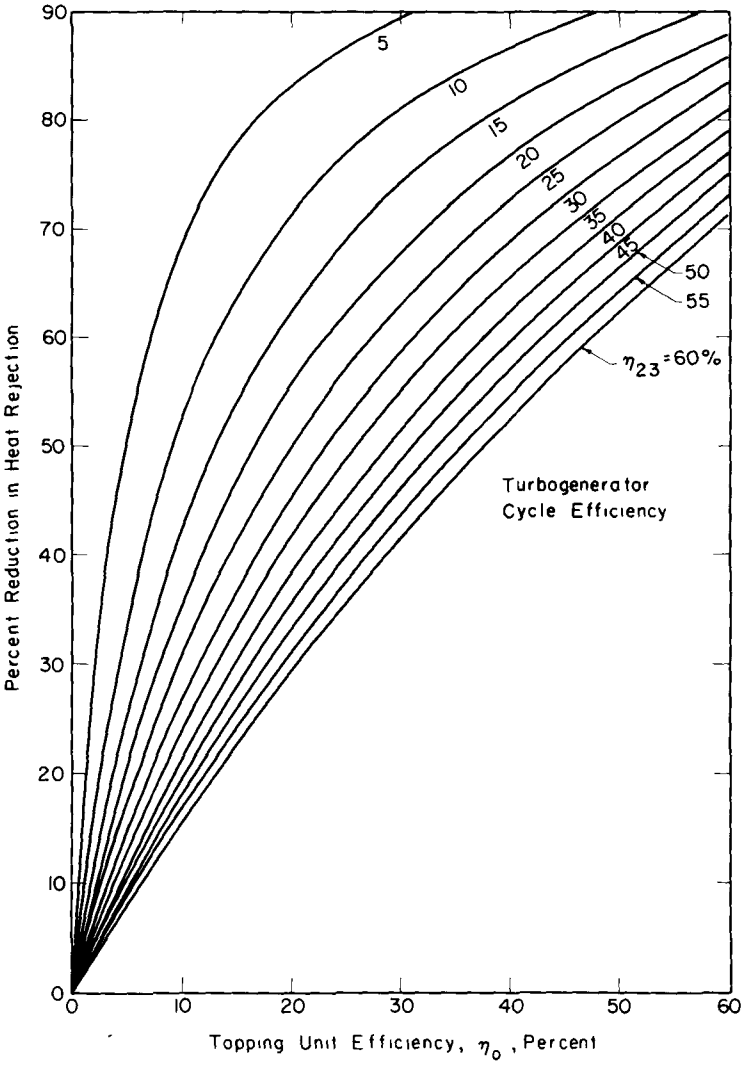

Fig. A.2 — Reduction in heat rejection due to topping.

REFERENCES

1. Nucleonics Reactor File, No 9, "Yankee," *Nucleonics, 19* 58 (March 1961).
2 W. R Corliss and D. G Harvey, *Radioisotopic Power Generation,* Prentice-Hall, Inc., Englewood Cliffs, New Jersey, 1964.
3. R D. Evans, *The Atomic Nucleus,* p. 484, McGraw-Hill, New York, 1955.
4 P. E Ohmart, "Method and Apparatus for Converting Ionic Energy into Electrical Energy," *J. Appl. Phys., 22* 1504 (1951).
5. A. Thomas and V. Ragosine, "Investigations on Utilization of Radioactivity Energy as a Source of Battery Power," 2nd Quarter Progress Report, DA-36-039 SC-42549, Tracerlab, Waltham, Mass , 1953
6. J. D. Cobine, *Gaseous Conductors,* pp. 53-55, Dover Publications, Inc., New York, 1941. Also note Sec. 6.3, p. 128.
7. S. C. Brown, *Basis Data of Plasma Physics,* p. 77 and pp. 195-197, M. I. T. Press and John Wiley & Sons, New York, 1959.
8. J. R Clark, "Thermal Pollution and Aquatic Life," *Scientific Am., 220* 19 (1969)

Appendix B

B-1 CONSERVATION EQUATIONS FOR CHARGED-PARTICLE MOTION IN ELECTRIC FIELDS

B-1.1 The Equation of Motion

The force on a unit positive charge in an electric field is, by definition, the electric-field intensity $\vec{E}$ at that point. Consequently, the force on a particle with charge +q is

$$\vec{F} = q\vec{E}. \tag{B.1}$$

The field $\vec{E}$ is the sum of the space-charge field $\vec{E}_\rho$ (due to the charged-particle density) and the applied field $\vec{E}_V$ (due to the potential across the device's electrodes), or

$$\vec{E} = \vec{E}_\rho + \vec{E}_V = \vec{E}_\rho - \nabla V. \tag{B.2}$$

The charged-particle density in the devices of interest here is generally small enough so that $\vec{E}_\rho$ can, to a good approximation, be neglected relative to $\vec{E}_V$. (As discussed in Chap. 7, the major exception where space-charge effects become important is the Thermonuclear Cell.) Then, according to Newton's second law of motion, it follows that

$$q\vec{E} = \frac{d}{dt}m\vec{v} = m\frac{d\vec{v}}{dt} + \vec{v}\frac{dm}{dt} \tag{B.3}$$

where the term involving dm/dt allows for a relativistic effect. Generally a relativistic correction is important only in cells involving high-energy electrons. It has been neglected in previous cell calculations except for Cohen's analysis of a Beta Cell[1] and Schock's analysis of secondary electrons accelerated during high-voltage operation of a Fission-Electric Cell[2]. (Relativistic effects are included in Sec. 2-3.2.)

Since we are not interested in detailed trajectory analyses, we now turn to conservation equations.

B-1.2 Conservation Equations

(a) Energy

The work done in moving the charged particle from point A to point B in the field $\vec{E}$ is

$$ {}_{A}W_{B} = \int_{A}^{B} \vec{F} \cdot d\vec{S} \tag{B.4} $$

where the scalar product is used to select the component of $\vec{F}$, which lies along the increment of path $d\vec{S}$ (see Fig. B.1).

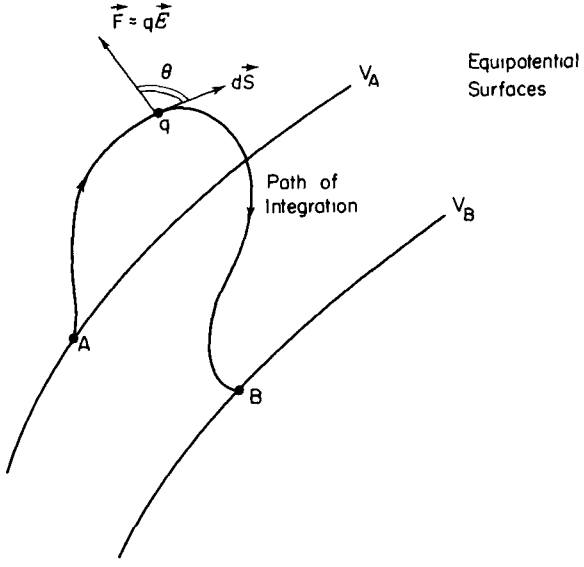

Fig. B 1 — The work performed in moving a charged particle in an electric field.

Substitution of Eqs. (B.1) and (B.2) into this expression gives

$$ {}_{A}W_{B} = q \int_{A}^{B} \vec{E} \cdot d\vec{S} = -q \int_{A}^{B} dV = q(V_A - V_B). \tag{B.5} $$

This result depends only on the beginning and end points, not on the specific path (the definition of a conservative force). For an electron, q is equal to $-e$, so the potential energy *given up* by an electron in going from point A to B is $(V_B - V_A)$ eV.

Next, we relate this expression for work to the change in kinetic energy of the particle. Using Eqs. (B.3) and (B 5), we find

$$ {}_{A}W_{B} = \int_{A}^{B} \vec{v} \cdot d(m\vec{v}) = \int_{v_A}^{v_B} m\vec{v} \cdot d\vec{v} + \int_{m_A}^{m_B} v^2 \, dm. \tag{B.6} $$

The relativistic mass $m(v)$ is given by

$$ m(v) \equiv m_0 \left[1 - \left(\frac{v}{c}\right)^2\right]^{-1/2} \tag{B.7} $$

where m_0 is the particle's rest mass and c is the speed of light in vacuum (a good summary of relativistic relations is given in Appendix D of Ref. 3). If this expression is used for m in Eq. (B.6), we find that

$$ {}_{A}W_{B} = m_0 c^2 \left\{\left[1 - \left(\frac{v_B}{c}\right)^2\right]^{-1/2} - \left[1 - \left(\frac{v_A}{c}\right)^2\right]^{-1/2}\right\} \equiv E_B - E_A \tag{B.8} $$

where E_j is the *total energy* (kinetic *plus* mass equivalent) i.e., it is defined as

$$ E_j \equiv m(v_j)\, c^2. \tag{B.9} $$

Combining Eqs. (B.5) and (B.8), we obtain the law governing energy conservation in an electric field

$$ q(V_A - V_B) = [m(v_B) - m(v_A)]c^2 \tag{B.10} $$

where $m(v_j)$ refers to the relativistic mass [Eq. (B.7)] corresponding to the speed at point j. For $v/c \ll 1$, relativistic corrections can be neglected so

$$ \begin{aligned} m(v)\, c^2 &\equiv m_0 c^2 \left[1 - \left(\frac{v}{c}\right)^2\right]^{-1/2} \\ &= m_0 c^2 \left[1 + \frac{1}{2}\left(\frac{v}{c}\right)^2 \ldots\right] \\ &\approx m_0 c^2 + \frac{1}{2} m_0 v^2. \end{aligned} \tag{B.11} $$

This represents the sum of the rest-mass energy equivalent and the kinetic energy associated with the rest mass. Energy conservation then reads

$$ q(V_A - V_B) = \frac{1}{2} m_0 v_B^2 - \frac{1}{2} m_0 v_A^2 = T_B - T_A \tag{B.12a} $$

where $T_{\vec{r}}$, the *kinetic energy* at location $\vec{r}$, is found from Eq. (B.9) to be

$$ T_{\vec{r}} \equiv (E_{\vec{r}} - m_0 c^2) = [m(v_{\vec{r}})c^2 - m_0 c^2]. \tag{B.12b} $$

(b) Linear Momentum

It must be remembered that Eq. (B.3) is a vector equation; hence, if the force component in any direction (say x_1) is zero, we have

$$\frac{d}{dt} m v_{x_1} = 0 \qquad (i = 1, 2, \text{ or } 3) \tag{B.13}$$

so that

$$m v_{x_1} \equiv p_{x_1} = \text{constant.} \tag{B.14}$$

(c) Angular Momentum

Both spherical and cylindrical electrodes are of interest and both geometries require the use of angular-momentum equations.

The spherical case is most straightforward in that it represents a central-force problem where the magnitude of the force depends only on the distance between the particle and the center of the sphere, and its direction lies along this radius. For such cases, it can be shown directly from Newton's second law (Eq. B.3) that the angular momentum $\vec{L}$ is constant since

$$\vec{F}(\vec{r}) = |\vec{F}(\vec{r})|\frac{\vec{r}}{r} = \frac{d}{dt}(m\vec{v}) = m\frac{d\vec{v}}{dt} + \vec{v}\frac{dm}{dt} \tag{B.15}$$

where

$$r = |\vec{r}| = (x^2 + y^2 + z^2)^{1/2} \tag{B.16}$$

and the particle is at $\vec{r}$. But, by definition, the velocity is

$$\vec{v} = \frac{d}{dt}\vec{r} \tag{B.17}$$

so that

$$F(\vec{r}) = m\left(\frac{d^2\vec{r}}{dt^2}\right) + \left(\frac{d\vec{r}}{dt}\right)\left(\frac{dm}{dt}\right). \tag{B.18}$$

Cross multiplying this vectorially by $\vec{r}$, we find

$$\left[m\vec{r} \times \frac{d^2\vec{r}}{dt}\right] + \left[\vec{r} \times \left(\frac{d\vec{r}}{dt}\right)\left(\frac{dm}{dt}\right)\right] = 0 \tag{B.19}$$

since $(\vec{r} \times \vec{r})$ is zero. But, since

$$\left(\frac{d\vec{r}}{dt}\right) \times \left(\frac{d\vec{r}}{dt}\right)$$

is also zero, Eq. (B.19) may be rewritten to give

$$\frac{d}{dt}\left(\vec{r} \times m\frac{d\vec{r}}{dt}\right) = \frac{d}{dt}(\vec{r} \times m\vec{v}) = \frac{d}{dt}(\vec{r} \times \vec{p}) = \frac{d\vec{L}}{dt} = 0 \qquad \text{(B.20)}$$

which proves that the angular momentum vector $\vec{L}$ is constant. Since $\vec{L}$ lies in a plane perpendicular to the one containing $\vec{r}$ and $\vec{p}$ (see Fig. B.2), the motion itself occurs in a single plane.

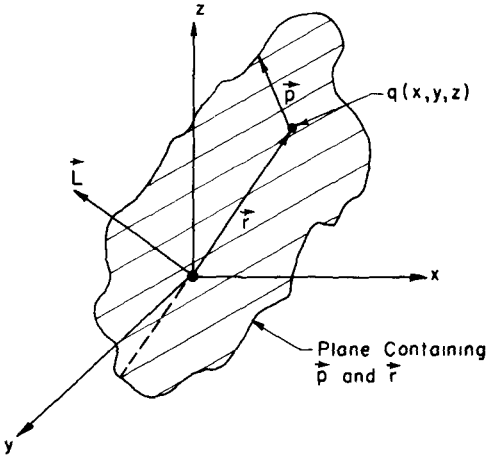

Fig. B.2—Angular momentum in spherical geometry.

One must be careful in problems involving cylindrical electrodes. Practical devices will generally have a large length to diameter ratio, but a cylinder of infinite length is considered here. The geometry is shown in Fig. B.3. The charge q is located at a point with coordinates $(\vec{R},z)$ and has velocity $\vec{v}$. We first resolve $\vec{v}$ into two components, v_z and $v_\perp$, such that $v_\perp$ is in a plane perpendicular to the z-axis. The angular momentum $\vec{L}_\perp$, defined relative to the z-*axis*, is

$$\vec{L}_\perp \equiv \vec{R} \times \vec{p}_\perp = \vec{R} \times m\vec{v}_\perp. \qquad \text{(B.21)}$$

Now, since the field is dependent only upon $\vec{R}$, the same arguments as used for a central force field may be applied, and

$$\vec{L}_{\perp} = \text{a constant vector.} \tag{B.22}$$

Referring to Fig. B.3, we see that

$$|\vec{L}_{\perp}| = Rmv_T = Rm|\vec{v}| \cos \psi \sin \phi = \text{constant} \tag{B.23}$$

where the tangential velocity component v_T is defined in the figure and the direction of $\vec{L}_{\perp}$ is parallel to the z-axis.

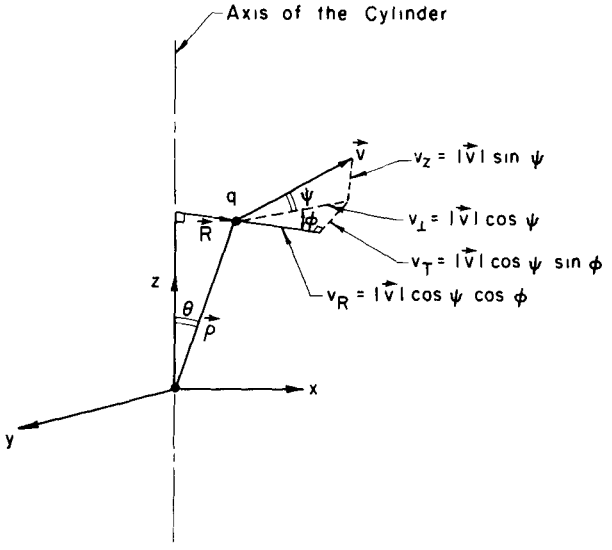

Fig. B.3 — Cylindrical coordinates.

REFERENCES

1. A. J. Cohen, "A Numerical Analysis of Direct Nuclear Electrogenerator Cells That Use Cerium-144 Beta-Emitting Radioisotope Sources," Report NASA-TN-D-2070, NASA Lewis Research Center, November 1963.
2. A. Schock, "A Direct Nuclear Electrogenerator — Analysis of Cylindrical Electrode Configuration," Report AFOSR-TN-59-590, Air Force Office of Scientific Research, 1959.
3. R. D. Evans, *The Atomic Nucleus*, McGraw-Hill, New York, 1955.

Appendix C

C-1 CALCULATION OF THE FISSION FRAGMENT ENERGY DISTRIBUTION

Nuclear fission has traditionally been visualized in terms of the liquid drop model[1]. The entrance of a neutron into the drop supplies excess energy, and it splits despite restoring forces represented in the analogy by surface tension. As the fragments separate, momentum will be conserved; i.e.,

$$M_1 v_{01} = M_2 v_{02} \tag{C.1}$$

or, in terms of kinetic energy T, this reduces to

$$M_1 T_{01} = M_2 T_{02}. \tag{C.2}$$

The subscript 0 indicates the initial state immediately after fission; 1 indicates the heavy fragment and 2 the light fragment.

Also the sum of the fragment energies equals the total kinetic energy released T_{0T}, or

$$T_{01} + T_{02} = T_{0T}. \tag{C.3}$$

Experimental data can be used to evaluate T_{0T} or, as a first estimate, it can be calculated assuming that the fragments are forced apart due to their charge, giving

$$T_{0T} \approx \frac{e^2 Z_1 Z_2}{r_1 + r_2} = \frac{e^2 Z_1 Z_2}{R_0 (A_1^{1/3} + A_2^{1/3})} . \tag{C.4}$$

This assumes that, immediately following fission, the fragment nuclei are touching and spherical in shape, and their radii r have been estimated using the classical expression (Ref. 2, p. 30)

$$r \approx R_0 A^{1/3} = (1.2 \times 10^{-13}) A^{1/3} \tag{C.5}$$

where R_0 is the nuclear unit radius and A is the mass number.

The use of Eq. (C.4) generally gives a value of T_{0T} about 20% larger than that observed experimentally (Ref. 2, p. 387).

Assuming T_{0T} is known, we can solve Eqs. (C.2) and (C.3) for T_{01} or T_{02} in terms of the mass ratio, giving

$$\frac{T_{01}}{T_{0T}} = \frac{M_2}{M_1 + M_2}. \tag{C.6}$$

But the masses are related by

$$M_1 + M_2 = M_U - \left(\nu M_n + \Delta M_B\right) \tag{C.7}$$

where subscript U designates the fissioning nucleus (e.g., uranium), n designates a neutron, ν represents the number of neutrons emitted, and ΔM_B is the mass defect due to the change in binding energy. (Note: M_U must include the added neutron in the case of neutron bombardment.) There is a statistical variation of ν about some average $\bar{\nu}$, and, as a result, there will be a statistical variation of M_2 around a mean value for any fixed M_1, and vice versa. For the present purposes, we can neglect this effect, as well as the mass defect, so Eq. (C.6) can be written

$$\frac{T_{01}}{T_{0T}} = \left[\frac{M_U - (\bar{\nu}M_n + M_1)}{M_U - \bar{\nu}M_n}\right]. \tag{C.8}$$

The experimental yield curve in effect gives a probable distribution of the mass M_1 (or M_2). Thus, Eq. (C.8) can be used to convert this to an energy distribution curve similar to the one shown in Fig. 3.8.

C-2 THE VAVILOV DISTRIBUTION

Straggling corrections for thin plates can be made using calculations by Seltzer and Berger[3] based on the original work of Vavilov[4]. He has shown that the probability $T(\Delta T, \tau)$ of a particle suffering an energy loss ΔT per unit energy loss during transmission through a thin plate of thickness τ is

$$T(\Delta T, \tau)\ d(\Delta T) = \frac{1}{\xi}\,\phi_V(\Delta_\nu, \kappa, \gamma^2)\ d\Delta_\nu \tag{C.9}$$

where

$$\Delta_\nu = \frac{\Delta T - \langle \Delta T \rangle}{\epsilon_{max}} - \kappa(1 + \gamma^2 - 0.577) \tag{C.10a}$$

$$\kappa = \xi/\epsilon_{max} \tag{C.10b}$$

$$\xi = 0.30058 \frac{m_0 c^2}{\gamma^2} \frac{Z}{A} \tau \qquad \gamma = v_0/c \tag{C.10c}$$

$$\epsilon_{max} = \frac{2m_0 c^2 \gamma^2}{1-\gamma^2}\left[1 + \frac{2m_0}{M}\frac{1}{\sqrt{1-\gamma^2}} + \left(\frac{m_0}{M}\right)^2\right]^{-1}. \tag{C.10d}$$

Here, A and Z are, respectively, the atomic weight and atomic number of the stopping material, while M is the rest mass and v_0 the initial speed of the penetrating particle, and m_0 is the electron rest mass.

The function ϕ_ν, as calculated by Seltzer and Berger[3], is shown in Fig. C.1 for various values of κ, which depend only on the stopping material and its thickness. Once this is fixed, the distribution around $\langle \Delta T \rangle$ can be found since Δ_ν is a function of $\Delta T - \langle \Delta T \rangle$.

The mean loss $\langle \Delta T \rangle$ is given by Seltzer and Berger as

$$\langle \Delta T \rangle = \xi \left\{ \ln \left[\frac{2m_0 c^2 \gamma^2 \epsilon_{max}}{I^2(1-\gamma^2)} \right] - 2\gamma^2 - 2\frac{C}{Z} - \delta \right\} \tag{C.11}$$

where I is the mean excitation energy of the stopping material, $2(C/Z)$ is a shell correction, and δ is a density effect correction, discussed in more detail in Ref. 3. Note that $\langle \Delta T \rangle$ is a linear function of ξ or the plate thickness τ.

The parameter κ is effectively the ratio of the average energy loss per collision to the maximum loss. When $\kappa = 0$, the well-known Landau distribution (pp. 65-66, Ref. 5) is obtained. Vavilov has shown that, as $\kappa \to 1$, his distribution can be represented in terms of Airey's function (p. 193, Ref. 3), but, for $\kappa \gg 1$, the distribution reduces to a Gaussian form, namely,

$$T(\Delta T, \tau) = \frac{1}{\xi\sqrt{(2\pi/\kappa)[1 - (\gamma^2/2)]}} \exp\left\{ \frac{-\kappa(\Delta T - \langle \Delta T \rangle)^2}{2\xi^2[1 - (\gamma^2/2)]} \right\}. \tag{C.12}$$

As discussed earlier, the most probable energy loss ΔT_p will differ from the mean loss due to asymmetries in the distribution. Seltzer and Berger[3] have calculated ΔT_p as a function of κ for $\gamma^2 = 0.5$, and their results are shown in Fig. C.2. The width of the distribution is also given in this figure. They assumed a Vavilov distribution, but, for cases where the Landau distribution is valid, ΔT_p is given by (p. 65, Ref. 5)

$$\Delta T_p = \xi \left\{ \ln \left[\frac{2m_0 v^2 \xi}{I^2(1-\gamma^2)} \right] - \gamma^2 + 0.373 \right\}. \tag{C.13}$$

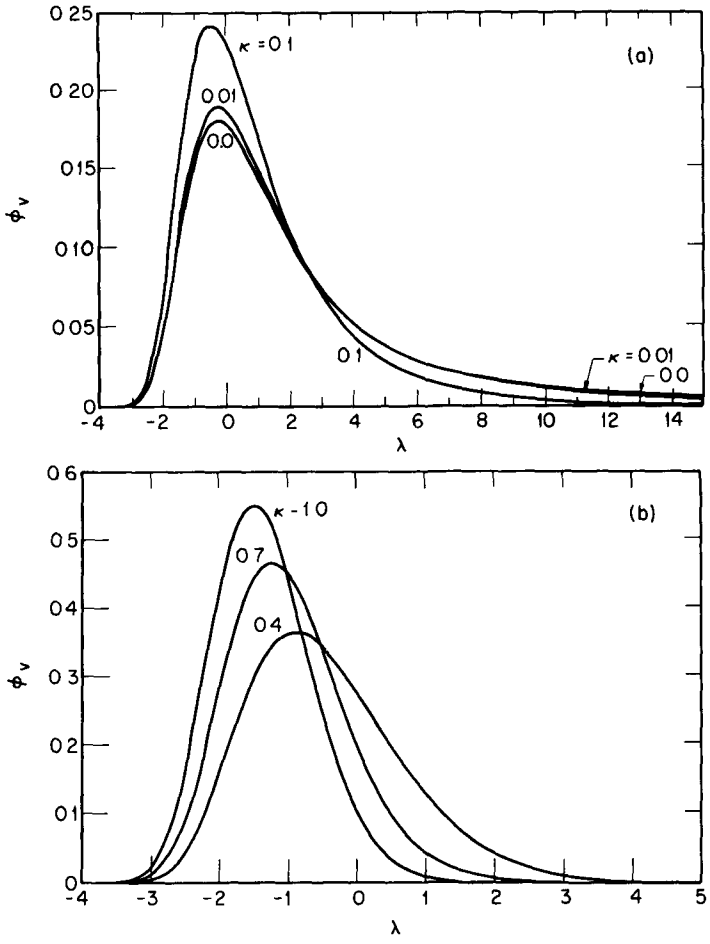

Fig C.1—The Vavilov distribution for $\gamma^2 = 0\ 9$. (a) $\kappa = 0$ (Landau), 0 01, and 0 1. (b) $\kappa = 0\ 4$, 0 7, and 1 0 (From Seltzer and Berger, Ref 3)

Note that ΔT_p deviates somewhat from linear dependence on the thickness τ since the bracketed quantity depends on τ through the logarithmic term.

Strictly speaking, the Vavilov distribution is *valid only for thin plates or small energy losses*, and the problem of a thick plate is considerably more complex. Some studies of this problem have been reported (p. 188, Ref. 3, and p. 330, Ref. 5), but the results are inconclusive. However, in general, it appears that the distribution curves approach a Gaussian shape as the plate thickness increases.

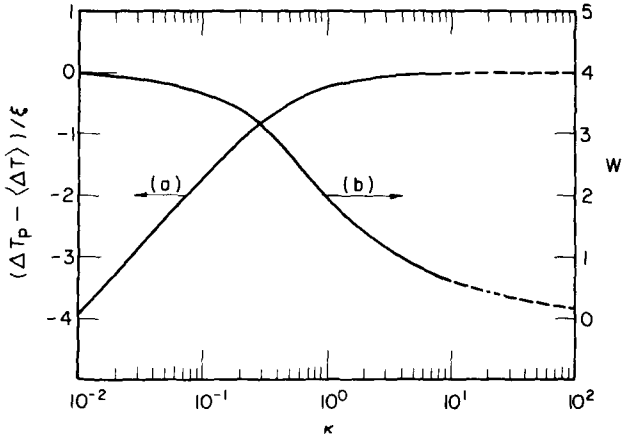

Fig. C.2 — The most probable energy loss and width of the Vavilov distribution for $\gamma^2 = 0.5$. (From Seltzer and Berger, Ref. 3. To obtain the most probable energy loss ΔT_p, the value of $(\Delta T_p - \langle \Delta T \rangle)/\xi$ is read from curve (a), and $\langle \Delta T \rangle$ and ξ are calculated according to Eqs. (C 11) and (C 10) Curve (b) is a plot of the quantity $W = (\Delta_1 - \Delta_2)/\xi$ with Δ_1 and Δ_2 being the two values of the energy loss at which the Vavilov distribution has fallen to 50% of its peak value.)

REFERENCES

1. E K. Hyde, *The Nuclear Properties of the Heavy Elements — III, Fission Phenomena*, Prentice-Hall, Inc., Englewood Cliffs, New Jersey, 1964.
2. R. D. Evans, *The Atomic Nucleus*, Chaps. 18 and 22, McGraw-Hill, New York, 1955.
3. S. M. Seltzer and M. J. Berger, "Energy-Loss Straggling of Protons and Mesons Tabulation of the Vavilov Distribution," pp. 187-203 of *Studies in Penetration of Charged Particles in Matter*, Nuclear Science Series Report No. 39, Committee on Nuclear Science, National Academy of Sciences — National Research Council, Washington, D C , 1964
4. P. V. Vavilov, *Zh. Eksperim Teor. Fiz, 32* 920 (1957), Transl., *Soviet Phys JETP, 5* 749 (1957).
5. S. V. Starodubtsev and A. M. Romanov, *The Passage of Charged Particles Through Matter*, Translated from Russian, Israel Program for Scientific Translations, Jerusalem, 1965. (Available, Clearinghouse for Fed. Sci. and Tech. Inf., Springfield, Va.)

Appendix D

D-1 PLANE KERNELS

Consider Fig. D.1, which depicts a plane source at z′. Its strength, $S(z',\mu,T_0)$ represents the number of particles born per second per unit of surface at z′ with direction cosine μ per unit μ, and kinetic energy T_0 per unit energy. Because of its definition, the source is represented as a delta function in space, giving

$$S(z',\mu,T_0) \equiv Q(\mu,T_0)\ \delta(z'-z) \tag{D.1}$$

where the energy–angle dependence is described by the function Q. The continuity equation is then

$$\nabla \cdot J(z,\mu;z',T_0) = Q(\mu,T_0)\ \delta(z'-z). \tag{D.2}$$

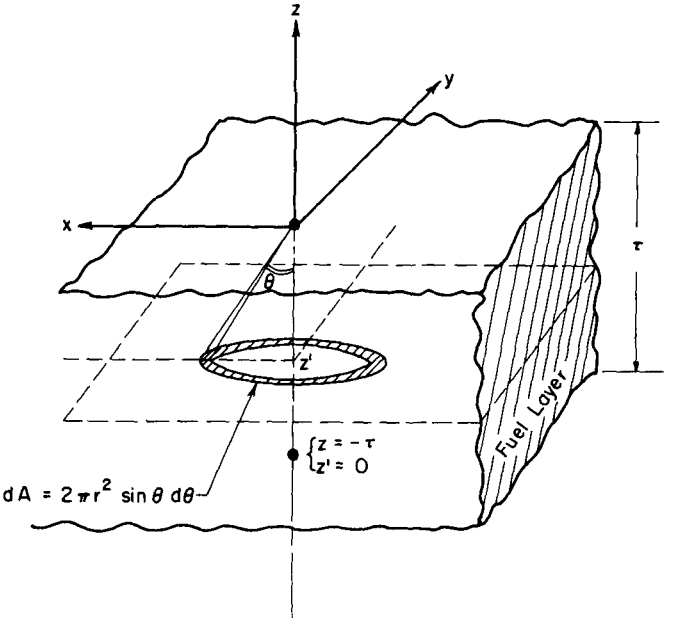

Fig. D.1—Geometry for the plane emitter analysis.

Operating on both sides with $\int_{z'-\epsilon}^{z'+\epsilon} dz$ and letting $\epsilon \to 0$, we find

$$[J(z, \mu; z', T_0)]_{z \to z'} = Q(\mu, T_0) \tag{D.3}$$

which demonstrates that a plane source is equivalent to specifying the *current* at z'. (While this may seem obvious here, in problems where both flux and current are involved, it is often confusing to know which should be used in the source boundary condition.)

The "plane kernel" can now be derived using this boundary condition. This kernel is defined as the current at the surface of a source free slab with a plane source of unit strength located at z'. For such a case, the current at the surface is simply

$$\begin{aligned} J(\tau, \mu; z', T_0) &= [J(z, \mu; z', T_0)]_{z \to z'} T[(\tau - z')/\mu, T_0] \\ &= Q(\mu, T_0)\, T[(\tau - z')/\mu, T_0] \end{aligned} \tag{D.4}$$

where the transmission function T is defined in Eq. (4.3). The angular distribution assigned to the source must be the same as that required for the problem where the kernel is ultimately to be used. In the present case, we will illustrate the problem for an isotropic emission, where J reduces to

$$J(\tau, \mu; z', T_0) = \frac{Q(T_0)}{2}\, h\left[\mu - \frac{\tau - z'}{\lambda(T_0)}\right]. \tag{D.5}$$

The step function $h(x)$ is the mean range form of T used in Eq. (4.3).

Consider, for simplicity, a thick plate so $\tau > \lambda(T_0)$. Then, integration of Eq. (D.5) over μ yields

$$\frac{J(\tau; z', T_0)}{Q(T_0)} = \begin{cases} \frac{1}{2}\left[1 - \frac{\tau - z'}{\lambda(T_0)}\right] & \left\{[\tau - \lambda(T_0)] \le z' \le \tau\right\} \quad \text{(D.6a)} \\ 0 & \left\{z' < [\tau - \lambda(T_0)]\right\} \quad \text{(D.6b)} \end{cases}$$

which is the required isotropic source "plane kernel" for the current. (Note that division of the current by $Q(T_0)$ normalizes it to a unit source strength.) The utility of this kernel can be illustrated as follows: If the spatial distribution of the actual source in the plate is given as $S(z', T_0)$, the total current from the plate can be found by integration of the plane kernel over this distribution, and this gives

$$J(\tau; T_0) = \int_{\tau - \lambda}^{\tau} \left[\frac{J(\tau; z', T_0)}{Q(T_0)}\right] S(z', T_0)\, dz'. \tag{D.7}$$

For a uniformly distributed source, S reduces to

$$S(z', T_0) \rightarrow S(T_0) \tag{D.8}$$

and Eq. (D.7) is easily evaluated, in which case

$$J(\tau; T_0) = \frac{S(T_0)}{4} \lambda(T_0). \tag{D.9}$$

This agrees with the earlier result for thick plates given by Eq. (4.9).

This method may also be used to calculate the energy spectrum of the current, the energy and charge currents, and the flux. These calculations are quite similar to those carried out for the point kernel in the initial sections of Chap. 4, the main problem involved being the proper selection of integration limits. For convenience a listing of plane and point kernels for both the flux and current are presented in Table D.1, along with integrated values.

Table D.1—A SUMMARY OF SOME USEFUL KERNELS AND TOTAL FLUXES AND CURRENTS(†,‡)

Point Kernels	Plane Kernels
$J(\tau,\mu;r,T_0) = S_{PT}(\mu,T_0)\ T(r,T_0)$	$J(\tau,\mu;z',T_0) = S_{PL}(\mu,T_0)\ T[(\tau - z')/\mu, T_0]$
$\phi(\tau,\mu;r,T_0) = \frac{S_{PT}(\mu,T_0)}{\mu}\ T(r,T_0)$	$\phi(\tau,\mu;z',T_0) = \frac{S_{PL}(\mu,T_0)}{\mu}\ T[(\tau - z')/\mu, T_0]$
$J^*(\tau;r,T_0) = \frac{S_{PT}(T_0)}{4}\ T(r,T_0)$	$J^*(\tau;z',T_0) = \frac{S_{PL}(T_0)}{2}\left[1 - \frac{\tau - z'}{\lambda(T_0)}\right] T(\tau - z', T_0)$
$\phi^*(\tau;r,T_0) = \frac{S_{PT}(T_0)}{2}\ T(r,T_0)$	$\phi^*(\tau;z',T_0) = \frac{S_{PL}(T_0)}{2}\left\{\ln\left[\frac{\lambda(T_0)}{\tau - z'}\right]\right\} T(\tau - z', T_0)$

After Integration over dr or dz'

$$J(\tau,\mu;T_0) = S(\mu,T_0)\ \mu \times \begin{cases} \lambda(T_0) & [\tau/\lambda(T_0) \geq \mu \geq 0] \\ \tau/\mu & [1 \geq \mu \geq \tau/\lambda(T_0)] \end{cases}$$

$$\phi(\tau,\mu;T_0) = J(\tau,\mu;T_0)/\mu$$

$$J^*(\tau;T_0) = \frac{S(T_0)}{2} \times \begin{cases} \tau\left[1 - \frac{\tau}{2\lambda(T_0)}\right] & [\tau \leq \lambda(T_0)] \\ \lambda(T_0)/2 & [\tau \geq \lambda(T_0)] \end{cases}$$

$$\phi^*(\tau;T_0) = \begin{cases} 2J^*(\tau;T_0) & [\tau > \lambda(T_0)] \\ \frac{S_0\tau}{2}\{1 + \ln[\lambda(T_0)/\tau]\} & [\tau < \lambda(T_0)] \end{cases}$$

†$T(r,T_0) \equiv \{1 - \int_0^r dr'\ \delta[r' - \lambda(T_0)]\}$.

‡The superscript * indicates that an isotropic source has been assumed, i.e., $S(\mu,T_0) \rightarrow S(T_0)/2$.

The plane kernel method may save some labor in certain problems, and it is particularly suited to cases where the source, unlike that used in Eq. (D.8), turns out to depend on z'. This situation is encountered in a Gamma-Electric Cell where gamma-ray attenuation is included, or in a Fission-Electric Cell where the neutron flux is attenuated across the fuel layer.

D-2 THE DIRAC CHORD METHOD

D-2.1 The Chord-Length Distribution

The chord length $s(\vec{\Omega})$ for the arbitrary convex solid of Fig. D.2 represents the straight-line distance between points on the solid surface defined by dA_s and $-\vec{\Omega}$. Thus, $s(\vec{\Omega})$ will lie inside the solid and coincide in direction with the source location vector $\vec{r}$ (Fig. D.2).

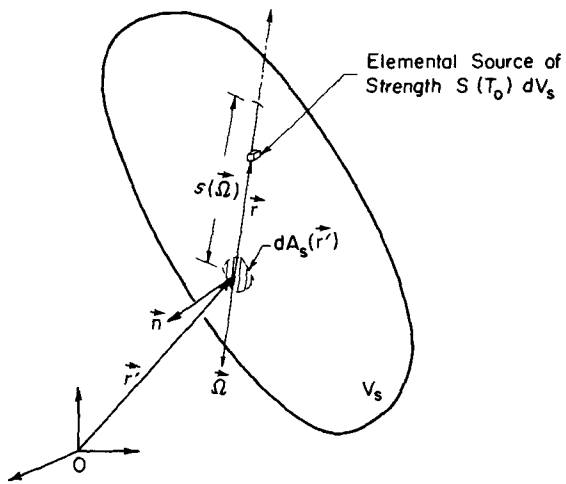

Fig. D.2 — Coordinates for chord calculations for an arbitrary convex solid.

A key point in Dirac's development [1] is the evaluation of the chord length distribution $\Phi(s)$ defined as the probability that a chord will have a length s per unit s. The solid is visualized as being composed of a series of tubes extending from dA_s and surrounding each chord $s(\vec{\Omega})$, as illustrated in Fig. D.3. The cross-sectional area of a tube perpendicular to $\vec{\Omega}$ is then given by $\vec{n} \cdot \vec{\Omega}\, dA_s$ where $\vec{n}$ is a unit vector normal to the surface and directed outwardly. The number of chords lying in the tube is taken to be proportional to this cross-sectional area, and the total number having a fixed length s is found by integrat-

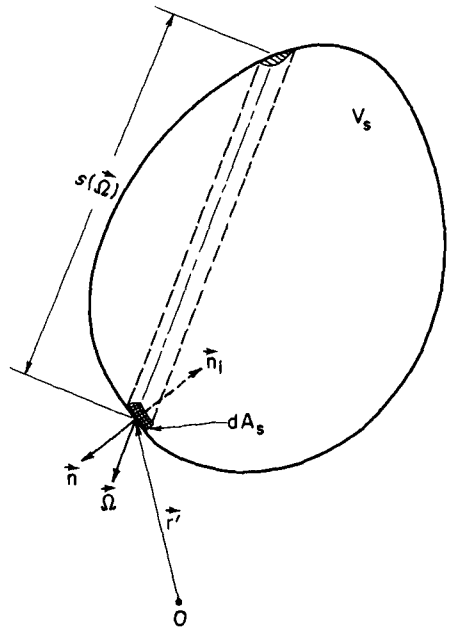

Fig. D.3 — The tube concept.

ing over all directions $\vec{\Omega}(s)$ that permit this length followed by integration over the entire surface. Normalization by the total number of chords then gives

$$\Phi(s) = \frac{\int dA_s \int_{\vec{\Omega}=\vec{\Omega}(s)} (\vec{n}\cdot\vec{\Omega})\, d\vec{\Omega}}{\int dA_s \int_{\vec{\Omega}} \vec{n}\cdot\vec{\Omega}\, d\vec{\Omega}}$$

$$= \frac{1}{\pi A_s} \int dA_s \int_{\vec{\Omega}=\vec{\Omega}(s)} (\vec{n}\cdot\vec{\Omega})\, d\vec{\Omega}. \qquad \text{(D.10)}$$

It is convenient to write this in terms of the average chord length, which, based on Eq. (D.10), can be shown to be

$$\bar{s} = \int s\,\Phi(s)\, ds$$

$$= \frac{4V_s}{A_s} \qquad \text{(D.11)}$$

where A_s is the surface area and V_s is the volume of the solid. (We have freely interchanged the order of integration here and have utilized the fact that the indicated integration over s is equivalent to extending the range of integration of $\vec{\Omega}$ from $\vec{\Omega}(s)$ to all $\vec{\Omega}$. Since the solid can be visualized as being composed of a number of parallel tube bundles of

volume $(\vec{n}\cdot\vec{\Omega})s\ dA_s$, the integration over this expression is equivalent to integration over an elemental volume dV.)

Substitution of $\bar{s}$ into Eq. (D.10) gives the desired form for the chord length distribution as

$$\Phi(s) = \frac{\bar{s}}{4\pi V_s} \int dA_s \int_{\vec{\Omega}(s)} (\vec{n}\cdot\vec{\Omega})\, d\vec{\Omega}. \tag{D.12}$$

D-2.2 Application to Escape Probability Calculations

To date, this method has been restricted to the case of a uniform isotropic source[1–5], which can be written as

$$S(\vec{r}, T_0, \vec{\Omega}) = \frac{S(T_0)}{4\pi}. \tag{D.13}$$

The definition of the escape probability $E(T_0)$ [Eq. (4.45)] is now generalized to include convex shapes by using the form

$$E(T_0) = \frac{J(\tau;T_0)}{S(T_0)\,\tau} \rightarrow \frac{\int dA_s(\vec{r}')\ J(\vec{r}';T_0)}{S(T_0)\ V_s}. \tag{D.14}$$

The numerator and denominator have both been integrated over the surface area of the solid, and $J(\vec{r}';T_0)$ is the current associated with the elemental area dA_s at $\vec{r}'$ shown in Fig. D.2. Now, if the current $J(\vec{r}';T_0)$ is written as an integral over the angular current and the source volume, Eq. (D.14) becomes

$$\begin{aligned} E(T_0) &= \frac{\int dA_s \int\int J(\vec{r}',\vec{\Omega};r,T_0)\, dr\, d\vec{\Omega}}{S(T_0)\ V_s} \\ &= \frac{1}{4\pi V_s} \int dA_s \int_{\vec{n}\cdot\vec{\Omega}>0} d\vec{\Omega}\,(\vec{n}\cdot\vec{\Omega}) \int_0^{s(\vec{\Omega})} T(r,T_0)\, dr \\ &= \frac{1}{4\pi V_s} \int dA_s \int_{\vec{n}\cdot\vec{\Omega}>0} d\vec{\Omega}\ (\vec{n}\cdot\vec{\Omega})\ \text{min.}\ [\lambda(T_0), s(\vec{\Omega})] \end{aligned} \tag{D.15}$$

where Eqs. (4.2) and (D.13) have been used along with the fact that an escaping particle could not have traveled a distance larger than the chord length $s(\vec{\Omega})$ or the mean range $\lambda(T_0)$. Here min. [x,y] represents the smallest of the two values, x or y.

Next, the integral over $\vec{\Omega}$ is divided into an integral over angles corresponding to a fixed chord length s followed by integration over all $\vec{\Omega}$—just the reverse of the procedure used earlier in Eq. (D.11).

Interchanging the order of integration then gives

$$E(T_0) = \frac{1}{4\pi V_s} \int ds \, \min.[\lambda(T_0), s] \int_{A_s} \int_{\vec{\Omega}(s)} (\vec{n} \cdot \vec{\Omega}) \, d\vec{\Omega} \, dA_s$$

$$= \frac{1}{\bar{s}} \int_{s^-}^{s^+} ds \, \min. \, [\lambda(T_0), s] \; \Phi(s) \tag{D.16}$$

where the chord length distribution has been introduced by comparison with Eq. (D.12) and the limits s^- and s^+ represent the minimum and maximum chord lengths, respectively.

A slightly different form of Eq. (D.16), obtained by careful examination of the limits, is

$$E(T_0) = 1 - \frac{1}{\bar{s}} \int_{\max.[s^-, \lambda(T_0)]}^{s^+} [s - \lambda(T_0)] \, \Phi(s) \, ds. \tag{D.17}$$

Equation (D.16), or alternately Eq. (D.17), represents a key result of the method. If the chord distribution $\Phi(s)$ is known, it can be used in these equations to obtain the escape probability with a minimum of labor. Only a single integration is required in contrast to the several integrations that would be necessary if one started directly with a current formulation such as that given in the first line of Eq. (D.15). It must be remembered, however, that this savings in labor is only possible if $\Phi(s)$ has already been evaluated.

For convenience chord-length distributions for a slab, sphere, and cylinder taken from Case et al.[2] are given in Table D.2 (distributions for the hemisphere, oblate spheroid, and oblate hemispheroid are also presented in this reference). Escape probabilities calculated from Eq. (D.17) are also given in Table D.2 and plotted in Fig. D.4. Note that the result given for the slab case is consistent with Eq. (4.48) provided the latter is adjusted to allow two-sided emission.

Figure D.4 shows that as $\xi \to 0$ (i.e., when the characteristic dimension of the solid is large relative to the range), the escape probability is independent of the shape. Since, in this limit, the particles cannot traverse the solid, its shape cannot have an influence.

Also note that, for large solids ($\xi \to 0$), the escaping current remains constant but the escape fraction approaches zero. Only those particles born a distance λ from the surface can escape; hence, as the solid's dimensions are increased beyond λ, the number per second crossing a square centimeter of surface area is fixed, but an increasing number of particles born deep in the interior of the solid are stopped.

Table D.2— SOME CHORD-LENGTH DISTRIBUTIONS AND CORRESPONDING ESCAPE PROBABILITIES

Configuration	Chord-Length Distribution*		Escape Probability†	
Sphere (radius a)	$s/2a^2$	$(s \leq 2a)$	$\frac{\xi}{12}\left[3-\left(\frac{\xi}{6}\right)^2\right]$	$(\xi \leq 6)$
	0	$(s > 2a)$	1	$(\xi \geq 6)$
Infinite slab (thickness a, assuming two-sided emission)	0	$(s < a)$	$\xi/4$	$(\xi \leq 2)$
	$2a^2/s^3$	$(s \geq a)$	$1 - (1/\xi)$	$(\xi \geq 2)$
Infinite cylinder (radius a)	$\frac{16a^2}{s^3}\int_0^{\min.(1,s/2a)} dx\{x^4(1-x^2)^{-1/2} \times [(s/2a)^2 - x^2]^{-1/2}\}$		$\frac{\xi}{4}\left[1 - 2\sum_{j=1}^{\infty} g(j)\left(\frac{\xi}{4}\right)^{2j}\right]$	$(\xi \leq 4)$
			$1 - 2\sum_{j=1}^{\infty} g(j)\left(\frac{4}{\xi}\right)^{2j}$	$(\xi \geq 4)$

*From Case et al., Ref. 2.

†From Lewis, Ref. 4. Note: $\xi \equiv \lambda(T_0)\,(A_s/V_s)$, and $g(j) = [1 \cdot 3^2 \cdot 5^2 \ldots (2j-3)^2 \cdot (2j-1)]/[2^2 \cdot 4^2 \cdot 6^2 \ldots (2j)^2 \cdot (2j+2)]$

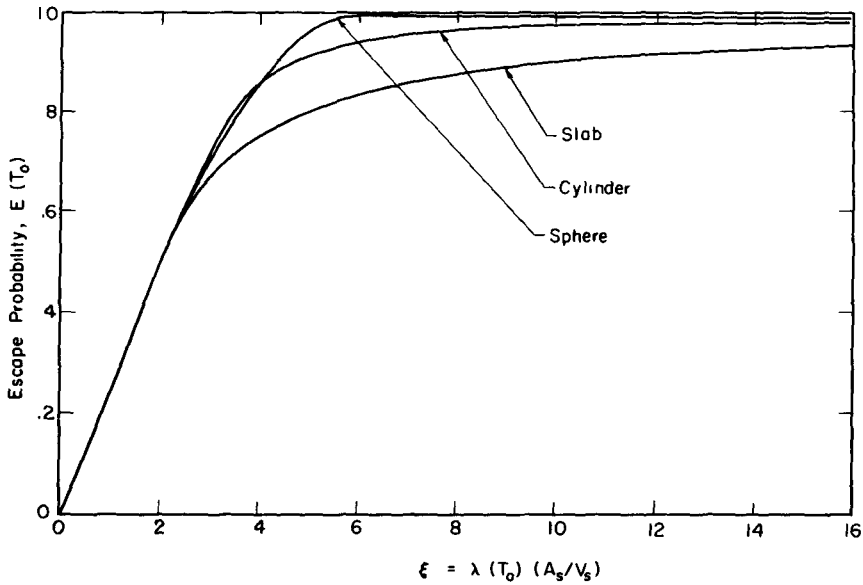

Fig. D.4—Escape probabilities for fission fragments from UO_2. (From Lewis and Pfeffer, Ref. 5.)

D-2.3 Application to Current Energy Spectrum Calculations

The chord length distribution can also be used to evaluate the energy spectrum of the escaping current. To accomplish this, we return to the definition of the escape probability given in Eq. (D.15) and assume that the integrations over dA_s and $d\vec{\Omega}$ have been completed, so

$$E(T_0) = \frac{\int dr\ J_A(r,T_0)}{S(T_0)\ V_s}. \tag{D.18}$$

The subscript A indicates the current has been integrated over the total surface, so $J_A(r,T_0)$ represents the total number of escaping particles per second due to a source in dr at r. Now, the escape probability due to all particles traveling a distance less than r′, found by integrating between 0 and r′, is given by

$$E(r \lesssim r', T_0) = \frac{1}{S(T_0)\ V_s} \int_0^{r'} dr\ J_A(r,T_0). \tag{D.19}$$

(We need not be concerned about r' exceeding λ or s^+ since then J_A itself will go to zero.) Differentiating this result gives

$$\frac{dE(r \lesssim r', T_0)}{dr'} = \frac{J_A(r', T_0)}{S(T_0)\, V_s} \equiv H(r', T_0) \tag{D.20}$$

where $H(r', T_0)$ represents the probability that an escaping particle travels a distance r' per unit distance.

The escape probability for particles traveling a distance *less* than r' can be obtained from Eq. (D.17) by replacing $\lambda(T_0)$ by r', which gives

$$E(r \lesssim r', T_0) = 1 - \frac{1}{\bar{s}} \int_{\max.(s^-, r')}^{s^+} [s - r']\, \Phi(s)\, ds. \tag{D.21}$$

This is valid since r' is now the maximum distance traveled in the same sense that $\lambda(T_0)$ was in the original derivation. The dependence on T_0 is still included because the maximum value of r' is a function of T_0 through $\lambda(T_0)$. Differentiation of this equation with respect to r' and use of the definition of H [Eq. (D.20)] give

$$H(r', T_0) = \frac{1}{\bar{s}} \int_{\max.(s^-, r')}^{s^+} \Phi(s)\, ds \tag{D.22}$$

which can be used to find the total surface current J_A since it follows from Eq. (D.20) that

$$J_A(r', T_0) = S(T_0)\, V_s\, H(r', T_0). \tag{D.23}$$

The energy spectrum of the current can also be found from this result. Using the transformation method of Sec. 4-1.2, we write

$$J_A(T; T_0) = \frac{J[r'(T), T_0]}{|dT/dr'|}$$

$$= \frac{S(T_0)\, V_s}{\bar{s}\, |dT/dr'|} \int_{\max.[s^-, r'(T)]}^{s^+} \Phi(s)\, ds \tag{D.24}$$

and both $r'(T)$ and dT/dr' can be found directly from the slowing model of Chap. 3 [Eqs. (3.27) and (3.28)].

As before, appropriate average quantities are easily evaluated once $J_A(T; T_0)$ is known, e.g., the average energy becomes

Table D.3— PATH LENGTH DISTRIBUTIONS AND CURRENT SPECTRA*

Geometry	Path Length Distribution, $H(r',T_0)$		Energy Spectrum, $H(T,T_0) = \frac{J_A(T,T_0)}{S(T_0)\ V_s}$	
Sphere (radius a)	$\frac{3}{4a}\left[1 - \frac{(r')^2}{4a^2}\right]$	$(r' \le 2a)$	$\frac{(n+1)\xi}{4T_0}\left(\frac{T}{T_0}\right)^n\left\{1 - \left(\frac{\xi}{6}\right)^2\left[1 - \left(\frac{T}{T_0}\right)^{n+1}\right]^2\right\}$	$\frac{T}{T_0} \ge \left(1 - \frac{6}{\xi}\right)^{1/(n+1)}$
	0	$(r' \ge 2a)$	0	$\frac{T}{T_0} \le \left(1 - \frac{6}{\xi}\right)^{1/(n+1)}$
Infinite slab (thickness a)	$\frac{1}{2a}$	$(r' \le a)$	$\frac{n+1}{\xi T_0}\left(\frac{T}{T_0}\right)^n\left[1 - \left(\frac{T}{T_0}\right)^{n+1}\right]^{-2}$	$\frac{T}{T_0} \le \left(1 - \frac{2}{\xi}\right)^{1/(n+1)}$
	$\frac{a}{2(r')^2}$	$(r' \ge a)$	$\frac{\xi(n+1)}{4T_0}\left(\frac{T}{T_0}\right)^n$	$\frac{T}{T_0} \ge \left(1 - \frac{2}{\xi}\right)^{1/(n+1)}$
Infinite cylinder† (radius a)	$\frac{1}{2a}\left[1 - 2\sum_{j=1}^{\infty} g(j)\ (2j+1)\left(\frac{r'}{2a}\right)^{2j}\right]$	$(r' < 2a)$	$\frac{\xi(n+1)}{2T_0}\left(\frac{T}{T_0}\right)^n \sum_{j\ 1}^{\infty} g(j)\ 2j\left(\frac{\xi}{4}\right)^{-(2j+1)}\left[1 - \left(\frac{T}{T_0}\right)^{n+1}\right]^{-(2j+1)}$	$\frac{T}{T_0} < \left(1 - \frac{4}{\xi}\right)^{1/(n+1)}$
	$\frac{2}{3\pi a}$	$(r' = 2a)$	$\frac{\xi(n+1)}{3\pi T_0}\left(1 - \frac{4}{\xi}\right)^{n/(n+1)}$	$\frac{T}{T_0} = \left(1 - \frac{4}{\xi}\right)^{1/(n+1)}$
	$\frac{1}{a}\sum_{j\ 1}^{\infty} g(j)\ 2j\left(\frac{2a}{r'}\right)^{2j+1}$	$(r' > 2a)$	$\frac{\xi(n+1)}{4T_0}\left(\frac{T}{T_0}\right)^n\left[1 - 2\sum_{j-1}^{\infty} g(j)\ (2j+1)\left(\frac{\xi}{4}\right)^{2j}\left[1 - \left(\frac{T}{T_0}\right)^{n+1}\right]^{2j}\right.$	$\frac{T}{T_0} > \left(1 - \frac{4}{\xi}\right)^{1/(n+1)}$

*From Lewis, Ref. 4.
†g(j) is defined in Table D.2.

$$\langle T\rangle_A \equiv \frac{\int_0^{T_0} T\, J_A(T;T_0)\, dT}{\int_0^{T_0} J_A(T;T_0)\, dT} = \frac{1}{E(T_0)} \int_0^{T_0} dT\, r'(T) \int_{\max[s^-, r'(T)]}^{s^+} ds\, \Phi(s). \qquad (D.25)$$

Path length distributions from calculations by Lewis[4] based on Eq. (D.22) and the chord distributions given in Table D.2 are summarized in Table D.3. Values for $J_A(T;T_0)$ derived from Eq. (D.24) are also listed. A plot of $J_A(T;T_0)$ for plane, spherical cylindrical configurations are shown in Figs. D.5a, b, and c where n has been taken to

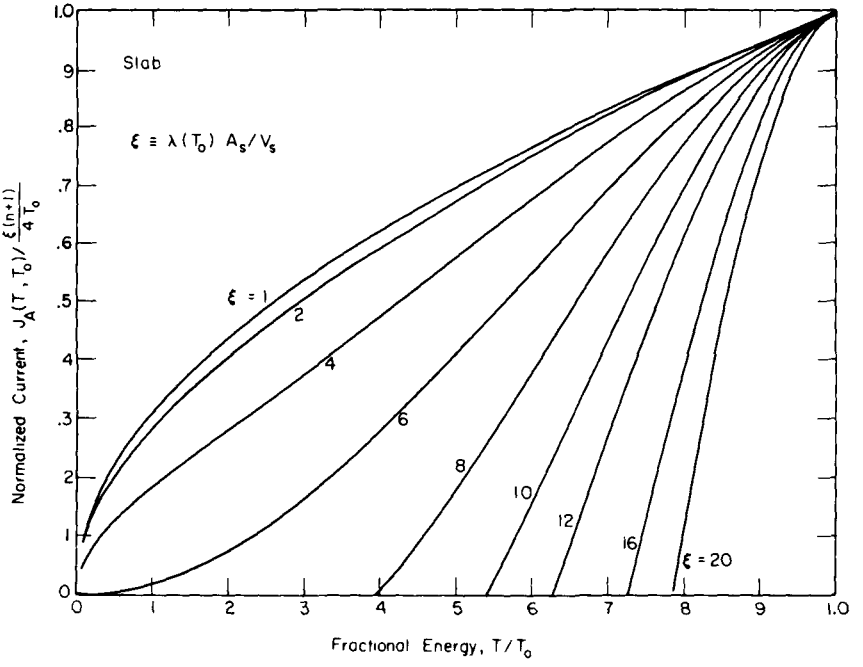

Fig. D.5(a) — Energy spectra for n = 1/2 for a slab emitter. (From Lewis, Ref. 4.)

be ½, corresponding roughly to alpha particles or protons. A plot of $[1 - (\langle T\rangle_A/T_0)]$, the average fractional energy loss in the solid, is shown for various geometries in Fig. D.6, p. 475.

Several asymptotic results are also useful. Lewis[4] points out that, if the solid dimensions are much larger than $\lambda(T_0)$, the argument in Eq. (D.22) can be replaced by a delta function so that $H \to 1/\bar{s}$. Thus, in this limit, current energy spectrum of Eq. (D.24) reduces to

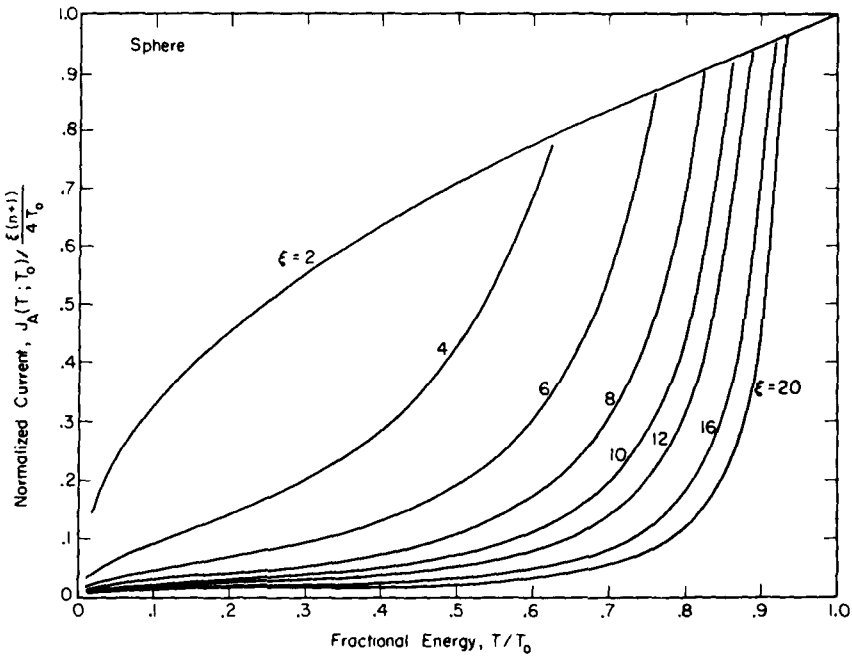

Fig. D.5(b) — Energy spectra for n = 1/2 for a spherical emitter. (From Lewis, Ref. 4.)

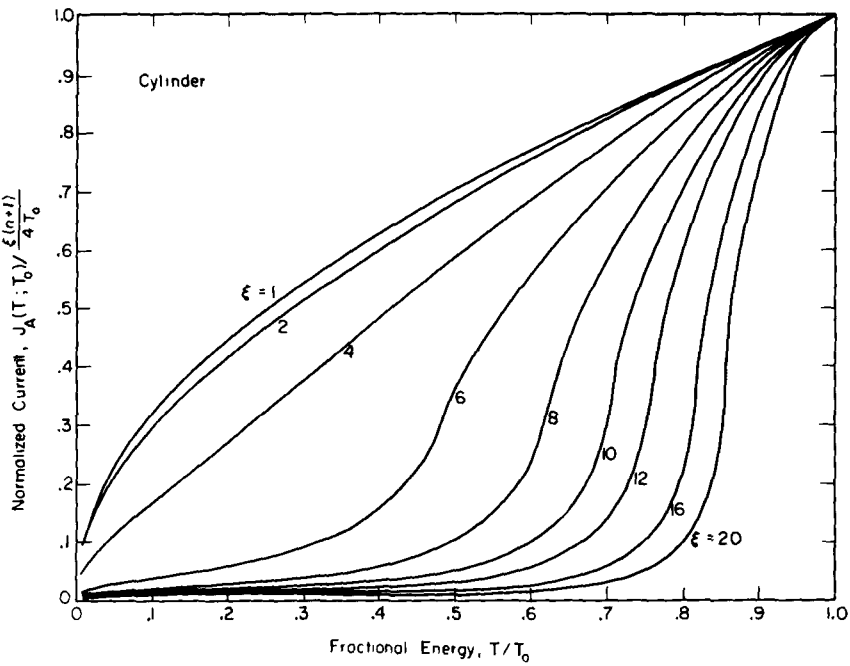

Fig. D.5(c) — Energy spectra for n = 1/2 for a cylindrical emitter. (From Lewis, Ref. 4.)

$$\left[J_A(T;T_0)\right]_{\xi\to 0} \to \frac{S(T_0)\,V_s}{\bar{s}\,|dT/dr'|} = \frac{(n+1)\,S(T_0)\,A_s\lambda(T_0)}{4T_0}\left(\frac{T_0}{T}\right)^n \qquad (D.26)$$

where Eq. (3.28) has been used to evaluate $|dT/dr'|$. Since $J_A = JA_s$, this result is consistent with Eq. (4.14). As might be expected, it is independent of geometry, since (as noted earlier) in this limit, all escaping particles originate over a volume that extends a depth λ in from the surface regardless of the shape of the solid. Substitution of Eq. (D.26) into Eq. (D.25) gives an asymptotic form for $\langle T\rangle_A$

$$\langle T\rangle_A = \frac{n+1}{n+2}\,T_0 \qquad (\xi \to 0) \qquad (D.27)$$

which agrees with Eq. (4.28).

If the source has a distributed energy spectrum, these results (all of which apply to a monoenergetic source) must be integrated over the actual spectrum in the same fashion as Eq. (4.18).

These methods have been used by Lewis and Pfeffer[5] to study fission fragment emission from UO_2. Their results are in excellent agreement with more involved calculations of Kahn et al.[6], who used a combined analytic–Monte Carlo approach. Kahn et al. have in turn tested their analysis against an extensive series of experimental measurements for UO_2 layers ranging from 0.0286 to 9.07μ thick[6]. Two typical results are shown in Figs. D.7a and b, and, as seen, the agreement is excellent considering the wide range of thicknesses involved.

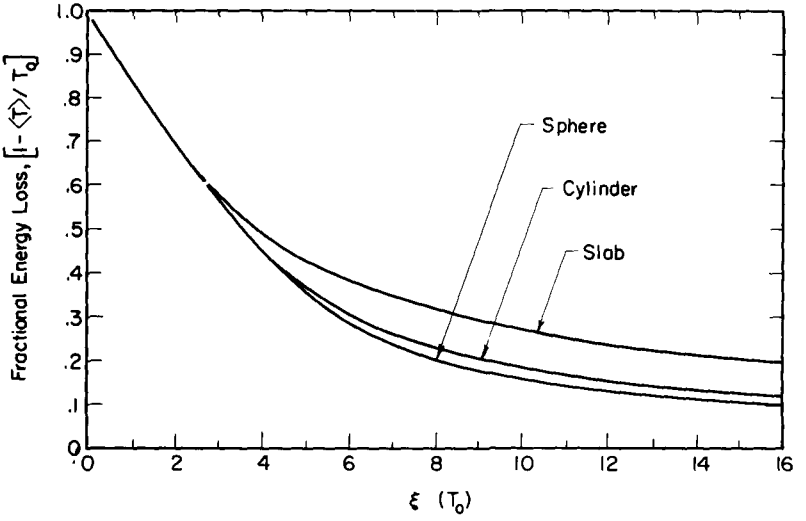

Fig. D.6—Average energy loss in the source assuming n = ½. (From Lewis, Ref. 4)

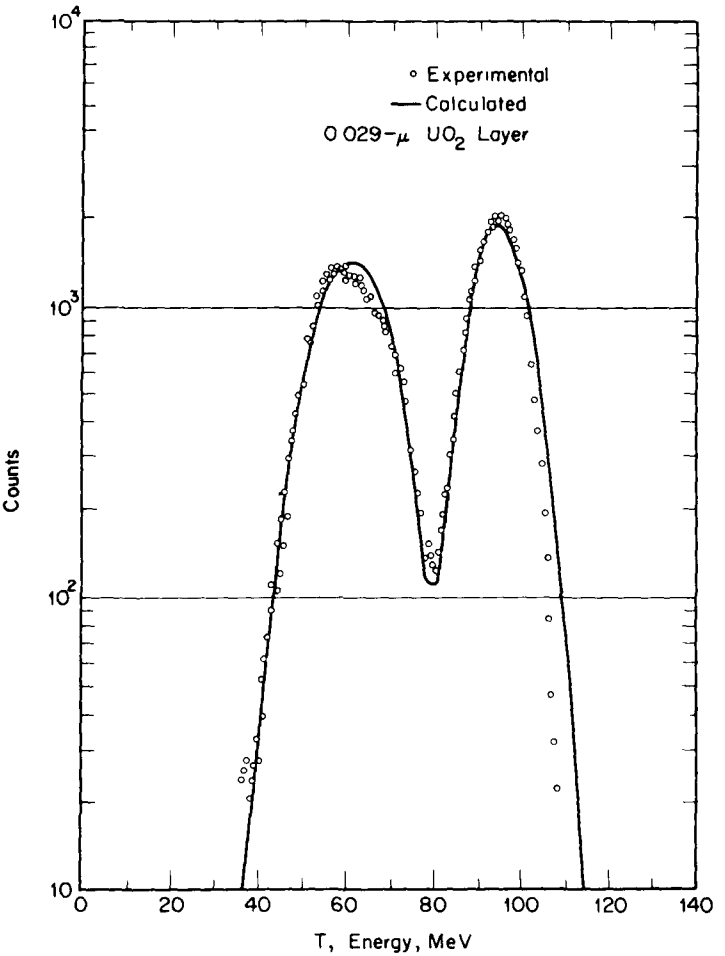

Fig. D.7(a) — Calculated and experimental current energy spectra for fission fragments emerging from a UO_2 layer 0.0286 μ thick. (From Kahn et al., Ref. 6.)

REFERENCES

1. P. A. M. Dirac, "Approximate Rate of Neutron Multiplication of a Solid of Arbitrary Shape and Uniform Density," British Report MS-D-5 (Declassified), Part I, 1943.
2. K. M. Case, F. de Hoffmann, and G. Placzek, *Introduction to the Theory of Neutron Diffusion* Vol. I, Los Alamos Scientific Laboratory, June 1953.
3. R. V. Meghreblian and D. K. Holmes, *Reactor Analysis*, pp. 373-377, McGraw-Hill, New York, 1960.

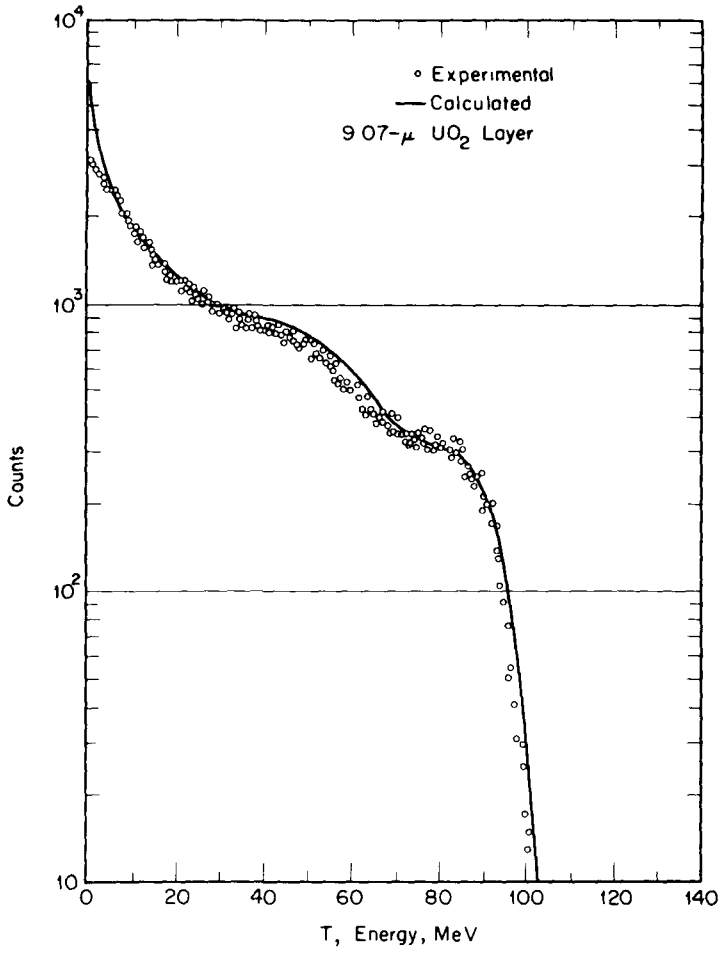

Fig. D.7(b) — Calculated and experimental current energy spectra for fission fragments emerging from a UO_2 layer 9.07 μ thick. (From Kahn et al., Ref. 6.)

4. E. E. Lewis, "A Generalization of the Dirac Chord Method to Include Charged Particle Phenomena," *Nucl Sci and Eng , 25* 359 (1966).
5. E. E. Lewis and R. P. Pfeffer, "The Influence of Source Geometry on Fission Fragment Escape Probabilities," *Nucl Sci and Eng., 27* 581 (1967).
6 S. Kahn, R. Harman, and V. Forgue, "Energy Distribution of Fission Fragments from Uranium Dioxide Films," *Nucl Sci and Eng , 23* 8 (1965).

Appendix E

E-1 PARAMETERS FOR THE IONIZATION—DIFFUSION MODEL

The evaluation of the various parameters involved in Eq. (5.8) is discussed in some detail in the following sections.

E-1.1 Diffusion Length for Low-Energy Secondaries

We assume that, as discussed in Sec. 5-3.2, inelastic scattering is the dominant process involved in the diffusion of low-energy secondaries. Then, if Σ_{ss} and Σ_{as} represent the macroscopic inelastic scattering and absorption cross sections, respectively, the diffusion length L_s can be expressed, following normal practice, as

$$L_s = \sqrt{D_s/\Sigma_{as}} = 1/\sqrt{3\Sigma_{ss}\Sigma_{as}} \tag{E.1}$$

where the diffusion coefficient D_s has been identified with $(3\Sigma_{ss})^{-1}$. The required cross sections can be evaluated as follows: Absorption is used here in the sense of representing any secondary electron whose energy has dropped below the minimum required for escape. Thus, if $\langle n_c \rangle$ represents the average number of inelastic collisions that occur before this minimum energy is reached, the mean free path for absorption can be related to the mean free path for scattering by

$$\lambda_{as} \approx \langle n_c \rangle \lambda_{ss}. \tag{E.2a}$$

Since $\lambda = (\Sigma)^{-1}$, this is equivalent to

$$\Sigma_{as} = \Sigma_{ss}/\langle n_c \rangle. \tag{E.2b}$$

Sternglass[1] has pointed out that the microscopic inelastic scattering cross section σ_{ss} should be proportional to the geometric area associated with the outermost filled shells of the target atoms, and, based on typical measurements of covalent radii, he suggests that

$$\sigma_{ss} \approx c(1.6Z^{1/3})10^{-16} \qquad \text{cm}^2 . \tag{E.3}$$

Here, c is a constant of proportionality, and Z is the atomic number of the target. The macroscopic cross section then becomes

$$\Sigma_{ss} \approx cN(1.6Z^{1/3})10^{-16} \qquad cm^{-1} \tag{E.4}$$

where N represents the atoms per cubic centimeter of the target.

Combining Eqs. (E.1) through (E.4), we obtain the following expression for the diffusion length

$$L_s = \frac{6.25 \times 10^{15}}{\alpha N Z^{1/3}} \tag{E.5a}$$

where

$$\alpha = c\sqrt{3/\langle n_c \rangle}. \tag{E.5b}$$

It might be expected that α would not vary greatly for materials within a given class, e.g., for metals as opposed to insulators.

As discussed in Sec. 5-3.2, $\langle n_c \rangle$ typically ranges between 2 to 5 for metals, so, to a first approximation, $\alpha \approx c$. Based on experimental data for platinum, Sternglass[1] suggests that α be assigned the value 1/4 for metals. In contrast, as pointed out in Sec. 5-4.7, the energy band structure of insulators results in much larger values of $\langle n_c \rangle$, and the data presented in Table 5.5, indicate that α is roughly 0.02 for materials such as MgO.

E-1.2 Energy Expended per Secondary

The mean energy expended per secondary formed E_{se} might be expected to have roughly the same magnitude as that observed in gases because, as indicated in Chap. 3, high-energy ions predominantly interact with the heavily populated bound shells having binding energies only weakly dependent on the phase state of the material. It is also well known that, despite large differences in ionization and excitation energies for various gases, the energy required for ion pair production remains amazingly constant. Based on these observations and data for heavy gases, Sternglass[1] has suggested that $E_{se} \approx 25$ eV for metals. (There is some question about this assignment since, as noted by Ghosh and Khare[2], electron excitation measurements suggest the use of a somewhat larger value.) Insulators again present special problems, and, as discussed in Sec. 5-4.7, E_{se} for them is generally of the order of 5 to 10 eV.

E-1.3 Surface Transmission Probability

The surface transmission probability P_s represents a touchy point in the development. As illustrated in Fig. E.1, the key question is the identification of the potential barrier that is "seen" by the secondary. At first thought, the work function ϕ might appear to be the logical choice; however, a large part of the work function results

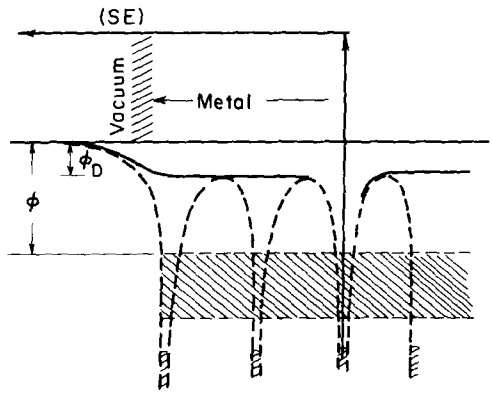

Fig E.1 — Schematic illustration of the formation of a secondary electron (SE) in a metal and its escape across the surface potential barrier. (After Sternglass, Ref. 1.)

from polarization effects associated with the image, exchange, and correlation forces that are encountered as an electron leaves the surface[3], and the secondary crosses the escape zone so rapidly relative to the relaxation time of conduction electrons (10^{-13} to 10^{-14} sec) that these effects do not have time to come into full force. This leaves the surface dipole potential ϕ_D as the dominant barrier (Fig. E.1). It is due to the asymmetric charge distribution that arises because the electron cloud projects outward beyond the positive ion-core charges at the surface. (For further details see Refs. 1 and 4.) Thus, the size of ϕ_D does not vary greatly from one material to another, and it is considerably smaller than the total work function; e.g., typical values for metals range from 0.1 to 0.5 eV.

Having identified ϕ_D as the barrier height, we are left with the step-barrier transmission problem illustrated in Fig. E 2, where a one-dimensional step is used to approximate the actual surface–vacuum interface. The transmission factor P_s, based on wave mechanics, is found to be (Ref. 5, p. 859)

$$P_s = \frac{4k_1k_2}{(k_1 + k_2)^2} \tag{E.6}$$

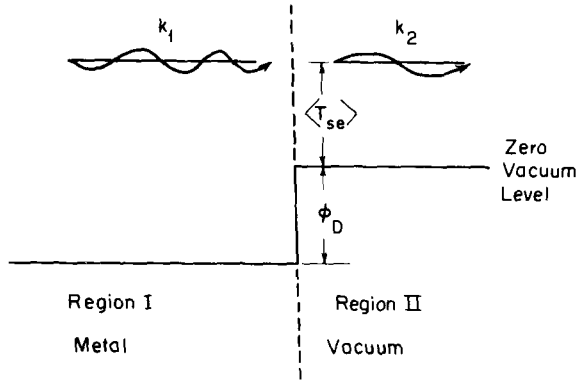

Fig. E.2 — The idealized surface barrier problem.

where k_j is defined as the particle wave number in the j*th* region, which, in terms of a particle of wave length λ_j and kinetic energy T_j, is simply

$$k_j = \frac{2\pi}{\lambda_j} = \frac{2\pi}{h} \sqrt{2mT_j} \tag{E.7}$$

where h is Planck's constant. Based on the nomenclature defined in Fig. E.2, we find

$$k_1 = \frac{2\pi}{h} \sqrt{2m_e[\langle T_{se} \rangle + \phi_D]} \tag{E.8}$$

and

$$k_2 = \frac{2\pi}{h} \sqrt{2m_e \langle T_{se} \rangle}. \tag{E.9}$$

The average secondary-electron energy $\langle T_{se} \rangle$, defined relative to the zero vacuum level, is typically 6 to 8 eV[1]. Thus, to a good approximation, $(\phi_D / \langle T_{se} \rangle) \ll 1$, and, using this fact, we can expand Eq. (E.6) to obtain

$$P_s \approx 1 - \frac{\phi_D}{2\langle T_{se} \rangle} . \tag{E.10}$$

For the typical values of ϕ_D and $\langle T_{se} \rangle$ noted above, P_s ranges from 0.90 to 0.99, which indicates that the barrier is quite transparent.

Absolute values are perhaps not so important as the conclusion that, since the barrier primarily involves ϕ_D, the transmission factor will be fairly insensitive to differences in total work function, conductivity, and crystal structure. (This assumes a smooth surface. Abnormally rough surfaces may cause a significant reduction in the transmission factor[1].) This insensitivity to the work function was observed in early secondary emission experiments, but a number of years passed before it was understood.

E-1.4 Source Normalization

The source normalization A_s was introduced through the escape probability P(x) given in Eq. (5.7). This probability is, in effect, the current escaping the surface (x = 0) due to a plane source of unit strength at x. The equivalent probability of reaching the plane x′ in

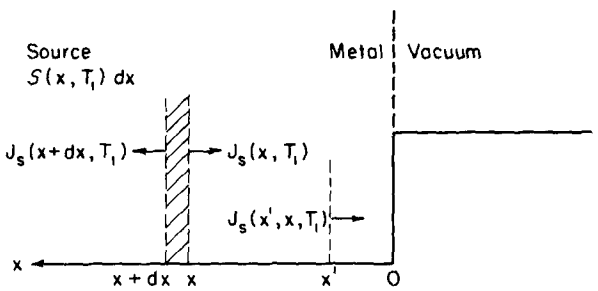

Fig E 3—The secondary-electron source in dx at x.

the interior of the target (see Fig. E.3; an interior plane at x′ is chosen to eliminate the surface transmission factor P_s) is given by

$$P(|x - x'|) \equiv \frac{J_s(x';x,T_1)}{S(x,T_1)} = A_s e^{-(x-x')/L_s} . \tag{E.11}$$

Here, $J_s(x';x,T_1)$ is the secondary-electron current at x′ due to the source $S(x,T_1)$, and division by S normalizes the probability to a unit source strength. Taking the limit of Eq. (E.11) as $x' \to x$, we obtain

$$A_s = \frac{[J_s(x';x,T_1)]_{x'\to x}}{S(x,T_1)} = \frac{\int_0^{+1} S(x,\mu;T_1)\,d\mu}{\int_{-1}^{+1} S(x,\mu;T_1)\,d\mu}. \tag{E.12}$$

The right-hand side of Eq. (E.12) follows directly from Eq. (D.3) and the definition of $S(x,T_1)$. This result demonstrates the basic role of A_s as a source normalization, and the key problem involved in its evaluation is a knowledge of the angular distribution of the source. For

example, if $S(x,\mu;T_1)$ is isotropic, it may be brought out from under the integrals, and A_s is found to be 1/2. Physically, this simply states that, for an isotropic source, half the electrons contribute to the current moving to the right while half contribute to the current in the opposite direction.

However, the actual angular distribution of secondaries produced along the track of a charged particle is not a simple isotropic distribution. Low-energy secondaries (as opposed to δ-rays) are emitted roughly at right angles to the track with a distribution that seems to be fairly symmetrical about a plane perpendicular to the track[1]. Thus, for the case of interest here, where the ion beam is normal to the surface, the contribution to forward and backward secondary currents will still be approximately equal, and $A_s = 1/2$ remains a valid first estimate.

One added complication is that, as used in Eq. (5.8), A_s represents a normalization for the low-energy secondaries produced by δ-rays as well as those produced directly in "soft" collisions of the primary ion, and the δ-ray tracks generally will not be perpendicular to the surface. However, as illustrated in Fig. 5.4, their directions will tend to be randomized by collisions so the composite angular distribution of the secondaries they ultimately produce will approach an isotropic distribution. Because of this and also because the δ-ray contribution is often of lesser importance, we will continue to use $A_s = 1/2$ for normal ion incidence.

Clearly, A_s should be adjusted for non-normal bombardment. The problem becomes quite complicated, however, and we avoid a detailed derivation by using a semiempirical yield correlation [Eq. (5.33)] when angular effects are discussed in Sec. 5-4.4.

E-1.5 δ-Ray Contribution

The δ-ray contribution to the yield is incorporated in the fractional δ-ray energy return function $f(x;T_1)$. As defined in Eq. (5.4), its evaluation requires a knowledge of $g(x;x',T_1)$, which gives the fraction of the energy going into δ-ray production at x' that is ultimately available for secondary production as the δ-rays slow at x per unit volume. To find g, we consider the problem of a medium containing a discrete *energy* source $S_{\delta E}$ at x'. This source is found by multiplying the particle source of Eq. (D.1) by $T_{\delta 0}$, the initial δ-ray energy, which gives

$$S_{\delta E}(x,\mu_\delta,T_{\delta 0}) = Q(\mu_\delta,T_{\delta 0})\ \delta(x'-x)\ T_{\delta 0}\ . \tag{E.13}$$

As discussed in Sec. 5-6, the Rutherford scattering formula can be used to predict the distribution of initial directions, and energy-

momentum conservation gives a unique relation between μ_δ and $T_{\delta 0}$. However, to avoid undue complexity in the present calculation, we will simply use average initial values, $\bar{\mu}_\delta$ and $\bar{T}_{\delta 0}$, to characterize the source distribution, so Q becomes

$$Q(\mu_\delta, T_{\delta 0}) \approx \delta(\mu_\delta - \bar{\mu}_\delta)\ \delta(T_{\delta 0} - \bar{T}_{\delta 0}). \tag{E.14}$$

The δ-rays will have initial energies extending up to 1 keV or so; hence, the slowing model developed in Chap. 3 provides a reasonable approximation for their transport. There is, in fact, some precedence for using such a model in similar situations[6–8]. In this case, the average δ-ray track is represented by a straight line as illustrated in

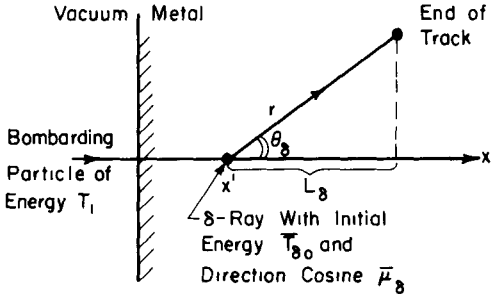

Fig. E.4—The δ-ray model.

Fig. E.4. Then Eqs. (3.28), (4.21), and (D.4) can be applied directly to find the angular energy current at x due to the source of Eq. (E.13), and this gives

$$J_{\delta E}(x,\mu;x',T_{\delta 0}) = T_{\delta 0}\, Q(\mu_\delta, T_{\delta 0}) \times \left\{ T\left[(x-x')/\mu_\delta,\ T_{\delta 0}\right] \left(1 - \frac{x-x'}{\mu_\delta \lambda_\delta}\right)^{1/(n+1)} \right\} \tag{E.15}$$

where λ_δ is the mean range corresponding to $T_{\delta 0}$ and T is the transmission function as defined in Eq. (4.3). Note that the slowing parameter n appearing here applies to the δ-rays and not to the primary ion.

Now, the energy current $J_{\delta E}(x;x',T_1)$ associated with δ-rays produced at x' by an ion of energy T_1 is found by integrating over all allowed δ-ray energies and angles. In light of Eq. (E.14) this simply gives

$$J_{\delta E}(x;x',T_1) = \bar{T}_{\delta 0} \left\{ T\left[(x-x')/\bar{\mu}_\delta,\ \bar{T}_{\delta 0}\right] \left(1 - \frac{x-x'}{L_\delta}\right)^{1/(n+1)} \right\} \tag{E.16}$$

where the characteristic length

$$L_\delta \equiv \bar{\mu}_\delta \lambda_\delta(\bar{T}_{\delta 0}) \tag{E.17}$$

represents the mean δ-ray displacement in the x-direction.

The desired function g can now be found by noting that it corresponds to the energy loss rate associated with $J_{\delta E}$; thus, application of the energy continuity relation [Eq. (4.25)] gives

$$g(x;x',T_1) = \frac{-\nabla \cdot J_{\delta E}(x;x';T_1)}{\iiint S_{\delta E}\, dx\, d\mu_\delta\, dT_{\delta 0}} \tag{E.18}$$

where the integral over $S_{\delta E}$ normalizes $J_{\delta E}$ to a unit source strength (required because g is defined on a fractional basis).

Substitution of Eqs. (E.13), (E.14), and (E.16) into this relation gives

$$g(x;x',T_1) = \begin{cases} \dfrac{1}{(n+1)L_\delta}\left(1 - \dfrac{x - x'}{L_\delta}\right)^{-[n/(n+1)]} & [0 < (x - x') < L_\delta] \quad \text{(E.19a)} \\ 0 & \text{(otherwise)} \quad \text{(E.19b)} \end{cases}$$

This form of g reflects two aspects of the transport model used in its derivation: First, the requirement that $(x - x') > 0$ restricts all δ-ray motion to the forward direction relative to the ion motion. (The possibility of backscattering is considered in the next section.) Second, the fact that $g \to 0$ as $(x - x') \to L_\delta$ simply reflects the assumption that the δ-rays can be represented by a mean initial direction cosine and a mean range.

This result for g can now be substituted into Eq. (5.4) to find $f(x;T_1)$. However, before the required integration can be carried out, the variation of $\langle dT_i/dx\rangle^{(2)}$ with space must be specified. For yield calculations involving high-energy ion bombardment, if the entrance side of the target is of interest, $\langle dT_i/dx\rangle^{(2)}$ can be approximated by its value at the surface as indicated in Eq. (5.5). (Note: This is not valid for the exit side of a fairly thick foil, where an explicit slowing law must be used to relate $\langle dT_1/dx\rangle^{(2)}$ at this face to the entering energy of the ion.) Under this assumption, $\langle dT_1/dx\rangle^{(2)}$ can be removed from the integral in Eq. (5.4), and, after carrying out the indicated integration, we find

$$f(x;T_i) = \begin{cases} 1 - (1 - x/L_\delta)^{1/n+1} & (x/L_\delta \lesssim 1) \quad \text{(E.20a)} \\ 1 & (x/L_\delta > 1). \quad \text{(E.20b)} \end{cases}$$

This relation will normally be used with $n = 1$ corresponding to δ-rays with energies below 0.5 MeV (Table 3.4). The limit $f(x;T_i) \to 1$ for $x/L_\delta > 1$ implies that an equilibrium is achieved in the interior of the target where the energy going into δ-ray production in a unit volume at x is just matched by the δ-ray energy losses in this volume. This can be explained as follows: For $x/L_\delta > 1$, the boundary is so far removed relative to the δ-ray range that this region is equivalent to an infinite medium relative to δ-ray transport. Then, as long as $\langle dT_i/dx \rangle^{(2)}$ is constant, the situation is analogous to an infinite medium containing uniform sinks and sources. Thus, the current $J_{\delta E}$ must be constant so $\nabla \cdot J_{\delta E} = 0$ for $x/L_\delta > 1$, and it follows from the continuity relation [Eq. (4.25)] that $S_{\delta E} = L_{\delta E}$ or that the energy going into δ-rays is matched by losses as stated above. Then, since $f(x;T_i)$ represents $[L_{\delta E}(x)/S_{\delta E}(x)]$, it is indeed unity under these conditions.

The assumption used in this argument that $\langle dT_i/dx \rangle^{(2)}$ is a constant is more precisely stated as, "It should not vary much over a distance equal to L_δ." Since, as discussed in Sec. 5-3.2, δ-ray ranges are generally much smaller than the ion range, this assumption is probably more accurate than might have been expected at first thought.

E-1.6 δ-Ray Backscattering Contribution

The preceding derivation of $f(x;T_i)$ neglected the possibility of a δ-ray backscattering into the region $(x < x')$. As shown in Sec. 5-7, backscattering is most important for high-Z materials, and, for such cases, it is possible to make a rough correction by replacing Eq. (E.19) with a modified form of g, namely

$$g(x;x',T_i) = \begin{cases} \dfrac{B}{(n+1)L_\delta}\left(1 - \dfrac{x - x'}{L_\delta}\right)^{-[n/(n+1)]} & [0 < (x - x') < L_\delta] \quad \text{(E.21a)} \\ G \exp\left[-\dfrac{(x' - x)}{L_B}\right] & [(x - x') < 0]. \quad \text{(E.21b)} \end{cases}$$

Here, B and G are normalization constants determined below, and the form of Eq. (E.21b) represents the solution of a diffusion-type process with a characteristic length L_B. This form is selected, somewhat arbitrarily, on the basis that backscattered δ-rays will suffer a

considerable reduction in energy due to the large angle scattering necessary to reverse directions. Thus, in contrast to the forward component, their motion should approach a diffusion-like process. (The original derivation by Sternglass[1] used this form for both forward and backward components.)

Two conditions are required to find the normalization constants: An equilibrium should still be achieved deep in the target so we require that $f(x;T_1) \to 1$ for $x/L_\delta \gtrsim 1$ as before. Also, we require that g be a continuous function of x including the point where $x = x'$ This is based on the physical argument that, even though the gradient of the energy deposition rate could change drastically at the source plane $(x = x')$, there should not be an actual discontinuity between forward and backward directions. Application of these two conditions gives

$$B = \left[1 + \frac{L_B}{(n+1)L_\delta}\right]^{-1} \tag{E.22a}$$

and

$$G = \frac{B}{(n+1)L_\delta} \tag{E.22b}$$

The remaining task is the evaluation of the diffusion length L_B for the backscattered δ-rays. For δ-rays born at x', the fraction of the energy returned to the region $(x < x')$, represented as $f(x < x'; T_1)$, can be calculated directly from g since, by definition

$$f(x < x', T_1) = \int_{-\infty}^{x} g(x;x',T_1)\, dx = L_B G. \tag{E.23}$$

However, this fraction can also be identified as the product of the number of δ-rays that are reflected and the fractional energy carried by them, which is precisely $r\bar{K}$, where r is the reflection coefficient and $\bar{K}$ is the fractional energy return defined in Sec. 5-7. Thus, $L_B G = r\bar{K}$ and the use of Eq (E.22b) for G gives

$$L_B = (n+1)L_\delta\left(\frac{r\bar{K}}{1 - r\bar{K}}\right) \tag{E.24}$$

This equation can be solved for L_B by using standard range relations to find L_δ, Fig 5.30 for r, and Eq. (5.125) or Fig. 5.32 to find $\bar{K}$. Some feeling for the magnitude of L_B can be obtained by noting that r typically ranges between 0.2 to 0.5 for materials of interest, while $\bar{K}$ is roughly 0.4 to 0.6, so the ratio L_R is

$$L_R \equiv \frac{L_B}{(n+1)L_\delta} \approx 0.1 \text{ to } 0.4. \tag{E.25}$$

In conclusion, if Eqs. (E.21a and b) are used to evaluate $f(x;T_i)$, we find

$$f(x;T_i) = \begin{cases} 1 - \left[\dfrac{(1 - x/L_\delta)^{1/(n+1)}}{1 - L_R}\right] & (x/L_\delta \leq 1) \quad \text{(E.26a)} \\ 1 & (x/L_\delta > 1) \quad \text{(E.26b)} \end{cases}$$

and this form, with $n = 1$, is used in Sec. 5-3. Based on the typical range of L_R presented in Eq. (E.25), we see that the backscattering correction is normally less than 30%, and hence it is frequently neglected, especially for low-Z materials.

E-2 A SEMIEMPIRICAL MODEL

Schultz and Pomerantz[9] have suggested that the detailed theoretical description of low-energy secondary-electron emission due to high-energy bombardment may be replaced by a simplified expression under the approximations that:

- The rate of production of secondaries is proportional to the stopping power $\langle dT_i/dx \rangle$ of the target material.
- The secondaries are characterized by a mean range in the solid.

Using these assumptions, they find that secondary-electron yield Δ can be expressed as

$$\Delta = \frac{L}{\epsilon}\left\langle \frac{dT_i}{dx} \right\rangle_{x=0} \sec\theta \tag{E.27}$$

where L is the thickness of the region in which escaping secondary electrons are produced, ϵ is the average energy required to produce one emerging secondary electron, and θ is the angle of incidence of the primary particle from the normal to the target surface.

Comparison of this result with Eq. (5.12) shows that the Schultz–Pomerantz model is in effect equivalent to Δ_0, the yield exclusive of δ-ray contributions, with

$$\frac{L}{\epsilon} = \frac{L_s P_s A_s}{2E_{se}}. \tag{E.28}$$

As seen from Table 5.1, this factor depends somewhat on the atomic number of the target through L_s; however, as suggested by Schultz and

Pomerantz, as a first approximation, $\epsilon/\rho L$ may be considered as constant for a specific class of materials (metals, insulators, etc.), independent of the bombarding particle. (Here ρ is the density of the target, thus ρL gives the escape zone thickness in g/cm^2.) This point can be tested since, if the stopping power $\langle dT_i/dx \rangle$ is known, the ratio $\epsilon/\rho L$ can be found from yield measurements. Table E.1 displays representative values reported by several investigators[9-13] for bombardment of metals by various high-energy particles. (Some additional data of this type also appear in Table 5.5.)

As seen from Table E.1, the factor $\epsilon/\rho L$ does display a rather remarkable constancy for a range of materials and primary particles. Assuming that only those secondary electrons formed within 10 to 100 Å of the surface can escape ($L \approx 10^{-7}$ cm), the characteristic value of ϵ is in the range of 10 to 100 eV.

This affords a particularly simple model for use where accuracy is not critical; otherwise the full yield expression such as that obtained in Eq. (5.11) should be used.

Table E.1—THE FACTOR $\epsilon/\rho L$ AS DETERMINED FROM YIELD DATA

	$\epsilon/\rho L$ [(keV cm^2)/mg]				
Target Material	Schultz and Pomerantz[9] (0.3 to 1.6-MeV Electrons)	Kanter[10] (1 to 10-keV Electrons)	Aarset et al.[11] (2-MeV Protons)	Anno[12] (3-MeV Alpha Particles)	Anno[13] (Fission Fragments)
C	150	210			
Al	90	100	169		
Ni	100				
Au			66	164*	
UO_2					127*

*Data corrected by a factor of 2.0 to correspond to impinging primaries rather than emerging ones, based on Eq. (5.45).

REFERENCES

1. E. J. Sternglass, "Theory of Secondary Electron Emission by High Speed Ions," *Phys. Rev., 108:* 1012 (1957).
2. S. N. Ghosh, and S. P. Khare, "Secondary Electron Emissions from Metal Surface by High-Energy Ion and Neutral Atom Bombardment," *Phys. Rev., 125:* 1254 (1962).
3. J. Millman and S. Seeley, *Electronics*, pp. 98-106, McGraw-Hill, New York, 1951.
4. C. Herring and M. H. Nicholas, "Thermionic Emission," *Rev Modern Phys., 21:* 185 (1949).
5. R. D. Evans, *The Atomic Nucleus*, pp. 574-581, McGraw-Hill, New York, 1955.
6. H. T. Sampson, *A Theoretical and Experimental Analysis of the Gamma-Electric Cell*, Ph. D. Thesis, Nucl. Eng. Program, Univ. of Illinois, 1967.

7. J. A. Sawyer and V. A. J. van Lint, "Calculation of High-Energy Secondary Electron Emission," *J. Appl. Phys., 35:* 1706 (1964).
8. J. Stevens and J. F. Artuso, "Nuclear Studies of the Compton Diode, Fiscal Year 1966," TR No. S-349-R, EG&G 1183-2110, the EG&G Co., Santa Barbara, Calif., Nov. 1966.
9. A. Schultz and M. Pomerantz, "Secondary Electron Emission Produced by Relativistic Primary Electrons," *Phys. Rev., 130:* 2135 (1963).
10. H. Kanter, "Energy Dissipation and Secondary Electron Emission in Solids," *Phys. Rev., 121:* 677 (1961).
11. B. Aarset, R. W. Cloud, and J. G. Trump, "Electron Emission from Metals Under High-Energy Hydrogen Ion Bombardment," *J. Appl. Phys., 25:* 1365 (1954).
12. J. N. Anno, "Secondary Electron Production from Alpha Particles Emerging from Gold," *J. Appl. Phys., 34:* 3495 (1963).
13. J. N. Anno, "Secondary Electron Production from Fission Fragments Emerging from Thin Layers of Uranium Dioxide," *J. Appl. Phys., 33:* 1678 (1962).

Appendix F

F-1 ADDITIONAL EQUIVALENT CIRCUIT RESULTS

F-1.1 Voltage–Load Curves

The current–voltage and current–load curves provide a general description of cell operation. However, for completeness we note that yet a third presentation can be obtained by eliminating i_L between Eqs. (6.7) and (6.8) to obtain the voltage as an explicit function of load resistance. Alternately, i_L can be eliminated between Eqs. (6.9) and (6.13). In either case, it is found that

$$\beta_0 = \frac{\gamma^2}{2}\left(1 + \frac{2}{\gamma} - \sqrt{1 + \frac{4}{\gamma}}\right) \tag{F.1}$$

where γ is defined in Eq. (6.14). A plot of β_0 as a function of the resistance ratio R_L/R_I is shown in Fig. F.1 for various values of the cell characteristic ρ_c. This plot, if used in conjunction with the current–voltage curves of Fig. 6.2, completely defines cell operation and eliminates the need for the current–load curves of Fig. 6.4. In practice,

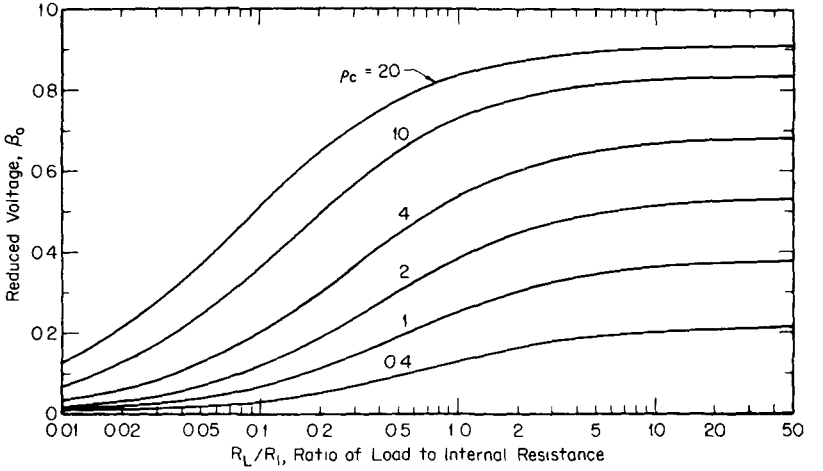

Fig. F.1—Voltage–load curves for various values of the cell characteristic. (For a planar cell with isotropic emission and zero fuel-layer thickness.)

the personal preference of the designer will probably determine which two of the three sets of performance curves will be constructed. (It must be remembered that the curves shown here are for the special case of an isotropic emitter parallel-plate cell with a zero-thickness fuel layer. They are convenient to illustrate the interrelationship of the parameters, but new curves should be constructed for each specific design under consideration.)

F-1.2 Application to Other Geometries

Some feeling for the differences between the various geometries can be gained by considering current–voltage curves. Equation (6.6) is a general relation, valid for all geometries, and, by dividing both sides of it by the short-circuit current i(0), we obtain

$$\frac{i_L}{i(0)} = \frac{i(\beta_0)/i(0)}{[1 + (R_L/R_I)]} . \tag{F.2}$$

After substitution of Eq. (6.8) for R_L and some algebra, it is found that

$$\frac{i_L}{i(0)} = \left[\frac{i(\beta_0)}{i(0)}\right] - \frac{\beta_0}{\rho_c} \tag{F.3}$$

which is a generalized form of Eq. (6.9).

The current–voltage curves illustrated in Fig. F.2 were constructed using values of $i(\beta_0)/i(0)$ taken from Chap. 2 for isotropic emission. Curves are shown for an ideal cell ($\rho_c = \infty$) and also a "typical value" of $\rho_c = 1.0$ for spherical- and parallel-plate cells as well as a plane electrode Dielectric-Volume-Emitter (DVE) Cell.

Several interesting features are observed. For spherical electrodes, the leakage currents with $\rho_c = 1.0$ cause a significant reduction in the currents at lower voltages where a constant current would occur in the ideal case of $\rho_c = \infty$.

The ideal DVE Cell is characterized by a current that goes to zero asymptotically as $\beta_0 \to \infty$. However, when $\rho_c = 1$, leakage currents in this cell force the current to zero at a finite voltage well below $\beta_0 = 1.0$.

These effects carry over to the power and efficiency curves in much the same fashion as illustrated in Chap. 6 for the parallel-plate cell.

F-1.3 Transient Analysis

Frequently, the time required to build up a certain voltage across the load is of interest. The present case differs from the "periodic

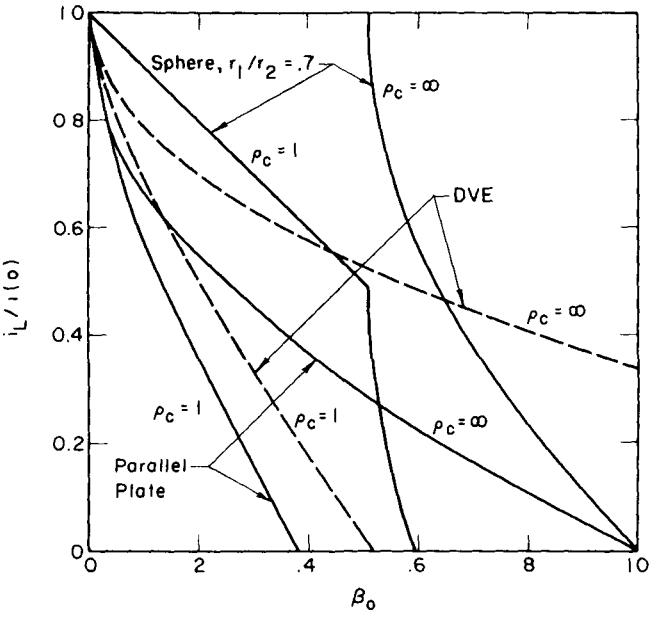

Fig. F.2—Effect of ρ_c on the current–voltage curves for several geometries. (Neglects particle energy losses in transport through fuel and/or insulator layers.)

charging" analysis presented for an ideal cell in Sec. 2-3.7 in that part of the current will now pass through R_I and R_L rather than charging the capacitance C_c.

Then, following an analysis similar to Sec. 2-3.7, we find that Eq. (2.35) is replaced by

$$\frac{t_{\beta_0}}{t_0} = \int_0^{\beta_0} \frac{d\beta_0}{i(\beta_0)/i(0) - \beta_0/\gamma} \tag{F.4}$$

where t_0 is the cell time constant R_0C_c defined in Chap. 2. If the isotropic-plate cell is again used for purposes of illustration, $i(\beta_0)/i(0)$ can be replaced by $(1 - \sqrt{\beta_0})$, and direct integration of Eq. (F.4) gives

$$\frac{t_{\beta_0}}{t_0} = \gamma \left\{ \frac{1}{\theta} \ln \left[\frac{1 + 2\sqrt{\beta_0}/\gamma(1-\theta)}{1 + 2\sqrt{\beta_0}/\gamma(1+\theta)} \right] - \ln \left[1 - \sqrt{\beta_0} - (\beta_0/\gamma) \right] \right\} \tag{F.5}$$

where

$$\theta = \sqrt{1 + \frac{4}{\gamma}}. \tag{F.6}$$

A plot of this result is shown in Fig. F.3 for various values of γ defined in Eq. (6.14b). As anticipated, as γ decreases, the time required to reach a given voltage increases. Note that the asymptotic voltage lines correspond to the β_{0M} values derived in Eq. (6.11) for steady state operation.

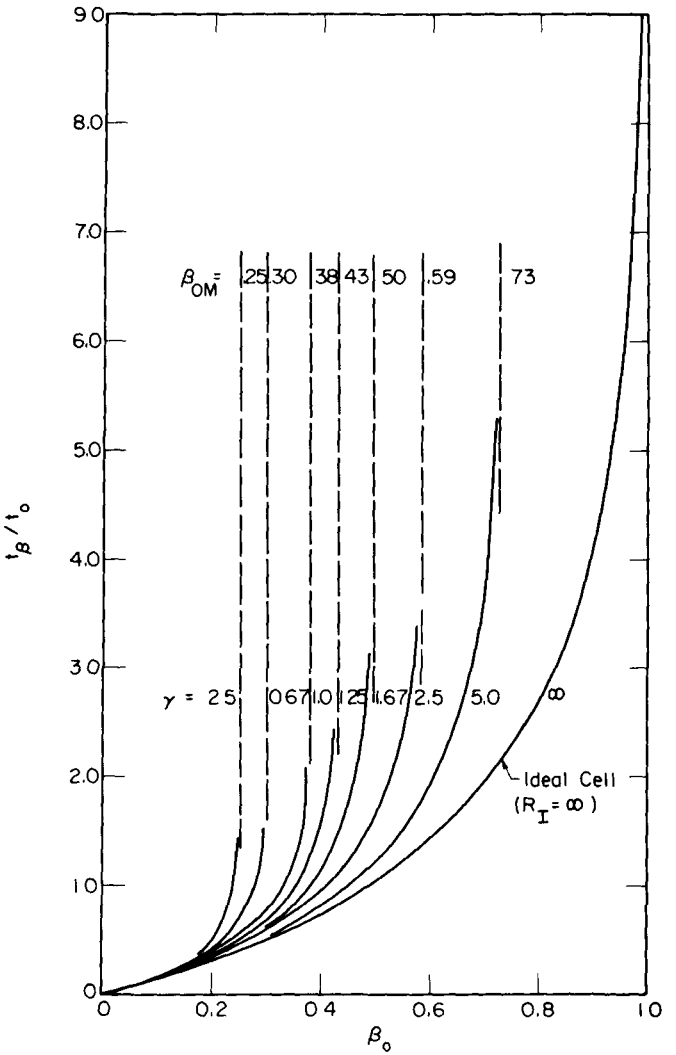

Fig. F.3—Charging time vs the resistance ratio. (For a planar cell with isotropic emission and zero fuel-layer thickness.)

Some limiting cases are of interest. First, if $R_I = R_L = \infty$, $\gamma \to \infty$ and Eq. (F.5) reduces to the idealized case considered earlier Eq. (2.39a) for a parallel-plate cell. However, the more common situation encountered is an open circuit ($R_L = \infty$) with a finite insulator resistance R_I. Then $R \to R_I$, and, since R_I is likely to be in the megohm range, the characteristic γ may be of the order of one or less. In this case, as seen from the figure, the charging time and maximum voltage will be strongly affected by γ, i.e., by the insulator resistance.

Appendix G

Although space limitations prevent an exhaustive coverage, the following problems are included for use in self study or teaching situations. Some answers are given for spot checks. The problems are arranged by chapter and not by degree of difficulty.

1.1 Based on your knowledge of radioisotopes, discuss the relative merits of an Alpha Cell vs a Beta Cell. Tables 1.1 and 1.2 may be helpful, but do not limit your remarks to the particular fuels shown there. Compare your answer to appropriate sections of Chap. 7.

1.2 Using the techniques of Appendix A, estimate the current and power density obtainable from a plate-type cell that has a ^{10}B fuel layer and is placed in a neutron flux of 10^{13} neutrons/(cm^2 sec). Assume that the alpha and lithium ranges are both roughly 5 μ in boron.

1.3 Consider a proton beam with energies uniformly distributed between 50 keV and 2 MeV. Compare the efficiency possible with an arrangement of three collectors [similar to that of Fig. 1.9(d)] to that for a single collector system. Assume all plates are held at the optimum voltage and neglect angular effects; i.e., assume all particles are directed perpendicularly to the collector plate(s). [Answer: 75 vs 50%]

1.4 It is pointed out in Sec. 1-4 that radiation induced ionization might be utilized in an electrogasdynamic generator. Suggest a possible arrangement for this, and comment on why the radiation should be viewed as a "catalyst" in this case. Using the parameters of Ref. 21, estimate the current possible with gamma radiation from a 1000-Ci ^{60}Co source.

1.5 Show that, if the Ionization-Electric Cell were not limited by Eq. (1.2), it would be possible to violate the second law of thermodynamics.

1.6 Consider a double topping scheme such as that illustrated by the use of both a radiation cell and MHD cycle in Fig. 1.8. Assume $\eta_0 = 20\%$, $\eta_{12} = 30\%$, and $\eta_{23} = 35\%$. Evaluate the increase in plant efficiency and also the reduction in heat rejection relative to the use of MHD topping alone.

2.1 Recoil protons due to a 10-MeV neutron beam striking a thin polyethylene slab are collected in a plate-type cell:

a. Show that the proton source distribution can be represented by a cosine distribution whereas the proton's initial energy varies as the cosine squared.

b. Incorporating the source angle–energy distribution, but otherwise assuming an ideal cell, find the maximum cell efficiency and the corresponding reduced voltage. [Answer: 14.7% and $\beta_0 = 4/9$ based on $V_{max} = 10$ MV]

c. Assume that the collector is composed of a material in which the proton range is $\lambda_p = 0.1T_p$ (cm), where T_p is the initial proton energy. Find a collector thickness such that one-half the protons reaching the collector pass through it during operation at the optimum voltage found above. Continue to treat the emitter under ideal-cell assumptions. [Answer: 0.31 cm]

2.2 Derive in detail the current–voltage characteristic for a cylindrical plate cell as indicated in Sec. 2-5. Verify that the maximum efficiency for isotropic emission is 19.2%.

2.3 A first-order correction for gamma attenuation across a DVE Cell can be made assuming that the gamma intensity $I_\gamma(t)$ after passing through a thickness t of the dielectric can be represented in terms of the relaxation length λ_γ as $I_\gamma(t) = I_\gamma(0) \exp(-t/\lambda_\gamma) \approx I_\gamma(0)[1 - t/\lambda_\gamma]$, where $t \ll \lambda_\gamma$. Assume that the average Compton electron range $\lambda_e \ll \lambda_\gamma$ and the cell thickness d is chosen such that $\lambda_e < d < \lambda_\gamma$. Find an expression for the current J(U) as a function of the voltage gradient U, assuming a linear potential drop and the average cosine source model.

$$\left[\text{Answer: } \frac{J(U)}{S_0 \lambda_e q} = \begin{cases} \left(1 - \dfrac{d}{\lambda_\gamma}\right)\bar{\mu} + \dfrac{\lambda_e}{\lambda_\gamma}\left(\dfrac{\bar{\mu}^2}{2}\right) + \cdots & (U < U_M) \\ \left(1 - \dfrac{d}{\lambda_\gamma}\right)\dfrac{\bar{\mu} U_M}{U} + \dfrac{\lambda_e}{\lambda_\gamma}\left(\dfrac{U_M}{U}\right)^2 \dfrac{\bar{\mu}^2}{2} + \cdots & (U > U_M) \end{cases}\right]$$

2.4 Assume that the "expected" potential diagram for a DVE Cell shown in Fig. 2.25 can be represented by two straight lines which cross at a potential minimum value of V_s (negative). This simply neglects the rounding at the minimum shown in Fig. 2.25. Treat V_s, hence d', as known; also take $d' > \lambda_e$.

a. Find an expression for the current J(U).

b. In practice ohmic-type leakage currents will occur in the dielectric due to its finite resistance and the large voltage gradients. Indicate the directions(s) of flow consistent with the preceding diagram, and discuss their effect on cell operation.

c. Given that the resistivity of the dielectric is α_0 (Ω cm), estimate the size of V_s. To do this, assume that the emitter electrode is so thin that gamma interactions in it can be neglected; i.e., no Compton electrons cross the emitter–dielectric interface. (The circuit is completed by an ohmic current at this interface.)

3.1 Consider protons slowing in aluminum.

a. Compare the range for a 1-MeV proton in aluminum found from Fig. 3.6 with that predicted by the theory of Sec. 3-3.1. Comment about possible causes for any differences. Which answer would you expect to be most accurate? [Answer, first part: 11 μ vs 17.6 μ, respectively]

b. Using proton range values from Fig. 3.6 for 1 to 10 MeV in aluminum, find an appropriate value of the slowing parameter n for protons and compare it with Table 3.4. Again using Fig. 3.6, comment on the dependence of n on the target material.

3.2 Estimate the percentage of its total track length that a 5-MeV proton slowing in O_2 spends in energy region I. Take an approximate breakpoint energy from Fig. 3.2a. [Answer: 99.8%] Repeat for slowing in gold. Can you draw any general conclusions about the variation of the percentage with initial energy? With density and/or atomic number of the target?

3.3 It is generally assumed that the range distribution $P(\lambda, T_0)$ for ions is a Gaussian; cf. Eq. (3.63).

a. Find an expression for the corresponding transmission function $T(r, T_0)$. [Answer: See Eq. (4.49)].

b. Make a rough sketch of $T(r, T_0)$ vs r which illustrates the difference between this result and the Mar transmission function.

c. Comment on the relation between the average and most probable energies for both functions.

d. Set up an expression for the straggling parameter S corresponding to the Mar transmission function. Comment on how this result compares with Eq. (3.64). [Answer: Use Eq. (3.64) with $\overline{\lambda} = (T_0^c/D)^{1/b}$ $(1/b)\ \Gamma\ (1/b)$]

3.4 Consider a parallel beam of electrons of energy T_0 bombarding a thin target of thickness τ. Find the average energy of the transmitted beam using the Mar transmission function. [Hint: One method is to use the definition $\langle T \rangle = \int_0^{T_0} T\ P(T, T_0)\ dT$]

4.1 Given the range of an 80-MeV fission fragment in uranium metal as 21 mg/cm^2, find the particle and energy currents at the surface of a 10.5-μ-thick ^{235}U foil placed in a thermal neutron flux of 10^{12} neutrons/(cm^2 sec). For simplicity, assume that the fragment energy spectrum is approximately given by

$$S(T_0) \approx 0.42\ \delta(T_0 - 67) + 0.58\ \delta(T_0 - 98)$$

where T_0 is in million electron volts. The density of ^{235}U is 18.1 g/cm^3.

4.2 Various approaches are possible in current calculations.

a. Derive Eq. (4.8) by integration in reverse order; i.e., integrate over μ first.

b. Starting with the plane kernel of Eq. (D.4), Appendix D, derive Eq. (4.12).

c. Verify the results indicated in Table D.1 for $\phi^*(\tau;z',T_0)$ and $\phi^*(\tau;T_0)$.

d. Using the chord-length distribution for a sphere from Table D.2, verify the escape probability $E(T_0)$ and the energy spectrum $H(T,T_0)$ given in Tables D.2 and D.3, respectively.

4.3 Consider a parallel-plate cell fueled with a thick layer of a beta-emitting radioisotope. The *initial* energy spectrum of the betas can be represented by Fermi's distribution (p. 548, Ref. 2, Chap. 3)

$$n(\epsilon) \approx \epsilon\sqrt{\epsilon^2 - 1}\ (\epsilon_0 - \epsilon)^2$$

where ϵ depends on the initial beta energy T_0 through

$$\epsilon \approx \frac{T_0}{m_0c^2} + 1$$

and ϵ_0 represents the maximum or end-point energy. Find an appropriate current–voltage relation for this cell. [Hint: Eq. (4.82) can be used as a kernel.]

4.4 Recoil protons are obtained by 10-MeV neutron bombardment of a polyethylene sheet. Then, as in Problem 2.1, the initial angular and energy distribution of the protons can be represented as

$$P(\mu_0) = \begin{cases} 2\mu_0 & (0 < \mu_0 < 1) \\ 0 & (-1 < \mu_0 < 0) \end{cases}$$

and

$$T_p = T_n\ \mu_0^2$$

where T_p and T_n are the initial proton and neutron energies, respectively. The range for 10-MeV protons in polyethylene is defined as λ_0 (but remember that λ depends on T_p).

For convenience in calculations, use $n = \frac{1}{2}$ and $m = 0$ to approximate the values of Table 3.4.

a. Consider a parallel-plate cell with a polyethylene thickness τ such that $\tau > \lambda_0$ but still thin enough so that neutron attenuation is negligible. Assuming that the polyethylene has been treated so that it is, in effect, a good electrical conductor, calculate the current–voltage characteristic; cf. Sec. 4-3.

[Answer: $$J_q(\beta_n) = \frac{q_0 S_0 \lambda(T_n)}{3}\left[1 - \beta_n^{3/2}\left(1 - \frac{3}{2}\ln \beta_n\right)\right]$$

where β_n has been normalized by T_n, i.e., the maximum proton energy]

b. Assume that a DVE-Cell configuration is used with an untreated polyethylene so that a high resistivity is maintained in the dielectric volume. Following Sec. 4-5, set up an equation that describes the cell current–voltage characteristic.

4.5 Verify that the particle current $J_{II}(z)$ in the source-free region of a "two-region" problem is of the following form if $n_I = n_{II} = n$:

$$\frac{J_{II}(z)}{\tau S(T_0)} = \begin{cases} \dfrac{1}{4\tau/\lambda_I}(1-z)^2 & \left[z > \left(1 - \dfrac{\tau}{\lambda_I}\right)\right] \\ \dfrac{1}{4}\left(2 - \dfrac{\tau}{\lambda_I} - 2z\right) & \left[z < \left(1 - \dfrac{\tau}{\lambda_I}\right)\right]. \end{cases}$$

5.1 Compare the low-energy secondary yield predicted by Eq. (5.19) with that from the thermionic model [i.e., Eq. (5.1)] for 1-MeV protons incident on gold. For simplicity, use $n = 1.0$. [Answer: 0.11 vs 0.04 for the thermionic model]

5.2 Estimate the low-energy secondary yield for 1-MeV gamma radiation incident on aluminum. [Answer: $\Delta(h\nu_0) = 7.7 \times 10^{-10}$] Using Fig. 5.22, comment on the ratio of the low-to-high-energy component for gamma radiation. Would ion bombardment result in a similar ratio? Explain.

5.3 Based on Eq. (5.70), compare the energy leading to a maximum yield for protons as opposed to electrons bombarding an aluminum target. For simplicity, take $n = 1$ for both particles. [Answer: 7.2 vs 0.5 keV, respectively]

5.4 Consider secondary emission at a fuel-layer surface.

a. Sketch approximate yield curves for fission fragments equivalent to Figs. 5.6 and 5.18. Be sure to indicate your reasoning.

b. Verify that the charge ratio vs thickness plot of Fig. 5.8 should be approximately constant with a value equal to $44(T_0)^{1/2}/q_0$, where T_0

and q_0 are the average initial energy and charge of the fragment, respectively.

c. Make a rough sketch of a plot similar to Fig. 5.8 for alpha particles born in a ^{10}B coating.

5.5 Calculate the high-energy secondary yield for ions bombarding a foil assuming that:

- Rutherford scattering produces the δ-rays (Table 5.6).
- The foil thickness τ is such that ion attenuation can be neglected but is large relative to the electron range.
- The Mar transmission factor describes δ-ray transport.

[Hint: Recall the definition of the average range in terms of the transmission function.]

$$\left[\text{Answer:} \quad \Delta = \Sigma_0 \Gamma\left(\frac{1}{b}\right) \frac{T_{iM}^{c/b}}{D^{1/b}(2c - b)}\right.$$

$$\left.\text{where} \quad \Sigma_0 = N_e \left(\frac{M}{m_e}\right)^2 \frac{\pi e^4 Z^2}{2T_i^2} \quad \text{and} \quad T_{iM} = \frac{4m_e}{M} T_i\right]$$

5.6 Consider an isotropic, monoenergetic flux of low-energy ions incident on one face of a foil of thickness τ. Derive an expression for and sketch the yield on the opposite (exit) face of the foil as a function of τ.

5.7 As a first approximation, assume that the angular distribution for Compton electrons produced by high-energy photons can be represented as a cosine distribution. Using this, the energy–angle relation of Table 5.6, and the technique of Secs. 5-6.1 and 5-6.2, find an expression for the yield assuming a "thick" target. Take n = 0 for the electrons.

$$\left[\text{Answer:} \quad \Delta = \frac{\mu_a}{\bar{T}_{\delta 0}} \frac{4m_0c^2}{C} \left\{\frac{A^{3/2}}{2}\left[\ln\left|\frac{\sqrt{A}+1}{\sqrt{A}-1}\right|\right] - A - \frac{1}{3}\right\}\right.$$

$$\left.\text{where } \bar{T}_{\delta 0} = 2m_0c^2\left[A \ln\left(\frac{A}{A-1}\right) - 1\right]\right.$$

with μ_a defined by Eq. (5.26) and C by Eq. (3.24)]

Evaluate this result for 1-MeV photons incident on aluminum, and compare it with Figs. 5.22 and 5.25. Discuss any differences. Is the present result consistent with that for problem 5.2?

6.1 It is proposed that a more realistic equivalent circuit would include another internal resistance, R_I', in the line between C_c and R_I in Fig. 6.1.

a. Based on this circuit, obtain an expression for the current i_L vs the reduced voltage β_0. Derive an explicit result for an ideal parallel-plate cell with isotopic emission and show that it is consistent with Eq. (6.9).

[Answer, for parallel-plate cell:

$$\frac{i_L}{i(0)} = 1 + \frac{1}{2}\frac{R_I'}{R_0} - \frac{1}{2}\sqrt{\left(\frac{R_I'}{R_0}\right)^2 + 4\left(\beta_0 + \frac{R_I'}{R_0}\right)} - \frac{\beta_0}{\rho_c}$$

where $R_0 = V_0/i(0)$, $\rho_c = R_I/R_0$, and $\beta_0 = V_L/V_0$.]

b. Derive an expression for η_c/η_c^*.

c. What physical processes might be accounted for by R_I'? [Hint: Remember that i^2R_I' represents an internal energy loss.]

6.2 A grid significantly influences cell operation.

a. Using Fig. 6.13, obtain an expression for the grid current. Show that the grid and anode currents add to give the cathode current.

b. Find an expression for the maximum (open-circuit) voltage, β_{0M}, which allows for both grid and leakage currents. Check your result against curve 9 in Fig. 6.14 and also show that it is consistent with Eq. (6.11).

[Answer:

$$\beta_{0M} = \frac{\rho_c^2}{2}\left[\frac{2k_1}{\rho_c} + (k_1k_2)^2\right] - \frac{\rho_c}{2}\sqrt{\rho_c^2\left[\frac{2k_1}{\rho_c} + (k_1k_2)^2\right]^2 - 4k_1^2}$$

where k_1 and k_2 are given in Eqs. (6.37b and c), respectively.]

c. Using Fig. 6.15(b), estimate the amplification or μ-factor for Cell No. 1 of Fig. 7.17. Does this check with the value of 41 quoted in Sec. 6-2.3? [It may be necessary to extrapolate Fig. 6.15(b) or, alternately, to assume an equivalent plate model with Fig. 6.15(a).]

6.3 Derive Eq. (6.44) for the magnetic cutoff. Show how to include initial electron energies.

6.4 Voltage breakdown limits are important in various ways.

a. Using Cranberg's breakdown criteria and $\mu = 41$, predict whether voltage breakdown will first occur between the anode–grid, the anode–cathode, or the grid–cathode for Cell No. 1 in Fig. 7.17.

b. Does the onset of microdischarging shown in Figs 7 14 and 7.15 occur at the breakdown-voltage point? Discuss your answer

c. Compare the separation distance required to maintain 1 MV on two parallel plates separated by vacuum as opposed to using PMMA (polymethylmethacrylate, commonly called Lucite) for insulation

6 5 Consider radiation-induced conductivity

a. Using data from Table 6.4 and the corresponding text, estimate the value of σ_0 for polyethylene and compare it with that given in Table 6.3. [Answer Estimated value is 2.6×10^{-16} $(\Omega\ \text{cm})^{-1}$]

b. Obtain a modified form of Eq. (6 57) assuming an exponential trap distribution, i.e., replace Eq. (6.55) by

$$M(T) \propto \exp \frac{T - T_0}{kT}$$

where T_0 is a reference energy corresponding to the bottom of the conduction band. [Hint Treat Eq (6 57) as a kernel and integrate over the modified distribution.]

6 6 Consider radiation-induced space-charge effects.

a. The theory leading to Eq. (6.67) does not mention soft electrons produced by the photon and by the Compton electrons as they slow. Discuss the validity of neglecting them.

b. Obtain an equation equivalent to Eq (6 67) for the space charge due to low-q ion bombardment. Assume *both* the ion and δ-rays produced by it are trapped at the end of their track.

c. Equation (6.67) is derived assuming that the motion of the Compton electrons is not affected by space-charge effects. However, the space charge might build up under continued irradiation to a size at which it can alter the Compton trajectories. Using as simple a model as possible, modify the theory to include this. Find an expression for the movement of the point of maximum negative charge (L_δ in Fig. 6.25) with time during irradiation. [For further discussion of this point, see E. Kennedy, "Computation of Electron Transport in Dielectrics," *Trans. Am. Nucl. Soc., 11(1)* 407 (June 1968)] Does your theory show that, as indicated in the text, potentials larger than the electron equivalent can be generated?

7 1 The FEC is a key, but complicated, concept

a. Discuss the point made in Sec. 7-2 that the increase in FEC efficiency in going to cylindrical or spherical electrodes is offset by an increased fuel thickness assuming that the fuel volume is held constant.

b. Verify the shape of the magnetron curves shown in Fig. 7.11. Do you agree that higher voltages could be achieved with larger fields?

Discuss in more detail the argument that sweep rings might not be required at higher voltages.

7.2 Several alpha and beta cells were discussed.

a. Verify Miller's estimates for the ^{210}Po cell discussed in Sec. 7-3.

b. It is noted in Sec. 7-3 that the initial BMI Alpha Cell short-circuit current was about 10^{-8} A. Is this consistent with the frequency and size of the microdischarges that limited voltage buildup?

c. Assuming 700-kV operation, what fraction of the beta current would pass through the 5 mg/cm^2 collector described in Sec. 7-4.1 for the high-powered BEC?

d. Under what conditions would you select spherical Cell A of Table 7.1 instead of Cell D?

7.3 Recalculate the current–voltage curve and maximum voltage of Fig. 7.27 using the techniques developed in earlier chapters.

7.4 A variety of neutron detectors is conceivable.

a. Which of the detectors listed in Table 7.2 would offer the fastest time response? Why?

b. Using order of magnitude estimates, verify the sensitivity listed for the cadmium emitter detector.

7.5 Consider the solid-dielectric type GEC.

a. It is noted in connection with the GEC of Fig. 7.36 that a similar design with a 2.5-cm-thick plexiglass insulator produced 8.8×10^{-11} A for an incident energy flux from ^{60}Co of 1.7×10^5 ergs/sec over a 64 cm^2 area. Confirm the corresponding calculated value of 7.65×10^{-11} A using Eq. (7.1). Would substitution of a polyethylene insulator increase or decrease the current?

b. Discuss the relative merits of polyethylene, silicone, teflon, Lucite, epoxy, glass, and polybutene oil for the insulator in the GEC.

c. Compare the methods for reducing the energy dependence of solid-dielectric GEC's to those in the vacuum-type GEC.

d. Discuss the contribution of electrons due to the photoelectric effect and pair production in the GEC. If possible, derive the governing equations for these currents.

7.6 Consider the Thermonuclear-Electric Cell.

a. Verify that the efficiency of the multiple collector design for the mirror reactor of Fig. 7.63 is approximately equal to $(1 - 1/N)$, where N is the number of collectors. [Hint: Review your solution to Problem 1.3.]

b. Discuss the relative merits of the metal-vapor–charge-exchange collector suggested in Sec. 7-7 as opposed to the magnetic analyzer of Fig. 1.9(d).

c. Estimate and compare space-charge fields encountered in a typical Thermonuclear-Electric Cell and a Fission-Electric Cell.

Index